

Geological disasters and its prevention in deep mining

Edited by

Shuren Wang, Hongyuan Liu, Lianchong Li and
Chengguo Zhang

Published in

Frontiers in Earth Science



FRONTIERS EBOOK COPYRIGHT STATEMENT

The copyright in the text of individual articles in this ebook is the property of their respective authors or their respective institutions or funders. The copyright in graphics and images within each article may be subject to copyright of other parties. In both cases this is subject to a license granted to Frontiers.

The compilation of articles constituting this ebook is the property of Frontiers.

Each article within this ebook, and the ebook itself, are published under the most recent version of the Creative Commons CC-BY licence. The version current at the date of publication of this ebook is CC-BY 4.0. If the CC-BY licence is updated, the licence granted by Frontiers is automatically updated to the new version.

When exercising any right under the CC-BY licence, Frontiers must be attributed as the original publisher of the article or ebook, as applicable.

Authors have the responsibility of ensuring that any graphics or other materials which are the property of others may be included in the CC-BY licence, but this should be checked before relying on the CC-BY licence to reproduce those materials. Any copyright notices relating to those materials must be complied with.

Copyright and source acknowledgement notices may not be removed and must be displayed in any copy, derivative work or partial copy which includes the elements in question.

All copyright, and all rights therein, are protected by national and international copyright laws. The above represents a summary only. For further information please read Frontiers' Conditions for Website Use and Copyright Statement, and the applicable CC-BY licence.

ISSN 1664-8714
ISBN 978-2-83251-311-8
DOI 10.3389/978-2-83251-311-8

About Frontiers

Frontiers is more than just an open access publisher of scholarly articles: it is a pioneering approach to the world of academia, radically improving the way scholarly research is managed. The grand vision of Frontiers is a world where all people have an equal opportunity to seek, share and generate knowledge. Frontiers provides immediate and permanent online open access to all its publications, but this alone is not enough to realize our grand goals.

Frontiers journal series

The Frontiers journal series is a multi-tier and interdisciplinary set of open-access, online journals, promising a paradigm shift from the current review, selection and dissemination processes in academic publishing. All Frontiers journals are driven by researchers for researchers; therefore, they constitute a service to the scholarly community. At the same time, the *Frontiers journal series* operates on a revolutionary invention, the tiered publishing system, initially addressing specific communities of scholars, and gradually climbing up to broader public understanding, thus serving the interests of the lay society, too.

Dedication to quality

Each Frontiers article is a landmark of the highest quality, thanks to genuinely collaborative interactions between authors and review editors, who include some of the world's best academicians. Research must be certified by peers before entering a stream of knowledge that may eventually reach the public - and shape society; therefore, Frontiers only applies the most rigorous and unbiased reviews. Frontiers revolutionizes research publishing by freely delivering the most outstanding research, evaluated with no bias from both the academic and social point of view. By applying the most advanced information technologies, Frontiers is catapulting scholarly publishing into a new generation.

What are Frontiers Research Topics?

Frontiers Research Topics are very popular trademarks of the *Frontiers journals series*: they are collections of at least ten articles, all centered on a particular subject. With their unique mix of varied contributions from Original Research to Review Articles, Frontiers Research Topics unify the most influential researchers, the latest key findings and historical advances in a hot research area.

Find out more on how to host your own Frontiers Research Topic or contribute to one as an author by contacting the Frontiers editorial office: frontiersin.org/about/contact

Geological disasters and its prevention in deep mining

Topic editors

Shuren Wang — Henan Polytechnic University, China

Hongyuan Liu — University of Tasmania, Australia

Lianchong Li — Northeastern University, China

Chengguo Zhang — University of New South Wales, Australia

Citation

Wang, S., Liu, H., Li, L., Zhang, C., eds. (2023). *Geological disasters and its prevention in deep mining*. Lausanne: Frontiers Media SA.

doi: 10.3389/978-2-83251-311-8

Table of contents

05	Editorial: Geological disasters and its prevention in deep mining Shuren Wang, Hongyuan Liu, Lianchong Li and Chengguo Zhang
08	Study on Surrounding Rock Deformation Laws of an Argillaceous Soft Rock Roadway Based on the Creep Damage Model Fengbin Chen, Rui Su, Liuhua Yang, Xiaolin Yang, Huazhe Jiao and Changxing Zhu
19	Analysis on the Shear Stress Propagation Mechanism in the Rock Reinforcement System Jianhang Chen, Hui Li, Shankun Zhao, Hongbao Zhao, Cun Zhang, Junwen Zhang and Danqi Li
26	Behavior of large shaft sinking headframe subjected to uneven foundation settlement Bo Wang, Zhiqiang Liu and Shuai Yuan
37	A New Blasting Permeability Enhancement Scheme For Deep-Buried Soft Coal Mining Face Based on Borehole Deformation Characteristics Dequan Xuan, Jianhua Zhang, Gang Huang, Peng Li and Zhifeng Zhang
46	A novel evaluation method of mining goaf ground activation under high-speed railway load Lian-Wei Ren, Peng-Fei He, You-Feng Zou, Chao Yang, Zhi-Lin Dun, Zheng-Sheng Zou and Chunyu Shi
61	Morphological characteristics and permeability evolution of deep mine gas drainage boreholes Xiao Liu, Tianxiang Jing, Haixiao Lin, Dequan Xuan, Yong Li and Sen Xu
76	Model test study on the rock mass deformation law of a soft rock tunnel under different ground stresses Zhengguo Zhu, Zhichun Fang, Fei Xu, Zhiming Han, Xiaolong Guo and Chaoyi Ma
92	Study on Stability Control of Gob-Side Entry Retaining Structure Without Filling Wall in Hard Roof Long Jing-kui, Qi Chao-xin, Cao Zuo-yong, Lan Hong and Yu Wen-kai
104	Experimental and numerical investigation on compressive strength and crack behavior of rock-like specimens with open flaws under confining loads Shaorui Sun, Jin Wang, Huilin Le, Haotian Fan and Wuchao Wang

- 118 **Theoretical analysis of the reasonable support capacity based on voussoir beam structure for a given load of the loose body under an extremely close goaf**
Yuqi Ren, Yang Li, Xinghai Lei, Xiangji Ou, Nan Wang, Guoshuai Li and Kunpeng Yang
- 131 **Assembled design and compressive performance simulation of mine waterproof wall based on concrete 3D printing**
Chuangnan Ren, Baobin Gao, Chenhui Geng and Wenjie Zhu
- 140 **Experimental study on rockburst fragment characteristic of granite under different loading rates in true triaxial condition**
Feiyue Sun, Jiaqi Guo, Junqi Fan and Xiliang Liu
- 155 **Research on the gas migration trend and mechanism of the transition flow regime in coal based on MRT-LBM simulation**
Yanwei Liu, Haojie Jia, Hongkai Han, Weiqin Zuo, Jin Shi, Ping Chang, Jian Miao, Yanyan He and Jie Peng
- 168 **Regional prediction and prevention analysis of rockburst hazard based on the Gaussian process for binary classification**
Tianwei Lan, Zhijia Zhang, Jiawei Sun, Wenqi Zhao, Mancang Zhang, Weidong Jia, Mingwei Liu and Xutao Guo
- 177 **Study on the evolution and prediction of fracture depth of surrounding rock in deep mining roadway based on numerical analysis and borehole detection**
Huaibin Li, Xingdong Zhao, Bibo Dai, Zujun Huang and Qiankun Zhu



OPEN ACCESS

EDITED AND REVIEWED BY

Yanlin Zhao,
Hunan University of Science and
Technology, China

*CORRESPONDENCE

Shuren Wang,
w_sr88@163.com

SPECIALTY SECTION

This article was submitted to
Geohazards and Georisks,
a section of the journal
Frontiers in Earth Science

RECEIVED 17 October 2022

ACCEPTED 04 November 2022

PUBLISHED 28 December 2022

CITATION

Wang S, Liu H, Li L and Zhang C (2022),
Editorial: Geological disasters and its
prevention in deep mining.
Front. Earth Sci. 10:1071841.
doi: 10.3389/feart.2022.1071841

COPYRIGHT

© 2022 Wang, Liu, Li and Zhang. This is
an open-access article distributed
under the terms of the [Creative
Commons Attribution License \(CC BY\)](#).
The use, distribution or reproduction in
other forums is permitted, provided the
original author(s) and the copyright
owner(s) are credited and that the
original publication in this journal is
cited, in accordance with accepted
academic practice. No use, distribution
or reproduction is permitted which does
not comply with these terms.

Editorial: Geological disasters and its prevention in deep mining

Shuren Wang^{1*}, Hongyuan Liu², Lianchong Li³ and
Chengguo Zhang⁴

¹School of Civil Engineering, Henan Polytechnic University, Jiaozuo, China, ²School of Engineering, University of Tasmania, Hobart, TAS, Australia, ³School of Resources and Civil Engineering, Northeastern University, Shenyang, China, ⁴School of Minerals and Energy Resources Engineering, University of New South Wales, Sydney, NSW, Australia

KEYWORDS

deep mining, disaster mechanism, soft rock, large deformation, rockburst

Editorial on the Research Topic

[Geological disasters and its prevention in deep mining](#)

Introduction

With the gradual depletion of shallow mineral resources, the mining of deep mineral resources has become inevitable. The geological disasters such as large deformations of soft rocks, rock bursts, and gas outbursts induced by the deep mining have brought great challenges and seriously threatened the safety of mine productions. Under the conditions of high ground stresses, high water pressures and strong engineering disturbances, the nonlinear behavior of deep coals and rocks is more prevalent in deep mining, which may further complicate the forming mechanisms, patterns and dynamics of the geological disasters. Thus, deep mining-induced disasters have the characteristics of sudden, complexity and nonlinearity, and are more difficult to effectively forecast and control. Since the traditional mining theory lags behind the mining engineering practice, it is urgent to develop new theories and methods to solve the theoretical and technical challenges of deep mining.

We then provide a forum for professionals and academics to communicate their impactful research on Geological Disaster and Its Prevention in Deep Mining, which results in the 15 papers being published in this Research Topic that might be of your interest. These papers mainly cover the following six aspects, such as experiment on mechanical characteristics of rock samples, rockburst prediction and mine waterproofing, surface deformation and foundation subsidence, gas migration and its enhancement drainage, deformation characteristics of surrounding rock in roadway, and stability and support of mining field. Please visit the following website for more information: <https://www.frontiersin.org/research-topics/34613/geological-disasters-and-its-prevention-in-deep-mining#overview>.

Experiment on mechanical characteristics of rock samples

Rock reinforcement plays a significant role in maintaining the stability of excavated structures, such as tunnels and underground roadways. However, shear failure in the rock reinforcement system, especially the shear failure at the rock reinforcement bolt surface, induces a threat to the rock reinforcement system. To reveal the shear stress (SS) propagation mechanism, [Chen et al.](#) presented the SS propagation process in the rock reinforcement system. They stated that the numerical simulation was a better choice when studying the SS propagation mechanism of rock reinforcement bolts, combining experimental tests and analytical simulation. Engineering problems are related to the failure of geological materials, especially that of jointed rock masses. To investigate the influence of confining stress and inclination angle on cracking behavior and failure mechanism, [Sun et al.](#) conducted triaxial compression tests on rock-like samples containing parallel opening flaws. They investigated the influence of the width-to-length ratio of opening flaws on compressive strength to verify the improved theory reliability. Comparing their numerical results with the two kinds of theoretical results, they concluded that the width-to-length ratio had an obvious impact on compressive strength and the opening fracture intensity factor.

Rockburst prediction and mine waterproofing

After the identification of the intrinsic relationship between multiple factors of coal mines and rockbursts, [Lan et al.](#) established a prediction model based on the Gaussian process for binary classification. They proposed the prediction criteria of the rockburst hazard probability, determined the hazard probability value of the prediction area by applying neural network and fuzzy inference methods, and put forward the prevention technical scheme for the rockburst hazard. To study the effect of loading rate on rockbursts, [Sun et al.](#) conducted the indoor test of single-face fast unloading-three directions and five-face stress-vertical continuous loading under different loading rates using a new true-triaxial rockburst test system. They found that the fragmentation degree of rockburst fragments increased with the loading increasing. The loading rate has a significant effect on the energy consumption of rockburst fragments. It is necessary to introduce concrete 3D printing technology for the construction of coal mine waterproof walls to adapt to more complex construction environment. [Ren et al.](#) tested the compressive properties of 3D printed concrete under different printing methods and force directions. They found that 3D printing mine waterproof walls can meet the engineering requirements.

Surface deformation and foundation subsidence

To make a reasonable safety evaluation of the high-speed railway construction in the mined-out areas, [Ren et al.](#) analyzed the safety depth of the mined-out areas under the impact of high-speed railway loading. They found that the depth of train load disturbance was linearly related to the train axle weight and roadbed height but it was a sinusoidal function of the train speed. They proposed a formula for calculating the depth of train load disturbance, which provided a certain reference for the construction of high-speed railways in the mined-out areas. Deep mining is an inevitable trend in the world, for which the construction of deep and large vertical shafts is the primary task. The design of the shaft sinking headframe is challenging due to the significant differences in the geometry and working load compared to conventional steel structures. [Wang et al.](#) investigated the mechanical behavior of the SA-3 shaft sinking headframe under uneven foundation settlement and normal working-load conditions. They found that the most unfavorable condition for the stress of members was the diagonal double foundation settlement, and the most unfavorable condition was the same-side double foundation settlement.

Gas migration and its enhancement drainage

Hydraulic flushing is the main means of gas extraction. [Liu et al.](#) studied the pore morphology and permeability evolution of the hydraulic flushing hole. They found that the shape of the hydraulic punch hole was ellipsoid with three different axes, and its horizontal section was approximately an ellipse. The permeability of the coal increases with the extension of extraction time, while the permeability of the equivalent ellipsoid pore decreases with the increase in coal water content. To enhance permeability by blasting in deep coal mining with a hard roof whose gas drainage requirement is higher, the charging and control holes are easy to be deformed and damaged, seriously affecting the blasting implementation and effect. [Xuan et al.](#) proposed a new blasting permeability enhancement scheme for the deep-buried soft coal mining face with a hard roof. To reveal the mechanism of gas flow in a low-permeability coal seam, [Liu et al.](#) established a new multiple-relaxation-time lattice Boltzmann method model of gas migration and simulated the gas flow in coal pores with different micro/nanopore sizes. They found that the dimensionless permeability coefficient increased with decreasing pore size under the same pressure.

Deformation characteristics of surrounding rock in roadway

Argillaceous soft rocks are susceptible to a more serious creep phenomenon if encountering water. [Chen et al.](#) established a creep constitutive model and analyzed the creep range and cross-sectional deformation of argillaceous surrounding rocks of a roadway under dry and damp states. They found that the argillaceous surrounding rocks were prone to viscoelastic deformation during the creep process. The damp state has an obvious time effect on the damage of surrounding rocks. Since it was difficult to monitor the deformation of a rockmass in front of a tunnel, [Zhu et al.](#) conducted the model test and concluded that it was necessary to pre-reinforce the core rockmass in front of the tunnel to control the advanced deformation of the tunnel. The longitudinal load-bearing arch in front of the tunnel face can effectively control the extrusion deformation of the core rockmass to expand forward. The failure of surrounding rock in deep hard rock roadway is closely related to mining disturbance. [Li et al.](#) proposed a comprehensive method of numerical analysis and borehole detection, and they revealed the evolution law of fracture depth of the surrounding rock under the mining influence.

Stability analysis and control of mining field

Given the growing popularity of fully mechanized longwall mining, hydraulic shields have emerged as the most crucial pieces of equipment whose rated support capacities are a significant assurance for safe extraction of coal seams. [Ren et al.](#) studied the reasonable shield support capacity under an extremely close goaf. They found that the thickness of the main roof had the greatest influence on the shield support capacity. Presplitting the main roof is proposed as an effective method for controlling the breaking length and reducing the shield support capacity based on existing research. In view of the deformation and

instability law of hard roof without side filling retaining roadway and based on the systematic construction and analysis of the force and bearing model of roadway retaining structure, [Long et al.](#) proposed the control mechanical model and calculation method of roadway retaining, which took the anchor roof beam and the key block above to form the cantilever beam together, with the anchor solid coal side as the foundation support. This method can better improve the structure for stability, adaptability and engineering applicability, which is successfully applied in engineering practice.

We hope that these articles provide readers with valuable information on recent developments in science, technology, and related researches for achieving the goals of geological disaster prediction and prevention in deep mining.

Author contributions

All authors listed have made a substantial, direct, and intellectual contribution to the work and approved it for publication.

Conflict of interest

The authors declare that the research was conducted in the absence of any commercial or financial relationships that could be construed as a potential conflict of interest.

Publisher's note

All claims expressed in this article are solely those of the authors and do not necessarily represent those of their affiliated organizations, or those of the publisher, the editors and the reviewers. Any product that may be evaluated in this article, or claim that may be made by its manufacturer, is not guaranteed or endorsed by the publisher.



Study on Surrounding Rock Deformation Laws of an Argillaceous Soft Rock Roadway Based on the Creep Damage Model

Fengbin Chen, Rui Su, Liuhua Yang*, Xiaolin Yang, Huazhe Jiao and Changxing Zhu

School of Civil Engineering, Henan Polytechnic University, Jiaozuo, China

OPEN ACCESS

Edited by:

Hongyuan Liu,
University of Tasmania, Australia

Reviewed by:

Lei Fan,
Hunan University of Science and
Technology, China
Chao Yuan,
Hunan University of Science and
Technology, China

*Correspondence:

Liuhua Yang
yanglh2005@163.com

Specialty section:

This article was submitted to
Geohazards and Georisks,
a section of the journal
Frontiers in Earth Science

Received: 06 April 2022

Accepted: 31 May 2022

Published: 23 June 2022

Citation:

Chen F, Su R, Yang L, Yang X, Jiao H
and Zhu C (2022) Study on
Surrounding Rock Deformation Laws
of an Argillaceous Soft Rock Roadway
Based on the Creep Damage Model.
Front. Earth Sci. 10:914170.
doi: 10.3389/feart.2022.914170

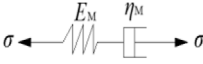
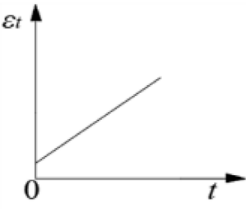
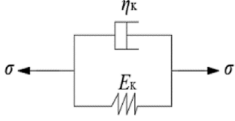
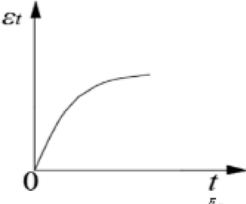
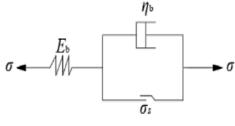
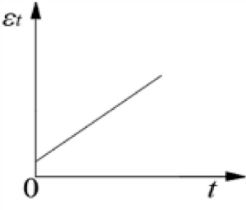
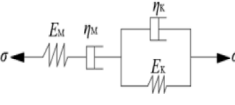
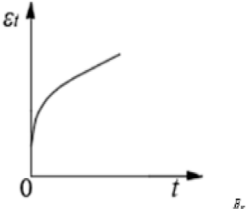
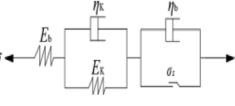
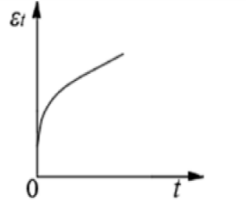
The indexes of argillaceous soft rocks in Western China, such as rock strength and softening coefficient, are much smaller than those of soft rocks commonly seen in other areas. Such argillaceous soft rocks are susceptible to a more serious creep phenomenon if encountering water. Accordingly, the study theoretically constructed a constitutive creep model considering the weakening coefficient and damage of surrounding rocks. Next, the viability of this model was verified by combining numerical simulation and field monitoring. Accordingly, this study conducted a comparative analysis on the creep range and cross-sectional deformation of argillaceous surrounding rocks of a roadway in a titled stratum under dry and damp states. Results showed that the Cvisc model considering the weakening coefficient of surrounding rocks was applicable to the decay creep and uniform creep stage, and that considering the damage of surrounding rocks was applicable to the accelerated creep stage. During the creep process, the argillaceous surrounding rocks were prone to viscoelastic deformation. The damp state had an obvious time effect on the damage of surrounding rocks. Specifically, the creep range was expanded under a damp state at 18 days compared with that under a dry state, and the change in the left and upper displacements was especially significant. The roadway cross-section changed asymmetrically under both dry and damp states, where it was changed into an approximate deflected rhombic shape under the dry state and into an approximate deflected trapezoidal shape under the damp state. Additionally, the roadway cross-sectional change under the humid state was evidently greater than that under the dry state.

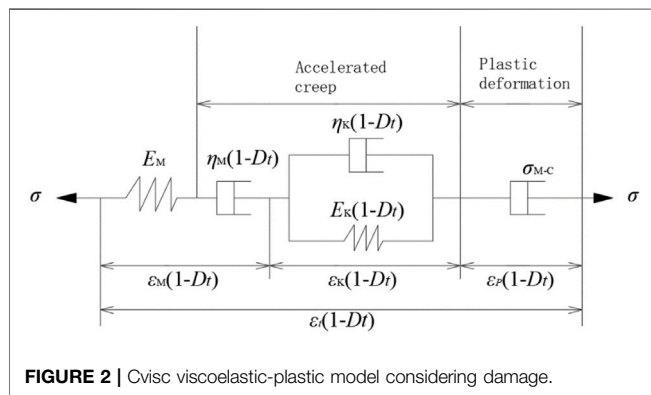
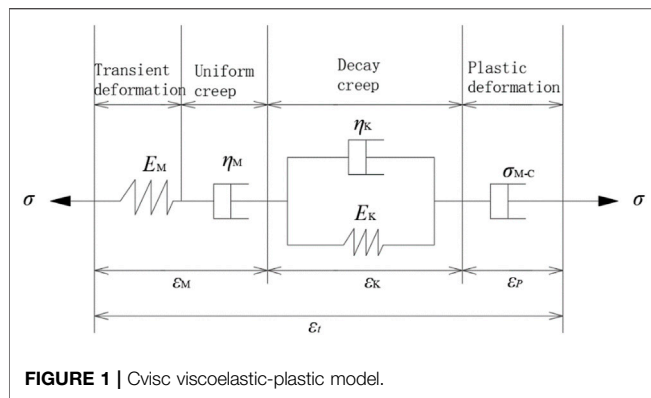
Keywords: argillaceous surrounding rock, damage, cvisc model, creep, time effect

INTRODUCTION

Rocks are primarily divided into magmatic, sedimentary, and metamorphic rocks, where sedimentary rocks play a dominant role, including limestones, sandstones, shales, and mudstones, which are especially susceptible to creep when encountering water (Xu, 2007; Zhang et al., 2011; Li et al., 2014). With the passing of time, the surrounding rocks on the roadway surface were gradually eroded by the moisture in the atmosphere, thus losing self-supporting ability. Consequently, the roadway is subjected to serious deformation, which further causes stability problems in terms of numerous aboveground and underground rock engineering. Therefore, argillaceous soft rock roadways need repeated renovation

TABLE 1 | Rheological model and main deformation characteristics.

Model Name	Main deformation characteristics of the model	Mechanical model	Stress-Strain-time relation
Maxwell (H-N)	Transient deformation, uniform creep, relaxation		 $\varepsilon_t = \frac{\sigma_0}{E_H} + \frac{\sigma}{\eta_H} t$
Kelvin (H N)	Decay creep, residual elasticity		 $\varepsilon_t = \frac{\sigma}{E_K} (1 - e^{-\frac{E_K}{\eta_K} t})$
Bingham (N S)	Transient deformation, uniform creep, relaxation, residual elasticity		 $\varepsilon_t = \frac{\sigma_0}{E_b} + \frac{\sigma - \sigma_s}{\eta_b} t$
Burgers (H-N(H N))	Transient deformation, decay creep, uniform creep, relaxation, residual elasticity		 $\varepsilon_t = \frac{\sigma_0}{E_g} + \frac{\sigma}{\eta_g} t + \frac{\sigma}{E_x} (1 - e^{-\frac{E_x}{\eta_x} t})$
Kormanura (H-(H N)-(N S))	Transient deformation, decay creep, uniform creep, relaxation, residual elasticity		 $\varepsilon_t = \frac{\sigma_0}{E_k} + \frac{\sigma_0}{E_x} (1 - e^{-\frac{E_x}{\eta_x} t}) + \frac{\sigma - \sigma_s}{\eta_b} t$



and are usually stuck in a vicious circle of “roadway formation-failure-repair-secondary failure-secondary repair.” Roadway support is a major problem confusing mine safety and efficient production and one of the technical problems requiring urgent solutions in engineering (Wang and Wang, 2000; Chen et al., 2007; Lu et al., 2007).

With regard to the deformation instability problem of soft rock roadways, rock creep and soft rock characteristics have been extensively investigated by domestic (Chinese) and foreign scholars. Wang H J et al. explored the influence of different horizontal stresses on roadway deformation via FLAC^{3D} and pointed out that confining pressure was positively correlated with the creep rate of rock masses (Wang et al., 2014). Ma G Y et al. studied the mechanical properties of double-layer initial support for deep high-stress tunnels by constructing a damage evolution model considering the elastoplastic deviatoric strain decrement; they subsequently concluded that the rock deformation could be well reflected by the constitutive elastoplastic creep damage evolution model (Ma et al., 2021). Xu W Y et al. stated that if introduced into nonlinear functions, the generalized Bingham creep model could reflect the decay, steady-state, and accelerated creep stages during the creep process well (Xu et al., 2006). Xie Y P et al. probed the total creep characteristics of carbonaceous slate specimens by establishing a hardening damage model and pointed out that the Cvisc model improved on the basis of damage theory which could reflect rock creep well (Xie et al., 2021). Yang D S et al. studied the relationships of gas permeability and creep properties of mudstones with the

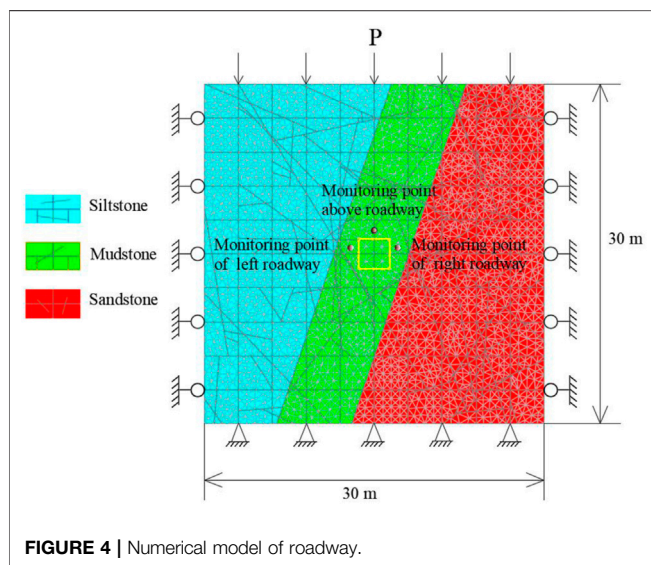
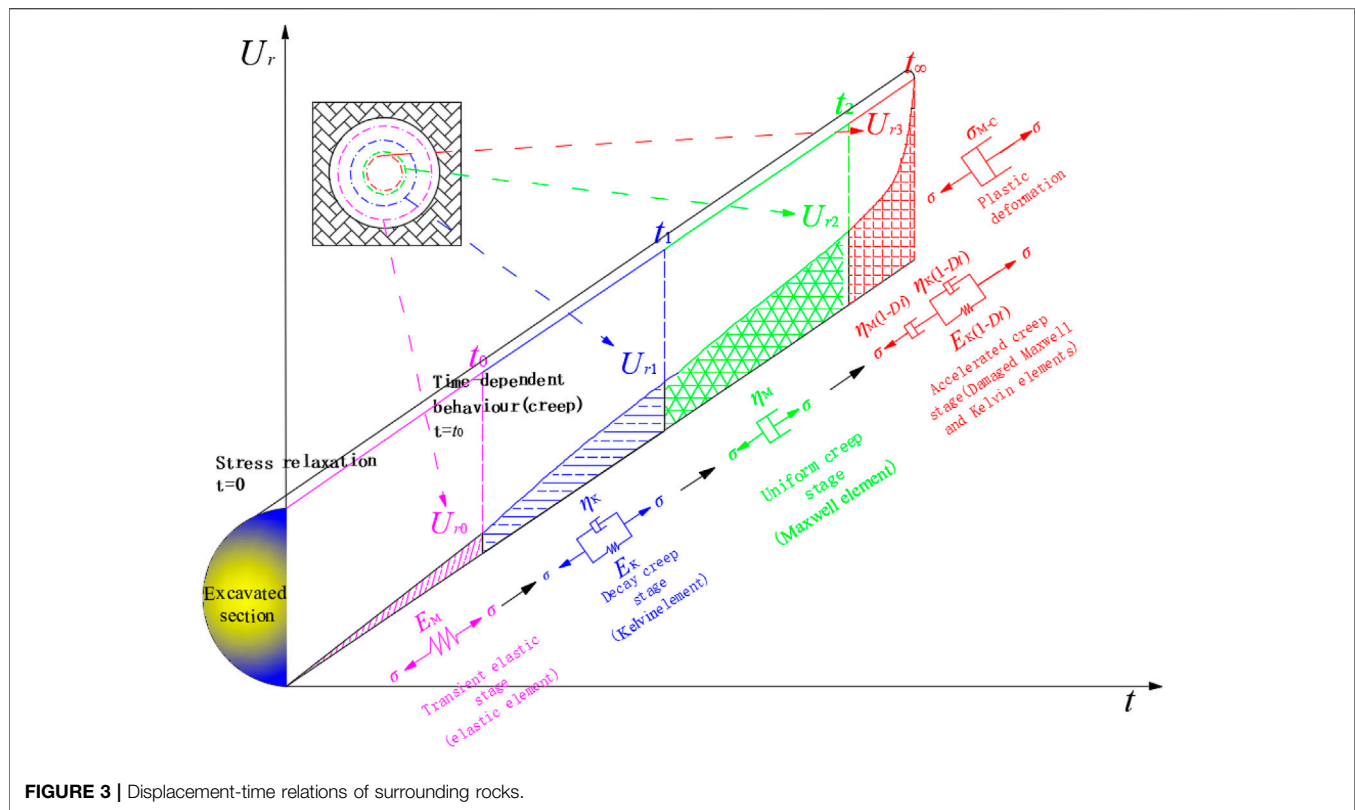
moisture content (Yang et al., 2010; Yang et al., 2011). Huang Y B et al. explored the failure mechanism of deep soft rock chambers via numerical simulation and proposed an optimized recovery scheme (Huang et al., 2021). Liu G et al. analyzed the changes in the crustal stress before and after the excavation of a soft rock roadway and the influence on the change and failure of surrounding rocks; then, they discussed about the deformation failure mechanism of high-stress soft surrounding rocks from the angles of the changes in the confining pressure and strength of rock masses and engineering rock masses (Liu et al., 2000). Wu G J et al. built a nonlinear creep damage equation and indicated the positive correlation between damage and deviatoric stress (Wu et al., 2010).

The above study results have a very good guiding effect on the deformation of soft rock roadways, but the constitutive surrounding rock creep model thoroughly considers the damage and weakening coefficient of surrounding rocks. Additionally, the literature has scarcely explored the deformation laws of argillaceous soft rocks under a damp environment. In this study, a constitutive soft rock model considering the damage and weakening coefficient of surrounding rocks was constructed on the basis of the classical Cvisc constitutive model. Next, the reasonability of this constitutive model was verified by combining numerical simulation and field monitoring. On this basis, this research comparatively analyzed the creep range of surrounding rocks in an argillaceous soft rock roadway and the roadway cross-sectional deformation laws under dry and damp states, expecting to provide a basis for the field support design and facilitate mine safety and efficient production.

CONSTITUTIVE DAMAGE MODELING FOR ARGILLACEOUS SOFT ROCKS

Mechanical studies show that rock deformation not only includes transient elastic and plastic deformation characteristics unrelated to time but also includes rheological deformation characteristics related to time (Zhang and Xu, 2006). During deep tunnel excavation, the deformation with time characteristic accounts for 70% of the total deformation, and rheological deformation plays a dominant role under deep conditions (Paraskevopoulou and Diederichs, 2018). To conveniently explore the rheological behaviors of rock masses, three basic units—elastomer (H), viscous body (N), and plastic body (S)—are typically combined in different forms with the main rheological models and deformation behaviors as seen in **Table 1** (Zhu et al., 2011; Zhao, 2017):

The above classical rheological models can describe well the partial creep properties of rock masses, but transient plastic deformation and accelerated creep deformation are neglected. In deep environment, rock masses are generally characterized by typical whole creep stage characteristics, namely, decay creep, uniform creep, and accelerated creep. As pointed out in the literature (Li et al., 2014), the Cvisc model is a combination of Burgers model and Mohr-Coulomb model, where the former can describe the constitutive viscoelastic relations in the creep process well, and the latter is capable of describing the constitutive elastoplastic relations. **Figure 1** displays the Cvisc viscoelastic-plastic model:



As shown in **Figure 1**, the Cvisc viscoelastic-plastic model can describe the transient deformation, decay creep, uniform creep, and plastic deformation in the creep process of soft rocks, with the following constitutive equation:

$$\varepsilon_t = \frac{\sigma}{E_M} + \frac{\sigma}{\eta_M} t + \frac{\sigma}{E_K} \left(1 - e^{-\frac{E_K}{\eta_K} t} \right) + \varepsilon_p \quad (1)$$

where ε_t is the total strain, ε_p stands for the plastic strain, σ is the horizontal stress, and t represents time. E_M , η_M , E_K , and η_K represent the elasticity modulus and viscosity coefficient of Maxwell body and Kelvin body.

During the creep process of soft rocks subjected to argillization when encountering water, their deformation is largely affected by the damage degree inside the material and the intensity of water environment. According to relevant literature (Zhao, 2017), rock damage occurs in the accelerated creep stage during the creep process, and the damage variable D_t presents the Weibull distribution with time t , expressed by the following equation:

$$D_t = 1 - e^{-at^\beta} \quad (2)$$

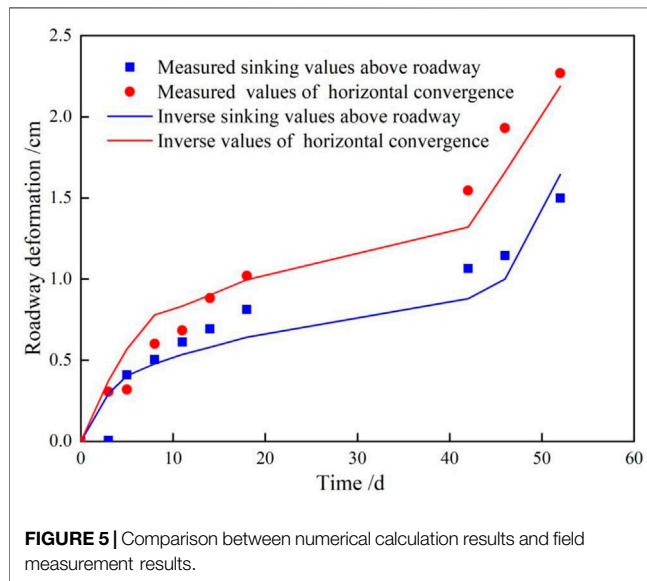
The influence of water environment on creep was considered by introducing the weakening coefficient λ of surrounding rocks. Then, λ was substituted into **Eq. 1** to obtain the constitutive equations of transient deformation, decay creep, uniform creep, and plastic deformation during the creep process as follows:

$$\varepsilon_t = (1 - \lambda) \left[\frac{\sigma}{E_M} + \frac{\sigma}{\eta_M} t + \frac{\sigma}{E_K} \left(1 - e^{-\frac{E_K}{\eta_K} t} \right) \right] + \varepsilon_p \quad (3)$$

The Cvisc model considering damage could describe the accelerated creep stage (Wang et al., 2014) (Cai and Lai, 2003; Chen et al., 2022). In addition, if damage was considered for the components subjected to decay creep, uniform creep, and plastic deformation in **Eq. 1**; **Figure 2** presents the Cvisc viscoelastic-plastic model considering damage:

TABLE 2 | Physical and mechanical parameters of roadway surrounding rock.

Lithology	Density/Kg·m ⁻³	Bulk modulus/GPa	Shear modulus/GPa	Poisson ratio	Cohesion/MPa	Angle of friction/°	Tensile strength/MPa
Siltstone	2,440	2.28	1.17	0.28	2.1	38	1.57
Mudstone	2,325	1.35	0.77	0.26	0.3	34	0.25
Sandstone	2,546	2.52	3.7	0.3	2.64	36	2.06

**FIGURE 5** | Comparison between numerical calculation results and field measurement results.**TABLE 3** | Creep parameters of roadway surrounding rock.

Lithology	E_M /GPa	η_M /GPa·d	E_K /GPa	η_K /GPa·d
Mudstone	950	4.0×10^4	0.15	9.0

The constitutive equation for the accelerated creep stage during the creep process could be obtained by combining Eqs 2 and 3 on the bases of effective stress model and strain equivalence principle:

$$\begin{aligned} \varepsilon_t &= (1 - \lambda) \left\{ \frac{\sigma}{E_M} + \left[\frac{\sigma}{\eta_M} t + \frac{\sigma}{E_K} \left(1 - e^{-\frac{E_K}{\eta_K} t} \right) + \varepsilon_p \right] \left(\frac{1}{1 - D_t} \right) \right\} \\ &= (1 - \lambda) \left\{ \frac{\sigma}{E_M} + \left[\frac{\sigma}{\eta_M} t + \frac{\sigma}{E_K} \left(1 - e^{-\frac{E_K}{\eta_K} t} \right) + \varepsilon_p \right] \left(e^{\alpha t^\beta} \right) \right\} \end{aligned} \quad (4)$$

Eqs 3 and 4 are the constitutive equations for the whole rock creep process (transient deformation, decay creep, uniform creep, accelerated creep, and plastic deformation) and consider the effects of rock damage variable D_t and surrounding rock weakening coefficient λ on creep. As pointed out in relevant literature (Paraskevopoulou and Diederichs, 2018), the displacement of surrounding rocks is in direct proportion to strain during the excavation of the underground tunnel. The

forementioned strain-time relations in Eqs 3 and 4 were used to obtain the displacement-time relations of the surrounding rocks during tunnel excavation as shown in Figure 3.

From Figure 3, the whole time-dependent displacement process around the surrounding rocks could be well reflected by different rheological components within different time periods. This phenomenon indicates that the displacement-time relations of surrounding rocks could be accurately described by the constitutive Eqs 3 and 4 of soft rock creep that considered the rock damage variable D_t and surrounding rock weakening coefficient λ .

NUMERICAL CALCULATION OF THE DEFORMATION FAILURE OF SURROUNDING ROCKS IN AN ARGILLACEOUS SOFT ROCK ROADWAY

Modeling

In a copper mine, the exploitation depth already reaches 600 m, and the surrounding rocks in its roadway are mostly mudstones and sandstones, accompanied by bedding development, low strength, and proneness to argillization when encountering water (Shen, 2014; Yang et al., 2018; Wu et al., 2020). According to the geological information of this copper mine, a 2D plane strain calculation model (Figure 4) of this deep roadway was constructed using the UDEC discrete element software. To eliminate the influence of boundary effect on the model calculation, both the length and height of the model were set as 5 times of the tunnel diameter (30 m), and the monitoring points were arranged at the vault and 0.3 m depth of the left and right walls, respectively.

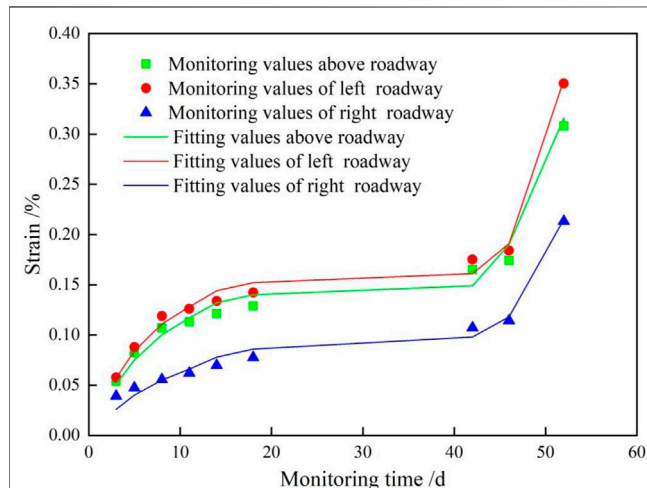
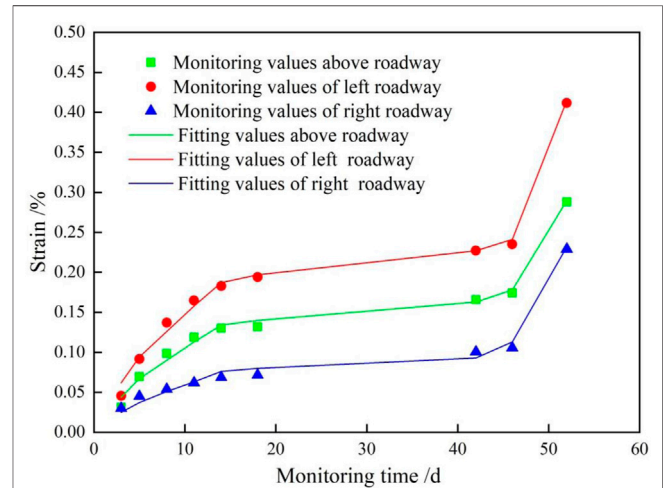
The pressure applied above the model was $P = \gamma h$, where γ is the average volume weight of rock strata above the model. The horizontally applied stress was μP ($\mu = 0.42$), and the horizontal displacements at the left and right sides and the vertical displacement at the bottom were restricted. In this model, the random fractures conforming to the geological survey results of this copper mine and the horizontal and vertical fractures preventing the automatic deletion of isolated random fractures in the model calculation were generated through the Monte Carlo method (Yu, 2015). Table 2 shows the reduced physical and mechanical parameters of this roadway.

Inversion of Model Creep Parameters

A precondition for numerical model calculation lies in the accurate numerical calculation of parameters. The BP neural

TABLE 4 | Fitting parameters of Formulas 3 and 4 under the dry state.

Location	σ / MPa	E_M / GPa	η_M /GPa·d	E_K / GPa	η_K / GPa·d	ε_p / $\times 10^{-7}$	α	B	Correlation coefficient
Vault	0.775	128.7	1.177×10^4	0.520	3.699	8.999	0.0025	1.770	0.961
Left side	1.610	125.6	1.071×10^4	1.012	6.826	8.999	0.0004	2.221	0.995
Right side	1.630	109.1	1.0963×10^4	1.670	16.706	9.001	0.0019	1.861	0.946

**FIGURE 6** | Relationship between numerical monitoring data and theoretical analysis in dry state.**FIGURE 7** | Relationship between numerical monitoring data and theoretical analysis in the damp state.**TABLE 5** | Fitting parameters of formulas 3 and 4 in the damp state.

Location	σ / MPa	E_M / GPa	η_M /GPa·d	E_K / GPa	η_K / GPa·d	ε_p / $\times 10^{-7}$	λ	A	β	Correlation coefficient
Vault	0.421	864.3	1.636×10^4	0.109	1.029	1.001	0.576	0.0048	1.618	0.985
Left wall	0.763	881.0	3.372×10^4	0.172	1.102	1.324	0.635	0.0024	1.792	0.992
Right wall	0.952	101.3	3.832×10^4	0.196	1.931	8.999	0.616	0.00001	3.064	0.964

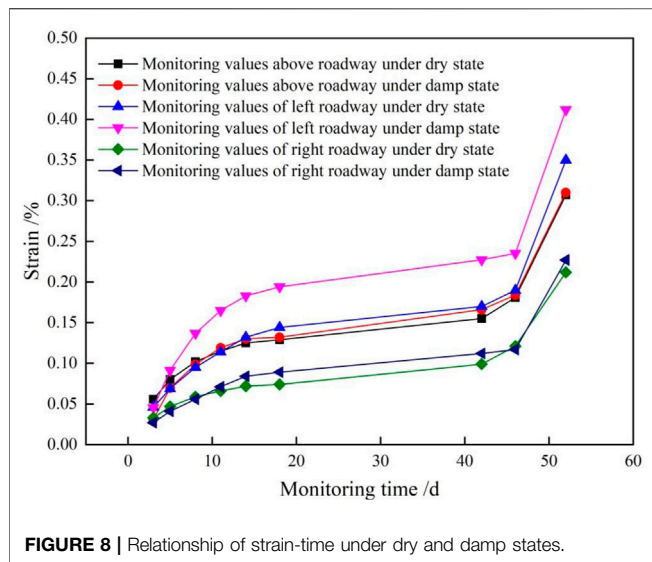
network can realize any nonlinear relation between input parameters and target parameters and acquire target prediction parameters, meeting the accuracy requirement by adjusting the initial weight and threshold (Chen, 2020). To restore the properties of surrounding rocks in the roadway as much as possible, the Cvisc constitutive model was adopted for the mudstones of this roadway during numerical model calculation and Mohr-Coulomb constitutive model for other rock strata (Zha et al., 2021). Finally, the mean square errors between the numerically calculated displacements at monitoring points and the actually monitored displacements were made into an input set and the creep parameters (E_M , η_M , E_K , and η_K) into an output set for the prediction through the BP neural network until they meet the accuracy requirement. **Figure 5** presents the numerical calculation results and actual monitoring results.

By analyzing **Figure 5**, the numerical calculation results largely accorded with the field measurement

results, proving that the inversion parameters could accurately reflect the deformation of surrounding rocks in the roadway. **Table 3** presents the parameters finally obtained by inversion.

ANALYSIS OF CALCULATION RESULTS

In the literature (Zhang et al., 2009), the softening coefficient of surrounding rocks in the roadway of this copper mine was obtained through uniaxial compression experiments as 0.12–0.21, indicating that the strength of surrounding rocks was largely affected by water. Given that groundwater prevention measures were already taken in the roadway excavation process of this mine, the strength of mudstones was weakened using the softening coefficient of 0.21 considering the influence of water on mudstone strength. To analyze the influence of dampness-induced



argillization on the deformation of surrounding rocks, the creep range of surrounding rocks and roadway cross-sectional deformation laws under dry and damp states were comparatively analyzed using the numerical model in Section 3.1.

Verification of Constitutive Model

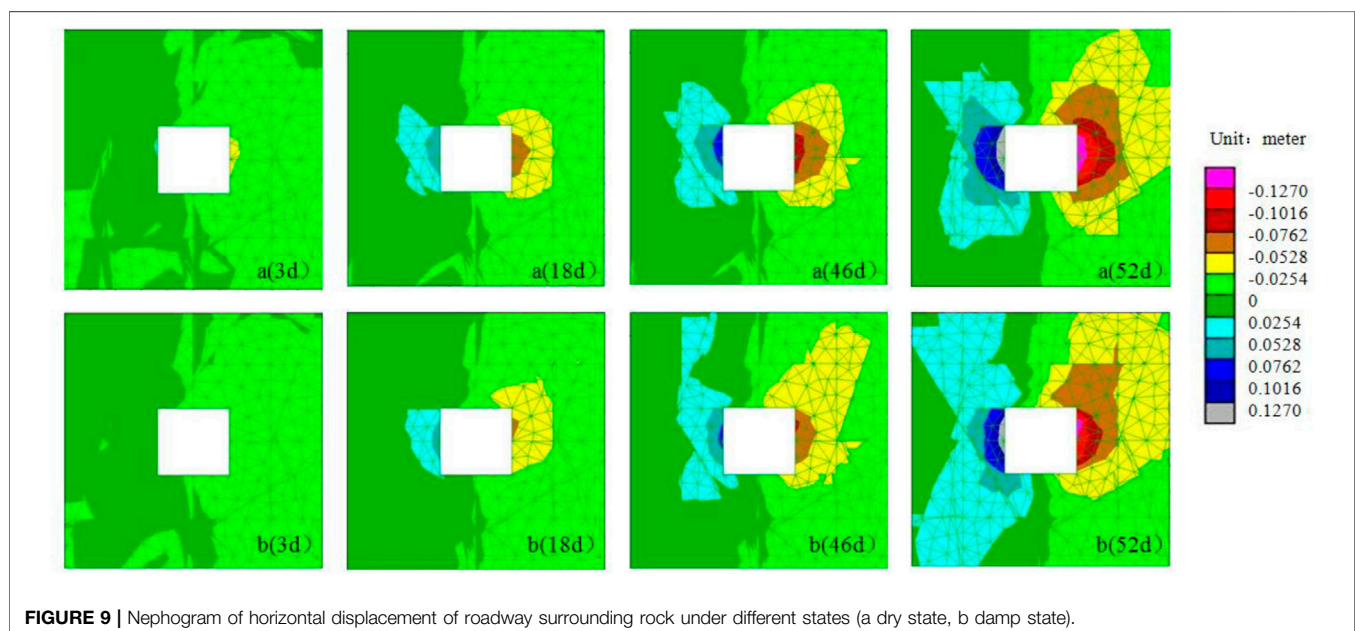
The creep parameters obtained through inversion in Section 3.2 were applied to the numerical model calculation, where the weakening coefficient λ of surrounding rocks was taken as 0 under the dry state. After the roadway excavation was stabilized, the strain and time of the roadway vault, left wall, and right wall were monitored. Next, the monitored data were fitted using Eqs 3 and 4, in which the stress level was the average stress within each time period. Table 4 lists the main fitted parameters under the dry state, and Figure 6 displays the fitting results.

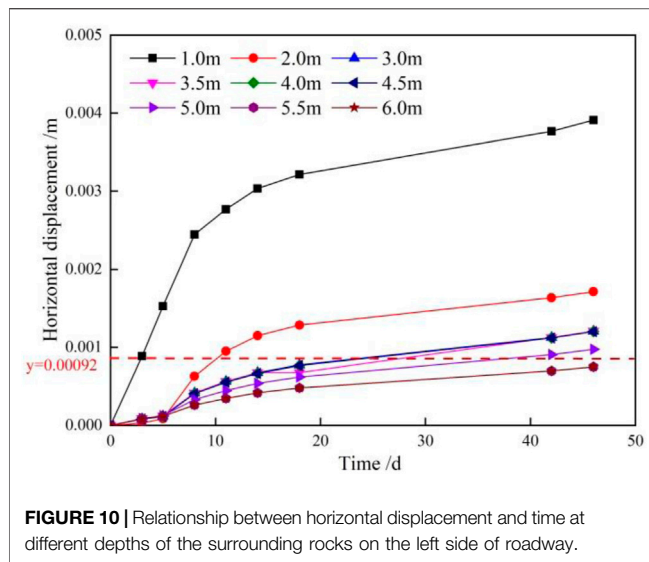
As seen in Table 4, the creep parameters EM , ηM , EK , and ηK basically had consistent orders of magnitude with those in Table 3, accompanied by high correlation coefficients. Thus, Eqs 3 and 4 could accurately describe the surrounding rock deformation-time relations under the dry state. The plastic deformations ε_p at roadway vault, left wall, and right wall were all small, indicating that surrounding rocks were subjected to viscoelastic deformation in creep stages under the dry state.

Table 5 lists the main parameters fitted through Eqs 3 and 4 under the damp state, and Figure 7 illustrates the fitting results. As could be known from Table 5, the creep parameters EM , ηM , EK , and ηK basically had consistent orders of magnitude with those in Table 3, accompanied by high correlation coefficients. This finding manifests that Eqs 3 and 4 could accurately describe the surrounding rock deformation-time relations under the damp

TABLE 6 | Creep rates of surrounding rocks in different stages under dry and damp states.

Location	Average creep rate in dry condition %/d			Average creep rate in damp condition %/d		
	3–18 days	18–46 days	46–52 days	3–18 days	18–46 days	46–52 days
Vault	0.00501	0.0016	0.0223	0.0067	0.0015	0.0191
Left side	0.00561	0.0015	0.0277	0.0099	0.00146	0.0294
Right side	0.00256	0.0013	0.0165	0.00257	0.0012	0.0205



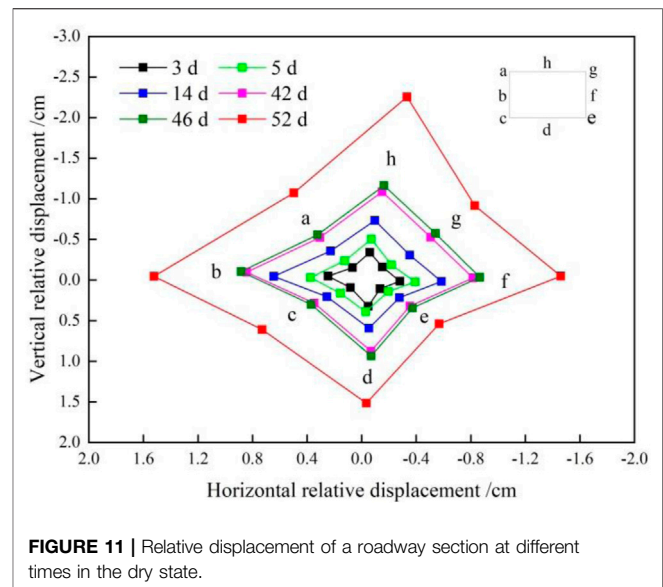


state. Moreover, the plastic deformations ε_p at roadway vault, left wall, and right wall were all smaller than those under the dry state, indicating that due to the increase in water content of the surrounding rocks under the damp state, the viscoelastic deformation of surrounding rocks was more obvious in the creep stages. The λ value was kept at approximately 0.6, indicating that the surrounding rocks substantially deteriorated by the dampness-induced argillization so that the final deformation of surrounding rocks was greater than that under the dry state.

As shown in **Figures 6, 7**, the monitoring data under dry and damp states were fitted very well by **Eqs 3 and 4**. Under the damp state, the maximum strains at roadway vault, left wall, and right wall were 0.29, 0.41 and 0.23%, respectively, and those under the dry state were 0.3, 0.35, and 0.21%, respectively. This finding indicates that the dampness-induced argillization of surrounding rocks impacted the left wall of the roadway in a titled stratum but slightly influenced the roadway vault and right wall.

Figure 8 displays the strain-time relations under dry and damp states. **Figure 8** shows that under both dry and damp states, the creep of surrounding rocks at different positions presented typical decay creep (3–18 days), uniform creep (18–46 days), and accelerated creep (46–52 days) with the passing of time. During the creep process, the strains at the roadway vault and right wall under the damp state were slightly greater than those under the dry state, and the strain at the left wall under the damp state was significantly greater than that under the dry state.

As aforementioned, the creep rates of surrounding rocks at different positions in the strain decay and accelerated stages were both higher than that in the uniform stage, thereby using the creep rate in the uniform stage as reference for analysis. **Table 6** displays the creep rates of the surrounding rocks in different stages under dry and damp states. Under the dry state, the average creep rate of surrounding rocks at different positions in the decay stage was 1.97–3.74 times of that in the uniform stage, and that in the accelerated stage was 12.69–18.46 times of that in the uniform stage. Under the damp state, the average creep rate of



surrounding rocks at different positions in the decay stage was 2.14–6.78 times of that in the uniform stage, and that in the accelerated stage was 12.73–20.14 times of that in the uniform stage. By comparison, the strain of surrounding rocks under the damp state was increased compared with under the dry state. Thus, the dampness-induced argillization accelerated the damage inside surrounding rocks. Finally, the damp state was positively correlated with the strain of surrounding rocks.

Determining the Creep Range for Surrounding Rocks

After the roadway excavation was stabilized, surrounding rocks crept, thus slowly reducing the roadway cross section. As could be known from **Figure 5**, the horizontal convergence deformation at two roadway walls was greater than the subsidence deformation at the roadway vault. Accordingly, the horizontal displacement was taken as an example to analyze the creep range of surrounding rocks. **Figure 9** exhibits the horizontal displacement nephograms of surrounding rocks in the roadway under dry and damp states within different time periods.

As could be observed from **Figure 9**, the scope of influence of horizontal displacement was gradually enlarged with the lapse of creep time. At 3–18 days, the scope of influence of horizontal displacement of surrounding rocks was small, and that under the dry state was basically consistent with that under the damp state. This finding indicates that under both states, the surrounding rocks deformed slowly at 3–18 days, during which the deformation of surrounding rocks had little to do with the dampness-induced argillization state of surrounding rocks. At 18–46 days, the scope of influence of horizontal displacement was gradually enlarged, and that under the damp state was slightly larger than that under the dry state. This finding indicates that the damage of surrounding rocks under the damp state was slightly greater than that under the dry state. At 18–46 days, the deformation of surrounding rocks was positively correlated

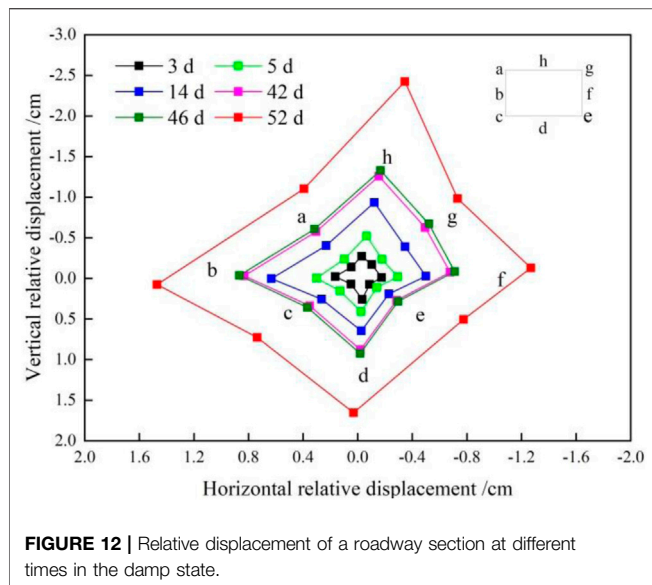


FIGURE 12 | Relative displacement of a roadway section at different times in the damp state.

with the dampness-induced argillization state of surrounding rocks. At 46–52 days, the scope of influence of horizontal displacement of surrounding rocks substantially expanded, and that under the damp state was larger than that under the dry state. This finding manifests that the damage of surrounding rocks under the damp state was greater than that under the dry state. Consequently, it took less time for surrounding rocks to experience the same deformation. In this stage, the deformation of surrounding rocks showed a significant positive correlation with their damp state. The above analysis results showed that after the argillization of surrounding rocks when encountering water, their deformation was enlarged. However, the dampness-induced argillization state had an obvious time effect on the damage of surrounding rocks, and surrounding rocks were damaged more evidently under the damp state after a certain time point.

The stability of surrounding rocks could be reflected by their deformation rate. When the deformation was smaller than 0.02 mm/d, the surrounding rocks could be considered to be basically stable (Hou, 2017). Under the dry state, **Figure 10** displays the horizontal displacement-time relations at different depths on the left side of surrounding rocks in this roadway. As could be known from **Figures 6, 7**, after 46 days, the surrounding rocks were in an accelerated creep stage. Thus, the creep range of surrounding rocks was distinguished by keeping their deformation rate at 0.02 mm/d (cumulative horizontal displacement: 0.00092 m) within 46 days.

As observed from **Figure 10**, the horizontal displacement of surrounding rocks was in a direct proportion to time and inversely proportional to the depth, and the cumulative horizontal displacement of surrounding rocks within the depth range of 1.0–5.5 m of surrounding rocks on the left side was greater than 0.00092 m. Thus, the creep range of surrounding rocks on the left side of this roadway was 1.0–5.5 m. Similarly, under the dry state, the creep ranges of surrounding rocks above the roadway at its right side and beneath it were 1.0–5.0, 1.0–4.5,

and 1.0–3.5 m, respectively. Hence, the creep range of surrounding rocks was asymmetric under the dry state, and the overall creep range presented a clockwise reduction from the surrounding rocks on the left side of this roadway.

Under the damp state, the creep ranges of surrounding rocks on the left side of this roadway, above it, on its right side, and beneath it were 1.0–5.5, 1.0–5.5, 1.0–4.5, and 1.0–4.0 m, respectively. This finding manifests that the creep range of surrounding rocks under the damp state was relatively consistent with that under the dry state, but that under the damp state was larger than that under the dry state.

Analysis of Roadway Cross-Sectional Deformation

Owing to the creep of surrounding rocks in this roadway, the roadway cross section was reduced. Additionally, its shape also deviated from the original design, thus impacting the normal basic functions of this roadway. **Figure 11** presents the time-dependent changes in relative horizontal and vertical displacements at main monitoring points on the rectangular roadway cross section under the dry state.

As could be known from **Figure 11**, under the dry state, the relative horizontal displacement of roadway cross section in a tilted stratum under the dry state was -1.5 to 1.5 cm, and the relative vertical displacement was -2.2 to 1.5 cm. In addition, the relative displacement at each monitoring point was in a direct proportion to time. At monitoring point d, relative vertical displacement played a dominant role, which led to floor heaving of this roadway. At monitoring points b and f, relative horizontal displacement dominated, and the horizontal displacement at point b was greater than that at point f. Thus, the left wall largely caved than the right wall did. At monitoring points a, c, e, g, and h, both relative horizontal and vertical displacements occurred, leading to the inward reduction of roadway cross section, and the displacement at point h indicated the vault settlement and deviation to the left. At monitoring points b, f, h, and d, the relative displacement substantially influenced the cross-sectional change in this roadway, the overall cross-sectional change was asymmetric (approximate to a deflecting rhombus), and finally, the cross-sectional shape was basically identical with that in relevant literature (Li et al., 2021).

Figure 12 shows the time-dependent changes in relative horizontal and vertical displacements at main monitoring points on the rectangular roadway cross section under the damp state.

As could be known from **Figure 12**, the main factors influencing the relative displacement-time relations and cross-sectional changes of this roadway in a tilted stratum under the damp state were basically consistent with those under the dry state, the relative horizontal displacement was -1.2–1.6 cm, and the relative vertical displacement was -2.5 to 1.6 cm. The relative displacement range in both horizontal and vertical directions was larger than that under the dry state. Thus, under the damp state, the damage in the surrounding rocks was aggravated, the overall roadway cross section changed asymmetrically (approximating a

deflecting trapezoid), and the final roadway cross-sectional shape basically coincided with the relevant literature (Li et al., 2021).

CONCLUSION

- 1) The Cvisc model considering the weakening coefficient of surrounding rocks is applicable to the decay and uniform creep stages, and that considering damage is applicable to the accelerated creep stage. During the creep process, surrounding rocks were subjected to viscoelastic deformation;
- 2) At 3–18 days, surrounding rocks basically crept under the dry state identically with that under the damp state. After 18 days, the creep range under the damp state expanded than that under the dry state, and the damage in surrounding rocks under the damp state had an obvious time effect;
- 3) Under the dry state, the maximum creep ranges of surrounding rocks on the left side of the roadway, above it, on its right side, and beneath it were 5.5, 5.0, 4.5, and 3.5 m, respectively. Those under the damp state were 5.5, 5.5, 4.5, and 4.0 m, respectively. The overall creep range was asymmetric, being reduced clockwise from the left side of this roadway;
- 4) Under the dry state, the relative horizontal displacement of this roadway was -1.5 to 1.5 cm, and the relative vertical displacement was -2.2 to 1.5 cm. The cross section of this roadway changed asymmetrically, resembling a deflecting rhombus or trapezoid under the dry state. Additionally, the

change laws under the damp state were basically consistent with those under the dry state, but the roadway cross section largely changed under the damp state in an approximately deflecting trapezoid.

DATA AVAILABILITY STATEMENT

The raw data supporting the conclusion of this article will be made available by the authors, without undue reservation.

AUTHOR CONTRIBUTIONS

Conceptualization, FC; methodology, LY; software, RS; validation, XY; formal analysis, HJ; investigation, CZ; writing—review and editing, RS. All authors have read and agreed to the published version of the manuscript.

FUNDING

This study was financially supported by the National Natural Science Foundation of China (No. 51874119), Key R & D and promotion projects in Henan Province (key scientific and technological projects) (No. 212102310602).

REFERENCES

- Cai, M. F., and Lai, X. P. (2003). Monitoring and Analysis of Nonlinear Dynamic Damage of Transport Roadway Supported by Composite Hard Rock Materials in Linglong Gold Mine. *J. Univ. Sci. Technol. Beijing* 10 (2), 10.
- Chen, Y. J., Xie, B. X., Cao, P., and Shi, X. Z. (2007). Scale Effect of Soft Rock Rheology. *J. Univ. Sci. Technol. Beijing* 30 (5), 468. doi:10.3321/j.issn:1001-053X.2008.05.002
- Chen, X. Y., Wang, X. F., Zhang, D. S., Qin, D. D., Wang, Y., Wang, J. Y., et al. (2022). Creep and Control of the Deep Soft Rock Roadway (DSRR): Insights from Laboratory Testing and Practice in Pingdingshan Mining Area. *Rock Mech. Rock Eng.* 55, 363. doi:10.1007/s00603-021-02670-1
- Chen, L. (2020). *Study on Fracture Evolution and Instability Mechanism of Large Dip Coal Seam Roadway Considering the Effect of Mining*. China: CUMT.
- Hou, C. J. (2017). Key Technologies for Surrounding Rock Control in Deep Roadway. *Int. J. Min. Sci. Technol.* 46 (5), 970. doi:10.13247/j.cnki.jcumt.000660
- Huang, Y. B., Wang, Y., Gao, H. K., Jiang, Z. H., Li, K., and Chen, K. (2021). Failure Mechanism and Construction Process Optimization of Deep Soft Rock Chamber Group. *Int. J. Min. Sci. Technol.* 50 (1), 69. doi:10.13247/j.cnki.jcumt.001232
- Li, T. C., Lu, Z., Liu, J. Z., and Ma, X. Q. (2014). Deformation and Failure Process Analysis of Rectangular Roadway in Muddy Weakly Cemented Soft Rock Strata. *Rock Soil Mech.* 35 (4), 1077. doi:10.16285/j.rsm.2014.04.020
- Li, J., Qiang, X. B., Ma, N. J., and Li, B. (2021). Formation Mechanism and Engineering Application of the Directionality of Butterfly Leaf in the Butterfly Plastic Zone of Roadway Rock Surrounded. *J. China Coal Soc.* 46 (9), 2838. doi:10.13225/j.cnki.jccs.2021.1150
- Liu, G., Nie, D. X., and Han, W. J. (2000). Deformation and Failure of Surrounding Rocks of Roadway in High Stressed Soft Rocks. *J. Rock Mech. Geotech. Eng.* (6), 726. doi:10.3321/j.issn:1000-6915.2000.06.009
- Lu, T., Liu, Y., and Xu, F. (2007). Deformation and Failure of Stratified Weak Roof Strata of Longwall Roadway. *J. Univ. Sci. Technol. Beijing, Mineral, Metallurgy, Material* 14 (5), 387–394. doi:10.1016/s1005-8850(07)60077-2
- Ma, G. Y., He, C., Chen, Z. Q., Ma, C. C., Yang, W. B., and Lai, X. H. (2021). Research on Mechanical Properties of Double Primar: Support Method of Deep Buried Tunnel Based on Damage Evolution Rheological Model. *J. Cent. South Univ.* 52 (8), 2897. doi:10.11817/j.issn.1672-7207.2021.08.034
- Paraskevopoulou, C., and Diederichs, M. (2018). Analysis of Time-dependent Deformation in Tunnels Using the Convergence-Confinement Method. *Tunn. Undergr. Space Technol.* 71, 62. doi:10.1016/j.tust.2017.07.001
- Shen, B. T. (2014). Coal Mine Roadway Stability in Soft Rock: A Case Study. *Rock Mech. Rock Eng.* 47 (1), 2225. doi:10.1007/s00603-013-0528-y
- Wang, C., and Wang, Y. (2000). Deformational Behaviour of Roadways in Soft Rocks in Underground Coal Mines and Principles for Stability Control. *Int. J. Rock Mech. Min. Sci.* 37 (6), 937. doi:10.1016/s1365-1609(00)00026-5
- Wang, H. J., Li, S. C., Wu, A. X., Yi, H. B., Sun, W., Wang, X. N., et al. (2014). Theoretical Analysis for Rheological Characteristics of Surrounding Rock and On-Site Monitoring in Longshou Mine. *J. Rock Mech. Geotech. Eng.* 33 (S2), 3676. doi:10.13722/j.cnki.jrme.2014.s2.035
- Wu, G. J., Chen, W. Z., Cao, J. J., and Tan, X. J. (2010). Nonlinear Creep Damage Model of Engineered Rock and its Application. *J. Rock Mech. Geotech. Eng.* 29 (6), 1184.
- Wu, G. J., Chen, W. Z., Jia, S. P., Tan, X. J., Zheng, P. Q., Tian, H. M., et al. (2020). Deformation Characteristics of a Roadway in Steeply Inclined Formations and its Improved Support. *Int. J. Rock Mech. Min. Sci.* 130, 104324. doi:10.1016/j.jrmm.2020.104324
- Xie, Y. P., Chen, Q. N., He, Y. C., Chen, Z. H., Tian, W. Q., Zhou, Y. J., et al. (2021). Creep Model Construction and Application of Carbonaceous Slate with Muscovite and Graphite under Deep High Geostress Environment. *J. Cent. South Univ.* 52 (2), 568. doi:10.11817/j.issn.1672-7207.2021.02.025
- Xu, W. Y., Zhou, J. W., Yang, S. Q., and Shi, C. (2006). Study on Creep Damage Constitutive Relation of Greenschist Specimen. *J. Rock Mech. Geotech. Eng.* (S1), 3093. doi:10.3321/j.issn:1000-6915.2006.z1.077
- Xu, X. L. (2007). *Study on Weakening Mechanism and Dynamic Process Control of Surrounding Rock in Argillaceous Roadway*. China: CUMT.
- Yang, D., Billiotte, J., and Su, K. (2010). Characterization of the Hydromechanical Behavior of Argillaceous Rocks with Effective Gas Permeability under Deviatoric Stress. *Eng. Geol.* 114 (3–4), 116. doi:10.1016/j.enggeo.2010.04.002

- Yang, D., Bornert, M., Chanchole, S., Wang, L., Valli, P., and Gatmiri, B. (2011). Experimental Investigation of the Delayed Behavior of Unsaturated Argillaceous Rocks by Means of Digital Image Correlation Techniques. *Appl. Clay Sci.* 54 (1), 53. doi:10.1016/j.clay.2011.07.012
- Yang, X. X., Han, Y., and Liu, N. (2018). Analysis on Bolting and Shotcreting with Wire Mesh Supporting Technology of Soft Rock Roadway. *Min. RD* 38 (6), 11.
- Yu, B. C. (2015). *Studies on the Stability of Surrounding Rock and Seepage Characteristics of Karst Hydraulic Tunnel Based on Monte-Carlo Stochastic Fracture Network*. China: SWJTU.
- Zha, E. S., Zhang, Z. T., Zhang, R., Wu, S. Y., Li, C. B., Ren, L., et al. (2021). Long-term Mechanical and Acoustic Emission Characteristics of Creep in Deeply Buried Jinping Marble Considering Excavation Disturbance. *Int. J. Rock Mech. Min. Sci.* 139 (2), 104603. doi:10.1016/j.ijrmms.2020.104603
- Zhang, W. K., and Xu, W. Y. (2006). Analysis of a New Visco-Elasto-Plastic Model for Jointed Rock Mass. *J. Rock Mech. Geotech. Eng.* (S1), 2894. doi:10.3321/j.issn:1000-6915.2006.z1.04
- Zhang, N., Li, G. C., and Xu, X. L. (2009). Argillation of a Roof Weak Interlayer Due to Water Seepage and its Influence on Roadway Stability. *Int. J. Min. Sci. Technol.* 38 (6), 757. doi:10.3321/j.issn:1000-1964.2009.06.001
- Zhang, N., Li, G. C., and Xu, X. L. (2011). *Theory and Practice of Surrounding Rock Control in Argillaceous Roadway*. China: CUMTP.
- Zhao, J. J. (2017). *Study on Creep Behavior and Creep Model of Deep Gypsum Mudstone*. Shandong: CUP.
- Zhu, Z. H., Zhao, Y. L., Xu, Y. F., and Sun, X. K. (2011). Teaching Research on Eight Typical Rheological Combination Models of Rock Mechanics. *ETAP* 3 (6), 85. doi:10.3969/j.issn.1674-5884.2011.06.031

Conflict of Interest: The authors declare that the research was conducted in the absence of any commercial or financial relationships that could be construed as a potential conflict of interest.

Publisher's Note: All claims expressed in this article are solely those of the authors and do not necessarily represent those of their affiliated organizations, or those of the publisher, the editors and the reviewers. Any product that may be evaluated in this article, or claim that may be made by its manufacturer, is not guaranteed or endorsed by the publisher.

Copyright © 2022 Chen, Su, Yang, Yang, Jiao and Zhu. This is an open-access article distributed under the terms of the Creative Commons Attribution License (CC BY). The use, distribution or reproduction in other forums is permitted, provided the original author(s) and the copyright owner(s) are credited and that the original publication in this journal is cited, in accordance with accepted academic practice. No use, distribution or reproduction is permitted which does not comply with these terms.



Analysis on the Shear Stress Propagation Mechanism in the Rock Reinforcement System

Jianhang Chen^{1,2}, Hui Li³, Shankun Zhao⁴, Hongbao Zhao², Cun Zhang², Junwen Zhang^{2*} and Danqi Li^{5*}

¹State Key Laboratory of Water Resource Protection and Utilization in Coal Mining, Beijing, China, ²School of Energy and Mining Engineering, China University of Mining and Technology (Beijing), Beijing, China, ³China National Coal Group Corporation, Beijing, China, ⁴Mine Safety Technology Branch of China Coal Research Institute, Beijing, China, ⁵WA School of Mines, Minerals, Energy and Chemical Engineering, Curtin University, Perth, WA, Australia

OPEN ACCESS

Edited by:

Shuren Wang,
Henan Polytechnic University, China

Reviewed by:

Saisai Wu,
Xi'an University of Architecture and
Technology, China
Yingchun Li,
Dalian University of Technology, China

*Correspondence:

Danqi Li
danqi.li@curtin.edu.au
Junwen Zhang
zhangjunwen1977@163.com

Specialty section:

This article was submitted to
Geohazards and Georisks,
a section of the journal
Frontiers in Earth Science

Received: 08 May 2022

Accepted: 19 May 2022

Published: 27 June 2022

Citation:

Chen J, Li H, Zhao S, Zhao H, Zhang C,
Zhang J and Li D (2022) Analysis on the
Shear Stress Propagation Mechanism
in the Rock Reinforcement System.
Front. Earth Sci. 10:938808.
doi: 10.3389/feart.2022.938808

Rock reinforcement is significant in maintaining the stability of excavated structures, such as tunnels and underground roadways. However, shear failure in the rock reinforcement system, especially the shear failure at the rock reinforcement bolt surface, induces a threat to the rock reinforcement system. To reveal the shear stress (SS) propagation mechanism in the rock reinforcement system, this article conducted a literature review. First, the investigation approaches that were used by previous researchers to study the SS propagation were summarized. The advantages and disadvantages of experimental tests, analytical simulation, and numerical simulation were compared and analyzed. Then, the SS propagation process in the rock reinforcement system was presented. Two typical SS propagation modes were explained. More attention was given to the SS propagation mode in which the maximum SS propagates from the external end of rock reinforcement bolts to the internal end of rock reinforcement bolts. After that, a discussion section was given. In the discussion section, the significance of the SS propagation was further emphasized. Moreover, the limitations in the analytical simulation and numerical simulation were indicated. It is concluded that when studying the SS propagation mechanism of rock reinforcement bolts, combining experimental tests, analytical simulation, and numerical simulation is a better choice. This study is beneficial for revealing the SS propagation mechanism of the rock reinforcement system.

Keywords: rock mechanics, fracture development, rock reinforcement, deformation failure, decoupling behavior

INTRODUCTION

In rock mechanics, failure of rock masses is commonly encountered (Wang et al., 2021a). This is because fractures distribute non-uniformly in rock masses (Nikolenko et al., 2021; Yang et al., 2021). Moreover, experiment work proves that rock masses which are full of fractures are quite low in strength (Gao et al., 2021).

This is more prominent when the rock masses are subjected to manual excavations (Zhang et al., 2021). For example, in civil engineering and mining engineering, excavation activities are performed to create tunnels, chambers, or roadways (Chen et al., 2022). These tunnels and roadways will be later used in serving transportation and ventilation (Yao et al., 2020).

It is ensured that this manual excavation disturbs the initial stability of rock masses (Wu et al., 2018). Moreover, due to manual excavations, stress concentration occurs in rock masses (Chen et al., 2020; Zhang et al., 2022). Consequently, fractures are likely to develop in rock masses (Zhang et al., 2020a; Chen et al., 2021a; Yang et al., 2022). This further weakens the rock mass strength.

To guarantee the safety of the rock mass excavation, rock reinforcement bolts are commonly used (Li et al., 2021a; Wang et al., 2021b; Chang et al., 2021). Experimental work proves that rock reinforcement bolts can combine the jointed rock mass. Moreover, once rock masses converge, shear deformation will occur in the grout column. Consequently, stress can be transferred in the rock reinforcement system (Thompson et al., 2012).

During the loading process, the shear stress (SS) propagation plays a significant role (Wang et al., 2020a). Therefore, proper understanding of the SS propagation mechanism in the rock reinforcement system is quite significant.

This article aims at revealing the SS propagation mechanism in the rock reinforcement system. To realize this purpose, a literature review was conducted. This study is beneficial to propose new reinforcement approaches to prevent rock mass failure.

PREVIOUS STUDY ON THE SS PROPAGATION

Investigation Approaches

To study the SS propagation mechanism in the rock reinforcement system, previous researchers adopted various approaches. Generally, investigation approaches can be classified into three different types: experimental tests (Marian et al., 2021), analytical simulation (Liu et al., 2017; Li et al., 2021b), and numerical simulation (Chen et al., 2021a).

Experimental tests should be the most credible one. Specifically, strain gauges are adhered on the bolt surface (Wang et al., 2019). Then, this instrumented bolt is installed in a rock block. Grout is used to bond the bolt with the rock block (Chen et al., 2021b; Yu et al., 2021). After full curing, the bolt is pulled out. During testing, tensile force distribution along with the bolt can be measured. Then, **Eq. 1** is adopted to simply calculate the SS at the bolt surface (Aoki et al., 2003).

$$\tau = \frac{D_b E (\varepsilon_1 - \varepsilon_2)}{4\Delta L}, \quad (1)$$

where τ is SS at the bolt surface, D_b is the bolt diameter, E is the elastic modulus of the bolt, ε is the tensile strain of the bolt, and ΔL is the spacing between two adjacent strain gauges.

This approach has been used by a number of researchers (Wang et al., 2020b). However, a shortcoming is that the attached strain gauges are likely to be stripped from the bolt surface. To solve this issue, Chekired and Benmokrane (Chekired et al., 1997) developed the tension measuring device. This device can be mounted on the bolt to measure the strain distribution.

Additionally, Martin and Pakalnis (Martin et al., 2008) proposed replacing the central wire in the cable bolt with a modified wire. Specifically, along with this modified wire, strain gauges were attached.

In addition, analytical simulation is an efficient approach to study the SS propagation mechanism (Chen et al., 2021c). Specifically, although the bolt may have a long length, the infinitesimal method can be used to analyze the SS at the bolt surface, as shown in **Eq. 2** (Ma et al., 2019):

$$\tau = \frac{D_b}{4} \frac{d\sigma_b(x)}{dx}, \quad (2)$$

where $d\sigma_b(x)$ is the increment of the tensile stress in the bolt.

Then, it is assumed that the bolt surface has the same mechanical property (Zou and Zhang, 2019). A bond-slip equation can be used to depict the relationship between the SS at the bolt surface and the slip (Zhang et al., 2020b). By incorporating the bond-slip equation into **Eq. 2**, analytical equations can be developed.

This analytical approach was initially proposed by Farmer (Farmer, 1975). However, at that period, the decoupling behavior was not considered. Later, this analytical method was adopted by others (Zhu et al., 2021). Aydan and Ichikawa (Aydan et al., 1985) made a significant improvement on analytical simulation. Their innovation is that the classic trilinear equation was proposed to describe the slip behavior of the bolt surface. Based on the trilinear equation, the bolt surface encountered the elastic, softening, and decoupling behavior. Therefore, the coupling and decoupling behavior of the bolt surface can be simulated.

Moreover, the trilinear equation may be simplified into the bilinear equation to evaluate the SS propagation of the bolt surface (Cai et al., 2004). The main difference between the bilinear equation and the trilinear equation is that there is no linear softening behavior in the bilinear equation.

In recent years, numerical simulation has become more popular in rock reinforcement analysis. It is because numerical simulation is powerful in establishing and calculating complicated structures (Mohamed et al., 2020). As for the rock reinforcement analysis, more research was focused on using the structure element, such as the cable or pile. There is a significant difference between the cable and pile. Specifically, the cable only considers the longitudinal performance of rock reinforcement bolts. In contrast, the pile can analyze both the longitudinal performance and the lateral performance of rock reinforcement bolts.

The advantage is that numerical elements have already been created by commercial companies. Therefore, users can conveniently adopt the structure element to simulate different rock reinforcement cases. In contrast, the shortcoming is that the original constitutive equation may not truly reflect the proper behavior of the rock reinforcement system. For example, in the structure element of the cable, the bolt surface is assumed to deform following an elastic perfectly plastic equation, as shown in **Eq. 3** (Nemcik et al., 2014).

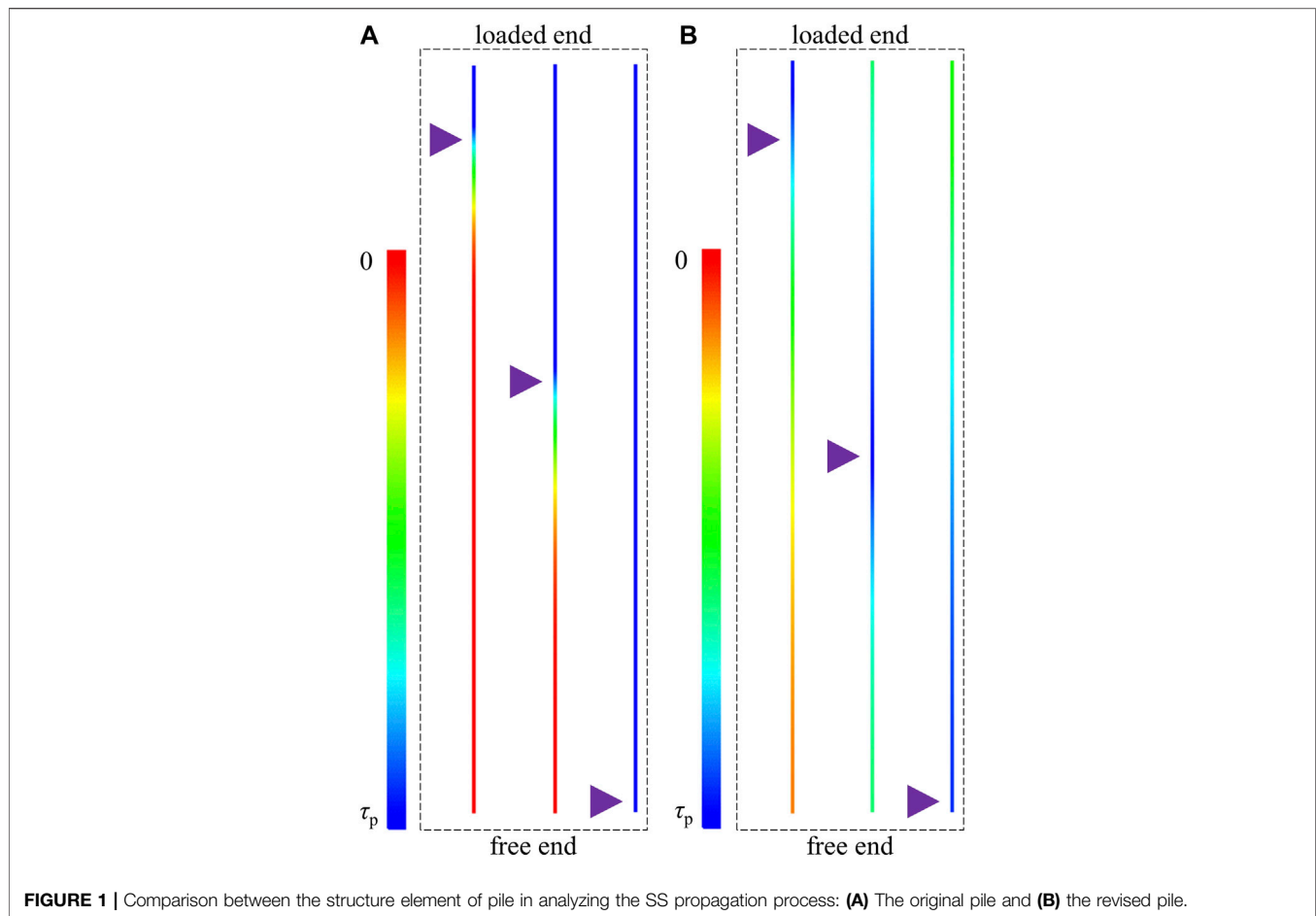


FIGURE 1 | Comparison between the structure element of pile in analyzing the SS propagation process: **(A)** The original pile and **(B)** the revised pile.

$$\begin{cases} \tau = k_g \delta (\delta \leq \delta_p) \\ \tau = \tau_p (\delta > \delta_p) \end{cases}, \quad (3)$$

where k_g is the shear stiffness of the grout column, δ is the slip of the bolt surface, δ_p is the slip of the bolt surface when the peak strength reaches, and τ_p is the peak strength of the bolt surface.

It neglects the post-failure behavior of the bolt surface. Therefore, it cannot truly simulate the loading performance of bolts without modification.

Nevertheless, the commercial software usually reserves the secondary development interface. For example, for the structure element of the cable, the Itasca Company prepared a number of FISH functions (Chen et al., 2021d). For the structure element of the pile, the Itasca Company created the TABLE function (Chen and Li, 2022). Therefore, users can use these FISH functions or TABLE function to modify the original rock reinforcement elements. For example, **Figure 1** shows the comparison between the original pile and the revised pile. Apparently, with the original pile, at the end of the SS propagation process, the SS at the full bolt surface equaled the peak strength. This overestimated the loading capacity of bolts. In contrast, with the modified pile, there was always a non-uniform SS distribution at the bolt surface. This was more consistent with the experimental test results. Consequently, it

saw a wide application of the commercial numerical tools in the rock reinforcement analysis (Shang et al., 2018).

SS Propagation Mechanism

Based on the previous research, it is accepted that the SS at the bolt surface may have a uniform distribution if the anchor length was short enough (Blanco Martín et al., 2010). Benmokrane and Chennouf (Benmokrane et al., 1995) indicated that when the anchor length is less than four times the bolt diameter, the SS can be treated equal. Based on this concept, **Eq. 4** was used to calculate the SS at the bolt surface (Ma et al., 2013):

$$\tau = \frac{F}{\pi D_b L}, \quad (4)$$

where F is the pulling force and L is the anchor length.

It should be noted that **Eq. 4** is valid when the anchor length is constant during the pulling process. Nevertheless, it is more common to encounter the scenario where the anchor length decreases gradually. Then, **Eq. 5** can be used to calculate the SS (Ma et al., 2013).

$$\tau = \frac{F}{\pi D_b (L - u_b)}, \quad (5)$$

where u_b is the pulling displacement.

More importantly, rock reinforcement bolts usually have a long length (Cao et al., 2013). In this case, after the bolt is subjected to tensile loading, a non-uniform SS distribution occurs. For the laboratory monotonous loading condition, the bolt usually has two ends. One is embedded in the rock block, and it is called the internal end. By contrast, the other one is left outside and it is called the external end. Since there is a non-uniform SS distribution, SS propagation between the two ends of the bolts generates.

Some research indicated that the maximum SS under each loading level was likely to occur around the same position (Teymen and Kılıç, 2018). Moreover, that position was close to the borehole collar.

In contrast, it is more common to see that during the initial load process, the SS at the borehole collar increased gradually. With the loading increasing, the SS at the borehole collar increased to the peak strength. Then, it started dropping. More interestingly, the maximum SS moved toward the internal end direction. This SS propagation ended when the SS at the internal end of the bolt reached the peak strength.

As a validation of this SS propagation concept, Rong and Zhu (Rong et al., 2004) conducted laboratory pull-out tests on bolts. Strain gauges were attached on the bolt surface to record the tensile force distribution. Later, Ma and Nemcik (Ma et al., 2013) analyzed these experimental data. Eq. 1 was used to calculate the SS at the bolt surface. The analysis results showed that at the initial loading grade, the SS at the borehole collar increased gradually. However, after a certain loading level, the SS at the borehole collar reached the peak strength. With the loading level further increasing, the maximum SS propagated gradually toward the external end. This analysis result was consistent with the above SS propagation concept. Therefore, the experimental work and the corresponding data analysis proved the reliability of the SS propagation concept.

Additionally, the analytical simulation and numerical simulation can better reflect the SS propagation process. Ren and Yang (Ren et al., 2010) used the classic trilinear equation to depict the slip behavior of the bolt surface. They analyzed the SS propagation process at the bolt surface. The results showed that the maximum SS at the bolt surface propagated from the external end to the internal end. Moreover, although each point at the bolt surface experienced the elastic, softening, and decoupling behavior, the full bolt surface underwent five different grades. They were the elasticity, elasticity-weakening, elasticity-weakening-decoupling, weakening-decoupling, and decoupling grades. Later, Blanco Martín and Tijani (Blanco Martín et al., 2013) indicated that when the trilinear equation was used to depict the slip behavior of the bolt surface, the full bolt surface may undergo a pure softening grade.

It should be mentioned that when different bond-slip equations are used, the full bolt surface may undergo different grades. For example, Chen and Liu (Chen et al., 2021e) indicated that when a bilinear equation was used to depict the slip behavior of the bolt surface, the full bolt surface only experienced three grades: the elastic grade, elastic-decoupling grade, and decoupling grade.

Although different bond-slip equations can be used, the SS propagation mechanism was consistent. Specifically, the maximum SS at the bolt surface consistently propagated from the external end to the internal end, as shown in Figure 2.

This finding was also confirmed with the numerical simulation. Nemcik and Ma (Nemcik et al., 2014) modified the original structure element in FLAC2D and simulated the SS propagation process at the bolt surface. A non-linear bond-slip equation was used. The results showed that each point at the bolt surface obeyed the same non-linear bond-slip equation. With the loading level increasing, the maximum SS at the bolt surface propagated toward the internal end. This finding was consistent with the others (Nie et al., 2018).

DISCUSSION

The SS at the bolt surface plays a significant role in determining the loading capacity of bolts (Wu et al., 2019). Under the static loading condition, the loading capacity of the bolts equals the sum of the shear force at the bolt surface (Ho et al., 2019). Since the SS at the bolt surface can be calculated directly with the shear force at the bolt surface, as shown in Eq. 6, there is a close relationship between the SS at the bolt surface and the loading capacity of the bolts (Zuo et al., 2019).

$$\tau = \frac{F_s}{A_s}, \quad (6)$$

where F_s is the shear force at the bolt surface and A_s is the contact area between the bolt and the grout column.

Therefore, it is valuable to understand the SS propagation mechanism of bolts. To realize this purpose, previous researchers used various approaches. It is believed that the experimental approach is more credible. This is because compared with the experimental approach, the analytical simulation and numerical simulation usually relied on a number of assumptions (Yokota et al., 2019). Whether those assumptions are reasonable is doubted. In the analytical simulation, it is usually assumed that the bolt, grout column, and surrounding rock masses deform elastically. In fact, in experimental tests, failure of the rock masses may occur because of the radial dilation at the bolt surface. Therefore, under this scenario, the analytical simulation which assumes that only slip failure occurs at the bolt surface may not be trustable.

Similarly, in the numerical simulation, rock masses are simulated with different elastoplastic equations. Among kinds of equations, the Mohr–Coulomb equation is more commonly used. This equation is relatively simpler and its input parameters can be acquired directly from experimental tests. However, it cannot properly simulate the post-failure behavior of rock masses. Specifically, after the peak, the strain softening behavior and residual behavior of rock masses cannot be properly simulated. In this case, the interaction between the numerical rock mass and bolts cannot be the same as in the reality. This is also the reason why the numerical simulation work should be calibrated and compared with experimental results.

Nevertheless, this is not to deny the significance of analytical simulation and numerical simulation. In fact, these two approaches are more effective for researchers to understand the SS propagation mechanism of bolts. Therefore, it is suggested that combining the experimental tests, analytical simulation, and numerical simulation is a better choice for studying the SS propagation mechanism of bolts.

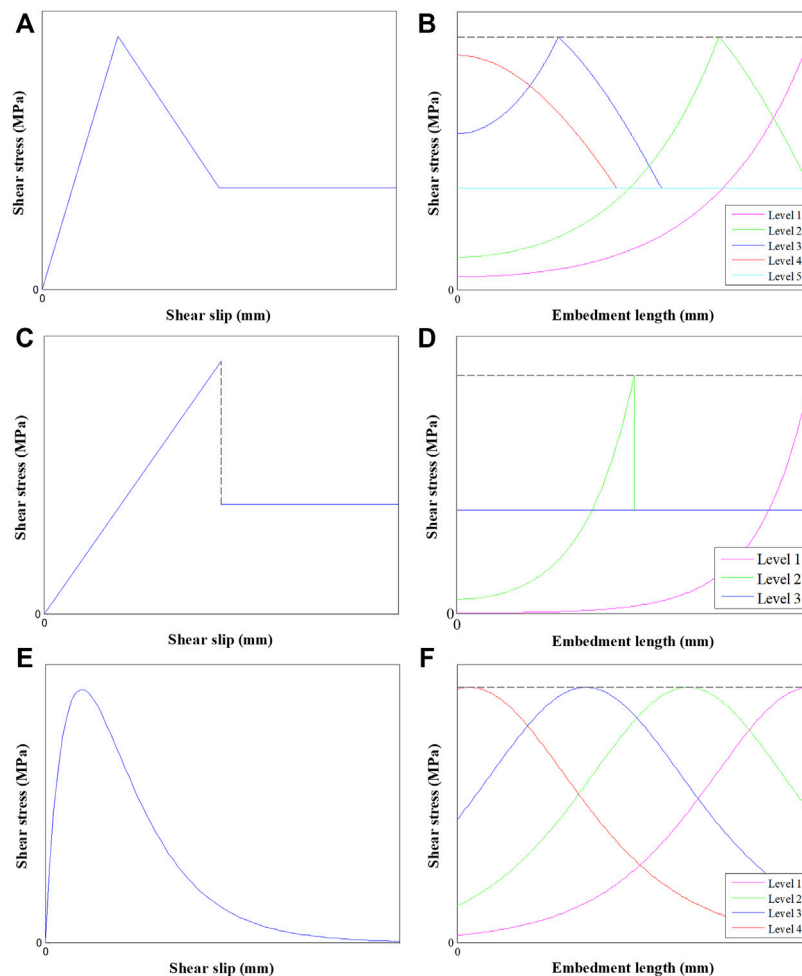


FIGURE 2 | SS propagation process: **(A)** Trilinear equation, **(B)** the corresponding SS propagation process, **(C)** bilinear equation, **(D)** the corresponding SS propagation process, **(E)** non-linear equation, and **(F)** the corresponding SS propagation process.

CONCLUSION

This article conducted a literature review on the SS propagation mechanism of rock reinforcement bolts. The previous investigation approaches were summarized. It is concluded that previous researchers usually used experimental tests, analytical simulation, and numerical simulation. Among those approaches, the experimental approach is more widely used. The experimental test results are also more likely to be accepted by others. By contrast, the analytical approach had more degree of freedom. With this approach, researchers can use different bond-slip equations to depict the slip behavior of the bolt surface. As for the numerical simulation, it is convenient for users since the original constitutive equation has already been created by the developer. Moreover, developers usually reserve the secondary development interface for users to modify the original constitutive equations.

As for the SS propagation mechanism, it is more commonly agreed that during the pulling process of bolts, the SS at the borehole collar firstly increased. With the loading level increasing, the SS at the borehole collar gradually reaches the

peak strength. Then, with the further increasing of the loading level, the maximum SS starts propagating toward the internal end. This phenomenon was consistently observed in experimental tests, analytical simulation, and numerical simulation.

AUTHOR CONTRIBUTIONS

Writing: JC, HL, SZ, HZ, and CZ; conceptualization: JZ and DL.

FUNDING

The National Natural Science Foundation of China (52034009, 51904302, 52174093, and 52104155), Open Fund of State Key Laboratory of Water Resource Protection and Utilization in Coal Mining (Grant No. WPUKFJJ 2019-08), Yue Qi Distinguished Scholar Project (800015Z1179), and the Beijing Municipal Natural Science Foundation (8212032).

REFERENCES

- Aoki, T., Shibata, K., Nakahara, F., Maeno, Y., Kawano, R., and Obara, Y. (2003). "Pull Tests of Long-Embedded Cablebolts," in Proceedings of Conference Pull tests of long-embedded cablebolts, Gauteng, South Africa, September 08 2003, 45–48.
- Aydan, O., Ichikawa, Y., and Kawamoto, K. (1985). Load Bearing Capacity and Stress Distributions In/along Rockbolts with Inelastic Behaviour of Interfaces, Proceedings of Conference Load bearing capacity and stress distributions in/along rockbolts with inelastic behaviour of interfaces, Nagoya, 1281–1292.
- Benmokrane, B., Chennouf, A., and Mitri, H. S. (1995). Laboratory Evaluation of Cement-Based Grouts and Grouted Rock Anchors. *Int. J. Rock Mech. Min. Sci. Geomechanics Abstr.* 32, 633–642. doi:10.1016/0148-9062(95)00021-8
- Blanco Martín, L., Tijani, M., and Hadj-Hassen, F. (2010). A New Analytical Solution to the Mechanical Behaviour of Fully Grouted Rockbolts Subjected to Pull-Out Tests. *Constr. Build. Mater.* 25, 1–18. doi:10.1016/j.conbuildmat.2010.07.011
- Blanco Martín, L., Tijani, M., Hadj-Hassen, F., and Noiret, A. (2013). Assessment of the Bolt-Grout Interface Behaviour of Fully Grouted Rockbolts from Laboratory Experiments under Axial Loads. *Int. J. Rock Mech. Min. Sci.* 63, 50–61. doi:10.1016/j.ijrmms.2013.06.007
- Cai, Y., Esaki, T., and Jiang, Y. (2004). A Rock Bolt and Rock Mass Interaction Model. *Int. J. Rock Mech. Min. Sci.* 41, 1055–1067. doi:10.1016/j.ijrmms.2004.04.005
- Cao, C., Jan, N., Ren, T., and Naj, A. (2013). A Study of Rock Bolting Failure Modes. *Int. J. Min. Sci. Technol.* 23, 79–88. doi:10.1016/j.ijmst.2013.01.012
- Chang, J., He, K., Pang, D., Li, D., Li, C., and Sun, B. (2021). Influence of Anchorage Length and Pretension on the Working Resistance of Rock Bolt Based on its Tensile Characteristics. *Int. J. Coal Sci. Technol.* 8, 1384–1399. doi:10.1007/s40789-021-00459-9
- Chekired, M., Benmokrane, B., and Mitri, H. S. (1997). Laboratory Evaluation of a New Cable Bolt Tension Measuring Device. *Int. J. Rock Mech. Min. Sci.* 34, 1–13. doi:10.1016/s1365-1609(97)00076-2
- Chen, Y., Teng, J., Bin Sadiq, R. A., and Zhang, K. (2020). Experimental Study of Bolt-Anchoring Mechanism for Bedded Rock Mass. *Int. J. Geomech.* 20, 1–12. doi:10.1061/(asce)gm.1943-5622.0001561
- Chen, Y., Zuo, J., Liu, D., Li, Y., and Wang, Z. (2021). Experimental and Numerical Study of Coal-Rock Bimaterial Composite Bodies under Triaxial Compression. *Int. J. Coal Sci. Technol.* 8, 908–924. 1-17. doi:10.1007/s40789-021-00409-5
- Chen, J., Hagan, P. C., and Saydam, S. (2021). An Experimental Study of the Specimen Geometry Effect on the Axial Performance of Cement-Based Grouts. *Constr. Build. Mater.* 310, 125167. doi:10.1016/j.conbuildmat.2021.125167
- Chen, J., Zhao, Y., Zhao, H., Zhang, J., Zhang, C., and Li, D. (2021). Analytic Study on the Force Transfer of Full Encapsulating Rockbolts Subjected to Tensile Force. *Int. J. Appl. Mech.* 13, 1–13. doi:10.1142/s1758825121500976
- Chen, J., Zhao, H., He, F., Zhang, J., and Tao, K. (2021). Studying the Performance of Fully Encapsulated Rock Bolts with Modified Structural Elements. *Int. J. Coal Sci. Technol.* 8, 64–76. doi:10.1007/s40789-020-00388-z
- Chen, J., Liu, P., Zhao, H., Zhang, C., and Zhang, J. (2021). Analytical Studying the Axial Performance of Fully Encapsulated Rock Bolts. *Eng. Fail. Anal.* 128, 1–16. doi:10.1016/j.engfailanal.2021.105580
- Chen, J., and Li, D. (2022). Numerical Simulation of Fully Encapsulated Rock Bolts with a Tri-linear Constitutive Relation. *Tunn. Undergr. Space Technol.* 120, 1–13. doi:10.1016/j.tust.2021.104265
- Chen, J., Liu, P., Liu, L., Zeng, B., Zhao, H., Zhang, C., et al. (2022). Anchorage Performance of a Modified Cable Anchor Subjected to Different Joint Opening Conditions. *Constr. Build. Mater.* 336, 1–12. doi:10.1016/j.conbuildmat.2022.127558
- Farmer, I. W. (1975). Stress Distribution along a Resin Grouted Rock Anchor. *Int. J. Rock Mech. Min. Sci. Geomechanics Abstr.* 12, 347–351. doi:10.1016/0148-9062(75)90168-0
- Gao, H., Wang, Q., Jiang, B., Zhang, P., Jiang, Z., and Wang, Y. (2021). Relationship between Rock Uniaxial Compressive Strength and Digital Core Drilling Parameters and its Forecast Method. *Int. J. Coal Sci. Technol.* 8, 605–613. doi:10.1007/s40789-020-00383-4
- Ho, D.-A., Bost, M., and Rajot, J.-P. (2019). Numerical Study of the Bolt-Grout Interface for Fully Grouted Rockbolt under Different Confining Conditions. *Int. J. Rock Mech. Min. Sci.* 119, 168–179. doi:10.1016/j.ijrmms.2019.04.017
- Li, D., Cai, M., and Masoumi, H. (2021). A Constitutive Model for Modified Cable Bolts Exhibiting Cone Shaped Failure Mode. *Int. J. Rock Mech. Min. Sci.* 145, 104855. doi:10.1016/j.ijrmms.2021.104855
- Li, D., Li, Y., Chen, J., and Masoumi, H. (2021). An Analytical Model for Axial Performance of Rock Bolts under Constant Confining Pressure Based on Continuously Yielding Criterion. *Tunn. Undergr. Space Technol.* 113, 103955. doi:10.1016/j.tust.2021.103955
- Liu, J., Yang, H., Wen, H., and Zhou, X. (2017). Analytical Model for the Load Transmission Law of Rock Bolt Subjected to Open and Sliding Joint Displacements. *Int. J. Rock Mech. Min. Sci.* 100, 1–9. doi:10.1016/j.ijrmms.2017.01.018
- Ma, S., Nemcik, J., and Aziz, N. (2013). An Analytical Model of Fully Grouted Rock Bolts Subjected to Tensile Load. *Constr. Build. Mater.* 49, 519–526. doi:10.1016/j.conbuildmat.2013.08.084
- Ma, H.-C., Tan, X.-H., Qian, J.-Z., and Hou, X.-L. (2019). Theoretical Analysis of Anchorage Mechanism for Rock Bolt Including Local Stripping Bolt. *Int. J. Rock Mech. Min. Sci.* 122, 104080. doi:10.1016/j.ijrmms.2019.104080
- Marian, W., Krzysztof, K., Jacek, N., Marcin, S., and Wioleta, B. (2021). An Exsitu Underground Coal Gasification Experiment with a Siderite Interlayer: Course of the Process. *Int. J. Coal Sci. Technol.* 8, 1447–1460. doi:10.1007/s40789-021-00456-y
- Martin, L., Pakalnis, R., and Milne, D. (2008). *Determination of Physical Properties of Cable Bolts in Cement Grout Pull Tests Using Instrumented King Wires*. Spokane: National Institute for Occupational Safety and Health Spokane, 1–8.
- Mohamed, K., Rashed, G., and Radakovic-Guzina, Z. (2020). Loading Characteristics of Mechanical Rib Bolts Determined through Testing and Numerical Modeling. *Int. J. Min. Sci. Technol.* 30, 17–24. doi:10.1016/j.ijmst.2019.12.016
- Nemcik, J., Ma, S., Aziz, N., Ren, T., and Geng, X. (2014). Numerical Modelling of Failure Propagation in Fully Grouted Rock Bolts Subjected to Tensile Load. *Int. J. Rock Mech. Min. Sci.* 71, 293–300. doi:10.1016/j.ijrmms.2014.07.007
- Nie, W., Zhao, Z. Y., Ma, S. Q., and Guo, W. (2018). Effects of Joints on the Reinforced Rock Units of Fully-Grouted Rockbolts. *Tunn. Undergr. Space Technol.* 71, 15–26. doi:10.1016/j.tust.2017.07.005
- Nikolenko, P. V., Epshtein, S. A., Shkuratnik, V. L., and Anufrenkova, P. S. (2021). Experimental Study of Coal Fracture Dynamics under the Influence of Cyclic Freezing-Thawing Using Shear Elastic Waves. *Int. J. Coal Sci. Technol.* 8, 562–574. doi:10.1007/s40789-020-00352-x
- Ren, F. F., Yang, Z. J., Chen, J. F., and Chen, W. W. (2010). An Analytical Analysis of the Full-Range Behaviour of Grouted Rockbolts Based on a Tri-linear Bond-Slip Model. *Constr. Build. Mater.* 24, 361–370. doi:10.1016/j.conbuildmat.2009.08.021
- Rong, G., Zhu, H., and Zhou, C. (2004). Testing Study on Working Mechanism of Fully Grouted Bolts of Thread Steel and Smooth Steel. *Chin. J. Rock Mech. Eng.* 23, 469–475. (In Chinese). doi:10.3321/j.issn:1000-6915.2004.03.021
- Shang, J., Yokota, Y., Zhao, Z., and Dang, W. (2018). DEM Simulation of Mortar-Bolt Interface Behaviour Subjected to Shearing. *Constr. Build. Mater.* 185, 120–137. doi:10.1016/j.conbuildmat.2018.07.044
- Teymen, A., and Kılıç, A. (2018). Effect of Grout Strength on the Stress Distribution (Tensile) of Fully-Grouted Rockbolts. *Tunn. Undergr. Space Technol.* 77, 280–287. doi:10.1016/j.tust.2018.04.022
- Thompson, A. G., Villaescusa, E., and Windsor, C. R. (2012). Ground Support Terminology and Classification: An Update. *Geotech. Geol. Eng.* 30, 553–580. doi:10.1007/s10706-012-9495-4
- Wang, S., Xiao, H. G., Zou, Z. S., Cao, C., Wang, Y. H., and Wang, Z. L. (2019). Mechanical Performances of Transverse Rib Bar during Pull-Out Test. *Int. J. Appl. Mech.* 11, 1–15. doi:10.1142/s1758825119500480
- Wang, S., Wang, Z., Gong, J., Wang, Y., and Huang, Q. (2020). Coupling Effect Analysis of Tension and Reverse Torque during Axial Tensile Test of Anchor Cable. *Dynaii* 95, 288–293. doi:10.6036/9603
- Wang, S. R., Wang, Y. H., Gong, J., Wang, Z. L., Huang, Q. X., and Kong, F. L. (2020). Failure Mechanism and Constitutive Relation for an Anchorage Segment of an Anchor Cable under Pull-Out Loading. *Acta Mech.* 231, 3305–3317. doi:10.1007/s00707-020-02717-4
- Wang, Z., Wang, T., Wu, S., and Hao, Y. (2021). Investigation of Microcracking Behaviors in Brittle Rock Using Polygonal Grain-based

- Distinct Method. *Int. J. Numer. Anal. Methods Geomechanics* 45, 1871–1899. doi:10.1002/nag.3246
- Wang, S., Wang, Y., Wang, Z., Gong, J., and Li, C. (2021). Anchoring Performances Analysis of Tension-Torsion Grouted Anchor under Free and Non-free Rotating Conditions. *Dynaii* 96, 166–172. doi:10.6036/9985
- Wu, S., Chen, H., Lamei Ramandi, H., Hagan, P. C., Hebblewhite, B., Crosky, A., et al. (2018). Investigation of Cable Bolts for Stress Corrosion Cracking Failure. *Constr. Build. Mater.* 187, 1224–1231. doi:10.1016/j.conbuildmat.2018.08.066
- Wu, S., Ramandi, H. L., Chen, H., Crosky, A., Hagan, P., and Saydam, S. (2019). Mineralogically Influenced Stress Corrosion Cracking of Rockbolts and Cable Bolts in Underground Mines. *Int. J. Rock Mech. Min. Sci.* 119, 109–116. doi:10.1016/j.ijrmms.2019.04.011
- Yang, H., Krause, M., and Renner, J. (2021). Determination of Fracture Toughness of Mode I Fractures from Three-point Bending Tests at Elevated Confining Pressures. *Rock Mech. Rock Eng.* 54, 5295–5317. doi:10.1007/s00603-021-02432-z
- Yang, H., Renner, J., Brackmann, L., and Röttger, A. (2022). Normal Indentation of Rock Specimens with a Blunt Tool: Role of Specimen Size and Indenter Geometry. *Rock Mech. Rock Eng.* 55, 2027–2047. doi:10.1007/s00603-021-02732-4
- Yao, H., Wang, H., Li, Y., and Jin, L. (2020). Three-dimensional Spatial and Temporal Distributions of Dust in Roadway Tunneling. *Int. J. Coal Sci. Technol.* 7, 88–96. doi:10.1007/s40789-020-00302-7
- Yokota, Y., Zhao, Z., Nie, W., Date, K., Iwano, K., and Okada, Y. (2019). Experimental and Numerical Study on the Interface Behaviour between the Rock Bolt and Bond Material. *Rock Mech. Rock Eng.* 52, 869–879. doi:10.1007/s00603-018-1629-4
- Yu, H., Jia, H., Liu, S., Liu, Z., and Li, B. (2021). Macro and Micro Grouting Process and the Influence Mechanism of Cracks in Soft Coal Seam. *Int. J. Coal Sci. Technol.* 8, 969–982. doi:10.1007/s40789-020-00404-2
- Zhang, Z., Deng, M., Bai, J., Yu, X., Wu, Q., and Jiang, L. (2020). Strain Energy Evolution and Conversion under Triaxial Unloading Confining Pressure Tests Due to Gob-Side Entry Retained. *Int. J. Rock Mech. Min. Sci.* 126, 1–10. doi:10.1016/j.ijrmms.2019.104184
- Zhang, W., Huang, L., and Juang, C. H. (2020). An Analytical Model for Estimating the Force and Displacement of Fully Grouted Rock Bolts. *Comput. Geotechnics* 117, 1–10. doi:10.1016/j.compgeo.2019.103222
- Zhang, Z., Deng, M., Bai, J., Yan, S., and Yu, X. (2021). Stability Control of Gob-Side Entry Retained under the Gob with Close Distance Coal Seams. *Int. J. Min. Sci. Technol.* 31, 321–332. doi:10.1016/j.ijmst.2020.11.002
- Zhang, C., Zhao, Y., Han, P., and Bai, Q. (2022). Coal Pillar Failure Analysis and Instability Evaluation Methods: A Short Review and Prospect. *Eng. Fail. Anal.* 138, 1–19. doi:10.1016/j.engfailanal.2022.106344
- Zhu, S., Chen, C., Mao, F., and Cai, H. (2021). Application of Disturbed State Concept for Load-Transfer Modeling of Recoverable Anchors in Layer Soils. *Comput. Geotechnics* 137, 1–16. doi:10.1016/j.compgeo.2021.104292
- Zou, J., and Zhang, P. (2019). Analytical Model of Fully Grouted Bolts in Pull-Out Tests and *In Situ* Rock Masses. *Int. J. Rock Mech. Min. Sci.* 113, 278–294. doi:10.1016/j.ijrmms.2018.11.015
- Zuo, J.-p., Wen, J.-h., Li, Y.-d., Sun, Y.-j., Wang, J.-t., Jiang, Y.-q., et al. (2019). Investigation on the Interaction Mechanism and Failure Behavior between Bolt and Rock-like Mass. *Tunn. Undergr. Space Technol.* 93, 103070. doi:10.1016/j.tust.2019.103070

Conflict of Interest: HL is employed by the company China National Coal Group Corporation.

The remaining authors declare that the research was conducted in the absence of any commercial or financial relationships that could be construed as a potential conflict of interest.

Publisher's Note: All claims expressed in this article are solely those of the authors and do not necessarily represent those of their affiliated organizations, or those of the publisher, the editors, and the reviewers. Any product that may be evaluated in this article, or claim that may be made by its manufacturer, is not guaranteed or endorsed by the publisher.

Copyright © 2022 Chen, Li, Zhao, Zhao, Zhang, Zhang and Li. This is an open-access article distributed under the terms of the Creative Commons Attribution License (CC BY). The use, distribution or reproduction in other forums is permitted, provided the original author(s) and the copyright owner(s) are credited and that the original publication in this journal is cited, in accordance with accepted academic practice. No use, distribution or reproduction is permitted which does not comply with these terms.



OPEN ACCESS

EDITED BY
Shuren Wang,
Henan Polytechnic University, China

REVIEWED BY
Jin Yu,
Huaqiao University, China
Yukun Ji,
Independent Researcher, Switzerland

*CORRESPONDENCE
Bo Wang,
wangbo1983@cumt.edu.cn

SPECIALTY SECTION
This article was submitted to
Geohazards and Georisks,
a section of the journal
Frontiers in Earth Science

RECEIVED 11 May 2022
ACCEPTED 28 June 2022
PUBLISHED 22 July 2022

CITATION
Wang B, Liu Z and Yuan S (2022),
Behavior of large shaft sinking
headframe subjected to uneven
foundation settlement.
Front. Earth Sci. 10:941126.
doi: 10.3389/feart.2022.941126

COPYRIGHT
© 2022 Wang, Liu and Yuan. This is an
open-access article distributed under
the terms of the [Creative Commons
Attribution License \(CC BY\)](https://creativecommons.org/licenses/by/4.0/). The use,
distribution or reproduction in other
forums is permitted, provided the
original author(s) and the copyright
owner(s) are credited and that the
original publication in this journal is
cited, in accordance with accepted
academic practice. No use, distribution
or reproduction is permitted which does
not comply with these terms.

Behavior of large shaft sinking headframe subjected to uneven foundation settlement

Bo Wang^{1,2*}, Zhiqiang Liu^{1,2} and Shuai Yuan²

¹State Key Laboratory for Geomechanics and Deep Underground Engineering, China University of Mining and Technology, Xuzhou, China, ²School of Mechanics and Civil Engineering, China University of Mining and Technology, Xuzhou, China

Deep mining is an inevitable trend in China and the world, for which the construction of deep and large vertical shafts is the primary task. A shaft sinking headframe is a basic structure for supporting various hoisting and sinking equipment during vertical shaft construction. The design of the shaft sinking headframe is challenging due to the significant differences in the geometry and working load compared to conventional steel structures. Recently, the effect of uneven foundation settlement on the shaft sinking headframe has been of great concern when sinking shafts by the freezing sinking method or in permafrost soil areas. In this study, finite element calculations were performed to investigate the mechanical behavior of the SA-3 shaft sinking headframe under uneven foundation settlement (0.001–0.006 *L*) and normal working-load conditions. The results indicate that the most unfavorable condition for the stress of members is the diagonal double foundation settlement, and in the view of the geometric offset, the most unfavorable condition is the same-side double foundation settlement. The corner members near the settled foundation were changed from a state of compression to tension. Uneven foundation settlement of less than 0.001 *L* is acceptable for the safety and service performance of the shaft sinking headframe. These criteria can be used for reference in engineering practice.

KEYWORDS

shaft sinking headframe, uneven foundation settlement, FE analysis, mechanical behavior, deep mining

Introduction

Shaft sinking headframes are a basic structure for supporting various hoisting and sinking equipment during shaft construction. It mainly consists of a sheave wheel platform and a muck discharging platform (Wang, 2018a). After shaft construction, the shaft sinking headframe will be replaced by a permanent headframe to meet the needs of mine production. Therefore, in the general sense of engineering, the shaft sinking headframe is a temporary structure and needs to have advantages of installation, simple structure, and convenient transport.

During the period from 1965 to 1986, seven steel pipe shaft sinking headframes were widely used in China and finalized as types I, II, III, III_G, IV, IV_G, and V by the Ministry of

Coal Industry of China (Wang, 1988). However, with the increasing demand for deep mining, the vertical shafts being sunk in China are tending to get deeper or larger (Yu and Shi, 1991; Qi and Pu, 2013; Liu et al., 2017a). Until recently, the maximum vertical shaft depth in China was 1915 m (under construction, auxiliary shaft of Sanshandao Gold Mine) and the maximum vertical shaft internal diameter was 11 m (under construction, auxiliary shaft of Sanshandao Gold Mine), respectively. To meet the demands of deep (depth of 1,000–1,500 m), large (internal diameter of 10–12 m) vertical shaft constructions, several new large shaft sinking headframes have been developed by researchers and engineers, such as Wang (Wang et al., 2012; Wang, 2018b), who presented the design idea and application of two new shaft sinking headframes and classified them as type VI and VII. Liu et al. (Liu et al., 2017a; Liu et al., 2017b) also proposed a series of new large shaft sinking headframes based on the study of the National High Technology Research and Development Program of China (Study of key technology and equipment on large sinking headframes and shaft wall hanging method). The new large shaft sinking headframes can be divided into two categories: the SA set with a single sheave wheel platform and the SM set with a double sheave wheel platform (Wang et al., 2017). For each category, three specifications, which are suitable for internal shaft diameters of 6–8 m, 8–10 m, and 10–12 m, respectively, are included. These developments in the shaft sinking headframe have successfully supported deep and large shaft construction in China (Wang et al., 2019).

Design of the shaft sinking headframe is challenging due to the significant differences in the geometry, rigidity, and behavior of shaft sinking headframes compared to conventional steel structures (Shu et al., 2016; Hardy, 2019). The differences are related to the main purpose of the shaft sinking headframe, which is the support of hoisting and sinking equipment. However, for the design of shaft sinking headframes, there are no special codes and standards to refer to, nor are there regulations for the behavior of shaft sinking headframes against the differential foundation settlements (Xiao et al., 2009; Lu and Ma, 2016; Wang, 2018b). The structure of the shaft sinking headframe is redundant and sensitive to uneven foundation settlement. On the one hand, uneven foundation settlement will induce large secondary stress in members and thus reduce their bearing capacity. On the other hand, it will cause inclination of the shaft sinking headframe, which directly affects the overall stability of the shaft sinking headframe, causes offset of the hoisting centerline, and thus, affects the safety of the hoisting system.

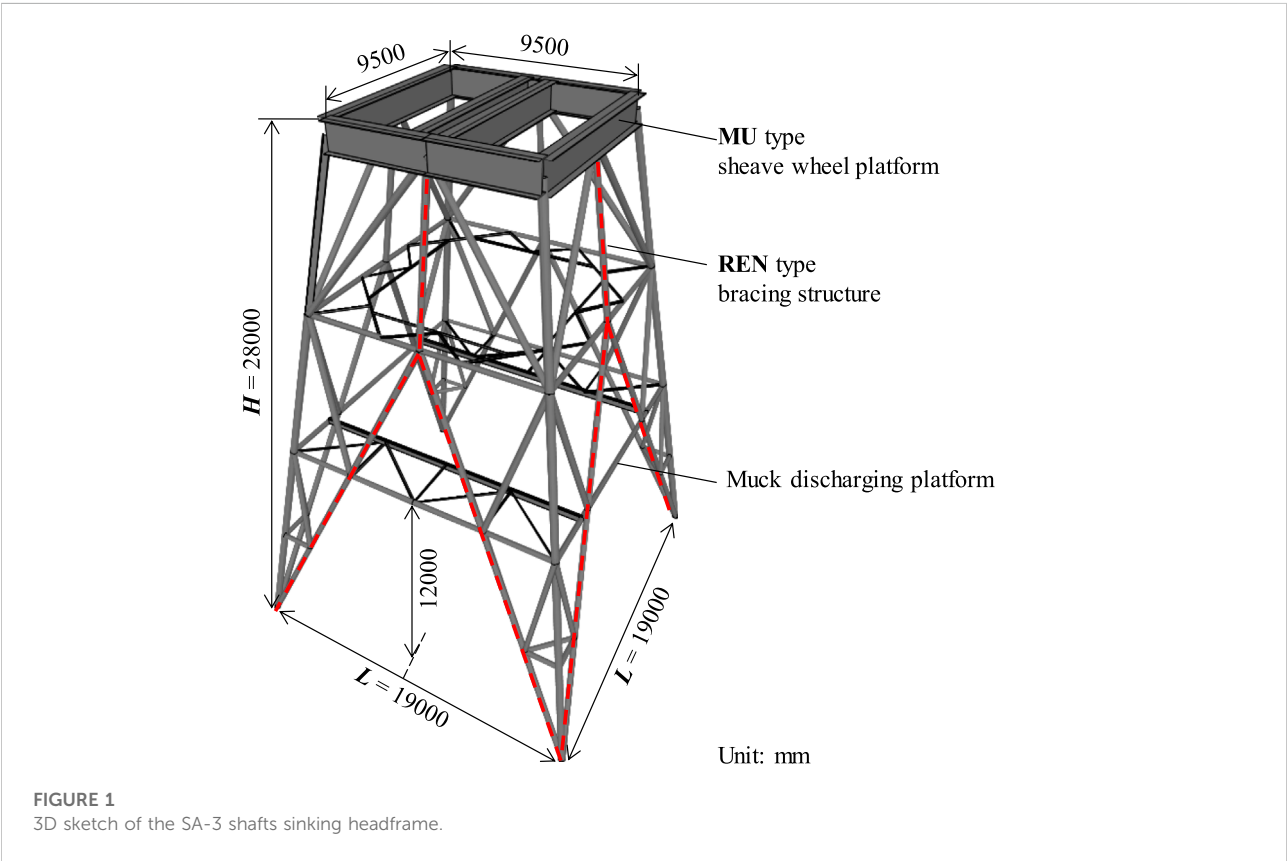
As noted by Liu et al. (Liu et al., 2005), when using the freezing sinking method or in permafrost soil areas, the frost heave and thawing settlement may cause uneven uplift or settlement of the foundation and thus result in large secondary stress, excessive deformation, overall tilting, and even collapse of the shaft sinking headframe. The effect of the uneven settlement of the foundation on the superstructure has

been of much concern to engineers. Chen and Shi (Chen and Shi, 1999; Chen, 2014) studied the strain and stress of a multi-rope hoisting steel headframe (permanent shaft headframe) subjected to the unequal settlement of foundations through model tests and theoretical analysis. The weak aspects of the steel shaft permanent headframe were: the torsion of members; weak axial strength of cross section of members; rigidity of the corner post; and sensitivity to uneven settlement. Liu and Zheng (Liu and Zheng, 2004) simulated the ground as an elastic support to investigate the influence of the ground's unequal settlement on the steel structure's behavior and found that the distance of the columns was an important factor affecting the internal force redistribution caused by unequal settlement. Wang et al. (Wu, 2006) investigated the uneven settlement of the Xinli auxiliary shaft tower and found that the differential settlement between the southeast corner and northwest corner of the shaft tower was about 80 mm during a 250 day monitoring period. The research indicated that the melting of frozen soil, load eccentricity, and groundwater pumping were the three main factors affecting the uneven subsidence of the shaft tower foundation. Xiao et al. (Yang and Chen, 2015) presented details of uneven settlement and reinforcement of a type V shaft sinking headframe foundation after the freezing and sinking of the south return-air shaft at Tunliu Mine. After thawing the frozen wall, the shaft sinking headframe foundation sunk 15, 67, 14, and 88 mm in the southeast, northeast, southwest, and northwest, respectively, and, correspondingly, the east and west sides of the sheave wheel platform moved northward by 124 and 143 mm. Although it is important to consider the total displacement of the foundation, the differential settlement is very important to the behavior of the shaft sinking headframe and must be considered in its structural design (Dong et al., 2000). Due to the complicated physical and engineering properties of subsoil, phenomenon of uneven foundation settlement is inevitable in many cases and it can further lead to many engineering problems such as bearing capacity losses and even overturning of superstructure. At present, few studies focus on the behavior of shaft sinking headframes under uneven foundation settlement. The related technical qualifications and application scope are not yet clear.

Therefore, in this paper, we took a type SA-3 shaft sinking headframe as an example to study its behavior and influence mechanism under the uneven settlement of foundations. The type SA-3 is one of the newly developed shaft sinking headframes with a single sheave wheel platform and has been used at the Sishanling auxiliary shaft, which has a net diameter of 10 m and a depth of 1,503 m. The resultant stress of the SA-3 shaft sinking headframe due to an imposed uneven settlement was analyzed using a finite element model. Compared with those reported earlier by other researchers, the maximum allowable value of the uneven settlement of foundations under normal working conditions was put forward.

TABLE 1 Main parameters of the SA-3 shaft sinking headframe.

Type	Shaft specification (m)		Bearing capacity (kN)		Self-weight of headframe (×10 ³ kg)
	Internal diameter	Depth	Normal working	Rope breaking	
SA-3	10-12	1,200	4,898	10,664	188



Main parameters and analyze methods

Main parameters of the SA-3 shaft sinking headframe

The SA-3 shaft sinking headframe was designed for sinking vertical shafts with an internal diameter of 10–12 m and a depth of 1,200 m. The structure and major dimensions of the SA-3 shaft sinking headframe are shown in Table 1 and Figure 1.

The SA-3 shaft sinking headframe adopts an MU type sheave wheel platform and an REN type bracing frame and achieves a maximum bearing capacity greater than 10,000 kN under the rope breaking condition. The height of the SA-3 shaft sinking headframe is 28 m, and sizes of the sheave wheel platform and bottom section of the SA-3 shaft sinking headframe are 9.5 and 19 m, respectively.

As shown in Figure 2, the sinking equipment on the SA-3 shaft sinking headframe mainly includes: four hoisting buckets (one double-hook hoisting and two single-hook hoisting), two central rotary muckers, a movable metal form (four wire ropes for suspending), a four-layer sinking platform (six wire ropes for suspending, four of them are used as guide ropes for the bucket), and a safety ladder, cables, pipes, etc.

Loads acting on the shaft sinking headframe generally include permanent, variable, and special loads. Permanent loads refer to the self-weight of the shaft sinking headframe and sinking equipment. Variable loads refer to the loads that may change during shaft sinking, such as the working load of the hoisting wire rope, wind load, etc. Special loads refer to the breaking load of the hoisting wire rope, because the bucket is running at high speeds, and accidents, like jamming, serious over-winding, or cable slipping away from the sheave, are more

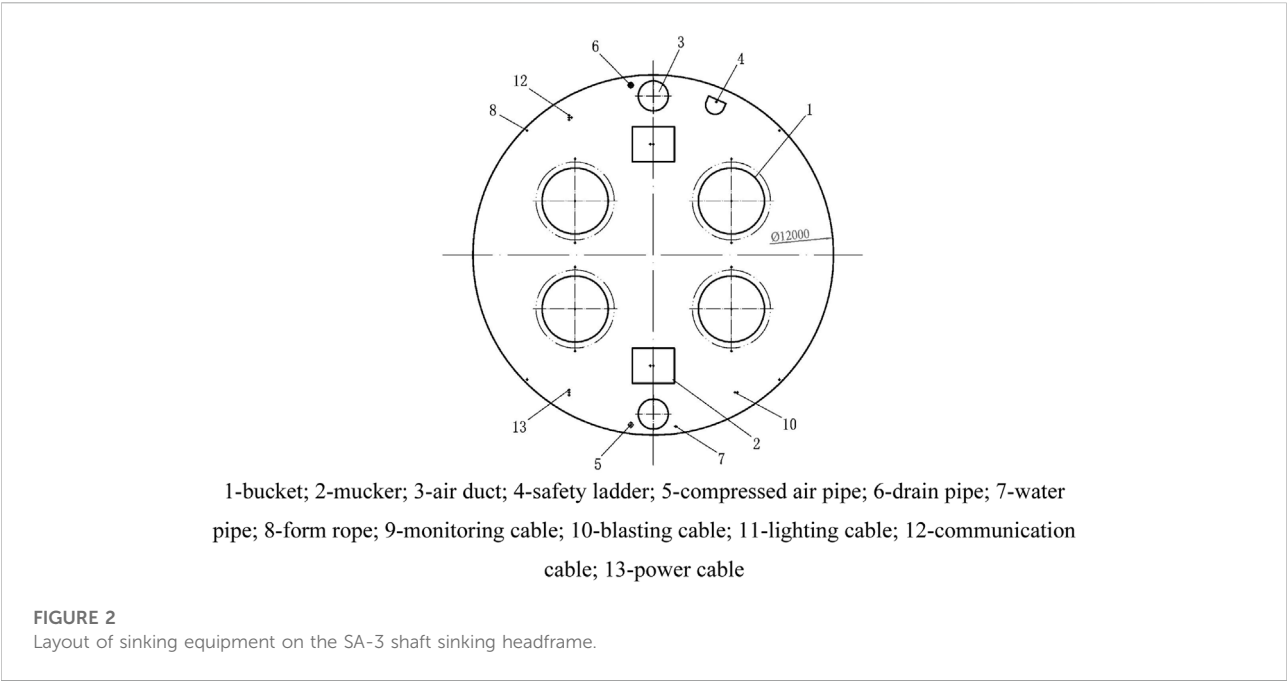


TABLE 2 Loads applied to the SA-3 shaft sinking headframe under normal working conditions.

Load condition	Main hoisting (kN)		Secondary hoisting (kN)		Guide ropes (kN)	Mucker (kN)	Form ropes (kN)	Safety ladder (kN)	Cables (kN)			Total (kN)
	1st	2nd	1st	2nd					Blasting	Communication	Power	
Normal working	273	273	273	273	236*8	216*2	281*4	58	54	120	130	4,898
Rope breaking	2,104	546	2,104	2,104	236*8	216*2	281*4	58	54	120	130	10,664

likely to happen. In design, the following two load conditions shall be taken into consideration: the normal working condition and the rope breaking condition.

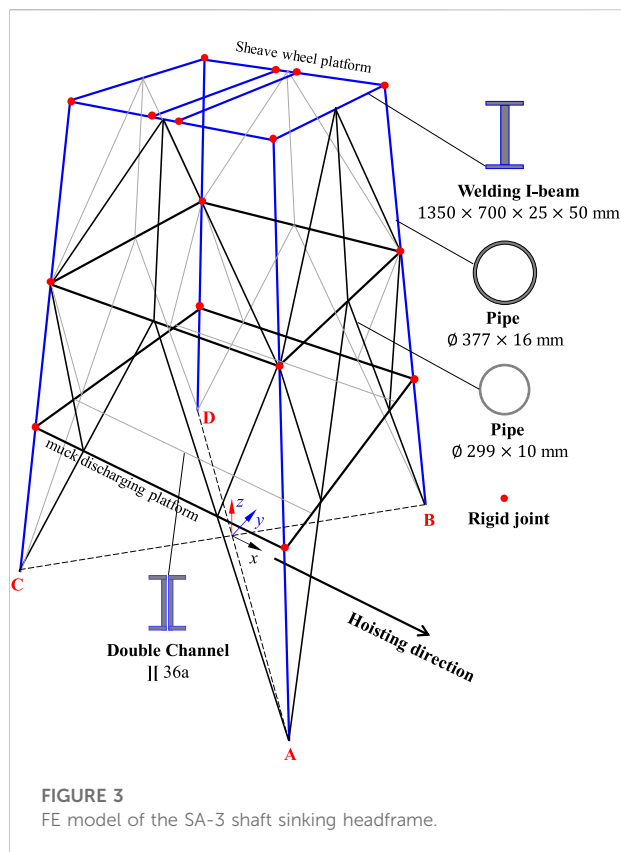
In the normal working conditions, the weight of the shaft sinking headframe and accessory equipment and the working loads of various hoisting and suspending ropes are included.

In the rope breaking condition, the considered loads include the weight of the shaft sinking headframe and accessory equipment, the breaking load of one hoisting rope, the double working load of the yoke rope, and the working load of the other ropes. In general, the partial factors of the permanent and variable loads are selected as 1.2 and 1.4 under normal working conditions and are selected as 1.0 under rope breaking conditions. The values of the loads under the working and rope breaking conditions are listed in Table 2. It can be seen that the total loads applied to the SA-3 shaft sinking headframe under normal working conditions and rope breading

conditions are approximately 5,000 kN and 10,000 kN, respectively.

Finite element analysis of the SA-3 shaft sinking headframe

The finite element (FE) analysis method is effective for evaluating the behavior and strength of the space steel pipe truss structure. In this paper, SAP 2000 was used to model the behavior of the SA-3 shaft sinking headframe subjected to uneven foundation settlement. As shown in Figure 3, a finite element model was built in accordance with the SA-3 structural design drawings. Sections of the boundary beam and middle beam on the sheave wheel platform were welded I-beams with dimensions of H1350 × 700 × 25 × 50 mm. Sections of the main bracing structure members are pipes with dimensions of Ø377 ×



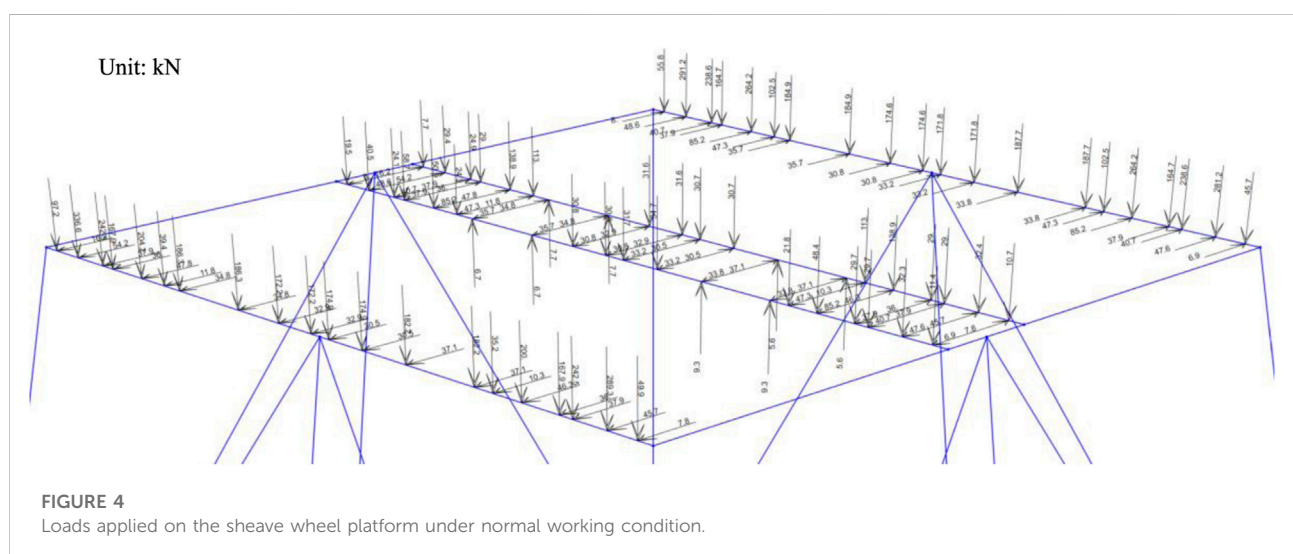
16 mm and $\text{Ø}299 \times 10$ mm, respectively. The main beam on the muck discharging platform is double channels of $\text{||}36\text{a}$. Because this study focuses on the behavior of the structural member, the connections between the members were not addressed. We assumed that the beam-to-beam joint and beam-to-corner post joint are rigid connections (red point shown in Figure 3) and other joints of the members are pinned for FE modeling. This

assumption more properly presents the real structural behavior of the shaft sinking headframe. In SAP 2000, the pin connections of the members can be simulated by releasing one or more of the element degrees of freedom from the joint. For rigid connections, the three translational and three rotational degrees of freedom of the frame element are continuous. For pin connections, rotation at the end of the element should be released, and this assures that the moment is zero.

In the FE analysis, only normal working conditions were considered. Based on the layout of the sinking equipment on the SA-3 shaft sinking headframe, loads under normal working conditions were applied to the FE model. Figure 4 shows the loads applied on the sheave wheel platform, each load was resolved into vertical and horizontal components at the connection of the secondary beam (for installation of hoisting and suspension sheaves) and applied to the FE model as a concentrated load. The weight of the members is calculated automatically by the program. The reliability of the FE model was verified by comparison with model test results in the structural design stage of the SA-3 shaft sinking headframe.

Uneven foundation settlement of the SA-3 shaft sinking headframe

The foundation form of the shaft sinking four posts is independent of the foundation, and the settlement does not affect either. Therefore, there are various possible combinations of uneven settlement between the four post foundations, such as single, same-side, diagonal, double, and three-foundation settlement. According to the symmetrical characteristics of the bracing structure of the SA-3 shaft sinking headframe, the effect of three foundation settlements will be similar to a single foundation settlement, more specifically, it will be similar to the effect of single foundation



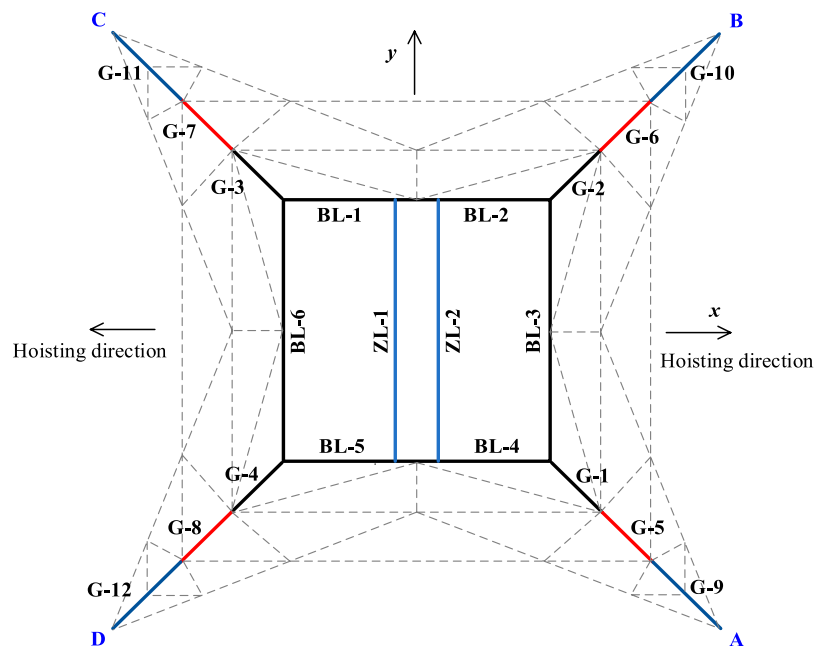


FIGURE 5
Diagram of uneven foundation settlement of the SA-3 shaft sinking headframe.

TABLE 3 Combinations of the uneven foundation settlement on the SA-3 shaft sinking headframe.

Case	Combination of foundation	Load condition	Settlement of foundation (mm)		
			A	B	C
1–6	Single foundation	Normal working	20/40/60/80/100/120	—	—
7–12	Same-side double foundation	Normal working	20/40/60/80/100/120	20/40/60/80/100/120	—
13–18	Diagonal double foundation	Normal working	20/40/60/80/100/120	—	20/40/60/80/100/120

uplift. The effect of same-side double foundation settlement is more likely to cause inclination and reduce the overall stability of the shaft sinking headframe. Referring to the standard for the design of mine headframes in China (GB 50385-2018), the allowable foundation deformation of mine headframes is as follows: for a single-diagonal-bracing steel headframe, the settlement difference between foundations should not exceed $0.001 L$, in which L is the center-to-center spacing of the adjacent foundation; for a double-diagonal-bracing steel headframe, the settlement difference between foundations should not exceed $0.0005 L$; and for both, the maximum settlement should be less than 80 mm.

Based on the above considerations, in this study, the following three combinations of uneven foundation settlements are discussed: Single, same-side, and diagonal double foundation settlement with a maximum uneven

settlement of 160 mm. Details of the considered uneven foundation settlement combinations are shown in Figure 5 and Table 3.

Results and analysis

Mechanical performance of the SA-3 subjected to uneven foundation settlement

Figure 6 shows the axial force diagram of members caused by the settlement of a single foundation A under normal working conditions. From the figure, it can be seen that the axial force of the members near foundations A and C was changed from compression to tension, whilst the members near foundations

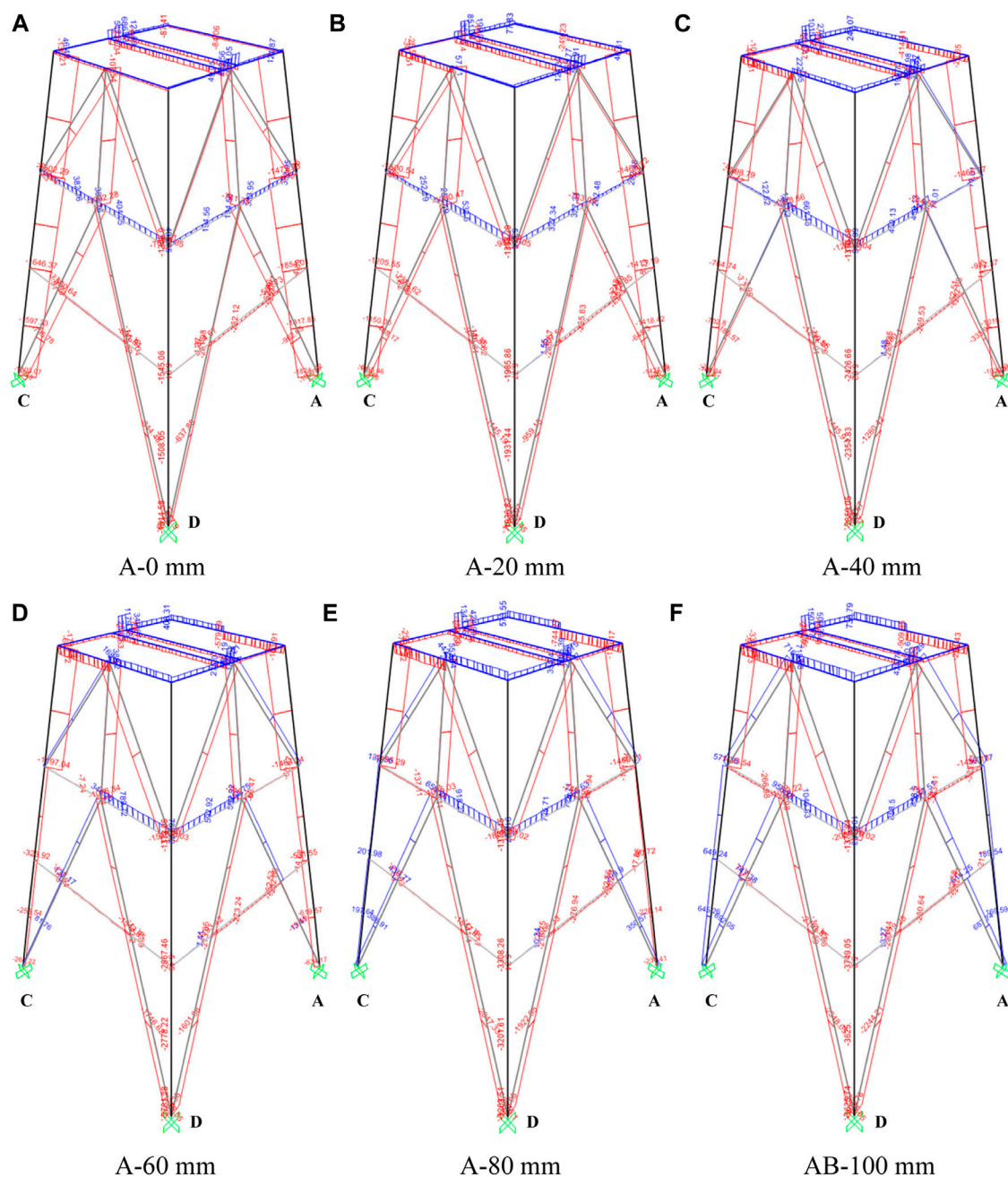


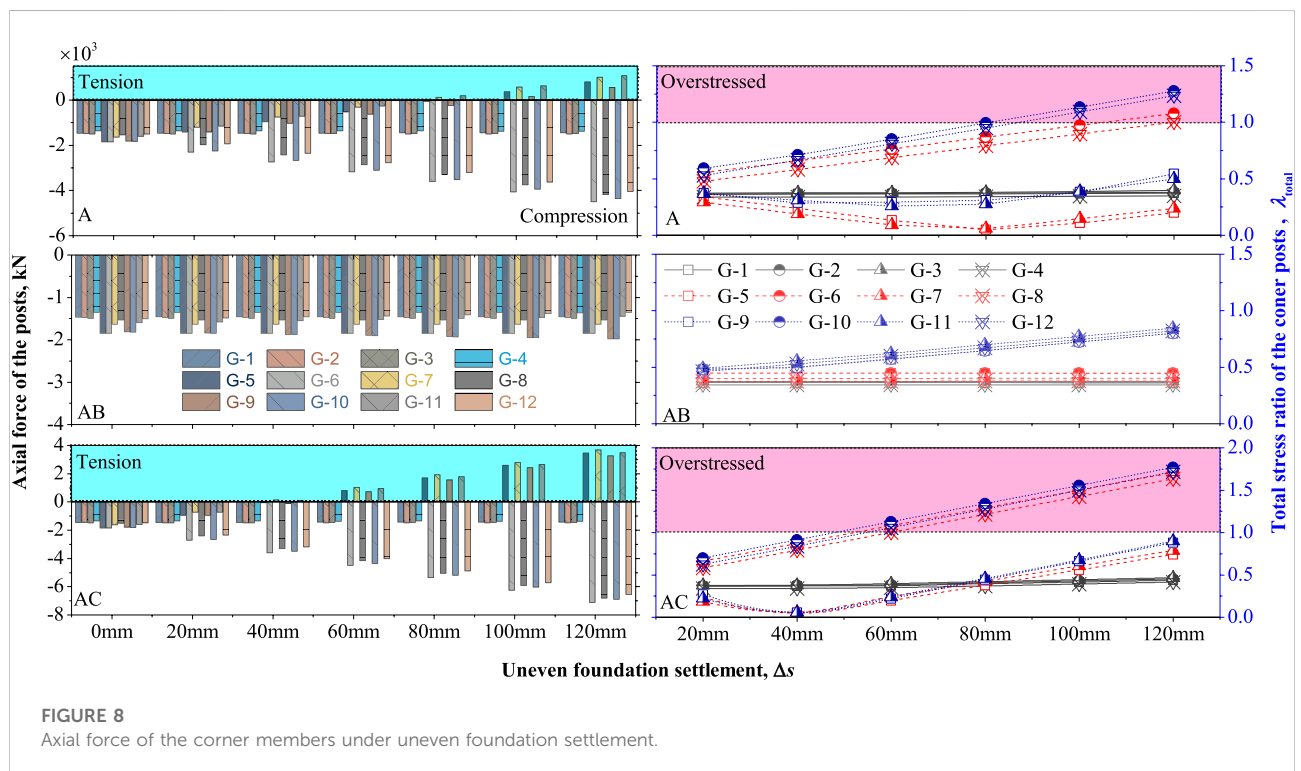
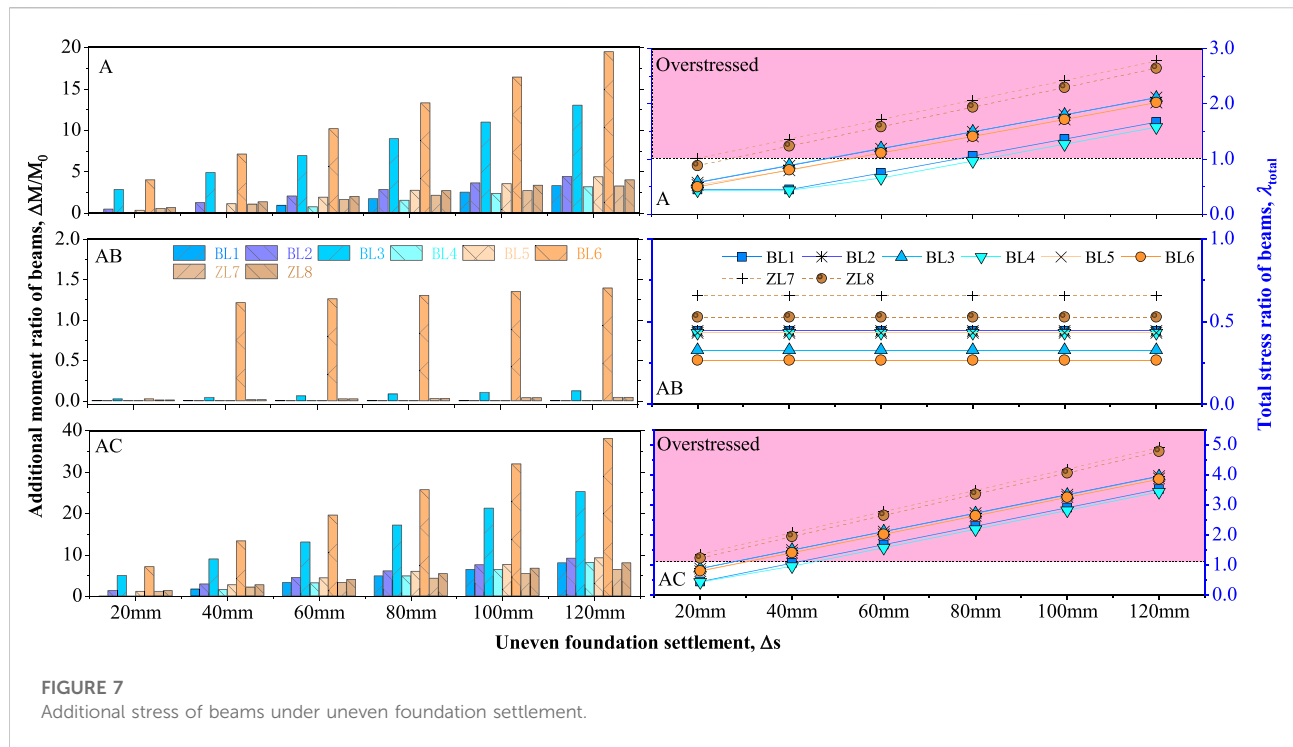
FIGURE 6

Axial force of the members versus the settlement of a single foundation A. (A) A-0 mm (B) A-20 mm (C) A-40 mm (D) A-60 mm (E) A-80 mm (F) AB-100 mm

B and D were subjected to compression and their axial force increased as the foundation settlement increased.

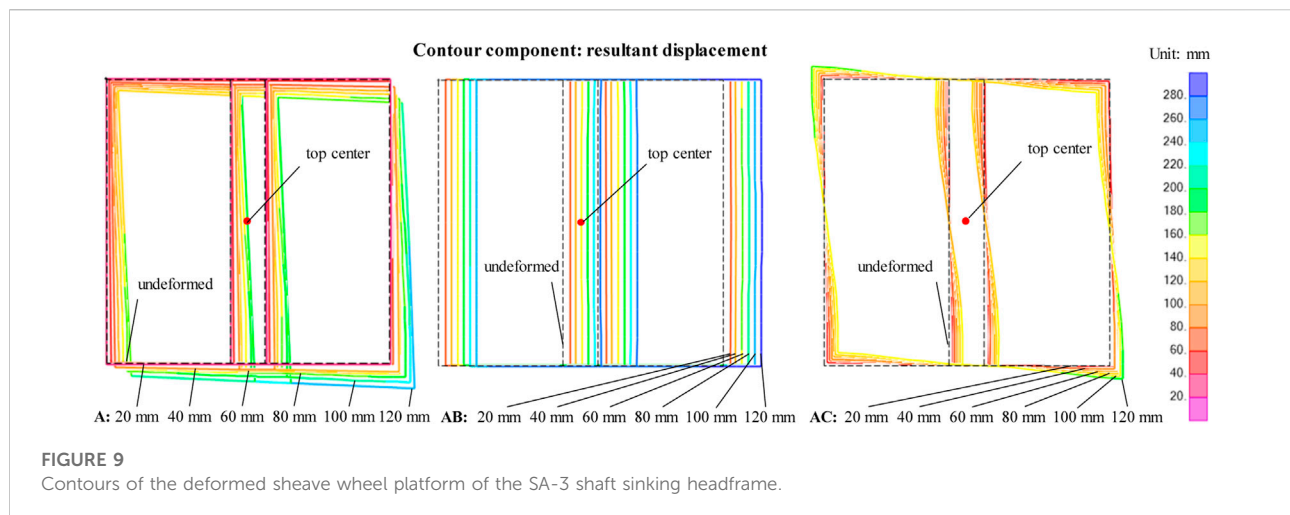
The additional stress ratio ($\Delta\lambda_{\text{total}}$, which is the additional total stress ratio caused by uneven foundation settlement compared to the initial state of members under normal working conditions) of beams on the sheave wheel platform and total stress ratios ($\lambda_{\text{total}} = \lambda_N + \lambda_{M\text{maj}} + \lambda_{M\text{min}}$, in which λ_N is the

axial stress ratio, $\lambda_{M\text{maj}}$ is the moment stress ratio in the principal axis direction, and $\lambda_{M\text{min}}$ is the moment stress ratio in the secondary axis direction) of the corner members are plotted in Figures 7, 8. Figure 7 shows that additional stress occurs in the middle beams, ZL-1 and ZL-2. The additional stress ratio is about 35% under a single foundation settlement of 20 mm ($0.001 L = 19 \text{ mm}$), and approximately 141% under a diagonal double



foundation settlement of 20 mm. In Figure 8, the results show that the axial force of the corner posts has essential variations under single foundation settlement and diagonal double

foundation settlement. The states of the corner posts, G-5, G-9 (foundation A side), G-7, and G-11 (foundation C side), changed from compression to tension. In view of the total



stress ratio, 60 mm of single foundation settlement (max. additional stress ratio is 51% in G-3) and 40 mm of diagonal double foundation settlement (max. additional stress ratio is 82% in G-2) are acceptable for the safety of the corner members.

Deformation behavior of the SA-3 subjected to uneven foundation settlement

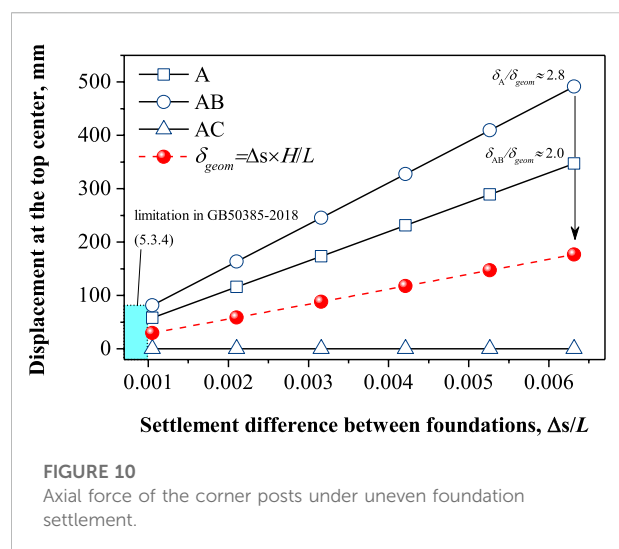
Figure 9 shows the contours of the displacement of the deformed sheave wheel platform under various foundation settlements. The results show that the displacements were mainly toward the side of the settled foundation and increased as the uneven foundation settlement increased. At the maximum foundation settlement of 120 mm, displacements of the top corners reached 263 mm, 288 mm, and 175 mm under a combination of single A, double AB, and AC foundation settlement.

The ratio of the resultant displacement to the geometric offset is important in evaluating the ability of the shaft sinking headframe subjected to uneven foundation settlement. The geometric offsets at the top center position of the shaft sinking headframe can be approximately calculated according to the following formula:

$$\delta_{geom} = \frac{\Delta s \cdot H}{L} \quad (1)$$

Here Δs is the settlement difference between foundations in mm; H is the top surface height of the sheave wheel platform; and L is the distance between the corner members at the bottom of the SA-3 shaft sinking headframe.

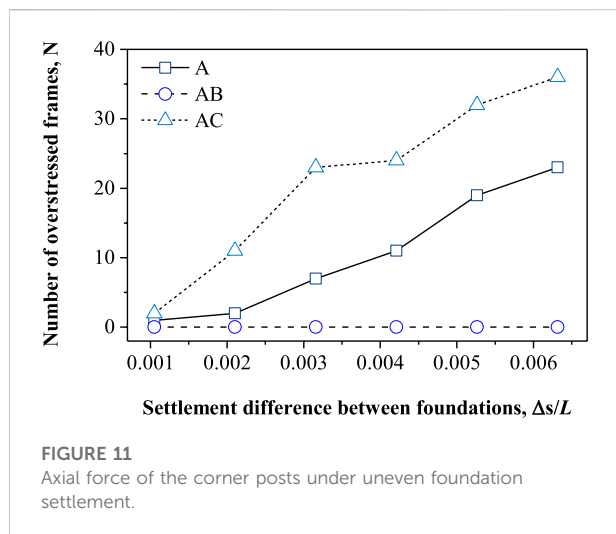
Figure 10 shows the analyzed displacement in the X-Y plane at the top center position of the SA-3 shaft sinking headframe by FE analysis. It can be seen that the resultant displacement in the



X-Y plane occurred under the conditions of the same-side double and single foundation settlement. The displacement in the X-Y plane increased almost linearly with the foundation settlement. The ratios of the resultant displacement in the X-Y plane to the geometric offset were 2.0 and 2.8, respectively. There was no significant displacement in the X-Y plane at the top center of the SA-3 shaft sinking headframe under the condition of the diagonal double foundation settlement.

Discussion

As mentioned above, uneven foundation settlement can cause additional stress on members and geometric offset on sheaves, which affects the safety and service performance of the shaft sinking headframe. The accurate prediction of the adverse effects of



uneven foundation settlement on shaft sinking headframe is of practical importance. In general, the total stress ratio of the members should be less than 1.0 (standard for designing steel structures: GB 50017-2017) and the distance between the sinking platform and the concrete shaft lining should not exceed 100 mm (code for construction of shaft and roadway of coal mine: GB 50511-2010). Therefore, determining the criteria of uneven foundation settlement should consider both the stress and deformation behavior of the shaft sinking headframe structure. Figure 11 plots the number of overstressed frames versus the uneven foundation settlement ratio ($\Delta s/L$). It shows that the numbers of overstressed frames under the foundation settlement of AC and A were larger, and the number of overstressed frames under the foundation settlement of AB was comparatively small. For safety considerations, the number of overstressed frames can be ignored when the uneven foundation settlement is less than $0.001 L$. Meanwhile, as shown in Figure 10, displacement at the top center of the sheave wheel platform was less than 100 mm when the uneven foundation settlement was less than $0.001 L$. This result is consistent with the standard for design of mine headframes (GB 50385-2018), which makes the result reliable and very useful in engineering practice. At present, although there are grouting reinforcement and rectification technologies to deal with the uneven foundation settlement under emergency conditions, we should pay more attention to geotechnical investigation and to prevent the uneven settlement of foundations.

Conclusion

In this study, an FE analysis was performed to investigate the effects of uneven foundation settlement on the mechanical and deformation behavior of the shaft sinking headframe. The criterion of the shaft sinking headframe subjected to uneven foundation settlement was discussed. The main conclusions are as follows:

- 1) Uneven foundation settlement can cause additional stress of members and geometric offset of sheaves and affect the safety and service performance of the shaft sinking headframe. The most unfavorable condition for the stress of members is diagonal double foundation settlement. In contrast, the most unfavorable condition for the geometric offset of the structure is same-side double foundation settlement.
- 2) The axial force of the members near the settled foundation changed from compression to tension, whilst the members near the unsettled foundation were subjected to compression and their axial force increased as the uneven foundation settlement increased.
- 3) Displacement in the X-Y plane mostly occurred under conditions of same-side double and single foundation settlement. The displacement in the X-Y plane increased almost linearly with the uneven foundation settlement.
- 4) Acceptable uneven foundation settlement for the shaft sinking headframe can be determined as $0.001 L$. This result is reliable and can be used for reference in engineering practice.

Data availability statement

The original contributions presented in the study are included in the article/Supplementary material; further inquiries can be directed to the corresponding author.

Author contributions

Data curation: SY; writing, original draft preparation: BW; writing, review, and editing: ZL.

Funding

This research was supported by the National Science Foundation of China (Grant Nos 51874286 and 51408595) and the Natural Science Foundation of Jiangsu Province of China (Grant No. BK20140203).

Acknowledgments

The authors gratefully appreciate the support.

Conflict of interest

The authors declare that the research was conducted in the absence of any commercial or financial relationships that could be construed as a potential conflict of interest.

Publisher's note

All claims expressed in this article are solely those of the authors and do not necessarily represent those of their affiliated

organizations, or those of the publisher, the editors, and the reviewers. Any product that may be evaluated in this article, or claim that may be made by its manufacturer, is not guaranteed or endorsed by the publisher.

References

- Chen, H., and Shi, T. S. (1999). Research on experimental model of multirope hoisting steel headframe influenced by artificially frozen ground. *J. China Univ. Min. Technol.* 28, 574–577.
- Chen, J. J. (2014). *Study on the structure selection and mechanical properties of the large sinking headframe*. Xuzhou: China University of Mining and Technology. [masters dissertation].
- Dong, J., Deng, H. Z., Ma, X., Wang, Z. M., and Jiao, L. P. (2000). Nonlinear full process analysis of steel super structural damage due to uneven ground settlement. *China Civ. Eng. J.* 33, 101–106.
- Hardy, M. (2019). "Seismic elastic behaviour of mine headframes," in *Proceedings of the 4th international conference on shaft design and construction* (Toronto: The Canadian Institute of Mining, Metallurgy and Petroleum), 203–212.
- Liu, B., Wang, W. M., and Chen, Z. D. (2005). Settlement analysis of permanent headframe of Liangbaosi auxiliary shaft. *Mine Constr. Technol.* 26, 36–39.
- Liu, C., and Zheng, G. (2004). Analysis of the influence of ground unequal settlement on the structure with elastic support model method. *J. Build. Struct.* 25, 124–128.
- Liu, Z. Q., Hong, B. Q., and Long, Z. Y. (2017). 60 years science and research achievements of Mine construction. *Mine Constr. Technol.* 38, 1–6.
- Liu, Z. Q., Wang, B., Du, J. M., and Li, M. L. (2017). New mine shaft sinking headframe with single platform applied to construction of deep and large diameter mine shaft. *Coal Sci. Technol.* 45, 24–29.
- Lu, Z. K., and Ma, Z. C. (2016). Influence of differential foundation settlement on steel headframe. *Coal Eng.* 48, 28–30.
- Qi, H. G., and Pu, Y. N. (2013). Current situation and development trend of deep mine shaft construction technology. *Mine Constr. Technol.* 34, 4–7.
- Shu, Q. J., Yuan, G. L., Huang, Z. H., and Ye, S. (2016). The behaviour of the power transmission tower subjected to horizontal support's movements. *Eng. Struct.* 123, 166–180. doi:10.1016/j.engstruct.2016.05.027
- Wang, B., Liu, Z. Q., and Du, J. M. (2019). "Design and application of new series of large shaft sinking headframe," in *Proceedings of the 4th international conference on shaft design and construction* (Toronto: The Canadian Institute of Mining, Metallurgy and Petroleum), 399–405.
- Wang, B., Liu, Z. Q., Du, J. M., Wang, S., and Fan, H. (2017). Design method of double platform sinking headframe of large mine shaft. *Coal Sci. Technol.* 45, 161–167.
- Wang, J. F. (1988). *Illustration books of shaft sinking engineering*. 1st ed. Beijing: China Coal Communications Industry Publishing Home.
- Wang, P. (2018). *The influence of various burst loads on the bearing capacity and stability of steel derrick*. Xuzhou: China University of Mining and Technology. [masters dissertation].
- Wang, P. Y. (2018). Development and prospect of construction technique for super-large diameter deep vertical shaft. *Coal Eng.* 50, 47–50.
- Wang, S. H., You, C. A., Ma, Z. Z., Qiu, Y., and Lv, Y. X. (2012). Analysis on unequal settlement of auxiliary shaft tower in Xinli. *Geotech. Investig. Surv.* 2, 33–37.
- Wu, Q. M. (2006). *Study on the influence of frost heave on derrick foundation in freezing sinking*. [masters dissertation]. Huainan: Anhui University of Science and Technology.
- Xiao, Q. F., Li, M., Chen, B. J., Wang, L., and Huang, F. C. (2009). Treatment of uneven foundation settlement of freezing shaft sinking headframe. *Mine Constr. Technol.* 30, 37–39.
- Yang, R. S., and Chen, J. (2015). Development status and prospects of mine shaft construction equipment and technology. *Mine Constr. Technol.* 36, 1–4.
- Yu, G. Y., and Shi, T. S. (1991). A study on the calculation of the sinking headframe. *J. China Univ. Min. Technol.* 20, 8–13.



A New Blasting Permeability Enhancement Scheme For Deep-Buried Soft Coal Mining Face Based on Borehole Deformation Characteristics

Dequan Xuan¹, Jianhua Zhang², Gang Huang^{2*}, Peng Li³ and Zhifeng Zhang⁴

¹School of Safety Science and Emergency Management, Wuhan University of Technology, Wuhan, China, ²School of Resources and Environmental Engineering, Wuhan University of Technology, Wuhan, China, ³School of Energy and Environment, Zhongyuan University of Technology, Zhengzhou, China, ⁴Xin'an Coal Mine, Henan Dayou Energy Co., Luoyan, China

OPEN ACCESS

Edited by:

Shuren Wang,
Henan Polytechnic University, China

Reviewed by:

Zhibiao Guo,
China University of Mining and
Technology, Beijing, China
Lang Liu,
Xi'an University of Science and
Technology, China

*Correspondence:

Gang Huang
huanggong2016@whut.edu.cn

Specialty section:

This article was submitted to
Geohazards and Georisks,
a section of the journal
Frontiers in Earth Science

Received: 09 May 2022

Accepted: 21 June 2022

Published: 11 August 2022

Citation:

Xuan D, Zhang J, Huang G, Li P and
Zhang Z (2022) A New Blasting
Permeability Enhancement Scheme
For Deep-Buried Soft Coal Mining
Face Based on Borehole
Deformation Characteristics.
Front. Earth Sci. 10:939360.
doi: 10.3389/feart.2022.939360

When blasting to enhance permeability in deep-buried soft coal mining face with a hard roof whose gas drainage requirement is higher, the charging hole and control hole (which doubles as drainage hole) are easy to be deformed and damaged, seriously affecting the blasting implementation and effect. Combining with the stratum characteristics of soft coal seam and hard surrounding rock, the idea of arranging boreholes near the surrounding rock to reduce deformation, inspired by the end effect, is put forward. Then, the experimental research on the deformation characteristics of boreholes at different distances from the surrounding rock is carried out, and the results show that the closer the borehole is to the roof (floor), the smaller the deformation, under the same stress conditions and within a certain distance. Based on this, a new scheme of arranging control holes and blasting holes near the roof and floor is proposed and designed. The field test results show that the blasting of 60 m deep holes are successfully realized and the remarkable permeability enhancement effect is achieved, verifying the feasibility and effectiveness of the improved scheme. This study explores a new blasting permeability enhancement scheme with practical value and reference significance for deep-buried soft coal mining face with a hard roof.

Keywords: blasting, permeability enhancement, deep buried, soft coal, borehole deformation

INTRODUCTION

Gas dynamic disasters with noteworthy burstiness, destructiveness, and complexity often cause huge casualties and property losses (Yu et al., 2013; Wang et al., 2021), and its most important and fundamental technical means of prevention and control is gas drainage (Li, 2015; Zhou et al., 2016; Nikitenko and Glukhikh, 2021). However, coal seams with the risk of gas-dynamic disasters are always not only with high gas content but of poor permeability, resulting in a small drainage radius and poor drainage effect, which requires permeability enhancement to strengthen gas drainage (Lei et al., 2016; Cheng and Pan, 2020; Zhang et al., 2020).

Among a variety of common technologies of permeability enhancement, controlled blasting with the advantages of simple process and high efficiency, has been more and more widely studied and applied (Bhandari, 1980; Zhang and Liu, 2013; Guo et al., 2020). It is found that the gas drainage rate

of the working face was increased by more than 17% in the pre-drainage test of underground deep hole pre-splitting blasting (Wang et al., 2012). By analyzing the changes in coal stress and longitudinal wave velocity in different blasting ranges, Zhicheng Xie and others predicted the effective cracking radius and effective influence radius and then optimized the drilling layout, and brought the net drainage quantity after blasting which is 1.54~2.24 times higher than that before blasting (Xie et al., 2017). To improve the gas drainage effect of a coal seam with high gas content and low permeability, hydraulic-controlled blasting of a deep hole was carried out to provide pressure relief and to increase the permeability of a coal seam. The mechanism for pressure relief and permeability improvement caused by the hydraulic-controlled blasting was then analyzed. It was found that the outcomes were the result of joint action by the blasting force and the hydraulic pressure (Ye et al., 2017). Based on the analysis of the influence of the charging structure on the propagation characteristics of explosion stress waves and the zoning of blasting cracks, the field test of coal seam deep hole-shaped charge blasting was designed and carried out. The results showed that the charging structure affects the permeability enhancement effect of coal seam deep hole-shaped charge blasting (Guo et al., 2018a). It is calculated that the single drilled fracture crack extension range is 3.11~5.24 m according to the coal seam deep-hole pre-splitting blasting joint mechanism and fracture propagation mechanics model, providing a theoretical basis for choosing the appropriate hole spacing (Ti et al., 2018). The multi-hole pre-splitting blasting technology is proposed and applied and it was found that the permeability of the coal seam which improved by deep hole pre-splitting blasting was 2.5 times than that of the original coal seam (Huang et al., 2019). To reduce gas disasters in low permeability and high-gas coal seams and improve gas pre-drainage efficiency, by comparing and analyzing the damage distribution nephogram of coal and rock mass under the influence of different millisecond blasting time intervals and the blasting effect of the simulation model, the optimal layout parameters of multilayer through cracks were obtained theoretically (Zhao et al., 2021).

These research and application results of blasting permeability enhancement technology have played an important role in coal seam gas control, but most are aimed at shallow or hard coal seams, and focused on the blasting mechanism, charging structure, or permeability enhancement effect. Few studies have been carried out on the problem that the charging hole and control hole (doubles as drainage hole) are easy to be deformed and damaged in deep-buried soft coal seams, which seriously affects the blasting implementation and effect. With the increase of mining intensity and depth, gas dynamic disasters become more and more serious and complex. Not only does the high incidence zone expand from the coal roadway heading face to the mining face with a much wider range, but gas dynamic disasters of the mining face directly covered with hard rock, under the disturbance of roof breaking, often occur in the case of “low threshold”, namely lower than the conventional critical index (Yin et al., 2017; Zhao et al., 2020). It brings many problems to the gas drainage work based on blasting to enhance permeability. First, the deformation and damage of

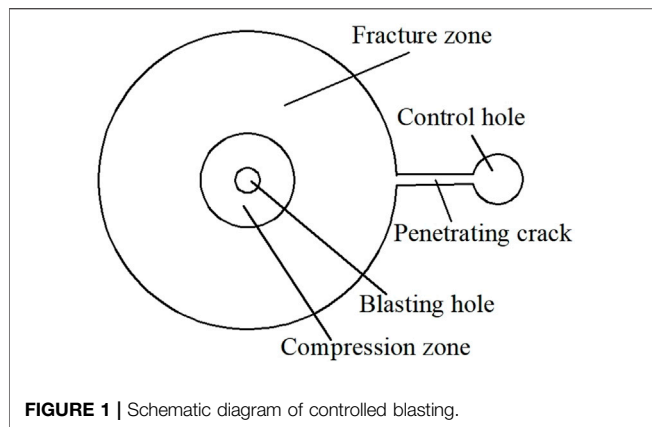
blasting holes and control holes in deep-buried soft coal seams are much more severe, resulting in slow drilling speed, small hole forming depth, low hole forming rate, and short holding time, which makes it difficult to charge in ultra-deep hole required by mining face and easy to block the control hole (doubles as drainage hole) seriously hindering gas drainage (Xue and Feng, 2018; Zhang et al., 2021). Second, with the increase of gas pressure and the decrease of permeability in deep coal bodies, the difficulty of gas drainage increases, but the standard indicators of the mining face are stricter due to the gas dynamic disasters which often occur in the case of “low threshold” under the disturbance of roof breaking. These factors have become the bottleneck problem of deep buried soft coal face gas prevention strengthened by controlled blasting permeability enhancement technology.

Aiming at this, taking 14,020 mining faces of Xin'an Coal Mine as the research background, the targeted research is carried out. On the basis of the permeability enhancement mechanism of deep hole controlled blasting in coal body combined with the stratum characteristics of soft coal seam and hard surrounding rock, the experimental research on the deformation characteristics of boreholes at different distances from the surrounding rock is carried out, and on this basis, a new blasting scheme which can control the borehole deformation and promote the implementation and permeability enhancement is designed. Finally, field tests are carried out to verify the feasibility and effectiveness of the new scheme.

RESEARCH BACKGROUND

The research takes 14,020 mining faces of Xin'an Coal Mine as the background. Xin'an Coal Mine is located in the west of the Henan Province. The only minable No. 21 coal seam in the minefield is of simple structure and stable horizon. As a result of multi-period strong tectonic movements, the whole coal seam universally develops into class III–V soft coal shaped like earth and powder, with less obvious bedding and very low mechanical strength. The coal seam is covered with thick hard sandstone at close range and underlying hard mudstone, forming good engineering geological conditions. Since the “low threshold” gas dynamic disaster of the mining face has occurred many times after the mine enters deep mining, the drainage evaluation indexes gas pressure and gas content are tightened from the original 0.74 Mpa and 8 m³/t to 0.6 Mpa and 6 m³/t, respectively.

The 14020 mining face is located in mining area 14 in the west of the mine. The buried depth of the coal seam in the mining face is about 600 m, the thickness varies from 2.8 to 3.2 m, with an average of 3.1 m; and the dip angle varies from 5° to 8°, with an average of 6°. The false roof of the mining face is not developed, and the direct roof is sandstone with an average thickness of 3 m. The basic roof is medium-grained sandstone with an average thickness of 8.6 m and hard lithology. The false bottom of the mining face is not developed, and the direct bottom is sandy mudstone with an average thickness of 2 m. The basic bottom is mudstone with an average thickness of 10 m.



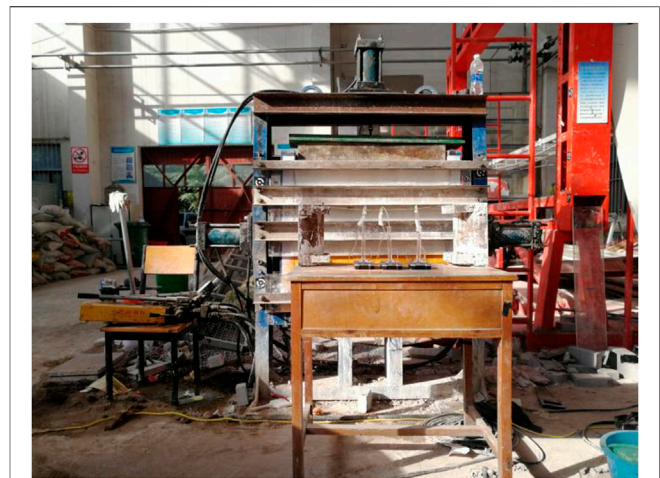
MECHANISM ANALYSIS OF CONTROLLED BLASTING TO INCREASE PERMEABILITY

Analysis of Cracking Effect of Controlled Blasting

When ordinary blasting in the medium far from the free surface, strong shock waves and a large amount of high temperature and high-pressure gas are generated instantly. When the shock wave acts on the medium around the blasting hole, it will form dynamic stress whose strength is far greater than the medium compressive strength, resulting in the strong compression of the medium and the expansion of the original blasting hole, which also consumes a considerable part of energy. After that, the shock wave decays into a stress wave and continues to propagate around, causing the medium under its action to produce radial compression and circumferential tension. When the circumferential tensile stress exceeds the dynamic tensile strength of the medium, radial cracks radiating outward from the explosion center generate and expand continually with the propagation of stress waves until the tensile stress is lower than the medium tensile strength.

After the radial cracks are formed, the high temperature and high-pressure explosive gas quickly flows into these radial cracks promoting the cracks' further expansion in the action pattern of wedges. As the explosive gas expands and cools down, its pressure drops to a certain extent, and the compressive elastic energy accumulated in the medium will be released, forming an unloading wave to propagate towards the center of the blast hole, which turns the medium into a radial tensile state and producing circumferential cracks. The area formed by the intersection of radial fractures and circumferential fractures is called the fracture area. When the stress wave propagates further forward, it has attenuated to the point of being only able to make the medium particles vibrate and propagate in the form of the seismic wave rather than destroy the medium and finally decays to disappear.

Under the strong blasting compression, unlike the near area of the blasting hole in brittle hard rock will be crushed to form a crushing circle, the near area of the blasting hole in plastic soft coal will be locally compacted forming a compaction circle, which consumes more blasting energy and greatly reduces the crack range and permeability enhancement effect (Shakeran et al., 2016;



Cao et al., 2020). For this reason, the controlled blasting technology of adding a control hole at a certain distance from the blasting hole is introduced. When the explosion stress wave propagates to the auxiliary free surface provided by the additional control hole, it will produce reflection forming a tensile stress wave. The reflected wave not only causes the tensile failure of the coal body near the control hole wall but propagates to the center of the blasting hole and superimposes its generated stress on the stress field at the tip of the radial fracture promoting the expansion of radial and circumferential fracture (Guo et al., 2020). In addition, the combined action of the tensile stress caused by the reflected wave and the weak discontinuous wave behind the strong intermittent shock wave front makes the edge of the control hole produce a crack pointing to the blasting hole center and connect with the radial cracks generated firstly (Figure 1).

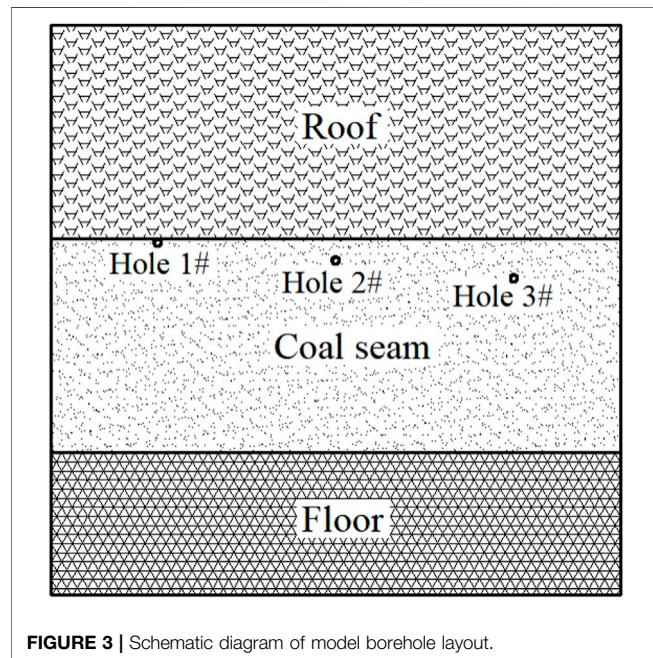
It should be noted that, in addition to the aforementioned functions in blasting cracking, the control hole also compensates for the space required for coal fracture avoiding or greatly reducing the compaction of coal, and improves the utilization rate of blasting energy forming a broader crack network in coal seam (Guo et al., 2018b).

Analysis of Permeability Enhancement Effect of Controlled Blasting

When the gas is extracted by a borehole, the free gas in the coal body flows into the drainage borehole under the action of its pressure and drainage negative pressure, which causes the pressure to decrease and breaks the original dynamic balance state between adsorbed gas and free gas in the coal body, so that part of the adsorbed gas is desorbed into free gas, and then enters the drainage borehole through the coal matrix and fissure in turn. This gas migration expands from the near area of the drainage hole wall to the deep and weakens gradually with the decrease of the drainage negative pressure caused by the increase of the radial distance.

TABLE 1 | Physical model proportioning parameters.

Stratum	Prototype		Model		Proportion and Dosage of Model Materials			
	Thickness(m)	Strength (MPa)	Thickness (cm)	Strength (MPa)	Sand (kg)	Calcium Carbonate (kg)	Cement (kg)	Plaster (kg)
roof	3	64	30	4	68	0	4.08	9.52
coal seam	3.1	3.2	31	0.2	60	3.6	0	8.4
floor	1.9	41.5	19	2.6	46.6	0	2.34	5.49

**FIGURE 3** | Schematic diagram of model borehole layout.

According to the law of mass conservation, the migration process of gas in coal body conforms to the following equation:

$$\frac{\partial m}{\partial t} + \nabla \cdot (\rho q_g) = Qp,$$

where m is the gas content of coal, kg/m^3 ; t is the gas migration time of coal body, s ; ρ is the density of the gas, kg/m^3 ; q_g is the gas seepage velocity in coal, m/s ; Qp is the gas source term in the coal body, $\text{kg/m}^3\text{s}$.

According to the linear seepage characteristics of Darcy's law, ignoring the influence of gravity on drainage gas migration:

$$q_g = -\frac{k}{\mu} \nabla p,$$

where k is the permeability of coal body, m^2 ; μ is the dynamic viscosity of gas in coal, $\text{Pa} \cdot \text{s}$. It is obvious that gas migration is positively correlated with coal permeability and pressure gradient, and inversely correlated with gas viscosity. When taking controlled blasting in the coal seam, the stress and temperature of the coal around the blasting hole rise sharply, substantial flow channel cracks that can improve coal permeability are produced, and the exposed area and internal energy increases which promotes the desorption and reduce gas

viscosity, effectively improving the gas drainage effect in many ways (Nie and Li, 2012; Kong et al., 2021).

DEFORMATION CHARACTERISTICS OF BOREHOLES WITH DIFFERENT DISTANCES FROM SURROUNDING ROCK

In the deep-buried soft coal mining face with a hard roof whose gas drainage requirement is higher, the implementation and permeability enhancement effect of controlled blasting is severely restricted since the borehole is easy to be deformed and damaged. Combining with the stratum characteristics of soft coal seam and hard surrounding rock in the mining face, the idea of arranging boreholes near the surrounding rock to reduce its deformation, was inspired by the relevant research results such as the end effect (Xu et al., 2017; Wang et al., 2022), is put forward and the simulation test of borehole deformation characteristics at different distances from the surrounding rock is carried out in order to provide guidance for improving the scheme design of controlled blasting to enhance permeability.

In order to conveniently and economically control the test conditions and observe the deformation and failure of rock mass, the simulation test for the deformation characteristics of boreholes with different distances from the surrounding rock is carried out, taking the 14,020 mining face of Xin'an Coal Mine as the background.

Simulation Test System of Borehole Deformation

The simulation test system of borehole deformation is shown in **Figure 2**. The loading device is a steel frame structure with full restraint around mainly composed of a strong rigid reaction frame, three parallel movable loading plates, the front and rear transparent limit guards reinforced with channel steel, and a loading system. It can carry out the test of front and rear plane rigid restraint and surrounding loading to the specimen with the maximum size of $800 \text{ mm} \times 800 \text{ mm} \times 200 \text{ mm}$. Considering the size of the simulated borehole is small and using the traditional embedded displacement sensor to measure the deformation of the surrounding rock of the borehole will affect the stress distribution and deformation of the surrounding rock of the model borehole, the pouch drainage method is designed to measure the deformation of the borehole. In order to facilitate observation and improve data accuracy, an electronic scale with an accuracy of 0.001 g is used to measure the discharge water.

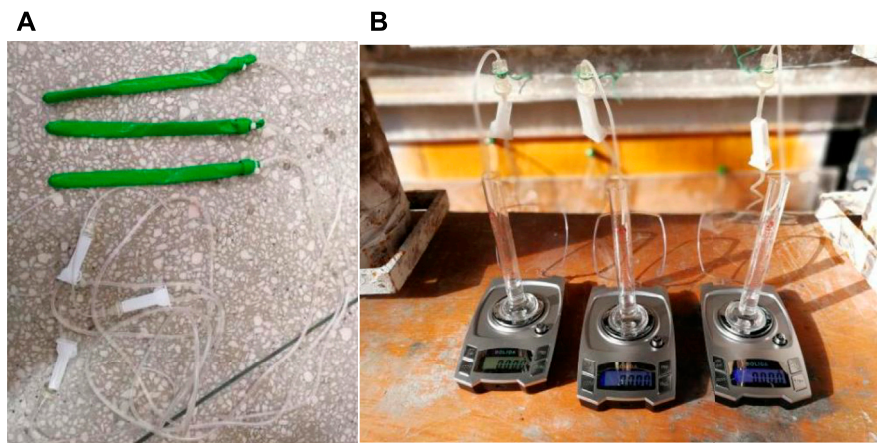


FIGURE 4 | Borehole deformation measuring device. (A) pouch, (B) electronic scale.

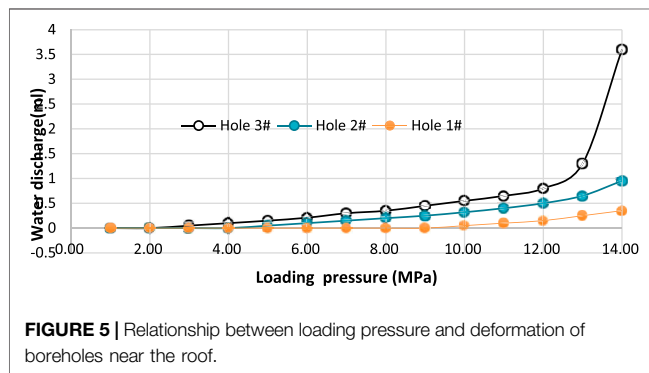


FIGURE 5 | Relationship between loading pressure and deformation of boreholes near the roof.

Design and Implementation of Similarity Test

Comprehensively considering the test purpose and the performance of the simulation test device, the similarity model includes their strata: direct roof, coal seam, and direct bottom. According to the strata occurrence characteristics and mechanical parameters of 14,020 mining faces of Xin'an Coal Mine, the model materials of each layer are selected with strength as the main index and used to build a physical model according to the geometric similarity ratio of 10, the unit weight ratio of 1.6 and the stress ratio of 16. After consulting literature materials and similar conversions (Li et al., 2007), the model is made of sand, calcium carbonate, cement, and gypsum according to the ratio and dosage shown in **Table 1**.

After the materials of each layer are separately prepared and mixed according to the proportion, add 1% borax solution whose amount is 1/10 of its total weight and stir well, and then lay and compact layer by layer. Before laying each layer of the model, the front and rear guard plates of the experimental device shall be fixed neatly and firmly. For more convenient observation, the coal and rock stratum is sprayed orange and white, respectively.

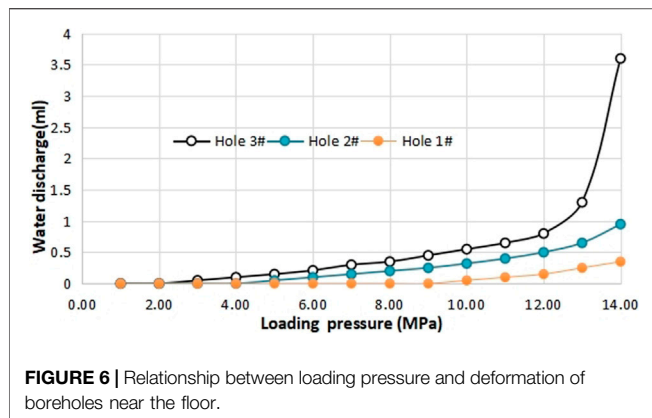
The laid model is dried for 3 days, and then the simulated borehole is excavated with an electric drill. Since it is difficult to completely repeat the process of model building, drying, and loading, the boreholes at different distances from the roof are carried out loading deformation tests on the same model and in the same loading process. According to the size of the model and borehole, it is designed to sequentially excavate three boreholes along a coal seam with a diameter of 10 mm and length of 200 mm from the position 150 mm away from the side in the model coal seam. The three boreholes are 5, 30, and 55 mm away from the roof, respectively, and their horizontal spacing is 250 mm (**Figure 3**).

Then, the borehole deformation measuring device is installed. A pouch made of the long balloon with the length equal to the drilling depth and the diameter slightly larger than the drilling diameter is first put into every borehole (**Figure 4A**). Then, one end of a tube with a valve is tightly connected with the pouch's mouth, and the other end extends into the measuring cup placed on the precision electronic scale (**Figure 4B**); and then, using a syringe, the pouch and the tube is completely filled with water, keeping the pouch pressed against the borehole wall and the height of the tube outer end slightly higher than the drilling hole, so that the water is extruded when and only the pouch is synchronously deformed with the borehole wall which flows wholly into the measuring cup (**Figure 4**).

When the aforementioned preparations are completed, the loading deformation test is carried out on the model. According to the actual situation that the side pressure coefficient of 14,020 mining face in Xin'an mine is about 1, two-way equal pressure (upper and lower, right and left) loading is slowly carried out and the borehole deformation and pouch drainage are continuously observed during the test.

Test Results Analysis

According to the water discharge measurement results reflecting the borehole deformation, the relationship between the loading



pressure of the oil cylinder and the surrounding rock deformation of boreholes at a different distance from the roof are obtained (Figure 5).

As can be seen, when the pressure loaded by the oil cylinder is 1~2 MPa, the water discharge of the three boreholes is 0 ml. When the loading pressure reaches 3 MPa, the No.3 hole that is farthest from the roof begins to drip. When the loading pressure reaches 5 MPa, the No.2 hole begins to drip. Until the loading pressure reaches 10 MPa, the No.1 hole nearest to the roof begins to drip. The water discharge of boreholes gradually increases with the increase of loading pressure. When the loading pressure reaches 14 MPa, the water discharge of borehole No.3 suddenly increases rapidly to 3.6 ml, and then the borehole collapses. At this time, the No.2 hole produces obvious deformation but no instability and the water discharge was 0.95 ml. While, the No.1 hole produces slight deformation, and the water discharge is only 0.35 ml.

With reference to the aforementioned scheme, a similar loading deformation test of boreholes at different distances from the floor is carried out, and basically consistent results are obtained (Figure 6), which will not be described here to avoid repetition.

It can be found that, through the aforementioned simulation test results, within a certain distance, under the same stress conditions the closer the borehole is to the roof (floor), the smaller the deformation, which provides a direction and basis for improving the layout design of blasting boreholes.

SCHEME DESIGN AND FIELD TEST OF DEEP HOLE CONTROLLED BLASTING TO ENHANCE PERMEABILITY

Borehole Layout

In light of the aforementioned deformation characteristics, test results of boreholes at different distances from the surrounding rock, and comprehensively considering the blasting purpose, site conditions, drilling equipment, explosive specification, and operation safety, the blasting hole is arranged adjacent to the coal seam floor and its diameter is designed to be 65 mm, for the convenience of hole forming and charging as well as avoiding blasting to break the

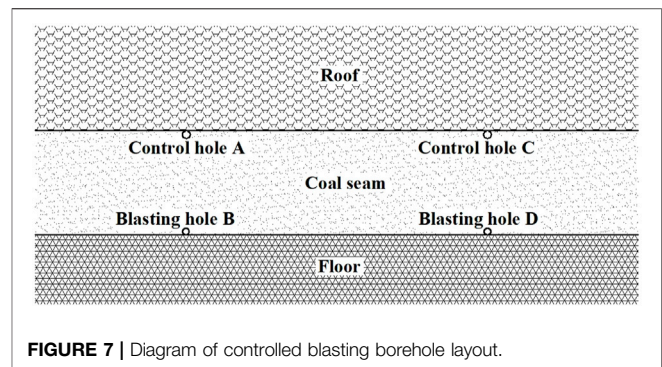


TABLE 2 | Relevant parameters of coal seam blasting calculation.

Parameter Name (unit)	Parameter Value
tensile strength σ_t (MPa)	0.15
Poisson's ratio ν	0.32
detonation velocity D (m/s)	3,000
explosive density ρ (kg/m ³)	1,150

roof affecting the safe mining of the mining face. The control hole is arranged adjacent to the roof and its diameter is designed to be 113 mm, so as to better guide the blasting energy and compensate for the space required for coal fracture, promoting the formation of a blasting joint network and gas drainage.

In order to investigate the actual effect of the improved scheme, as shown in Figure 7, two groups of controlled blasting permeability enhancement tests were designed and implemented in Xin'an 14,020 mining face. In the figure, holes A and C are control holes (doubles as drainage holes), while holes B and D are blasting holes. Their dip angles are designed according to the dip angle of the coal seam of 6°, and the orientation is perpendicular to the center line of the roadway. The depth is set as half the width of the mining face of 60 m, according to the need for gas drainage covering the mining face.

Blasting Parameters

For the safety of blasting operation, coal mine-permitted three-level emulsion explosive is selected, and radial uncoupled axial continuous charging is adopted. The radial uncoupling coefficient is controlled at 1.2~1.8 to improve the cracking effect of blasting in coal seam (Gong et al., 2006).

According to relevant research, the relationship between uncoupled blasting crack radius and explosive radius is as follows (Liu et al., 2018):

$$r_p = (b\sigma_d/\sigma_t)^{1/\alpha} r_c,$$

where r_c is the explosive radius; $b = \nu/(1 - \nu)$, ν is the Poisson's ratio of coal; α is the stress wave reduction index, $\alpha = 2 - \mu/(1 - \mu)$; μ is the dynamic Poisson's ratio of coal body, generally taken 0.8 times of Poisson's ratio ν ; σ_t is the tensile strength of coal; σ_d is the initial radial stress caused by stress wave, which is calculated as follows:

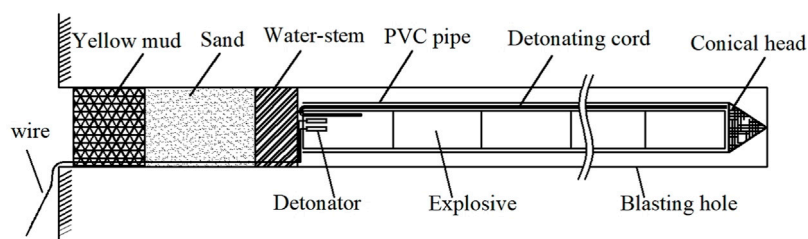


FIGURE 8 | Schematic diagram of controlled blasting charge structure.

TABLE 3 | Drainage data of blasting permeability enhancement hole and traditional hole.

Borehole	Concentration (%)	Mixed Flow Volume (m ³ /min)	Pure Gas Flow Volume (m ³ /min)
traditional drainage hole	36.5	0.064	0.023
test hole A	53.1	0.066	0.035
test hole C	45.5	0.072	0.033

$$\sigma_d = \frac{\rho_0 D^2}{8} \left(\frac{r_c}{r_b} \right)^6 n,$$

where D is the detonation velocity; ρ_0 is the explosive density; r_b is the radius of the blasting hole; n is the pressure increase coefficient, generally taken as 10.

According to the aforementioned borehole layout scheme and actual relevant parameters of blasting in 14,020 mining faces of Xin'an mine (Table 2), the calculated diameter of the explosive roll is 40 mm, which can meet the requirements of fracture range for coal seam permeability enhancement.

To ensure the reliability of detonating and avoid the pipe effect, double millisecond delay electric detonators with parallel connections are selected for forwarding initiation in the design, and the allowable detonating cord of the coal mine is placed along the full length of the explosive column in the auxiliary charging PVC pipe with an inner diameter of about 45 mm.

The blocking length in gas-bearing coal is generally 20 ~ 40% of the blasting hole depth. According to the field measurement, the pressure relief zone width and equivalent discharged gas width of roadway in Xin'an mine are 15 and 21 m, respectively. Comprehensively considering the blasting safety and the permeability enhancement needs of the mining face, the blocking length is taken as 20.0 m, the charging length 40 m, and the charging amount 62 kg.

Field Test

The field test is carried out in Xin'an 14,020 mining faces according to the design scheme. First, drill the control hole and connect the pipe for gas drainage in time. Then, drill the blasting hole and fully discharge the drilling cuttings in the holes with compressed air. Afterward, a positive charge with the help of an antistatic PVC pipe with screwed joints. For smooth pipe delivery, the front end of the foremost PVC pipe

is equipped with a conical head. Connect and charge the PVC pipes one by one and send them into the blasting hole. The explosive rolls shall be closely adjacent to each other, and the allowable detonating cord of the coal mine shall be placed along the full length of the explosive column. The explosive roll at the outermost end shall be inserted into two same types allowable Millisecond Electric Detonators of a coal mine with a parallel connection.

When plugging the blast hole after charging, first fill with water-stem at the inner end 2 m, then fill 12 m long sand into the borehole with compressed air hole sealer, and finally fill 6 m yellow mud and tamp it section by section with tamping bar (Figure 8). After checking and confirming the safety, blasting shall be carried out.

From the field drilling, it is found that the drilling speed of boreholes adjacent to surrounding rock is more than 50% higher than that of the traditional boreholes with the same diameter arranged in the middle of the coal seam, and the borehole forming performance is significantly improved.

Within 1 week after blasting, the gas drainage parameters of boreholes A and C are observed every day. It is found that compared with the traditional nonblasting drainage borehole with the same diameter, depth, and drainage time drilled in the middle of the coal seam, the average gas concentration and gas pure flow volume within 1 week after blasting is significantly increased (Table 3). The drainage concentration and drainage pure flow volume of test hole A increased by 45.5 and 52.2%, respectively, and those of test hole C increased by 25.5 and 43.5%, respectively.

CONCLUSION

- 1) Based on the blasting cracking mechanism and the law of gas migration, the mechanism of controlling blasting permeability

enhancement is further clarified: under the action of blasting, the stress and temperature of the coal around the blasting hole rise sharply, and substantial flow channel cracks that can improve coal permeability are produced, the exposed area and internal energy increases which promote the desorption and reduce gas viscosity, effectively improving the gas drainage effect in many ways.

- 2) Aiming at the problem that the borehole in a deep soft coal seam is easy to deform and destroy which affects the implementation of controlled blasting and the effect of permeability enhancement, the assumption of arranging the borehole near the surrounding rock to reduce its deformation is put forward, and the simulation test of borehole deformation characteristics at different distances from the surrounding rock is carried out. The results show that under the same stress condition, the closer the borehole is to the roof (bottom plate), the smaller the deformation, which provides the direction and basis for improving the layout design of blasting boreholes.
- 3) In light of the deformation characteristics test results of boreholes at different distances from the surrounding rock, and comprehensively considering the blasting purpose, site conditions, drilling equipment, explosive specifications, and construction safety, a new scheme of arranging, respectively, control hole and blasting hole near the roof and floor is proposed and designed, and the effectiveness and practicability of the new scheme are verified by field tests. The field test results show that the new scheme significantly improves the drilling speed and the borehole forming performance, successfully realizes the controlled blasting of a 60 m ultra-deep hole, and effectively improves the concentration and pure gas flow volume of drainage gas.

- 4) This study explores a new blasting permeability enhancement scheme with practical value and reference significance for deep-buried soft coal mining face with a hard roof.

DATA AVAILABILITY STATEMENT

The original contributions presented in the study are included in the article/Supplementary Material, further inquiries can be directed to the corresponding author.

AUTHOR CONTRIBUTIONS

DX: Conceptualization, Methodology, Formal Analysis, Writing—Original Draft. JZ: Methodology, Project Administration. GH: Visualization, Writing—review, and editing. PL: Funding, Resources, Supervision. ZZ: Investigation, Validation, Data Curation. All authors have read and agreed to the published version of the manuscript.

FUNDING

This study is supported by the Youth Project of the National Natural Science Foundation of China (51804356).

ACKNOWLEDGMENTS

Many thanks to the National Nature Science Foundation of China for the financial support under Grant 51804356, and the relevant staff of the Xin'an Coal Mine for their great help.

REFERENCES

- Baisheng, B., and Xiangchun, X. (2012). Mechanism Research on Coal and Gas Outburst during Vibration Blasting. *Saf. Sci.* 50 (4), 741–744. doi:10.1016/j.ssci.2011.08.041
- Bhandari, S. (1980). On the Role of Stress Waves and Quasi-Static Gas Pressure in Rock Fragmentation by Blasting, 365, 383. doi:10.1016/B978-0-08-025442-5.50036-6
- Cao, Y., Ma, Y., Mao, X., Yang, T., and Wang, Y. (20202020). Experimental Study on Crack Distribution and Regional Electrical Resistivity Response of Soft Coal Seams after Multi-Hole Blasting. *J. Saf. Sci. Technol.* 16 (10), 71–77. doi:10.11731/j.issn.1673-193x.2020.10.011
- Cheng, Y., and Pan, Z. (2020). Reservoir Properties of Chinese Tectonic Coal: a Review. *Fuel* 260, 116350. doi:10.1016/j.fuel.2019.116350
- Gong, M., Liu, W., Wang, D., Wu, H., Chen, T., and Qiu, D. (2006). Controlled Blasting Technique to Improve Gas Pre-drainage Effect in a Coal Mine. *J. Univ. Sci. Technol. Beijing* 2006 (03), 223–226. doi:10.13374/j.issn1001-053x.2006.03.005
- Guo, D., Lv, P., Zhao, J., and Zhang, C. (2020). Research Progress on Permeability Improvement Mechanisms and Technologies of Coalbed Deep-Hole Cumulative Blasting. *Int. J. Coal Sci. Technol.* 7 (1), 329–336. doi:10.1007/s40789-020-00320-5
- Guo, D. Y., Zhao, J. C., Zhang, C., and Zhu, T. G. (2018b). Mechanism of Control Hole on Coal Crack Initiation and Propagation under Deep-Hole Cumulative Blasting in Coal Seam. *Chin. J. Rock Mech. Eng.* 37 (04), 919–930. doi:10.13722/j.cnki.jrme.2017.1038
- Guo, D., Zhang, C., Zhu, T., and Pan, J. (2018a2018). Effect of Charge Structure on Deep-Hole Cumulative Blasting to Improve Coal Seam Permeability. *Chin. J. Eng.* 40 (12), 1488–1494. doi:10.13374/j.issn2095-9389.2018.12.006
- Huang, C., Zhang, Y., He, J., Luo, Y., and Sun, Z. (2019). Permeability Improvements of an Outburst-prone Coal Seam by Means of Presplitting and Blasting with Multiple Deep Boreholes. *Energy Sci. Eng.* 7 (5), 2223–2236. doi:10.1002/ese3.426
- Kong, X., Li, S., Wang, E., Wang, X., Zhou, Y., Ji, P., et al. (2021). Experimental and Numerical Investigations on Dynamic Mechanical Responses and Failure Process of Gas-Bearing Coal under Impact Load. *Soil Dyn. Earthq. Eng.* 142, 106579. doi:10.1016/j.soildyn.2021.106579
- Lei, Y., Liu, J., Zhang, S., Zhang, W., and Wang, H. (2016). Contrast Test of Different Permeability Improvement Technologies for Gas-Rich Low-Permeability Coal Seams. *J. Nat. Gas Sci. Eng.* 33, 1282–1290. doi:10.1016/j.jngse.2016.06.066
- Li, H. (2015). Discussion on Ways of Mine Gas Drainage and Extraction. *Amr* 1073-1076, 2189–2193. doi:10.4028/www.scientific.net/AMR.1073-1076.2189
- Li, X., Lu, Y., Kang, Y., and Rao, B. (2007). *Rock Mechanics Experiment Simulation Technology*. Beijing: Science Press.
- Liu, Z., Cao, Y., Zhu, G., Wang, C., and Jing, G. (2018). Pressure Relief Effect of Uncoupled Blasting Technology in High Stress Area. *Explos. SHOCK WAVES* 38 (02), 390–396. doi:10.11883/bzycj-2016-0180

- Nikitenko, S. M., and Glukhikh, S. A. (2021). Gas Drainage in Coal Mines: Current Condition and Prospects. *IOP Conf. Ser. Earth Environ. Sci.* 823 (1), 012019. doi:10.1088/1755-1315/823/1/012019
- Shakeran, M., Eslami, A., and Ahmadpour, M. (2016). Geotechnical Aspects of Explosive Compaction. *Shock Vib.* 2016 (8), 6719271. doi:10.1155/2016/6719271
- Ti, Z., Zhang, F., Pan, X., Ma, Z., and Shang, Z. (2018). Permeability Enhancement of Deep Hole Pre-splitting Blasting in the Low Permeability Coal Seam of the Nanting Coal Mine. *Plos One* 13 (6), e0199835. doi:10.1371/journal.pone.0199835
- Wang, F., Zhang, P., Cui, B., Sun, Z., and Zhang, K. (2021). Research Progress of Disaster Factors and a Prevention Alarm Index of Coal and Gas Outbursts. *Arab. J. Geosci.* 14 (19). doi:10.1007/s12517-021-07540-2
- Wang, L., Li, X. X., and Zhao, Y. X. (2012). The Practice about Deep Hole Pre-split Blasting in Mining Faces of Low Permeability Extra-thick Seam. *Amr* 524–527, 781–785. doi:10.4028/www.scientific.net/AMR.524-527.781
- Wang, Y., Liu, X., Pang, B., and Yu, Y. (2022). Numerical and Experimental Study on End Effect of Waste-Soil Samples under Uniaxial Compression. *Geofluids* 2022, 1–11. doi:10.1155/2022/3014164
- Xie, Z., Zhang, D., Song, Z., Li, M., Liu, L., and Sun, D. (2017). Optimization of Drilling Layouts Based on Controlled Presplitting Blasting through Strata for Gas Drainage in Coal Roadway Strips. *Energies* 10 (8), 1228. doi:10.3390/en10081228
- Xu, Y., Cai, M., Zhang, X., and Feng, X. T. (2017). Influence of End Effect on Rock Strength in True Triaxial Compression Test. *Can. Geotech. J.* 54, 862–880. doi:10.1139/cgj-2016-0393. doi:10.1139/cgj-2016-0393
- Xue, F., and Feng, X. (2018). Spatial and Temporal Distribution Law and Influencing Factors of the Mining-Induced Deformation and Failure of Gas Boreholes. *Adv. Mater. Sci. Eng.* 2018, 1–15. doi:10.1155/2018/9580526
- Ye, Q., Jia, Z. Z., and Zheng, C. (2017). Study on Hydraulic-Controlled Blasting Technology for Pressure Relief and Permeability Improvement in a Deep Hole. *J. Petroleum Sci. Eng.* 159, 433–442. doi:10.1016/j.petrol.2017.09.045
- Yin, G., Li, X., Lu, J., and Li, M. (2017). Disaster-causing Mechanism of Compound Dynamic Disaster in Deep Mining under Static and Dynamic Load Conditions. *Mtan Xuebao/Journal China Coal Soc.* 42 (9), 2316–2326. doi:10.13225/j.cnki.jccs.2017.0139
- Yu, Z. J., Jiang, F. C., Mao, X. X., and Wang, J. (2013). Hazard of Coal Mine Gas and its Preventive Measures. *Amr* 724–725, 1289–1292. doi:10.4028/www.scientific.net/AMR.724-725.1289
- Zhang, C., Wang, E., Xu, J., and Peng, S. (2020). Experimental Investigation on Mechanics and Seepage Characteristics of Tectonic and Intact Coal Containing Gas. *Appl. Sci.* 10 (20), 7290. doi:10.3390/app10207290
- Zhang, W. Q., and Liu, J. (2013). Study on Methods of Exploring the Loosening Radius of Deep-Hole Controlling Blasting. *Amr* 734–737, 650–655. doi:10.4028/www.scientific.net/AMR.734-737.650
- Zhang, X. B., Shen, S. S., Feng, X. J., Ming, Y., and Liu, J. J. (2021). Influence of Deformation and Instability of Borehole on Gas Extraction in Deep Mining Soft Coal Seam. *Adv. Civ. Eng.* 2021 (1), 1–11. doi:10.1155/2021/6689277
- Zhao, D., Wang, M., Gao, X., and Engineering, M. (2021). Study on the Technology of Enhancing Permeability by Deep Hole Presplitting Blasting in Sanyuan Coal Mine. *Sci. Rep.* 11. doi:10.1038/s41598-021-98922-9
- Zhao, Y., Lin, B., Liu, T., Zheng, Y., Kong, H., Li, Q., et al. (2020). Mechanism of Multifield Coupling-Induced Outburst in Mining-Disturbed Coal Seam. *Fuel* 272 (4), 117716. doi:10.1016/j.fuel.2020.117716
- Zhou, H., Dai, H., and Ge, C. (2016). Quality and Quantity of Pre-drainage Methane and Responding Strategies in Chinese Outburst Coal Mines. *Arab. J. Geosci.* 9 (6), 445. doi:10.1007/s12517-016-2488-5

Conflict of Interest: Author ZZ was employed by Xin'an Coal Mine, Henan Dayou Energy Co.

The remaining authors declare that the research was conducted in the absence of any commercial or financial relationships that could be construed as a potential conflict of interest.

Publisher's Note: All claims expressed in this article are solely those of the authors and do not necessarily represent those of their affiliated organizations, or those of the publisher, the editors, and the reviewers. Any product that may be evaluated in this article, or claim that may be made by its manufacturer, is not guaranteed or endorsed by the publisher.

Copyright © 2022 Xuan, Zhang, Huang, Li and Zhang. This is an open-access article distributed under the terms of the Creative Commons Attribution License (CC BY). The use, distribution or reproduction in other forums is permitted, provided the original author(s) and the copyright owner(s) are credited and that the original publication in this journal is cited, in accordance with accepted academic practice. No use, distribution or reproduction is permitted which does not comply with these terms.



OPEN ACCESS

EDITED BY
Hongyuan Liu,
University of Tasmania, Australia

REVIEWED BY
Rusong Nie,
Central South University, China
Magdalena Tutak,
Silesian University of Technology,
Poland

*CORRESPONDENCE
Peng-Fei He,
212008010028@home.hpu.edu.cn

SPECIALTY SECTION
This article was submitted to
Geohazards and Georisks,
a section of the journal
Frontiers in Earth Science

RECEIVED 29 April 2022
ACCEPTED 20 July 2022
PUBLISHED 17 August 2022

CITATION
Ren L-W, He P-F, Zou Y-F, Yang C,
Dun Z-L, Zou Z-S and Shi C (2022), A
novel evaluation method of mining goaf
ground activation under high-speed
railway load.
Front. Earth Sci. 10:931466.
doi: 10.3389/feart.2022.931466

COPYRIGHT
© 2022 Ren, He, Zou, Yang, Dun, Zou
and Shi. This is an open-access article
distributed under the terms of the
[Creative Commons Attribution License](#)
(CC BY). The use, distribution or
reproduction in other forums is
permitted, provided the original
author(s) and the copyright owner(s) are
credited and that the original
publication in this journal is cited, in
accordance with accepted academic
practice. No use, distribution or
reproduction is permitted which does
not comply with these terms.

A novel evaluation method of mining goaf ground activation under high-speed railway load

Lian-Wei Ren¹, Peng-Fei He^{1*}, You-Feng Zou², Chao Yang³,
Zhi-Lin Dun¹, Zheng-Sheng Zou¹ and Chunyu Shi⁴

¹School of Civil Engineering, Henan Polytechnic University, Jiaozuo, China, ²School of Surveying and Land Information Engineering, Henan Polytechnic University, Jiaozuo, China, ³WSP Australia, Newcastle, NSW, Australia, ⁴Taiyuan Design Research Institute for Coal Industry, Taiyuan, China

With the continuous improvement of infrastructure, some high-speed railway lines will inevitably cross the goaf ground, and there is less research on the safety of high-speed rail construction in goaf ground. To make a reasonable and accurate safety evaluation of the high-speed railway construction in the mine goaf ground, machine learning combined with numerical simulation is used to evaluate the safety depth of goaf under the impact of high-speed railway load. An optimal algorithm is selected among BP, RBF, and PSO-RBF neural networks based on the accuracy of the predicted height of a caving fracture zone. Numerical models for simulating high-speed railway founded on goaf are set up using the commercial software package FLAC3D, where factors such as subgrade height, train speed, and axle load are investigated in terms of train load disturbance depth and the extent of the caving fracture zone. The results indicate that the PSO-RBF neural network has an error of 2.76% in predicting the height of the caving fracture zone; the depth of train load disturbance is linearly related to the axle weight and roadbed height but is a sinusoidal function of the train speed. Based on the numerical simulation results, a formula for calculating the depth of train load disturbance is proposed, which provides a certain reference value for the construction of high-speed railways in the goaf ground.

KEYWORDS

goaf ground, activation evaluation, high-speed railway, combined method, disaster prevention

1 Introduction

Stringent ground settlement criteria are required for construction and operation of high-speed railways. When high-speed railways cross goaf zones, the dynamic load generated by trains could destabilize the existing stable goaf, resulting in settlement and inclination of subgrade and endangering the driving safety of high-speed railways (Lei et al., 2013; Liang et al., 2016). The waste of land caused by mining activities has become an important issue restricting sustainable development (Bian et al., 2012; Yu et al., 2018). Taking Qinshui coalfield in Shanxi Province as an example, due to the goaf site area of nearly 3000 square kilometers formed by coal mining, the high-speed railway line inevitably passes through the goaf site. As shown in Figure 1, the built Tai-jiao section, Shi-tai section, and Tai-xi section and the Qing-

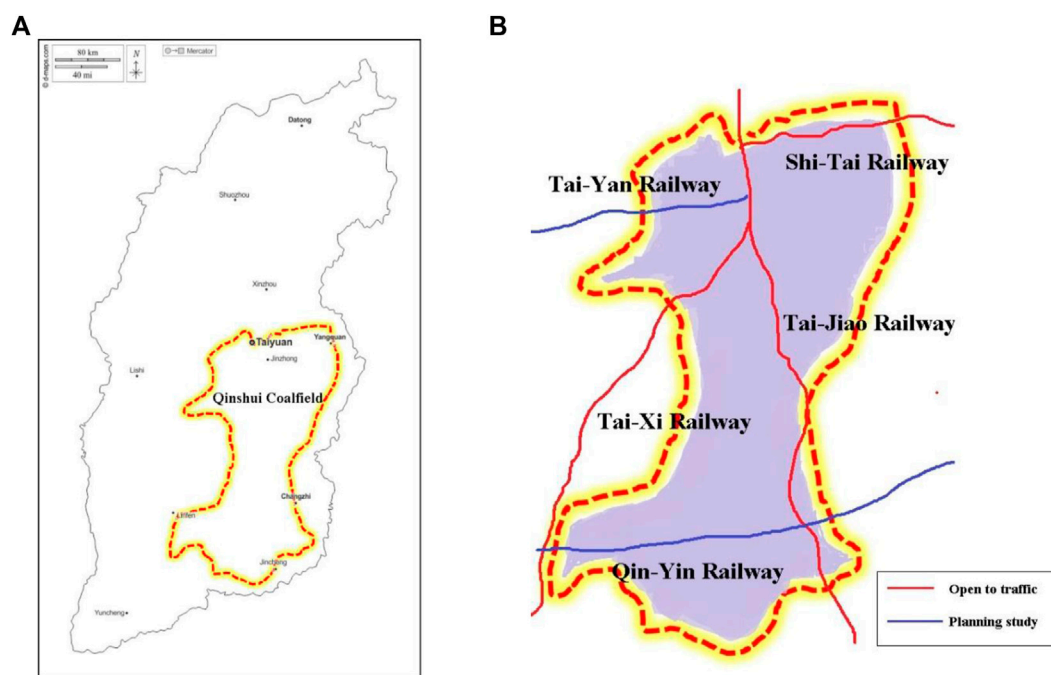


FIGURE 1

Study area: (A) Qinshui coalfield location in Shanxi Province, China; (B) high-speed railway line through Qinshui coalfield.

Yin high-speed railway and Tai-yan high-speed railway under planning and research all pass through the goaf site.

At present, domestic and international research is focused on the stability of goaf ground and stability under building loads (static loads). Guo et al. (2019) proposed an evaluation model of a goaf expressway with seven evaluation factors based on fuzzy theory, calculated the factor weight by gray correlation method, and applied the model to Wuyun Expressway to prove the reliability of the model. Liu et al. (2011) proposed a fuzzy matter-element model which used the AHP and matter-element extension method to identify the risk level of goaf zones. Maria et al. (2013) used the calculation method based on material resistance to analyze the sensitivity of goaf roof stability to the variation of roof material properties. Ashok et al. (2012) proposed a concept of panel stability based on Salamon stability (Merwe, 2003) criterion, which is further applied to analyze the critical failure modes of coal pillars. Debasis and Choi (2006) conducted sensitivity checks on various factors affecting the stability of aged goafs and used fuzzy collection theory to predict the occurrence probability of surface subsidence pits. Dong et al. (2008) proposed an evaluation index system based on uncertainty measure theory to predict the risk of goaf. Henry et al. (1989) summarized four mine collapse mechanisms, namely, single-force source, dual-force opposition, shear dislocation, and tensile force. However, there are fewer research results on the safety of high-speed railway construction at the goaf ground. Unlike other construction loads, high-speed railway loads are not only

influenced by vehicle speed, roadbed height, and axle weight but also have the characteristics of strong periodicity and large changes. Once the activation and deformation of the extraction area by train load occurs, it will cause great hidden danger to the safety of high-speed railway traffic.

In this study, the machine learning method is used to predict the height of the caving fracture zone induced by construction and operation of high-speed railways. The numerical simulation method is used to obtain the train dynamic load disturbance depth under various working conditions by changing the embankment height, train speed, and train axle load. A calculation formula is provided to predict the train load disturbance depth, which can be combined with the caving fracture zone to evaluate the safety of foundations for high-speed railways.

2 Critical depth-to-thickness ratio of a high-speed railway goaf ground

2.1 Failure characteristics of overlay rock in coal mine goaf

Along with the coal seam being mined out, stress redistribution occurs in the goaf, and the original structure is destroyed. Upon completion of stress redistribution, a relatively

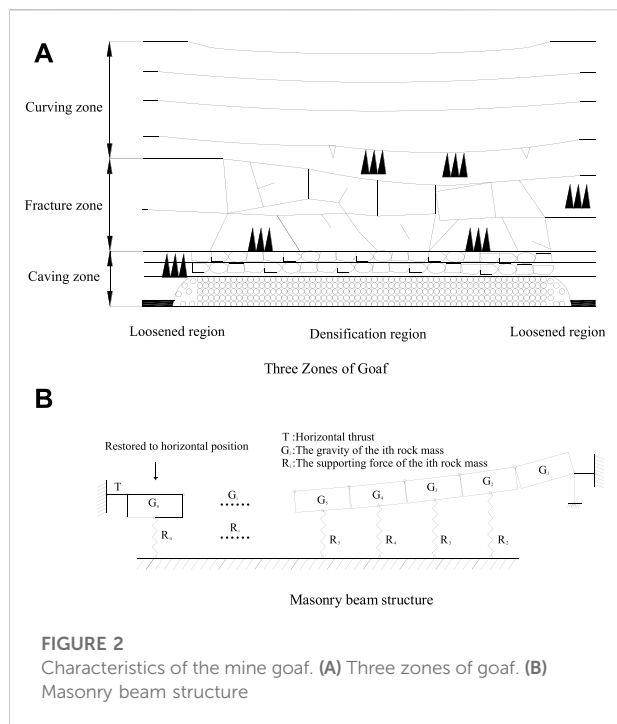


FIGURE 2
Characteristics of the mine goaf. (A) Three zones of goaf. (B) Masonry beam structure

stable mining-induced secondary rock structure is finally formed. The overlying strata can be divided into the caving zone, fracture zone, and bending zone, as shown in Figure 2A, after mining by the long arm caving method. The caving zone is mainly destroyed by the original overlying roof. The rock stratum breaks, and the caving fills the mining area. The caving zone is denser in the middle, but there are more cavities on the sides. The fracture zone induced by the bending of the rock layer is located above the caving zone. Different from the caving zone, the fracture zone maintains its layered structure and has more cracks in the rock layer. The bending zone mainly refers to the rock (soil) layer from the fracture zone to the surface. The vertical displacement of each rock layer in the bending zone is basically the same, though there are some separations and cracks. Masonry beam structures may also be present in the caving zone and fracture zone Figure 2B.

2.2 Critical mining depth-to-thickness ratio

According to the overlay rock failure characteristics of goaf, the broken rock mass and cracks in goaf exist mostly in the caving zone and fracture zone. When the broken rock mass is compacted or the cracks are closed by external force, the goaf will be reactivated and deformed, resulting in surface subsidence and affecting the safety of surface buildings.

In general, the evaluation of the stability grade of the goaf site is based on the location of the depth of the additional stress influence and the depth of the caving fracture zone. Through numerical simulation, theoretical analysis, and model experiment, Zhang (2005) and Guo (2001) pointed out that the primary factor affecting the construction site of goaf should be the mining depth-to-thickness ratio. When the goaf site has a certain mining depth-to-thickness ratio, the existence of goaf has no effect on the foundation of buildings. Therefore, before traditional evaluation, it is necessary to preliminarily determine the mining depth-thickness ratio. If the condition is not met, the influence grade is divided by the relationship between the influence depth of additional stress and the depth of the caving fracture zone.

In order to determine the critical mining depth-to-thickness ratio, Zhang (2005) analyzed the simulation results of 12 calculation models and 144 calculation schemes and obtained the critical mining depth-to-thickness ratio under different loads and different action positions, as shown in Table 1 (building load).

Compared with the traditional building foundation, the high-speed railway engineering foundation has more strict requirements for settlement and inclination. When calculating the critical ratio in Table 1 (building load), due to the high degree of compaction and full filling in the middle area of the goaf, the safety factor is found to be 1.2. In the edge area, the structure similar to the masonry beam is formed after the rupture of the hard rock stratum. There are voids and uncompacted areas, and the safety factor is 1.5. In this study, the safety factor of the middle region is increased to 1.5, and that of the edge region is increased to 2.0. The criterion of the critical depth-to-thickness ratio of high-speed railway engineering is obtained (train load).

2.3 Load position

As shown in Figure 2B, the outer edge area mainly refers to the area from the open-off cut to the restoration level of the masonry beam rock block. The formula for calculating the length of this region can be obtained from the masonry beam theory (Qian, 1981):

$$n = \text{int}(H/L_z \tan \varphi) + 1, \quad (1)$$

$$L_z = h_i \sqrt{\sigma_t / 3 \left(\sum h_i + h_i \right) \gamma}, \quad (2)$$

$$L = n \times L_z, \quad (3)$$

where n is the number of rock blocks in the masonry beam structure, H is mining depth, φ is fully mining angle, L_z is the length of periodic weighting step distance, h_i is the thickness of the key layer, $\sum h_i$ is the thickness of the upper weak rock layer, σ_t is the ultimate tensile stress of the key layer, γ is the volumetric force of the rock layer, and L is the length of the outer edge region.

TABLE 1 Determination of critical mining depth-to-thickness ratio of load.

Load type	Load location	Load size (MPa)			
		≤0.036	0.036–0.072	0.072–0.108	0.108–0.180
Building load	Intermediate zone		19	30	45
	Outer edge region	20	24	45	56
	Inner edge region	24	38	60	
Train load	Intermediate zone		24	38	56
	Outer edge region	27	32	60	75
	Inner edge region	32	51	80	

TABLE 2 Irregularity selection.

Controlling condition	Wave-length/m	Arch rise/mm
Driving smoothness (1)	10	3.5
Dynamic additional load (2)	2	0.4
Waveform wear (3)	0.5	0.08

The inner edge area refers to the area where the rock block restores the horizontal position to the stop line. The compactness of the inner edge area is better than that of the outer edge area. For safety, Eqs 1–3 are also adopted for regional determination.

The compaction area is located in the middle of the inner and outer edge areas. Due to sufficient collapse of rock mass, there are fewer cracks in this area and the safety is high.

2.4 Foundation base load

The calculation of load mainly comprises static load of subgrade and dynamic load of a train. Liang and Cai (1999) proposed a sine function formula of train load considering geometric irregularity, which comprises single-wheel static load and dynamic load caused by geometric irregularity. The value of irregularity is shown in Table 2.

$$F(t) = P_0 + \sum_{i=1}^3 P_i \sin(\omega_i t), \quad (4)$$

$$P_i = m_0 a_i \omega_i^2, \quad (5)$$

$$\omega_i = 2\pi V / L_i, \quad (6)$$

where P_0 is the single-wheel static load, kN; ω_i is circular frequency under various conditions; m_0 is unsprung mass, kg; a_i is arch rise under various conditions, mm; V is train speed, m/s; and L_i is wave-lengths under various conditions, m.

Based on the measured data of dynamic stress attenuation law, Bian et al. (2010) obtained the attenuation formula of subgrade dynamic stress:

$$\eta = 1 - z / (a + b \times z), \quad (7)$$

where z is the subgrade height, a and b are the fitting coefficients, and the mean values of the fitting coefficients a and b of ballasted track are 0.64 and 0.86, respectively.

In summary, the calculation formula of the base load can be obtained:

$$\sigma = \sum \gamma_i z_i + P_0 / W + \eta \sum_{i=1}^3 P_i \sin(\omega_i t) / W, \quad (8)$$

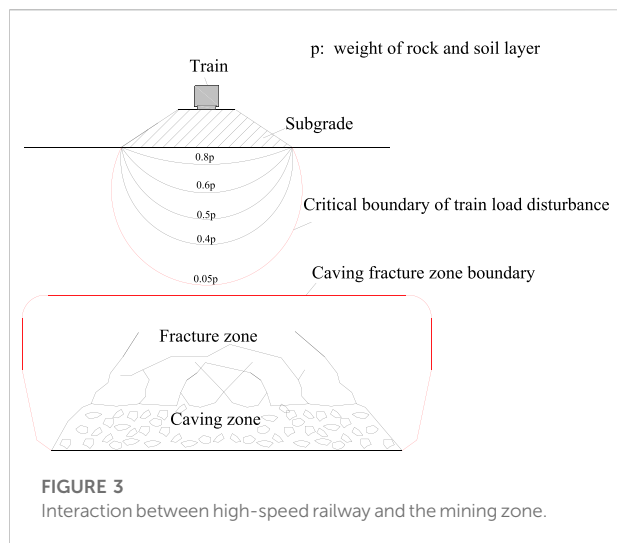
where γ_i is the bulk density of the subgrade material for layer i , z_i is height of the subgrade material of layer i , and W is the foundation base width.

3 Influence degree of goaf ground activation

When the critical depth-to-thickness ratio of the goaf site does not meet the standards given in Table 1, the influence degree of reactivation needs to be determined. The additional load distributed from the foundation of any structures above, once its value is no more than 10% of the weight of the overburden rock-soil mass, is considered to impose no significant effect on the rock and soil mass at this depth. Due to a stringent requirement for subgrade settlement for the construction and operation of high-speed railways, a critical influence depth of train load, H_a , is defined as the disturbance depth at which the distributed additional stress from the train load is 5% of the weight of rock and soil above.

The relationship between the critical influence depth of train load and the depth position of the caving fracture zone is depicted in Figure 3.

Because of strict requirements for high-speed railway ground deformation, the more stringent evaluation criteria should be adopted after considering China code's criteria (The Professional Standards Compilation Group of People's Republic of China, 2014): 1) when the buried depth of the caving fracture zone is greater than or equal to 2.5 times the load influence depth, the



influence is little; 2) when the buried depth of the caving fracture zone is less than 2.5 times the load influence depth and greater than or equal to the load influence depth, the influence is moderate; 3) when the buried depth of the caving fracture zone is less than the load influence depth, the influence is great.

4 Height prediction of the caving fracture zone

This study compares the depth of train load disturbance (H_a) and the depth of the caving fracture zone (H_{lf}) to determine the “re-activation” of the goaf ground. Prediction of the height of the caving fracture zone is commonly based on the empirical formula in GB 51044 (2014). This method is relatively straight-forward, but it will produce a less accurate prediction of the safety depth of the goaf ground for considering only the coal seam mining thickness.

Machine learning, as an objective and effective prediction variable or classification method, has been widely used in geotechnical engineering (Tan et al., 2011; Cai et al., 2020; Mahmoodzadeh et al., 2021). There are many factors affecting the development height of the caving fracture zone. As such, a reasonable influencing factor system is critical for a more accurate prediction based on the machine learning method. As per Guo et al. (2021), seven factors are selected in this study: overburden structure, buried depth, dip angle, mining thickness, working face size, coal mining method and layered mining number. Thirty-eight sets of data as provided in Wang et al. (2016) are adopted to train and test samples, which are listed in Table 3.

4.1 Introduction of machine learning methods

The back-propagation (BP) neural network is a widely used neural network trained according to the error back-propagation algorithm. The BP neural network adopts the gradient descent method, but which tends to terminate the learning by only achieving a local optimal value. As such, the prediction accuracy of using a BP neural network is not high.

The RBF neural network is a feedforward nonlinear neural network. The RBF (radial basis function) neural network consists of three layers, namely, the input layer, hidden layer and output layer. The radial basis function of multivariable nonlinear interpolation is adopted to transfer the input layer data to the hidden layer instead of the “weight” function used in the BP neural network. A linear interpolation is adopted in the RBF neural network when the hidden layer outputs to the output layer. In this way, the mapping of the network from input to output is nonlinear, but the network output is linear for variables. The “weight” factor of the network can be directly solved based on a set of linear equations. In this study, the RBF neural network algorithm is further combined with the PSO-RBF-neural network algorithm (Qin et al., 2005) for learning, and the results are compared with those based on the BP neural network. The optimal algorithm is then selected in order to overcome the local convergence issue of the BP neural network.

4.2 Error analysis and selection

According to the results of sample training and testing, the performance diagrams of each algorithm are provided in Figure 4. The PSO-RBF algorithm is found to provide the highest fitting degree.

Equation 9 is adopted to calculate the error between the training set and the testing set for each algorithm mentioned above:

$$E = \sum_{i=1}^n |y_{pi} - y_i| / y_i, \quad (9)$$

where E is error of the training set or testing set, y_{pi} is the i th predicted value, y_i is the i th measured value and n is the total number of objects in the set.

The results in terms of the error of the training set and test set based on Eq. 9 are provided in Table 5. It shows that some algorithms have a high fitting degree on the training set but a low fitting degree on the test set. This might be attributed to a relatively small number of samples (38 groups). A comprehensive error is thus defined in Eq. 10:

$$E_S = 0.4E_{train} + 0.6E_{test}, \quad (10)$$

TABLE 3 Learning samples.

NO.	Overburden structure ¹	Buried depth (m)	Dip angle (°)	Mining thickness (m)	Working face size (m)	Coal mining method ²	Layered mining number	Measured value
1	1	231	8	6.2	167	1	2	90.7
2	4	168	5.5	3.1	137	3	1	27.8
3	1	270	18	1.8	100	2	1	33
4	4	359	2.3	3.6	146	4	1	30
5	1	200	76	8	89	4	1	48
6	1	209.5	30	4.5	77	1	2	47.3
7	1	43	60	3	30	3	1	35
8	4	49	5	4	135	3	1	45
9	1	1024	32	6.5	180	4	1	75.6
10	4	230	37	2	85	2	1	52.5
11	3	120	8	1.2	75	2	1	31
12	1	434.6	8	8.7	153	4	1	64.5
13	2	320	6	1.7	65	2	1	27.5
14	3	475	28	5.13	149	3	1	45
15	3	173	20	3.8	70	1	2	26.7
16	2	409	9	8.13	193	4	1	72.9
17	2	130	5	6.3	136	1	2	52.2
18	2	93	62	1.8	73	2	1	16.6
19	1	260.94	2	5.2	265.5	3	1	153.9
20	3	467	8	11.4	207	4	1	228
21	2	288	6.5	8.61	169	4	1	65.5
22	2	520	12	3	174	3	1	102.3
23	1	391	25	5.6	230	1	2	57.3
24	2	285	6	1.6	180	2	1	30.8
25	2	479	4	6.6	170	4	1	66.6
26	2	325	5	5.6	160	1	2	51.5
27	4	113.3	14.5	2.45	188.8	3	1	34.98
28	4	262.8	2.5	8.8	143	1	2	39
29	4	225	23	6	174	1	3	58.4
30	4	329	8	8.1	134	4	1	83.9
31	3	341	6	5.3	99.5	1	2	45
32	3	52	9	4.3	90	1	2	40.3
33	1	89	7	2.03	69	2	1	45.86
34	2	420	23	3.7	70	3	1	56.8
35	4	350	9	4	136	3	1	35
36	1	400	5.75	5.77	154	4	1	70.7
37	2	418.6	6	8.7	198	4	1	65.5
38	1	272	11.5	8	120	4	1	62

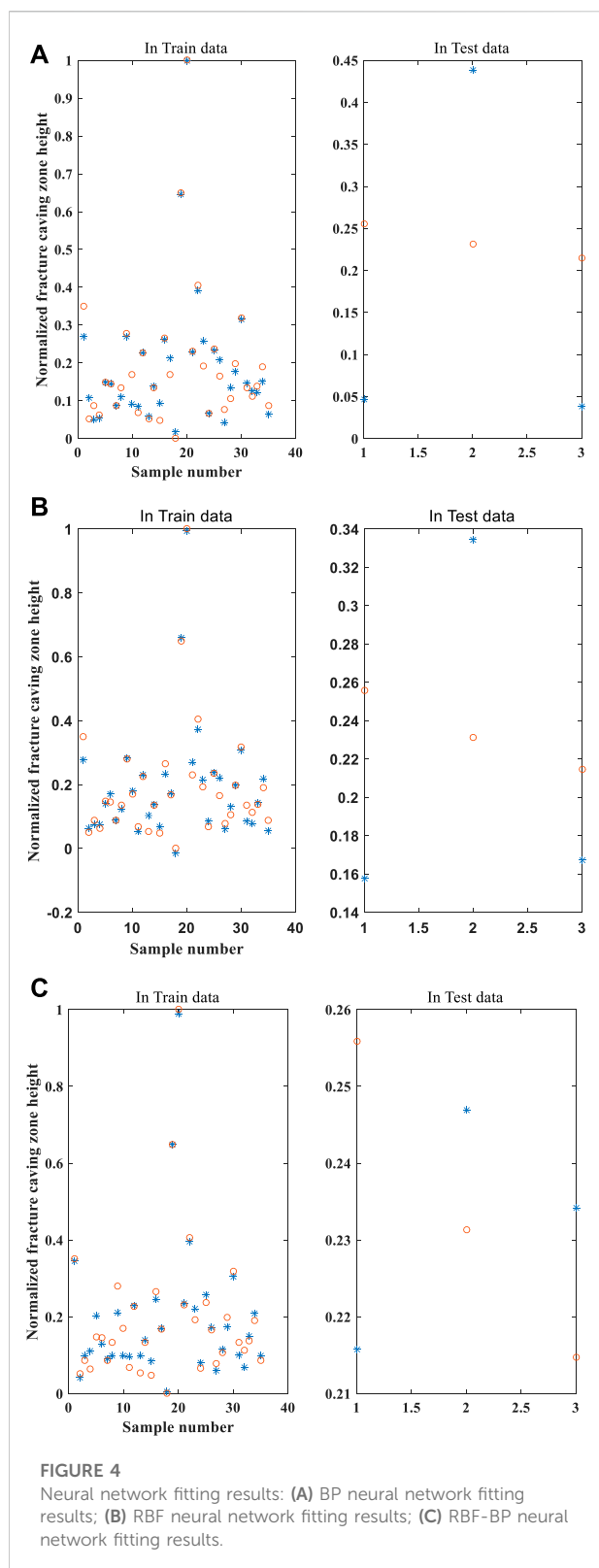
1) The overburden structure includes the hard–hard type (Index 1), the hard–weak type (Index 2), the weak–hard type (Index 3), and the weak–weak type (Index 4).

2) The coal mining methods are blast mining (Index 1), fully mechanized mining (Index 2), layer mining (Index 3), and fully mechanized caving (Index 4).

where E_s is composite error, E_{train} is the error of the training set, and E_{test} is the error of the test set.

The calculation of Eq. 10 shows that in the case of the same training samples and test samples, the PSO-RBF neural network algorithm provides a minimum comprehensive

error of 2.76%, while the RBF and BP neural network algorithms provide 8.048% and 12.84%. The PSO-RBF neural network algorithm performs even better than the GA-BP prediction model (2016) and thus will be used to predict the height of the caving fracture zone.



5 Numerical simulation of train load disturbance depth

A lot of research works have been carried out to investigate the dynamic response of soil under the influence of train load. Xia et al. (2009) proposed a coupling model to simulate the train-track-soil dynamic response by considering the track irregularity condition and the vibration induced by track irregularity. Galvin and Dominguez (2009, 2010a, 2010b) established the train-track-subgrade finite element model to analyze the dynamic response of three typical tracks under train load.

As a commonly used numerical analysis software in geotechnical engineering, FLAC3D is widely used in slope stability (Zhou and Qin, 2020), mining engineering (Booth et al., 2016), and geotechnical engineering (Yang et al., 2020). To accurately obtain the depth of ground disturbance under train load, FLAC3D software is used to simulate this study.

5.1 Prediction of disturbance depth

5.1.1 Train load simulation

Lamaran and Derdas (2002) simulated the load as the sum of the static load and additional dynamic load as a function of train speed, sleeper spacing, rail properties, and wheel weight. Auke and Gerard (2001) pointed out that the geometric irregularity caused by rail wear will produce huge wheel-rail impact force. Manabe (2004) studied the rail vibration caused by multiple wheelsets under track irregularity. Various geometric irregularities can also contribute to the variation of the train dynamic load magnitude (Jenkins et al., 1974). At present, the commonly used train load simulation formula is composed of a series of sine functions. In this study, the sine function of Eq. 4 considering irregularity is taken as the function of simulating train load.

5.1.2 High-speed railway subgrade–foundation model

According to the geotechnical engineering investigation results of the research railway section, the subgrade–foundation structure model is established as shown in Figure 5.

The length of the model is 64.8 m, and the height is 55 m.

5.1.3 Constitutive model and parameters

The British Derby Railway Research Center indicates that the dynamic behavior of a traditional ballast track subgrade is similar to that of an elastic damping material. In this study, a

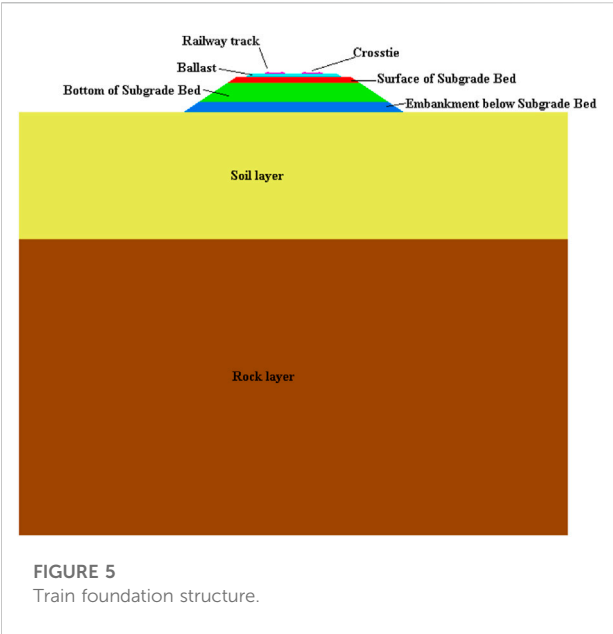


FIGURE 5
Train foundation structure.

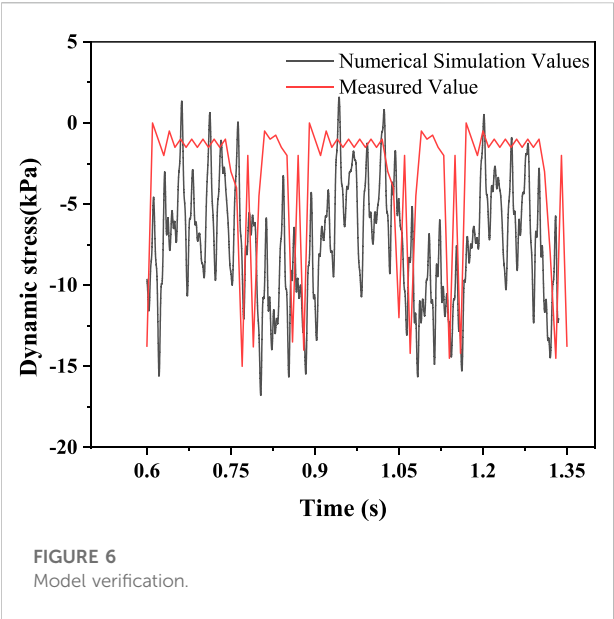


FIGURE 6
Model verification.

TABLE 4 Parameters of subgrade and soil layers.

	Thickness (m)	Bulk modulus K (MPa)	Shear modulus G (MPa)	Density γ (kN/m^3)	Effective cohesion c' (kPa)	Effective internal friction angle ϕ' ($^\circ$)
Railway track	0.2	17680	14960	25	-	-
Crosstie	0.15	17680	14960	25	-	-
Ballast	0.35	2960	2310	23.44	-	-
Surface of subgrade bed	0.7	76	175	22	-	-
Bottom of subgrade bed	2.3	38	98	20	-	-
Embankment below subgrade bed	-	38	98	20	-	-
Yellow clay	15	9.5	4.4	18.6	20	30
Sandstone	35	1302	1059	22	2000	35

Mohr–Coulomb constitutive model is used for the rock and soil layer, and an elastic constitutive model is used for subgrade structure. The material parameters of each layer are shown in Table 4.

5.1.4 Boundary condition and damping

A viscous boundary condition is adopted in FLAC3D to absorb the vibration wave and improve the calculation efficiency. Rayleigh damping is selected in this study, with a damping ratio parameter of 0.5%.

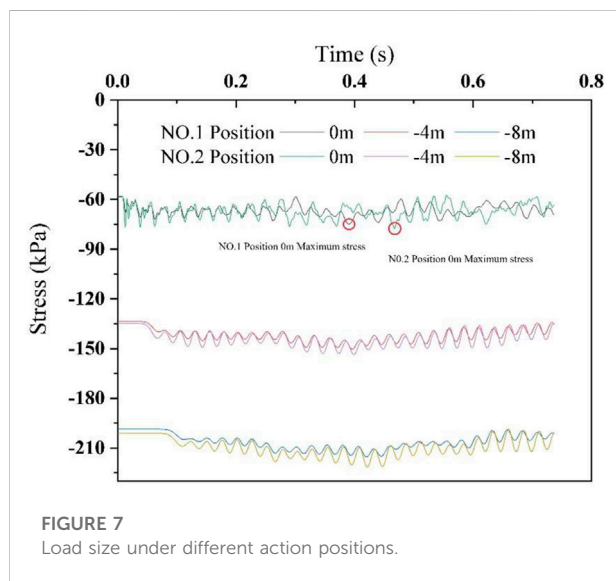
5.1.5 Model validation

The numerical model is first validated against the monitoring data obtained from the Qinhuangdao–Shenyang

passenger line (Nie, 2005). The dynamic stress at the bottom of the foundation bed predicted in this numerical simulation and the measured values are provided in Figure 6. It can be seen that the numerical model can capture the upper bound and lower bound values for the dynamic stress and the variation period. It can be seen from Figure 6 that the simulated dynamic stress value changes faster than the measured value because the simulated dynamic stress considers the geometric irregularity. When the train runs several times, it will be partially worn, which makes the train travel on the railway similar to a jumping state. The measured value is measured when the railway has just been built and the track is relatively smooth.

TABLE 5 Experimental groups.

Group	Axle load (t)	Train speed (km/h)	Embankment height (m)
Axle load group	14	250	4.15
	18	250	4.15
	22	250	4.15
	26	250	4.15
	30	250	4.15
Train speed group	22	150	4.15
	22	200	4.15
	22	250	4.15
	22	300	4.15
	22	350	4.15
Embankment height group	22	250	3.35
	22	250	3.75
	22	250	4.15
	22	250	4.55
	22	250	4.95



5.2 Disturbance depth formula

In this study, FLAC3D software is used to simulate the depth of train load disturbance as a function of axle load, speed, and embankment height, and twelve groups of models are designed by control variables as shown in Table 5. The depth of load disturbance was determined by comparing the maximum additional stress at each monitoring point with the 5% self-weight of the rock and soil mass at the point.

When two high-speed trains meet at the goaf ground, the load on the goaf ground is the largest. In order to accurately determine the disturbance depth of train load, stress monitoring points are set between the single rail and double rail in the same numerical model so as to determine the location of the maximum disturbance depth. The results are shown in Figure 7.

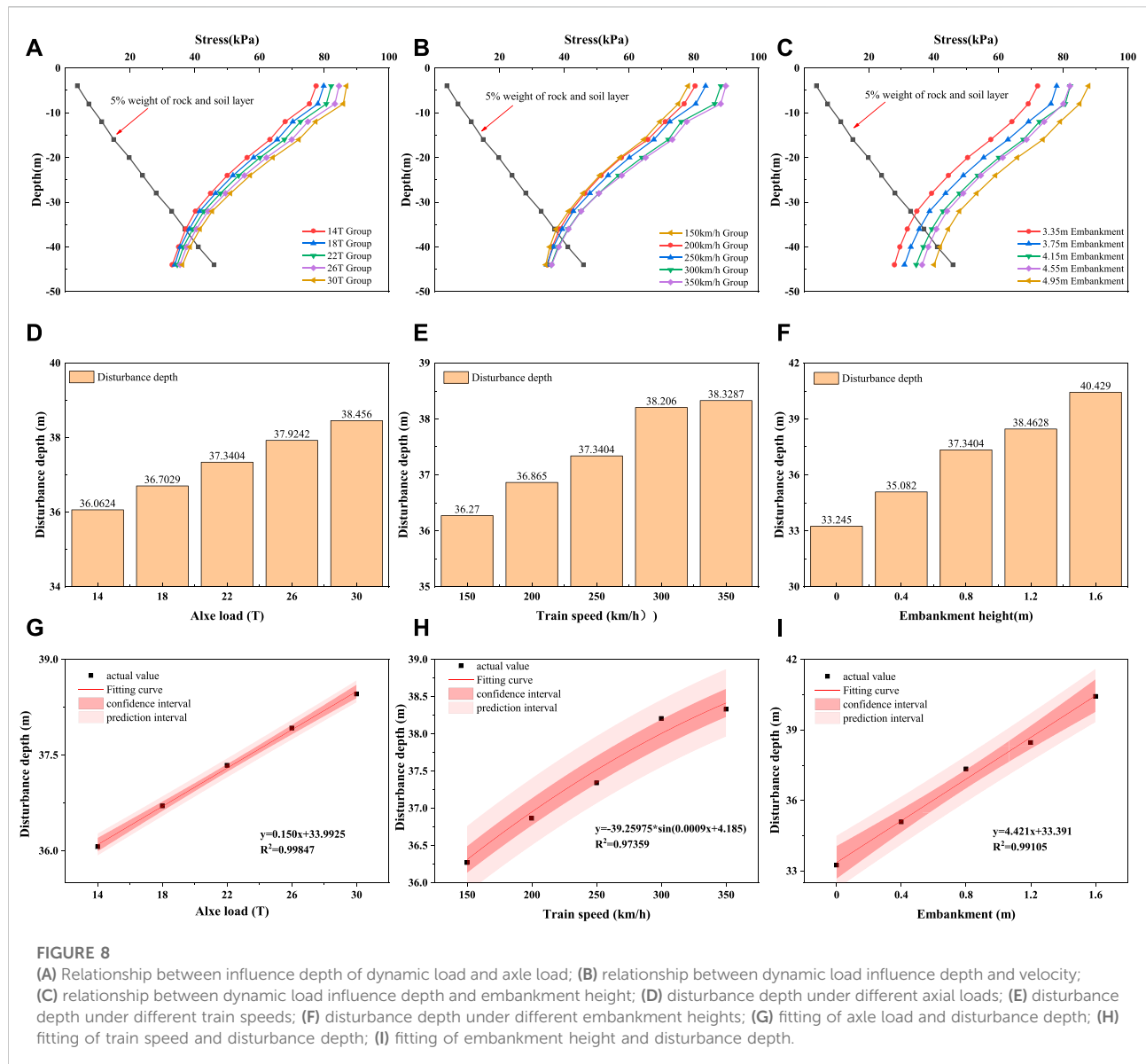
At -4 and -8 m, the load of the monitoring points between the double track is always greater than that between the single track. At 0 m, the load fluctuates greatly, but it is still the maximum value of the monitoring points between the double track. So, the position between the two tracks is selected to arrange monitoring points for determining the maximum disturbance depth. The diagram of stress change and disturbance depth for each group is shown in Figure 8.

5.2.1 Influence analysis of train axle load

In this study, the influence depth under the five grades of axle load listed in Table 5 is studied. As shown in Figures 8A,D, the increase of axle load would increase the additional dynamic stress on the base and increases the influence depth significantly. This is because the axle load directly affects the unilateral static wheel load, and the size of the unilateral static wheel load accounts for a large proportion of the dynamic load (see Eq. 4).

5.2.2 Influence analysis of train speed

Five grades of varying train speed between 150 and 350 km/h, as listed in Table 5, are used to study the change of dynamic load influence depth. It can be seen from Eq. 4 that the increase of train speed would result in a corresponding increase in the force

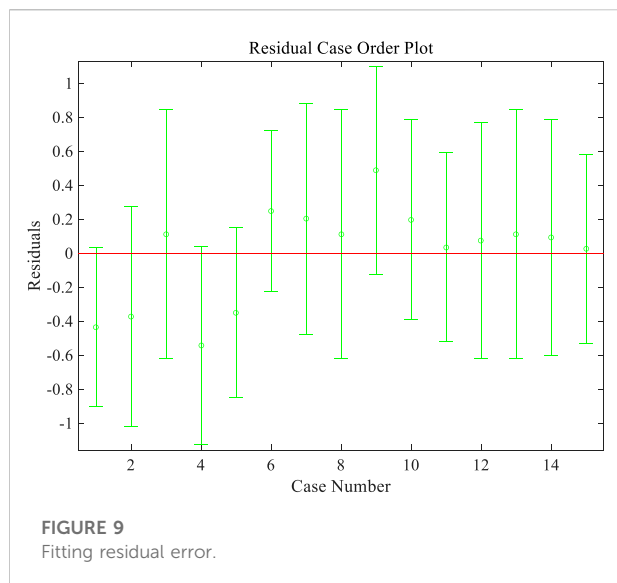


acting on the rail, which should be attributed to the impact of the change of speed on the circular frequency under various control conditions. The influence depth, as indicated in Figure 8B, is observed to increase linearly with the train speed increases from 150 to 300 km/h but remains nearly constant when the train speed increases from 300 to 350 km/h. This observation is consistent with the findings of Bian et al. (2014). Such impacts of train speed on influence depth should be attributed to a shorter duration of train load with the train speed increasing.

5.2.3 Influence analysis of embankment height

Five groups of embankment height, namely, 3.35 m, 3.75 m, 4.15 m, 4.55 m, and 4.95 m are studied regarding their influence

on the depth of train dynamic load. As shown in Figures 8C,F, with the increase of embankment height, the static load imposed on the foundation by the embankment would increase, which, thereby, would increase the influence depth of train load. In fact, due to the characteristics of high-speed rail, dozens of high-speed railway will pass through every day, and increasing the embankment height can effectively reduce the impact of dynamic load on the site. For example, the curve of 4.15 and 4.55 m embankments in Figure 8C shows that the additional load under the condition of 4.15 m is basically the same as that under the condition of 4.55 m at the monitoring point of 4 m below the base. Although the static load of the 4.55 m embankment is larger than that of the 4.15 m embankment, the increase of embankment height makes the disturbance consumption of



train dynamic load increase, resulting in the additional stress being equal at the base of 4 m.

5.2.4 Disturbance depth of train load

Figures 8A–F show that the disturbance depth is dependent on the additional stress, the latter of which is a function of the axle load, train speed, and embankment height. These three factors are mutually independent. As such, the relationship between the disturbance depth and each factor can be obtained by data fitting. A comprehensive formula by superposition can be obtained for the critical disturbance depth of train load.

The fitting results of the relationship between the three factors and disturbance depth are shown in Figures 8G–I. A linear relationship is apparent between the two factors of axle load and embankment height and the disturbance depth. A sine function relationship is, however, observed between the train speed and disturbance depth, which should be attributed to the loading function (a sine function, Eq. 4) used in this study.

As shown in Eq. 11, the relationship between the critical disturbance depth of train dynamic load and the three factors, i.e., axle load, speed and embankment height can be obtained as

$$H_d = a_0 + a_1G + a_2H + a_3 \sin(0.0009v + 4.185), \quad (11)$$

where H_d is the critical disturbance depth of train dynamic load, m; G is axle load, ton; H is height of embankment below subgrade bed, m; v is train speed, km/h; and a_0 , a_1 , a_2 , and a_3 are fitting coefficients.

By using a multiple linear regression analysis, the following values for the fitting coefficients can be obtained:

$$a_0 = -7.283; a_1 = 0.150; a_2 = 4.437; a_3 = -39.448.$$

Substituting a_0 , a_1 , a_2 , and a_3 into Eq. 11, the formula for calculating the critical depth of train dynamic load disturbance is shown in Eq. 12.

$$H_d = -7.283 + 0.150G + 4.437H - 39.448(0.0009v + 4.185). \quad (12)$$

The residuals obtained by this multiple linear regression are shown in Figure 9. The confidence interval of residual values at each data point contains 0 points, and the R^2 value of this formula is 0.97, indicating that this fitting can better reflect the original data.

6 Case study

6.1 Engineering geology

In order to verify the validity of the judgment method and the correctness of the FLAC3D model, an engineering example, DK259 + 690–DK259 + 710 road section of Tai-Jiao high-speed railway, as shown in Figure 10, is used to verify the approach provided above. The high-speed rail line crosses No. 2 goaf, which has a buried depth of goaf about 46.6 m and a maximum mining height of about 6.5 m. The dip angle of the coal seam is 2° – 5° and was mined by blast mining. The backfilling material is sandstone and mudstone gravels, and the backfilling structure is loose. The high-speed railway is constructed with ballast track, and the height of the embankment below the subgrade bed is 0 m. The ground profile and the design parameters are the same as those adopted in this study above (Figure 6 and Table 4). The design train speed is 250 km/h, the design axle load is 22 t, and the railway trunk line is 40 m from open-off cut.

6.2 Critical mining depth-to-thickness ratio determination

The goaf site of the railway trunk line is determined according to Eqs 1–3, and relevant data are inserted: h_i is 3 m, Σh_i is 10 m, γ is 2.5×10^4 N/m³, σ_t is 10 MPa, and H is 46.6 m. The calculation shows that L_z is 9 m and n is 5. The length of the outer edge and inner edge is 45 m. Therefore, the location of the high-speed railway project is the outer edge area.

The mining depth-to-thickness ratio of the goaf site is only 7, which does not meet the critical value of any working condition in Table 1. Therefore, the relationship between the depth of the caving fracture zone and the disturbance depth is used to determine the influence level of goaf activation.

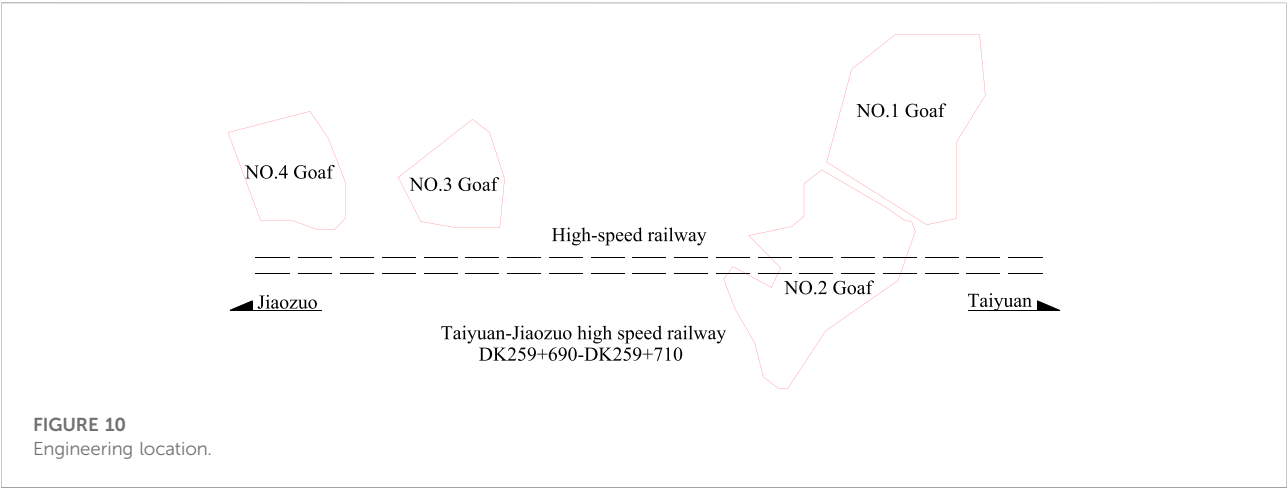


FIGURE 10
Engineering location.

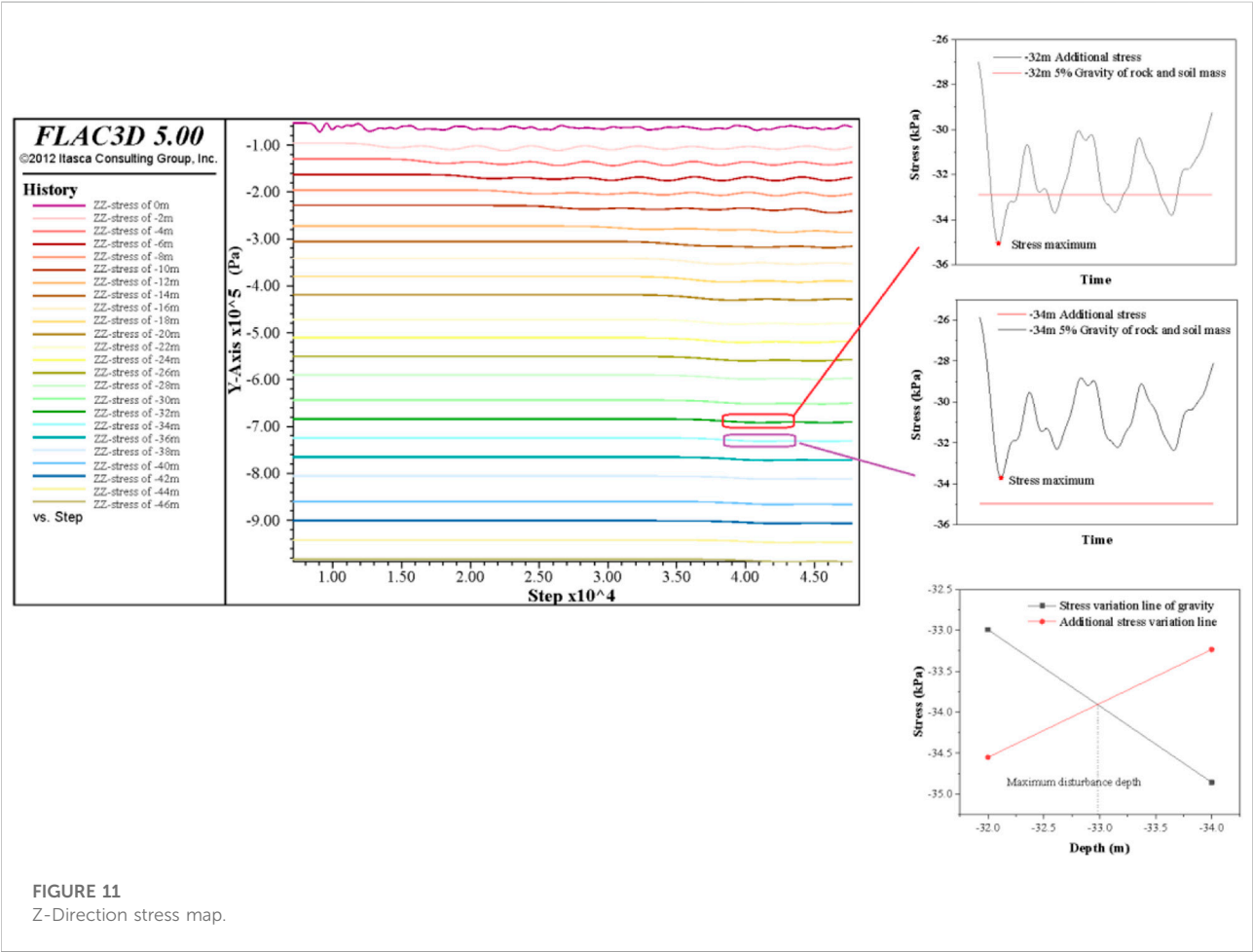


FIGURE 11
Z-Direction stress map.

6.3 Height prediction of the caving fracture zone

The height of the caving fracture zone in the goaf is predicted by the PSO-RBF algorithm. The engineering condition of the goaf is normalized and compiled, with an input matrix being obtained:

$$X = [1 \ 0.001 \ 0.0405 \ 0.5196 \ 0.3830 \ 0 \ 0].$$

The trained grid is used to train the input matrix, and the height of the caving fracture zone in the goaf is calculated to be 39.37 m.

6.4 Train load disturbance depth prediction

To verify numerical simulation and Eq.12, these two methods are compared by predicting the disturbance depth of the train dynamic load.

The numerical simulation model produces the Z direction stress figure. As shown in Figure 11, the influence depth under this condition is 32.96 m. At the same time, the numerical simulation model results show that the maximum stress load at 0 m is 72.56 kPa, and the result obtained by Eq. 8 is 80.682 kPa, indicating that the equation is reasonable.

With the train parameters substituted into Eq. 12, the dynamic load disturbance depth is predicted to be 33.675 m. The difference between the values predicted by these two methods is only 0.679 m.

Calculations of the height of the caving fracture zone and the depth of train load disturbance show that the critical disturbance boundary of the train dynamic load is expected to intrude into the top boundary of the caving fracture zone. The dynamic load of the train would impact the caving fracture zone, closure of the separation layer and cracks, and reactivate goaf deformation. The influence level of the goaf site is significant.

Grouting treatment was carried out during the construction of high-speed railway in this section to fill the separation layer and cracks in the caving fracture zone to improve the foundation performance. This is consistent with the predicted results of the research method and indicates that the method has some engineering reference value.

7 Conclusion

Due to the high-intensity and long-term mining of China's coal resources, a large area of goaf sites have been formed. In addition, with the rapid development of high-speed railway, some key lines will inevitably cross the coal mine goaf site. The activation evaluation criteria of goaf ground are one of the urgent problems to be solved to ensure the safe operation and maintenance of high-speed railways. Based on the neural

network and numerical simulation, the combined methods for the goaf ground activation criteria of high-speed railway are proposed. The main conclusions are as follows:

- 1) The criteria for determining the critical mining depth-to-thickness ratio of high-speed railway in the goaf site is given, the zoning formula of the goaf site is proposed, and the simplified formula of combined action under subgrade and train load is obtained.
- 2) The BP, RBF, and PSO-RBF neural networks are used to learn the 38 mine goaf samples, and the error of each model for sample learning and testing is obtained. The PSO-RBF neural network model has the lowest error, which can be used to predict the height of the caving fracture zone in the goaf site.
- 3) One evaluation criterion for the influence degree of goaf ground stability of high-speed railway is proposed, and a simple and effective numerical simulation model about applying train dynamic load is established. Comparisons on the additional dynamic stress and self-weight stress of the goaf ground are drawn, the disturbance depth of train dynamic load is predicted, and the influence degree of goaf ground stability is judged.
- 4) Activation judging formula with high availability and reliability is deduced. By changing the embankment height, train speed, and train axle load, the FLAC3D model was used to simulate various working conditions. The results show that the disturbance depth of train dynamic load has a good functional relationship with the abovementioned three factors. The calculation formula of critical depth of train dynamic load disturbance is given by using the superposition principle and multiple linear regression analysis.
- 5) An example verification process through a line section of the Taijiao high-speed railway proves that the method has a certain reference value in the safety evaluation of high-speed railway construction projects at the site of the mining area, but it cannot provide detailed hazard classification, such as the corresponding measures to be taken for each level of hazard.

Data availability statement

The original contributions presented in the study are included in the article/Supplementary Material; further inquiries can be directed to the corresponding author.

Author contributions

LR: Conceptualization, Methodology, Software, Investigation, Formal Analysis; PH: Data Curation, Writing–Original Draft, YZ: Visualization, Investigation; CY: Resources, Supervision; ZD: Software, Validation; ZZ: Visualization, Writing–Review & Editing; CS: Numerical model modification and debugging.

Funding

Funding for this work was supported by the National Natural Science Foundation of China (No. U1810203).

Conflict of interest

Author CY is employed by WSP Australia and Author CS is employed by Taiyuan Design Research Institute for Coal Industry.

The remaining authors declare that the research was conducted in the absence of any commercial or financial

relationships that could be construed as a potential conflict of interest.

Publisher's note

All claims expressed in this article are solely those of the authors and do not necessarily represent those of their affiliated organizations, or those of the publisher, the editors, and the reviewers. Any product that may be evaluated in this article, or claim that may be made by its manufacturer, is not guaranteed or endorsed by the publisher.

References

- Ashok, J., and Shrivastva, B. K. (2012). Stability analysis of the proposed hybrid method of partial extraction for underground coal mining. *Int. J. Rock Mech. Min. Sci.* 52, 103–111. doi:10.1016/j.ijrmms.2012.03.002
- Auke, D., Herman, G., and Holscher, P. (2001). Elastic Waves Generated by high-speed trains[J]. *J. Comp. Acous.* 9 (3), 833–840. doi:10.1142/s0218396x01001133
- Bian, X. C., Jiang, H. G., Cheng, C., Chen, Y. M., Chen, R. P., and Jiang, J. (2014). Full-scale model testing on a ballastless high-speed railway under simulated train moving loads. *Soil Dyn. Earthq. Eng.* 66 (11), 368–384. doi:10.1016/j.soildyn.2014.08.003
- Bian, X. C., Jiang, H. G., and Chen, Y. M. (2010). Accumulative deformation in railway track induced by high-speed traffic loading of the trains. *Earthq. Eng. Vib.* 9 (3), 319–326. doi:10.1007/s11803-010-0016-2
- Bian, Z. F., Miao, X. X., Lei, S. G., Chen, S. E., Wang, W. F., and Sruthers, Sue (2012). The challenges of reusing mining and mineral-processing wastes. *Science* 337, 702–703. doi:10.1126/science.1224757
- Booth Andrew, J., Marshall Alec, M., and Ro, S. (2016). Probabilistic analysis of a coal mine roadway including correlation control between model input parameters. *Comput. geotechnics.* 74 (4), 151–162. doi:10.1016/j.compgeo.2016.01.008
- Cai, B., Pan, G. L., and Fu, F. (2020). Prediction of the postfire flexural capacity of rc beam using GA-BPNN machine learning. *J. Perform. Constr. Facil.* 34 (6). doi:10.1061/(ASCE)CF.1943-5509.0001514
- Deb, D., and Choi, S. O. (2006). Analysis of sinkhole occurrences over abandoned mines using fuzzy reasoning: A case study. *Geotech. Geol. Eng. (Dordr.)* 24 (5), 1243–1258. doi:10.1007/s10706-005-1404-7
- Dong, L. J., Peng, G. J., Fu, Y. H., Bai, Y. F., and Liu, Y. F. (2008). Unascertained measurement classifying model of goaf collapse prediction. *J. Coal Sci. Eng. China.* 14 (2), 221–224. doi:10.1007/s12404-008-0046-9
- Galvin, P., Romero, A., and Dominguez, J. (2009). Experimental and numerical analyses of vibrations induced by high-speed trains on the Córdoba-Málaga line. *Soil Dyn. Earthq. Eng.* 29 (4), 641–657. doi:10.1016/j.soildyn.2008.07.001
- Galvin, P., Romero, A., and Dominguez, J. (2010a). Fully three-dimensional analysis of high-speed train-track-soil-structure dynamic interaction. *J. Sound Vib.* 329 (24), 5147–5163. doi:10.1016/j.jsv.2010.06.016
- Galvin, P., Romero, A., and Dominguez, J. (2010b). Vibrations induced by HST passage on ballast and non-ballast tracks. *Soil Dyn. Earthq. Eng.* 30 (9), 862–873. doi:10.1016/j.soildyn.2010.02.004
- Guo, G. L. (2001). *Deformation mechanism and control of building foundation above old goaf[M]*. Xuzhou: China University of Mining and Technology press. (in Chinese).
- Guo, Q., Li, Y., Meng, X. R., Guo, G. L., and Lv, X. (2019). Instability risk assessment of expressway construction site above an abandoned goaf: A case study in China. *Environ. Earth Sci.* 78 (20), 588. doi:10.1007/s12665-019-8599-z
- Guo, Q. B., Meng, X. R., Li, Y. M., Lv, X., and Liu, C. (2021). A prediction model for the surface residual subsidence in an abandoned goaf for sustainable development of resource-exhausted cities. *J. Clean. Prod.* 2021, 123803. doi:10.1016/j.jclepro.2020.123803
- Henry, S. H., Wetmiller, R. J., and Gendzwil, D. J. (1989). Don J.gendzwil. Induced seismicity in mines in Canada—an overview[J]. *Pure Appl. Geophys.* 129 (3), 423–453. doi:10.1007/BF00874518
- Jenkins, H. H., Stephenson, J. E., Clayton, G. A., Morland, G. W., and Lyon, D. (1974). The effect of track and vehicle parameters on wheel/rail vertical dynamic loads[J]. *J. Railw. Eng. Soc.* 3 (1), 2–16.
- Lamaran, G., and Derdas, M. (2002). Evaluation of dynamic load on rail track sleepers used on vehicle-track modeling and analysis[J]. *Int. J. Struct. Stab. Dyn.* 2 (3), 355–374.
- Lei, S., Cui, Z., Zhang, H., and Han, L. (2013). Analysis and treatment of the fault activation below the dynamic foundation in the goaf area[J]. *Disaster Adv.* 6, 337–342.
- Liang, B., and Cai, Y. (1999). Dynamic analysis on subgrade of high-speed railways in geometric irregular condition[J]. *J. China Railw. Soc.* 1999 (02), 93–97. (in Chinese).
- Liang, X., Cheng, Q., Wu, J. J., and Chen, J. (2016). Model test of the group piles foundation of a high-speed railway bridge in mined-out area. *Front. Struct. Civ. Eng.* 10 (4), 488–498. doi:10.1007/s11709-016-0338-x
- Liu, W. S., Li, F. Y., and Guo, X. T. (2011). “Comprehensive evaluation of the stability of coal mining subsidence based on fuzzy matter-element Theory[C],” in *Natural resources and sustainable development. Part 1* (Freienbach, Switzerland: Trans Tech Publications), 237–241.
- Mahmoodzadeh, A., Mohammadi, M., Ibrahim, H., Abdulharmid, S. N., Ali, H. F. H., Farid Hama Ali, H., et al. (2021). Artificial intelligence forecasting models of uniaxial compressive strength. *Transp. Geotech.* 27, 100499. doi:10.1016/j.trgeo.2020.100499
- Manabe, K. (2004). Multiple-wheel induced vibration of rail with surface irregularity. *QR. RTRI.* 45 (3), 136–141. doi:10.2219/rtriqr.45.136
- María-Belén, P. G., Alcalde-Gonzalo, J., Ramírez-Oyanguren, P., and Francisco-José Suárez-Domínguez-Alvarez-Fernández, M. I. (2013). Longwall mining stability in take-off phase. *J. Appl. Math.* 2013 (5), 859803–859813. doi:10.1155/2013/859803
- Merwe, J. (2003). New pillar strength formula for South African coal[J]. *Journal-South Afr. Inst. Min. Metallurgy.* 103 (5), 281–292.
- Nie, Z. H. (2005). *Study on vertical dynamic response of the track/subgrade in high-speed railway[D]*. Changsha, China: Central South University. (in Chinese).
- Qian, M. G. (1981). A study of the behaviour of overlying strata in longwall mining and its application to strata control[J]. *Dev. Geotechnical Eng.* 32, 13–17.
- Qin, Z., Chen, J., Liu, Y., and Lu, J. (2005). “Evolving RBF neural networks for pattern classification[C],” in *International Conference on Computational & Information Science.* (Berlin Heidelberg: Springer).

Tan, X. H., Bi, W. H., Hou, X. H., and Wang, W. (2011). Reliability analysis using radial basis function networks and support vector machines. *Comput. Geotechnics*. 38 (2), 178–186. doi:10.1016/j.compgeo.2010.11.002

The Professional Standards Compilation Group of People's Republic of China (2014). *Code for investigation of geotechnical engineering in the coal mine goaf[S]*. Beijing: China Planning Press.

Wang, J. T., Guo, G. L., and Guo, Q. B. (2016). Application of grey system theory and GA-BP neural network model in control and prediction of water-flowing fractured zone's height[J]. *Coal Technol.* 35 (08), 126–128. (in Chinese).

Xia, H., and CaoRoeck, Y. M. G. D. (2009). Theoretical modeling and characteristic analysis of moving-train induced ground vibrations[J]. *J. Vib. Eng.* 329 (7), 819–832.

Yang, J., Yin, Z. Y., Liu, X. F., and Gao, F. P. (2020). Numerical analysis for the role of soil properties to the load transfer in clay foundation due to the traffic load of the metro tunnel. *Transp. Geotech.* 23, 100336. doi:10.1016/j.trgeo.2020.100336

Yu, Y., Chen, S. E., Deng, K. Z., Wang, P., and Fan, H. D. (2018). Subsidence mechanism and stability assessment methods for partial extraction mines for sustainable development of mining cities—a Review. *Sustainability* 10 (1), 113. doi:10.3390/su10010113

Zhang, Y. B. (2005). *Research on the stability of building foundation above old mine goafs and its damage regula[D]*. Taiyuan, China: Taiyuan University of Technology. (in Chinese).

Zhou, J. F., and Qin, C. B. (2020). Finite-element upper-bound analysis of seismic slope stability considering pseudo-dynamic approach. *Comput. geotechnics*. 122 (6), 103530–103530.16. doi:10.1016/j.compgeo.2020.103530



OPEN ACCESS

EDITED BY

Hongyuan Liu,
University of Tasmania, Australia

REVIEWED BY

Mingjing Lu,
SINOPEC, China
Shu Longyong,
China Coal Research Institute, China

*CORRESPONDENCE

Xiao Liu,
liuxiao@hpu.edu.cn

SPECIALTY SECTION

This article was submitted to
Geohazards and Georisks,
a section of the journal
Frontiers in Earth Science

RECEIVED 29 March 2022

ACCEPTED 27 June 2022

PUBLISHED 19 August 2022

CITATION

Liu X, Jing T, Lin H, Xuan D, Li Y and Xu S
(2022), Morphological characteristics
and permeability evolution of deep mine
gas drainage boreholes.
Front. Earth Sci. 10:906923.
doi: 10.3389/feart.2022.906923

COPYRIGHT

© 2022 Liu, Jing, Lin, Xuan, Li and Xu.
This is an open-access article
distributed under the terms of the
[Creative Commons Attribution License
\(CC BY\)](https://creativecommons.org/licenses/by/4.0/). The use, distribution or
reproduction in other forums is
permitted, provided the original
author(s) and the copyright owner(s) are
credited and that the original
publication in this journal is cited, in
accordance with accepted academic
practice. No use, distribution or
reproduction is permitted which does
not comply with these terms.

Morphological characteristics and permeability evolution of deep mine gas drainage boreholes

Xiao Liu^{1*}, Tianxiang Jing¹, Haixiao Lin¹, Dequan Xuan², Yong Li¹ and Sen Xu¹

¹Henan Polytechnic University, Jiaozuo, China, ²Ventilation Department of Henan Dayou Energy Co. Ltd, Yima, China

Structural coal has low permeability and high gas content. The increase of mining depth seriously restricts the safe mining of deep mines. Hydraulic flushing is the main means of gas extraction. The shape of the hydraulic flushing hole is an important basis to determine the pumping radius, which is widely regarded as a cylinder. However, due to the differences in the stress level, water force, friction and external moisture, the pore morphology, and permeability evolution need to be further studied. At present, the hole shape for hydraulic punching is equivalent to a cylinder in drilling design and evaluation, which is one of the important bases to determine the effective extraction radius. However, the hole shape is affected by many factors, so the scientific equivalent to a cylinder remains to be discussed. The BR-PKN equation describing the hole shape is established by introducing and combining the Bergmark–Roos equation and PKN model, and the hole's shape is shown by MATLAB. To verify its accuracy, YZD18.5 is used as an onsite logging tool for data acquisition and analysis, and the hole section is drawn. The BR-PKN equation and permeability evolution model are simulated by COMSOL Multiphysics, and the permeability evolution law of conventional cylinder with hydraulic flushing is compared and analyzed. The results show that 1) the shape of the hydraulic punch hole is ellipsoid with three different axes, and its horizontal section is approximately an ellipse; 2) within the influence range of quasi-ellipsoid holes, the permeability changes in the long and short axis of quasi-ellipsoid holes are similar. The permeability evolution curve of the coal first increases, then decreases, and finally, flattens with the increase of distance from borehole, and the permeability of the coal body increases with the extension of extraction time; 3) the permeability of the equivalent ellipsoid pore decreases with the increase in coal water content. The effective radius in the long and short axes of the minimum cross section of the quasi-ellipsoid hole is 0.89 and 0.95 times the effective extraction radius of the equivalent cylinder, which provides a basis for a drilling layout.

KEYWORDS

hydraulic flushing, hole shape, the moisture content, numerical simulation, extraction of radius

1 Introduction

After a long period of intense tectonic activity, coal is primarily formed after extrusion, shear deformation, and cohesion of low strength and low permeability. With the increase in mining depth, the distribution of tectonic coal tends to expand. Unloading is a deep mine gas disaster management technology. Hydraulic punching is a tectonic coal unloading extraction gas effective technique, and its role is mainly reflected in the following three aspects (Wu et al., 2002; Wang et al., 2013; Jiang et al., 2018; Liu and Liu, 2019; He et al., 2021): 1) high-pressure water is used to break the coal body, forming a certain range of pressure relief area around the hole, in which the permeability increases substantially, so as to achieve the purpose of gas extraction; 2) wetting coal reduces its elastic potential energy; and 3) water lock reduces gas desorption speed. The pore shape is a key influencing factor in the design of gas drainage. Scholars generally regard the process of hydraulic flushing as a uniform pore expansion, that is, a cylinder with regular pore shape (Wei et al., 2014; Yang et al., 2018; Ren, 2019). However, after flushing, the stress state of the coal body around the hole will change, and the shape of the hole will change correspondingly under the influence of stress, which is not a regular cylinder, thus affecting the gas extraction design.

External moisture is an important part of coal. When external moisture enters coal, it will affect the permeability characteristics and structure of the coal. After hydraulic flushing, the external moisture of the coal around the hole changes, and the permeability of coal will also change under the influence of external moisture. To explore the relationship between water and coal reservoir permeability, many scholars have carried on fruitful research. For example, Jianping Wei conducted independent research and development of the gas coal and rock triaxial seepage test system, determination of coal sample under different moisture content and confining pressure and gas pressure combination of seepage flow, moisture content, and the relationship between the coal containing gas permeability characteristics of expression (Yuan et al., 2015). Li et al. (2020) established a coal-rock permeability model considering the comprehensive effect of water content and fracture compressibility and analyzed the response mechanism of effective compressibility coefficient and permeability of coal rock under different water content conditions. Hao et al. (2016) explored hydraulic flushing around coal gas migration rule and established a creep-under the coupled action of seepage flow hydraulic flushing on the surrounding coal permeability dynamic evolution model, and their results show that hydraulic flushing measures can greatly improve the permeability of the coal

body around drilling and coal permeability depending on the space distance, which can quickly reduce the negative power function relationship. On the basis of studying the process of hydraulic flushing and hole shape, this paper studies the hole shape produced by hydraulic flushing and the evolution of coal permeability around the pore with time by means of theoretical analysis and numerical simulation. The results can provide a theoretical basis for the design of mine gas extraction and data support.

2 Methods

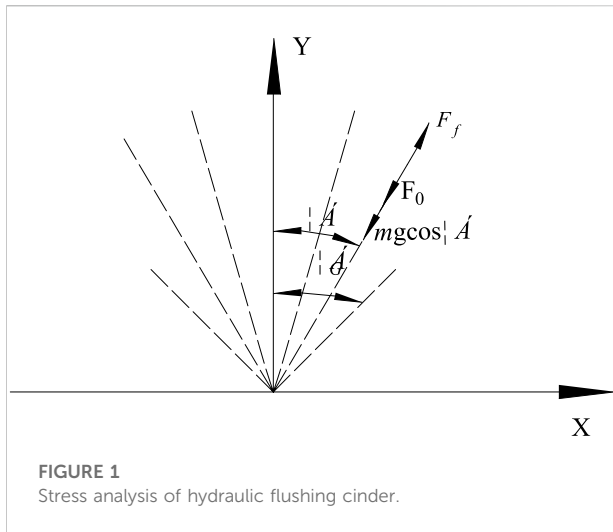
2.1 Establishing a hole shape equation for hydraulic flushing

Bergmark–Roos ore drawing theory establishes a mathematical model of loose ore and rock flow from the mechanical point of view. It is assumed that ore and rock particles move continuously from the initial position to the ore drawing port in the shortest distance. The relationship between the gravity of ore and the direct friction of surrounding particles is analyzed from the force of particles in the movement, and the formation principle of ore drawing ellipsoid is clarified. This is a significant development in ore drawing theory research (Ma et al., 2016; Tao et al., 2010; Melo et al., 2007; Kuchta, 2002; Zhang et al., 2019; Liu et al., 2020). The maximum and minimum horizontal principal stresses are the key factors affecting the shape of hydraulic flushing holes. In the horizontal section of the hole after hydraulic flushing, coal and rock are regarded as elastic and brittle materials, the height of the hole is fixed, and the force of water is a constant, which is highly consistent with the PKN model (Tao, 2009; Garikapati et al., 2019; Zheng et al., 2019). In this study, based on the characteristics of coal extraction by water jet and the influence of horizontal stress, the Bergmark–Roos and PKN models were used to establish the shape equation of hydraulic flushing. The BR-PKN equation is as follows:

$$s = \frac{H}{1 - \cos \alpha_G} (\cos \alpha - \cos \alpha_G), \quad (1)$$

where s is the moving distance of particles, m; H is the height of ore body, m; α is the angle between the particle moving trace and the vertical direction, °; and α_G is the maximum angle of dispersion movement, which is determined by the following formula:

$$\alpha_G = 45 - \varphi_0/2, \quad (2)$$



where φ_0 is the internal friction angle of particles, which changes with particle size and particle roughness. The coarser the particles, the greater the value.

The stress analysis of hydraulic punching coal cinder is shown in Figure 1.

The resultant force F of each component force on coal cinder along the trajectory direction of coal cinder production is

$$F = mg \cos \alpha + F_0 - F_f,$$

where M is mass of coal and rock bulk, kg; G is the acceleration of gravity, 9.81 N/kg ; F_0 is the force of punching water on coal cinder, N , constant value; and F_f is the friction force between coal and rock bulk, N . Because F_0 is a constant value, so F_0/m is a constant, let $F_0/m = ge$, e is a constant.

According to the stress analysis of the horizontal section of the hole, the horizontal section is not regular round, and has long axis and short axis. Its short semi-axis r_1 is

$$r_1 = s \sin \alpha = H \frac{\cos \alpha + e - \cos \alpha_G}{1 + e - \cos \alpha_G} \sin \alpha. \quad (3)$$

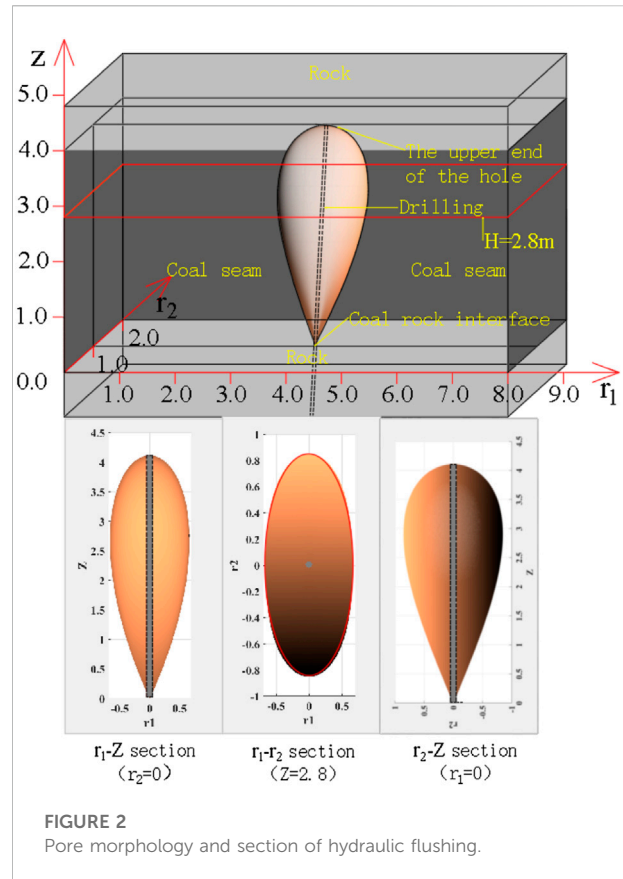
Hole height Z is

$$Z = s \cos \alpha = H \frac{\cos \alpha + e - \cos \alpha_G}{1 + e - \cos \alpha_G} \cos \alpha. \quad (4)$$

The long half-axis r_2 of the horizontal section can be obtained by the following formula:

$$r_2 = \frac{QH(1 + e - \cos \alpha_G) \left[2xe^x \operatorname{erfc}(x) + 2/\sqrt{\pi} - 1 \right]}{32\pi C^3 \sqrt{\pi} \sin \alpha (\cos \alpha + e - \cos \alpha_G)}, \quad (5)$$

where Q is the change of hole volume, $Q = H^* \frac{dA}{dt}$, m^3/min ; C is the coefficient, taken as 1; t is the movement time of coal and rock bulk; $x = \frac{2C\sqrt{\pi}}{H}$; and $\operatorname{erfc}(x)$ is the error compensation function of x .



2.2 Drawing of the hole shape equation based on MATLAB

The coal seam thickness of 14250 working face of Xin'an Coal Mine is $0.3\text{--}13.1 \text{ m}$, and the average coal thickness is about 4 m . The deduced BR-PKN equation suitable for coal cinder output of hydraulic flushing is displayed in three dimensions by MATLAB, and the shape and section of hydraulic flushing holes are expressed in Figure 2. It is found that the shape of hydraulic flushing holes is a quasi-ellipsoid with a slightly larger top than bottom. The horizontal section of the hole ($r_1\text{--}r_2$ section) is a flat ellipse.

2.3 Field verification of the shape characteristics of hydraulic flushing holes

The hole's shape in hydraulic flushing is restricted by many factors, such as coal-rock bulk gravity, coal-rock friction, water force, stress and so on. Through theoretical derivation, it is found that the hole's shape is ellipsoid-like. To verify the feasibility of BR-PKN equation and verify that the holes' shape is ellipsoid, the hydraulic flushing test was carried out in the cutting bottom plate roadway of

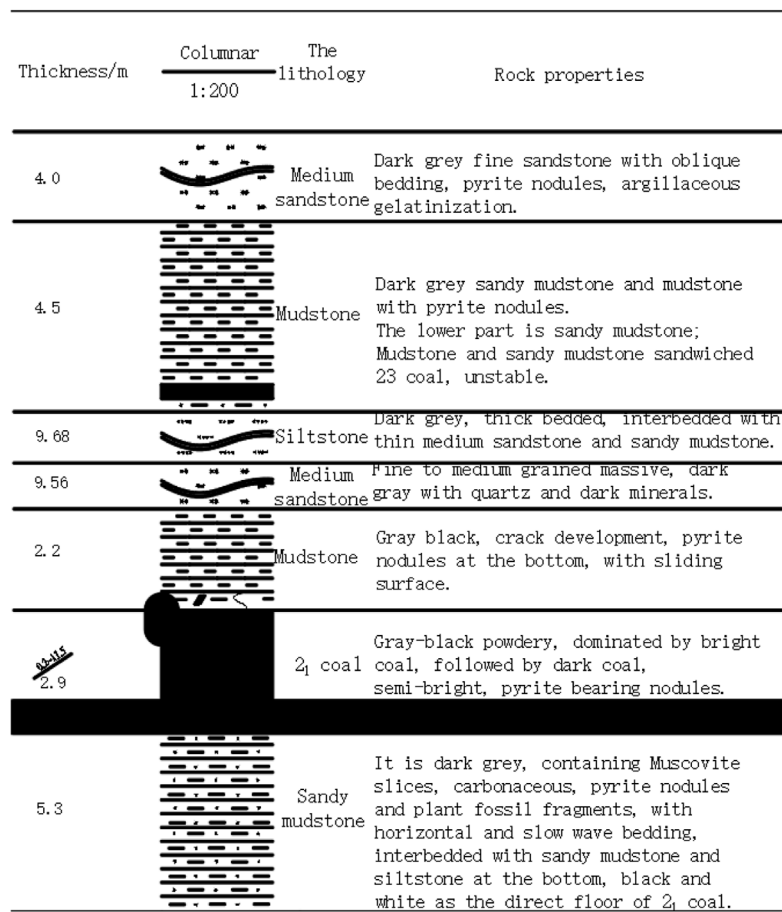


FIGURE 3
Strata histogram of Xin'an Coal Mine.

14250 working face in Xin'an mine. [Figure 3](#) is the stratum bar chart of Xin'an Coal Mine

2.3.1 Test equipment

YZD18.5 mine lateral resistivity video imaging logging tool is mainly composed of a probe, host control box, host control panel, and push rod.

Working principle: select the appropriate detection method according to the demand, then carry out onsite layout and construction, and select the corresponding detection method according to the construction method. The instrument can analyze the rock stratum structure of the borehole through video (e.g., layered lithology, rock hole fracture development, water outlet point characteristics, roof separation, etc.), automatically generate the borehole orientation profile, borehole plane trajectory, and borehole histogram according to the scale through the detection data. There is a camera ahead, which can realize automatic continuous measurement. With the continuous deepening of the push rod in

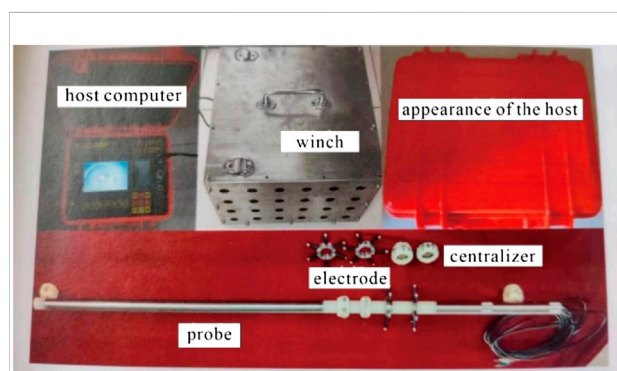


FIGURE 4
YZD18.5 mine lateral resistivity video imaging logging tool.

the hole, the instrument can collect parameters such as different hole section diameters and shapes along the hole direction of hydraulic flushing.

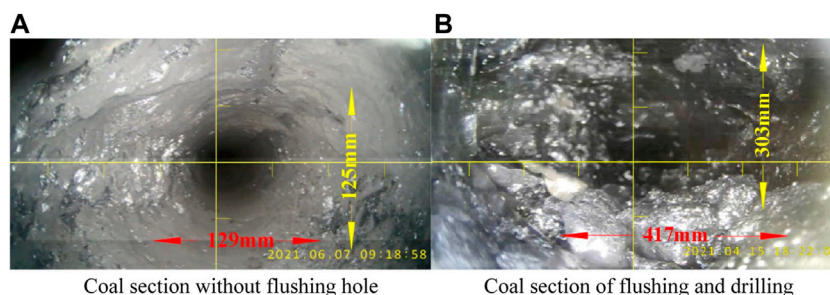


FIGURE 5

Borehole aperture peep view. (A) Coal section without flushing hole. (B) Coal section of flushing and drilling.

Instrument parameters: the video resolution is 1280 * 960, the probe angle of view is 120°, and the effective sight distance is 300mm; the data acquisition frequency is 15 points/second; the measurement range of borehole inclination is -90° to 90°, and the measurement accuracy is +0.1°; the detection depth is 0–200m, and the hole depth error is less than 0.5%. Figure 4 shows YZD18.5 mine lateral resistivity video imaging logging tool.

2.3.2 Test procedure

- 1) Select the drill hole after hydraulic flushing, blow out the coal and rock slag in the hole with compressed air to minimize the residue, ensure the smooth drilling, and maintain the drilling shape after hydraulic flushing to the greatest extent
- 2) The YZD18.5 mine lateral resistivity video imaging logging tool is used for borehole peeping, the collected video files are analyzed, and the standards including acquisition frequency, frequency, and image definition are formulated after many tests
- 3) The collected image information is summarized and processed in CAD, a section diagram of the hydraulic flushing hole's shape is drawn, and the hydraulic flushing hole's shape is analyzed

2.3.3 Data acquisition and analysis

When the probe of YZD18.5 mining lateral resistivity video imaging logging tool enters the borehole, it is necessary to install the centralizer of corresponding model to ensure that the probe remains in the center of the borehole. The borehole diameter is 113 mm, and the centralizer with diameter of 93 mm is selected. After the probe enters the borehole, it will collect the hole information on the path. When the probe rod reaches the hole bottom and saves the data, the data acquisition is completed.

We then analyze the video files obtained after data acquisition, consider the observation angle of the probe, the effective detection distance of the probe, the forward speed of the probe, the data acquisition frequency and other factors, and use the intercepting frame function on the premise of ensuring the clarity and high accuracy of the image according to the actual test on the site. We

plan to collect images every 0.15 m along the hole axis and every 90° along the hole circumference. The gray value of the collected image information is analyzed by schlieren method, the spatial position information contains in the hole section is obtained, and the hole's shape section is drawn, as is shown in Figure 5.

2.3.4 Data processing

Two holes 9-03# and 7-09# are selected to draw the hole morphology diagram, as shown in Figure 6.

In Figure 6, the spatial information of about 40 images was used to draw the sectional map of the cavity morphology. r_1 -Z and r_2 -Z sections are quasi-ellipsoids with the upper part slightly larger than the lower part and the right-hand side is slightly larger than the left-hand side, and the maximum values of long semi-axis and short semi-axis are obtained at about $z = 0.6H$. The r_1 - r_2 section shows an approximate ellipse, and the values of r_1 and r_2 are close to a constant value. The cross-sectional view of the hole's shape is roughly the same as the three-dimensional display of BR-PKN equation deduced above in MATLAB; that is, the hole's shape after flushing is an ellipsoid with a slightly larger top than the bottom.

2.4 Adsorption-permeability model of coal and rock considering water content

The pore and fissure of coal seam are the main factors affecting the permeability of coal seam, which directly affect the adsorption capacity and permeability characteristics of coal:

$$\varphi = \frac{V_p}{V_b} = \frac{V_{p0} + \Delta V_p}{V_{b0} + \Delta V_b} = 1 - \frac{V_{s0} + \Delta V_s}{V_{b0} + \Delta V_b} = 1 - \frac{1 - \varphi_0}{1 + \varepsilon_v} \left(1 + \frac{\Delta V_s}{V_{s0}} \right), \quad (6)$$

where φ - porosity of coal and rock, %; φ_0 - Initial porosity of coal, %; V_p - volume of coal pore and fissure, and ΔV_p - variation; V_{p0} - initial coal pore fissure volume; V_b - total coal and rock volume, ΔV_b - variation; V_{b0} - initial total coal and rock volume; V_{s0} - coal-

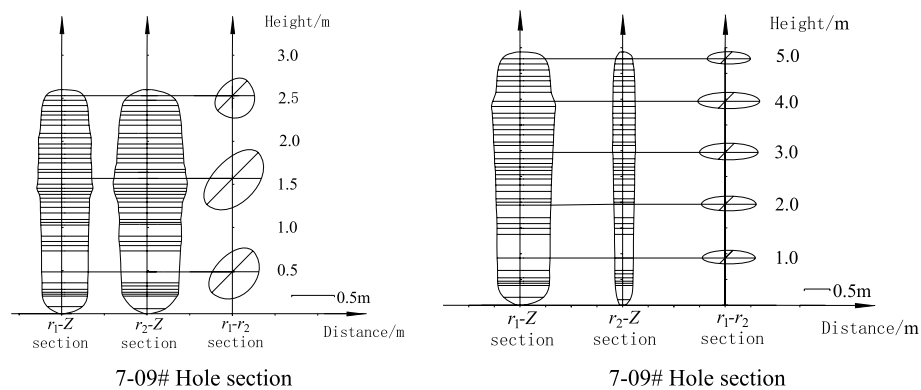


FIGURE 6
Drilling for hydraulic flushing. (A) 7-09# hole section. (B) 7-09# hole section.

rock skeleton volume; V_s - coal-rock skeleton volume change; and V_ε - Volumetric strain of coal mass.

The internal deformation of coal rock is mainly composed of three parts, which are caused by temperature, gas pressure and adsorption/desorption. Assuming that the temperature of coal and rock is constant, the deformation caused by temperature can be ignored, and only the deformation caused by gas pressure and adsorption/desorption can be expressed as

$$\Delta V_s = -V_{s0}(\varepsilon_p - \varepsilon_{sw}), \quad (7)$$

where the strain caused by gas pressure ε_p can be expressed as

$$\varepsilon_p = \frac{\Delta p}{K_s}, \quad (8)$$

where Δp - gas pressure change, $\Delta p = p_0 - p$, MPa.

Under the condition of uniform surface properties of adsorbents, the adsorption amount of methane in coal and rock was calculated by the Langmuir isothermal adsorption model:

$$V_0 = \frac{abp}{1 + bp}, \quad (9)$$

where V_0 - gas adsorption capacity (cm^3/g), a - adsorption constant (cm^3/g), b - adsorption constant (MPa^{-1}), and p - gas pressure (Mpa).

When there is water on the surface of coal and rock fissure, there will be adsorption of gas. When the water reaches a certain amount, there will be “water lock effect”, which will slow down the release rate of gas and affect the adsorption characteristics of coal and rock (Maggs, 1946; Hu

and Wu, 2014). Therefore, the existence of water content should be considered in the establishment of the adsorption model:

$$V = \frac{abp}{1 + bp} \exp(-\lambda m), \quad (10)$$

where V - solid adsorption gas volume (cm^2/g), λ - reduction coefficient of adsorption capacity of coal by humidity, and m - water content (%).

Adsorption deformation of coal rock after adsorption of gas can be obtained by Bangham's theory:

$$\frac{\Delta l}{l} = \gamma \pi, \quad (11)$$

where l - coal-rock width (m), Δl - coal-rock width change value (m), π - surface free energy (J), and γ - deformation constant.

F. A. P. Maggs proposed the relationship between deformation constant and physical and mechanical properties of solids as follows (Tao et al., 2017):

$$\gamma = \frac{\eta \rho_c}{K_s}, \quad (12)$$

where ρ_c - density of coal and rock mass (kg/m^3), η - specific surface area of solid (cm^2), and K_s - adsorption modulus (MPa).

In Gibbs surface adsorption equation, the surface free energy generated by the relative movement between molecules can be described as

$$\pi = RT \int_0^p \Gamma d(\ln p), \quad (13)$$

where R - Ideal gas constant, Γ - surface excess, and T - temperature (K). When the adsorbed substance is CH_4 , the surface excess Γ can be described as

$$\Gamma = \frac{n}{\eta} = \frac{V}{Vm\eta}, \quad (14)$$

where n - total surface excess of adsorbed gas; V_m - molar volume of gas. By substituting Eqs 9, 11–13 into Eq. 12, the linear deformation of coal rock can be obtained as follows:

$$\frac{\Delta l}{l} = \frac{\alpha \rho_c RT}{V_m K_s} \exp(-\lambda m) \int_0^p \frac{bp}{1+bp} dp. \quad (15)$$

Therefore, the adsorption deformation of coal rock is

$$\varepsilon_{sw} = \frac{3\Delta l}{l} = \frac{3\alpha \rho_c RT}{V_0 E_A} \exp(-\lambda m) \int_0^p \frac{bp}{1+bp} dp. \quad (16)$$

Substituting Eqs 7, 8, 16 into Eq. 6, the expression of porosity φ can be obtained:

$$\begin{aligned} \varphi &= 1 - \frac{1 - \varphi_0}{1 + \varepsilon_v} (1 - \varepsilon_p + \varepsilon_{sw}) \\ &= 1 - \frac{1 - \varphi_0}{1 + \varepsilon_v} \left[1 - \frac{\Delta p}{K_s} + \frac{3\alpha \rho_s RT}{V_m K_s} \exp(-\lambda m) \ln(1 + bp) \right]. \end{aligned} \quad (17)$$

The permeability of coal is closely related to its stress state, and the change of stress will lead to the change of coal skeleton and pore volume. Permeability and porosity are closely related. According to the relationship between permeability and porosity,

$$k = \frac{\varphi}{K_Z S_p^2}. \quad (18)$$

Among them,

$$S_p = \frac{A_s}{V_p}, \quad (19)$$

where K - permeability, m^2 ; K_Z - dimensionless constant, value 5; S_p - pore surface area per unit pore volume of coal, cm^2 ; and A_s - total surface area of pores in coal, cm^2 . When the permeability changes from the initial state k_0 , the porosity can also be re-expressed:

$$\varphi = \frac{V_{p0} + (\Delta V_b - \Delta V_s)}{V_{b0} + \Delta V_{b0}}, \quad (20)$$

$$S_p = \frac{A_{s0}(1 + \partial)}{V_{p0} + (\Delta V_b - \Delta V_s)}, \quad (21)$$

where ∂ is the increase coefficient of pore surface area of coal rock, %.

Therefore, the ratio of changed permeability to initial permeability can be obtained:

$$\frac{k}{k_0} = \frac{1}{1 + e} \frac{1}{(1 + \partial)^2} \left(\frac{V_{p0} + \Delta V_p}{V_{p0}} \right). \quad (22)$$

According to the work of Tao (2009),

$$\frac{V_{p0} + \Delta V_p}{V_{p0}} = 1 + \frac{e}{\varphi_0} - \frac{\Delta V_s}{V_{s0}} \frac{(1 - \varphi_0)}{\varphi_0}. \quad (23)$$

Then, the permeability evolution model considering water content can be obtained:

$$k = \frac{1}{1 + e} \left[1 + \frac{e}{\varphi_0} + \frac{\Delta P(1 - \varphi_0)}{\varphi_0 K_s} - \frac{3\alpha \rho_s RT}{V_m K_s} \exp(-\lambda m) \ln(1 + bp) \right]^3. \quad (24)$$

3 Results

3.1 Geometric model and boundary conditions

Xin'an Mine is mainly mined in the Permian coal seam group 1, the thickness of the coal seam is 0.3–13.1 m, the thickness of coal seam is 0.3–13.1 m, the average coal thickness is about 4m, the whole layer soft coal, the firmness coefficient $f=0.17$, the homogenization is strong, the coal seam density $\rho=1400 \text{ kg/m}^3$, the coal seam gas content is $4.0 \text{ m}^3/\text{t} \sim 14.0 \text{ m}^3/\text{t}$, The original gas pressure was 0.4–1.4 MPa, and the coal was extracted by hydraulic flushing technology of the floor roadway through layer, and 1t coal is produced per meter of coal section during hydraulic flushing. Based on this, a numerical calculation geometric model is established, and the maximum punch aperture of the long axis and short axis is 0.76 and 0.63m, respectively. The model parameters are shown in Table 1.

3.2 Permeability evolution of hydraulic flushing coal based on quasi-ellipsoid

During hydraulic flushing, a water jet is used to stimulate coal breaking in a coal seam. During coal breaking, the external moisture of coal seam is increased and the spatial distribution characteristics of permeability of coal body in hydraulic hole are affected. Therefore, the permeability evolution law of coal body under different water bearing conditions is carried out based on the shape of hydraulic flushing hole. COMSOL Multiphysics simulation software was used to simulate the permeability changes of coal body in the long and short-axis directions of equivalent ellipsoid holes and equivalent cylindrical holes at 0, 1, 10, 30, 60 and 90 days after hydraulic drilling under different water cut conditions, on the basis of ellipsoid hole shape, as shown in Figures 7, 8. And Figures 9 shows the comparison of coal permeability along the long and short axes of ellipsoid when water content is 6%. In these figures, the arc length on the abscissa represents the normal distance from the hole (m), and

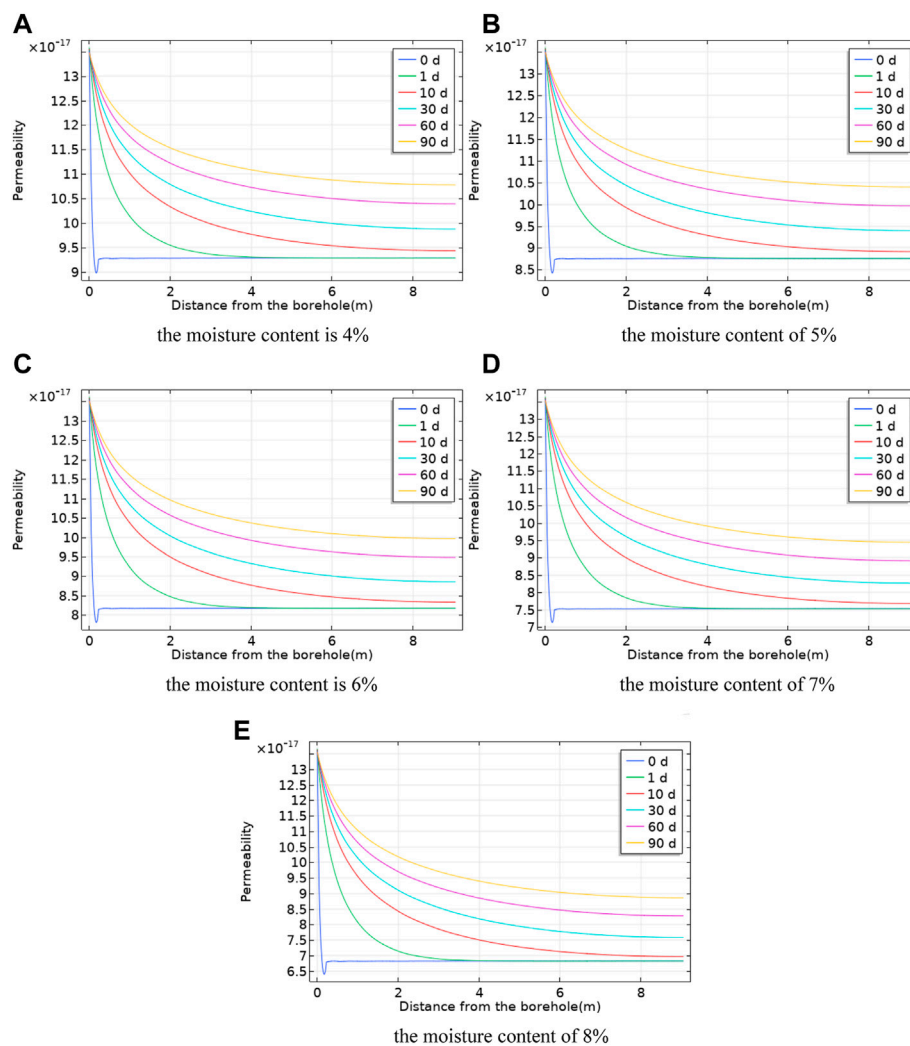


FIGURE 7

Evolution of coal permeability along the long axis of equivalent ellipsoid-like holes under different water content. (A) The moisture content is 4%, (B) the moisture content is 5%, (C) the moisture content is 6%, (D) the moisture content is 7%, and (E) the moisture content is 8%.

the ordinate represents the permeability of coal around the hole (m^2).

3.2.1 Permeability evolution of the long axis of the equivalent ellipsoidal cavity

According to the permeability curve after hydraulic flushing and the stress state of coal around the hole, the area around hydraulic flushing can be divided into three zones (Hao et al., 2014; Fan et al., 2021). The first is the increased permeability zone; that is, the stress decreased zone, which is 0–2.1 m away from the hole. The coal permeability in this zone increases obviously, and it always exists with the extension of time, and the permeability continues to increase with the extension of time, but the increase rate is small. The second is the decreased permeability zone; that is, the increased stress zone, which is 2.1–6.0 m away from the hole. The permeability of this zone

decreases rapidly but it is still larger than the original permeability. Moreover, this zone always exists with the extension of time, and the permeability continues to increase with the extension of time, with a slightly larger increase than that of the increased permeability zone. In the third zone, the permeability flat area, namely the original rock stress area, the distance from the hole is greater than 6.0 m. The stress to the original rock stress in this region is not affected by hydraulic flushing. The penetration of the area gradually overcomes the original permeability, the change is very small with the extension of time, and there is a small increase of permeability.

As can be seen from Figure 7, with the same water content, the coal permeability along the long axis of the equivalent ellipsoid hole shows a trend of uniform growth with the extension of extraction time. With the increase of the distance from the hole, the permeability first increases, then

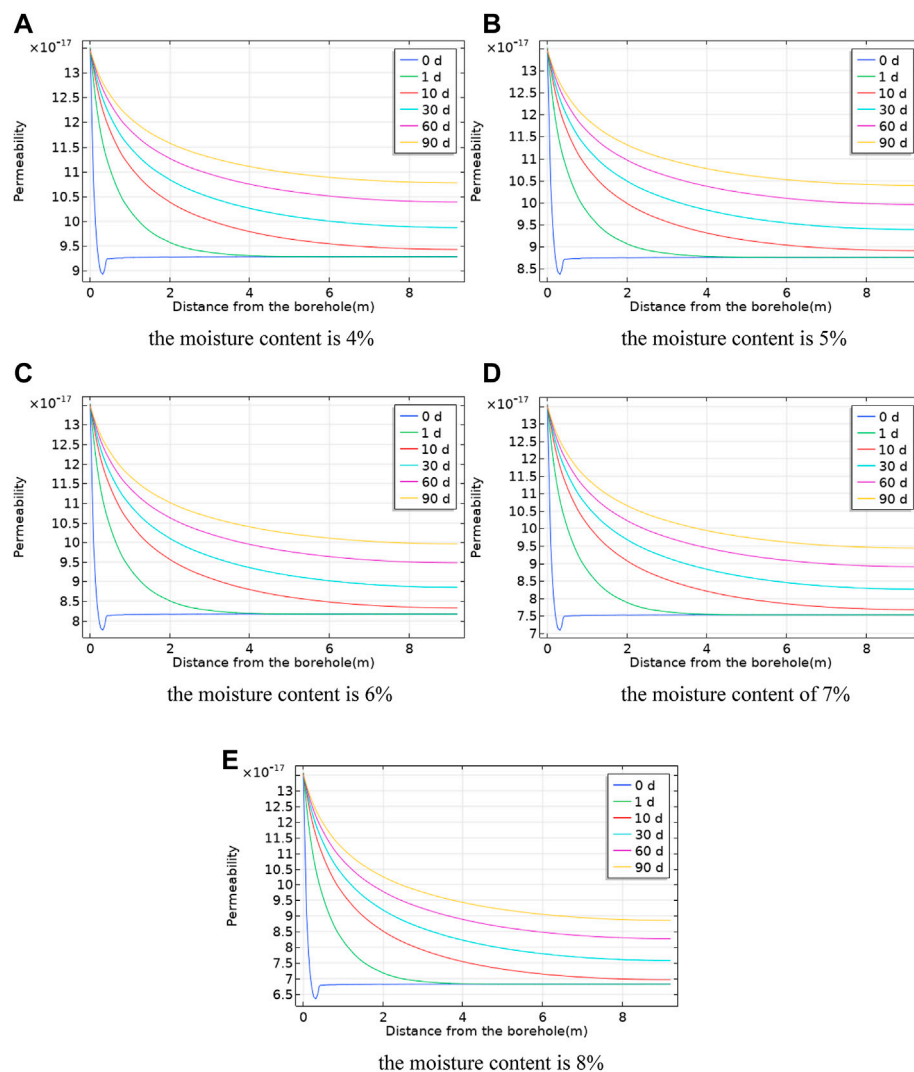


FIGURE 8

Evolution of coal permeability along the short axis of equivalent ellipsoid-like holes under different water content conditions. (A) The moisture content is 4%, (B) the moisture content is 5%, (C) the moisture content is 6%, (D) the moisture content is 7%, and (E) the moisture content is 8%.

decreases rapidly, and finally tends to be stable. In 0 days of permeability, with the increase of the distance between holes distance fell sharply, and there is a peak at 0.3 m away from the hole location. Permeability then increases because after the hydraulic flushing there is an increased stress anomaly zone around the hole, the area affected by ground stress and force transmission shifts, and the effective stress increases after the coal by water jet impact by compaction. The porosity of coal becomes smaller, resulting in the decrease of permeability in this area. With the extension of time, the coal body gradually recovers. With the increase of water content, the permeability evolution is basically consistent, but the permeability gradually decreases. When the

extraction time is 90 days, the water cut is 4%, 5%, 6%, 7%, and 8%, the maximum permeability is the same, which increases by 23.8% compared with the original permeability. Compared with the original permeability, and the stable permeability decreases by 0.9%, 4.6%, 8.3%, 14.8%, and 19.4%, respectively, compared with the original permeability.

3.2.2 Evolution of coal permeability along the short axis of equivalent ellipsoid

It can be found that the evolution curve of coal permeability along the short axis increases first, then decreases, and finally flattens with the increase of distance from the borehole, which is almost consistent with the

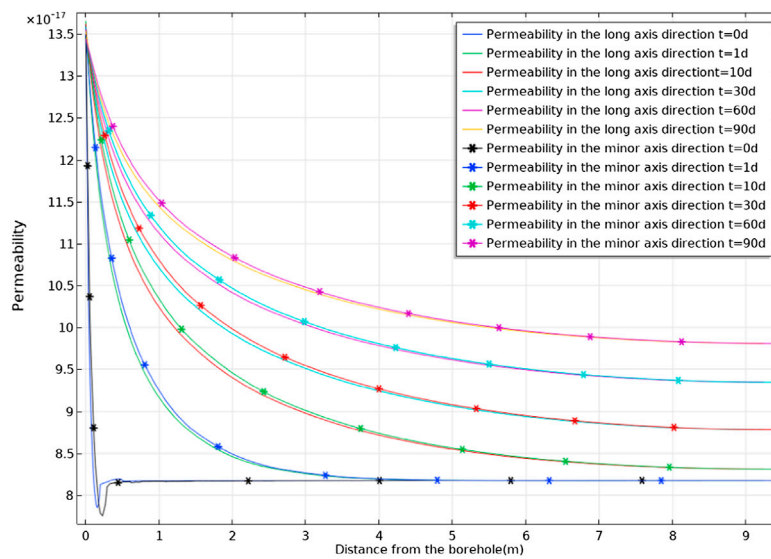


FIGURE 9

Comparison of coal permeability along the long and short axes of ellipsoid when water content is 6%.

permeability along the long axis and slightly smaller in value than that along the long axis.

By observing Figures 7, 8, it can be found that the permeability of coal in the short-axis direction has the following characteristics compared with that in the long-axis direction:

- 1) The variation law of coal permeability in the short-axis direction of the equivalent ellipsoid hole is roughly consistent with that in the long axis direction.
- 2) The permeability of the long axis and the short axis changes with the change of stress. The stress value of the long axis and the short axis is almost the same when the distance from the borehole is greater than 4 m, which explains the phenomenon that the evolution curves of the permeability of the long axis same as the short axis when the distance from the borehole is greater than 4 m.

3.3 Simulation of the effective radius of hydraulic flushing based on quasi-ellipsoid

COMSOL Multiphysics software was used to simulate the extraction radius of the derived equivalent ellipsoid hole. The area where the gas content is reduced to less than $6 \text{ m}^3/\text{t}$ is considered as the influence range of effective extraction radius (Li et al., 2011; Wen et al., 2012; Hu et al., 2020; Xu et al., 2020; Xie et al., 2021). COMSOL Multiphysics software was used to set the coal quantity as 1 t/m , the extraction time as 3 months, the

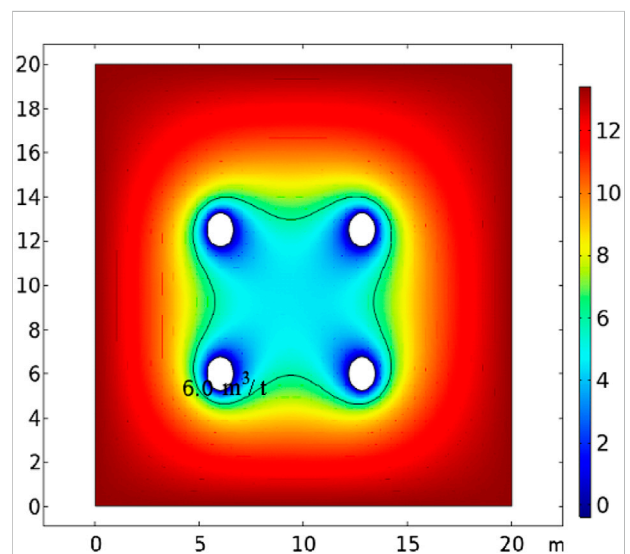
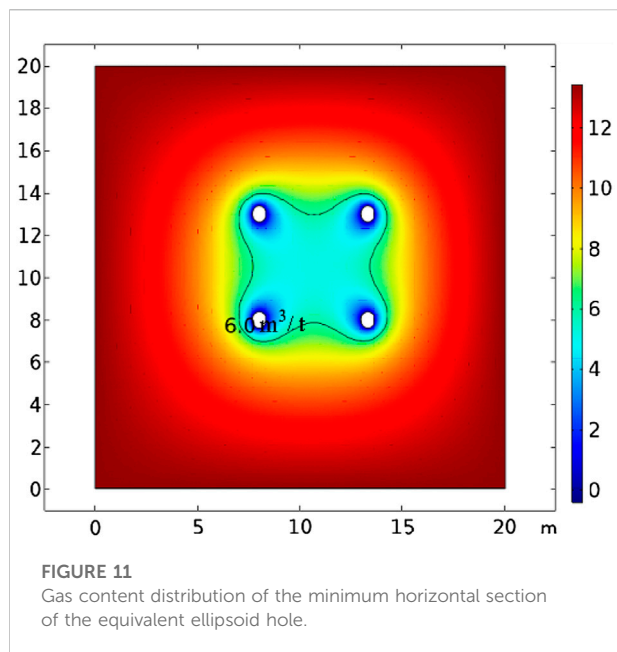


FIGURE 10

Gas distribution of the maximum horizontal section of the equivalent ellipsoid hole.

spacing of boreholes as 6.60m, and the hole depth as 4.00 m. The drilling sections of equivalent ellipsoid are different. Here, only the maximum and minimum horizontal sections are analyzed. The minimum horizontal section is obtained when it is near the roof and floor of coal seam, and the maximum long axis and short axis are about half of the maximum horizontal section. The



maximum horizontal section of short semi-axis r_{1m} and long semi-axis r_{2m} are 0.63 and 0.76 m, respectively, while the minimum section of short semi-axis r_1 and long semi-axis r_2 are 0.315 and 0.38 m, respectively. After 90 days of drainage, the gas content distribution around the borehole is shown in Figures 10, 11.

Figures 10, 11 show the gas content isolines after 90 days of extraction, and areas below the isolines of $6 \text{ m}^3/\text{t}$ are

regarded as effective extraction ranges. It is found that the maximum effective extraction radius of the equivalent ellipsoid hole is 3.25 m in the long-axis direction and 3.40 m in the short-axis direction. The minimum effective extraction radius in the long-axis direction of the cross-section is 2.50 m and the effective extraction radius in the short-axis direction is 2.65 m.

3.4 Comparison of ellipsoid-like and cylindrical holes

3.4.1 Permeability correlation

Figure 12 shows the moisture content of 6% when the equivalent of evolution of coal permeability curves around the cylinder holes. When the moisture content is 6%, the coal permeability of two horizontal directions are perpendicular to each other, which in the equivalent cylinder showed a uniform growth trend. With the increase of the distance from the hole, the permeability first increases, after rapidly decreases, and finally tends to be stable. With the increase of water content, the permeability evolution is basically consistent, but the permeability gradually decreases. At 90 days of extraction, the maximum permeability at a water cut of 6% increased by 23.8% compared to the original permeability and the stationary permeability decreased by 10.6% compared to the original permeability.

Figure 13 shows the evolution curve of coal permeability around the quasi-ellipsoid hole and cylindrical hole with different distances from the hole under the condition of 6% water content. The dotted

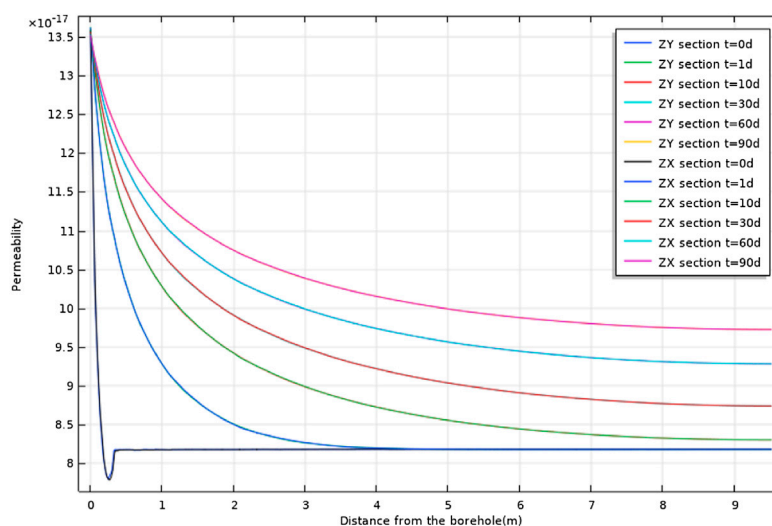


FIGURE 12
Permeability evolution of coal around cylinder hole when water content is 6%.

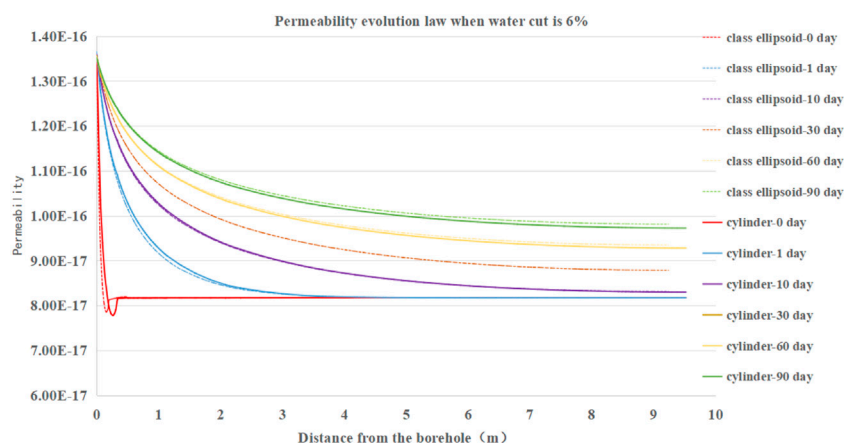


FIGURE 13
Permeability evolution under different pore morphology when water content is 6%.

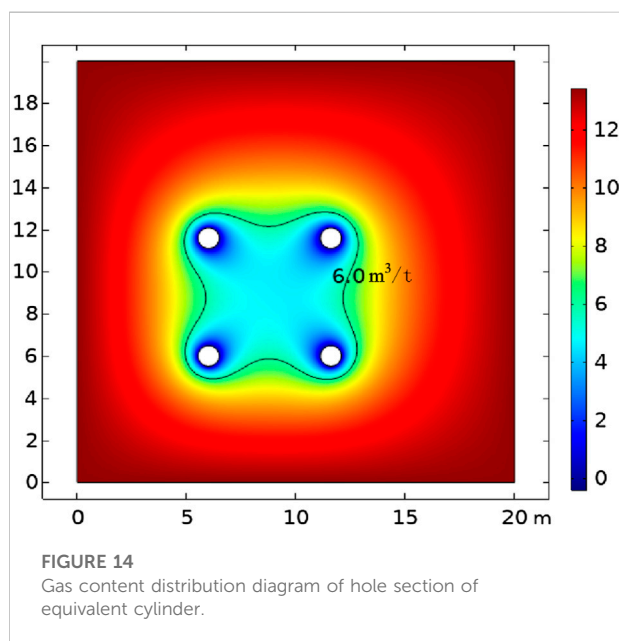


FIGURE 14
Gas content distribution diagram of hole section of equivalent cylinder.

line in the figure represents the evolution law of coal permeability around the equivalent quasi-ellipsoid hole, and the solid line represents the permeability and evolution law around the equivalent cylindrical hole. By comparing the permeability curves of the two holes, it can be found that

- 1) The permeability evolution of the two pore shapes has the same change trend with water content, and both of them show that the permeability decreases with the increase of water content
- 2) When the time is the same, the water content is 6% and the coal output is 1 t/m, the permeability of coal around the long

axis of the equivalent ellipsoid hole is less than that of the equivalent cylinder hole within 0–30 days after flushing, and that of coal around the long axis of the equivalent ellipsoid hole is greater than that of the equivalent cylinder hole during 60–90 days

3.4.2 Comparison of effective extraction range

Figure 14 shows the gas content distribution diagram of the section of the equivalent cylinder hole. It can be found that the effective drainage radius of the equivalent cylinder hole by hydraulic flushing is 6.6 m after 90 days of drainage. A comparison with Figures 10, 11 shows that

- 1) The maximum effective extraction radius of the quasi-ellipsoid hole in the longitudinal direction is 1.16 times that of the equivalent cylindrical hole, and the effective extraction radius in the short-axis direction is 1.21 times that of the cylindrical hole
- 2) The effective extraction radius of the minimum section of the quasi-ellipsoid in the long-axis direction is 0.89 times that of the equivalent cylinder, and the effective extraction radius in the short-axis direction is 0.95 times that of the cylinder

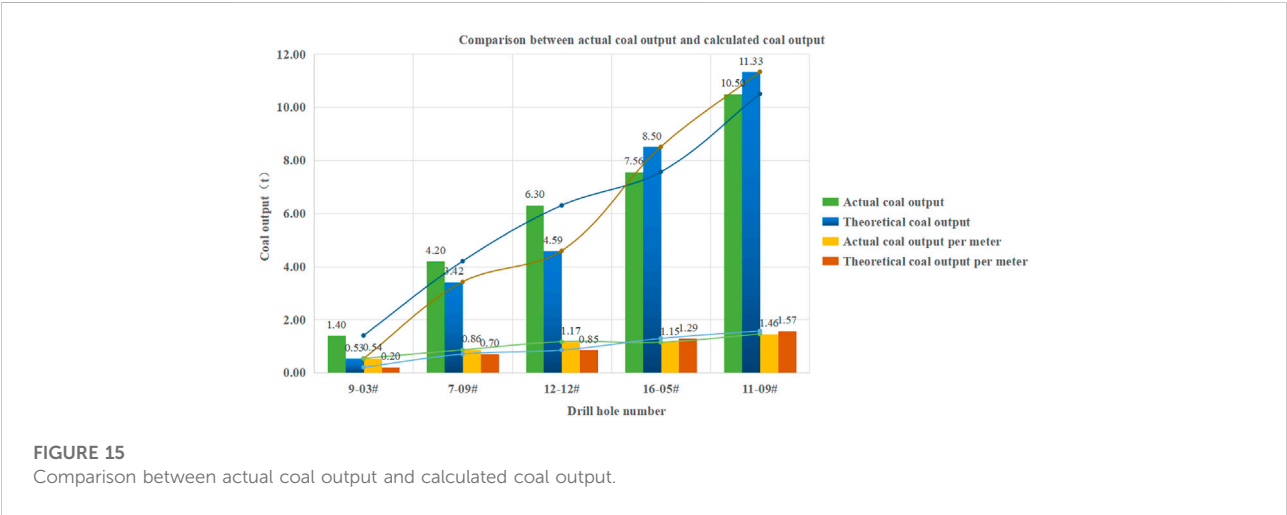
This suggests that in the actual hole pattern for the class under the condition of ellipsoid, an equivalent cylinder hole arrangement is not reasonable in the evaluation of extraction of prone to extraction standards. However, the existence of blank tape, ellipsoid to class hole of radius of the cross-section of short axis efficient extraction-based layout borehole can effectively avoid extraction of white space, improve the effect of the gas extraction, and ensure the safety of mine production.

TABLE 1 Numerical model parameters.

Parameter	Initial porosity /%	Initial porosity/m ²	Poisson's ratio of coal	The coefficient of Klinkenberg a/MPa	Adsorption constant a/(m ³ /t)	Adsorption constant b/MPa ⁻¹	The temperature /K
The values	0.0494	1.09*10 ⁻¹⁶	0.32	0.76	32	0.72	293
Parameter	The density of coal rho/(t/m ³)	Modulus of elasticity E/GPa	Elastic modulus of solid skeleton Ks/GPa	Initial gas pressure /MPa	Atmospheric pressure /kPa	Initial gas density /(kg/m ³)	
The values	1.40	2.20	3.20	1.40	101	0.716	

TABLE 2 Hydraulic flushing drilling parameters.

Borehole no.	Dip angle(°)	Hole depth /m	Length of coal section	Actual coal output /t	Calculated coal quantity /t	Calculation of the maximum long half-axis r ₁ /m	Calculation of the maximum minor axle r ₂ /m
			H/m				
9-03	34	14.40	2.60	1.40	0.53	0.42	0.51
7-09	72	18.80	4.90	4.20	3.42	0.79	0.94
12-12	35	31.80	5.40	6.30	4.59	0.87	1.04
16-05	44	26.00	6.60	7.56	8.50	1.07	1.29
11-09	75	20.00	7.20	10.50	11.33	1.13	1.42



3.5 Test data analysis

After the test, boreholes with different coal thicknesses in the bottom roadway at 14250 working face were selected to collect drilling parameters of hydraulic punching. The specific drilling parameters are shown in Table 2.

In Table 2, coal extraction volume is composed of coal extraction volume from hydraulic flushing and coal extraction volume from drilling. By substituting test data into Eq. 5, parameters $b=0.04$ and $\alpha_G=18^\circ$ are fitted. Figure 15 shows the comparison between the actual coal output and the calculated coal output.

As can be seen from Figure 15, with the increase of coal thickness from the borehole, the coal output presents a rising trend, and the average coal output per meter increases with the increase of coal thickness. The coal thickness of hole 9-03# is 2.60m, and the actual average coal output is 0.54 t/m. The coal thickness of hole 11-09# is 7.60m, and the actual average coal yield is 1.46 t/m; that is, the average coal yield from hole 11-09 increases with the increase of coal thickness. The calculated maximum short-axis r_1 and long-axis r_2 of the hole also increased, and the ratio of r_2 to r_1 remained roughly at about 1.20.

4 Conclusion

- 1) For the shape of the hole after hydraulic flushing, the BR-PKN equation was established by combining the Bergmark–Roos equation and the PKN model, and the numerical simulation was carried out. The shape of the hole was displayed in MATLAB in three dimensions, and it was found that the shape of the hole was a quasi-ellipsoid with the upper part slightly larger than the lower part and the horizontal section approximately elliptic.
- 2) When the water content is constant, the permeability of coal around the equivalent ellipsoid hole increases gradually with time. With the increase of the distance from the hole, the permeability increases first, then decreases rapidly, and finally tends to be stable. When the water content increases, the permeability of coal generally decreases, which indicates that the increase of coal external moisture will inhibit the permeability characteristics of coal seam.
- 3) When the water content is 6%, and the coal output is 1 t/m, the permeability of coal around the long axis of the equivalent ellipsoid hole is less than that of the equivalent cylinder hole in 0–30 days after flushing, and it is greater than that of the equivalent cylinder hole in 60–90 days.
- 4) When the extraction time is 90 days and the water content is 6%, the effective extraction radius of the minimum section of quasi-ellipsoid is 2.50 m along the long axis and 2.65 m along the short axis, which are 0.89 and 0.95 times of the hydraulic hole of equivalent cylinder, respectively. Combined with the above data, it is necessary to optimize the spacing of extraction holes. It is recommended that the spacing of drilling rows be 5.00 m (direction of maximum horizontal principal stress) and 5.30 m (direction of minimum horizontal principal stress).
- 5) The present study is in the vertical coal layers of drilling on the basis of research on the hydraulic flushing holes form. However, in practice the hydraulic flushing hole shape is affected by factors such as the dip angle of the coal seam and borehole inclination. These factors need further multi-factor coupling under the condition of

hole shape characteristic research to optimize the extraction from drilling and to provide theoretical basis for design and evaluation.

Data availability statement

The original contributions presented in the study are included in the article/Supplementary Material; further inquiries can be directed to the corresponding author.

Author contributions

TJ and SX contributed to the writing of the manuscript. DX and YL made a contribution to the field work. XL and HL revised the manuscript. All authors have read and agreed to the published version of the manuscript.

Funding

This study was supported by the Youth Project of National Natural Science Foundation of China (51804100).

Acknowledgments

The authors thank Zhifeng Zhang, Lisheng Zhang, and the other personnel in the field test of the Xin'an Coal Mine for their help.

Conflict of interest

Author DX is employed by Ventilation Department of Henan Dayou Energy Co., Ltd.

The remaining authors declare that the research was conducted in the absence of any commercial or financial relationships that could be construed as a potential conflict of interest.

Publisher's note

All claims expressed in this article are solely those of the authors and do not necessarily represent those of their affiliated organizations, or those of the publisher, the editors, and the reviewers. Any product that may be evaluated in this article, or claim that may be made by its manufacturer, is not guaranteed or endorsed by the publisher.

References

- Fan, Y. P., Shu, L. Y., Huo, Z. G., Hao, J. W., and Li, Y. (2021). Numerical simulation of sectional hydraulic reaming for methane extraction from coal seams. *J. Nat. Gas Sci. Eng.* 95, 104180. doi:10.1016/j.jngse.2021.104180
- Garikapati, Hasini, Verhoosel, Clemens V., Harald van Brummelen, E., Zlotnik, S., and Pedro, D. (2019). Sampling-based stochastic analysis of the PKN model for hydraulic fracturing. *Comput. Geosci.* 23 (1), 81–105. doi:10.1007/s10596-018-9784-y
- Hao, F. C., Sun, L. J., and Liu, M. J. (2014). Research on boreholes space optimization of hydraulic flushing considering press relief and gas drainage effect. *J. Min. Saf. Eng.* 31 (05), 756–763. doi:10.13545/j.issn1673-3363.2014.05.015
- Hao, F. C., Sun, L. J., and Zhao, F. J. (2016). Research on coal permeability spatio-temporal evolution around hydraulic flushing based on creep-seepage coupling. *J. Saf. Sci. Technol.* 12 (08), 16–22. doi:10.11731/j.issn.1673-193x.2016.08.003
- He, L. W., Dai, Y. C., Xue, S., Zheng, C. S., Han, B. Q., Guo, X., et al. (2021). Study on gas control methods optimization for mining safety. *Adv. Civ. Eng.* 1, 1. doi:10.1155/2021/4594330
- Hu, K., Xia, B. W., Liu, C. W., Lu, Y. Y., and Song, Z. Y. (2020). Effective methane extraction radius after high-pressure water jet slotting. *Geofluids* 1, 1. doi:10.1155/2020/8820540
- Hu, Y. L., and Wu, X. M. (2014). Research on coalbed methane reservoir water blocking damage mechanism and anti-water blocking. *J. China Coal Soc.* 39 (06), 1107–1111. doi:10.13225/j.cnki.jccs.2013.1024
- Jiang, J. Y., Yang, W. H., Cheng, Y. P., Lv, B. M., Zhang, K., Zhao, K., et al. (2018). Application of hydraulic flushing in coal seams to reduce hazardous outbursts in the mengjin mine, China. *Environ. Eng. Geoscience* 24 (4), 425–440. doi:10.2113/eeg-2110
- Kuchta, M. E. (2002). A revised of the Bergmark-Roos equation for describing the gravity flow of broken rock. *Min. Res. Eng.* 11 (4), 349–360. doi:10.1142/s0950609802001002
- Li, B. B., Cheng, Q. Y., Li, J. H., Wang, B., and Xu, J. (2020). Study on fracture compression and permeability of water-bearing coal. *Chin. J. Rock Mech. Eng.* 39 (10), 2069–2078. doi:10.3390/app9122549
- Li, B., Liu, M. J., Liu, Y. W., Wang, N. H., and Guo, X. L. (2011). Research on pressure relief scope of hydraulic flushing bore hole. *Procedia Eng.* 26, 382–387. doi:10.1016/j.proeng.2011.11.2182
- Liu, D., and Liu, W. (2019). Research on gas extraction technology: Hydraulic stamping and hydro fracture to pressure relief and permeability improvement. *Coal Sci. Technol.* 47 (3), 136–141. doi:10.1016/j.jngse.2019.103067
- Liu, Y. M., Wang, C. H., and Zhou, H. (2020). Optimization scheme of hydraulic fracturing simulation experiments using mixed-level uniform design method based on the PKN model. *J. Phys. Conf. Ser.* 1, 012165. doi:10.1088/1742-6596/1574/1/012165
- Ma, G., Liu, X., and Li, F. (2016). Study on morphology features of hydraulic flushing hole based on ore drawing theory. *Coal Sci. Technol.* 44 (11), 73–77. doi:10.13199/j.cnki.cst.2016.11.014
- Maggs, F. A. P. (1946). The adsorption-swelling of several carbonaceous solids. *Trans. Faraday Soc.* 42, B284–B288. doi:10.1039/TF946420B284
- Melo, F., Vivanco, C., Fuentes, C., and Apablaza, V. (2007). On drawbody shapes: From Bergmark-Roos to kinematic models. *Int. J. Rock Mech. Min. Sci.* 44 (1), 77–86. doi:10.1016/j.ijrmms.2006.04.010
- Ren, Z. J. (2019). Application of hydraulic punching technology in seam gas drainage in yuwu coal mine. *Coal Eng.* 51 (03), 65–70.
- Tao, G. Q., Yang, S. J., Liu, Z. D., and Ren, Q. Y. (2010). Research of ore drawing method of broken ore and rock based on Bergmark-Roos equation. *J. China Coal Soc.* 35 (05), 750–754. doi:10.1016/S1876-3804(11)60004-9
- Tao, Y. Q., Feng, D., Ma, G., Xu, J., and Peng, S. J. (2017). Study on physical simulation experiment of hydraulic borehole flushing and pressure released and permeability improved effect. *Coal Sci. Technol.* 45 (06), 55–60. doi:10.13199/j.cnki.cst.2017.06.009
- Tao, Y. Q. (2009). *Study on the gassy coal THM coupling model and coal and gas outburst simulation*[D]. China: Chongqing University.
- Wang, K., Li, B., Wei, J. P., and Li, P. (2013). Change regulation of coal seam permeability around hydraulic flushing borehole. *J. Min. Saf. Eng.* 30 (05), 778–784.
- Wei, J. P., Wei, L., and Wang, D. K. (2014). Experimental study of moisture content influences on permeability of coal containing gas. *J. China Coal Soc.* 39 (01), 97–103. doi:10.13225/j.cnki.jccs.2013.0209
- Wen, Z. H., Wei, J. P., Liu, Y. Z., and Zhang, H. T. (2012). Numerical simulation on effective influence radius of hydraulic flushing borehole. *Adv. Mat. Res.* 616–618, 1021–1026. doi:10.4028/www.scientific.net/amr.616-618.1021
- Wu, H. J., Li, X. L., Gao, X., Chen, D. Y., and Li, Z. (2002). Development and application of water sealing technology for gas drainage boreholes. *ACS omega* 7 (1), 733–743. doi:10.1021/acsomega.1c05385
- Xie, S. R., Cui, J. Q., Chen, D. D., and Chen, P. (2021). Numerical simulation study on gas drainage by interval hydraulic flushing in coal seam working face. *Energy Explor. Exploitation* 39 (4), 1123–1142. doi:10.1177/01445987211010274
- Xu, D. D., Tao, Y. Q., Zhou, Z. T., Hou, C., and Fabio, M. (2020). Study of the law of hydraulically punched boreholes on effective gas extraction radius under different coal outputs. *Shock Vib.* 1, 12. doi:10.1155/2020/8858091
- Yang, S., Liu, X. F., Zhang, C., Liu, Q. L., and Gong, C. Z. (2018). Numerical solution of effective radius of hydraulic punching based on klinkenberg effect. *Saf. Coal Mines* 49 (06), 152–155. doi:10.13347/j.cnki.mkaq.2018.06.040
- Yuan, L., Lin, B. Q., and Yang, W. (2015). Research progress and development direction of gas control with mine hydraulic technology in China coal mine. *Coal Sci. Technol.* 43 (01), 45–49. doi:10.13199/j.cnki.cst.2015.01.011
- Zhang, M. L., Zhang, T. Y., and Fan, J. Y. (2019). Calculation and analysis of fracture extension parameters based on PKN model. *Sci. Technol. Eng.* 19 (5), 116–123.
- Zheng, Y. F., Zhai, C., and Ni, G. H. (2019). Study on performance of fracturing fluid based on surfactant releasing water locking effect. *Saf. Coal Mines* 50 (11), 1–5. doi:10.13347/j.cnki.mkaq.2019.11.001



OPEN ACCESS

EDITED BY

Shuren Wang,
Henan Polytechnic University, China

REVIEWED BY

Wanjuan Ye,
Xi'an University of Science and
Technology, China
Yuyang Liu,
Chang'an University, China

*CORRESPONDENCE

Zhichun Fang,
fangzhichun777@126.com

SPECIALTY SECTION

This article was submitted to
Geohazards and Georisks,
a section of the journal
Frontiers in Earth Science

RECEIVED 06 June 2022

ACCEPTED 20 July 2022

PUBLISHED 22 August 2022

CITATION

Zhu Z, Fang Z, Xu F, Han Z, Guo X and
Ma C (2022), Model test study on the
rock mass deformation law of a soft
rock tunnel under different
ground stresses.
Front. Earth Sci. 10:962445.
doi: 10.3389/feart.2022.962445

COPYRIGHT

© 2022 Zhu, Fang, Xu, Han, Guo and Ma.
This is an open-access article
distributed under the terms of the
[Creative Commons Attribution License](https://creativecommons.org/licenses/by/4.0/)
(CC BY). The use, distribution or
reproduction in other forums is
permitted, provided the original
author(s) and the copyright owner(s) are
credited and that the original
publication in this journal is cited, in
accordance with accepted academic
practice. No use, distribution or
reproduction is permitted which does
not comply with these terms.

Model test study on the rock mass deformation law of a soft rock tunnel under different ground stresses

Zhengguo Zhu^{1,2}, Zhichun Fang^{1*}, Fei Xu³, Zhiming Han¹,
Xiaolong Guo¹ and Chaoyi Ma¹

¹Key Laboratory of Roads and Railway Engineering Safety Control (Shijiazhuang Tiedao University), Ministry of Education, Shijiazhuang, China, ²Hebei Province Technical Innovation Center of Safe and Effective Mining of Metal Mines, Shijiazhuang, China, ³School of Safety Engineering and Emergency Management, Shijiazhuang Tiedao University, Shijiazhuang, China

It is difficult to monitor the deformation of a rock mass in front of a tunnel owing to the large buried depth and complex geological conditions. In this study, by using a self-designed model test box as a carrier and using loess, sand, gypsum, cement, and water as the raw materials, the class V materials similar to the surrounding rock are obtained through an orthogonal test. These are used to study the deformation law of a rock mass in front of a tunnel in different ground stress soft rock. The results show that similar materials for the surrounding rock can meet the needs of the testing concerning the physical and mechanical properties and have economic and environmental protection advantages. The three-dimensional loading of a similar geological body is used to simulate the state of the rock mass. The real-time monitoring of the rock mass stress and deformation is conducted during a simulation of tunnel excavation, and the deformation laws of the rock mass and surrounding rock in front of the tunnel are obtained. In the range of 0.26 times the tunnel diameter in front of the tunnel in the high ground stress soft rock, the deformation of the core rock mass is the largest part of the tunnel deformation. Therefore, to reasonably control the advanced deformation of the tunnel, it is necessary to pre-reinforce the core rock mass within 0.26 times the tunnel diameter in front of the tunnel. At 1 times the diameter in front of the face, a longitudinal load-bearing arch is formed in the rock mass, and this effectively controls the extrusion deformation of the core rock mass to expand forward.

KEYWORDS

similar materials, model test, soft rock, deformation law, different ground stresses

1 Introduction

Under the condition of high ground stress, some tunnel-collapse accidents caused by improper control of the surrounding rock stress release often occur in the construction of soft rock tunnels, which has caused great losses to the project. Many scholars have studied the engineering problems of soft rock tunnels with high stress and achieved fruitful

results. Yang et al. (2017) found that owing to the complex tectonic stress of a deep rock mass, the stress field is a superposition of the gravity stress field and tectonic stress field; accordingly, it is mostly in a high-in-situ-stress state. Chen et al. (2021). Ma et al. (2021) found that tunnel-collapse accidents caused by improper control of the surrounding rock stress release, high ground stress, and discontinuity often occur in the construction process of soft rock tunnels, causing significant losses to the corresponding projects. A Kovacevic et al. (2021) and Cheng et al. (2018) found that to ensure the construction safety in a soft rock tunnel with high geo-stress and the stability and durability of the tunnel, it is necessary to initially study the deformation laws of the rock mass. At present, the control and monitoring processes for tunnel rock mass deformations are mainly concentrated on the surrounding rock of the excavated part. Zhang et al. (2019) and Sengani (2020) found that according to a geotechnical control deformation analysis method, all deformations of tunnel surrounding rock and instabilities caused by deformation are directly or indirectly related to the strength of the core rock mass in front of the tunnel face. Accordingly, it is necessary to control and monitor the stress release and deformation of the rock mass in front of the tunnel face. However, on the whole, these results are more inclined to construction technology and applicable to individual cases, while there are relatively few basic studies.

As an important means for studying geotechnical engineering problems, the tunnel model test is easy to operate and costs relatively less. Moreover, it can avoid certain immature theoretical problems and can directly reflect the deformation law of the rock mass as caused by tunnel excavation and interactions between the surrounding rock and support. Sun et al. (2018) conducted a physical modeling experiment to study the deformation mechanism of a tunnel excavated in deep-buried soft rock strata. Xiang et al. (2018) proposed a transparent soil model test technique and used a particle flow code (3D) numerical simulation to study the influences of the surrounding material (rock and soil) strengths and buried depths on the deformation and failure mechanisms. Hu et al. (2018) proposed a pre-supporting technique denoted the “Freeze-Sealing Pipe Roof method”, which combined a pipe-roofing method with an artificial ground freezing method and an innovative freezing scheme for the first time in China during the construction of the Gongbei Tunnel. Liu et al. (2019) relied on the Daban Mountain tunnel to build a model experiment system with a similarity ratio of 1:37, aiming to obtain the distribution law of a frost front in a cold-region tunnel under ventilation. There have also been great achievements in the study of tunnel face rock mass. Zhang et al. (2020) extended a traditional block theory to tunnels constructed using a tunnel boring machine (TBM) by incorporating a disc cutter–block interaction mechanism. Hao et al. (2021) conducted tests with 32 loading levels using three physical models combined with the numerical simulation to analyze the effect of the major principal stress

direction with respect to the tunnel’s long axis on the stability of an underground tunnel. Yu et al. (2021) established a thermo–hydro–mechanical-coupled finite element model and verified it *via* a model test in the laboratory; then, they used it to consider the failure mode of the lining structure and investigated the influence of the burial depth on the temperature field and soil–lining interaction. Niu et al. (2021) developed a back-analysis method combining a model test and numerical simulation and derived results from the similitude criterion for the model based on similarity theory and elasticity mechanics equations. Zhou et al. (2021) studied the seismic response law of a loess tunnel based on the shaking table model of a 1/40 loess tunnel and considered the adverse conditions from an El-Centro bidirectional seismic wave and rainfall to discuss the damping effect of the loess tunnel structure (e.g., by setting a damping layer). At present, the research on the deformation law of the rock mass in front of the tunnel is not thorough, and on the whole, these results are more inclined to the construction technology and suitable for individual cases, while there is relatively little research on the foundation. Starting from the theoretical research, this study analyzes the deformation law of the square rock mass in front of the tunnel face in high-stress soft rock, makes a detailed study of the deformation characteristics of the core rock mass in front of the tunnel face and the rock around the tunnel by using the method of model test, and finally finds out the control range of the square rock mass deformation in front of the tunnel face.

2 Preparation of similar materials

2.1 Three similarity theorems and single-value conditions of geomechanics

1) First similarity theorem

If the numerical values of the similarity criterion between two phenomena are the same or the similarity index is 1, then two phenomena satisfy the first similarity theorem. This similarity theorem defines the mathematical relationship between the similarity ratios of each similarity parameter.

2) Second similarity theorem

The second similarity theorem establishes a functional relationship between the similarity criteria of similar phenomena. This leads to the differential equation that similar phenomena should satisfy.

3) Third similarity theorem

The third similitude theorem can be regarded as obtaining the similarity conditions of specific phenomena by adding the

single-value conditions of each phenomenon, i.e., by substituting the special solution of the differential equation so that a phenomenon is different from other phenomena.

The aforementioned great similarity theorems have different meanings for workers who solve practical problems. The first similarity theorem is a theoretical concept; the second similarity theorem gives the existence and function of similarity criteria, which are often used to guide practical work. The third similarity theorem provides the necessary and sufficient conditions for the actual model test.

During the model test, the physical phenomena shown by the model should be similar to the prototype structure, i.e., the material, shape, and external load of the model should follow a certain similarity law. A similar scale refers to the ratio of physical quantities of the same dimension between the prototype structure and the model, which is often represented by the letter C .

1) Geometric conditions

The establishment of a model must be scaled according to the actual size of the prototype to achieve geometric similarity. If individual parts or components cannot be geometrically similar owing to the limitations of the test conditions, it should be ensured that their characteristics are similar to those of the prototype.

2) Medium conditions

As the similarity ratios selected for each model test parameter are different, the similarity indexes that should be met between the similarity ratios of geomechanically similar materials are shown in Eqs 1, 2:

$$\frac{C_\sigma}{C_\gamma C_L} = 1. \quad (1)$$

$$\frac{C_\sigma}{C_\epsilon C_E} = 1. \quad (2)$$

The dimensionless similarity constants are all 1, and the similarity constant is $C_E = 1$, so the calculation is shown in Eq. 3:

$$C_\sigma = C_E. \quad (3)$$

In the aforementioned equation the following are represented, C_σ -stress similarity ratio; C_γ -bulk density similarity ratio; C_L -geometric similarity ratio; C_ϵ -strain similarity ratio; C_E -elastic modulus similarity ratio.

3) Boundary conditions and initial conditions

The most difficult task when simulating similar conditions in geomechanics is simulating the stress state of the rock mass. A geological body is in a complex stress environment. To simulate the actual engineering conditions, it is necessary to simulate the



initial stress state of the stratum, which requires three-dimensional loading of similar geological bodies. The range of the stress redistribution caused by underground engineering construction is approximately 3–5 times the excavation space. Therefore, the size of the surrounding geological model is at least three times larger than that of the surrounding geological model.

2.2 Engineering background

Jianshan tunnel is located in Baiyin City, Gansu Province. The starting and ending mileage is DK277 + 300 ~ DK283 + 830. The total length of the tunnel is 6530 m. The physical and mechanical parameters of the surrounding rock 2 km away from the starting point of the tunnel are selected as the main parameters of the model test prototype. The surrounding rock within 1700 m of this section is an extremely fragile carbonaceous slate. Considering the influence of initial ground stress, the surrounding rock grade has been revised to grade V, and the average buried depth is 575 m (Figure 1).

The tunnel site area mainly includes fold and fault structures. The core of the fold structure exists near 2650 m from the beginning of the tunnel, and with an axial direction of 110°, the north occurrence is at W436°S and the south occurrence is at N13°W432°N. The underground water in the tunnel is formed by infiltration of atmospheric precipitation into the rock fissures and mainly penetrates downward along the fissures of the rock mass. The water abundance of underground water is also poor, and the underground water is unevenly distributed throughout the year. The increase of the underground water level follows a seasonal law: it rises significantly in July, August, and September.

The ground stress field in the tunnel area is obtained using a finite element multiple regression analysis method. From the magnitude of the expansion analysis results, when the lateral pressure coefficient $\lambda = 1.8$, the average value of the maximum horizontal principal stress, δ_H , at the tunnel axis is 15 MPa, and the average values of δ_h and δ_v at the tunnel axis are 9.7 MPa and

TABLE 1 Value range of material, physical, and mechanical parameters.

Physical and mechanical parameter	Bulk density γ (KN/m ³)	Elastic modulus E (GPa)	Cohesion c (KPa)	Internal friction angle ϕ (°)	Poisson's ratio ν
Raw rock material	17–21	1–3	60–100	20–25	0.35–0.45
Model material	17–21	0.02–0.06	1.2–2	20–25	0.35–0.45

TABLE 2 Orthogonal test design scheme.

Influence factor		Soil sand ratio	Proportion of cement (%)	Proportion of gypsum (%)	Water content (%)
level	1	4:6	5	7	10
	2	5:5	6	8	12
	3	6:4	7	9	14
Test number		Column number			
	1	1	1	1	1
	2	1	2	2	2
	3	1	3	3	3
	4	2	1	2	3
	5	2	2	3	1
	6	2	3	1	2
	7	3	1	3	2
	8	3	2	1	3
	9	3	3	2	1

The physical and mechanical parameters of the similar materials with different proportions as obtained by the orthogonal test are shown in Table 3.

6.5 MPa, respectively. The uniaxial compressive strength R_C of the surrounding rock is 30 MPa. According to the *engineering rock mass classification standard* (GB/T 50218-2014), when the strength stress ratio is between 2 and 4, the tunnel is considered to be in a high-stress state. According to this judgment, it is considered that the maximum buried depth of the tunnel of the project is in the state of high ground stress.

2.3 Preparation of similar materials

When the geometric similarity ratio of the model test is determined, for the qualitative model, it is generally taken as 100–200, and for the quantitative model, it is 20–50. In this test, considering the size of the existing model test box, if it was partially modified, it would not meet the requirements of the boundary conditions; hence, we chose to determine the appropriate similarity ratio according to the existing design.

The maximum width of the proposed tunnel is 6.8 m, the vertical height of the tunnel is 5.8 m, and the designed maximum diameter of the existing model in this study was 14 cm. The geometric similarity scale C_L was 50, and the bulk density similarity scale C_γ was 1, according to the similarity index of the geomechanical model test shown in Eq. 4:

$$C_\sigma = C_E = C_\gamma C_L. \quad (4)$$

Therefore, the similarity ratios of other physical quantities could be calculated as follows:

- 1) Similarity ratio of stress, modulus of elasticity, and cohesion: $C_\sigma=50$, $C_E=50$, $C_c=50$.
- 2) Similarity ratios of Poisson's ratio and internal friction angle: $C_\gamma=1$, $C_\phi=1$. According to the actual tunnel rock mass

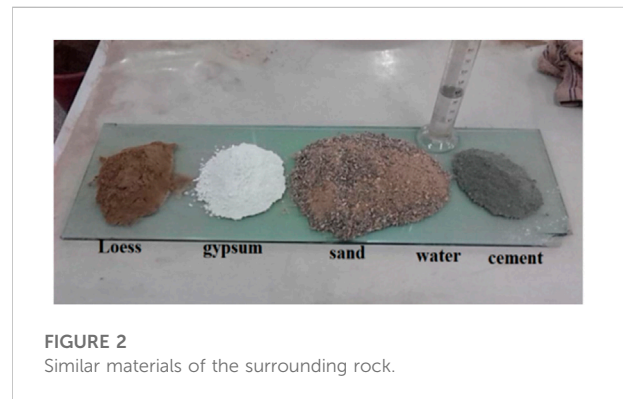


FIGURE 2
Similar materials of the surrounding rock.

TABLE 3 Physical and mechanical parameters of similar materials with different proportions.

Test number	Bulk density γ (KN/m ³)	Compression modulus E_s (MPa)	Cohesion c (kPa)	Internal friction angle φ (°)
1	21.39	10.096	17.53	37.53
2	19.89	9.323	10.31	28.28
3	19.28	8.929	2.65	30.97
4	22.14	7.367	8.11	25.28
5	24.55	6.732	3.49	26.30
6	19.26	6.543	10.75	20.70
7	20.35	4.494	6.13	19.56
8	16.13	4.274	3.36	25.22
9	20.28	4.801	1.52	20.27

parameters, the ranges of the theoretical values of physical and mechanical parameters of similar materials in the model test are as shown in Table 1.

Loess and quartz sand were used as the main raw materials, and gypsum and cement were used as cementing materials. Water was used as the regulating agent, and these materials were used as raw materials to develop similar materials for the rock mass (Figure 2).

In general, in the process of developing similar materials, adding quartz sand can reduce the cohesion of loess and increase the bulk density of similar materials; gypsum can reduce the bulk density of materials; the addition of cement can improve the strength of materials and can still be used as cement when mixed with water.

When there are many factors and multiple tests need to be arranged, orthogonal design is a more commonly used design method, which can skillfully arrange the tests, reduce the number of tests, and shorten the test cycle on the premise of achieving the same statistical effect. Orthogonal design not only considers the balanced dispersion of factor levels but also takes into account the neat and comparable level of factors, which is convenient for analyzing the interaction between factors. Orthogonal design is a method to scientifically arrange and analyze multi-factor and multi-level experiments by using an orthogonal table. The orthogonal table is a standardized table constructed on the basis of Latin square and orthogonal Latin square by applying combinatorial mathematics theory according to the idea of balanced dispersion. It is the basic tool of orthogonal design. The orthogonal test design scheme is shown in Table 2.

According to the aforementioned thought, different soil sand ratios, cement proportions, gypsum proportions, and water contents were selected as the four influencing factors, and three different proportions were selected for each influencing factor. Therefore, an L_9 (3^4) orthogonal table was selected to combine the tests.

According to a comparison of the data in Table 3 and Table 1, it can be seen that the physical and mechanical parameters of the



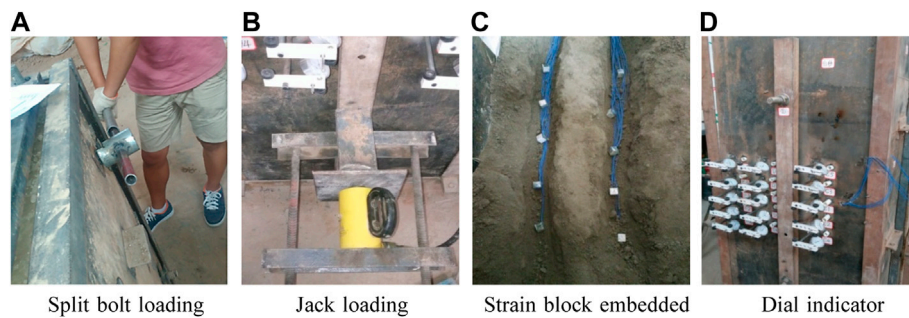
FIGURE 3
Model test box.

similar materials obtained from test No. 9 are within the theoretical value ranges of the model materials, thereby meeting the design requirements of the model test. Therefore, the proportions of similar materials in test No. 9 were selected as the formula for the similar materials in the model test, i.e., the soil to sand ratio was 6:4, the cement proportion was 7%, the gypsum proportion was 8%, and the water content was 10%.

3 Experimental design

3.1 Design of the model box and loading mode

According to the actual project considered in this test, the tunnel width was 13.6 m, the vertical height was 11.6 m, and the proposed geometric similarity scale CL was 50. The final design

**FIGURE 4**

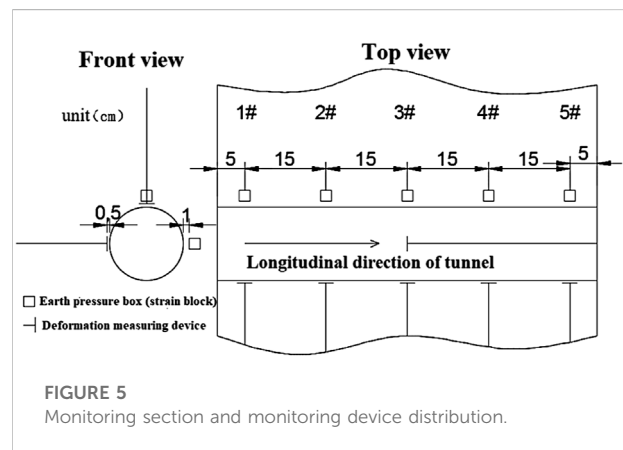
Model test loading and stress and deformation monitoring. (A) Split bolt loading; (B) jack loading; (C) strain block embedded; (D) dial indicator installation

of the test box size was 200 cm vertically, 200 cm horizontally, and 70 cm longitudinally (Figure 3). The frame of the model box was welded with 12 angle steel, and the six faces were designed as movable steel plates. The tunnel section in the test is approximately circular, and the tunnel diameter was 27.2 cm; this ensured that the tests conducted in the model box could meet the tunnel boundary conditions. This design not only saved a significant amount of cost but also ensured that the test could meet the theoretical requirements.

To simulate the high ground stress condition of the soft rock tunnel, the model needed to be loaded in three directions. This test adopted a loading mode comprising a combination of a pull rod and jack. The position of the tie rod was on the four corners of each surface of the model box, so there were four pairs of pull rods in the transverse, vertical, and longitudinal directions of the model box; when the rock mass was stressed, the relative panel was moved and pressurized by tightening the pull rod nut (Figure 4A). When the pull rod could not be tightened again, the reaction frame was considered sufficiently supported to load with the jack (Figure 4B). At the same time, the two hydraulic jacks on the top of the model system pass through mutually independent steel ropes (specification: $\Phi 20$) so as to exert reverse load on the internal surrounding rock. In order to avoid the possible deviation and instability of the steel wire rope under its flexibility, the jack base is firmly in contact with the top boundary surface of the model system, and the top of the jack piston is stably placed with channel steel to limit the sliding movement of the steel wire rope.

3.2 Stress and deformation monitoring in the test

The monitoring of the surrounding rock stress was realized by connecting the dh3818 strain gauge with an earth pressure box and strain block (Figure 4C). The earth pressure cell was a strain-type miniature earth pressure box for the model test, and the

**FIGURE 5**

Monitoring section and monitoring device distribution.

strain block was a measuring device comprising the nylon block and strain gauge.

The deformation monitoring was the key aspect of the test. The design of the monitoring device was required to allow for the deformation monitoring of the monitoring point without being affected by the surrounding rock mass. The deformation of the tunnel surrounding rock and core rock mass was mostly an inward convergence or longitudinal extrusion deformation. The deformation in other directions was not large, and it was difficult to monitor. Therefore, this test only monitored the convergence deformation of the surrounding rock and extrusion deformation of the core rock mass. In this way, the deformation considered in the test was only the vertical deformation of the vault, the lateral deformation of the wall waist, and the longitudinal deformation of the core rock mass (Figure 4D).

The tunnel excavation speed of the supporting project was 1.75 m per day. According to the proposed similarity ratio conversion, the tunnel excavation speed in the test was 7 cm per hour. The longitudinal length of the model test box was 100 cm. The monitoring section was set at the middle position

(50 cm). The other sections were selected as the longitudinal 5 cm, 20 cm, 50 cm, and 65 cm positions of the model (Figure 5).

Each section was equipped with two stress monitoring devices and two deformation monitoring devices, and their respective positions were located at the vault and wall waist of the tunnel. Because the stress and deformation of the arch crown section needed to be monitored simultaneously, the earth pressure box (strain block) and the deformation-monitoring device were staggered by 1 cm; owing to the symmetry of the wall waist, the earth pressure box (strain block) is arranged on one side, and the deformation-monitoring device was arranged on the other side. In addition, a deformation-monitoring device was arranged at the center of the face of the No. 3 section to monitor the longitudinal extrusion deformation of the core rock mass of the tunnel.

3.3 Test method and test comparison arrangement

1) Test method

After the test bench was filled with similar materials in the layers, compacted, and implanted with the stress- and deformation-monitoring device, loading was started, and the stress collection work was performed simultaneously. When the stress measured by the earth pressure box (strain block) reaches the test design value, it was considered that the surrounding rock had reached the designed initial stress state.

In the process of the test, it was found that the boundary conditions had great influence on the 1 # and 5 # sections. The deformation of the rock mass monitored at section 1 # was excessively large, and the tunnel excavation was completed when the rock mass deformation of section 5 # was very small, so the monitoring was not complete. Therefore, only the monitoring data of each measuring point of sections 2 #, 3 #, and 4 # were recorded, and the change of each footage excavation focused on the shape value.

2) Experimental comparison

To compare and study the deformation of the tunnel rock mass under different stress states of the surrounding rock with and without a lining, a double-layer wire mesh was selected as a lining-similar material, and the support was employed during excavation and jacking.

To study the deformation law of the rock mass under different stress states, the designed initial stress state of the rock mass had five groups: 0.1 MPa, 0.2 MPa, 0.3 MPa, 0.4 MPa, and 0.5 MPa, and each group was set with and without a lining.

3) Test arrangement

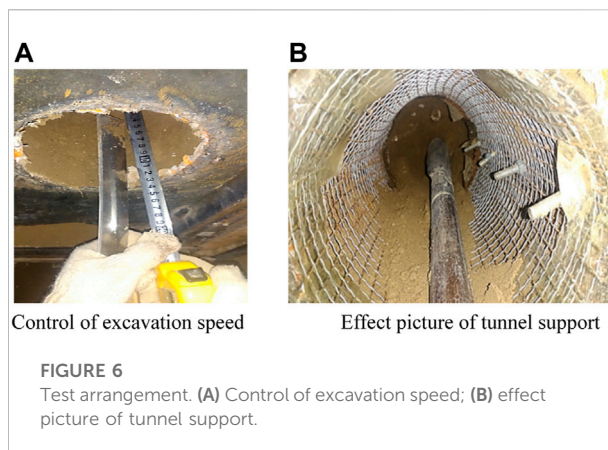


FIGURE 6
Test arrangement. (A) Control of excavation speed; (B) effect picture of tunnel support.

The divisional excavation method was used for tunnel excavation (Figure 6). In each group of test excavation, a constant speed of 7 cm per hour (1.75 m per day in actual engineering according to the proposed similarity ratio) was maintained (Figure 6A), and deformation and stress values were collected once for each excavation distance; among them, the lining test (Figure 6B) pushed the wire mesh lining to a certain distance for each distance.

4 Analysis of the deformation law of the rock mass in front of the tunnel face

4.1 Comparative analysis of the deformation law of the rock mass

Mentioned in his 2011 book ADECO-RS (Analysis of Controlled Deformation-Rock and Soil), Pietro Lunardi proposed the “New Italian Tunneling Method”, where the core of this method is to strengthen the rock and soil mass in front of the tunnel face in advance and improve its stiffness so as to control the deformation of the rock and soil mass in front of the tunnel face. In this approach, all deformations of the surrounding rock and instabilities caused by deformation are directly or indirectly related to the strength of the core rock mass in front of the face. The longitudinal extrusion deformation of the core rock mass in front of the tunnel face and surrounding rock pre-convergence should be included in the study of the deformation law, and the deformation analysis should be extended to a three-dimensional space.

Figure 7 shows the deformation of the tunnel vault and wall waist with and without the lining and the longitudinal extrusion deformation curve of the core rock mass at section 3 #.

From the deformation curve of the surrounding rock, it can be seen that the deformation of section 2# is larger than that of section 4#. The longitudinal design length of the model is 0.7 m,

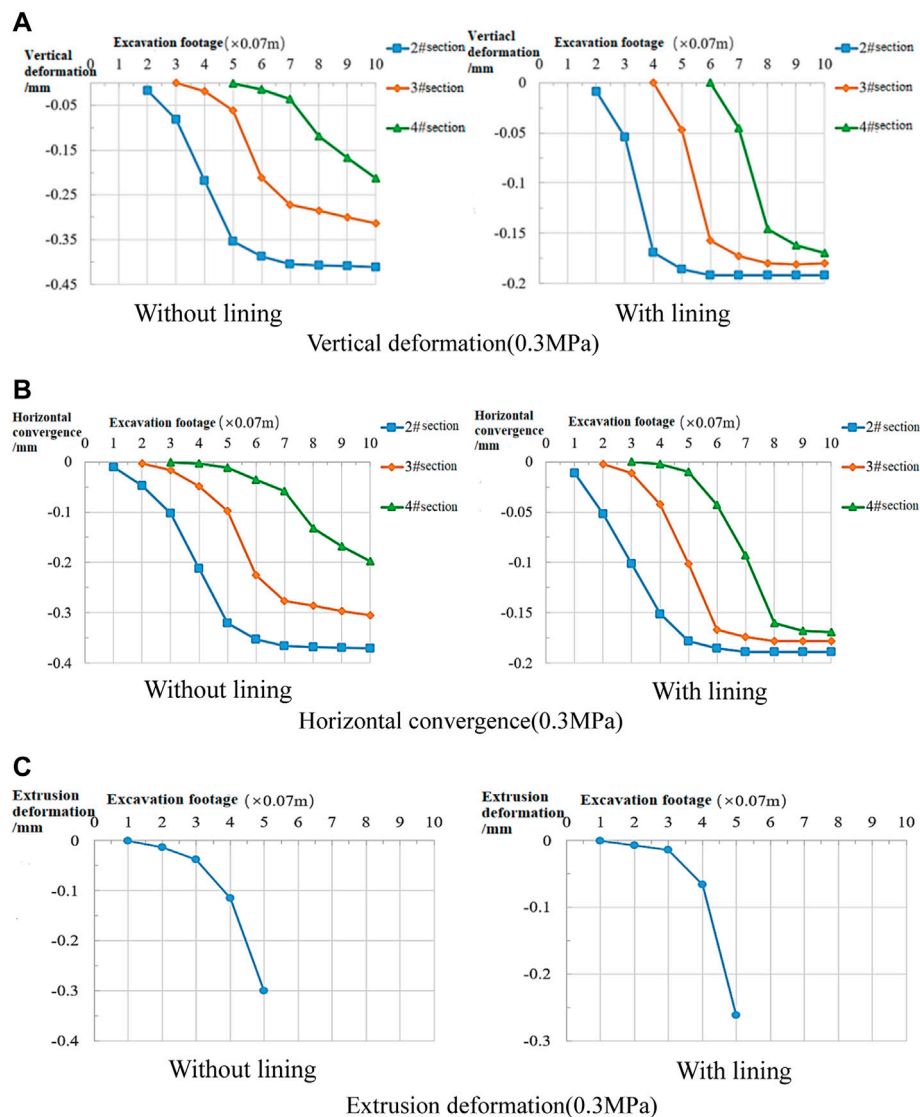


FIGURE 7
0.3 MPa test results. (A) Vertical deformation (0.3 MPa); (B) horizontal convergence (0.3 MPa); (C) extrusion deformation (0.3 MPa).

the position of section 2# is 0.2 m, section 3# is the middle (0.35 m), and section 4# is at 0.5 m; from the beginning of tunnel excavation to the excavation of section 2#, the stress in the entire model concentrates on the excavated side, resulting in a large deformation of section 2#; section 4# is in the second half of the model, and the rock mass to be excavated is only 0.2 m. With the excavation of the tunnel, the stress release of the surrounding rock in the model is large, so the deformation value measured in theory is too small and does not conform to the actual situation. Therefore, this study should be mainly based on the deformation law of the rock mass with section 3#, and section 2# and section 4# should correspond to the entrance and exit sections of the tunnel, respectively.

By comparing the data extracted from the map, it can be concluded that the tunnel rock mass begins to deform at the position of 14–28 cm ($0.5 D-1 D$, where D is the tunnel diameter) in front of the tunnel without the lining. The position where the lining test begins to deform is 7–28 cm ($0.26 D-1 D$) in front of the tunnel. The extrusion deformation of the core rock mass starts to deform at $1 D$ in front of the tunnel face regardless of whether there is a lining or not, which indicates that the size and range of the disturbance area of the rock mass in front of the tunnel face are not significantly different under the conditions of lining or not. According to this changing trend, the tunnel deformation is divided into six regions for discussion, as follows:

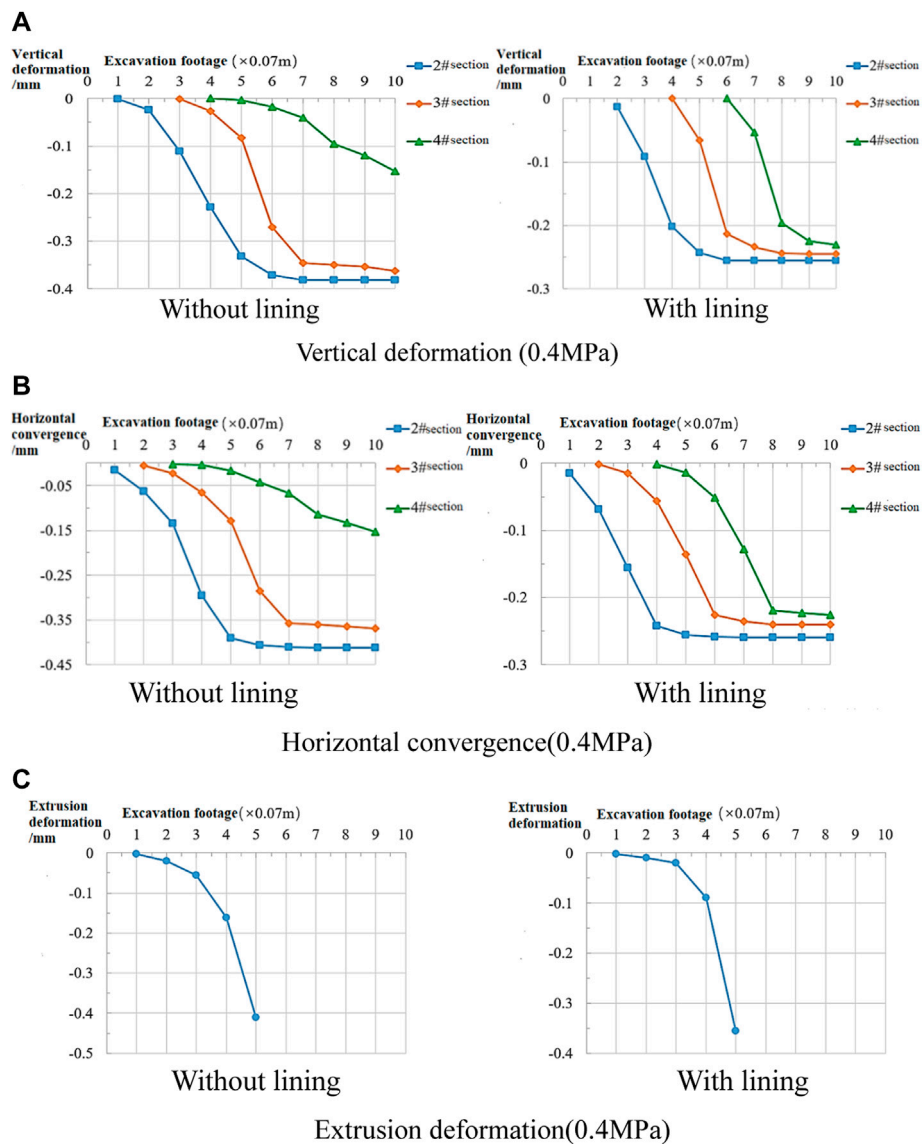


FIGURE 8

0.4 MPa test results. (A) Vertical deformation (0.4 MPa); (B) horizontal convergence (0.4 MPa); (C) extrusion deformation (0.4 MPa).

1) Rock mass beyond 0.5 D in front of the tunnel

The results show that the pre-convergence deformation of the arch crown and wall waist at 0.5 D in front of the tunnel is very small. The test on the vault with the lining does not detect the trend of deformation; however, the central position of the core rock mass has a relatively evident extrusion deformation. The extrusion deformation of the core rock mass measured in the lining test is 0.024 mm smaller than that in the non-lining test. Because the deformation of the rock mass at this position is very small, it is impossible to judge whether the lining affects the rock mass deformation in front of the tunnel.

2) 0.5 D—0.26 D rock mass in front of the tunnel

At the position 0.26 D away from the heading face, the rock mass is greatly disturbed, and the deformation is evident relative to that at 0.5 D away from the face. The results show that the extrusion deformation of core rock mass in the lining test is greater than that of wall waist, but the difference between them is small; however, the extrusion deformation of the core rock mass in a non-lining test is much larger than that of the arch crown and wall waist, i.e., 6.39 and 2.35 times of that of the arch crown and wall waist, respectively. It can be seen that the extrusion deformation of the tunnel face at the 0.26 D position in front of

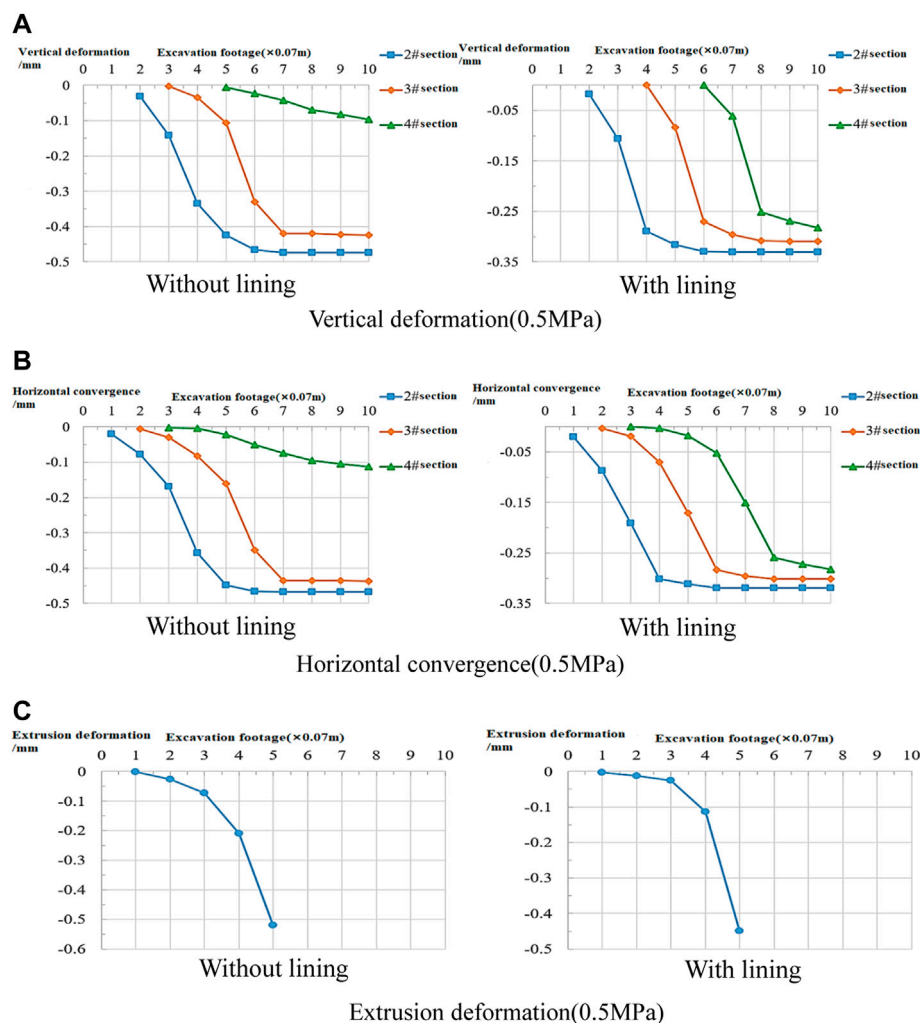


FIGURE 9
0.5 MPa test results. (A) Vertical deformation (0.5 MPa); (B) horizontal convergence (0.5 MPa); (C) extrusion deformation (0.5 MPa).

the tunnel becomes much larger than the pre-convergence of the surrounding rock in the section of the main deformation.

3) Rock mass of 0.26 D—face in front of the tunnel

In the tunnel face, the vertical displacement in the test of the vault with the lining is smaller than that of the test for the unlined vault, whereas the lateral displacement of the wall waist has no significant difference whether under the condition of a lining or not. The extrusion deformation of the core rock mass in this section is still far greater than the pre-convergence deformation of the surrounding rock. The extrusion deformation value of the core rock mass in the non-lining test is 4.92 and 3.06 times that of the arch crown and wall waist, respectively, and is 5.57 and 2.59 times of those in the lining test, respectively. The extrusion deformation of the core rock mass in the lining test is only 13%

less than that in the unlined test. The results show that the core rock mass extrusion deformation remains the largest part of the tunnel advance deformation, and the influence of the lining 0.26 D away from the tunnel face on the core rock extrusion deformation is very small.

4) Tunnel face position—the 0.26 D surrounding rock section behind the face

In this section, the deformation rate of the tunnel vault is fast, and the vertical deformation value of the surrounding rock of section 2# with or without the lining exceeds the lateral deformation value of the wall waist; although the lining test is not supported in this section, it can be seen that the surrounding rock deformation in this section is 23%–29% smaller than that in the unlined test and that the

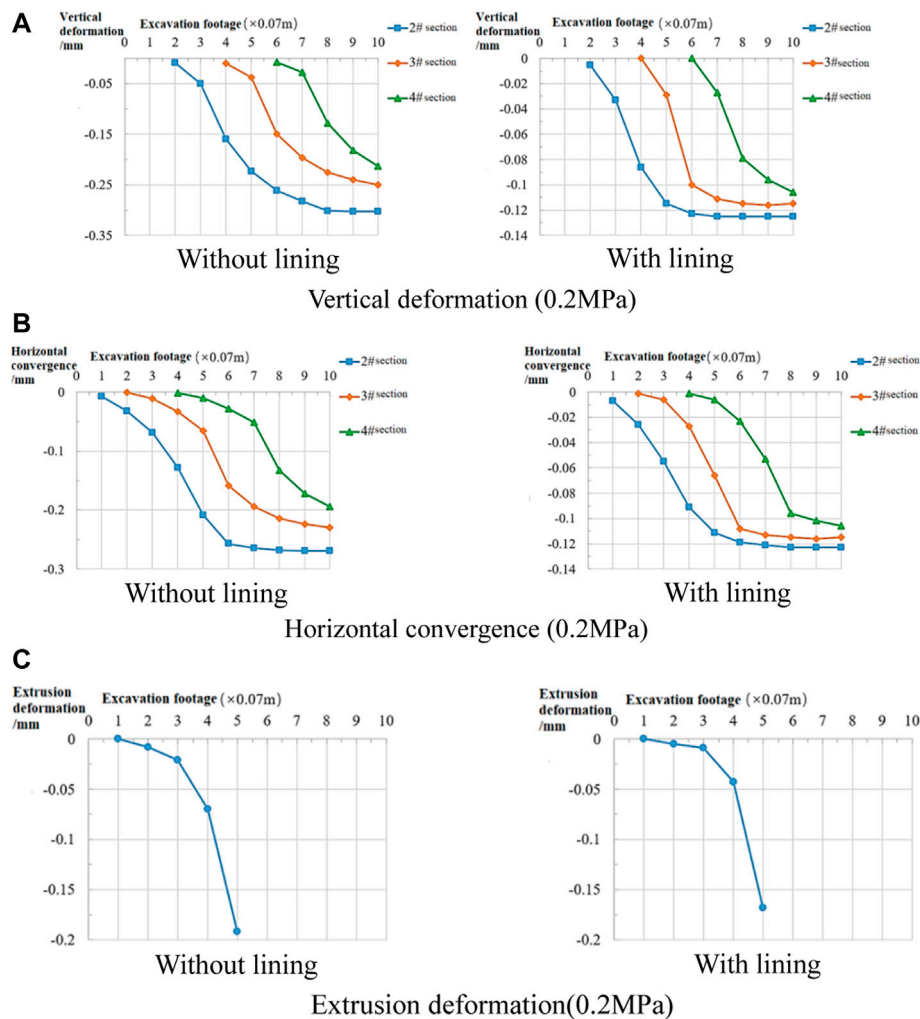


FIGURE 10
0.2 MPa test results. (A) Vertical deformation (0.2 MPa); (B) horizontal convergence (0.2 MPa); (C) extrusion deformation (0.2 MPa).

surrounding rock deformation has been controlled to a certain extent.

5) 0.26 D–0.5 D surrounding rock section behind the face

In this section, the deformation rate of the surrounding rock of the arch crown is still greater than that of the wall waist, and the deformation of the surrounding rock of section 2# is still greater than that of the wall waist. Although the deformation values of other sections are less than those of the wall waist, the deformation value of the surrounding rock in this section is reduced by 36%–47% compared with that without lining, so the deformation of the surrounding rock is obviously controlled.

6) 0.5 D–1 D surrounding rock section behind the face

The results show that the vertical deformation of the surrounding rock at each section exceeds the lateral deformation of the wall waist. The deformation of the surrounding rock in the lining test is reduced by 42%–53% compared with that in the non-lining test, and the surrounding rock deformation control effect is better.

In conclusion, the longitudinal extrusion deformation of the rock mass in front of the tunnel is the most important part of the tunnel's advanced deformation. The results show that the extrusion deformation at the central position of the tunnel face when the tunnel face reaches the lining is equivalent to the final deformation value when the tunnel vault and wall waist are stable, whereas those in the non-lining test are 1.45 and 1.47 times of the final deformation values of the vault and the wall waist, respectively. The results show that the extrusion deformation of the core rock mass is the most serious part of the advanced deformation of a soft rock tunnel with high ground

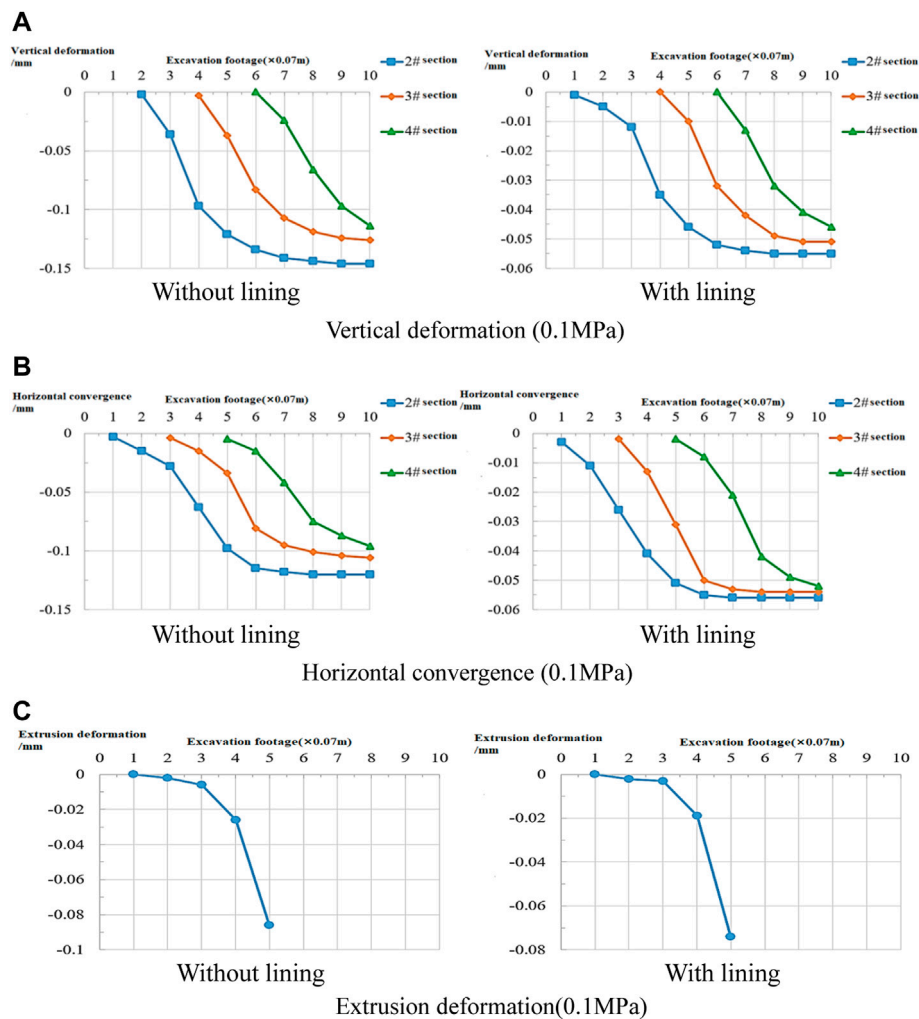


FIGURE 11

0.1 MPa test results. (A) Vertical deformation (0.1 MPa); (B) horizontal convergence (0.1 MPa); (C) extrusion deformation (0.1 MPa).

stress, and its deformation should be paid significant attention. At 0.26 D away from the face, the core rock mass in front of the tunnel begins to produce an evident longitudinal extrusion deformation and shows a large deformation rate in the rock section from 0.26 D to the face. Therefore, to control the extrusion deformation of the core rock mass of the tunnel, the strength of the rock mass from the face to the front 0.26 D should be strengthened.

4.2 Comparative analysis of the deformation law of the rock mass under different stress states

To study the change of the tunnel rock mass deformation law after increasing or reducing the initial ground stress, the

maximum ground stress is increased and decreased, respectively. In this test, according to the initial test arrangement, lined and unlined tests are conducted, and the rock deformation laws are compared and analyzed in detail.

1) Analysis of the deformation law of the rock mass after stress increases

It can be seen from Figure 8 that the deformation of each part of the rock mass increases with an increase in the stress. The results show that the deformation of the arch crown increases from 0.314 mm to 0.363 mm, i.e., by 16%, that of the wall waist increases from 0.305 mm to 0.369 mm, i.e., 21%, and the extrusion deformation of the core rock mass increases from 0.300 mm to 0.410 mm, i.e., 37%. In the lining test, the deformation of the vault increases from 0.181 mm to

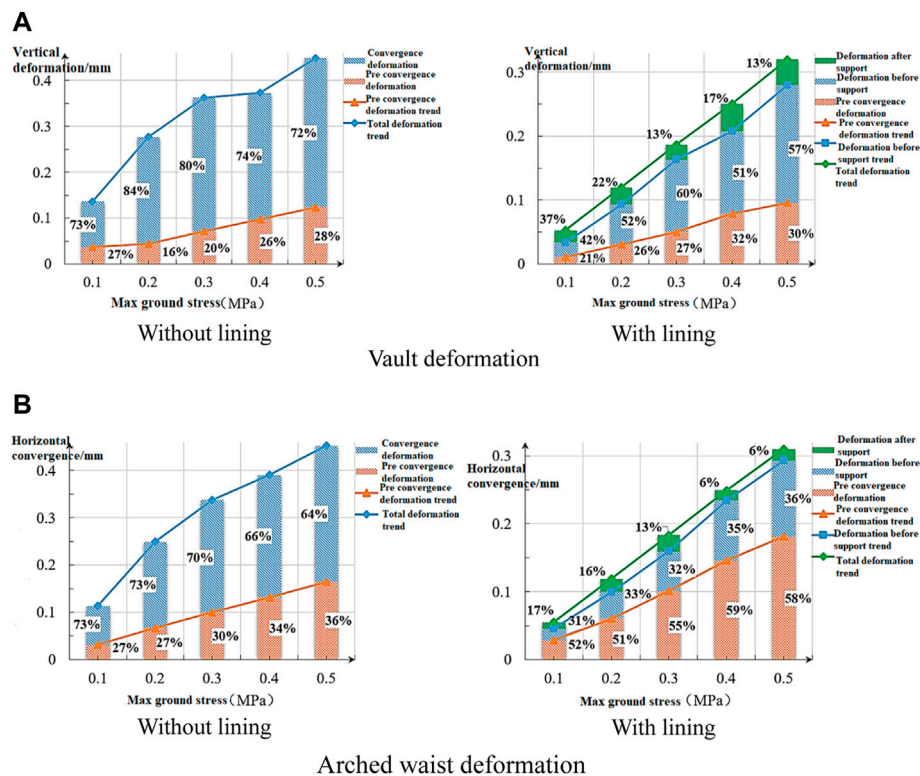


FIGURE 12

Deformation trend of the vault and arched waist under different stress states. (A) Vault deformation; (B) arched waist deformation.

0.245 mm, i.e., 35%, that of the wall waist increased from 0.178 mm to 0.240 mm, i.e., also by 35%, and the extrusion deformation of the core rock increased from 0.262 mm to 0.356 mm, i.e., 36%.

Figures 7–9 show that the deformation of each part of the rock mass increases with the increase of stress, and the proportion of advanced deformation also increases. However, the proportion of advanced deformation of section 2 # increases evidently, whereas that of section 4 # decreases. It can be seen that the release of the stress in the whole geological body tends to transfer to the excavation side, so the deformation rate of the rock mass in the first half of the tunnel excavation is faster, and the deformation value is larger. After the stress increases, the core rock mass extrusion deformation remains the most evident part of the tunnel surrounding rock advanced deformation. The analysis shows that a large part of the tunnel's advanced deformation is represented by extrusion of the core rock mass; therefore, with the increase of the advanced deformation of each part, the extrusion deformation of the core rock mass will evidently increase.

2) Analysis of the deformation law of the rock mass after stress decrease

Figure 10 shows that after a reduction of the ground stress, the deformation of the arch crown in the 3# section without the lining decreases by 20% from 0.314 mm to 0.250 mm, and that of the wall waist decreases by 25% from 0.305 mm to 0.230 mm; the extrusion deformation of the core rock mass decreases from 0.300 mm to 0.192 mm, i.e., by 36%. In the lining test, the deformation of the vault is reduced from 0.181 mm to 0.115 mm, i.e., by 36%; the wall waist is reduced from 0.178 mm to 0.115 mm, i.e., by 35%; the extrusion deformation of the core rock mass is reduced from 0.262 mm to 0.168 mm, i.e., by 36%.

Figure 11 shows that when the initial stress decreases, the deformation of each part of the rock mass decreases and the proportion of the advanced deformation also decreases. The disturbed range of the rock mass in front of the tunnel is shortened from 1D to 0.9 D, and the disturbance range is evidently reduced. Compared with the situation in which the disturbance area of the rock mass is within 1D in front of the face after the increase of initial stress, it can be found that under the stable condition of the tunnel, the disturbance range in front of the face does not expand with the increase of the initial stress. The main reason is that the deformation of the core rock mass in front of the face is limited. With the increase in the distance from the face, the disturbed rock mass compresses the core rock mass in the process of stress release. The higher the ground stress, the

TABLE 4 Proportion of the reduced deformation value of the surrounding rock after lining.

Type of deformation		0.1 MPa (%)	0.2 MPa	0.3 MPa	0.4 MPa	0.5 MPa
Vault	Convergence	73	23.7%	23%	20.5%	20.8%
	Preconvergence	53.9	59.4%	47%	36.1%	29.2%
Arched waist	Convergence	8.8	0	−3.1%	−5.4%	−6.2%
	Preconvergence	68.1	70.1%	62.8%	56.7%	52.9%
Face	Extrusion deformation	14	12.5%	12.7%	13.2%	13.5%

greater the extrusion effect (which controls the extrusion deformation of the core rock mass). Further analysis shows that the deformation of the core rock mass is controlled in the position close to the face. Simultaneously, the longitudinal bearing arch of the rock mass in front of the tunnel is also formed and prevents the extrusion deformation of the core rock mass from expanding to a larger range.

Based on the results of this test, a tunnel with the same section should have such an “ultimate longitudinal bearing arch” so that even under a higher initial stress environment, the maximum range of the rock disturbance caused by tunnel excavation to the rock mass in front of the tunnel is also on the inner side of the “ultimate longitudinal bearing arch.” The “ultimate longitudinal bearing arch” is actually the maximum upper limit of deformation that can be borne. The existence of the “ultimate longitudinal bearing arch” prevents the advanced deformation from expanding to a wider range and effectively controls the expansion of the extrusion deformation of the core rock mass to the front. From this test, the “ultimate longitudinal bearing arch” of the tunnel should be approximately 1D in front of the tunnel face.

4.3 Comparative analysis of deformation law of rock mass under different stress states

1) Analysis of deformation proportion of the surrounding rock in each part

It can be seen from Figure 12 that with an increase in the initial stress of the surrounding rock, the pre-convergence deformation of the surrounding rock has an evident increasing trend, and its law is evident. The ratio of the pre-convergence deformation value of the non-lining test arch crown to the final deformation value is between 16% and 28%, and with the increase of the initial stress, the proportion of the wall waist pre-convergence deformation value to the final deformation value is between 27% and 36%. The analysis shows that owing to the large transverse stress of the tunnel in this test, the final deformation of the vault and wall waist under different stress states is not

different, but the proportion of the pre-convergence of the surrounding rock in the final deformation value is different by 8%–11%, leading to a larger proportion of advance deformation in the direction of the greater surrounding rock stress.

The pre-convergence deformation of the arch crown with the lining is less than that without the lining. However, because the deformation of the surrounding rock is controlled by the lining, the proportion of the pre-convergence deformation in the final deformation value increases to 21%–32%. The pre-convergence deformation value of the wall waist is greater than that of the wall waist without the lining and accounts for 51%–59% of the final deformation value. This shows that after the deformation of the surrounding rock behind the face is controlled, the release of surrounding rock stress shifts to the unsupported section and front of the face, leading to the increase in the advanced deformation value of the surrounding rock.

In addition, the final convergence deformation of the surrounding rock of the tunnel with the lining is significantly smaller than that of the tunnel without the lining. After the lining, the convergence deformation of the vault only accounts for 13%–22% of the total deformation value, and the wall waist convergence deformation value only accounts for 6%–17% of the total deformation value. It can be seen that with the increase of the initial stress, the proportion of the convergence deformation value of the surrounding rock to the total deformation has a decreasing trend; this shows that the deformation rate of the surrounding rock is related to the stress of the stratum and that the deformation rate of the surrounding rock is evidently accelerated after the increase of initial stress. Therefore, the deformation of the surrounding rock under a high-stress state has already been completed before the lining with the same construction method. In practical engineering, tunnel support should be provided at a reasonable time, i.e., according to the different ground stress values.

2) Control of the surrounding rock deformation by the lining

It can be seen from Table 4 that the convergence deformation of the surrounding rock after the lining is well-controlled. The convergence deformation of the transverse arch waist with larger stress values decreases by 52.9%–68.1%, and that of the vertical vault with smaller stress values decreases by 29.2%–59.4%. It can

be seen that the lining evidently controls the deformation of the surrounding rock, especially in the direction of large stress.

With the increase of the initial stress, the proportion of the lining controlling the convergence deformation of the surrounding rock decreases; this is caused by the same construction method under different conditions and leads to a missed support opportunity. Accordingly, the timing of support construction should be strictly controlled in such projects. In this test, the pre-convergence deformation of the surrounding rock of the arch crown is reduced by 20.5%–23.7%, that of the wall waist is reduced by 6.2%–8.8%, and the extrusion deformation of the core rock mass is reduced by 12.5%–14%. After lining, the deformation of the surrounding rock in this section is controlled, and the rock mass tends to be stable, simultaneously, owing to the concentration of rock stress caused by excavation of the excavation site, the surrounding rock in the section without the lining and in a certain range in front of the tunnel is compressed longitudinally. The shear strength of the surrounding rock in each section of the tunnel in this section is larger than that in the test without the lining, so the advanced deformation is smaller than in the test without the lining test. Owing to the control of the longitudinal stress release in the direction of larger stress, the pre-convergence deformation of the surrounding rock (arch waist) in this direction increases.

5 Conclusion

This study considers the deformation law and deformation control of the rock mass in front of a tunnel in high-ground stress soft rock. The deformation characteristics of the core rock mass in front of the tunnel face and the surrounding rock mass around the tunnel are studied in detail by means of model tests, and the control range of the rock mass deformation in front of the tunnel is identified. The conclusions are as follows:

- 1) Loess and sand are used as the main aggregates, cement and gypsum are used as the cementing agents, and water is used for mixing. According to the orthogonal test, the physical and mechanical parameters of the similar materials of the grade V surrounding rock under the final ratio meet the requirements of the indoor model test under similar ratios and have the advantages of easy access to the basic materials, along with easy preparation, processing, and maintenance; moreover, these materials are economic and reasonable and harmless to the environment.
- 2) At a certain position in front of the tunnel, the core rock mass is compressed and compacted after being subjected to the stress concentration caused by tunnel excavation from the stratum, and a longitudinal bearing arch is formed at this position. This arch effectively controls the expansion of the extrusion deformation of the core rock mass to the front. The higher the stress state, the stronger the extrusion effect caused by the stress concentration; accordingly, it is inferred that there is an “ultimate longitudinal bearing arch” at a certain position in front of the tunnel face under the higher stress state, which prevents the extrusion deformation of the core rock mass of the tunnel with the same section from exceeding the scope of the bearing arch even under larger initial stress conditions. According to the analysis of the test, the “ultimate longitudinal bearing arch” of the tunnel should be formed at approximately 1D in front of the tunnel face.
- 3) The pre-convergence deformation of the lining test tunnel is smaller than that of the non-lining test tunnel, and the lining has a certain control effect on the advanced deformation of the tunnel. This is because in the lining test, the surrounding rock of the lining section tends to be stable after the lining construction, and owing to the stress concentration caused by the excavation, the surrounding rock in the surrounding rock section without the lining and the surrounding rock in front of the tunnel in a certain range are compressed longitudinally. This improves the shear strength of the surrounding rock of each section of the tunnel in this section and makes the pre-convergence deformation smaller than that of the test without the lining.
- 4) The deformation rate of the tunnel rock mass accelerated with an increase of the initial stress, and a reasonable time should be selected for the construction of tunnel support. Under a low-stress condition, the surrounding rock can bear a large part of the stress concentration caused by tunnel excavation by its strength, thereby making the stress release slow; however, after the initial stress increases, the deformation rate of the surrounding rock accelerates, so support should be provided as soon as possible. Therefore, a reasonable time should be chosen according to the different ground stress states.

Data availability statement

The raw data supporting the conclusions of this article will be made available by the authors, without undue reservation.

Author contributions

All the authors contributed to this manuscript. Conceptualization and writing, ZF and ZZ; methodology, FX and ZH; investigation, XG and CM; resources, ZZ. All authors have read and agreed to the published version of the manuscript.

Funding

This work is funded by the National Science Foundation of China (Grant No. 51978424), S & T program of Hebei Province in China (Grant No: 22375416D), Hebei Natural Science Foundation Project (Grant No. E2022210040), and the Key

Project of China Railway Construction Corporation Limited Science and Technology (Grant No:2019-A05).

Conflict of interest

The authors declare that the research was conducted in the absence of any commercial or financial relationships that could be construed as a potential conflict of interest.

References

- A Kovacevic, M. S., Bacic, M., Gavin, K., and Stipanovic, I. (2021). Assessment of long-term deformation of a tunnel in soft rock by utilizing particle swarm optimized neural network. *Tunn. Undergr. Space Technol.* 110, 103838. doi:10.1016/j.tust.2021.103838
- Chen, Z. Q., He, C., Wang, J., and Ma, C. C. (2021). Time-dependent squeezing deformation mechanism of tunnels in layered soft-rock stratum under high geo-stress. *J. Mt. Sci.* 18, 1371–1390. doi:10.1007/s11629-020-6356-0
- Cheng, L., Liu, Y. R., Pan, Y. W., Yang, Q., and Lv, Z. (2018). Effective stress law for rock masses and its application in impoundment analysis based on deformation reinforcement theory. *J. Cent. South Univ.* 25, 218–229. doi:10.1007/s11771-018-3731-x
- Hao, X. J., Zhang, Q., Sun, Z. W., Wang, S. H., Yang, K., Ren, B., et al. (2021). Effects of the major principal stress direction respect to the long axis of a tunnel on the tunnel stability: physical model tests and numerical simulation. *Tunn. Undergr. Space Technol.* 114, 103993. doi:10.1016/j.tust.2021.103993
- Hu, X. D., Fang, T., Chen, J., Ren, H., and Guo, W. (2018). A large-scale physical model test on frozen status in freeze-sealing pipe roof method for tunnel construction. *Tunn. Undergr. Space Technol.* 72, 55–63. doi:10.1016/j.tust.2017.10.004
- Liu, L. L., Li, Z., Liu, X. Y., and Li, Y. Y. (2019). Frost front research of a cold-region tunnel considering ventilation based on a physical model test. *Tunn. Undergr. Space Technol.* 77, 261–279. doi:10.1016/j.tust.2018.04.011
- Ma, C. D., Xu, J. Q., Tan, G. S., Xie, W. B., and Lv, Z. H. (2021). Research on supporting method for high stressed soft rock roadway in gentle dipping strata of red shale. *Minerals* 11, 423. doi:10.3390/min11040423
- Niu, H. S., Weng, X. L., Tian, C., and Wang, D. (2021). Model test and back analysis of shield tunnel load distribution in soft clay. *Adv. Mater. Sci. Eng.* 2021, 1–15. doi:10.1155/2021/9992348
- Sengani, F. (2020). Characterisation of rock fracturing ahead of the preconditioned mining faces in a hard rock mining. *Arab. J. Geosci.* 13, 670. doi:10.1007/s12517-020-05720-0
- Sun, X. M., Chen, F., Miao, C. Y., Song, P., Li, G., Zhao, C. W., et al. (2018). Physical modeling of deformation failure mechanism of surrounding rocks for the deep-buried tunnel in soft rock strata during the excavation. *Tunn. Undergr. Space Technol.* 74, 247–261. doi:10.1016/j.tust.2018.01.022
- Xiang, Y. Z., Liu, H. L., Zhang, W. G., Chu, J., Zhou, D., and Xiao, Y. (2018). Application of transparent soil model test and DEM simulation in study of tunnel failure mechanism. *Tunn. Undergr. Space Technol.* 74, 178–184. doi:10.1016/j.tust.2018.01.020
- Yang, F. J., Zhang, C. Q., Zhou, H., Liu, N., Zhang, Y., Azhar, M. U., et al. (2017). The long-term safety of a deeply buried soft rock tunnel lining under inside-to-outside seepage conditions. *Tunn. Undergr. Space Technol.* 67, 132–146. doi:10.1016/j.tust.2017.05.004
- Yu, Y., Ling, X. Z., Tang, L., Han, X., Geng, L., and Wei, S. W. (2021). Preliminary identification of the failure mode of shallow tunnels in soil subjected to frost heave: Model test and numerical simulation. *Transp. Geotech.* 29, 100555. doi:10.1016/j.trgeo.2021.100555
- Zhang, J. H., Zhang, L. Y., Wang, W. J., Zhang, D. B., and Zhang, B. (2020). Probabilistic analysis of three-dimensional tunnel face stability in soft rock masses using Hoek-Brown failure criterion. *Int. J. Numer. Anal. Methods Geomech.* 44, 1601–1616. doi:10.1002/nag.3085
- Zhang, Z. X., Wang, S. F., Huang, X., and Rostami, J. (2019). Application of block theory for evaluating face stability under disc cutters loading of TBM, case study of a water-conveyance tunnel project. *Tunn. Undergr. Space Technol.* 90, 249–263. doi:10.1016/j.tust.2019.05.002
- Zhou, X. H., Cheng, X. S., Qi, L., Wang, P., Chai, S. F., and Liu, Y. J. (2021). Shaking table model test of loess tunnel structure under rainfall. *KSCE J. Civ. Eng.* 25, 2225–2238. doi:10.1007/s12205-021-1064-z

Publisher's note

All claims expressed in this article are solely those of the authors and do not necessarily represent those of their affiliated organizations, or those of the publisher, the editors, and the reviewers. Any product that may be evaluated in this article, or claim that may be made by its manufacturer, is not guaranteed or endorsed by the publisher.



Study on Stability Control of Gob-Side Entry Retaining Structure Without Filling Wall in Hard Roof

Long Jing-kui^{1,2*}, Qi Chao-xin³, Cao Zuo-yong³, Lan Hong⁴ and Yu Wen-kai²

¹School of Architecture and Design, China University of Mining and Technology, Xuzhou, China, ²School of Mechanics and Civil Engineering, China University of Mining and Technology, Xuzhou, China, ³Guizhou Bureau of National Mine Safety Administration, Guiyang, China, ⁴Guizhou Lindong Coal Industry Co, Ltd., Guiyang, China

In view of the deformation and instability law of hard roof without side filling retaining roadway, based on the systematic construction and analysis of the force and bearing model of roadway retaining structure, this article proposes the control mechanical model and calculation method of roadway retaining, which takes the anchor roof beam and the key block above to form the cantilever beam together, with the anchor solid coal side as the foundation support. The research and practice show that under the condition of hard roof, the mechanical connection between the roof of gob-side entry retaining and the roof of mining face can be effectively cut off so as to improve the structural configuration and mechanical properties of the lateral roof of gob-side entry retaining and the key blocks above, and reduce the damage of upper strata subsidence and goaf roof collapse to the roof of roadway. Then, through strengthening by anchor to significantly enhance solid coal side, bearing capacity of anchor roof beam, so they can share the upper strata caused by the load and deflection of mining influence, in addition, the roof bolting, reinforcement of waste rock bolting supporting role can better improve the structure for stability, adaptability and engineering applicability, this method is successfully applied in engineering practice. It is worthy of further research and application.

OPEN ACCESS

Edited by:

Shuren Wang,
Henan Polytechnic University, China

Reviewed by:

Zhengzheng Cao,
Henan Polytechnic University, China
Xiangjun Chen,
Henan Polytechnic University, China

*Correspondence:

Long Jing-kui
jklong@cumt.edu.cn

Specialty section:

This article was submitted to
Geohazards and Georisks,
a section of the journal
Frontiers in Earth Science

Received: 16 June 2022

Accepted: 21 June 2022

Published: 23 August 2022

Citation:

Jing-kui L, Chao-xin Q, Zuo-yong C,
Hong L and Wen-kai Y (2022) Study on
Stability Control of Gob-Side Entry
Retaining Structure Without Filling Wall
in Hard Roof.
Front. Earth Sci. 10:970912.
doi: 10.3389/feart.2022.970912

Keywords: hard roof, gob-side entry retaining, no gateway sidewall back, stability control, mechanical model

1 INTRODUCTION

For a long time, coal pillar mining has been adopted in most mining areas of China's coal mines, resulting in the loss of produced coal accounting for about 40% of the total coal loss of the whole mine (Chen and Lu, 1994). The pillarless mining along a gob retaining roadway can improve the mining area's recovery rate by 10–20% and reduce the roadway driving rate by 25–30% (He et al., 2016). It can also realize y-type ventilation, control gas, relieve mining imbalance, and eliminate isolated working face. With significant economic benefits and technological advantages, it can better meet the goal of safe, economic, efficient, green, and sustainable mining. It has important strategic significance (Sun and Zhao, 1993; Qian et al., 2003).

According to roadway side support materials and action modes, it can be divided into filling support and non-filling support (Cao et al., 2016). The calculation models around the resistance of roadway side support mainly include the mechanical model of separated rock block, the mechanical model of roof tilt, the mechanical model of rectangular superimposed plate bending moment failure, the mechanical model of limit equilibrium beam of coal body, and the mechanical model of elastic thin strip (Chen, 2012). The research shows that the application and development of roadway side

filling support are affected by the complexity of the process, impedance lag, and high cost, while the non-filling support can effectively avoid these problems and realize the control of roadway roof and overlying rock strata more quickly (Hua et al., 2005). In fact, most coal mines, especially small- and medium-sized coal mines, are more likely to have the way of sideway filling without lane retention when conditions permit.

He et al. (2017a, 2017b), on the basis of the “roof cutting short-boom beam theory,” have put forward new technologies such as roof cutting pressure relief and 110 construction methods in recent years, which further promote the development of roadwayless side filling and retaining technology. Pre-split cutting top is to cut off the stress transfer path between goaf and roadway roof through pre-split action, shorten the length of the cantilever beam of the roof, and help the goaf roof collapse fully. The main technologies include slit pressure relief, drilling pressure relief, blasting pressure relief, and water injection softening. Kang et al. (2014), Sun et al. (2014), Zhang (2010) and other scholars have made many valuable research achievements in this regard.

As for the role of roadway anchoring and roadway side support, one view holds that roadway anchoring and roadway side support have no fundamental influence on the broken rule of the basic roof and cannot change the broken position and shape of the roof. The other holds that different roadway anchoring and roadway side support have different influences on the position, shape, and law of the basic roof breakage, which mainly depend on the strength and stiffness of roadway anchoring and roadway side support. In fact, strengthening roadway anchoring and roadway side support can improve the broken position and structural form of the basic roof, enhance the stability and adaptability of roadway retention structure, and significantly improve the effect of roadway retention.

Based on the previous research by others, the author takes the control of retaining roadway in hard roof as their search object. By systematically constructing the force and bearing model of goaf retaining roadway with no roadway side filling (referred to as non-filling retaining roadway, the same below), the feasibility, rationality and calculation method of bearing capacity of anchoring solid coal slope, anchoring roof beam and key blocks above on the retaining roadway structure are studied. And through effective roof cutting to improve the overburden structure configuration and stress field distribution, significantly improve the stability, adaptability and engineering applicability of roadway retaining structure, promote coal mine safety, economic, efficient and sustainable production

2 THE CONTROL PRINCIPLE OF HARD ROOF WITHOUT FILLING IS “ANCHORING - CUTTING - SUPPORTING - BLOCKING - CLOSING”

A hard basic roof refers to a layer of hard rock with good mechanical properties, good structural integrity, and bearing capacity above the direct roof of the coal seam. The direct

roof of the coal seam is generally a composite layered structure, with different strengths and stiffnesses in each layer. The bond between adjacent layers is weak, and the weak surface is developed, showing a heterogeneous layered occurrence form. In order to improve the bearing capacity of the roadway's direct roof, it is necessary to adopt high-strength materials to coordinate and strengthen the anchoring during tunneling, so that it has high strength and high stiffness that meet the requirements of roadway retaining bearing performance. After stoping the first working face, the cantilever beam structure will not be formed together with the goaf roof due to the strength of the anchor roof beam and the key block above. Compared with ordinary roadways, the load-bearing structure of roadway retaining is changed from roof, solid coal side, gangue side and floor “tetrahedron” to roof, solid coal side and floor “trihedron.” Under the comprehensive influence of key block overturning and subsidence, upper weak rock layer, and mining, there will be separation, deformation, and failure between the anchor roof beam and the basic roof, so it is necessary to optimize the position and state of the roadway side structure and reconstruct the bearing structure. Therefore, on the basis of previous research and practice, the control principle of “anchor-cut-support-stop-close” was proposed.

For the reserved roadway, it is necessary to consider its anchorage strength and stiffness to meet the mechanical property requirements of repeated mining failure. Therefore, the roadway cannot adopt the control mode of ordinary roadway, and it needs to adopt “bolt + anchor cable + anchor net + steel belt” to strengthen the anchoring of roadway roof and solid coal side. It means that the bolts are interlocked horizontally with W steel bands, and the bolts are interlocked longitudinally with T steel bands to form “anchor cable beam.” In addition, the layout density of anchor cable beam is appropriately strengthened to effectively improve the anchoring strength and stiffness of roof and solid coal side, so as to improve their bearing capacity and anti-deformation capacity, which is the “anchor” principle. In contrast, if the mining coal gang is going to be excavated when the working face is mined, the ordinary anchoring method can be adopted, and it only needs to meet the mining impact requirements.

Because it is a hard roof and the anchoring roof beam has good bearing capacity, the basic roof will form a single cantilever beam with large span above the lateral roof and goaf, which is very unfavorable to the stability of the roadway retaining structure. Therefore, a certain distance ahead of the working face is needed to cut off the mechanical connection between the roof of the roadway and the roof of the mining face in advance. When the goaf roof collapses, the stress transfer and damage to the roof of the roadway can be significantly reduced, which is the “cutting” principle. Considering the effect and influence of periodic pressure, the top-cutting distance should be greater than the fracture length of the basic roof along the advancing direction of the working face, generally 50m ahead of the working face.

In order to enhance the stability and adaptability of the lateral roof of roadway retention and prevent large overturning and subsidence of the direct roof and the basic roof above the roadway retention, “single column + steel beam” or hydraulic support should be adopted to support the roadway side to form the roof

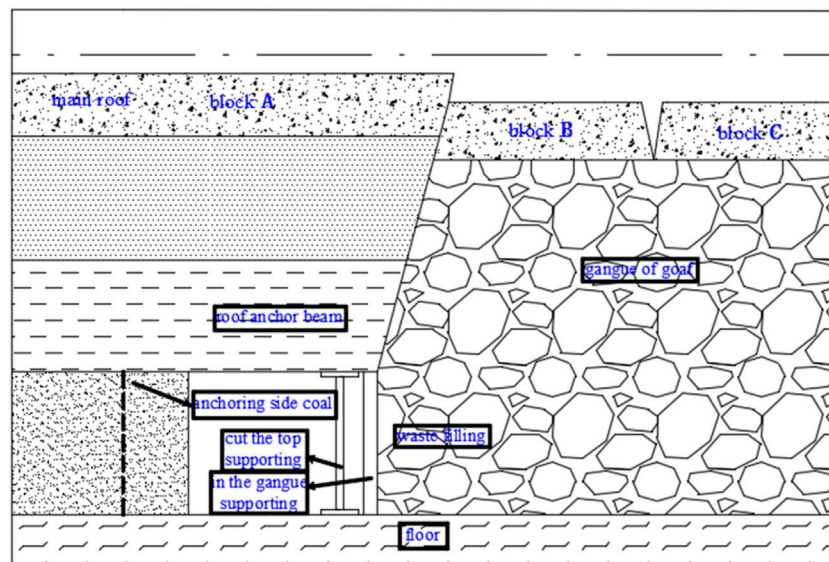


FIGURE 1 | Control diagram of “anchor - cut - support - block - close” of unfilled gob-side entry retaining structure.

cutting support structure. At the same time, through the joint action of roof cutting and caved gangue bursting, caved gangue usually fills the goaf and forms gangue support structure, thus forming a certain support force for the basic roof above the goaf and the lateral roof of roadway retaining. The principle of “support” is to make good use of the self-support function of gangues in goaf and the support function of roadway side cutting roof support structure.

In addition, in order to prevent the gangue in goaf from falling into the roadway, it is necessary to build a gangue retaining and supporting structure with steel beam and steel mesh before the caving, so that the gangue in goaf can form a new gangue side on the outside of the structure, which is the “retaining” principle. In addition, in order to prevent the gas or harmful gas in the goaf from flowing into the roadway and the air in the roadway from flowing into the goaf, it is advisable to use “wire mesh + sealing cloth + steel mesh” to construct a closed structure between the gangue retaining structure and the caved gangue in the goaf. If necessary, grouting or higher sealing treatment should be carried out on the gangue side, which is the “closed” principle.

As mentioned previously, by cutting the mechanical connection between the roadway and the roof of the stoping working face, the configuration and stress transfer path of the roadway retaining structure are optimized, and the roadway retaining structure is placed in the low-stress zone so as to weaken the damaging effect of upper rock strata activities on key blocks and the roadway retaining structure. On this basis, through the implementation of tunnel anchorage structure, cut the roof supporting structure and supporting structure of coal and gangue and gangue supporting structure of retaining the effective control to form has a good stability and adaptability for bearing structure, so that we can better meet the requirements of coal mining, it is the control principle of “anchor-cut - support - solid - block - close” for hard roof without filling roadway retention, as shown in **Figure 1**.

Compared with the side filling retaining roadway, the non-filling retaining roadway has high efficiency, simple construction process and technology, and most of its supporting materials can also be recycled, which significantly saves production cost. In addition, the bearing performance of the roadway roof and solid coal side can be adjusted by changing the control mode and parameters, including cutting roof support which has strong controllability, and it is easier to realize the cooperative bearing between them. For the hard layered roof, it is undoubtedly effective, efficient, and applicable to use this control principle and technology to realize lane retention, and it also has an important reference value for other conditions of roof lane retention. For example, under the condition of a thick layer soft rock roof of a coal mine in Guizhou, the authors successfully retained the roadway by effectively cutting the roof, strengthening the anchoring in the roadway, and cutting the roof support.

3 MIGRATION LAW OF HARD ROOF WITHOUT FILLING RETAINING ROADWAY

According to the cantilever beam hypothesis, masonry beam mechanical model, transfer rock beam mechanical model, key layer theory, large-small structure stability principle, and other theories (Allard and Swelsky, 1986; Zhu, 1987; Song, 1988; Qian, 1994; Ortlepp and Stacey, 1998; Hou and Li, 2001; Qian et al., 2010; Chen, 2012; Yuan et al., 2013), the key layer that has the greatest influence on the entry retention is mainly the basic roof, and the fracture position of the basic roof determines the structural characteristics of the lateral roof strata of the stope. It is necessary to study the influence of fracture, movement, and stability of the basic roof on the stability of roadway retaining structure. With the advancement of the working face, the overlying strata of the goaf collapsed, and the “O-X” fracture was formed by the initial pressure on the basic roof, while the masonry

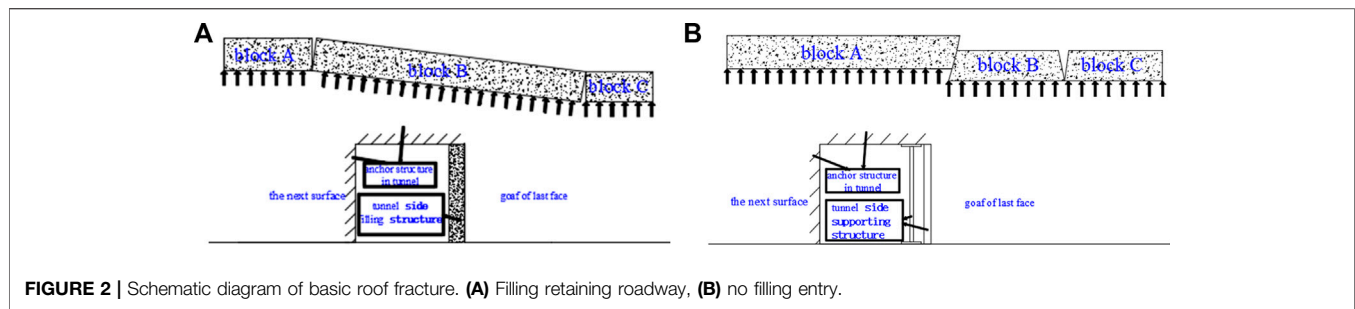


FIGURE 2 | Schematic diagram of basic roof fracture. (A) Filling retaining roadway, (B) no filling entry.

beam structure was formed along the direction of the working face by periodic pressure, and the curved triangle block was formed at the end of the working face. As for the filling and retaining roadway beside the roadway, due to the hysteresis of the loading at the side of the roadway, the arc-shaped triangular block will fracture, rotate, and sink under the overburdening pressure. Usually, the first fracture occurs above the side of the solid coal body, and finally three blocks A, B, and C are formed, as shown in **Figure 2A**.

Compared with ordinary roof roadway, the periodical pressure of hard roof stope is more intense, which is unfavorable to control the stability of roadway retention. However, according to the control principle of the hard roof, as the roof of roadway and the roof of working face have been effectively cut off, two blocks A and B are formed on the basic roof before mining. Under the advanced action of periodic pressure, the cutting condition between block A and B will be further intensified, and certain slippage and spacing will occur along the cutting surface. When the working face is pushed, the direct roof above the mined coal seam collapses first, which provides space for the settlement of the upper basic roof. Subsequently, block B will have obvious settlement, and the scattered between block A and block B will further increase, which is mainly related to the degree of gangue filling in the goaf and the degree of upper rock subsidence. Due to differences in structural performance and settlement sequence of the goaf roof, block B will also fracture during settlement, forming new blocks B and C, which are finally compacted on the gangue structure of goaf, as shown in **Figure 2B**. Therefore, to master the basic law of hard roof stope mine pressure, a reasonable control mode of roadway retention is adopted, which is the key to the safety of stope production and the stability of roadway retention structure.

4 STABILITY CONTROL MECHANISM OF ROADWAY RETAINING WITHOUT FILLING IN HARD ROOF

4.1 Stress and Load-Bearing Model of Roadway Retaining Structure

For the hard roof, the mechanical properties, fracture position, and geometric parameters of block A on the roof of entry retention are the key factors affecting the stability of entry retention structure. Under the action of its upper strata and its own gravity, block A will transfer the load to the anchoring roof beam in the way of bending subsidence, and then the anchoring roof beam will transfer to the roadway retaining structure such as

a solid coal wall, cutting roof support in a similar way. In order to simplify the construction of the mechanical model, it is assumed that 1) roadway roof and working face roof, especially block A and block B, can be effectively cut off; 2) the load generated by the rock strata at the basic top is mainly transmitted to the gangue of the entry retaining structure and the goaf through block A, B, and C, respectively; 3) through the synergistic anchoring effect of anchor rods, anchor cables, and composite components, the roadway roof is directly anchored into an integral rock beam, which forms a cantilever beam structure together with block A and plays a major role in the stability of roadway retention; and 4) the solid coal seam is continuous, homogeneous, and isotropic.

According to the control principle of the hard roof without filling and roof migration law, after the first working face is pushed over, the roadway retention structure mainly bears the load imposed by the self-gravity G_1 of soft rock in the upper part of block A, the bending load G_2 of block A, and the bending load G_3 of the anchoring roof beam. The supporting force F_1 of the solid coal side, the bearing capacity F_2 of block A, the bearing capacity F_3 of the anchoring roof beam, the supporting force F_4 of roof cutting support, the supporting force F_5 of gangue retaining support, the supporting force F_6 of goaf gangue supporting block B, the lateral supporting force F_7 of roadway roof, and the lateral supporting force F_8 of block B supporting block A are jointly undertaken. Thus, taking the boundary line of the loose area of solid coal side and the intersection point O under roadway roof as the origin, the force and bearing model of roadway retaining structure is established, as shown in **Figure 3A**. The basic mechanical equation of roadway retaining structure is as follows:

$$F_1 + F_2 + F_3 + F_4 + F_5 + F_6 + F_7 + F_8 = G_1 + G_2 + G_3 \quad (1)$$

Formula (1) considers the balance relationship between the force and load of the roadway retaining structure. When this relationship is satisfied, the roadway retaining structure is in a stable state.

4.2 Stability Control Mechanism of Roadway Retaining Without Filling in Hard Roof

According to **Formula (1)**, as long as the equilibrium state is not broken, the lane retention structure can remain stable. For actual engineering conditions, the basic structure remains the same, the change of movement is produced by the mining effect, and the structure bearing capacity because the control mode, control parameters and controlled time different and change, That is,

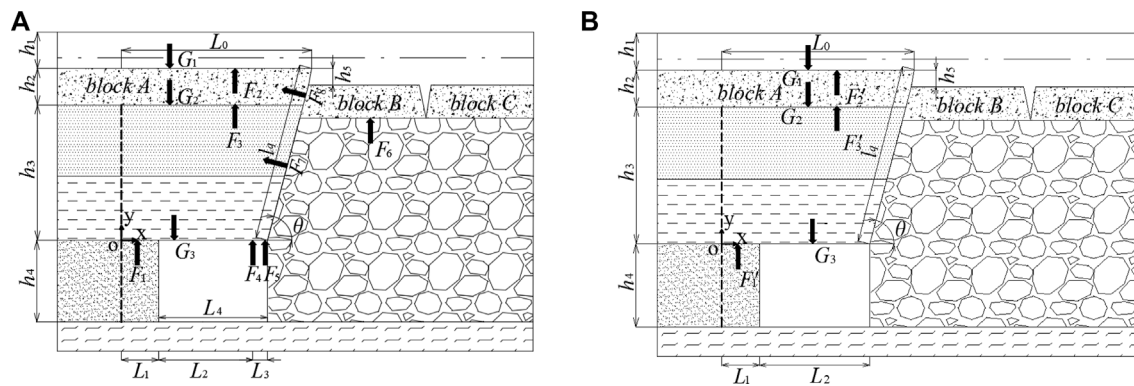


FIGURE 3 | Structural mechanics model diagram of gob-side entry retaining without filling. **(A)** Stress and load bearing model diagram, **(B)** stability control model diagram.

the structural bearing capacity is variable, when a lack of structure bearing capacity and advance damage can cause the structure for the overall destruction and instability. Therefore, it is necessary to optimize the mechanical model and calculation method of load-bearing structures from the perspective of enhancing the stability of retaining structure.

In practical engineering, this article considers that gangue may not be able to fill the goaf in time, which may result in insufficient support force F6 of gangue on block B, lateral support force F7 on roadway roof, and lateral support force F8 of block B on block A, and limited support force F4 of roof cutting support and F5 of gangue retaining support. Therefore, F4 ~ F8 on the left of **Formula (1)** is not included in the calculation of roadway retaining structure bearing capacity. In this case, the bearing capacity of anchoring solid coal wall and roof anchoring beam needs to be realized by strengthening anchoring, while the bearing capacity of block A can be realized by effectively cutting the roof and forming a short arm beam, as shown in **Figure 3B**:

$$F_1' + F_2' + F_3' = G_1 + G_2 + G_3 \quad (2)$$

where F'_1 is the load-bearing performance of the solid coal seam after strengthened anchoring, kN; F'_2 is the load-bearing performance of the roof after strengthened anchoring, kN; and F'_3 is the bearing performance after block A is cut off to form a short-boom beam, kN.

Formula (2) shows that under the condition of hard roof, if only the anchoring coal slope is considered, the anchoring roof beam and block A withstand, respectively, from deflection of strata above the load, and the load is realized by strengthening the anchoring or structural optimization; then, combined with the “reinforcing bearing” effect of F4 ~ F8 forces, the roadway retaining structure will be more stable because top-cutting support, retaining gangue support, and gangue support exist objectively. Notably, it is of great significance to carry out such treatment, which is the stability control mechanism of retaining the roadway without filling in the hard roof. The next step is to calculate the bearing capacity and related parameters of the anchoring solid coal wall, anchoring roof

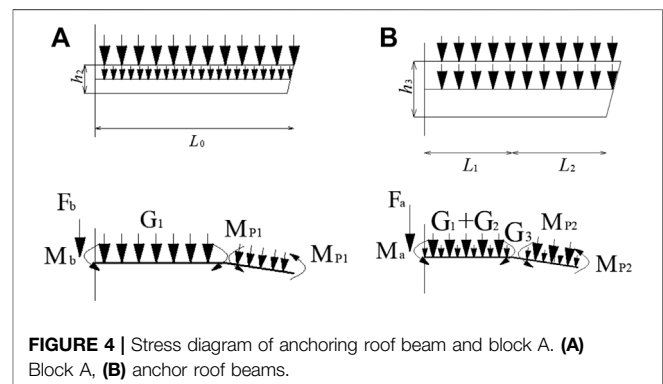


FIGURE 4 | Stress diagram of anchoring roof beam and block A. **(A)** Block A, **(B)** anchor roof beams.

beam, and block A, which meet the requirements of **Formula (2)**.

4.3 Mechanical Calculation of Stability Control Model of Roadway Retaining Structure

As shown in **Figure 3B**, according to the stability control mechanism of unfilled roadway retention in hard roof, and on the basis of satisfying the relationship between force and bearing capacity in **Formula (2)**, load-bearing performance, relevant mechanical parameters and control requirements should be provided by anchoring solid coal slope, anchoring roof beam and upper block A can be designed and constructed to provide load-bearing structure with good stability. Thus, the theoretical research is transformed into engineering practice, and verified and optimized in practice. Thus, the stress diagram of anchoring roof beam and block A is established, as shown in **Figure 4**.

4.3.1 Block A Geometric Parameters

- 1) Fracture length of the basic roof along the advancing direction of the working face. It can be obtained through on-site mine pressure monitoring or theoretical calculation (Qian et al., 2010):

$$L = h_2 \sqrt{\frac{R_t}{3q}} \quad (3)$$

where L is the fracture length of the basic roof along the advancing direction of the working face, m; h_2 is the basic top thickness, m; R_t is the tensile strength of block A, MPa; and q is the unit length self-gravity of the soft rock above the basic roof, kN/m.

- 2) The basic roof along the lateral fracture span. According to the yield line analysis of the plate (Jiang, 1993), it is considered that the lateral fracture span of block A is related to the length of the working face and the periodic compression step of the basic roof can be written as:

$$L' = \frac{2l_1}{17} \left[\sqrt{\left(10 \frac{L}{L_m}\right)^2 + 102} - 10 \frac{L}{L_m} \right] \quad (4)$$

where L' is the lateral fracture span of the basic roof, m, and L_m is the length of the working face, m; According to the calculation and analysis, when $L_m/L > 6$, the lateral fracture span L' is basically equal to the periodic compression step L , that is, $L' = L$.

- 3) Width of the loose zone of the solid coal wall. Under the influence of mining, the solid coal will form a certain loose area. The basic roof rock is regarded as a semi-infinite beam, and the elastic foundation beam model is used to obtain the width of the loose zone of solid coal wall (Qian and Zhao, 1987; Qian and He, 1989):

$$L_1 = \frac{\tan^{-1} \left[\frac{\beta(2\alpha M_0 s + r Q_0)}{r^2 M_0 + \alpha r Q_0} \right]}{\beta} \quad (5)$$

where $\beta = (\frac{\sqrt{K_c}}{2\sqrt{EI}} + \frac{N}{4EI})^{\frac{1}{2}}$, $\alpha = (\frac{\sqrt{K_c}}{2\sqrt{EI}} - \frac{N}{4EI})^{\frac{1}{2}}$, $s = \frac{N}{EI}$, $r = \frac{K_c}{EI}$; L_1 is the width of the loose zone of the solid coal seam, m; and K_c is the coefficient of Winkler foundation, which is related to the thickness and mechanical properties of the upper and lower strata, MPa/m. EI is the flexural stiffness of the basic roof beam; M_0 , Q_0 , N are the sectional internal forces corresponding to the possible fracture position of the solid coal side of the working face, kN.

4.3.2 Pre-Split Cutting Top Parameters

Under the condition of hard roof, the lateral fracture span L' along the basic roof is generally large, and under the action of upper rock, there will be great pressure and damage to the entranceway structure. Therefore, before the first face mining, the top cutting needs to be completed at a given angle and cut to the upper bound of block A. Roof cutting angle and depth (length) are related to the thickness of roof strata, mechanical properties, and natural caving angle of goaf, which can be determined according to the calculation of relevant parameters or actual engineering conditions. According to the roadway width, roof cutting angle, and other parameters, the span of block A after roof cutting is:

$$L_0 = L_1 + L_2 + \frac{h_2 + h_3}{\tan \theta} \quad (6)$$

where L_0 is the span of block A after cutting the top, m; L_2 is the width of roadway, m; h_3 is the thickness of the direct roof of the roadway, m; and θ is the cutting angle, °.

In order to make block A, the anchoring roof beam can form a short cantilever beam; the cutting angle is generally 5–10°, but it needs to be determined according to coal seam dip angle and roof rock structure to ensure the formation of a short-boom beam structure. According to Eqs 4 and 6, when $L_0 \approx L'$, there is no need to cut the top. According to the cutting angle, the cutting depth (length) is:

$$l_p = \frac{h_2 + h_3}{\sin \theta} \quad (7)$$

where l_p is the cutting top depth, m.

4.3.3 Self-Gravity of Upper Strata of Block A

Under the influence of mining, the upper weak rock layer will separate and sink, and act on block A in the way of self-gravity:

$$G_1 = L_0 h_1 \gamma_1 \quad (8)$$

where G_1 is the unit width self-gravity of the upper weak rock layer, kN; h_1 is the thickness of soft strata, m; and γ_1 is the bulk density of soft rock, kN/m³.

4.3.4 Bearing Capacity of Block A

As shown in Figure 4A, block A is subjected to force and load in the form of fixed beam, that is, the left boundary is constrained by the fixed end. When conducting mechanical analysis and calculation, lifting the fixed constraint is equivalent to bending moments F_b and M_b . According to the balance equation of bending moment and force, the following equation can be obtained:

$$F_b = -K_{G1} \frac{G_1}{L_0} \left(L_0 - \frac{h_2}{2 \tan \theta} \right) - G_2 \quad (9)$$

$$M_b = - \left(K_{G1} \frac{G_1}{L_0} + \frac{G_2}{L_0 - \frac{h_2}{2 \tan \theta}} \right) x \quad (10)$$

$$M_{P1} = -K_{G1} \frac{G_1}{L_0} \left(L_0 - \frac{h_2}{2 \tan \theta} \right) + K_{G1} \frac{G_1}{L_0} x, x \in \left(0, L_0 - \frac{h_2}{2 \tan \theta} \right) \quad (11)$$

$$F_{P2} = F_b + K_{G1} \frac{G_1}{L_0} x + \frac{G_2}{L_0 - \frac{h_2}{2 \tan \theta}} x \quad (12)$$

where M_{P1} is the bending moment of block A at the cutting position, kNm; F_{P2} is the force at the fracture position, kN; G_2 is the bending load of block A with unit width, kN; and K_{G1} is the load transfer coefficient of the overlying strata of block A, which can be:

$$G_2 = h_2 \left(L_0 - \frac{h_2}{2 \tan \theta} \right) \gamma_2 \quad (13)$$

where γ_2 is the bulk density of block A, kN/m³.

$$K_{G1} = \frac{L_0}{2h_2\gamma_4 \tan \varphi} \quad (14)$$

where φ is the friction angle within the rock layer and γ_4 is the lateral stress coefficient.

In addition, according to relevant formulas of material mechanics,

$$\sigma = \frac{6M_{p2}\sin\theta}{h_2^2} \leq [\sigma] \quad (15)$$

$$\tau_{max} = \frac{3F_{p2}\sin\theta}{h_2} \leq [\tau] \quad (16)$$

where σ is the tensile stress at the cutting position of block A, kN; $[\sigma]$ is the flexural strength of block A, kN/mm²; τ_{max} is the shear stress at the cutting position, kN; and $[\tau]$ is the shear strength of block A, kN/mm².

When Eqs 15 and 16 are satisfied, block A will not suffer from buckling failure. It can be seen that the mechanical properties of block A for the stability of entry retention can be obtained by changing the angle of cutting top and geometric parameters of entry retention structure, so that block A can remain stable.

4.3.5 Bearing Performance of Anchoring Roof Beams

As shown in Figure 4B, according to the mechanical characteristics of the hard roof, the anchoring roof beam is simplified as the cantilever beam for mechanical calculation. The left boundary of the beam is assumed to be a fixed end constraint. When mechanical analysis and calculation are carried out, lifting the fixed constraint is equivalent to bending moment F_a and M_a . According to the balance equation of bending moment and force, the following equation can be obtained:

$$F_a = - \left[K_{G2} \left(\frac{G_1}{L_0} + \frac{G_2}{L_0 - \frac{h_2}{2\tan\theta}} \right) + \frac{G_3}{L_0 - \frac{h_2 + \frac{1}{2}h_3}{\tan\theta}} \right] \left(L_1 + L_2 + \frac{h_3}{2\tan\theta} \right) \quad (17)$$

$$M_a = \frac{\left[K_{G2} \left(\frac{G_1}{L_0} + \frac{G_2}{L_0 - \frac{h_2}{2\tan\theta}} \right) + \frac{G_3}{L_0 - \frac{h_2 + \frac{1}{2}h_3}{\tan\theta}} \right] \left(L_1 + L_2 + \frac{h_3}{2\tan\theta} \right)^2}{2} \quad (18)$$

$$M_{p1} = \frac{\left[K_{G2} \left(\frac{G_1}{L_0} + \frac{G_2}{L_0 - \frac{h_2}{2\tan\theta}} \right) + \frac{G_3}{L_0 - \frac{h_2 + \frac{1}{2}h_3}{\tan\theta}} \right] \left(L_1 + L_2 + \frac{h_3}{2\tan\theta} \right)}{2} - \frac{\left[K_{G2} \left(\frac{G_1}{L_0} + \frac{G_2}{L_0 - \frac{h_2}{2\tan\theta}} \right) + \frac{G_3}{L_0 - \frac{h_2 + \frac{1}{2}h_3}{\tan\theta}} \right] x^2}{2}, x \in \left(a, L_1 + L_2 + \frac{h_3}{2\tan\theta} \right) \quad (19)$$

$$F_{p1} = \left[K_{G2} \left(\frac{G_1}{L_0} + \frac{G_2}{L_0 - \frac{h_2}{2\tan\theta}} \right) + \frac{G_3}{L_0 - \frac{h_2 + \frac{1}{2}h_3}{\tan\theta}} \right] x \quad (20)$$

where M_{p1} is the bending moment of the anchoring roof beam at the cutting position, kNm; F_{p1} is the force at the cutting position, kN; G_3 is the bending load of anchoring roof beam per unit width,

kN/m; and K_{G2} is the load transfer coefficient of the overlying strata of the anchoring roof beam:

$$G_3 = \left(L_0 - \frac{h_2 + \frac{1}{2}h_3}{\tan\theta} \right) \sum h_3\gamma_3 \quad (21)$$

where γ_3 is the bulk density of anchoring roof beam, kN/m³.

$$K_{G2} = \frac{L_0 - \frac{h_2}{\tan\theta}}{2h_3\gamma_4 \tan\varphi} \quad (22)$$

In addition, according to the formula of rectangular section stress calculation of material mechanics, the stress of beam per unit width is calculated as follows:

$$\sigma' = \frac{6M_{p1}\sin\theta}{h_3^2} \leq [\sigma'] \quad (23)$$

$$\tau_{max}' = \frac{3F_{p1}\sin\theta}{h_3} \leq [\tau']_{max} \quad (24)$$

where σ' is the tensile stress at the cutting position of the anchoring roof beam, kN; $[\sigma']$ is the bending strength of the anchoring roof beam, kN/mm²; τ_{max}' is the shear stress at the cutting position, kN; and $[\tau']_{max}$ is the shear strength of anchoring roof beam, kN/mm².

When Eqs 23 and 24 are satisfied, the anchoring roof beam will not bend and sink. It can be seen that the mechanical properties of the anchoring roof beam can be obtained by changing the cutting angle, geometric parameters of roadway retaining structure, and anchoring parameters of roadway roof, so that the anchoring roof beam can remain stable.

4.3.6 Anchor Solid Coal Side Support Force

During the process of roadway excavation to retaining, the stress of solid coal wall will be redistributed and abutment pressure will be formed at its wall. Under the premise of no control of the solid coal seam, the solid coal seam is subjected to vertical load, and two regions, namely, limit equilibrium zone and elastic zone, which will appear successively, as shown in Figure 5A.

Due to the irregularity of the stress characteristics of coal seam, the abutment pressure above the solid coal seam is simplified as a linear distribution form for convenient discussion (Ke, 2020). Taking any unit body within a certain range of solid coal seam as the research object, the abutment pressure above the solid coal seam can be regarded as two load distribution forms of uniform distribution and linear distribution, and its stress-simplified model can be obtained, as shown in Figure 5B. According to the analysis principle of stress components of a semi-infinite body under normal load, the stress components σ_x , σ_y , τ_{xy} generated by the unit body under partial load are calculated, respectively, and then the stress components at any point in the solid coal seam can be obtained by superposition of the stress components. Let the peak stress be $P_1 = k(G_1 + G_2 + G_3)$, $P_0 = G_1 + G_2 + G_3$. According to the elastic theory, the stress component at any point in the coal wall rock mass under uniformly distributed load is:

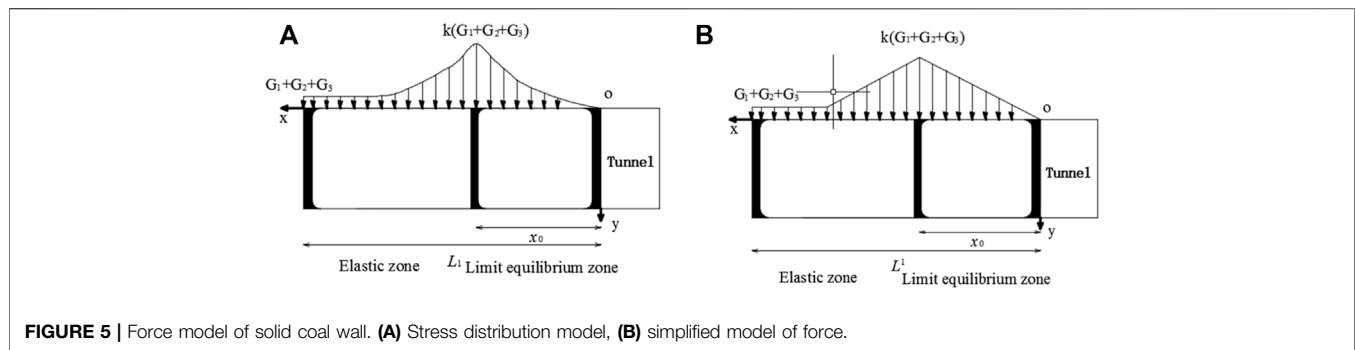


FIGURE 5 | Force model of solid coal wall. **(A)** Stress distribution model, **(B)** simplified model of force.

1) Linear load in limit equilibrium zone:

$$\sigma_{x1} = \frac{P_1}{\pi} \left[\frac{x}{x_0} \left(\arctan \frac{x}{y} - \arctan \frac{x-x_0}{y} \right) - \frac{y}{x_0} \ln \frac{x^2 + y^2}{(x-x_0)^2 + y^2} + \frac{2(x-x_0)y^2}{(x-x_0)^2 + y^2} \right] \quad (25)$$

$$\sigma_{y1} = \frac{P_1}{\pi} \left[\frac{x}{x_0} \left(\arctan \frac{x}{y} - \arctan \frac{x-x_0}{y} \right) - \frac{2(x-x_0)y}{(x-x_0)^2 + y^2} \right] \quad (26)$$

$$\tau_{xy1} = \frac{P_1}{\pi} \left[\frac{y^2 - (x-x_0)^2}{(x-x_0)^2 + y^2} - \frac{y}{x_0} \left(\arctan \frac{x}{y} - \arctan \frac{x-x_0}{y} \right) \right] \quad (27)$$

2) Uniform load in elastic zone:

$$\sigma_{x2} = \frac{P_1 - P_0}{\pi} \left[\arctan \frac{L_1 - x}{y} - \arctan \frac{x_0 - x}{y} - \frac{(L_1 - x)y}{(L_1 - x)^2 + y^2} + \frac{(x_0 - x)y}{(x_0 - x)^2 + y^2} \right] \quad (28)$$

$$\sigma_{y2} = \frac{P_1 - P_0}{\pi} \left[\arctan \frac{L_1 - x}{y} - \arctan \frac{x_0 - x}{y} + \frac{(L_1 - x)y}{(L_1 - x)^2 + y^2} - \frac{(x_0 - x)y}{(x_0 - x)^2 + y^2} \right] \quad (29)$$

$$\tau_{xy2} = \frac{P_1 - P_0}{\pi} \left[\frac{(L_1 - x)y}{(L_1 - x)^2 + y^2} - \frac{(x_0 - x)y}{(x_0 - x)^2 + y^2} \right] \quad (30)$$

3) Linear load in elastic zone:

$$\sigma_{x1} = \frac{P_1 - P_0}{\pi} \left[\frac{L_1 - x}{L_e} \left(\arctan \frac{L_1 - x}{L_1 - x_0} - \arctan \frac{x_0 - x}{y} \right) - \frac{y}{L_1 - x_0} \ln \frac{(L_1 - x)^2 + y^2}{(x_0 - x)^2 + y^2} + \frac{2(x_0 - x)y}{(x_0 - x)^2 + y^2} \right] \quad (31)$$

$$\sigma_{y1} = \frac{P_1 - P_0}{\pi} \left[\frac{L_1 - x}{L_1 - x_0} \left(\arctan \frac{L_1 - x}{L_1 - x_0} - \arctan \frac{x_0 - x}{y} \right) - \frac{2(x_0 - x)y}{(x_0 - x)^2 + y^2} \right] \quad (32)$$

$$\tau_{xy1} = \frac{P_1 - P_0}{\pi} \left[1 + \frac{(x_0 - x)^2 + y^2}{(x_0 - x)^2 + y^2} - \frac{y}{L_1 - x_0} \left(\arctan \frac{L_1 - x}{L_1 - x_0} - \arctan \frac{x_0 - x}{y} \right) \right] \quad (33)$$

By determining the stress component of any point in coal seam rock mass under the action of abutment pressure of each part, the stress component of this point can be obtained from the theory of elasticity:

$$\begin{cases} \sigma_x = \sigma_{x1} + \sigma_{x2} + \sigma_{x3} \\ \sigma_y = \sigma_{y1} + \sigma_{y2} + \sigma_{y3} \\ \tau_{xy} = \tau_{xy1} + \tau_{xy2} + \tau_{xy3} \end{cases} \quad (34)$$

Based on the Moore Coulomb criterion, the ultimate compressive strength of the anchored solid coal seam under triaxial stress is (Hui, 2021):

$$[\sigma_t] = 2c \frac{\cos \phi}{1 - \sin \phi} + \frac{1 + \sin \phi}{1 - \sin \phi} \sigma_m \quad (35)$$

where $[\sigma_t]$ is the ultimate compressive strength of anchored solid coal wall, MPa; σ_m refers to the solid lateral confining pressure of coal side, MPa. Since there is no confining pressure in the coal side, $\sigma_m = 0$. c is the cohesion of coal and rock mass, MPa; ϕ is the internal friction angle of coal and rock mass, $^\circ$.

Then, according to the formula of extreme value of mechanical normal stress of material:

$$\left. \begin{matrix} \sigma_{max} \\ \sigma_{min} \end{matrix} \right\} \frac{\sigma_x + \sigma_y}{2} \pm \sqrt{\left(\frac{\sigma_x - \sigma_y}{2} \right)^2 + \tau_{xy}^2} \quad (36)$$

where $\sigma_1, \sigma_2, \sigma_3$ are the stresses in three directions. The values of the two principal stresses can be obtained by using the aforementioned formula, and given that $\sigma_m = 0$, the three principal stresses can be obtained by ordering the three

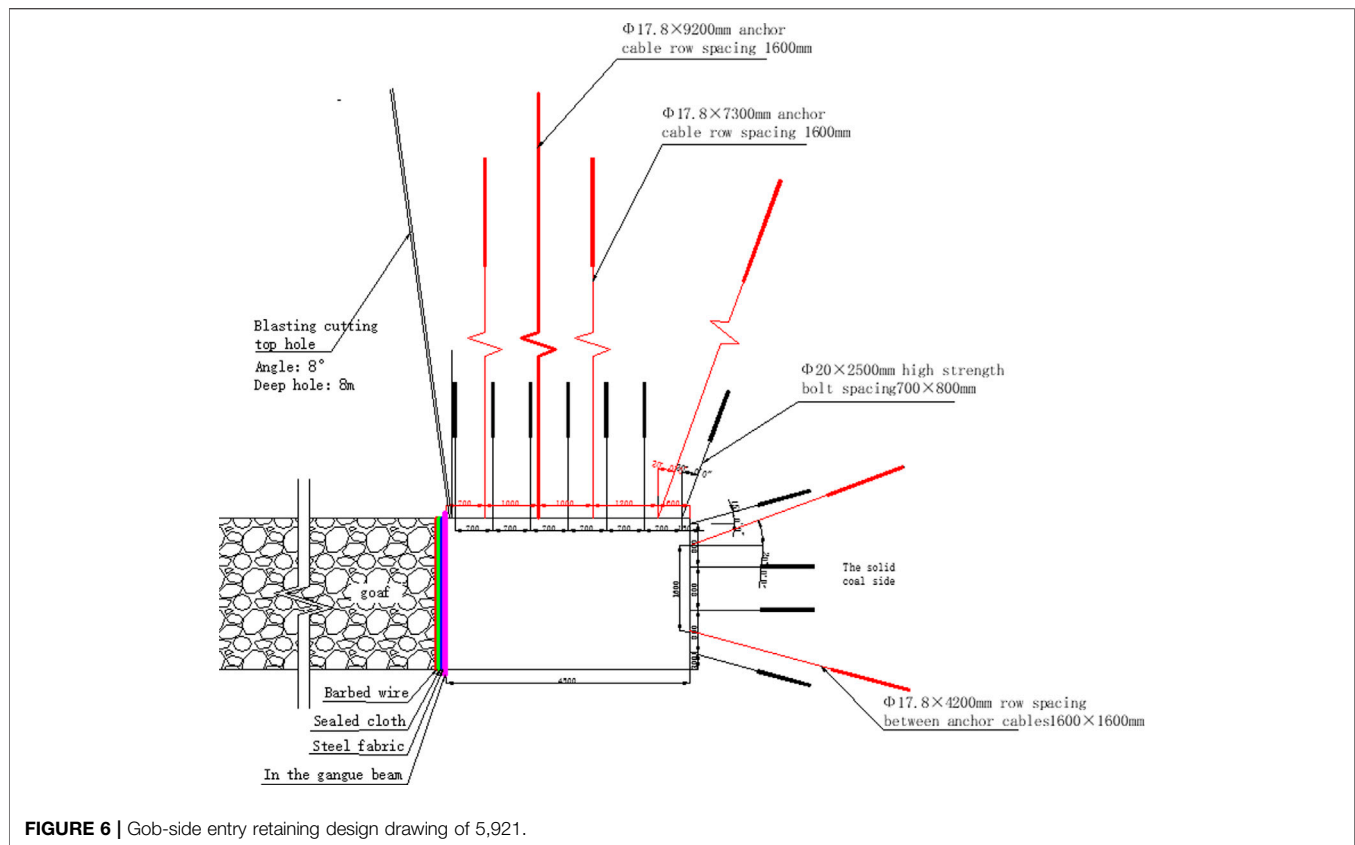


FIGURE 6 | Gob-side entry retaining design drawing of 5,921.

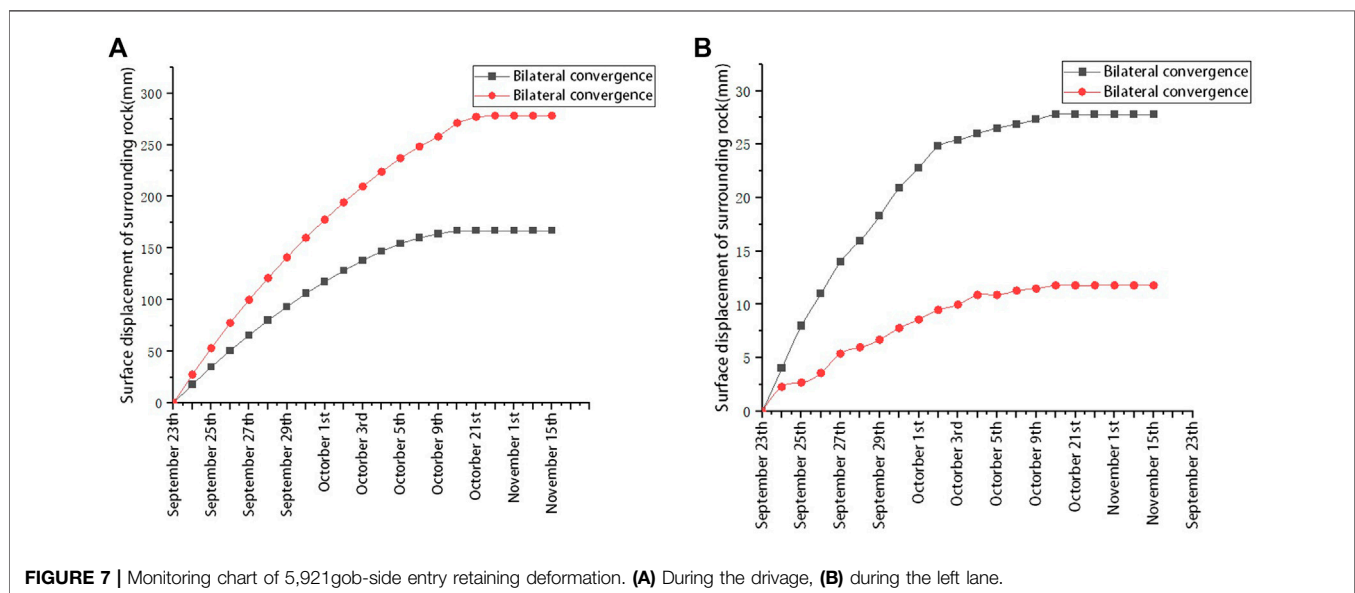


FIGURE 7 | Monitoring chart of 5,921gob-side entry retaining deformation. (A) During the drive, (B) during the left lane.

principal stresses in order of their numerical values, namely, σ_1 , σ_2 , σ_3 .

Finally, for safety reasons, the third strength theory is adopted, and the ultimate condition of instability failure of anchored solid coal wall is:

$$\sigma_1 - \sigma_3 \leq [\sigma_t] \quad (37)$$

where $[\sigma_t]$ is the ultimate compressive strength of anchored solid coal wall, MPa;

When Eq. 37 is satisfied, in other words, the stress at any point in the anchoring solid coal wall is less than its ultimate compressive strength, and the anchoring solid coal wall will not be damaged under compression. It can be seen that by strengthening the anchoring of the solid coal slope, changing

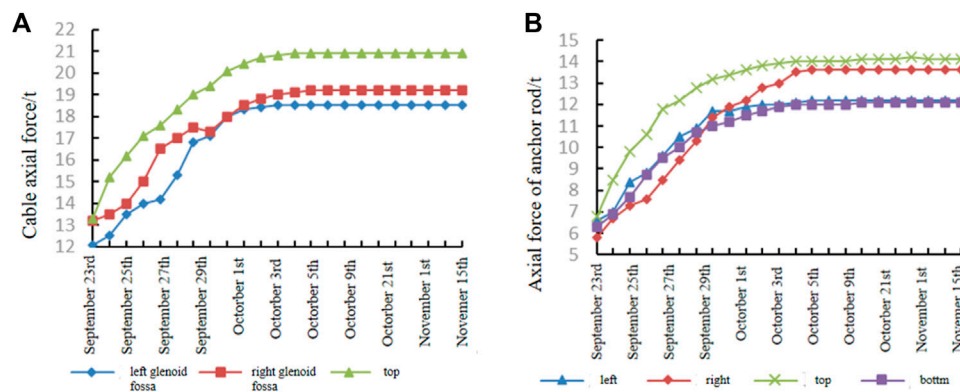


FIGURE 8 | Anchor-rod cable stress monitoring chart. (A) Anchor, (B) Anchor cable.

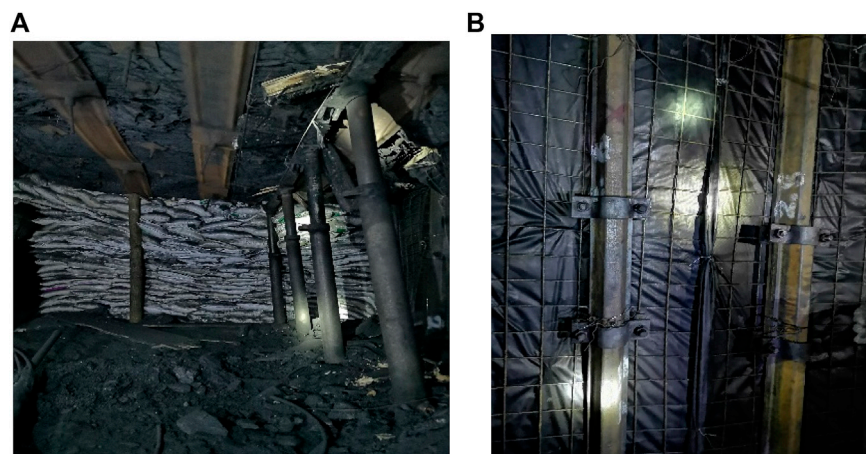


FIGURE 9 | Actual effect drawing of gob-side entry retaining. (A) Roof cutting support and lane retention space, (B) gangue retaining and support.

its mechanical property parameters and crushing range to obtain the mechanical properties of the solid coal slope for the stability of roadway retention, the stability of solid coal slope can be maintained and the structure of roadway retention is more stable.

4.4 Cooperative Bearing Relationship of Roadway Retaining Structure

Based on the previous analysis and calculation, relevant structural and mechanical properties parameters required to meet the stability of roadway entry retention can be obtained by changing the cutting angle, the anchoring performance of roadway solid coal wall and roof, and the geometric parameters of key blocks, so as to realize the construction and control of roadway entry retention structure. According to the stability control mechanism of roadway retaining structure, the following synergistic relationships should be satisfied among key load-bearing structures:

1) When the roof lithology is poor and the strength and stiffness of the anchoring roof beam are insufficient, it is necessary to

take effective ways to enhance the synergistic support effect of anchoring solid coal side, roof cutting support structure, retaining gangue support structure, and gangue support structure to realize the reinforcement control of the anchoring roof beam;

- 2) When the coal is soft and the bearing capacity of the anchoring coal seam is insufficient, the bearing capacity of the anchoring roof beam, the cutting roof support structure, and the gangue support structure should be strengthened to reduce the stress transfer and damage of the solid coal seam in the upper strata;
- 3) When the goaf roof caving is not sufficient and the bearing capacity of gangue support structure is limited, the anchorage strength and stiffness of roadway roof and solid coal side should be further improved, and the supporting force of roof cutting support structure should be increased to adapt to the destruction caused by the violent movement of overburdened strata;
- 4) By contrast, cutting roof bolting controllability is strong, according to the roof, solid coal wall, gangue collapse

degree and so on, the supporting force in the roadway and the side of the roadway can be adjusted. For example, to improve the support density or adopt hydraulic support, can effectively improve the bearing capacity of the roof support, and even play a key bearing role. There are also examples of the use of dense pillar to successfully retain the roadway.

5 FIELD TEST

5.1 Engineering Conditions

According to the aforementioned research methods, the practice of retaining roadways was carried out in the haulage lane of 5,921 working faces of the Longfeng Coal Mine in Guizhou province. The average thickness of the coal seam is 2.0 m, and the direct roof is a gray medium thick-bedded argillaceous siltstone with obvious horizontal bedding. There are soft rocks, thin coal seams, or coal lines in the middle, and the old roof is light gray medium thick-bedded fine sandstone with good stability. The direct bottom is a gray thin-bedded argillaceous siltstone, showing horizontal bedding. There is a floor-heave phenomenon during driving.

5.2 Anchorage Structure Design of Retaining Roadway

According to the control mechanism of non-filling lane retention and combined with the actual situation of the transport lane, the scheme design of important processes such as roadway anchor solid, roadway side support body, and directional blasting pre-splitting cutting roof were systematically carried out, as shown in **Figure 5**.

5.2.1 Control Parameters of Anchoring Roof Beam

Each section of the roof is drilled with 6 high-strength bolts. Because the loose ring is about 2,000 mm, the bolt specification is $\phi 20 \times 2,500$ mm, and the row distance is 700×800 mm. Located in the roof on the shoulder angle of mining face bolt straight drill, the roof shoulder angle of solid coal bolt and plumb line form 30° ; Bolt preload is 100 kN. A total of 4 anchor cables were drilled, among which the second anchor cable by the stopping side was $\phi 17.8 \times 9,200$ mm, which was drilled straight. The angle between the anchor cable at the shoulder angle of solid coal and the plumb line is 30° . The other two anchor cables are drilled vertical to the roof, with specifications of $\phi 18.9 \times 7,200$ mm. The spacing of anchor cables is shown in the figure, and the row spacing is 1,600 mm. Anchor cable preload is 200 kN.

5.2.2 Control Parameters of Anchoring Solid Coal Seam

Each section of solid coal wall is drilled with 4 bolts, and the row spacing is 800×800 mm. Other parameters are the same as those mentioned previously. In order to enhance the bearing performance of solid coal seam, two $\phi 17.8 \times 4,200$ mm short anchor cables are drilled in each section with row spacing of $1,600 \times 1,600$ mm. Other parameters are the same as those mentioned previously.

5.2.3 Control Parameters of Pre-Split Cutting top

The roof is cut by directional blasting, with a hole depth of 8,000 mm, drilling angle of 150° , and distance of 600 mm. There are 8~10 holes in the same group of initiation. The cutting top position is always about 50 m ahead of the working face, and pre-crack detection is carried out every 20 m to ensure the cutting top effect.

Other control parameters are shown in **Figure 6**.

5.3 The Control Effect

From the end of roadway excavation to the end of roadway retention, the construction quality inspection of anchor net cable, the stress monitoring of roadway deformation, and anchor bolt (cable) are strengthened to ensure the construction quality and achieve the expected control effect.

As shown in **Figure 7**, during roadway excavation, the maximum subsidence of the roof is no more than 15 mm, and the shrinkage of two sides is no more than 30 mm, indicating that strengthened anchoring significantly improves the strength and stiffness of roadway anchoring surrounding rock. During roadway retention, except for some small sections such as drilling field and fault, the maximum subsidence of roof under normal conditions is not more than 260 mm, and the shrinkage of two sides is not more than 180 mm, indicating that the anchorage structure of roadway retention has better stability and adaptability, and achieved better control effect.

As shown in **Figure 8** and **Figure 9**, the maximum axial force of bolt and cable during lane retention is no more than 140 and 220 kN, which are close to their initial anchoring force, with uniform force and no obvious stress concentration phenomenon, indicating that bolt and cable realize cooperative bearing and achieve the expected effect.

6 CONCLUSION

- 1) In view of the law of retaining roadway with hard roof and deformation and instability of overlying strata, the author take reasonable way to cut off the roof and the working face roof for the mechanical contact, to improve the position and state of strata structure and stress field distribution and reduce mining face goaf roadway roof caving the roof damage, so more conducive to the structural stability for control.
- 2) In this paper, combined with the actual construction of unfilled roadway retaining force and bearing model, the bearing characteristics of each bearing structure are analyzed, and it is proposed that the roadway solid coal side and roof are taken as the key bearing structures, and their bearing performance can be significantly improved by strengthening the anchoring effect, so that they jointly bear the bending load and mining influence imposed by the upper strata. The stability and adaptability of the whole roadway retaining structure can be improved by the reinforcing support of cutting roof support and gangue support.
- 3) Engineering practice shows that the control effect of unfilled roadway retention can be significantly improved by enhancing the cooperative bearing capacity of roadway anchorage structure and roadway side support structure, and the technical problems and difficulties in engineering practice are effectively solved.

- 4) In this article, the hard roof without filling roadway retention is taken as the research object, and the corresponding mechanical model and calculation method are established, which can provide a reference for other conditions of roof roadway retention and is worthy of further research and promotion.

DATA AVAILABILITY STATEMENT

The raw data supporting the conclusions of this article will be made available by the authors, without undue reservation.

AUTHOR CONTRIBUTIONS

LJ-K: In view of the deformation and instability law of the hard roof non-roadway side filling retaining roadway, the stress and bearing model of the retaining roadway structure is

REFERENCES

- Allard, K., and Swelsky, T. B. (1986). *Prediction Method of Roof Collapse. American Society of Mining Engineers. Status Quo of Rock Strata Control and Subsidence Prevention Technology in Longwall mining*[C]. Taiyuan: Shanxi Science Education Press.
- Cao, S. G., Chen, X. Z., Yang, H. Y., Wang, S., and Zou, D. J. (2016). Analysis of Side Control Technology and Applicable Conditions for Gob-Side Entry Retaining [J]. *Coal Sci. Technol.* 44 (4), 27–33.
- Chen, Y. (2012). *Study on Stability Mechanism and Control of Surrounding Rock Structure Movement of Gob-Side Entry retaining*[D]. Xuzhou: China University of Mining and Technology.
- Chen, Y. G., and Lu, S. L. (1994). *Surrounding Rock Control of Coal Mine Roadway in China*[M]. Xuzhou: China University of Mining and Technology Press.
- He, M. C., Chen, S. Y., Guo, Z. B., Yang, J., and Gao, Y. B. (2017b). Structural Control and Engineering Application of Surrounding Rock of Gob-Side Entry Retaining with Roof Cutting Pressure Relief [J]. *J. China Univ. Min. Technol.* 46 (9), 959–969.
- He, M. C., Song, Z. Q., Wang, A., Yang, H. H., Qi, H. G., and Guo, Z. B. (2017a). The Theory and 110 Construction Methods of Short-Wall Beam Cutting in Longwall Mining -- the Third Mining Science and Technology Reform[J]. *Coal Sci. Technol.* (1), 1–9+13.
- He, S. D., Zhang, Y., and Liu, W. (2016). Research Status and Prospect of Gob-Side Entry Retaining Technology[J]. *Mod. Min.* 563 (3), 6–10.
- Hou, C. J., and Li, X. H. (2001). Stability Principle of "large and Small" Structure of Surrounding Rock of Gob-Side Entry Retaining in Fully Mechanized [J]. *J. China coal Soc.* 26 (1), 1–7.
- Hua, X. Z., Ma, J. F., and Xu, T. J. (2005). Study on Surrounding Rock Control Mechanism of Gob-Side Retaining Roadway with Anchor Cable Reinforcement and its Application[J]. *Chin. J. Rock Mech. Eng.* 12, 2108–2112.
- Hui, X. D. (2021). *Narrow Section Bearing Evolution Characteristics and Coal Pillar Stability Control* [D]. Master thesis. Xuzhou, China: China University of Mining and Technology.
- Jiang, J. Q. (1993). *Stress and Movement of Surrounding Rock in Stope* [M]. Beijing: Coal Industry Press.
- Kang, H. P., Zhang, X., Wang, D. P., Tian, J. Z., Yi, Z. Y., and Jiang, W. (2022). Control Technology and Application of Surrounding Rock in Pillar - Free Mining[J]. *J. Coal Soc.* 47 (1), 16–44.
- Ke, D. (2020). *Close Distance Coal Seam Roadway Deformation Law of Surrounding Rock and the Control Technology Research* [D]. Master thesis. Xi'an, China: Xi'an University of Science and Technology.
- Ortlepp, W. D., and Stacey, T. R. (1998). Performance of Tunnel Support Under Large Deformation Static and Dynamic Loading. *Tunn. Undergr. Space Technol.* 13 (1), 15–21. doi:10.1016/S0886-7798(98)00022-4
- Qian, M., and He, F. (1989). The Behavior of the Main Roof in Longwall Mining-Weighting Span, fracture and Disturbance[J]. *J. Min. Metal. Fuel.* 37, 240–260.
- systematically constructed. The mechanical model and calculation method of the retaining roadway supported by the cantilever beam formed by the anchored roof beam and the key blocks above and the anchored solid coal wall are proposed. The technical scheme and relevant parameters of the engineering practice are designed, and the engineering test is guided. The first draft of this paper is written. QC-X, CZ-Y, LH, and YW-K: Participated in the theoretical analysis, engineering test scheme design, field implementation, and paper modification of the control of hard roof side entry filling and retaining roadway.
- FUNDING**
- The research was supported by the National Natural Science Foundation of China, 52174136.
- Qian, M., and Zhao, G. (1987). "The Behavior of the Main Roof Fracture in Longwall Mining and its Effect on Roof Pressure," in 28th US symposium on Rock Mechanics, June 29–July 1, 1987 (Tucson, Arizona: ARMA-87-1123).
- Qian, M. G., Shi, P. W., and Xu, J. (2010). *Mine Pressure and Strata control*[M]. Xuzhou: China University of Mining and Technology Press.
- Qian, M. G. (1994). Stability of Masonry Beams and its Application[J]. *Mine Press. Roof Manag.* 3, 6–10.
- Qian, M. G., Xu, J. L., and Miao, X. X. (2003). Green Mining Technology of Coal Mine[J]. *J. China Univ. Min. Technol.* 32 (4), 343–347.
- Song, Z. Q. (1988). *Practical Mine Pressure and control*[M]. Beijing: China University of Mining and Technology Press.
- Sun, H. H., and Zhao, B. L. (1993). *Theory and Practice of Gob-Side Entry Retaining* [M]. Beijing: China Coal Industry Press.
- Sun, X. M., Sun, X. M., Liu, X., Liang, G. F., Wang, D., and Jiang, Y. L. (2014). Research on Key Parameters of Gob-Side Entry Retaining in Thin Coal Seam under Pressure Relief by Cutting Roof[J]. *Chin. J. rock Mech. Eng.* 33 (7), 1449–1456.
- Yuan, L., Yuan, L., Xue, J. H., Zhang, N., and Lu, P. (2013). Present Situation and Prospect of Key Technologies of Coalbed Methane Extraction and Co-extraction of Coal and Gas[J]. *Coal Sci. Technol.* 41 (9), 6–11.
- Zhang, G. F. (2010). *Research on the Mechanism and Key Technology of Gob-Side Entry Retaining Formation by Cutting Roof Pressure relief*[D]. Beijing: China University of Mining and Technology.
- Zhu, D. E. (1987). *Breaking Law of Main Roof in Long Wall Face and its Application* [D]. Xuzhou: China University of mining and technology.
- Conflict of Interest:** LH was employed by Guizhou Lindong Coal Industry Co, Ltd.
- The remaining authors declare that the research was conducted in the absence of any commercial or financial relationships that could be construed as a potential conflict of interest.
- Publisher's Note:** All claims expressed in this article are solely those of the authors and do not necessarily represent those of their affiliated organizations, or those of the publisher, the editors, and the reviewers. Any product that may be evaluated in this article, or claim that may be made by its manufacturer, is not guaranteed or endorsed by the publisher.
- Copyright © 2022 Jing-kui, Chao-xin, Zuo-yong, Hong and Wen-kai. This is an open-access article distributed under the terms of the Creative Commons Attribution License (CC BY). The use, distribution or reproduction in other forums is permitted, provided the original author(s) and the copyright owner(s) are credited and that the original publication in this journal is cited, in accordance with accepted academic practice. No use, distribution or reproduction is permitted which does not comply with these terms.



OPEN ACCESS

EDITED BY

Shuren Wang,
Henan Polytechnic University, China

REVIEWED BY

Yingchun Li,
Dalian University of Technology, China
Dengke Wang,
Henan Polytechnic University, China

*CORRESPONDENCE

Jin Wang,
particlewj@hhu.edu.cn

SPECIALTY SECTION

This article was submitted to
Geohazards and Georisks,
a section of the journal
Frontiers in Earth Science

RECEIVED 17 June 2022

ACCEPTED 25 July 2022

PUBLISHED 25 August 2022

CITATION

Sun S, Wang J, Le H, Fan H and Wang W
(2022), Experimental and numerical
investigation on compressive strength
and crack behavior of rock-like
specimens with open flaws under
confining loads.
Front. Earth Sci. 10:972194.
doi: 10.3389/feart.2022.972194

COPYRIGHT

© 2022 Sun, Wang, Le, Fan and Wang.
This is an open-access article
distributed under the terms of the
[Creative Commons Attribution License](#)
(CC BY). The use, distribution or
reproduction in other forums is
permitted, provided the original
author(s) and the copyright owner(s) are
credited and that the original
publication in this journal is cited, in
accordance with accepted academic
practice. No use, distribution or
reproduction is permitted which does
not comply with these terms.

Experimental and numerical investigation on compressive strength and crack behavior of rock-like specimens with open flaws under confining loads

Shaorui Sun, Jin Wang*, Huilin Le, Haotian Fan and
Wuchao Wang

College of Earth Science and Engineering, Hohai University, Nanjing, China

Engineering problems are related to the failure of geological material, especially that of jointed rock masses. To investigate the influence of confining stress and inclination angle β on cracking behavior and failure mechanism, triaxial compression tests are conducted on rock-like samples containing parallel opening flaws. There are two patterns, namely, tensile failure and tensile-shear failure, and each occurrence has an equal frequency. Nine crack modes are summarized, and the most special one is mode 8, which is mainly observed in samples with $\beta = 60^\circ$ at high confining pressure. Both the compressive strength and internal friction in samples with $\beta = 60^\circ$ are the smallest in the experiments, and those in samples with $\beta = 65.31^\circ$ based on the improved theory are the smallest. The compressive strength decreases with the increase of inclination angle β when $0^\circ \leq \beta \leq 60^\circ$; however, it increases as inclination angle β increases when $60^\circ < \beta \leq 90^\circ$. This phenomenon is found in laboratory experiments and numerical tests and is almost even in accordance with theoretical results. Numerical compression tests are performed to investigate the influence of the width-to-length ratio of opening flaws on compressive strength and to verify the improved theory reliability. Compared numerical results with the two kinds of theoretical results, the width-to-length ratio has an obvious impact on compressive strength and the opening fracture intensity factor K_I .

KEYWORDS

opening flaw, crack type, compressive strength, fracture mechanism, numerical tests

1 Introduction

In geotechnical engineering, the occurrence of discontinuities in rock masses often results in a deterioration of strength. Compressive loading always contributes to the cracking of flaws, leading to rock mass failure (Lee and Jeon, 2011; Cao et al., 2015; Le et al., 2019a; Wan et al., 2019). In the past decades, a number of experimental and numerical researches on flawed rocks under uniaxial and biaxial loading have been carried

out (Bahaaddini et al., 2013; Fu et al., 2016; Huang et al., 2016; Chenchen Huang et al., 2019; Chen et al., 2020; Bao et al., 2021). However, it is triaxial compression that is better in replying to the cracking behavior and is more realistic to investigate into fracture mechanism since flawed rock mass, especially in underground excavation, is in three-dimensional geological stress.

Some previous research studies have confirmed that the path of different loading has an impact on the development of cracks and the compressive strength of rock masses. Five coalescence crack patterns were found in uniaxial compression; however, four patterns were found in biaxial compression (Bobet and Einstein, 1998), which is one less shearing pattern than uniaxial compression. The compressive strength of flawed rock mass is mainly related to the mechanical properties of rock-like material and infill material, the geometrical parameters of flaws and confining stress. A comprehensive understanding of the influence of three kinds of materials infilling Naghdeh limestone samples on failure was made, and it was found that the weaker the infilling materials, the more the possibility of cracking in them (Haeri et al., 2020). Moreover, the compressive strength of samples with an inclination angle of 60° was the smallest one. Conventional triaxial compression was performed on jointed rocks with two parallel flaws; four crack coalesces modes were identified in samples with different inclination angles under the confining stress 0, 5, 10, 15, and 20 MPa (Huang and Yang, 2018). To investigate the discontinuities in cracking behavior, three groups of specimens containing different numbers of flaws (type A, granite specimens without cracks; type B, rock specimens with one inclined crack; type C, rock specimens with two parallel pre-existing cracks C) were prepared for experimental and numerical triaxial compression, and the failure of type C was constantly shear at any confining pressure (Yao et al., 2019). It was known from the abovementioned research that the compressive strength increased with the increase of confining stress. However, there are not enough investigations on the influence of pre-existing flaw geometry on the rock's failure. Meanwhile, there are still difficulties in manual sample preparation due to the precise requirements of pre-existing flaws, especially opening flaws with a narrow width.

With the development of science and technology, more and more mature numerical simulation is one of the effective means to investigate the strength and deformation of rock mass (Guo et al., 2017; Cheng et al., 2019; Mu and Zhang, 2020; Wang et al., 2020). Compared to indoor experiments, there are fewer limitations to using the numerical method since many laborers and a specific area for the testing site are not required. Nine models with different joint numbers (1, 2, and 3) and joint angularities (0°, 45°, and 90°) were performed on the extended finite element method (X-FEM) (Haeri et al., 2020), and the failure process was fully demonstrated throughout. GPGPU was introduced to the finite element method to optimize modeling, and it was confirmed that more ductile flawed rock

masses and less liable to fracture with an increase in confining pressure (Mohammadnejad et al., 2019). The interaction integral technique in ANSYS was applied to accurately predict the crack propagation paths and the mixed-mode stress intensity factors of jointed rock masses (Alshoaibi, 2021). As the failure mechanism of composite rocks can be effectively explained from the perspective of the migration of particles, the distribution of contact force, and the development of tensile cracks and shear cracks, the discrete element method is widely adopted to investigate the mechanical response of rock materials on the micro level (Camones et al., 2013; Cui et al., 2020). It was indicated that there were five failure modes, determined by the flaw's orientation and step angle. Under triaxial compression, the cross-section of experimental specimens scanned by CT agreed with that of numerical models in PFC3D, and the numerical results well-revealed the failure mechanism of rock masses containing pre-existing flaws (Yan-Hua Huang et al., 2019). Therefore, numerical simulation has many advantages in the high accuracy of specimens' preparation, making it possible for investigating the strength and failure mechanism of rock masses containing opening flaws.

In this study, rock-like specimens contacting four opening flaws were subjected to triaxial compression tests to investigate the effects of flaws' inclination angle on compressive strength and cracking behavior in rock masses under different confining pressure. Types of cracks defined were used to determine the ultimate failure pattern, and the fracture theory of opening flaws was improved to make it more suitable for experimental results and reality. For verifying the reliability of this theory, numerical compression tests were performed. Numerical samples with min-width flaws were in high precision, and three width-to-length ratios were prepared to further understand the influencing factors of compressive strength. Results obtained from three methods (experiment, numerical simulation, and fracture theory) were expected to be compared and illustrated in the end.

2 Materials and methods

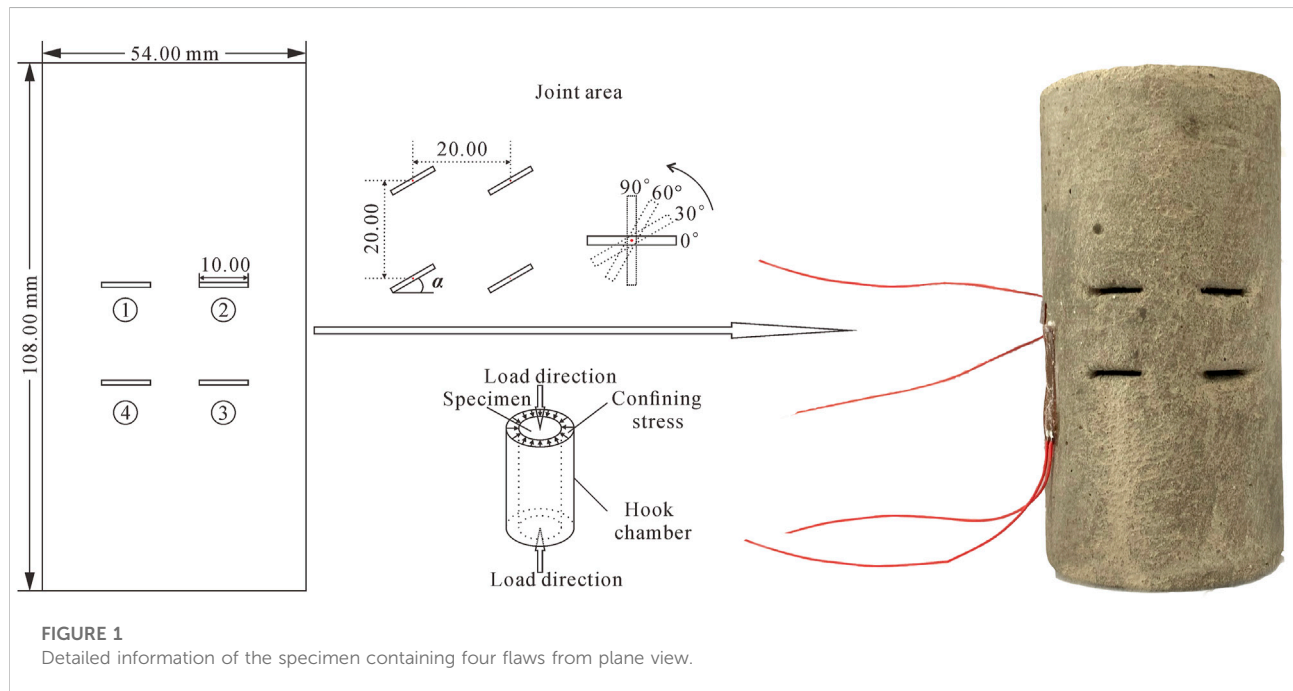
2.1 Specimens preparation

To reflect the brittle failure characteristics of rock mass with non-consecutive joints, cement mortar has been proved to be an ideal rock-like material for rock mechanics experiments. In this research study, specimens for triaxial loading tests were made of C32.5 Portland cement, fine sand, and water. The mechanical properties of the rock-like material with a cement-to-sand-to-water weight ratio of 1:2:0.4 were similar to those of sandstone are shown in Table 1. To reduce the effects of heterogeneity caused by formations of weak structural surfaces in the preparation process, the particle size of fine sand was selected to be less than 1 mm. Artificial flaws in specimens were

TABLE 1 Mechanical properties of the experimental material.

Type	UCS	Young's modulus	Poisson's ratio	Cohesion	Friction angle
	σ_c (MPa)	E (GPa)	ν	c (MPa)	φ (°)
Sandstone	20–170	3–35	0.02–0.20	4–40	25–60
Rock-like material	21.88	6.45	0.15	4.37	37.95

UCS, uniaxial compressive strength.



prefabricated using a steel sheet with a width of 10 mm and a thickness of 1 mm, and the flat sheet of steel was fixed at the designed position. These samples were cured for 28 days in a tank with a temperature of 20°C to avoid an uneven shrinkage resulting from dehydration and cement hydration. Two mutually perpendicular strain gauges were attached to the surface of each specimen to monitor strains in the vertical and horizontal directions, respectively.

The geometry of specimens is a cylinder shown in Figure 1, with a dimension of 108 mm in height and 54 mm in radius. Centers of the four pre-existing flaws remain consistent all the time, and the distance between each of the two adjacent centers is 20 mm. The inclination angle β is illustrated in Figure 1. In this experiment, five kinds of jointed specimens are composed of flaws with different inclination angles, and intact samples are used as control groups to calibrate microscopic parameters in numerical simulation. The evolution of flaws into transfixion under loading conditions can be clearly observed with these specimens.

2.2 Testing procedure

Triaxial compression tests were conducted by the ELE device, and the loading rate was 0.1 ~ 0.2 kN/s until the failure of specimens. It should be noted that centers of the Hooke chamber and of the jack were on the same line before loading to ensure force equality. In this experiment, confining stress was set to five levels which were 2.0, 4.0, 6.0, 8.0, and 10.0 MPa. Four kinds of flaws angle (0°, 30°, 60°, and 90°) were prefabricated to investigate the influence of inclination.

3 Experimental results

3.1 Samples coalescence and failure patterns

Compared to failure patterns under uniaxial compression, it is difficult to discover the crack mode which has been defined in

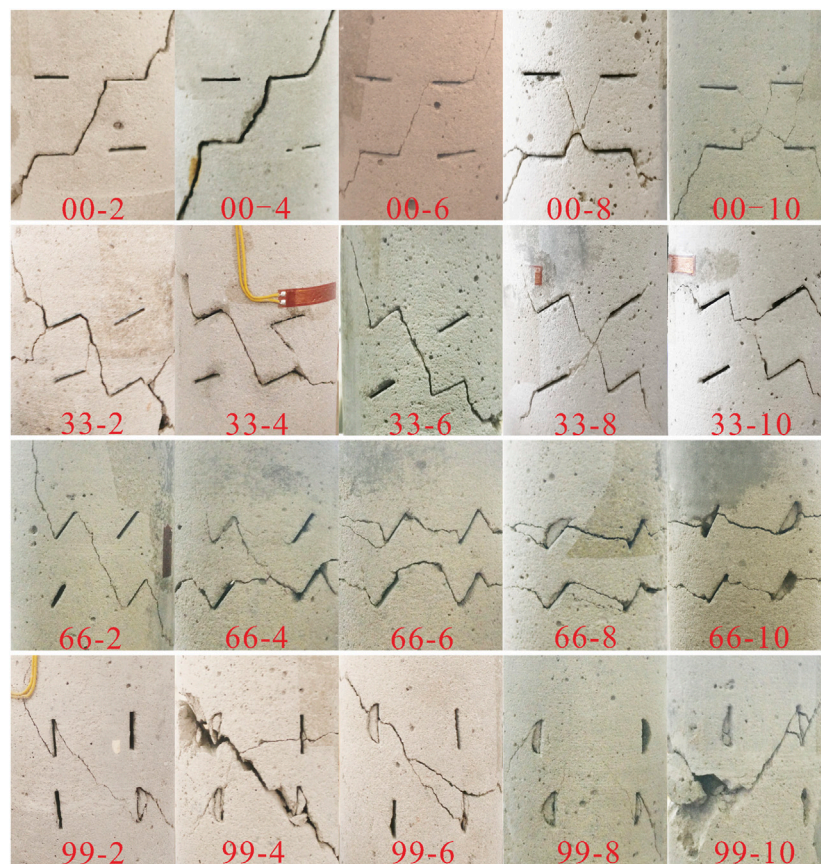


FIGURE 2

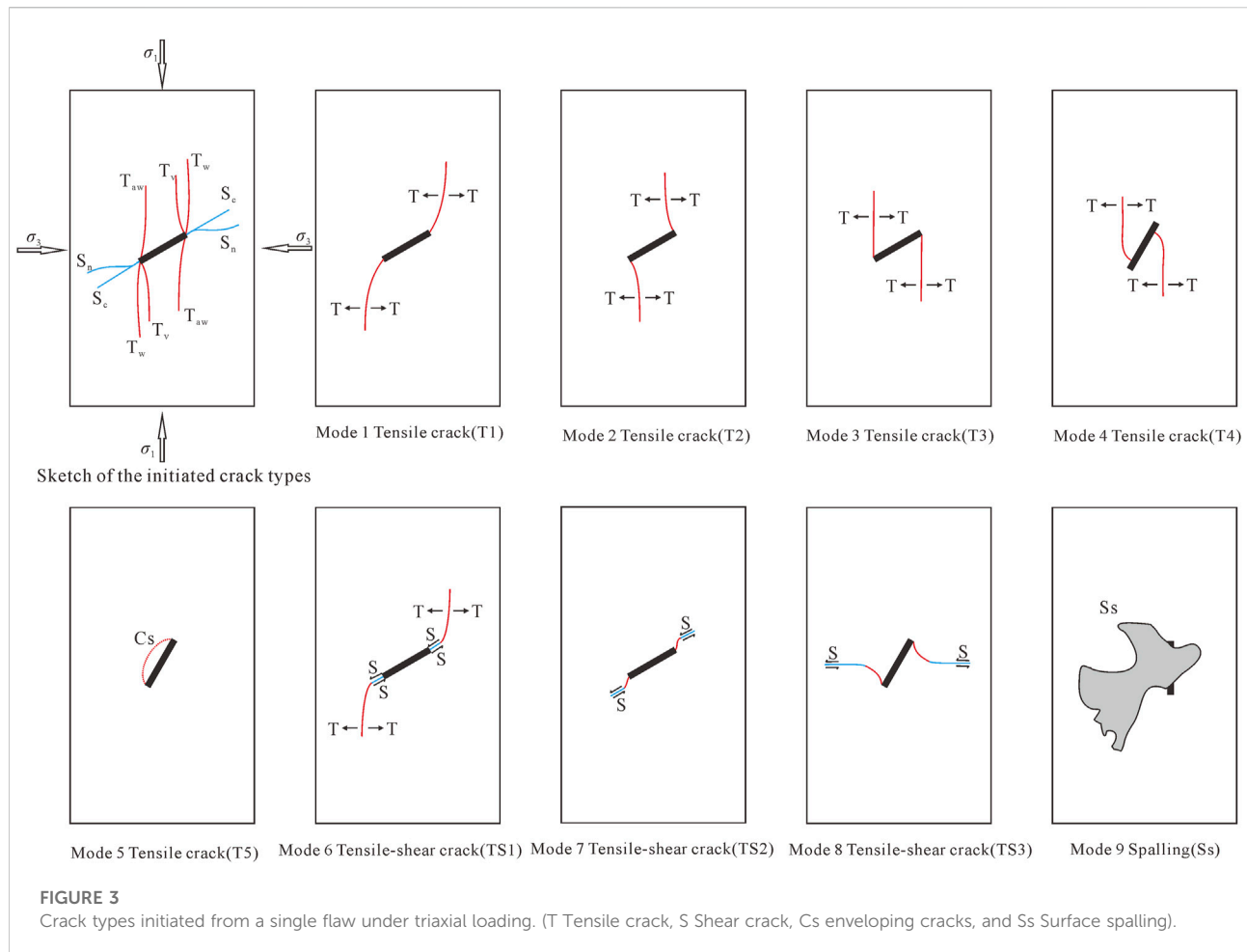
The ultimate failure of samples containing four opening flaws under triaxial compression. *The symbol "00-2" means that the sample with the inclination angle of 0° is loaded at the confining pressure of 2 MPa.

previous studies (Peng et al., 2021; Wong and Einstein, 2009; Yang and Jing, 2010) that a tensile crack initiates from the flaw tips and then propagates along the major stress under the biaxial or triaxial loading, due to the effect of confining stress. Based on the ultimate crack modes of rock-like samples shown in Figure 2, the failure patterns are summarized into two types: one is composed of pure tensile cracks, and another one is a mixed coalescence of tensile cracks and shear cracks. Moreover, there is no failure pattern that is only caused by shear cracks. According to the mechanical properties of single crack propagation in Figure 3, a total of nine crack modes are found. Five modes are tensile (mode 1~5), three modes are tensile-shear (mode 6~8), and one of them is a spalling surface (mode 9) which often appears after tensile cracks. Modes 1~4, 6~7, and 9 as common crack types of jointed rock masses failure have been summarized in many studies (Yang, 2011; Le et al., 2019b).

In mode 5, anti-wing cracks initiate from the two tips of pre-existing flaw and then extend to connection, and an elliptical crack surface is formed to envelop the flaw in the end. Short shear cracks shown in mode 7 are distributed near the pre-existing flaw

and are almost parallel to it. Their appearance is always accompanied by the propagation of tensile cracks. Different from the lateral crack found in the previous research (Yang and Jing, 2010), it always develops at the end of the anti-wing crack in mode 8 and is gradually vertical to the major principal stress. The surface of the lateral crack is smooth, and combined with Figure 3, this crack is identified as a shear crack.

Cracking evolution of all samples subjected to triaxial compression tests is demonstrated in Figure 4 and is in accordance with the conclusion (Bobet and Einstein, 1998): The coalescence of cracks (including flaws) is the main reason leading to the ultimate failure of flawed rock mass under biaxial compression. All crack types for each specimen are summarized in Table 2. It is of note that tensile crack is the most dominant crack during the loading of a specimen. Especially when $\beta = 90^\circ$, no matter what the confining pressure is, only the failure pattern that is composed of pure tensile cracks is discovered, and these two crack types (mode 3 and mode 5) are found in each specimen with that angle. When $\beta = 0^\circ$, there is only mode 1 under low confining pressure; however, the major tensile crack is mode



2 when $\beta = 30^\circ$. When the confining pressure is 8 and 10 MPa, these two crack types (mode 4 and mode 5) begin to appear in specimens with an inclination angle of 60° . With the increase of confining pressure, shear cracks gradually form in samples with $\beta = 0^\circ, 30^\circ$, and 60° , and the failure pattern changed from tensile failure to tensile-shear failure.

Based on the frequency of occurrence of crack types, mode 1 is thought to be the most dominant crack type in this study that just is not found in five kinds of samples (33-6, 33-8, 66-10, 99-2, and 99-10). The second type is mode 3, and the least one is mode 4. Mode 5 crack initiates in some samples with an angle of 60° at the large confining pressure (8 MPa, 10 MPa) and in all samples with an inclination angle of 90° . The main reason is that shear stress distributed on the pre-existing flaw surface increases as the inclination angle becomes larger. When the flaw is parallel to the axial loading, shearing is the strongest, leading it to be more prone to anti-wing cracks. Moreover, large confining pressure also contributes to shearing, resulting in anti-wing cracks intersecting to form an envelope surface. The special crack type, mode 8, is only observed in samples with $\beta = 30^\circ$ and $\sigma_3 = 10$ MPa and in samples with $\beta = 60^\circ$ and $\sigma_3 = 6, 8$, and 10 MPa.

3.2 Compressive strength and mechanical parameters of the specimens under confining loads

In order to obtain cohesion c and internal friction angle φ of samples, assuming that the relationship between confining pressure σ_3 and the corresponding compressive strength σ_1 is linear, linear regression is carried out in the least square method.

$$\sigma_1 = a\sigma_3 + b \quad (1)$$

in the equation, a is the slope of the resultant line, and b is the intercept of the resultant line on the σ_1 . Furthermore, c and internal friction φ are derived based on the Mohr–Coulomb criterion.

$$\varphi = \sin^{-1} \left(\frac{a-1}{a+1} \right) \quad (2)$$

$$c = \frac{b(1 - \sin \varphi)}{2 \cos \varphi} \quad (3)$$

The experimental results are processed according to the abovestated equations. Table 3 shows the compressive strength in the axial direction, cohesion c and internal friction

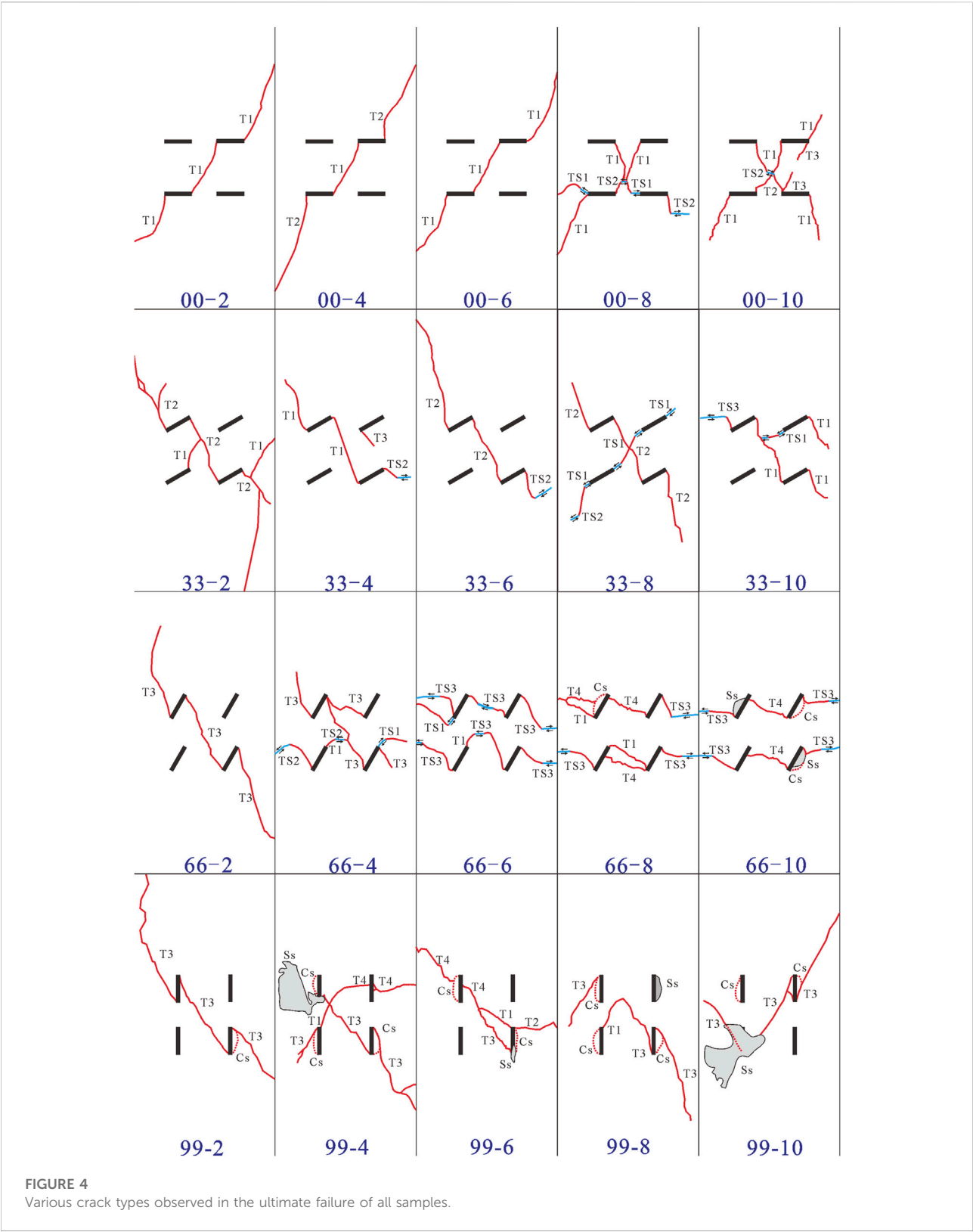


TABLE 2 Crack types of rock-like specimens containing four parallel flaws with different angles under triaxial loading test.

β (°)	σ_3 (MPa)	Tensile					Tensile-shear			Spalling
		Mode 1	Mode 2	Mode 3	Mode 4	Mode 5	Mode 6	Mode 7	Mode 8	Mode 9
0	2	✓								
	4	✓	✓							
	6	✓								
	8	✓					✓	✓		
	10	✓	✓	✓				✓		
30	2	✓	✓							
	4	✓		✓				✓		
	6		✓					✓		
	8		✓				✓	✓		
	10	✓					✓		✓	
60	2			✓						
	4	✓		✓			✓	✓		
	6	✓					✓		✓	
	8	✓			✓	✓			✓	
	10				✓	✓			✓	✓
90	2			✓		✓				
	4	✓		✓	✓	✓				✓
	6	✓	✓	✓	✓	✓				✓
	8	✓		✓		✓				✓
	10			✓		✓				✓

Crack types found in samples are marked with “✓.”

TABLE 3 Compressive strength and mechanical parameters of rock-like samples.

β (°)	Confining stress (MPa)					c (MPa)	φ (°)
	2.0	4.0	6.0	8.0	10.0		
Intact specimen	29.07	35.00	45.95	52.97	56.17	4.37	37.95
0	23.40	25.83	31.76	49.04	50.17	4.21	32.97
30	21.21	23.21	30.45	46.25	46.8	4.25	31.21
60	16.85	20.60	26.09	32.89	35.33	4.21	23.19
90	24.83	28.45	37.00	51.66	53.23	4.24	35.66

angle φ of jointed rock-like specimens with different inclination angles under corresponding confining stress. The compressive strength of intact specimens is always larger than that of jointed rock mass, no matter what the confining pressure is. Variations of compressive strength and internal friction as the inclination angle of flaws increases are described in Figure 5A. The compressive strength of samples with $\beta = 90^\circ$ is larger than that of samples with $\beta = 0^\circ$. Because the action of confining stress applied to samples is considered as leading opening flaws to internal closure, the specimen with $\beta = 90^\circ$ is easier to be closed

on account of the flaw surface perpendicular to the confining pressure. Hence, the compressive strength, cohesion c and internal friction angle φ of samples with $\beta = 90^\circ$ approach to those of intact samples.

An obvious experimental phenomenon is found: There is a V-shaped characteristic that the peak strength first decreased when $\beta < 60^\circ$ and then increased when $\beta > 60^\circ$. At any confining pressure, the compressive strength of samples with $\beta = 60^\circ$ is the minimum. The compressive strength of samples with $\beta = 30^\circ$ is very close to that of samples with $\beta = 0^\circ$. It is a further observation

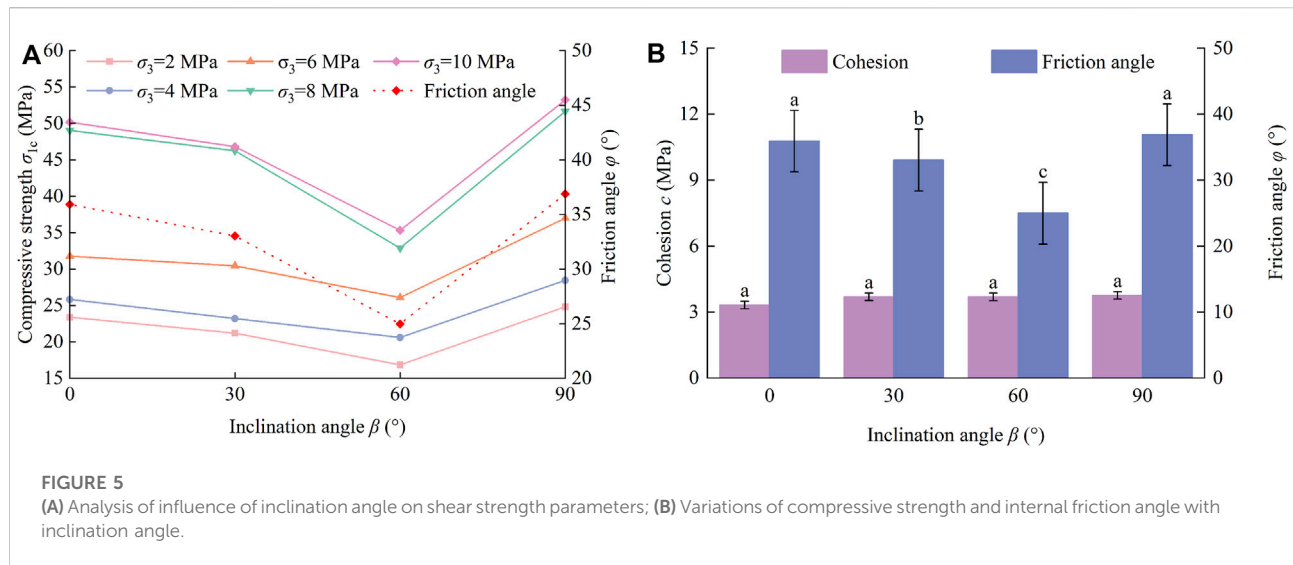


TABLE 4 Micro-parameters for bond parallel contact model.

Description of micro-parameters		Value	
Particle parameters		Parallel bond parameters	
Ratio of maximum radius to minimum radius of balls, R_{rat}	1.66	Cohesion bond strengths, R_n (MPa)	17.5
Density of particles, Q (kg/m ³)	2630	Tensile bond strengths, R_s (MPa)	26.4
Coefficient of friction, r_R	0.4	Angle of friction, (°)	28
Young's modulus of balls, E_c (GPa)	6.62	Effective modulus of bond, E_c (GPa)	6.62
Normal-to-shear stiffness ratio of balls	1.2	Normal-to-shear stiffness ratio of bond	1.2

that these curves in Figure 5A become flatter and flatter with the decrease of confining stress.

In Figure 5B, regression analysis is carried out for thoroughly investigating the influence of flaws angles, and the lowercase letters of the same column indicate the difference between cohesion, internal friction angle φ under the condition of different flaw angles (LSD): there is no significant effect of the inclination angle on cohesion ($p > 0.05$) but on internal friction angle ($p < 0.05$). The existence of pre-existing flaws does not have a significant effect on cohesion because cohesion is directly related to properties of rock material, such as mineral composition and density. The variation of the internal friction angle φ of jointed rock masses is in agreement with that of compressive strength, which decreases first and then increases with the increase of inclination, and the minimum one is found in samples with $\beta = 60^\circ$. When the confining pressure σ_3 and cohesion are determined, the compressive strength decreases as the internal friction angle decreases.

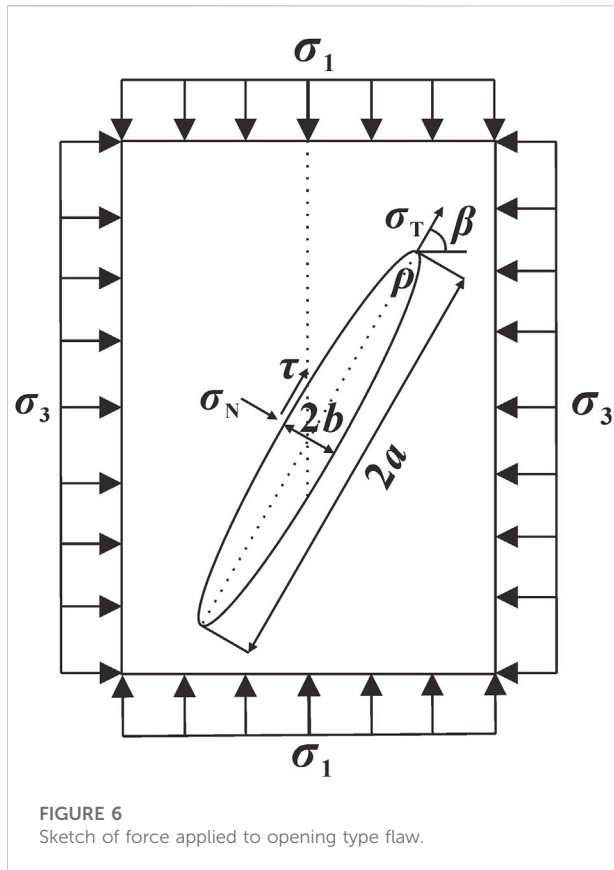
Lateral cracks in mode 8 initiate after anti-wing cracks and are defined as shear cracks because those surfaces are smooth and

flat; moreover, this mode is mainly discovered in samples with an inclination angle of 60° . It is speculated that there is a concentration of shear stress at the anti-wing crack end. In addition, the ratio of compressive strength and confining pressure in samples with $\beta = 60^\circ$ is smaller than other samples at high confining pressure, as Table 4 indicates, resulting in the crack gradually propagating along the lateral direction.

4 Discussion

4.1 Fracture mechanical theory of rock masses containing opened flaws

The stress state of a simplified diagram for an inclined opening flaw in the infinite body under the compressive loading is shown in Figure 6. The flaw is described as an ellipse with $2a$ mm in length and $2b$ mm in width, where the biaxial loads σ_1 and σ_3 are distributed uniformly on the edges.



The radius of curvature is ρ , and the angle of this flaw subjected to the direction of σ_3 is represented by the symbol β .

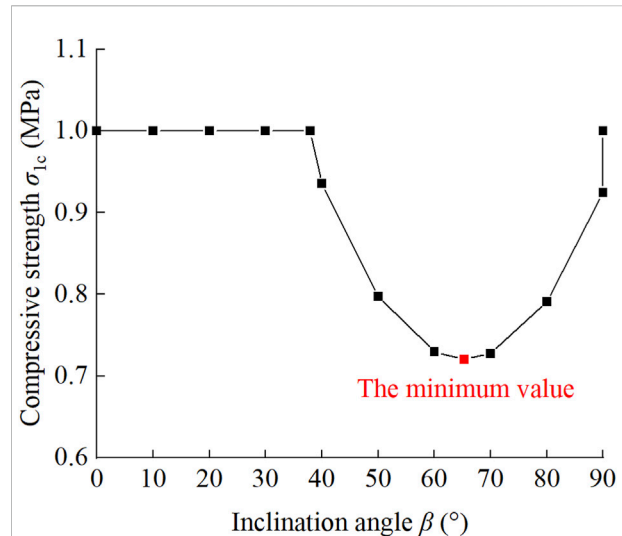
$$\left. \begin{aligned} \sigma_N &= \sigma_1 \cos^2 \beta + \sigma_3 \sin^2 \beta \\ \sigma_T &= \sigma_1 \sin^2 \beta + \sigma_3 \cos^2 \beta \\ \tau &= (\sigma_1 - \sigma_3) \sin \beta \cos \beta \end{aligned} \right\} \quad (4)$$

Based on the elastic mechanic, it is known that transverse compressive stress σ_T , normal stress σ_N and shear stress τ in the far field of the ellipse are represented by the Eq. 4. The stress intensity factor of opening mode is K_I , and that of sliding mode is K_{II} . A tensile stress perpendicular to σ_T will be produced by the transverse compressive stress at the prefabricated flaw tip (Muschelishvili, 1975), and k is introduced as the coefficient of pressure conductivity. The compressive stress σ is described by the following formula.

$$\left. \begin{aligned} \sigma &= k\sigma_T - \sigma_N \\ k &= \sqrt{\rho/a} \end{aligned} \right\} \quad (5)$$

$$\left. \begin{aligned} K_I &= \sigma \sqrt{\pi a} \\ K_{II} &= -\tau \sqrt{\pi a} \end{aligned} \right\} \quad (6)$$

Under triaxial compression, tensile-shear failure is found to be an important ultimate failure pattern of experimental samples in this study. In this pattern, only shear cracks initiated under



confining stress cause the ultimate failure of rock masses (Zhou, 1987).

$$\lambda_{12} \sum K_I + \sum K_{II} = K_{IIC} \quad (7)$$

In Eq. 7, λ_{12} is the compression-shear coefficient, and K_{IIC} is a material constant. Cracks always develop from the tip of the flaw, and when the width of the flaw is small, the tip can be considered as the endpoint of the major axis of the ellipse. Therefore, the radius of curvature ρ is expressed by b^2/a , and the compression-shear coefficient λ_{12} is considered as the friction coefficient f of rock material. When $\sigma_3 = \sigma_{3C}$, the compressive strength σ_{1C} of open-flawed rock mass is derived.

$$k = \frac{b}{a} \quad (8)$$

$$\sigma_{1C} = \frac{2}{\sqrt{\pi a}} \cdot \frac{K_{IIC} + f(1-k)\sqrt{\pi a}\sigma_{3C}}{\sin 2\beta - f(\cos 2\beta + 1) - fk(\cos 2\beta - 1)} + \sigma_{3C} \quad (9)$$

The angle β_u corresponding to the minimum compressive strength is calculated by the following equations: when

$$\frac{\partial \sigma_{1C}}{\partial \beta} = 0 \quad (10)$$

hence,

$$\beta_u = \frac{\pi}{2} - \frac{1}{2} \tan^{-1} \frac{1}{f(1+k)} \quad (11)$$

For open-flawed samples with 10 mm in length and 1 mm in width, made of rock-like material with an internal friction angle of 37.95° , the β_u calculated according to Eq. 11 is 65.31° at any confining pressure. In order to facilitate calculation, σ_{3C} in Eq. 9 is set to 0. The infinite flawed rock masses under uniaxial

condition is taken as the research object, and the fracture resistance R in Eq. 12, which is related to material properties and the width W mm of samples, is introduced to better describe the strength law (Ren et al., 2013). Both the compression-shear coefficient λ_{12} , the width-to-length ratio k , and the fracture resistance R are dimensionless parameters.

$$R = \frac{2}{\pi} \tan^{-1} \frac{\sigma_{1C} \sqrt{W}}{2K_{IIIC}} \quad (12)$$

Figure 7 demonstrates the relationship between compressive strength and inclination angle under uniaxial compression. This failure pattern occurs when the shear stress is larger than the frictional resistance, so when the inclination angle β is less than the internal friction angle φ , the compressive strength of the rock mass is close to the intact sample. It is clearly observed that the curves of inclination angle and compressive strength are V-shaped. When the angle increases from 0° to 65.31° , the compressive strength gradually decreases. When $\beta > 65.31^\circ$, the compressive strength increases with the increase of inclination angle. This is also in accordance with the experimental phenomenon found in Figure 5A.

4.2 Numerical verification tests for reliability

In the laboratory, when the pre-existing steel sheet is taken out from cement mortar, the opening flaw with a small width is easy to close. Therefore, numerical simulation is of great help in exploring the influence of flaw size. Numerical models are performed using the discrete element method to further verify relationships indicated in Eq. 9 between compressive strength and inclination angle and between compressive strength and flaws' size. The finite element method is used to verify the reliability of taking the geometrical parameter k of opening flaws into account.

4.2.1 Influencing factors of compressive strength

A two-dimensional model with the size of $108 \text{ mm} \times 54 \text{ mm}$ is filled with spherical particles named "balls" in PFC2D. The largest radius of balls is 0.332 mm , and the smallest is 0.2 mm . In the way of uniform distribution, it is constructed into a rectangular model with a density of 2630 g/cm^3 and consisting of 21046 balls. For a good calibration of microscopic parameters in Table 4, intact specimens are subjected to uniaxial and biaxial compression tests, respectively, and the results of mechanical parameters are: The Poisson ratio 0.15, the elastic modulus 6.46 GPa , the uniaxial compressive strength 21.52 MPa , and the axial peak strength is 29.80 MPa under the confining pressure of 2 MPa . Compared to the results of experiments shown in Table 1, the absolute values of errors are small, not more than 3.0% .

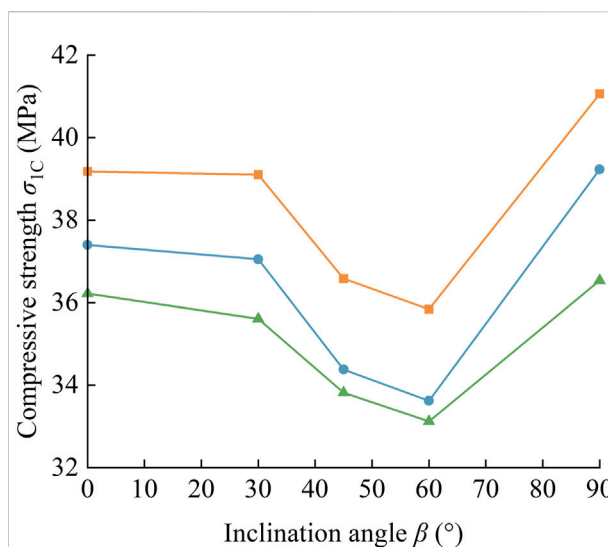


FIGURE 8
Effect between different width-to-length ratios and inclination angles on compressive strength of numerical samples containing opening flaw.

In the numerical compression test, the length of the open flaw is 20 mm , and three width-to-length ratios (0.05 , 0.1 , and 0.2) are prepared for making a thorough inquiry into the influence of opening flaw geometry. Under the confining pressure of 8 MPa , there is an obvious finding that tensile-shear failure is the most common failure pattern in numerical samples. As Figure 8 shows, the minimum compressive strength is found in the numerical sample with $\beta = 60^\circ$, no matter what the width-to-length ratio (0.05 , 0.1 , or 0.2) is. When the inclination angle grows from 0° to 60° , the compressive strength becomes larger; however, the compressive strength decreases with the increase of inclination angle when $\beta > 60^\circ$. For samples with the same inclination angle, their compressive strength decreases as the width-to-length ratio of the opening flaw increases. These findings also can be illustrated by Eq. 9 and confirm that the geometrical parameter k has an important influence on the compressive strength of open-flawed rock mass.

Figure 9 shows the ultimate modes of cracks in the numerical samples under the confining stress of 8 MPa . It is worth noting that with the increase of inclination angle, anti-wing cracks gradually develop near the pre-existing flaw. Shear failure is not found in any specimen, and mode 1 is the main failure pattern of specimens when $\beta = 0^\circ$, while mode 5 is found in all the specimens with an inclination angle of 90° . When $k = 0.05$, the development of a through crack is the main reason for sample failure. When $k = 0.2$, only the samples with $\beta = 0^\circ$ are destroyed by a through crack, while the main failure pattern of other specimens is mode 5. Therefore, it can be assumed that increasing the inclination angle, together with increasing the width, both positively affect the shearing on the

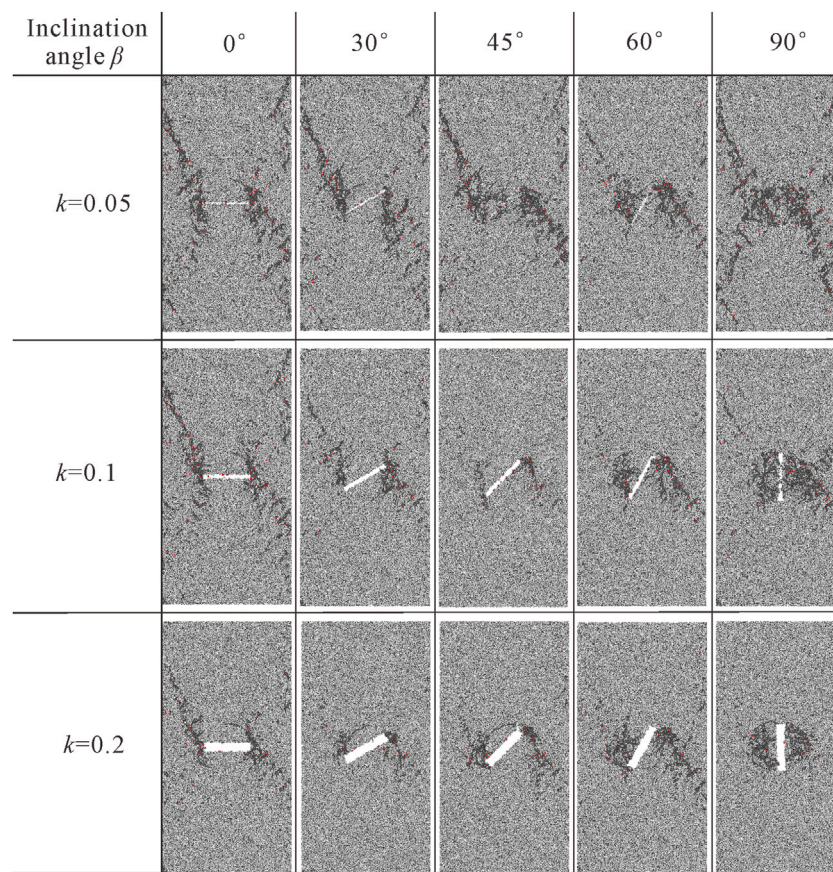


FIGURE 9

The ultimate failure modes of numerical samples with different width-to-length ratios and inclination angles.

flaw surface while the flaw's length is constant. Compared with others, the open flaw with an inclination angle of 90° is more susceptible to closure by the confining pressure, increasing its compressive strength.

4.2.2 Comparison of stress intensity factor

Without considering the influence of σ_T on the opening mode, the stress intensity factor of the opening mode is derived from the following equation. The improved effectiveness is investigated by ANSYS V19.2 in the finite element method. The material PLANE183 with eight nodes is used to deduct the singularity of the flaw tip, and details for meshing are demonstrated in Figure 10. The numerical model is a rectangle with a size of 108 mm \times 54 mm, and the length of the pre-existing flaw is 20 mm.

$$K_I' = \sigma_N \sqrt{\pi a} \quad (13)$$

The mechanical parameters in Table 1 are applied to the contact analysis procedure, such as coefficient of friction, elastic modulus, and Poisson's ratio. These two kinds of stress intensity

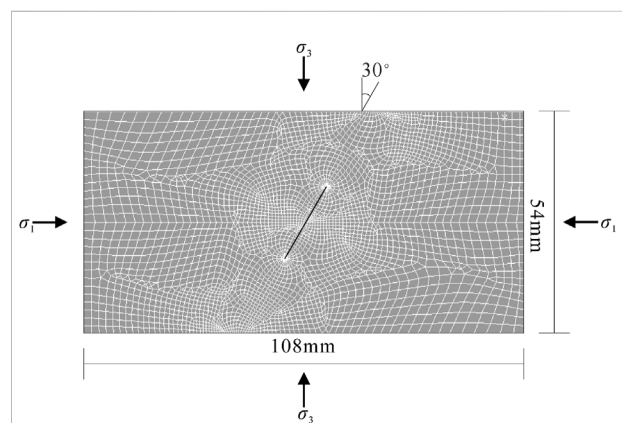


FIGURE 10

Meshing of the simulation model in ANSYS.

factors of open-flawed rock-like samples with different inclination angles are obtained in the method of interaction analysis at a confining pressure of 8 MPa in Table 5. The

TABLE 5 Values of stress intensity factors derived from different methods and relative error between them.

β (°)	Opening intensity factor K_I (MPa·m ^{-3/2})			Shear intensity factor K_{II} (MPa·m ^{-3/2})	
	Finite element method	Value of Eq. 13	Value of Eq. 6	Finite element method	Value of Eq. 3
0	6.90	6.94 (0.58%)	6.87 (0.43%)	0.00	0.00 (0.00)
30	5.43	5.55 (2.21%)	5.41 (0.37%)	2.39	2.38 (0.42%)
45	3.74	3.95 (5.61%)	3.75 (0.28%)	2.53	2.53 (0.00)
60	2.39	2.65 (10.88%)	2.39 (0.00)	2.14	2.15 (0.47%)
90	1.22	1.42 (16.39%)	1.05 (13.93%)	0.00	0.00 (0.00)

* Data in parentheses represent the absolute value of relative error between the analytical value calculated by different methods and the corresponding value.

opening fracture intensity factor K_I and the sliding fracture intensity factor K_{II} calculated from Eqs 6–13, respectively, are listed in Table 5. At present, the finite element method (FEM) is a mature method to calculate fracture mechanics of linear elastic material; therefore, the numerical results obtained by FEM are temporarily taken as true values, and the error analysis is carried out, respectively.

It can be seen from Table 5 that the value calculated based on Eq. 6 is closer to the numerical value of the opening fracture intensity factor K_I compared with Eq. 13, especially when the inclination angle is less than 90°. The sliding fracture intensity factor K_{II} calculated by the finite element method is very close to the one calculated by Eq. 6. It indicates that the improved fracture theory of opening flaw is workable and reliable. Therefore, the flaw's geometry is suggested to be considered as the influence factor of compressive strength of open-flawed rock mass, which makes the calculation more accurate.

5 Conclusion

A triaxial compressive test was carried out on rock-like specimens containing four parallel flaws, and nine crack modes and two failure patterns were found. The relationships between inclination angle and compressive strength and mechanical parameters, respectively, were summarized. Numerical biaxial tests were conducted to verify the reliability of the improved fracture theory of open-flawed rock mass.

- (1) Most cracks initiated during triaxial loading are tensile, and there is no failure pattern composed of pure shear cracks. One of the two failure patterns is tensile, and the other is tensile-shear with an equal frequency of occurrence. All samples with an inclination angle β of 90° are tensile failure patterns. For samples with $\beta = 0^\circ$, 30°, and 60°, shear cracks gradually appear, resulting in the tensile-shear failure at high confining stress.
- (2) Five modes of crack types are tensile, three modes are tensile-shear, and one is spalling surface. Mode 1 is the most

frequent crack type, but mode 8 is a special crack type that is mainly found in specimens with $\beta = 60^\circ$ at high confining pressure, where the lateral crack is shear initiating from the end of anti-wing tensile cracks. When confining stress σ_3 is 6 MPa, 8 MPa, and 10 MPa, the ratio of compressive strength σ_1 in samples with $\beta = 60^\circ$ is smaller than that of others, leading to the shear crack propagating along the lateral direction.

- (3) Both compressive strength and internal friction angle φ in samples with $\beta = 60^\circ$ are the smallest ones, and those of samples with $\beta = 90^\circ$ are the largest, which also is the closest to intact specimens, followed by those of samples with $\beta = 0^\circ$. However, the variation of inclination angle almost has no effect on the cohesion c of all samples.
- (4) Considering the influence of transverse compressive stress σ_T , an improved fracture theory of open-flawed rock is proposed, which takes the geometrical parameters of flaws into account. Based on the mechanical properties of the experimental material, the compressive strength of a flawed sample with $\beta = 65.31^\circ$ is the smallest according to theoretical equations. Moreover, when $0^\circ \leq \beta \leq 65.31^\circ$, the compressive strength decreases with the increase of inclination angle; however, the compressive strength increases when $65.31^\circ < \beta \leq 90^\circ$. This phenomenon is almost in accordance with the experimental results.
- (5) The compressive strength decrease as the width-to-length ratio of the opening flaw increases when the numerical biaxial compression test is performed using the discrete element method. The opening fracture intensity factor K_I calculated by the improved theory is closer to the numerical value obtained by the finite element method compared to that calculated by traditional theory.

Data availability statement

The raw data supporting the conclusion of this article will be made available by the authors, without undue reservation.

Author contributions

SS designed this research study. JW wrote the manuscript, led the data analysis, and interpreted the results. HL provided funding acquisition. Numerical analysis was guided by JW, HF, and WW. All authors contributed to manuscript revision and approved it for publication.

Funding

The research is funded by the Natural Science Foundation of China (Grant No. 42007256) and China's Postdoctoral Science Fund (No. 2021M690865) and supported by "The Fundamental Research Funds for the Central Universities" (No. B210201002).

References

- Alshoaibi, A. M. (2021). Numerical modeling of crack growth under mixed-mode loading. *Appl. Sci.* 11 (7), 2975. doi:10.3390/app11072975
- Bahaaddini, M., Sharrock, G., and Hebblewhite, B. K. (2013). Numerical investigation of the effect of joint geometrical parameters on the mechanical properties of a non-persistent jointed rock mass under uniaxial compression. *Comput. Geotechnics* 49, 206–225. doi:10.1016/j.compgeo.2012.10.012
- Bao, M., Chen, Z. H., Zhou, Z. H., Zhang, L. F., and Wang, J. M. (2021). Timeliness of collinear crack propagation in rock mass. *AIP Adv.* 11, 065120. doi:10.1063/5.0050868
- Bobet, A., and Einstein, H. H. (1998). Fracture coalescence in rock-type materials under uniaxial and biaxial compression. *Int. J. Rock Mech. Min. Sci.* 35, 863–888. doi:10.1016/S0148-9062(98)00005-9
- Camones, L. A. M., Vargas, E. D. A., Figueiredo, R. P., and Velloso, R. Q. (2013). Application of the discrete element method for modeling of rock crack propagation and coalescence in the step-path failure mechanism. *Eng. Geol.* 153, 80–94. doi:10.1016/j.enggeo.2012.11.013
- Cao, P., Liu, T. Y., Pu, C. Z., and Lin, H. (2015). Crack propagation and coalescence of brittle rock-like specimens with pre-existing cracks in compression. *Eng. Geol.* 187, 113–121. doi:10.1016/j.enggeo.2014.12.010
- Chen, M., Yang, S. Q., Ranjith, P. G., and Zhang, Y. C. (2020). Cracking behavior of rock containing non-persistent joints with various joints inclinations. *Theor. Appl. Fract. Mech.* 109, 102701–102717. doi:10.1016/j.tafmec.2020.102701
- Chenchen Huang, C. C., Yang, W. D., Duan, K., Fang, L. D., Wang, L., and Bo, C. J. (2019). Mechanical behaviors of the brittle rock-like specimens with multi-non-persistent joints under uniaxial compression. *Constr. Build. Mater.* 220, 426–443. doi:10.1016/j.conbuildmat.2019.05.159
- Cheng, Y., Jiao, Y. Y., and Tan, F. (2019). Numerical and experimental study on the cracking behavior of marble with en-echelon flaws. *Rock Mech. Rock Eng.* 52, 4319–4338. doi:10.1007/s00603-019-01849-x
- Cui, J., Jiang, Q., Li, S., Feng, X., Zhang, Y. L., and Shi, Y. E. (2020). Numerical study of anisotropic weakening mechanism and degree of non-persistent open joint set on rock strength with particle flow code. *KSCSE J. Civ. Eng.* 24, 988–1009. doi:10.1007/s12205-020-1482-3
- Fu, J. W., Chen, K., Zhu, W. S., Zhang, X. Z., and Li, X. J. (2016). Progressive failure of new modelling material with a single internal crack under biaxial compression and the 3-D numerical simulation. *Eng. Fract. Mech.* 165, 140–152. doi:10.1016/j.engfracmech.2016.08.002
- Guo, S. F., Qi, S. W., Zou, Y., and Zheng, B. (2017). Numerical studies on the failure process of heterogeneous brittle rocks or rock-like materials under uniaxial compression. *Materials* 10, 378–390. doi:10.3390/ma10040378
- Haeri, H., Sarfarazi, V., Ebneabbasi, P., Nazari maram, A., Shahbazian, A., Fatehi Marji, M., et al. (2020). XFEM and experimental simulation of failure mechanism of non-persistent joints in mortar under compression. *Constr. Build. Mater.* 236, 117500–117514. doi:10.1016/j.conbuildmat.2019.117500
- Huang, Y. H., and Yang, S. Q. (2018). Mechanical and cracking behavior of granite containing two coplanar flaws under conventional triaxial compression. *Int. J. Damage Mech.* 28, 590–610. doi:10.1177/1056789518780214
- Huang, Y. H., Yang, S. Q., and Zeng, W. (2016). Experimental and numerical study on loading rate effects of rock-like material specimens containing two unparallel fissures. *J. Central South Univ.* 23, 1474–1485. doi:10.1007/s11771-016-3200-3
- Le, H. L., Sun, S. R., and Wei, J. H. (2019a). Influence of types of grouting materials on compressive strength and crack behavior of rocklike specimens with single grout-infilled flaw under axial loads. *J. Mat. Civ. Eng.* 31, 1–6. doi:10.1061/(ASCE)MT.1943-5533.0002554
- Le, H. L., Sun, S. R., Xu, C. H., Li, L. Y., and Liu, Y. (2019b). Cracking behaviors and mechanical properties of rock-like specimens with two unparallel flaws under conventional triaxial compression. *Adv. Civ. Eng.* 2019, 1–15. doi:10.1155/2019/5849703
- Lee, H., and Jeon, S. (2011). An experimental and numerical study of fracture coalescence in pre-cracked specimens under uniaxial compression. *Int. J. Solids Struct.* 48, 979–999. doi:10.1016/j.ijsolstr.2010.12.001
- Mohammadnejad, M., Fukuda, D., Liu, H. Y., Dehkhoda, S., and Chan, A. (2019). GPGPU-parallelized 3D combined finite-discrete element modelling of rock fracture with adaptive contact activation approach. *Comput. Part. Mech.* 7, 849–867. doi:10.1007/s40571-019-00287-4
- Mu, L. L., and Zhang, Y. M. (2020). Cracking elements method with 6-node triangular element. *Finite Elem. Analysis Des.* 177, 103421–110355. doi:10.1016/j.fineld.2020.103421
- Muschelišvili, N. I. (1975). *Some basic problems of the mathematical theory of elasticity*. Leyden: Noordhoff International Publishing. doi:10.2307/2314307
- Peng, K., Wang, Y. Q., Zou, Q. L., Cheng, Y. Y., and Song, X. (2021). Experimental study of energy dissipation characteristics and crack coalescence modes of cracked sandstone under different cyclic loading paths. *Bull. Eng. Geol. Environ.* 80, 5881–5895. doi:10.1007/s10064-021-02290-7
- Ren, L., Xie, L. Z., and Ai, L. (2013). Preliminary study on strength of cracked rock specimen based on fracture mechanics. *Eng. Mech.* 30, 156–162. (in Chinese). doi:10.6052/j.issn.1000-4750.2011.07.0464
- Wan, W., Liu, J., Zhao, Y. L., and Fan, X. (2019). The effects of the rock bridge ligament angle and the confinement on crack coalescence in rock bridges: An experimental study and discrete element method. *Comptes Rendus Mécanique* 347, 490–503. doi:10.1016/j.crme.2018.12.006

Conflict of interest

The authors declare that the research was conducted in the absence of any commercial or financial relationships that could be construed as a potential conflict of interest.

Publisher's note

All claims expressed in this article are solely those of the authors and do not necessarily represent those of their affiliated organizations, or those of the publisher, the editors, and the reviewers. Any product that may be evaluated in this article, or claim that may be made by its manufacturer, is not guaranteed or endorsed by the publisher.

Wang, Y. X., Zhang, H., Lin, H., Zhao, Y. L., and Liu, Y. (2020). Fracture behaviour of central-flawed rock plate under uniaxial compression. *Theor. Appl. Fract. Mech.* 106, 102503–102518. doi:10.1016/j.tafmec.2020.102503

Wong, L. N. Y., and Einstein, H. H. (2009). Systematic evaluation of cracking behavior in specimens containing single flaws under uniaxial compression. *Int. J. Rock Mech. Min. Sci.* 46, 239–249. doi:10.1016/j.ijrmms.2008.03.006

Yan-Hua Huang, Y. H., Yang, S. Q., and Tian, W. L. (2019). Crack coalescence behavior of sandstone specimen containing two pre-existing flaws under different confining pressures. *Theor. Appl. Fract. Mech.* 99, 118–130. doi:10.1016/j.tafmec.2018.11.013

Yang, S. Q. (2011). Crack coalescence behavior of brittle sandstone samples containing two coplanar fissures in the process of deformation failure. *Eng. Fract. Mech.* 78, 3059–3081. doi:10.1016/j.engfracmech.2011.09.002

Yang, S. Q., and Jing, H. W. (2010). Strength failure and crack coalescence behavior of brittle sandstone samples containing a single fissure under uniaxial compression. *Int. J. Fract.* 168, 227–250. doi:10.1007/s10704-010-9576-4

Yao, W., Cai, Y. Y., Yu, J., Zhuo, J. F., Liu, S. Y., and Tu, B. X. (2019). Experimental and numerical study on mechanical and cracking behaviors of flawed granite under triaxial compression. *Measurement* 145, 573–582. doi:10.1016/j.measurement.2019.03.035

Zhou, Q. L. (1987). Compress shear fracture criterion of rock and its application. *Chin. J. Geotechnical Eng.* 9, 33–37. (in Chinese).



OPEN ACCESS

EDITED BY

Shuren Wang,
Henan Polytechnic University, China

REVIEWED BY

Zhijie Zhu,
Liaoning Technical University, China
Yingchun Li,
Dalian University of Technology, China

*CORRESPONDENCE

Yang Li,
liyancumtb@163.com

SPECIALTY SECTION

This article was submitted to
Geohazards and Georisks,
a section of the journal
Frontiers in Earth Science

RECEIVED 11 June 2022

ACCEPTED 22 July 2022

PUBLISHED 02 September 2022

CITATION

Ren Y, Li Y, Lei X, Ou X, Wang N, Li G and
Yang K (2022), Theoretical analysis of
the reasonable support capacity based
on voussoir beam structure for a given
load of the loose body under an
extremely close goaf.
Front. Earth Sci. 10:966660.
doi: 10.3389/feart.2022.966660

COPYRIGHT

© 2022 Ren, Li, Lei, Ou, Wang, Li and
Yang. This is an open-access article
distributed under the terms of the
[Creative Commons Attribution License
\(CC BY\)](https://creativecommons.org/licenses/by/4.0/). The use, distribution or
reproduction in other forums is
permitted, provided the original
author(s) and the copyright owner(s) are
credited and that the original
publication in this journal is cited, in
accordance with accepted academic
practice. No use, distribution or
reproduction is permitted which does
not comply with these terms.

Theoretical analysis of the reasonable support capacity based on voussoir beam structure for a given load of the loose body under an extremely close goaf

Yuqi Ren¹, Yang Li^{1*}, Xinghai Lei¹, Xiangji Ou¹, Nan Wang¹,
Guoshuai Li¹ and Kunpeng Yang²

¹School of Energy and Mining Engineering, China University of Mining and Technology-Beijing, Beijing, China, ²Beijing Tiandi Huatai Mining Management Co. Ltd, Beijing, China

Given the growing popularity of fully mechanized longwall mining, hydraulic shields have emerged as the most crucial pieces of equipment whose rated support capacities are a significant assurance for safe extraction of coal seams. Based on the extraction in the 1,692 panel of the No.9 coal seam in Qianjiaying coal mine, a detailed study of the reasonable shield support capacity under an extremely close goaf was conducted using field measurements, theoretical analyses, and system development. The results show that the ZY4800-13/32 shield employed in the 1,692 panel is unreasonable owing to its large surplus coefficient of support capacity and low support utilization rate. The voussoir beam structure is established for a given load of the loose body to calculate the shield support capacity when the lower coal seam is extracted under an extremely close goaf. The calculated shield support capacity required for the No.9 coal seam was 3,560.03 kN, so the rated support capacity should be 4,000 kN. A calculation and analysis scheme for the shield support capacity under the given load of loose body was developed using a GUI in Matlab, and this scheme was used to examine the influence degrees of the relevant parameters of the immediate roof, main roof, and loose body on the shield support capacity. The thickness of the main roof was found to have the greatest influence on the shield support capacity. Finally, presplitting the main roof was proposed as an effective method for controlling the breaking length and reducing the shield support capacity based on existing research.

KEYWORDS

shield support capacity, multiple coal seams, extremely close goaf, given load of the loose body, system development, influence degree

1 Introduction

As an important piece of equipment for controlling the ground pressure in the extraction of the coal seam, the hydraulic shield can effectively balance the roof pressure to ensure safe production. This means that the hydraulic shield must have a certain support capacity for the roof pressure (Stanislaw et al., 2016; Stanislaw et al., 2017; Cheng et al., 2018; Marcin and Stanislaw, 2019; Song et al., 2019; Sylwester et al., 2020). The maximum load capacity that a hydraulic shield can bear when acted upon by roof strata is called the rated support capacity, and the actual load capacity that the hydraulic shield can bear is referred to as its actual support capacity (Qian et al., 2010). During the first weighting or periodic weighting, the actual support capacity may exceed the rated support capacity, which can cause shield crushing and roof falling accidents that threaten the workers' safety. More seriously, the damage to the hydraulic shield can affect the normal production of the panel face. However, when the actual support capacity is less than 85% of the rated support capacity, the load utilization rate of the shield is considered to be low and unable to perform to its full potential. This means that the shield selection is unreasonable, resulting in increased cost per ton of coal. Therefore, determining the rated shield capacity is of great significance for the production of the panel face and even the coal mine (Li et al., 2021a).

At present, the main approaches used to determine the shield support capacity include the empirical estimation, on-site measurement, and voussoir beam structure analysis methods. In the empirical estimation method, the shield support capacity is approximately estimated by the product of 4–8 times of the mining height and bulk density. In the on-site measurement method, a large number of on-site measurement data, including roof-to-floor convergence and periodic weighting interval, are used to establish the initial, average, and final shield support capacities through regression and mathematical-statistical analyses. However, the movement of the roof strata must be considered when

determining the shield support capacity. Qian et al. (1996) and Cao et al. (1998) regarded the shield and surrounding rock as an organic whole and analyzed the coupling mechanism of the support and surrounding rock in detail. Wang et al. (2014) and Wang et al. (2015) established the binary criterion and argued that the shield support capacity should balance the roof load as well as maintain the stability of the coal wall. In addition, a new dynamic method to determine the shield support capacity was proposed using theoretical models and field measurements based on the first weighting of the support by the main roof. Wang et al. (2017) and Pang et al. (2020) analyzed the coupling relationship as well as control method for the strength, stiffness, and stability between the support and roof strata in the panel face based on coal seam extraction by the ultra-large-height mining method; a “two-factors” method for determining the shield support capacity was also proposed for ultra-large-height mining. Yan et al. (2011) and Yu et al. (2021) proposed a roof structure called the “short cantilever beam and hinged beam” structure using a new concept and discrimination method for the immediate roof and main roof in extraction by the large-height mining method; the calculation formula for the shield support capacity was also given. Zhang et al. (2021) analyzed the influence of the key stratum position on the shield support capacity for the large-height top-coal caving method. Kong et al. (2021) and Li et al. (2022) studied the roof structure and proposed improvement of the shield support capacity to avoid an unstable face-end roof.

Extant research on the shield support capacity is mostly focused on coal seam extraction using ultra-large- or large-height mining methods. However, there are few studies on the shield support capacity in the extraction of close multiple coal seams, especially those under an extremely close goaf. Studies on extraction of close multiple coal seams have investigated the stability and stress concentration of the pillar left in the goaf, reasonable position, and support scheme of the entry of the lower coal seam (Liu et al., 2016; Li et al., 2020; Sun et al., 2020; Zhang et al., 2020; Feng et al., 2021; Liu, 2013; Wu et al., 2022).

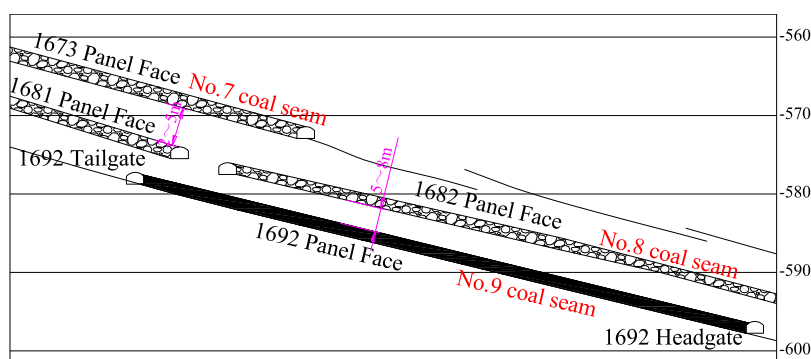


FIGURE 1
Distribution of the ultra-multiple coal seams.

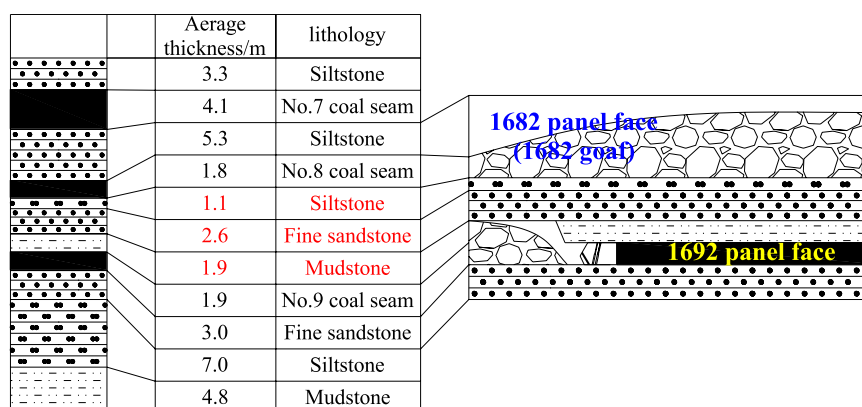


FIGURE 2

Column of rock mass and coal seam.

Generally, the shield support capacity in coal seam extraction includes the weight of the immediate and force generated by the movement of the blocks by breaking of the main roof. The movement of blocks formed by breaking of the main roof was often simplified to be caused by the uniformly distributed load on the blocks (Qian et al., 2010). However, under the extremely close goaf, the force on the blocks is no longer a uniformly distributed load.

Based on the above findings, a masonry beam structure with a given load of the loose body was proposed for coal seam extraction under an extremely close goaf according to the roof structure characteristics. The movement of blocks formed by breaking of the main roof was considered to be caused by the loose body of gangue in the upper goaf, which is arched. Furthermore, the shield support capacity was obtained by calculation. The rated support capacity in the No.9 coal seam in the Qianjiaying coal mine was calculated, and the rationality of the support selection was analyzed. At the same time, a calculation and analysis scheme of the shield support capacity under a given load of the loose body was developed to analyze the influence degrees of the related parameters of the immediate roof, main roof, and loose body.

2 Case overview

The Kailuan Coal Mine Group's Qianjiaying coal mine is a typical close multiple coal seam extraction mine, which is located in the Kaiping coalfield in Hebei Province, China. There are five minable coal seams distributed from the top to bottom within the 80 m coal-bearing strata, which are No.5, No.7, No.8, No.9, and No.12 coal seams. Among these, the vertical distance between the No.7, No.8, and No.9 coal seams is only 2–8 m, so these are typical ultra-close coal seams, as shown in Figure 1.

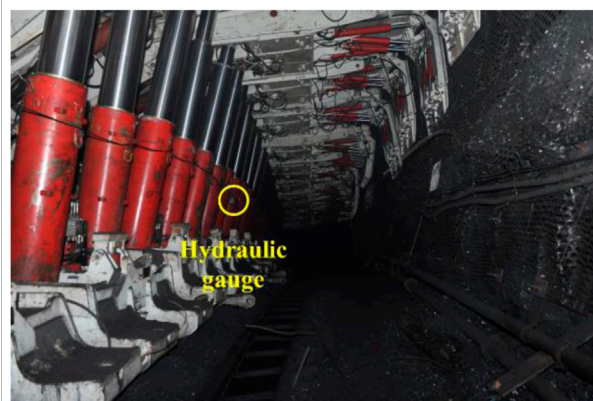


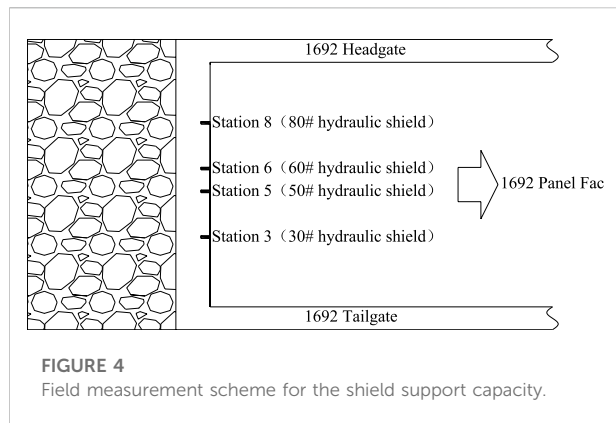
FIGURE 3

ZY4800-13/32 hydraulic shield.

At present, the 1,692 panel face is located in the No.6 district of the No.1 level; the No.9 coal seam is the main mining layer in the 1,692 panel face, with an average thickness of 1.9 m, average inclination angle of 17°, and average burial depth of 468.5–521.5 m. The fully mechanized coal mining method was adopted for this panel face, and the ZY4800-13/32 hydraulic shield was used to control the roof of the panel face. However, the 1,681 and 1,682 panel faces were extracted before the 1,692 panel extraction. The comprehensive column of coal and rock mass in the 1,692 panel is shown in Figure 2.

3 Field measurement of shield support capacity

The ZY4800-13/32 hydraulic shield was employed in the 1,692 panel face based on the production situation and support



selection experience, according to its user handbook, as shown in Figure 3. The rated and initial support capacities are 4,800 kN (39 MPa) and 3,877 kN (31.5 MPa), respectively.

3.1 Field measurement scheme

In the Qianjiaying coal mine, the inclined width of the 1,692 panel face is 160.8 m. From the tailgate to the headgate, there are a total of 107 hydraulic shields in the 1,692 panel face. As shown in Figure 4, a measuring station is arranged every 10 shields in the panel face for a total of 10 stations. The hydraulic

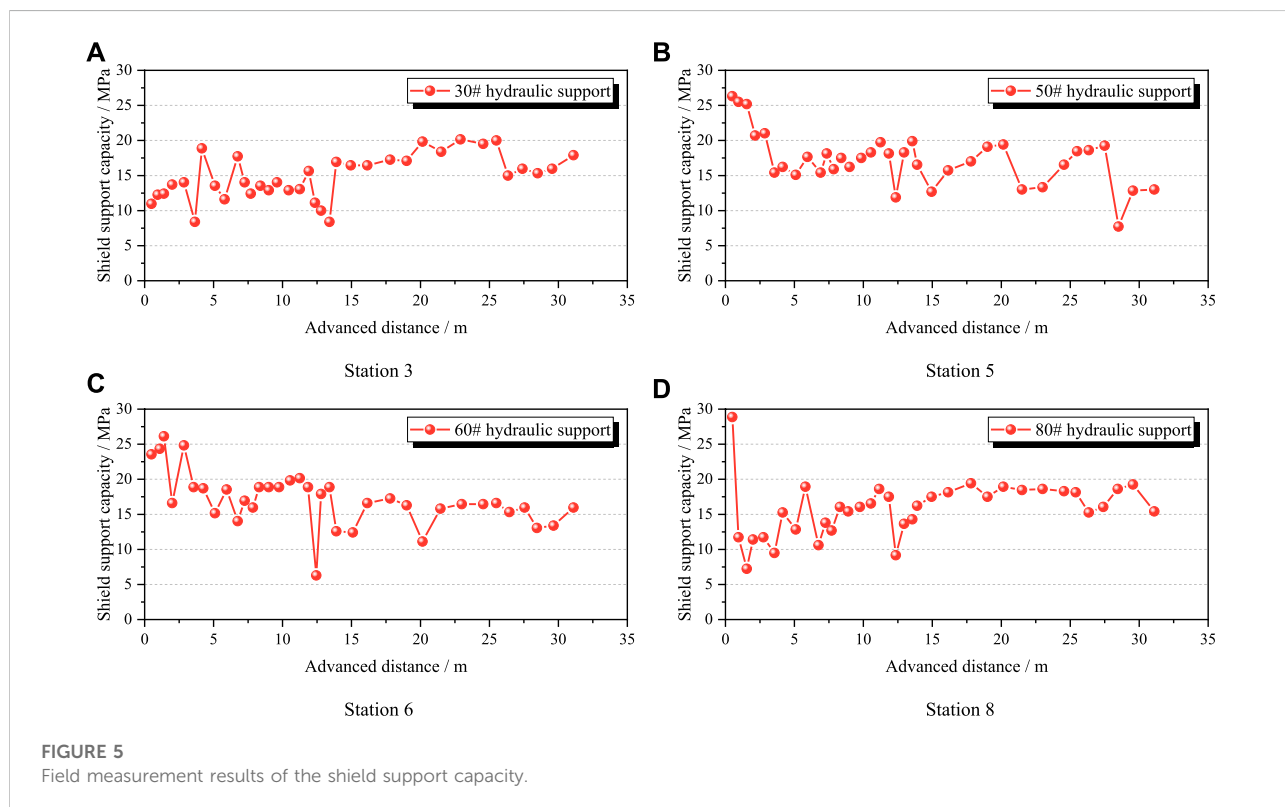
TABLE 1 Maximum, minimum, and average support capacities at each field measurement station.

Station	3	5	6	8	Average
Maximum support capacity/MPa	20.16	26.31	26.13	28.88	25.37
Minimum support capacity/MPa	8.39	7.72	6.29	7.24	7.41
Average support capacity/MPa	14.83	17.32	17.15	15.77	16.27

gauge readings of the left and right columns are recorded through the pressure gages installed on the columns. The average value between the left and right column readings is taken as the actual shield support capacity from field measurements.

3.2 Field measurement results

Figure 5 shows the field measurement results of the shield support capacities at stations 3, 5, 6, and 8. During the field measurements, the 1,692 panel face advanced by a total of 32 m. Table 1 presents the analysis results of the shield support capacity at each station. It is seen from Table 1 that the overall trend of variation of the shield support capacity is similar for each station. The average support capacity measured for the panel face was 16.27 MPa, which is 41.72% of the rated support capacity. During periodic weighting, the



maximum support capacity measured was 28.88 MPa, which was 73.85% of the rated support capacity. Therefore, the shield support capacity was generally low (less than 80%). The overall shield support capacity measured for the panel face was thus 6.29–28.88 MPa, with the shield load utilization rate being 16.13–73.85%, indicating a large surplus coefficient of support capacity and low support utilization rate by the 1,692 panel face. Based on the combination of coal mine production situation and shield selection experience, the shield load utilization rate of the ZY4800-13/32 hydraulic shield is not high, which means that the shield selection is unreasonable and can be optimized.

4 Calculation of shield support capacity

The interactions between the shield and roof strata are the bases of not only ground control but also roof stability testing. At the same time, they provide a reference for reasonable shield selection. Based on the observed results from the 1,692 panel face in the No.9 coal seam using ground penetrating radar and borehole television (Li et al., 2019; Li et al., 2021b; Li et al., 2021c), the roof structure model after coal seam extraction under an extremely close goaf is established. Further, the reasonable shield support capacity for coal seam extraction under an extremely close goaf is calculated.

4.1 Voussoir beam structure with given load of the loose body

The No.9 coal seam is extracted after the No.8 seam; the primary fissures in the roof strata of the No.9 coal seam are relatively developed but have good continuity and integrity. After extraction of the No.8 coal seam, its roof strata break and collapse into the gangue, which is then compacted in the goaf above the roof strata of the No.9 coal seam owing to its weight and loose body state (Li et al., 2008; Zhu et al., 2010). However, with the advancement of the panel face, the roof strata of the No.9 coal seam reach the limit span and may periodically break into rock blocks. The immediate roof of the No.9 coal seam breaks and collapses in the goaf, and the main roof of the No.9 coal seam breaks into articulated blocks; these articulated blocks generated by breaking of the main roof form a stable balance structure called the voussoir beam structure that bears the gangue in the goaf of the No.8 coal seam (Qian et al., 2010), as shown in Figure 6.

From Figure 6, the interactions between the hydraulic shield and roof strata include the support, cantilever beam of the immediate roof, voussoir beam of the main roof, and the load of the loose body. Therefore, coal seam extraction under an

extremely close goaf constitutes the articulated balance structure model of a voussoir beam with a given load of the loose body. The support capacity (P) mainly includes the weight of the immediate roof at the maximum control distance of the shield (Q_1) and force acting on the shield when the blocks of the voussoir beam are formed by the main roof slip instability (F), as shown in Eq. 1.

$$P = Q_1 + F. \quad (1)$$

In contrast to the conventional methods of estimating the load generated on the blocks by the breaking of the main roof, this study proposes using a given load of the loose body to estimate the load on the blocks; this means that the load is caused by the gangue above the blocks, which is different from the load applied by the intact strata. The load applied to the main roof by the intact strata (q_0) can be calculated using Eq. 2.

$$q_0 = \frac{E_1 h_1^3 \left(\sum_{i=1}^n \gamma_i h_i \right)}{\sum_{i=1}^n E_i h_i^3}, \quad (2)$$

where E_i is the elastic modulus of the i th main roof; γ_i is the bulk density of the i th stratum, kN/m^3 ; h_i is the thickness of the i th stratum, m.

4.2 Weight of the immediate roof (Q_1)

The weight of the immediate roof at the maximum control distance of the shield (Q_1) is calculated using Eq. 3.

$$Q_1 = \gamma_1 \times h_1 \times l_1, \quad (3)$$

where γ_1 is the bulk density of the immediate roof, kN/m^3 ; h_1 is the thickness of the immediate roof, m; l_1 is the length of the immediate roof, m, which can be calculated using Eq. 4.

$$l_1 = l_{k\max} \times K_f, \quad (4)$$

where $l_{k\max}$ is the maximum control distance of the shield, m; K_f is the allowance coefficient.

4.3 Force acting on the shield when the blocks of the voussoir beam are formed by the main roof slip instability (F)

The force acting on the support shield when the blocks of the voussoir beam are formed by the main roof slip instability mainly include the weight of the blocks, load on the blocks, and friction force of the sliding instability between the blocks. Based on the voussoir beam structure, the force acting on the support when the blocks of the beam are formed by the main roof slip instability is calculated using Eq. 5.

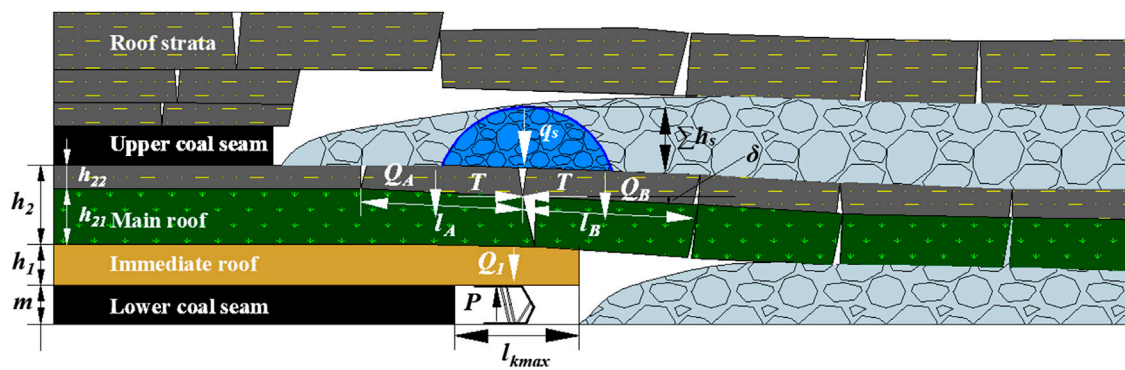


FIGURE 6
Roof structure characteristics after coal seam extraction.

$$\left\{ \begin{array}{l} F = Q_{A+B} - \frac{l_B \cdot Q_B}{2(h_B - \delta)} \tan(\varphi - \theta) \\ Q_{A+B} = Q_A + Q_B \\ Q_A = \gamma_A \times h_A \times l_A + P_s \\ Q_B = \gamma_B \times h_B \times l_B + P_s \\ \delta = h_B + m - K_p h_1 \\ \theta = \arctan \frac{\delta}{l_B} \end{array} \right. , \quad (5)$$

where Q_{A+B} includes the weight and load of rock blocks A and B, kN; l_A and l_B are the respective lengths of rock blocks A and B, m; Q_A and Q_B are the respective weight and load of rock blocks A and B, kN; h_A and h_B are the respective thicknesses of rock blocks A and B, which also constitute the thickness of the main roof, m; P_s is the given load on the rock blocks A and B, kN; δ is the subsidence of rock block B, m; m is the thickness of the coal seam, m; K_p is the bulk factor; φ is the internal friction angle of rock blocks A and B, °; θ is the breaking angle of rock blocks A and B, °.

For the thin strata between the upper and lower coal seams (such as the siltstone stratum above the No.9 coal seam), the breaking length can be simplified on the basis of the following reasons. On the one hand, these may be the immediate floor of the upper coal seam, and fissures may develop owing to extraction of the upper coal seam. On the other hand, their thickness and strength may be less than those of the hard strata above the lower coal seam (such as the fine sandstone stratum of the main roof of the No.9 coal seam); thus, the breaking length of the thin strata would be the same as that of the thick strata ideally. The breaking lengths of rock blocks A and B generated by breaking of the main roof can be calculated using Eq. 6, which is the general equation for calculating the periodic weighting of the main roof.

$$l_A = l_B = l_2 = h_2 \sqrt{\frac{R_{t2}}{3q}} \quad (6)$$

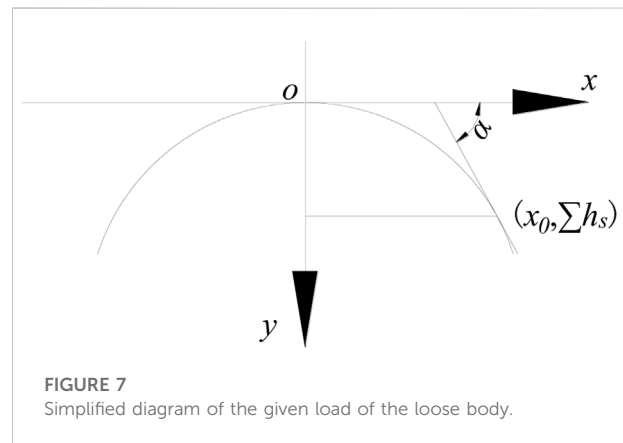


FIGURE 7
Simplified diagram of the given load of the loose body.

where l_2 is the periodic weighting interval of the main roof, m; h_2 is the thickness of the main roof, m; R_{t2} is the tensile strength of the main roof, kPa; q is the weight of the main roof, kPa.

The given load on the rock blocks A and B (P_s) can be calculated using Eqs. 7–13. After extraction of the upper coal seam, its roof strata break and collapse into the gangue, which may then be compacted in the goaf above the roof strata of the lower coal seam owing to its weight and loose body state. Above the roof strata of the lower coal seam, the collapsed gangue in the goaf of the upper coal seam is compacted and forms a parabolic loose body structure (Li et al., 2008; Zhu et al., 2010). The loads on rock blocks A and B generated by the breaking of the main roof are considered as the weight of the loose body. The shape of the loose body is simplified ideally as the parabolic shape of a loose arch. Figure 7 shows the simplified diagram of the given load of the loose body.

The tangent inclination at point $(x_0, \sum h_s)$ is assumed to be nearly equal to the natural repose angle (α) of the loose body structure. Then, the parabola's equation is assumed as

$$y = ax^2. \quad (7)$$

At the point $(x_0, \sum h_s)$, Eq. 7 becomes Eq. 8.

$$\sum h_s = ax_0^2. \quad (8)$$

At $x = x_0$, the derivative of Eq. 8 is

$$\tan \alpha = y'|_{x=x_0} = 2ax_0. \quad (9)$$

Hence,

$$a = \frac{\tan^2 \alpha}{4\sum h_s}. \quad (10)$$

Considering safety, a correction factor K_s is added such that Eq. 7 becomes

$$y = K_s \frac{\tan^2 \alpha}{4\sum h_s} x^2. \quad (11)$$

The area of the parabolically shaped loose body structure (S) is obtained as

$$S = 2 \left(\sum h_s \frac{l_s}{2} - \int_0^{\frac{l_s}{2}} K_s \frac{\tan^2 \alpha}{4\sum h_s} x^2 dx \right) = \sum h_s \cdot l_s - \frac{1}{48} K_s \frac{\tan^2 \alpha}{\sum h_s} l_s^3. \quad (12)$$

The given load for the parabolic shape of the loose body structure (P_s) is then

$$P_s = \left(\sum h_s \cdot l_s - \frac{1}{48} K_s \frac{\tan^2 \alpha}{\sum h_s} l_s^3 \right) \gamma_s, \quad (13)$$

where $\sum h_s$ is the height of the loose body structure, m; l_s is the span of the loose body structure, m; K_s is the correction factor; α is the natural repose angle of the loose body structure, °; γ_s is the bulk density of the loose body structure, kN/m³.

4.4 Calculation result

Through analyses of the geological and observed data from the 1,692 panel face of the Qianjiaying coal mine, the thickness (h_1) and bulk density (γ_1) of the immediate roof are 1.9 m and 22 kN/m³, respectively; the thickness (h_{21}), bulk density (γ_{21}), and tensile strength (R_{t21}) of the main roof are 2.6 m, 24 kN/m³, and 4.8 MPa, respectively; the thickness (h_{22}), bulk density (γ_{22}), and tensile strength (R_{t22}) of the siltstone above the main roof are 1.1 m, 24 kN/m³, and 5.2 MPa, respectively. The lengths (l_2) of siltstone and main roof are the same as the periodic weighting interval of the main roof, which is calculated to be 13.17 m. The internal friction angle (φ) between the blocks generated by the main roof is 28°. The maximum control distance of the shield (l_{kmax}) and allowance coefficient (K_f) are 5.1 m and 1.5, respectively. Thus, the length of the immediate roof (l_1) is calculated to be 7.65 m.

For the loose body of the collapsed and compacted gangue, the height ($\sum h_s$), span (l_s), natural repose angle (α), bulk density (γ_s), and correction factor (K_s) are 5.83 m, 13.17 m, 20°, 20 kN/m³, and 1.1, respectively.

The shield support capacity per unit area for the No.9 coal seam extraction is 2,637.06 kN after applying the above parameters to Eqs. 1–13. Considering the width of the shield as 1.5 m and load utilization coefficient as 0.9, the theoretically calculated result of the rated support capacity is 3,560.03 kN for extraction of the No.9 coal seam. Therefore, by taking the surplus into account, a shield with a rated support capacity of 4,000 kN (32.5 MPa) can be selected to meet the safety production requirements. The shield load utilization rate may then improve to 19.35–88.86% when combined with the field measurement data. The shield load utilization rate of the support is thus greatly improved, with a maximum value of 90%. In summary, the ZY4800-13/32 shield support employed in the 1,692 panel face is unreasonable in that its rated support capacity is too large.

5 Analysis of factors influencing the shield support capacity

From theoretical analysis, it is seen that the shield support capacity mainly bears the weight of the immediate roof at the maximum control distance of the shield as well as the force acting on the shield when the blocks of the voussoir beam are formed by the main roof slip instability. Based on the theoretical calculation equation, a calculation and analysis scheme of the shield support capacity under the given load of the loose body was developed to investigate the influences of the related parameters, including the immediate roof, main roof, and loose body, on the shield support capacity.

5.1 Development of calculation and analysis scheme

From the derived equation, a calculation and analysis scheme of the shield support capacity under the given load of the loose body is developed using the GUI features of Matlab. The proposed scheme mainly consists of three interfaces, namely cover, calculation, and analysis, and has two functions for calculation and analysis of the shield support capacity, as shown in Figure 8. The shield support capacity calculation is simplified, and dynamic data calculation is achieved by the system. In addition, the shield support capacity calculation efficiency is enhanced. The developed scheme effectively guides determination of the shield support capacity during mining production and constitutes a first attempt at an intelligent shield selection construction.



FIGURE 8 Calculation and analysis scheme of the shield support capacity under a given load of the loose body.

5.2 Analysis and discussion

5.2.1 Influences of related parameters of the immediate roof

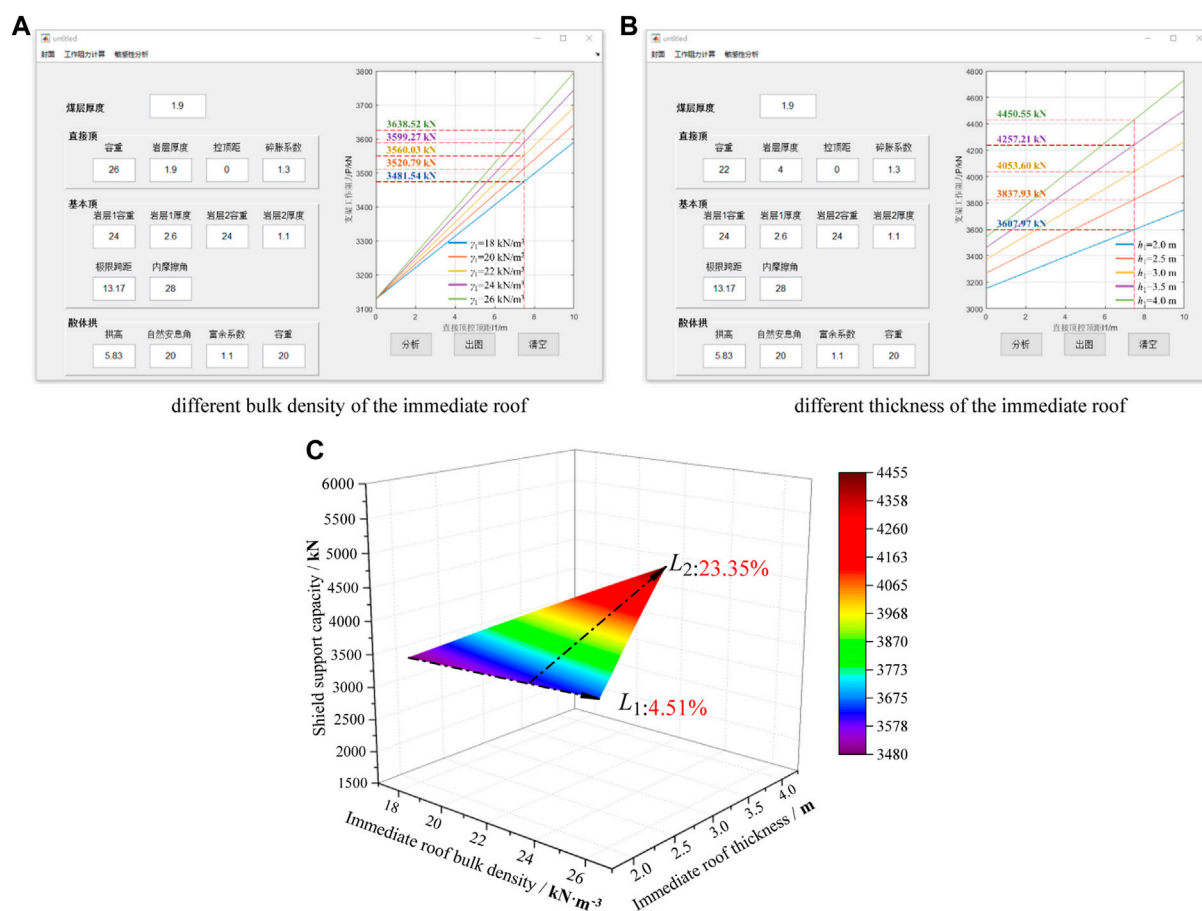
Figure 9 shows the influences of the bulk density, thickness, and control distance of the immediate roof on the shield support capacity when the parameters of the main roof and loose body are constant. From Figures 9A,B, the shield support capacity is seen to increase as the control distance of the immediate roof increases. Generally, the control distance of the immediate roof is related to the length of the shield top beam. The weight of the immediate roof within the control distance increases as the shield top beam length increases. Therefore, it is necessary to determine a reasonable length of the shield top beam during the shield design process to fully utilize the shield support characteristics.

From Figures 9A,B, the shield support capacity is observed to increase with increase in the bulk density and thickness of the immediate roof when its control distance remains constant. However, the bulk density and thickness of the immediate roof have different effects on the shield support capacity, as seen from Figure 9C. When the bulk density of the immediate roof increases from 18 to 26 kN/m³, the shield support capacity

increases from 3,481.54 to 3,638.52 kN, which is a 4.51% increase, as shown by L_1 in Figure 9C. When the thickness of the immediate roof increases from 2 to 4 m, the shield support capacity increases from 3,607.97 to 4,450.55 kN, which is a 23.35% increase, as shown by L_2 in Figure 9C. Obviously, the growth rate of L_1 is less than that of L_2 , i.e., the slope of L_1 is less than that of L_2 . Hence, the thickness of the immediate roof has a greater influence on the shield support capacity than the bulk density.

5.2.2 Influences of related parameters of the main roof

Figure 10 shows the influences of the bulk density, thickness, and limit span of the main roof on the shield support capacity when the parameters of the immediate roof and loose body are constant. From Figures 10A,B, the shield support capacity is seen to increase first and then decrease as the limit span of the main roof increases. Generally, the limit span of the main roof is its periodic weighting interval. From Figure 10A, the limit span of the main roof corresponding to the maximum shield support capacity is observed to be about 10 m where the main roof breaks because of the roof cutting effect of the shield. At this time, the load on the main roof also increases, resulting in accidents, such



Influence of bulk density and thickness of the immediate roof on shield support capacity

FIGURE 9

Relationship between related parameters of the immediate roof and shield support capacity.

as shield crushing due to ground pressure behaviors over a large area of the roof. The overburden lithology of coal-bearing strata is determined once it is formed; hence, the thickness of the main roof may change in the strike or tendency of the coal seam. According to Eq. 6, the greater the thickness of the main roof, the greater is its limit span and greater are the blocks generated by breaking of the main roof. Overall, some measures can be adopted to minimize the limit span of the main roof and reduce the chances of accidents by shield crushing, such as presplitting of the hard and thick roof (Wang et al., 2013; Huang et al., 2018; Liu et al., 2019; Chen et al., 2021; Xing et al., 2021).

From Figures 10A,B, the shield support capacity is observed to increase with increases in the bulk density and thickness of the main roof when its limit span remains constant. However, the bulk density and thickness of the main roof have different effects on the shield support capacity, as shown in Figure 10C. When the bulk density of the main roof increases from 18 to 26 kN/m³, the

shield support capacity increases from 3,320.33 to 3,639.93 kN, which is a 9.63% increase, as shown by L_3 in Figure 10C. When the thickness of the main roof increases from 2 to 4 m, the shield support capacity increases from 2,043.69 to 5,855.00 kN, which is an increase of 180.49%, as shown by L_4 in Figure 10C. Obviously, the growth rate of L_3 is less than that of L_4 , i.e., the slope of L_3 is less than that of L_4 . Hence, the thickness of the main roof has a greater influence on the shield support capacity than the bulk density.

5.2.3 Influences of related parameters of the loose body

Figure 11 shows the influences of the bulk density, height, and natural repose angle of the loose body on the shield support capacity when the parameters of the immediate roof and main roof are constant. From Figures 11A,B, the shield support capacity is seen to decrease as the natural repose angle of the loose body increases and increase as the bulk density and height

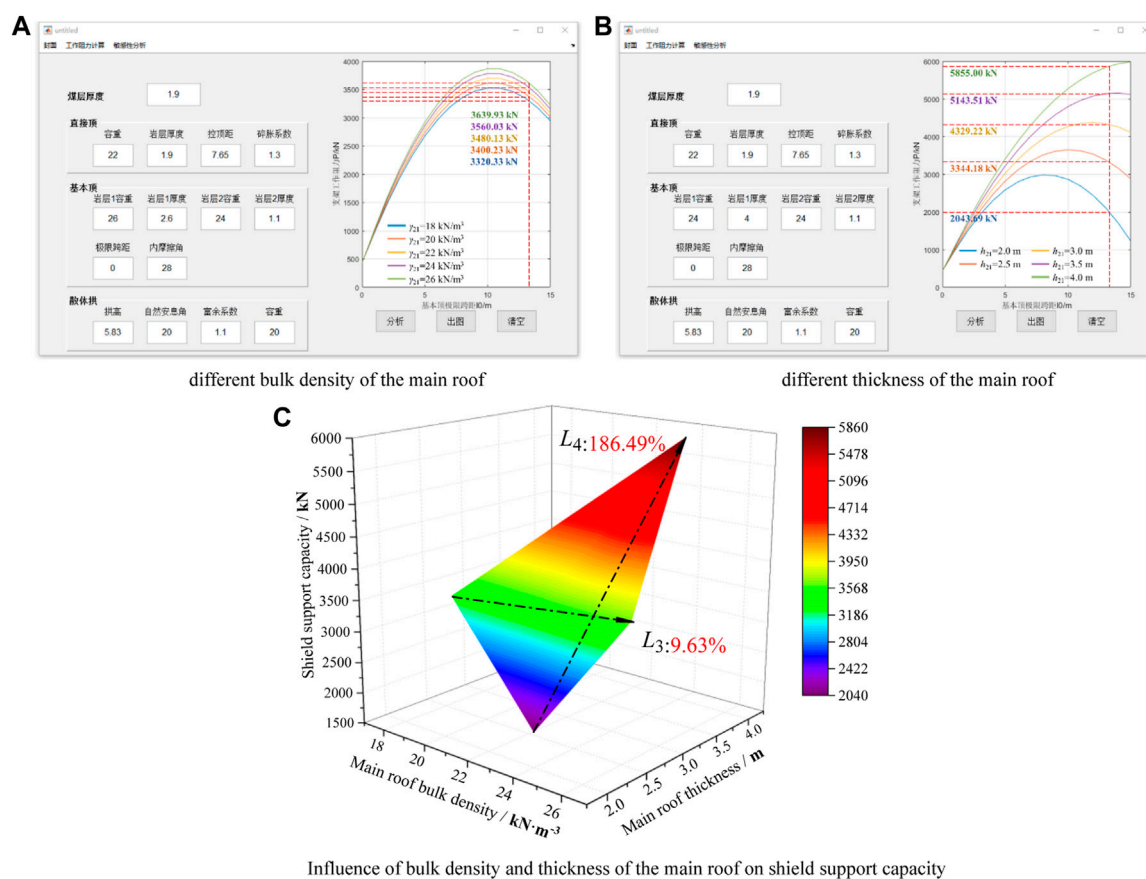


FIGURE 10

Relationship between related parameters of the main roof and shield support capacity.

of the loose body increase. Generally, the natural repose angle, bulk density, and height of the loose body formed by the collapsed gangue accumulation in the goaf after extraction of the upper coal seam are related to pressure. When the collapsed gangue in the goaf is gradually compacted under the action of the self-weight and roof load, the natural repose angle and height of the loose body decrease while the bulk density increases.

From Figures 11A,B, the shield support capacity is observed to increase with increasing bulk density and height of the loose body when the natural repose angle remains constant. However, the bulk density and height of the loose body have different effects on the shield support capacity, as shown in Figure 11C. When the bulk density of the loose body increases from 18 to 26 kN/m³, the shield support capacity increases from 3,383.64 to 4,089.19 kN, which is a 20.85% increase, as shown by L_5 in Figure 11C. When the height of the loose body increases from 5 to 7 m, the shield support capacity increases from 3,300.35 to 3,924.22 kN, which is an increase of 18.90%, as shown by L_6 in Figure 11C. Obviously, the growth rate of L_5 is greater than that of L_6 , i.e., the slope of L_5 is greater than that of L_6 . Hence, the bulk

density of the loose body has a greater influence on the shield support capacity than the height.

5.2.4 Discussion

Figure 12 shows the increasing percentage of shield support capacity when the relevant parameters of the immediate roof, main roof, and loose body are changed. It is assumed that the thickness of the main roof significantly influences the shield support capacity when only one parameter is changed and the other parameters are constant. During the initial stage of coal seam extraction under the goaf, the main roof between the goaf and lower coal seam will not break and collapse; as the extraction progresses, the main roof reaches the limit span and breaks into articulated blocks, forming the voussoir beam structure. On the one hand, the hydraulic shield for coal seam extraction under the goaf will bear the self-weight and load on the rock blocks generated by breaking of the main roof. On the other hand, the shield will bear the force of the sliding and instability of the rock blocks. It can be seen from Eqs. 1, 3, and 5 that increasing the thickness of the main roof increases the breaking length. Therefore, the two forces acting on the hydraulic support will also increase, which

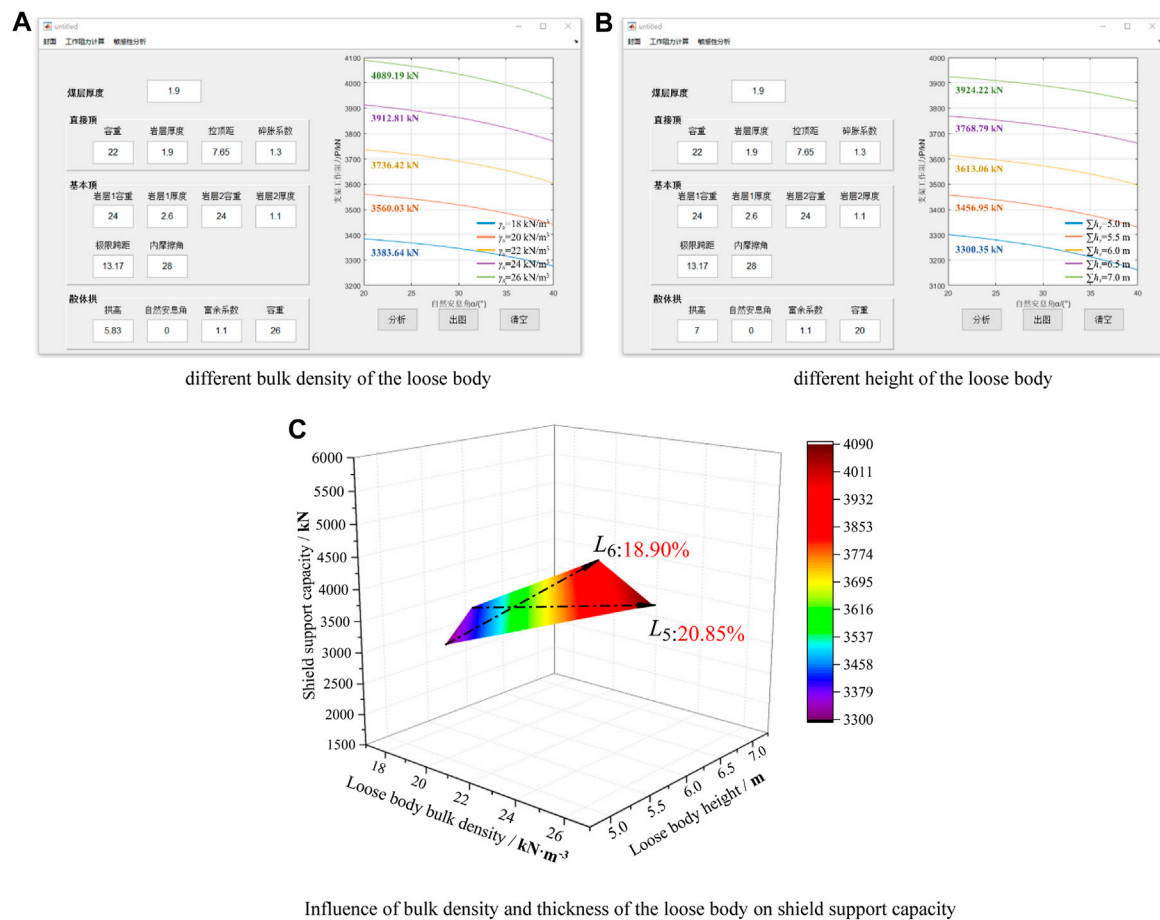


FIGURE 11

Relationship between related parameters of the loose body and shield support capacity.

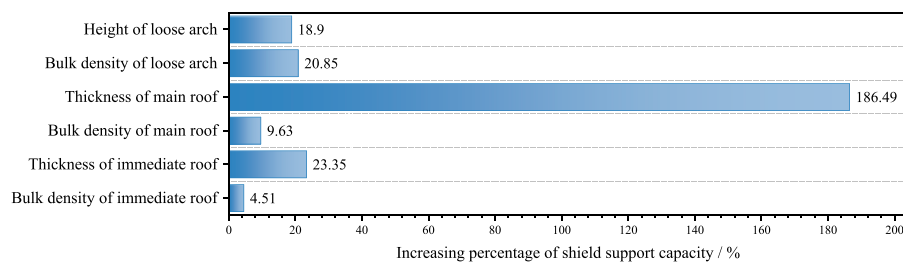


FIGURE 12

Influence degrees of various factors on the shield support capacity.

may cause shield crushing owing to ground pressure behaviors over a large area of the roof. In general, to avoid the occurrences of strong ground pressure behaviors in the panel face from excessive thickness of the main roof, scholars have increasingly conducted research in this field, such as presplitting of the sandstone in the main roof of the

Zhangji North coal mine (Ren et al., 2020), deep hole-shaped charge blasting of the hard roof in the Songshuzhen coal mine (Guo et al., 2013), far-field ground fracturing and near-field pressure blasting of the Jurassic and carboniferous coal seam extractions in the Datong mining area (Yu et al., 2019).

6 Conclusion

- 1) Through field measurement and analysis of the shield support capacity of the 1,692 panel face in the No.9 coal seam in the Qianjiaying coal mine, the existing shield selection was determined to be unreasonable. The ZY4800-13/32 shield employed in the 1,692 panel face was calculated to have a large surplus coefficient of the support capacity as well as low support utilization rate.
- 2) Based on extraction of the No.9 coal seam under an extremely close goaf after extraction of the No.8 coal seam, the voussoir beam structure with a given load of the loose body was established to calculate the shield support capacity. The shield support capacity for the No.9 coal seam was determined as 3,560.03 kN, so a rated support capacity of 4,000 kN should be selected to meet the requirements of production safety.
- 3) A GUI-based calculation and analysis scheme was developed using Matlab for the shield support capacity under the given load of the loose body. This scheme achieved both dynamic data calculation and improved calculation efficiency of the shield support capacity. The relationship between the support and roof strata was also analyzed visually.
- 4) Using the proposed calculation and analysis scheme, the influence degrees of the relevant parameters of the immediate roof, main roof, and loose body on the shield support capacity were examined. The thickness of the main roof had the greatest influence of approximately 186.49% increase on the shield support capacity. An increase in the thickness of the main roof resulted in an increase in the breaking length of the main roof; presplitting of the main roof was thus considered to be an effective method of controlling the breaking length to avoid shield crushing due to ground pressure behaviors over a large area of the roof when the load on the shield exceeded the rated support capacity.

Data availability statement

The original contributions presented in the study are included in the article/Supplementary Material, and further inquiries can be directed to the corresponding author.

References

- Cao, S., Qian, M., Liu, C., and Miao, X. (1998). New Research about Support and Surrounding Rock Relationship in Working Face. *J. China Coal Soc.* 23 (6), 575–579.
- Chen, B., Liu, C., and Wang, B. (2021). A Case Study of the Periodic Fracture Control of a Thick-Hard Roof Based on Deep-Hole Pre-splitting Blasting. *Energy Explor. Exploitation*, 1–23. doi:10.1177/01445987211036245
- Cheng, J., Wan, Z., and Ji, Y. (2018). Shield-roof Interaction in Longwall Panels: Insights from Field Data and Their Application to Ground Control. *Adv. Civ. Eng.* 2018, 1–18. doi:10.1155/2018/3031714
- Feng, G., Wang, S., Guo, Y., Zhang, Y., Bai, J., Niu, L., et al. (2021). Optimum Position of Roadway in the Middle Residual Coal Seam between the Upper and Lower Longwall Gobs. *Environ. Sci. Technol.* 55, 1–18. doi:10.1080/15567036.2021.1897709
- Guo, D., Shang, D., Lv, P., Wang, S., and Wang, J. (2013). Experimental Research of Deep-Hole Cumulative Blasting in Hard Roof Weakening. *J. China Coal Soc.* 38 (7), 1149–1153. doi:10.13225/j.cnki.jccs.2013.07.021
- Huang, B., Cheng, Q., Zhao, X., Xue, W., and Malcolm, S. (2018). Using Hydraulic Fracturing to Control Caving of the Hanging Roof during the Initial Mining Stages in a Longwall Coal Mine: a Case Study. *Arab. J. Geosci.* 11 (20), 603. doi:10.1007/s12517-018-3969-5
- Kong, D., Qiang, Li, Wu, G., and Song, G. (2021). Characteristics and Control Technology of Face-End Roof Leaks Subjected to Repeated Mining in Close-

Author contributions

Conceptualization: YL; data curation: YR, XO, and KY; formal analysis: YR and XO; funding acquisition: YL; investigation: YR, XL, NW, and GL; methodology: YL and YR; system: YR and XO; writing—original draft: YR.

Funding

This research was supported by the National Natural Science Foundation of China (No. 52074293) and the Natural Science Foundation of Hebei Province, China (No. E2020402041).

Acknowledgments

The authors acknowledge the above funds for supporting this research and editors and reviewers for their comments and suggestions.

Conflict of interest

Author KY is employed by Beijing Tiandi Huatai Mining Management Co., Ltd.

The remaining authors declare that the research was conducted in the absence of any commercial or financial relationships that could be construed as a potential conflict of interest.

Publisher's note

All claims expressed in this article are solely those of the authors and do not necessarily represent those of their affiliated organizations, or those of the publisher, the editors, and the reviewers. Any product that may be evaluated in this article or claim that may be made by its manufacturer is not guaranteed or endorsed by the publisher.

Distance Coal Seams. *Bull. Eng. Geol. Environ.* 80, 8363–8383. doi:10.1007/s10064-021-02438-5

Li, H., Liu, C., and Wang, L. (2008). Generating and Destabilization Evolutionary of Granular Arch Structure of Upper Immediate Roof. *J. China Coal Soc.* 33 (4), 378–381.

Li, X., He, W., and Xu, Z. (2020). Study on Law of Overlying Strata Breakage and Migration in Downward Mining of Extremely Close Coal Seams by Physical Similarity Simulation. *Adv. Civ. Eng.*, 1–9 doi:10.1155/2020/2898971

Li, Y., Ren, Y., Wang, N., Luo, J., Li, N., Liu, Y., et al. (2021a). A Novel Mining Method for Longwall Panel Face Passing through Parallel Abandoned Roadways. *Shock Vib.* 2021, 1–10. doi:10.1155/2021/9998561

Li, Y., Ren, Y., Peng, S. S., Cheng, H., Wang, N., and Luo, J. (2021b). Measurement of Overburden Failure Zones in Close-Multiple Coal Seams Mining. *Int. J. Min. Sci. Technol.* 31 (8), 43–50. doi:10.1016/j.ijmst.2020.12.009

Li, Y., Ren, Y., Wang, N., Jin, X., Ou, X., Luo, J., et al. (2021c). Structure Form and Evolution Characteristics of Collapsed Roof in Goaf. *J. China Coal Soc.* 46 (12), 3771–3780. doi:10.13225/j.cnki.jccs.2021.0272

Li, Y., Wang, J., Chen, Y., Wang, Z., and Wang, J. (2019). Overlying Strata Movement with Ground Penetrating Radar Detection in Close-Multiple Coal Seams Mining. *Int. J. Distributed Sens. Netw.* 15 (8), 155014771986985. doi:10.1177/1550147719869852

Liu, A. (2013). Research on Reasonable Position of Roadway for Close Multi-Seam and its Application. *Adv. Mat. Res.* 807–809, 2393–2397. doi:10.4028/www.scientific.net/amr.807-809.2393

Liu, H., Jin, D., Jiang, J., Wang, P., and Yang, J. (2019). Analysis of Overburden Structure and Pressure-Relief Effect of Hard Roof Blasting and Cutting. *Adv. Civ. Eng.*, 2019, 1–14. doi:10.1155/2019/1354652

Liu, X., Li, X., and Pan, W. (2016). Analysis on the Floor Stress Distribution and Roadway Position in the Close Distance Coal Seams. *Arab. J. Geosci.* 9 (2), 83. doi:10.1007/s12517-015-2035-9

Li, Q., Wu, G., Kong, D., Han, S., and Ma, Z. (2022). Study on Mechanism of End Face Roof Leaks Based on Stope Roof Structure Movement under Repeated Mining. *Eng. Fail. Anal.* 135, 106162. doi:10.1016/j.engfailanal.2022.106162

Marcin, W., and Stanislaw, P. (2019). Numerical Calculations of Shield Support Stress Based on Laboratory Test Results. *Comput. Geotechnics* 52 (4), 536–546. doi:10.1016/j.compgeo.2015.11.007

Pang, Y., Wang, G., and Yao, Q. (2020). Double-factor Control Method for Calculating Hydraulic Support Working Resistance for Longwall Mining with Large Mining Height. *Arab. J. Geosci.* 13 (6), 252. doi:10.1007/s12517-020-5208-0

Qian, M., Miao, X., He, F., and Liu, C. (1996). Mechanism of Coupling Effect between Supports in the Workings and the Rocks. *J. China Coal Soc.* 21 (1), 40–44.

Qian, M., Shi, P., and Xu, J. (2010). *Mining Pressure and Strata Control*. Xuzhou: China University of Mining and Technology Press.

Ren, S., Zhang, X., Tu, M., Sun, B., and Zhou, T. (2020). Research on Prevention and Control Technology of Strong Mining Pressure in Coal Seam with Thick and Hard Roof. *Min. Res. Dev.* 40 (9), 81–86. doi:10.13827/j.cnki.kyk.2020.09.016

Song, G., Ding, K., and Kong, D. (2019). Assessing Longwall Shield-Strata Interaction Using a Physical Model. *Q. J. Eng. Geol. Hydrogeology* 19 (3), 536–546. doi:10.1144/qjgegh2018-174

Stanislaw, P., Marek, P., and Andrzej, W. (2016). Applying the Ground Reaction Curve Concept to the Assessment of Shield Support Performance in Longwall Faces. *Arab. J. Geosci.* 9 (3), 167. doi:10.1007/s12517-015-2171-2

Stanislaw, P., Sylwester, R., Aleksander, W., and Alicja, K. (2017). Assessment of Roof Fall Risk in Longwall Coal Mines. *Int. J. Min. Reclam. Environ.* 31 (8), 558–574. doi:10.1080/17480930.2016.1200897

Sun, Z., Wu, Y., Lu, Z., Feng, Y., Chu, X., and Kang, Y. (2020). Stability Analysis and Derived Control Measures for Rock Surrounding a Roadway in a Lower Coal Seam under Concentrated Stress of a Coal Pillar. *Shock Vib.* 2020, 1–12. doi:10.1155/2020/6624983

Sylwester, R., Tomasz, J., and Stanislaw, P. (2020). Model Tests of the Effect of Active Roof Support on the Working Stability of a Longwall. *Comput. Geotechnics* 118, 103302. doi:10.1016/j.compgeo.2019.103302

Wang, F., Tu, S., Yuan, Y., Feng, Y., Fang, C., and Tu, H. (2013). Deep-hole Pre-split Blasting Mechanism and its Application for Controlled Roof Caving in Shallow Depth Seams. *Int. J. Rock Mech. Min. Sci.* 64, 112–121. doi:10.1016/j.ijrmms.2013.08.026

Wang, G., Pang, Y., Li, M., Ma, Y., and Liu, X. (2017). Hydraulic Support and Coal Wall Coupling Relationship in Ultra Large Height Mining Face. *J. China Coal Soc.* 42 (2), 518–526. doi:10.13225/j.cnki.jccs.2016.0699

Wang, J., Wang, L., and Guo, Y. (2014). Determining the Support Capacity Based on Roof and Coal Wall Control. *J. China Coal Soc.* 39 (8), 1619–1624. doi:10.13225/j.cnki.jccs.2014.9027

Wang, J., Yang, S., Yang, L., and Wang, Z. (2015). A Dynamic Method to Determine the Supports Capacity in Longwall Coal Mining. *Int. J. Min. Reclam. Environ.* 29 (4), 277–288. doi:10.1080/17480930.2014.891694

Wu, F., Yu, X., Zhao, G., Du, B., Lv, B., and Zhang, J. (2022). Characteristics of Stress Field and Damage Law of Coal Rock in Residual Pillar of Top Slice and its Application. *Front. Earth Sci. (Lausanne)* 10, 835531. doi:10.3389/feart.2022.835531

Xing, Y., Huang, B., Li, B., Liu, J., Cai, Q., and Hou, M. (2021). Investigations on the Directional Propagation of Hydraulic Fracture in Hard Roof of Mine: Utilizing a Set of Fractures and the Stress Disturbance of Hydraulic Fracture. *Lithosphere* 2021 (S1), 4328008. doi:10.2113/2021/4328008

Yan, S., Yi, X., Xu, H., Xu, G., Liu, Q., and Lei, Y. (2011). Roof Structure of Short Cantilever-Articulated Rock Beam and Calculation of Support Resistance in Full-Mechanized Face with Large Mining Height. *J. China Coal Soc.* 36 (11), 1816–1820. doi:10.13225/j.cnki.jccs.2011.11.022

Yu, B., Gao, R., Kuang, T., Huo, B., and Meng, X. (2019). Engineering Study on Fracturing High-Level Hard Rock Strata by Ground Hydraulic Action. *Tunn. Undergr. Space Technol.* 86, 156–164. doi:10.1016/j.tust.2019.01.019

Yu, L., Yan, S., and Liu, Q. (2012). Determination of support working resistance of top coal caving in extra thick coal seam. *J. China Coal Soc.* 37 (5), 737–742. doi:10.13225/j.cnki.jccs.2012.05.018

Zhang, B., Yang, Z., Chunxu, J., Guo, Z., and Li, H. (2021). Research on the Influence of the Key Stratum Position on the Support Working Resistance during Large Mining Height Top-Coal Caving Mining. *Adv. Civ. Eng.* 2020, 1–9. doi:10.1155/2021/6690280

Zhang, Z., Deng, M., Wang, X., Yu, W., Zhang, F., and Doan, D. V. (2020). Field and Numerical Investigations on the Lower Coal Seam Entry Failure Analysis under the Remnant Pillar. *Eng. Fail. Anal.* 115, 104638. doi:10.1016/j.engfailanal.2020.104638

Zhu, T., Zhang, B., Guorui, F., Zhang, X., and Kang, L. (2010). Roof Structure and Control in the Lower Seam Mining Field in the Ultra-close Multiple Seams. *J. China Coal Soc.* 35 (2), 190–193. doi:10.13225/j.cnki.jccs.2010.02.012



OPEN ACCESS

EDITED BY

Lianchong Li,
Northeastern University, China

REVIEWED BY

Wen-Chieh Cheng,
Xi'an University of Architecture and
Technology, China
Huashan Yang,
Guizhou Normal University, China

*CORRESPONDENCE

Baobin Gao,
gaobaobin@hpu.edu.cn

SPECIALTY SECTION

This article was submitted to
Geohazards and Georisks,
a section of the journal
Frontiers in Earth Science

RECEIVED 08 July 2022

ACCEPTED 29 August 2022

PUBLISHED 14 September 2022

CITATION

Ren C, Gao B, Geng C and Zhu W (2022),
Assembled design and compressive
performance simulation of mine
waterproof wall based on concrete
3D printing.
Front. Earth Sci. 10:989331.
doi: 10.3389/feart.2022.989331

COPYRIGHT

© 2022 Ren, Gao, Geng and Zhu. This is
an open-access article distributed
under the terms of the [Creative
Commons Attribution License \(CC BY\)](#).
The use, distribution or reproduction in
other forums is permitted, provided the
original author(s) and the copyright
owner(s) are credited and that the
original publication in this journal is
cited, in accordance with accepted
academic practice. No use, distribution
or reproduction is permitted which does
not comply with these terms.

Assembled design and compressive performance simulation of mine waterproof wall based on concrete 3D printing

Chuangnan Ren^{1,2}, Baobin Gao^{1,2,3*}, Chenhui Geng^{1,2} and Wenjie Zhu^{1,2}

¹State Collaborative Innovation Center of Coal Work Safety and Clean-efficiency Utilization, Jiaozuo, China, ²School of Safety Science and Engineering, Henan Polytechnic University, Jiaozuo, China, ³Henan Key Laboratory of Underground Engineering and Disaster Prevention, Jiaozuo, China

With the increase of mining depth, the deep mine waterproof wall project faces the test of worse construction environment and higher risk of water damage. With the development of intelligent construction technology, it is necessary to introduce concrete 3D printing technology for the construction of coal mine waterproof walls, so as to adapt to more complex construction environment and engineering needs. Through uniaxial compression tests, the compressive properties of 3D printed concrete were tested under different printing methods and force directions. The results showed that the compressive strength of the 3D printed concrete was higher under the conditions of printing path B and loading along the direction parallel to the bonding layer. According to test results, the mine waterproof wall structure based on concrete 3D printing was designed. Then, ABAQUS was used to simulate the compressive strength and deformation of the 3D printed waterproof wall. The results showed that the ultimate load of the 3D printing module was 6.697e⁴kN and the deformation range was controllable, which meet the engineering requirements. The advantages of 3D printing mine waterproof walls are more flexible in design, faster in manufacturing, and more intelligent in operation. This work provides new ideas for the design and construction of waterproof walls in deep mines.

KEYWORDS

concrete 3D printing, mine waterproofing wall, assembly design, compressive performance, mining engineering

Introduction

The hydrogeological and engineering geological conditions in deep underground mines have become increasingly complex with continuous increases in the depths of the mines and mining intensity worldwide (Chen et al., 2019; Gao et al., 2021). In China, water inrush disasters are a major threat to the safety of deep underground mines (Sun et al., 2017; Hu and Zhao, 2021; Jiang et al., 2022). Construction of mine waterproofing

walls is one of the most effective and widely applied methods for controlling groundwater and has been used for decades in underground mining (Hang et al., 2022). As the mining depth increases, the construction of mine waterproofing walls is facing the challenge of the worse construction environment and the higher risk of water damage.

Currently, mine waterproofing walls are constructed using the concrete pouring method. When this method is applied to the deep mine engineering site, two technical problems are exposed: on the one hand, the high temperature and high humidity construction environment is likely to cause gaps in the concrete pouring process, which brings hidden dangers to the engineering quality (Kreiger et al., 2019). On the other hand, the traditional construction method involves many sub-projects. It usually takes 2 months to build a waterproof wall, which is difficult to buy time for emergency rescue and disaster relief (Sui and Hang, 2016). In December 2013, the ESW retaining wall system independently developed by a coal mine in Henan Province, China, adopted the method of precast concrete modules to achieve rapid construction in 8 h. This technology subverts the traditional concrete pouring mode, and also provides new ideas for the construction of mine waterproof walls. Since then, the rapid construction of deep mine waterproof walls has become a hot spot in the field. Scholars and engineers have optimized the construction process and put forward new attempts (Gao et al., 2014; Gao and Wang, 2016; Sang, 2016; Gao et al., 2022), which have taken into account the construction conditions of deep mines, but lack green and intelligent measures.

In recent years, intelligent construction technology has achieved rapid development (Bos et al., 2016; Ma and Wang, 2018; Paul et al., 2018; Bai et al., 2021). Compared with prefabricated concrete slabs, 3D printing technology has the advantages of more flexible design, faster manufacturing, and smarter operation (Ma et al., 2018; Wang et al., 2020). In addition, concrete 3D printing can also improve the compression resistance and impermeability of concrete by adding admixtures (such as fibers) (Invernizzi et al., 2016; Rahul et al., 2019). With the development of intelligent construction technology, it is necessary to consider adopting more advanced methods for the construction of coal mine waterproof walls to achieve a faster, greener, safer and more intelligent construction mode.

In view of this, according to the mechanical properties test of 3D printed concrete, a waterproof wall structure based on concrete 3D printing was designed. The compressive performance of the waterproof wall was explored through finite element simulation analysis. Assembled design and compressive performance simulation of mine waterproof wall based on concrete 3D printing provides some new ideas for deep mine disaster prevention and control and the application of concrete 3D printing in mines.

Assembled design of 3D printed mine waterproof wall

Experimental materials

1) Material preparation. The design of 3D printed concrete material composition and mix ratio needs to be coordinated and compatible with the 3D printing system. On the basis of fully considering the properties of raw materials, various mixing principles and preparation methods, determine the proportions of various raw materials, and carry out ingredients according to Table 1.

Among them, the basalt fiber specifications are shown in Table 2. The fiber length is 18mm, which is slightly larger than the 15 mm diameter of the print head, which is beneficial to the orientation effect of the fiber composite material during the extrusion process.

2) Preparation of samples. The HC1008 3D printer was selected for the production of concrete samples. In order to explore the influence of different printing paths on the mechanical properties of concrete, two samples with different printing paths were made to test their mechanical properties. Two 3D printing paths are shown in Figure 1.

The samples were produced using a printing nozzle with a diameter of 15 mm, a printing layer height of 7 mm, and a printing speed of 20 mm/s. Finally, samples of 150 mm×150 mm×150 mm were obtained, as shown in Figure 2.

Experimental setup and method

According to the different stress directions of the samples, it can be divided into two forms: the direction perpendicular to the bonding layer and the direction parallel to the bonding layer. The force perpendicular to the bonding layer is defined as V, and the force parallel to the bonding layer is defined as H, as shown in Figure 3. According to the different printing paths and force directions, four groups (AV, AH, BV, BH) of 12 samples (50mm×50mm×50 mm) were made for uniaxial compression tests to test their compressive performance.

The RMT-150C rock mechanics test system was selected, which adopts the method of applying uniform load vertically on a single axis. The loading rate is 0.005 mm/s, and the vertical load is 1000 kN. The failure phenomenon of the sample is as follows: cracks parallel to the load direction appear on the outer surface of the sample and penetrate the entire sample.

Analysis of results

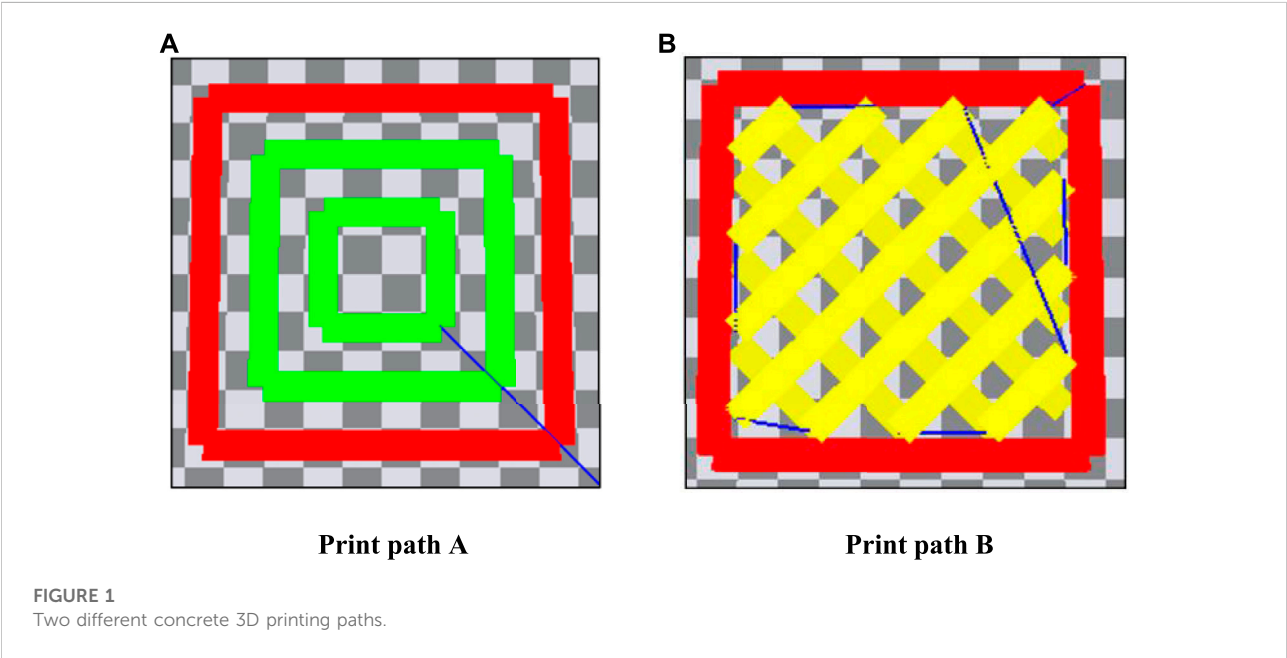
Under the condition of printing path A, the load-displacement curve of the sample is shown in Figure 4. It shows that under the condition of printing path A, when the

TABLE 1 The ratio of 3D printed concrete materials.

Material	Ordinary portland cement (%)	Silica fume (%)	Basalt fiber (%)	Quartz sand (%)	Water (%)	Set retarder (%)	Water-reducing admixture (%)	Early strength agent (%)
Proportion	100	30	0.5	130	28	0.5	1.2	2

TABLE 2 Specifications of basalt fiber.

Density (g/cm ³)	Diameter (um)	Length (mm)	Tensile strength (MPa)	Elastic Modulus (GPa)
2.55	13	18	1950	76.5



load is applied perpendicular to the bonding layer, the maximum compressive strength of the sample is 58.511 MPa, and the minimum compressive strength is 51.551 MPa. When the load is applied parallel to the bonding layer, the maximum compressive strength of the sample is 64.179 MPa, and the minimum compressive strength is 60.261 MPa.

Under the condition of printing path B, the load-displacement curve of the specimen is shown in Figure 5. It shows that: under the condition of printing path B, when the load is applied perpendicular to the bonding layer, the maximum compressive strength of the sample is 64.334 MPa, and the minimum compressive strength is 55.211 MPa. When the load is applied parallel to the bonding layer, the maximum compressive strength of the sample is 67.195 MPa, and the minimum compressive strength is 62.393 MPa.

In summary, the overall compressive strength of the samples in the printing path B is higher than that of the samples in the printing path A. This difference is mainly caused by the gap between the adhesive layers. Compared with printing path B, printing path A is more likely to form voids at the corners. Such voids will lead to poorer compactness of the structure, thereby affecting the compressive strength of the structure. Secondly, under the same printing path conditions, the compressive strength of the sample is higher when it is loaded in the direction parallel to the bonding layer. The main reason for this difference is: when loading parallel to the bonding layer, the extension direction of the 3D printing is parallel to the direction of the applied load, and a short column structure is generated inside the concrete, which enhances the compressive strength of the structure. The above experimental results can provide a



FIGURE 2
3D printed concrete samples.

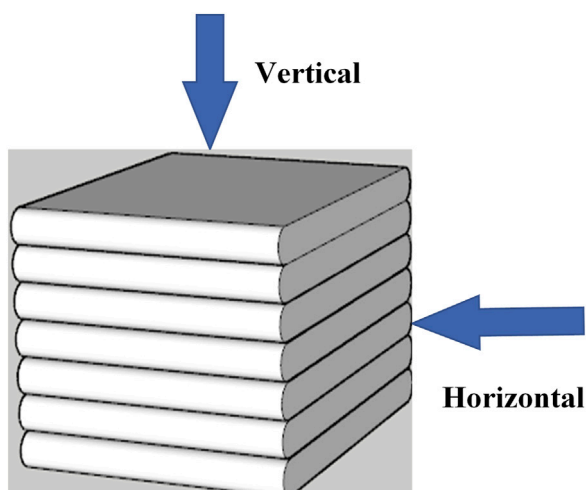


FIGURE 3
Schematic diagram of different force directions.

scientific basis for the design of assembly modules for 3D printed mine waterproof walls.

Assembly module design

The design of the mine waterproof wall is based on a mine in Jiaozuo City, Henan Province, China. The preliminary estimate of the water bearing pressure is 3~5 MPa. According to the design formula in the Chinese coal mine water prevention and control code, the total length of the waterproof wall is 6.6126 m. Considering the actual construction situation and ensuring the safety and stability of the sluice wall, the design

values are slightly larger than the calculated values, as shown in Table 3.

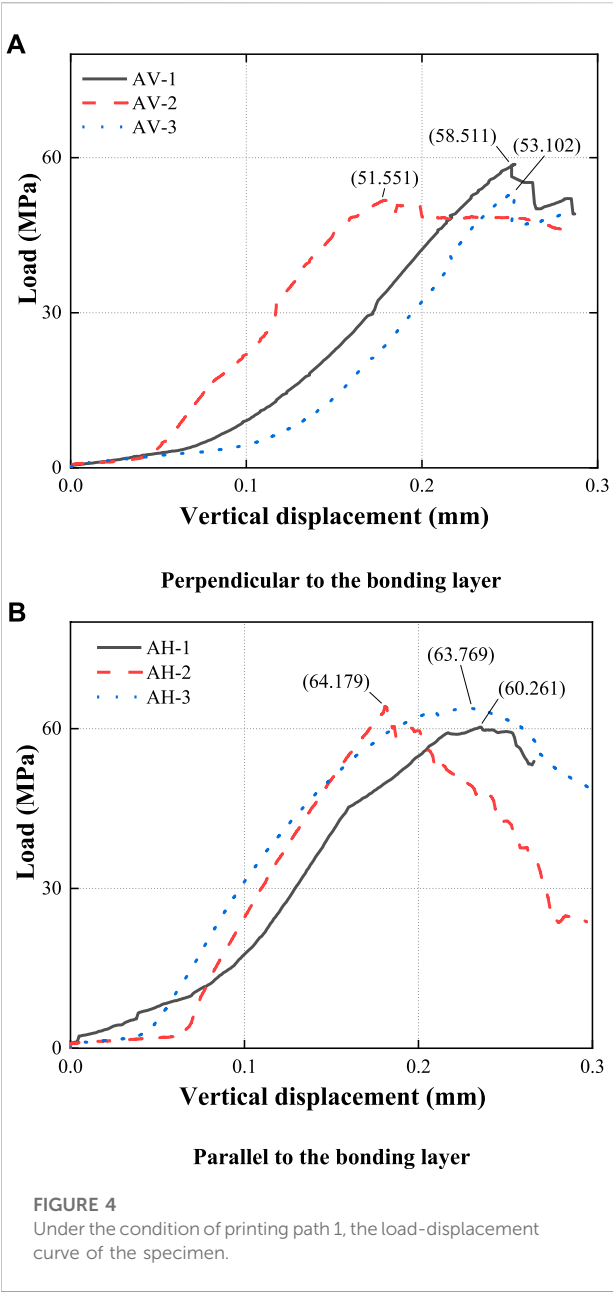
The assembly module is 4000 mm long, 4200 mm wide and 1200 mm thick, and the two ends are embedded in the base 300 mm. The protrusions are 400 mm thick and 1000 mm wide. Two bolt holes are preset at 150 mm inward on both sides of the groove, and the diameter of the bolt holes is 20 mm. In order to facilitate the fitting of the module protrusion and the module groove, the gap between the two is 20 mm. Specifically, as shown in Figure 6.

The assembly module adopts the printing path B, and the combined component is subjected to water pressure in the direction parallel to the bonding layer. A total of eight assembly modules are composed, as shown in Figure 7.

Simulation analysis of compressive performance of 3D printed mine waterproof wall

Construction of finite element model

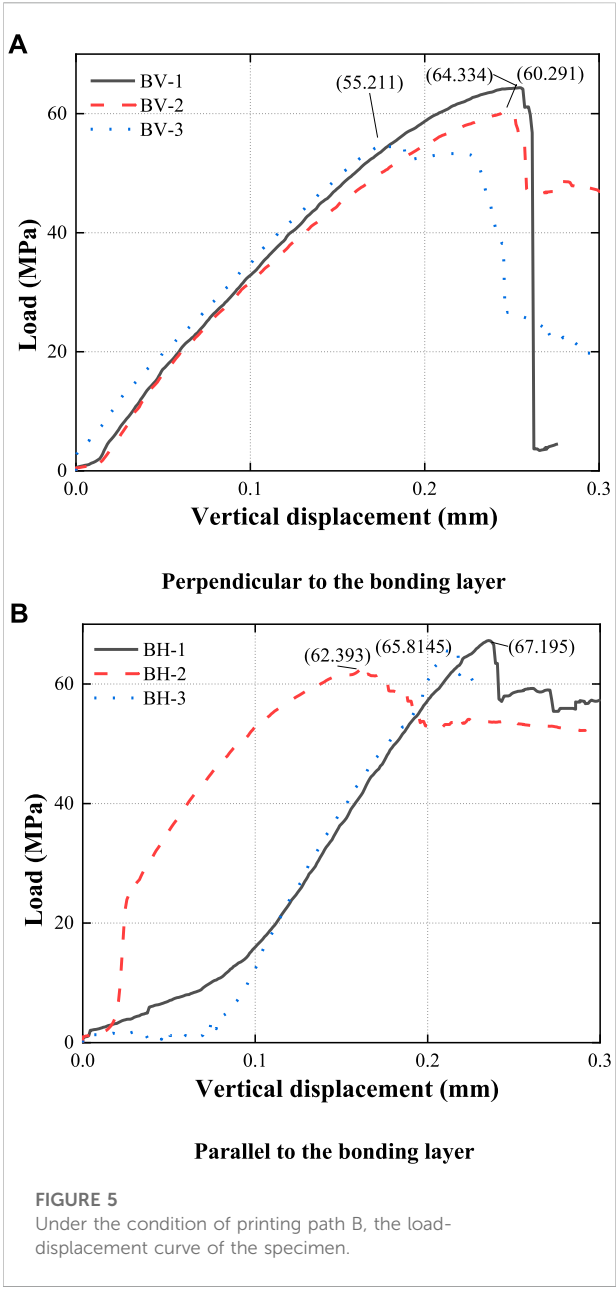
In order to explore the force characteristics of the 3D-printed mine waterproof wall under the action of water pressure and the pressure of the overlying rock, ABAQUS was used for simulation analysis. It was assumed that the upper and lower bases of the main body segment are rigid bodies and will not deform. Only the force transmission and the friction between the surfaces were considered between the assembly modules, and the modules would not have any seepage effect. CDP was adopted as the damage evolution constitutive model of concrete layer material damaged by macroscopic force. For the bonding layer, a Cohesive element was inserted to simulate the interlayer bonding. The concrete strength grade was C30. The meshing element size was



150 mm. As shown in Figure 8, a uniform load of 5 MPa is set in the horizontal direction to simulate the water pressure P . A uniform load of 10 MPa is set in the vertical direction to simulate the overburden pressure F .

Analysis of simulation results

The load-displacement curve of a monitoring point on the stress surface of the structure is shown in Figure 9. It can be seen from the figure that when the load reaches 3.035 e⁴kN and the displacement reaches 0.6mm, the damage starting point is



reached. At this time, the curve begins to rise nonlinearly, the stiffness of the structure decreases, and the structure is damaged. When the displacement reaches 2.4mm, the 3D printed structure

TABLE 3 Mine waterproof wall design parameter.

Technical parameter	Calculated	Designed
Chamber length/m	6.61	8
Maximum excavation area/m ²	20.83	20.83
Depth of embedded rock/m	0.62	1.5

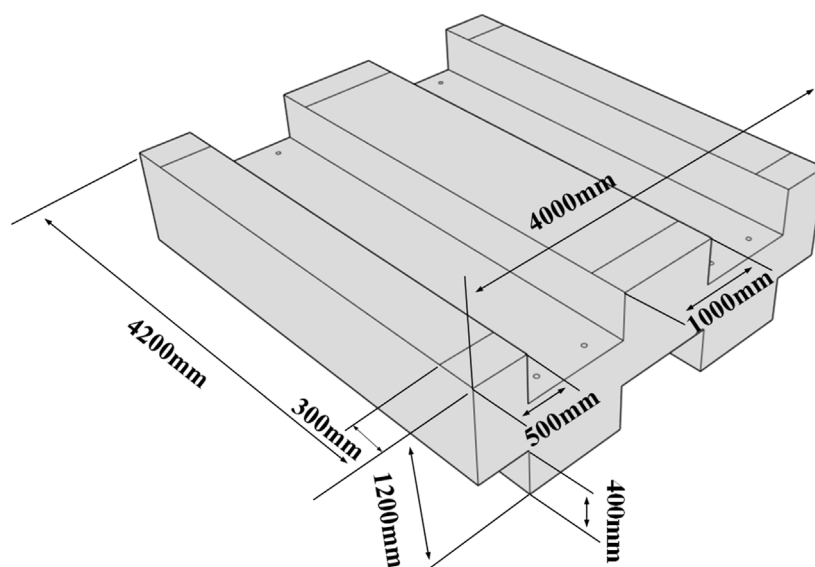


FIGURE 6
Design drawing of 3D printed concrete assembly module.

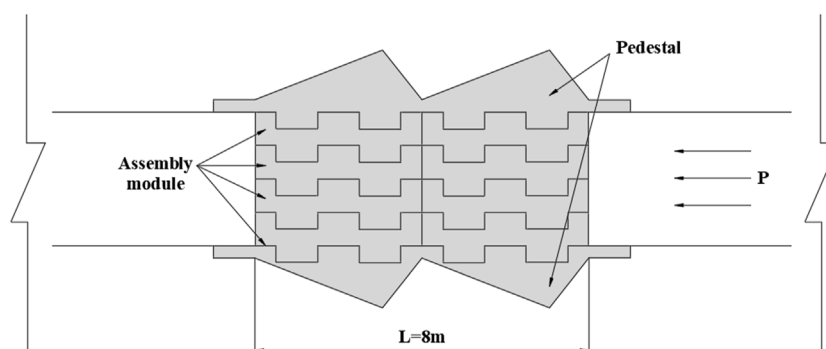


FIGURE 7
Design drawing of 3D printed mine waterproof wall.

reaches the ultimate load $6.697 \text{ e}^4 \text{ kN}$, which is slightly larger than that ($6.258 \text{ e}^4 \text{ kN}$) of the conventional structure.

Further, a simulation analysis was carried out for the structural deformation of the 3D printed waterproof wall and the traditional waterproof wall under the action of water pressure. Under the condition of 5 MPa water pressure, when the minimum deformation values are 0.1, 0.05, 0.01, and 0.001mm, the comparison of the deformation ranges of the two models is shown in Figure 10.

According to Figure 10 and the monitored data, the deformation range of the fabricated waterproof wall is slightly larger than that of the traditional one. The deformation range boundary of the traditional waterproof wall is a rounded arc, while the deformation range boundary of the prefabricated waterproof

wall is obviously affected by the assembly connection surface. But in general, the deformation range is controllable, which meets the engineering requirements. The advantages of 3D printing mine waterproof walls are more flexible in design, faster in manufacturing, and more intelligent in operation.

Discussions

- 1) The construction method of 3D printing mine waterproof wall. Based on the above research, a corresponding rapid construction method needs to be formed. At present, the research team has carried out the plan implementation on the project site. The assembly module is pre-printed and formed,

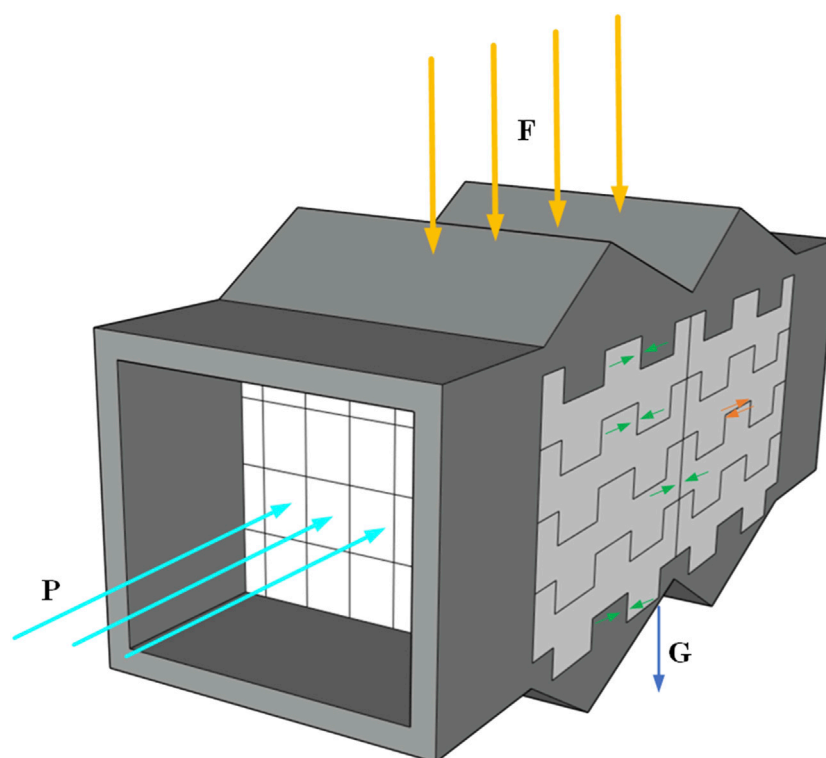


FIGURE 8
Force analysis of 3D printing mine waterproof wall.

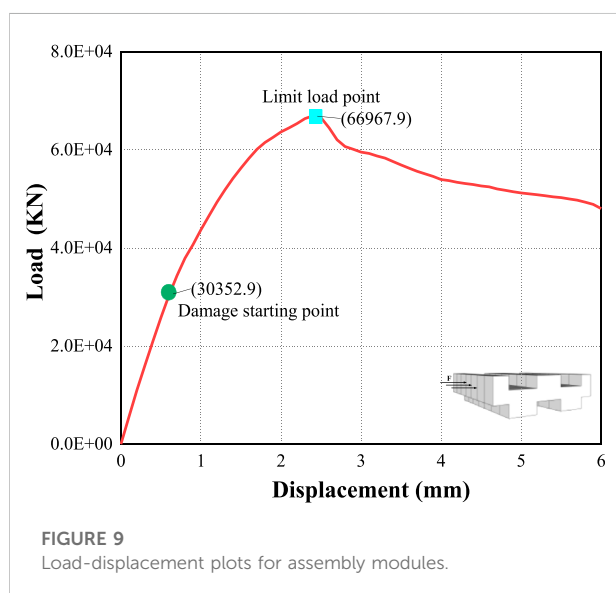


FIGURE 9
Load-displacement plots for assembly modules.

and the rapid assembly of the main section of the sluice wall is completed according to the top-down construction steps. After the assembled modules are assembled, there are a large number of contact seams between the modules, so

the sealing treatment and anti-seepage measures for these gaps are particularly important. The assembly modules are bolted on. The joint work between the modules adopts the hydraulic pressure bonding method of the rubber gasket. The waterproof and anti-seepage performance of the sluice wall structure is ensured by referring to the sealing connection method of the immersed tunnel.

- 2) Research on the impermeability of 3D printed mine waterproof walls. This work adopted an idealized model, focused on the compressive performance of 3D printed waterproof walls, and believed that the structure has sufficiently strong impermeability. However, as a waterproof structure in mines, it is necessary to conduct further research on the impermeability of 3D printed waterproof walls. The seepage characteristics of 3D printed concrete are different from those of traditional concrete, and the related theory and numerical model need to be improved.
- 3) Application prospect of 3D printing technology in coal mines. At present, 3D printing technology and prefabricated structures are rarely used in mine construction. With the upgrading and optimization of mine safety technology, it is necessary to consider expanding the application of prefabricated structures to mine engineering. This belongs to the field of interdisciplinary research. 3D printing technology and assembly process help to

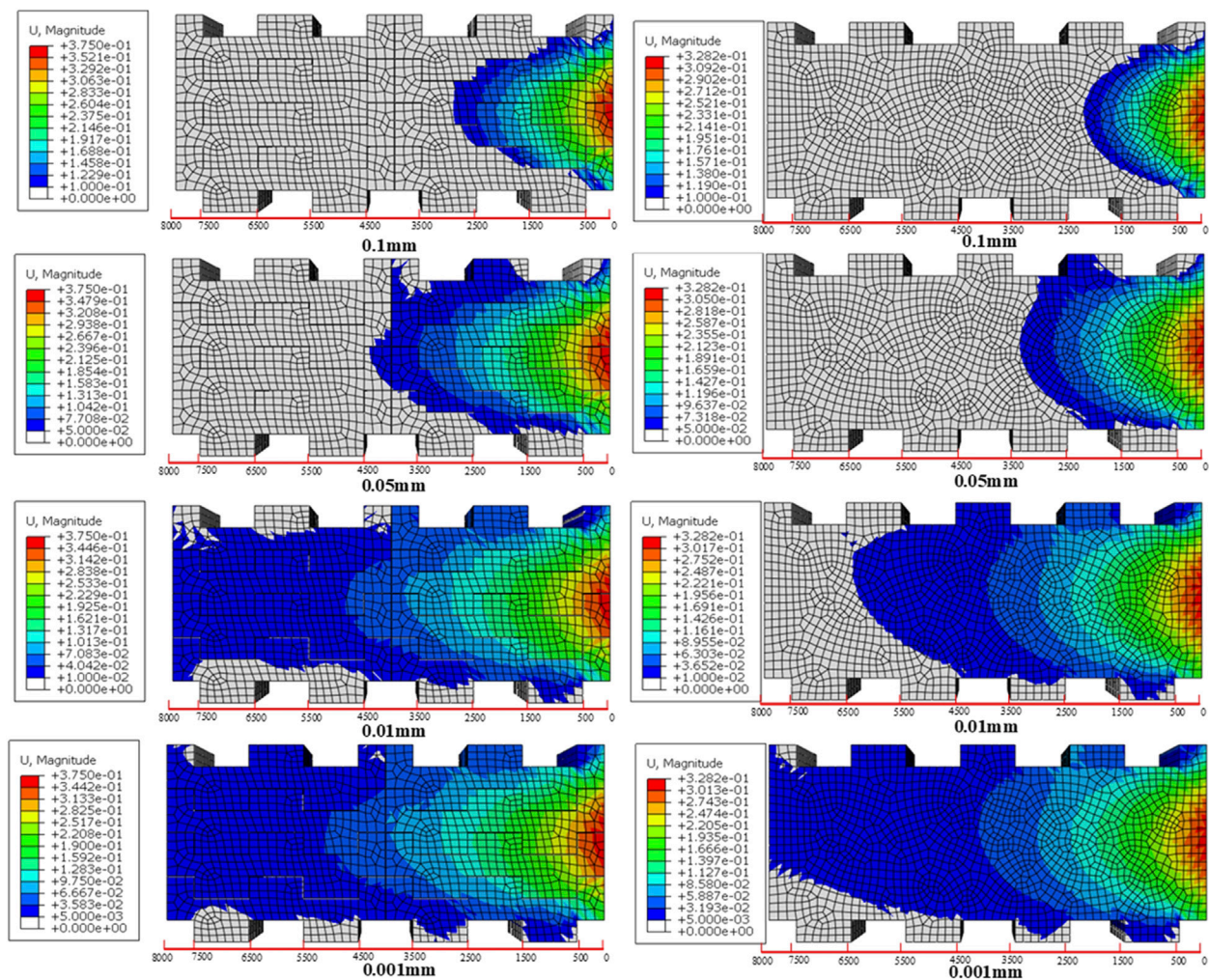


FIGURE 10
Comparison of the deformation range of the two models.

realize the intelligent construction of underground structures in coal mines. Relevant technological innovation and engineering applications need to be strengthened.

Conclusion

1) Four groups of 3D printed concrete were made according to two different printing paths and two force directions. The compressive properties of the 3D printed concrete were tested through uniaxial compression tests. The compressive strength of the 3D printed concrete was higher under the conditions of printing path B and loading along the direction parallel to the bonding layer. According to the test results, a mine waterproof wall structure based on concrete 3D printing was designed.

2) ABAQUS was used to simulate the compressive strength and deformation of the 3D printed waterproof wall. The 3D

printed structure could reach the ultimate load $6.697 \times 10^4 \text{ kN}$, which was slightly larger than that ($6.258 \times 10^4 \text{ kN}$) of the conventional structure. The deformation range of the 3D printed prefabricated waterproof wall was slightly larger than that of the traditional one. But in general, the deformation range is controllable, which meet the engineering requirements. The advantages of 3D printing mine waterproof walls are more flexible in design, faster in manufacturing, and more intelligent in operation.

3) The construction technology of 3D printing mine waterproof wall was discussed. The water pressure crimping method using rubber gaskets was envisaged to ensure the waterproof and impermeable performance of the waterproof wall structure. As a waterproof structure in mines, it is necessary to conduct further research on the impermeability of 3D printed waterproof walls. With the upgrading and optimization of mine safety technology, it is necessary to consider expanding the application of prefabricated structures to mine engineering.

Data availability statement

The original contributions presented in the study are included in the article/Supplementary Material, further inquiries can be directed to the corresponding author.

Author contributions

CR was responsible for the writing of the article and the construction of the framework; BG initially proposed the innovation of this article and provided great help for the optimization of the article; CG assisted in completing the simulation part and participated in the editing of the article; WZ assisted in completing the experimental part.

Funding

This study was supported by NSFC- Shanxi Coal-based Low-Carbon Joint Fund Key Project (Grant No. U1810203), and Key R&D and promotion projects in Henan Province (Grant No. 212102310013).

References

- Bai, X. D., Cheng, W. C., and Li, G. (2021). A comparative study of different machine learning algorithms in predicting EPB shield behaviour: A case study at the xi'an metro, China. *Acta Geotech.* 16 (12), 4061–4080. doi:10.1007/s11440-021-01383-7
- Bos, F., Wolfs, R., Ahmed, Z., and Salet, T. (2016). Additive manufacturing of concrete in construction: Potentials and challenges of 3D concrete printing. *Virtual Phys. Prototyp.* 11 (3), 209–225. doi:10.1080/17452759.2016.1209867
- Chen, X. J., Li, L. Y., Wang, L., and Qi, L. L. (2019). The current situation and prevention and control countermeasures for typical dynamic disasters in kilometer-deep mines in China. *Saf. Sci.* 115, 229–236. doi:10.1016/j.ssci.2019.02.010
- Gao, B. B., Ren, C. N., Dong, Q., and Chen, L. W. (2021). Study on dynamic behavior law and microseismic monitoring in stoping process of roadway with high Gas and wide coal pillar. *Shock Vib.* 2021, 1–14. doi:10.1155/2021/5135964
- Gao, B. B., Ren, C. N., and Song, S. P. (2022). A new evaluation method for water blocking performance of coal seam floor: Model construction, case application, and water-preserved strategy. *GEOFLOODS* 2022, 1–13. doi:10.1155/2022/1608734
- Gao, S. X., Wu, S. L., and Ma, H. Y. (2014). Numerical simulation of high-pressure floodgate wall based on FLAC^{3D}. *Saf. Coal Mines* 45 (7), 166–168. doi:10.13347/j.cnki.mkaq.2014.07.050
- Gao, Y., and Wang, J. M. (2016). Experiments on instant and automatic construction of movable floodgate wall in mines. *Res. Explor. Laboratory* 35 (3), 60–64.
- Hang, Y., Sui, W. H., and Yuan, S. C. (2022). Experimental investigation of the seepage failure between bulkheads and surrounding rocks in deep underground mines. *Bull. Eng. Geol. Environ.* 81 (9), 362. doi:10.1007/s10064-022-02859-w
- Hu, W. Y., and Zhao, C. H. (2021). Evolution of water hazard control technology in China's coal mines. *Mine Water Environ.* 40 (2), 334–344. doi:10.1007/s10230-020-00744-0
- Invernizzi, M., Natale, G., Levi, M., Turri, S., and Griffini, G. (2016). UV-assisted 3D printing of glass and carbon fiber-reinforced dual-cure polymer composites. *Materials* 9 (7), 583. doi:10.3390/ma9070583
- Jiang, H., Fan, G. W., Zhang, D. S., Zhang, S. Z., and Fan, Y. B. (2022). Evaluation of eco-environmental quality for the coal-mining region using multi-source data. *Sci. Rep.* 12 (1), 6623. doi:10.1038/s41598-022-09795-5
- Kreiger, E. L., Kreiger, M. A., and Case, M. P. (2019). Development of the construction processes for reinforced additively constructed concrete. *Addit. Manuf.* 28, 39–49. doi:10.1016/j.addma.2019.02.015
- Ma, G., Li, Z., and Wang, L. (2018). Printable properties of cementitious material containing copper tailings for extrusion based 3D printing. *Constr. Build. Mat.* 162, 613–627. doi:10.1016/j.conbuildmat.2017.12.051
- Ma, G., and Wang, L. (2018). A critical review of preparation design and workability measurement of concrete material for largescale 3D printing. *Front. Struct. Civ. Eng.* 12 (3), 382–400. doi:10.1007/s11709-017-0430-x
- Paul, S. C., van Zijl, G. P., Tan, M. J., and Gibson, I. (2018). A review of 3D concrete printing systems and materials properties: Current status and future research prospects. *Rapid Prototyp. J.* 24 (4), 784–798. doi:10.1108/RPJ-09-2016-0154
- Rahul, A. V., Santhanam, M., Meena, H., and Ghani, Z. (2019). Mechanical characterization of 3D printable concrete. *Constr. Build. Mater.* 227, 116710. doi:10.1016/j.conbuildmat.2019.116710
- Sang, Z. H. (2016). Fast construction technology of water gate wall under flowing water condition. *Coal Chem. Industry* 39 (12), 9–16. doi:10.19286/j.cnki.cci.2016.12.003
- Sui, W. H., and Hang, Y. (2016). Review and prospect on design and construction technology of mine water bulkhead. *Coal Sci. Technol.* 44 (8), 7–13. doi:10.13199/j.cnki.cst.2016.08.002
- Sun, W., Zhang, S., Guo, W., and Liu, W. (2017). Physical simulation of high-pressure water inrush through the floor of a deep mine. *Mine Water Environ.* 36 (4), 542–549. doi:10.1007/s10230-017-0443-7
- Wang, L., Tian, Z., Ma, G., and Zhang, M. (2020). Interlayer bonding improvement of 3D printed concrete with polymer modified mortar: Experiments and molecular dynamics studies. *Cem. Concr. Compos.* 110, 103571. doi:10.1016/j.cemconcomp.2020.103571

Acknowledgments

We would like to express our gratitude to engineers from Jiaozuo Coal Industry (Group) Co., Ltd for their help in the field tests. We thank the Key Laboratory of Resource Environment and Disaster Monitoring in Shanxi Province and the State Key Laboratory Cultivation Base for Gas Geology and Gas Control.

Conflict of interest

The authors declare that the research was conducted in the absence of any commercial or financial relationships that could be construed as a potential conflict of interest.

Publisher's note

All claims expressed in this article are solely those of the authors and do not necessarily represent those of their affiliated organizations, or those of the publisher, the editors and the reviewers. Any product that may be evaluated in this article, or claim that may be made by its manufacturer, is not guaranteed or endorsed by the publisher.



OPEN ACCESS

EDITED BY
Lianchong Li,
Northeastern University, China

REVIEWED BY
Guoshao Su,
Guangxi University, China
Kai Guan,
Northeastern University, China

*CORRESPONDENCE
Jiaqi Guo,
gj519@163.com

SPECIALTY SECTION
This article was submitted to
Geohazards and Georisks,
a section of the journal
Frontiers in Earth Science

RECEIVED 15 July 2022
ACCEPTED 22 August 2022
PUBLISHED 14 September 2022

CITATION
Sun F, Guo J, Fan J and Liu X (2022),
Experimental study on rockburst
fragment characteristic of granite under
different loading rates in true
triaxial condition.
Front. Earth Sci. 10:995143.
doi: 10.3389/feart.2022.995143

COPYRIGHT
© 2022 Sun, Guo, Fan and Liu. This is an
open-access article distributed under
the terms of the [Creative Commons
Attribution License \(CC BY\)](https://creativecommons.org/licenses/by/4.0/). The use,
distribution or reproduction in other
forums is permitted, provided the
original author(s) and the copyright
owner(s) are credited and that the
original publication in this journal is
cited, in accordance with accepted
academic practice. No use, distribution
or reproduction is permitted which does
not comply with these terms.

Experimental study on rockburst fragment characteristic of granite under different loading rates in true triaxial condition

Feiyue Sun¹, Jiaqi Guo^{1*}, Junqi Fan² and Xiliang Liu¹

¹School of Civil Engineering, Henan Polytechnic University, Jiaozuo, Henan, China, ²Research Institute for National Defense Engineering of Academy of Military Science PLA China, Luoyang, Henan, China

In order to study the effect of loading rate on rockburst, an indoor test of single-face fast unloading-three directions and five-face stress-vertical continuous loading is conducted under different loading rates using a new true-triaxial rockburst test system. The entire process of rockburst inoculation-occurrence-development is completely and accurately reproduced. The fragmentation degree, fractal dimension, and Weibull distribution characteristics of rockburst fragments under different loading rates are compared and analyzed. The results indicate that the rockburst ejection failure process can be summarized as four stages: grain ejection, rock spalling into plates, rock shearing into fragments, and rock fragment ejection. Rockburst fragments are mostly coarse-grained, medium-grained, and fine-grained. The macroscopic block characteristics of rockburst fragments reflect the fragmentation degree of rock, and the fragmentation degree of rockburst fragments increases with the loading rate. The fractal dimension shows the same trend with different loading rates, that is, the fractal dimension grows as the loading rate increases. As the loading rate increases, the crack expansion rate accelerates, which aggravates the damage to the rock specimen by decreasing its compressive strength and causing greater fragmentation when the specimen is failed. The loading rate has a significant effect on the energy consumption of rockburst fragments.

KEYWORDS

rockburst, true triaxial test, loading rate, rockburst fragments, fractal dimension

1 Introduction

With the construction of underground engineering to the deep earth, rockburst disasters caused by deep high ground stress are becoming more and more frequent. A rockburst has the characteristics of being sudden, local, instantaneous, and violent. When the rockburst disaster occurs, resulting in rock fragments produced by bursting loose, high-speed ejection or throwing, and other dynamic damage phenomena, it poses a serious threat to the safe construction of the project. Seventy-five people perished in an extremely strong rockburst at the Springhill mine in Canada (Hedley, 1992). An extremely

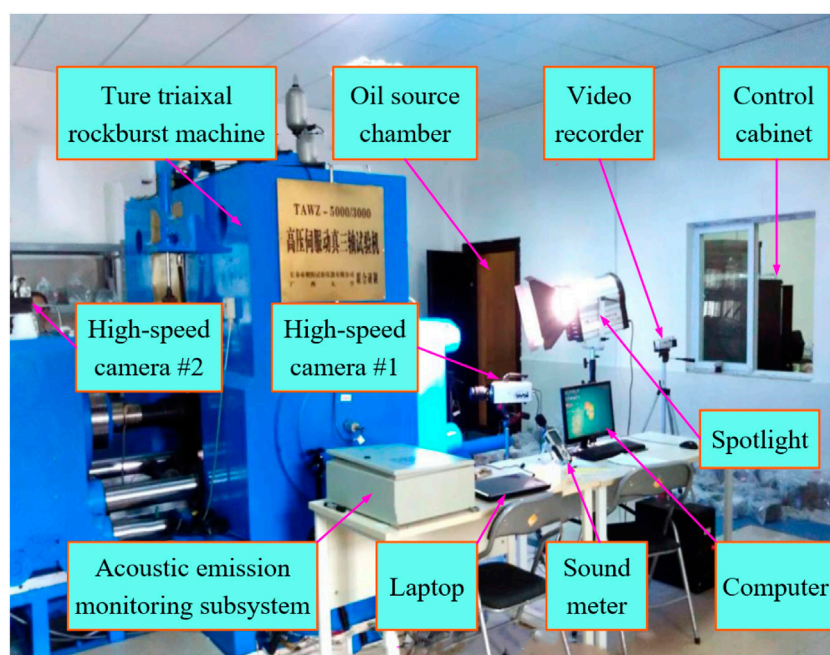


FIGURE 1

True-triaxial rockburst testing system (adapted from Su et al. 2016a).

strong rockburst in the drainage tunnel of the Jinping II hydropower project in China caused a serious accident that resulted in seven deaths and one injured (Hu et al., 2019b). During underground excavation, the occurrence of rockburst disasters is not only related to the rock mineral composition and internal rock structure but also to the surrounding rock stress state and excavation method. As well, external loading conditions such as loading rate have an equally significant influence on the mechanical behavior of rock. Therefore, the study of different loading rates on the failure characteristics, strength characteristics, energy evolution, and fragment characteristics of rock, to further elucidate the formation mechanism of rockburst disasters, has both theoretical significance and practical application value.

In the research on the effect of loading rate on rockburst, both domestic and international scholars have achieved some progress. Su et al. (2018) investigated the influence of loading rate on strainburst. Chen et al. (2019) studied the energy dissipation of fragments during rockburst. Lu et al. (2020) investigated the effects of loading rate on rock deformation, strength, and failure mode. Si et al. (2020) studied the influence of loading rate on rockburst in a circular tunnel. Khan et al. (2022) proposed a new rockburst tendency criterion based on energy evolution characteristics under different loading rates. The energy release characteristics of rockbursts are closely related to the fragmentation degree of rock fragments after destruction, and the

fractal dimension can partially reflect the physical mechanism of rock fragmentation evolution (Xie and Pariseau, 1993). Li et al. (2010), He et al. (2018), and Liu et al. (2021) analyzed the size feature and fragmentation degree of rockburst fragments. Li et al. (2014) clarified the variation law between fractal dimension and loading rate. Liu et al. (2014) determined the fractal dimension of rockburst fragments. Xia et al. (2014) studied the mass and shape distribution characteristics of rockburst fragments under different stress paths. Jiang et al. (2020a) discovered that the average size of rockburst fragments reduces as initial damage increases. Most of the abovementioned research results focus on the effect of loading rate on rock failure under uniaxial, biaxial, and conventional triaxial compression conditions. Existing research on rockburst fragments is still in the qualitative stage, and relevant quantitative research is yet to be carried out. Therefore, in order to more realistically reveal the characteristics of rockburst in the actual engineering context and to provide a more accurate description of the stress path transformation process during deep underground excavation, in this article, a true triaxial test of single-face fast unloading-three directions and five-face stress-vertical continuous loading will be conducted in order to investigate the failure characteristics, strength characteristics, energy evolution, and fragmentation characteristics of rock under different loading rates.

This article uses a novel true-triaxial rockburst test system, based on a new rockburst test method and a new loading and

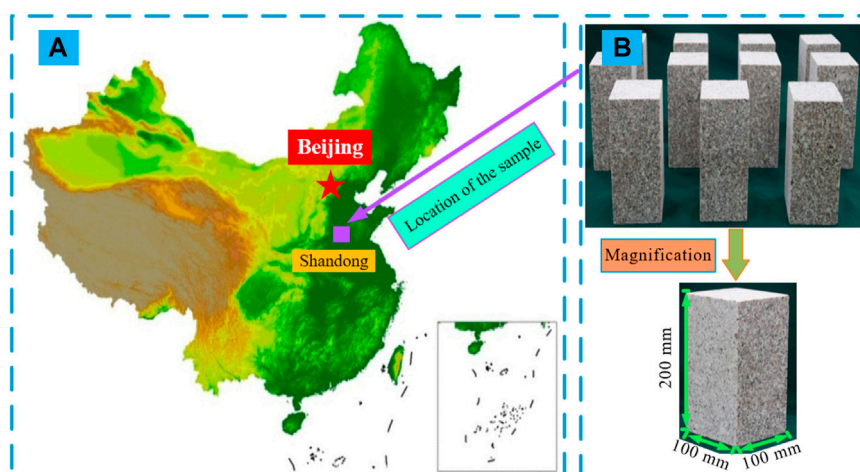


FIGURE 2
Location and photo of the sample. (A) Sampling location; (B) photo of rock specimens.

unloading path, to conduct an indoor physical simulation test of single-face fast unloading-three directions and five-face stress-vertical continuous loading under different loading rates. The entire process of rockburst incubation-occurrence-development is monitored in real time by an image acquisition system. Under different loading rates, the failure characteristics, strength characteristics, and energy evolution of granite specimens are compared and analyzed. Therefore, collecting the ejected fragments of specimens after the rockburst in order to measure the quality, size, and grain size of rockburst fragments. The statistical distribution and fractal characteristics of granite rockburst fragments are analyzed by quantitative means and methods in order to further elaborate on the rockburst phenomena under different loading rates.

2 The novel experimental method and design

2.1 Testing equipment

The test system mainly consists of a true-triaxial rockburst testing machine, a loading system, a control system, a real-time data signal acquisition and monitoring system, a high-speed camera system, and other subsystems (Figure 1). True-triaxial rockburst testing machine is a new high-pressure servo rigid press that has a maximum vertical loading pressure of 5,000 kN and a maximum horizontal loading pressure of 3,000 kN, through the full digital servo controller control can be realized in three vertical directions for independent loading and unloading. It has the special function of single-face fast unloading under the three directions and six-face loading

conditions. It can accurately simulate the process of rapid change of surrounding rock stress path at the moment of underground engineering excavation. With the aid of a high-speed camera, it is possible to observe the failure phenomenon of unloading faces in real time.

2.2 Rock sample preparation

Grayish-white granite samples were collected in Wenshang County, Shandong Province, China (Figure 2). To ensure the comparability of tests and decrease the impact of material heterogeneity and dispersion on the test results, all specimens were extracted from the same intact rock. Before true-triaxial rockburst tests, the rectangular prismatic specimens, 100 mm (length) \times 100 mm (width) \times 200 mm (height), were prepared, and all sides and ends of specimens were finely ground and polished to minimize the local stress concentration and produce flat and smooth end surfaces. To ensure that rock samples are uniformly pressured in all directions, the processing accuracy is strictly in accordance with the standard of the International Society for Rock Mechanics (Fairhurst and Hudson, 1999), with a flatness error of ± 0.05 mm for two opposite faces and a perpendicularity error of $\pm 0.25^\circ$ for two adjacent faces.

2.3 Testing methodology

2.3.1 Stress path design

Before excavation of the cavern, the rock mass was in a triaxial stress state. After the cavern excavation is unloaded, the

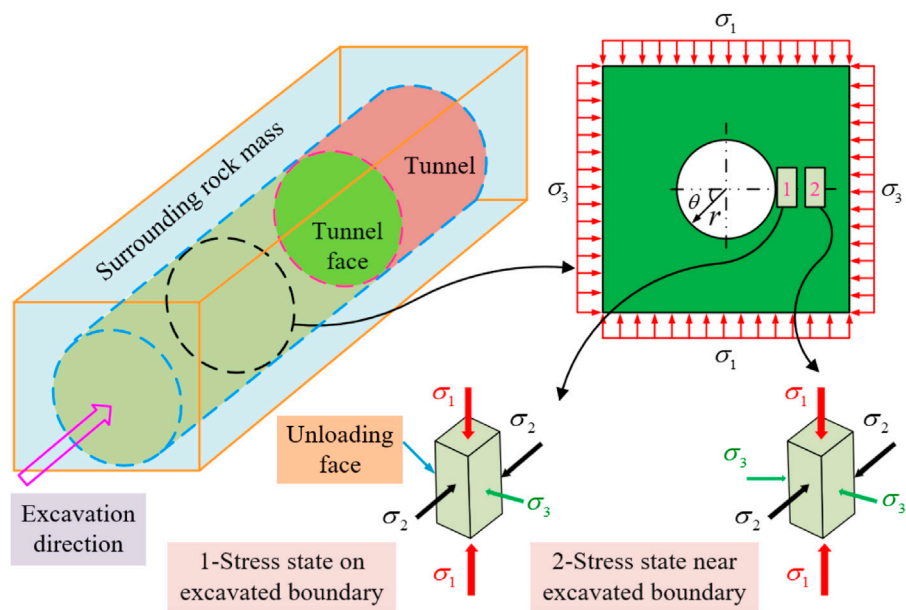


FIGURE 3

Stress state of rocks at and near the excavation boundary (adapted from Jiang et al. (2020b)).

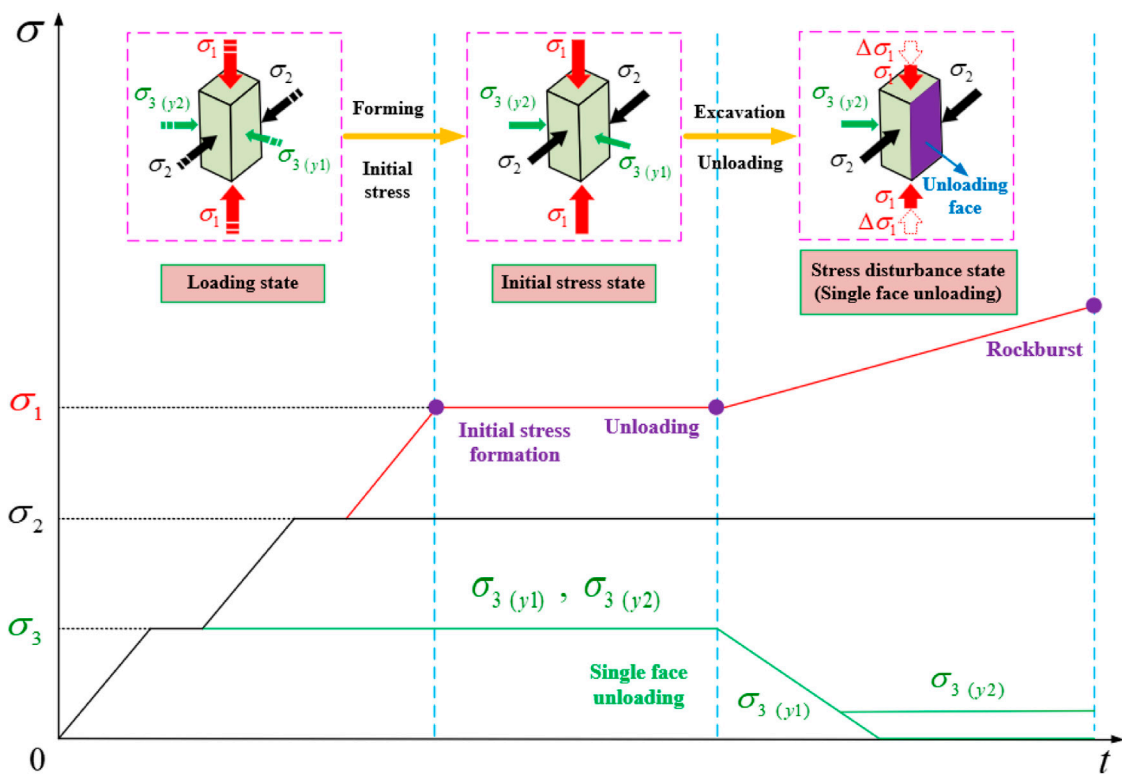


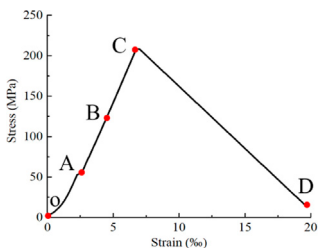
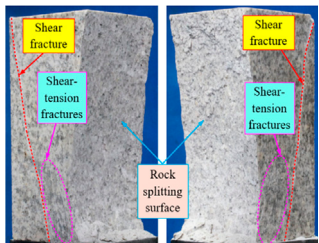
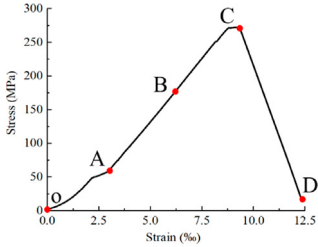
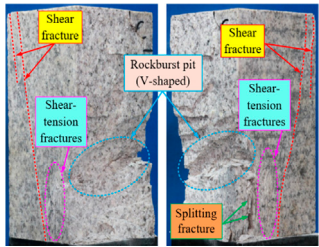
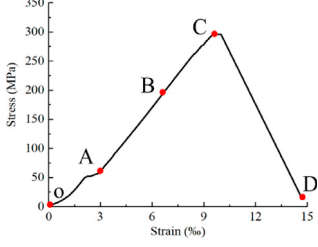
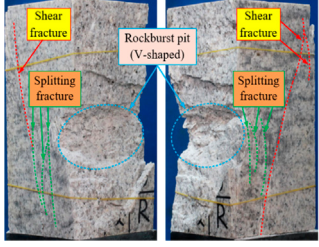
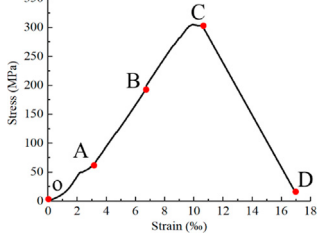
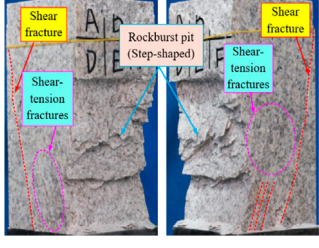
FIGURE 4

Sketch map of the test method and loading-unloading path of rockburst.

TABLE 1 Testing plan.

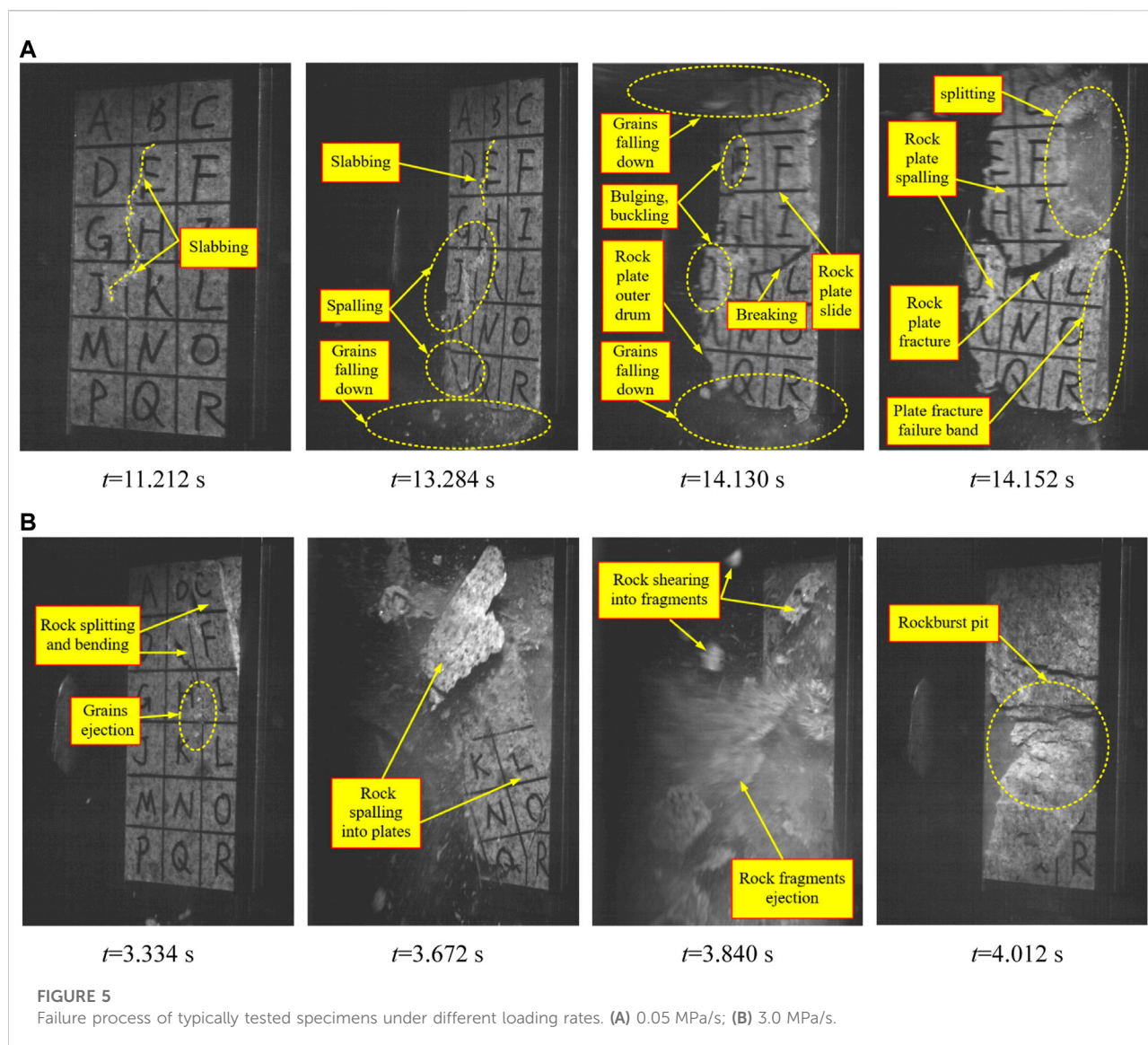
Specimen no.	Loading rate (MPa/s)	σ_2 (MPa)	$\sigma_{3(y2)}$ (MPa)
Z-1	0.05	55	5
Z-2	1.0	55	5
Z-3	3.0	55	5
Z-4	5.0	55	5

TABLE 2 Failure and ejection characteristics of the specimen with different loading rates.

Loading rate (MPa/s)	Axial stress–strain curve	Failure process	Failure mode
0.05 (Z-1)		When the vertical stress reaches 95% of the peak stress, the unloading face slabbing to form a thin rock plate. After about 0.022 s, the unloading rock plate spalling occurs on the unloading surface, forming a macroscopic slabbing failure band	
1.0 (Z-2)		When the vertical stress reaches 91% of the peak stress, grain ejection occurs on the unloading face, and the rock plate bends and slides. After about 1.708 s, the rock plate bulges and fractures, and the overall ejection damage occurs, accompanied by a bursting sound like a detonator blast, and the bursting sound is loud	
3.0 (Z-3)		When the vertical stress reaches 91% of the peak stress, small grain ejection and rock plate cracking at the upper part appear on the unloading face. After about 0.678 s, the rock plate fracture and ejection failure occurred, forming a rockburst pit, accompanied by a strong explosion sound-like explosive blasting, and the sound is strong	
5.0 (Z-4)		When the vertical stress reaches 95% of the peak stress, the rock plate breaks and spalling occurs on the unloading face. After about 0.076 s, ejection failure occurred on the unloading face, accompanied by a low sound like a shell explosion or muffled thunder, with a violent sound	

unloading face of rock mass appears, and its radial stress decreases sharply (the corresponding principal stress is σ_3), the tangential stress increases gradually (the corresponding principal stress is σ_1), and the principal stress along the

cavern axis remains the same as the initial stress field (the corresponding principal stress is σ_2), as depicted in Figure 3. For the rock unit in the area of concentrated compressive stress in the surrounding rock mass, the radial stress on the excavation



boundary is zero, while the radial stress in the rock mass at a certain distance from the excavation surface rises sharply along the diameter direction, and the rock unit is in a special stress state of “one-face zero load-three directions and five-face load”.

According to the stress path and boundary condition transformation process of the surrounding rock mass after excavation of an underground cavern (Figure 3), the true-triaxial rockburst test with single-face fast unloading-three directions and five-face stress-vertical continuous loading can accurately reproduce the stress transformation process of radial stress plunge and tangential stress concentration after excavation and unloading of deep underground engineering. In addition, engineering practice demonstrates that rockburst typically occurs within 1–3 days after excavation (Chen et al., 2012; Hu et al., 2019a), indicating that the gradual concentration of tangential stress is one of the main factors

leading to rockburst. Consequently, the process of continual concentration of tangential stress can be reproduced with vertical continuous loading. Figure 4 depicts the test method and loading-unloading path.

The specific testing procedures are described below: (I) the initial stress state of underground engineering rock mass before excavation is simulated according to the *in situ* stress field inversion of measured geostress in a project, and the initial stress state in three directions is $\sigma_1/\sigma_2/\sigma_3=74.58/54.96/39.51$ MPa (Ge and Hou, 2011). To achieve the loading and unloading in the tests, the values of σ_1 , σ_2 , and σ_3 under the initial ground stress condition in loading paths were set as 75, 55, and 40 MPa, respectively. First, the principal stresses σ_1 , σ_2 , and σ_3 were loaded simultaneously to the predetermined values and then held for about 2–3 min. Second, the principal stresses σ_1 and

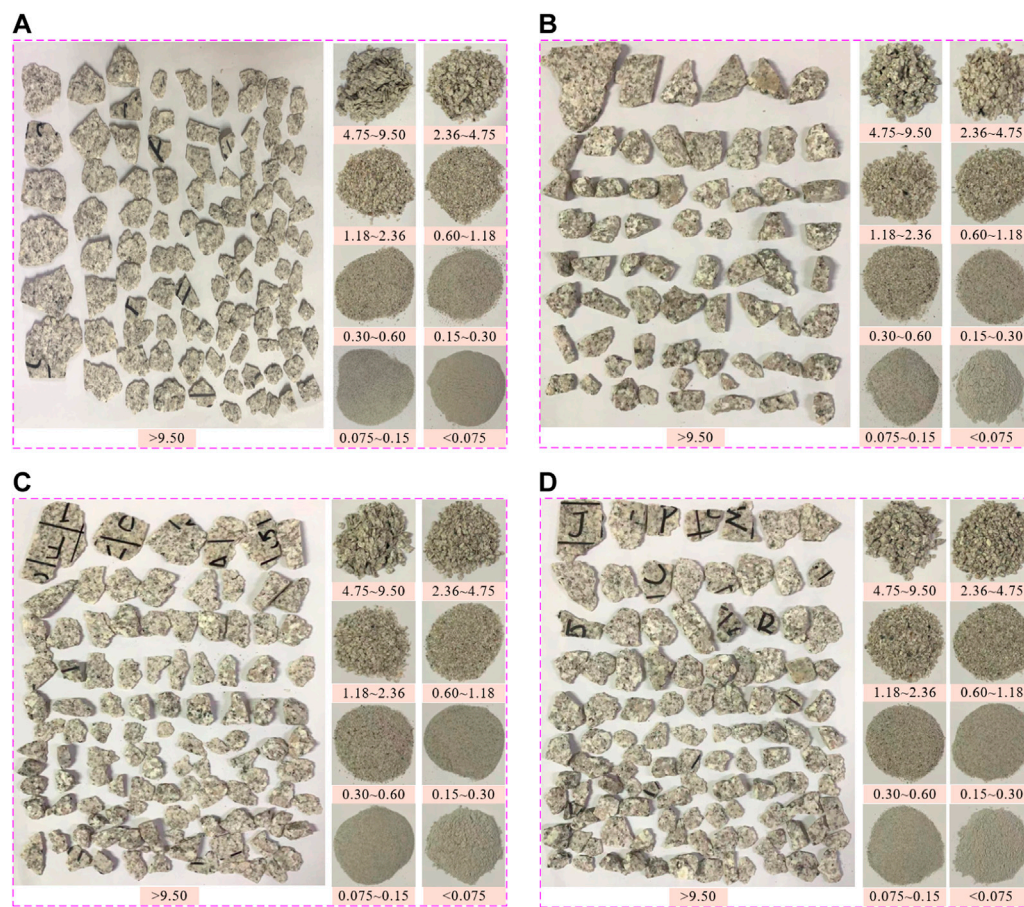


FIGURE 6

Fragment size distribution under different loading rates (unit: mm). (A) 0.05 MPa/s; (B) 1.0 MPa/s; (C) 3.0 MPa/s; (D) 5.0 MPa/s.

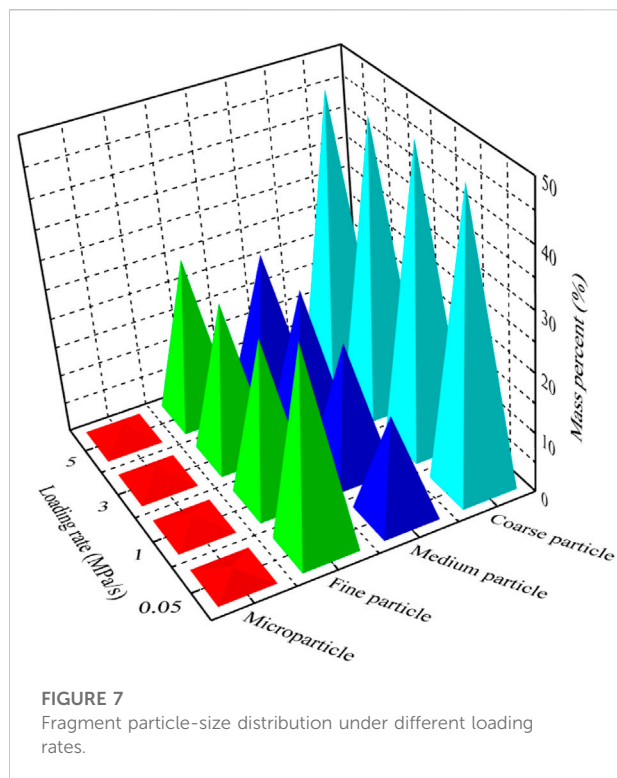
σ_2 were loaded simultaneously to the predetermined values and then held for about 2–3 min. Finally, the principal stress σ_1 was loaded to the predetermined values. After the initial stress state is applied, the specimen is stabilized for approximately 6–8 min under the triaxial stress state of $\sigma_1=75$ MPa, $\sigma_2=55$ MPa, and $\sigma_3=40$ MPa. (II) A single-face fast unloading device (two springs) is used to unload the stress $\sigma_{3(y1)}$ to zero on one face in the Y-direction, while rapidly reducing the stress $\sigma_{3(y2)}$ to a predetermined value on the other face in the Y-direction. In order to simulate the radial stress reduction after excavation unloading in underground engineering and to realize the conversion process, the stress path and boundary conditions near the excavation boundary must be under the effect of tangential stress. The stress $\sigma_{3(y2)}$ on the opposite face of the unloading face and the stress σ_2 in the X-direction are kept unchanged. Finally, the stress σ_2 in the vertical stress σ_1 is continuously increased at different loading rates until the specimen fails.

2.3.2 Testing plan

In this experiment, four different loading rates of 0.05, 1.0, 3.0, and 5.0 MPa/s were designed, with strain rates of 1.7×10^{-6} , 3.4×10^{-5} , 1.0×10^{-4} , and $1.7 \times 10^{-4} \text{ s}^{-1}$ corresponding to the four different loading rates. The specific test procedures are detailed in Table 1. In our test, at least three specimens were prepared for each test with a given loading path to guarantee the repeatability of the experimental results. The typical failure process of each tested specimen was chosen to investigate the rockburst.

3 Failure and ejection characteristics of rockburst

The stress–strain curves, failure process, and failure modes of granite specimens with different loading rates are shown in Table 2.



From Table 2, it is clear that at a loading rate of 0.05 MPa/s, rock samples exhibited static brittle failure characterized by slabbing. At loading rates of 1.0, 3.0, and 5.0 MPa/s, all rock specimens experienced varying degrees of rockburst dynamic failure, with rock specimens (Z-4) experiencing the most severe ejection failure. This indicates that the loading rate is sufficient to cause the accumulation of a large amount of elastic strain energy within the rock specimen, part of which is converted into dissipation energy required for the splitting of the rock plate and the potential shearing of rockburst pit into fragments (pieces), while most of the elastic strain energy is converted into kinetic energy required for the fragment ejection, prompting the rock sample to rockburst.

3.1 Stress–strain curve

By comparing the rock sample (Z-1) with static brittle failure, the typical stress–strain curves of rock samples with ejection failure exhibit the following characteristics: 1) the failure process of rock samples under different loading rates consists of four stages: the initial compaction stage (OA), the elastic deformation stage (AB), the pre-peak unstable fracture stage (BC), and the post-peak failure stage (CD). 2) The pre-peak curve has an obvious yield point, and the stress–strain curve between the yield point and peak point changes more gently, corresponding to the splitting failure at the unloading

face of the rock sample and shear failure in the range of potential rockburst pits.

3.2 Failure mode

The failure modes of rock samples under different loading rates are shown in Table 2. Z-1 rock samples exhibit a rock plate splitting phenomenon on the unloading face, a significant penetrating shear diagonal fracture on the inside of the rock body, and shear-tension fractures close to the unloading face, which are predominantly stable and slow slabbing failures. All Z-2~Z-4 rock samples exhibit clear multiple zoning failure characteristics, that is, the unloading face displays a V-shaped or step-shaped rockburst pit and tension produced by the splitting fracture, and the rockburst pit surface is uneven.

3.3 Ejection process of rockburst

Due to space constraints, the ejection failure process of a Z-3 granite sample is selected as an example to compare with the static brittle failure of the Z-1 granite sample. Figure 5 displays the detailed comparison. The ejection failure process can be divided into four stages, including grain ejection, rock spalling into plates, rock shearing into fragments, and rock fragment ejection.

4 Fragment characteristics of rockburst

4.1 Particle size grouping and mass distribution characteristics of fragments

According to the rockburst fragment classification method (Su et al., 2016b), fragments were classified into four classes based on particle size: particulate ($d < 0.075$ mm), fine-grained ($0.075 \text{ mm} \leq d < 4.75$ mm), medium-grained ($4.75 \text{ mm} \leq d < 9.5$ mm), and coarse-grained ($d \geq 9.5$ mm). Among them, fine-grained fragments containing six particle sizes (0.075–0.15 mm, 0.15–0.30 mm, 0.30–0.60 mm, 0.60–1.18 mm, 1.18–2.36 mm, and 2.36–4.75 mm). The masses of four grades were weighed by a high-sensitivity electronic scale. Figure 6 depicts photographs of fragment classification under different loading rates. Figure 7 illustrates the percentage distribution of rock fragments of each particle size class in the total mass of fragments under different loading rates.

Figure 7 illustrates that coarse-grained, medium-grained, and fine-grained fragments dominate the rockburst fragmentation mass. It demonstrates that as the loading

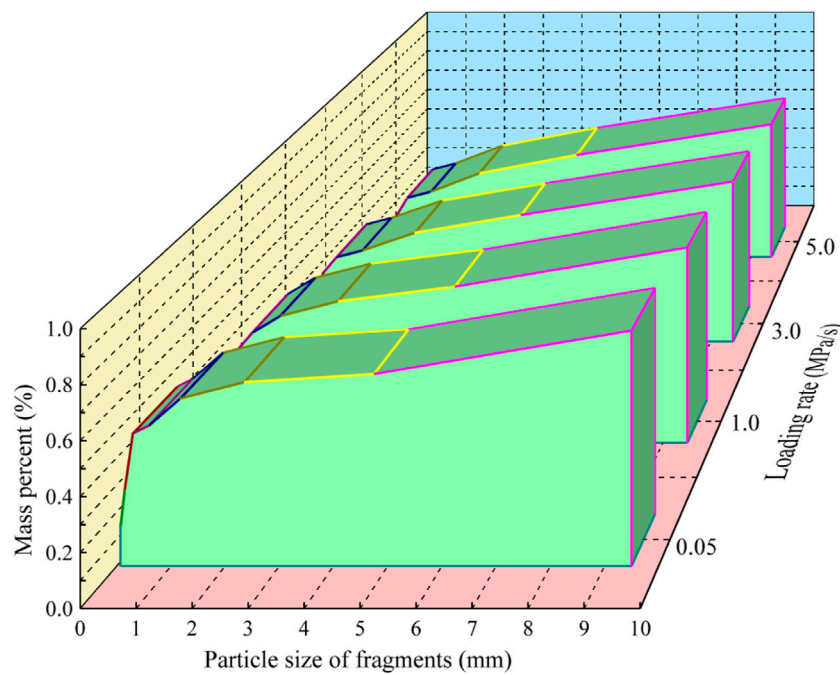


FIGURE 8

Weibull distribution curve of sample fragments.

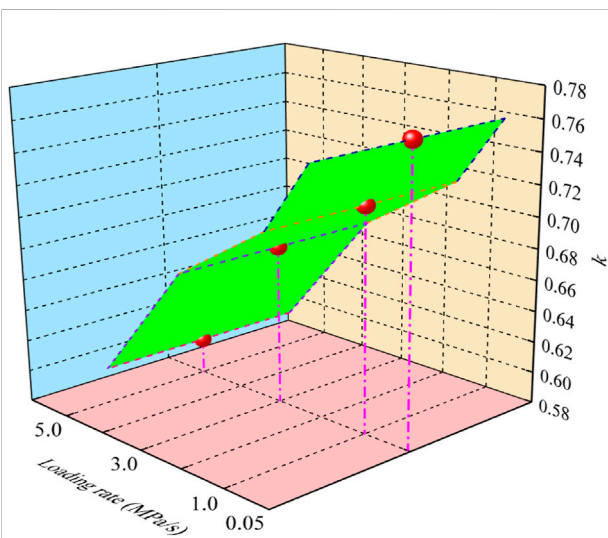


FIGURE 9

Size parameters of the Weibull distribution.

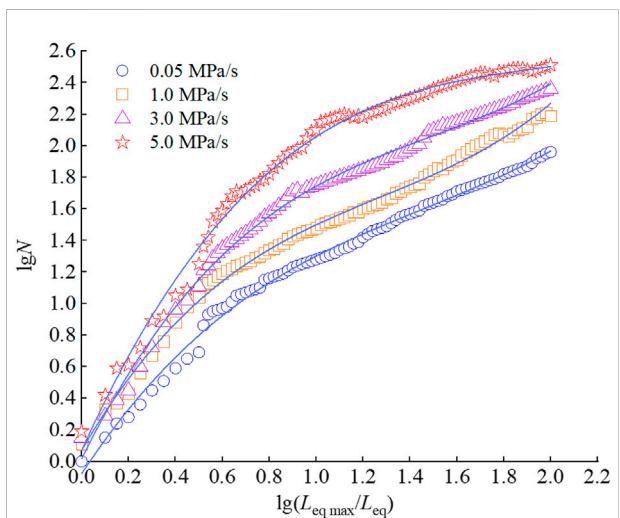


FIGURE 10

Relationship of granularity-quantity.

rate increases, under the action of vertical stress σ_1 , the fractured rock plate caused by the tension stress in the vertical direction unloading face increases significantly, and the rock plate is ejected under the action of shear as well as tensile-shear load, producing larger grain size fragments.

4.2 Weibull distribution of particle size

The Weibull distribution function can be used to fit and statistically analyze the particle size distribution of rockburst fragments, and the Weibull distribution function relationship is given below (Li et al., 2021):

TABLE 3 Calculation of granularity-quantity fractal values.

Loading rate (MPa/s)	Fitting curve	Correlation coefficient	Fractal dimension
0.05	$y = 0.2607x^3 - 1.1388x^2 + 2.2575x - 0.0782$	0.9945	2.14
1.0	$y = 0.3994x^3 - 1.5283x^2 + 2.5582x + 0.0701$	0.9948	2.42
3.0	$y = 0.3689x^3 - 1.6457x^2 + 3.0037x + 0.0167$	0.9953	2.64
5.0	$y = 0.2636x^3 - 1.5634x^2 + 3.2882x + 0.0696$	0.9932	2.78

$$G_{\text{weibull}}(x, \lambda, k) = 1 - \exp\left[-\left(\frac{x}{\lambda}\right)^k\right], \quad (1)$$

where k is the dimensional parameter; λ is the shape parameter; x is the maximum length value of the fragment particle group.

The size parameter k represents the average value of fragment size, and a smaller value of k indicates that the average fragment size is smaller, that is, the degree of fragmentation is more serious (Liu et al., 2022). Figure 8 depicts the Weibull distribution curve of rockburst fragments. The size parameter k obtained from the Weibull distribution curve is shown in Figure 9.

As shown in Figure 9, 1) the size parameter k decreases gradually with the increase in loading rate. It shows that the larger the loading rate within the selected range of tests, the smaller the average size of fragments after the occurrence of rockburst and the more severe the fragmentation of fragments, that is, the fragmentation degree of fragments increases with the increase in loading rate. 2) The use of the Weibull distribution function of rockburst test after the particle size distribution of fragmentation analysis, the quantitative comparison of fragmentation degree, can be used as a reference for quantifying the degree of rockburst serious index.

4.3 Fractal characteristics of fragments

Fractal theory can quantitatively describe various complex morphologies such as material fracture surfaces (Dlouhy and Strnadel, 2008). In particular, the fractal dimension reflects the complex morphologies that cannot be quantitatively expressed in the original Euclidean geometric space (Xie et al., 2004; Ping et al., 2015). Some researchers have utilized fractal methods to analyze the fragmentation degree of rockburst and the energy release characteristics of the failure process (Hu et al., 2002; Deng et al., 2007; Wang and Gao, 2007).

4.3.1 Granularity-quantity

For medium-grained and coarse-grained sizes, the measured length, width, and thickness values (l , w , and h , respectively) were converted into the equivalent side length of a square-by-rectangular shape L_{eq} (where $L_{\text{eq}} = (l \times w \times h)^{1/3}$). For particulate and fine-grained sizes, particle sieving is

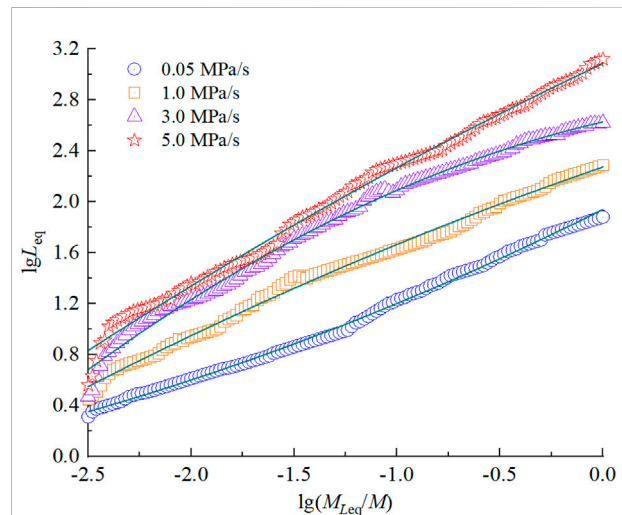


FIGURE 11
Relationship of granularity-mass.

performed, and the particle size is used as the equivalent side length value. The particle quantity is counted using the sampling statistics method. According to the granularity-quantity relationship equation (He et al., 2009), the fractal dimension of fractured pieces can be calculated as follows:

$$N = N_0 \left(\frac{L_{\text{eq}}}{L_{\text{eq max}}} \right)^{-D}, \quad (2)$$

where N is the number of fragments with characteristic granularity equivalent to edge length $\geq L_{\text{eq}}$, N_0 is the number of fragments with maximum characteristic scale $L_{\text{eq max}}$, and D is the fractal dimension.

The $\lg N - \lg (L_{\text{eq max}}/L_{\text{eq}})$ fitting curve is plotted as shown in Figure 10. Among them, the slope of the straight-line segment of the fitted curve is the fractal dimension, and the specific values are shown in Table 3.

4.3.2 Granularity-mass

The maximum length, width, and thickness values measured for coarse-grained fragments were converted to equivalent edge lengths, and the sieve grain size was utilized to determine equivalent edge lengths for medium-grained, fine-grained, and particulate fragments. The fragment granularity-equivalent edge

TABLE 4 Calculation of granularity-mass fractal values.

Loading rate (MPa/s)	Fitting curve	Correlation coefficient	Fractal dimension
0.05	$y = 0.0688x^2 + 0.8075x + 1.9394$	0.9974	1.81
1.0	$y = -0.0541x^2 + 0.5546x + 2.2731$	0.9951	1.98
3.0	$y = -0.1613x^2 + 0.3755x + 2.6274$	0.9945	2.21
5.0	$y = -0.0563x^2 + 0.7615x + 3.0866$	0.9942	2.56

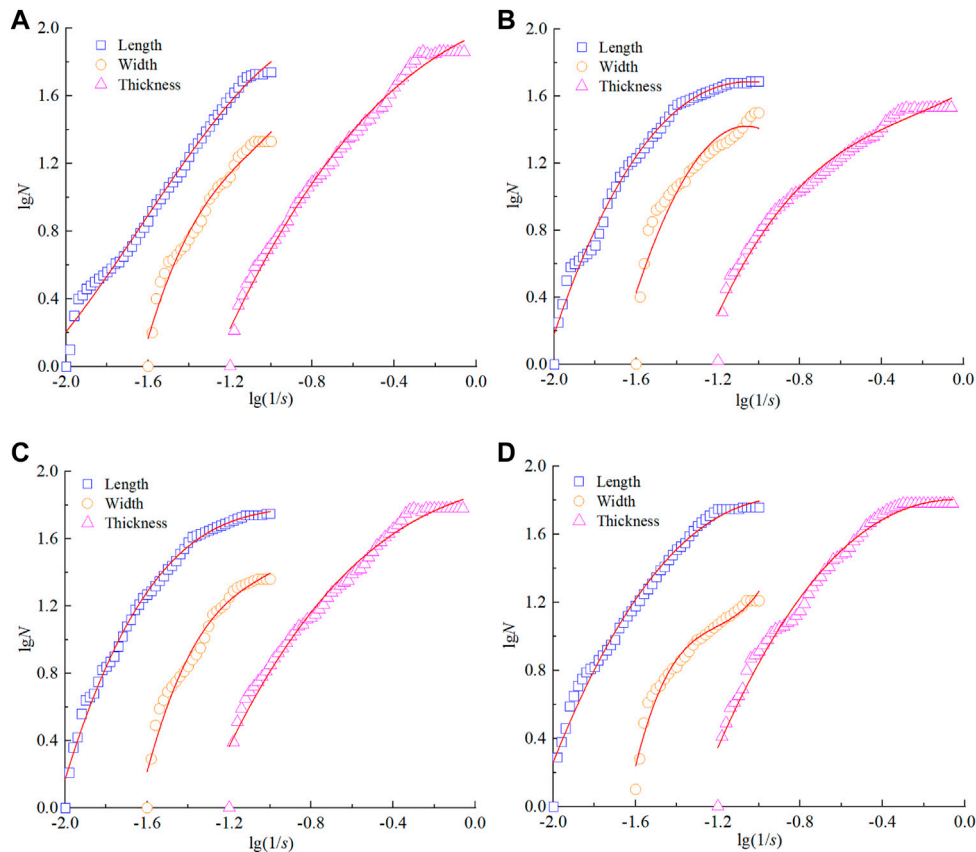


FIGURE 12
Fractal dimension of three sizes. (A) 0.05 MPa/s; (B) 1.0 MPa/s; (C) 3.0 MPa/s; (D) 5.0 MPa/s.

length was utilized to calculate the fractional dimension D . The formula was calculated as follows (He et al., 2009):

$$D = 3 - \alpha, \quad (3)$$

$$\alpha = \frac{\lg(M_{L_{eq}}/M)}{\lg L_{eq}}, \quad (4)$$

where α is the slope value of $M_{L_{eq}}/M - L_{eq}$ in double logarithmic coordinates; $M_{L_{eq}}/M$ is the cumulative percentage of fragments with equivalent side lengths less than L_{eq} , $M_{L_{eq}}$ is the mass of

fragments, corresponding to equivalent side lengths equal to L_{eq} , and M is the total mass of fragments in the calculated dimensions.

The fitted curve of $\lg(M_{L_{eq}}/M) - \lg L_{eq}$ was plotted as shown in Figure 11. The granularity-mass fractal dimension is calculated by combining Eqs 3 and 4, and the specific values are shown in Table 4.

4.3.3 Length/width/thickness-quantity

First, the length, width, and thickness of rockburst fragments are measured (all are the maximum dimensions in that

TABLE 5 Fractal dimension calculation of three sizes.

Loading rate (MPa/s)	Three sizes (mm)	Fitting curve	Correlation coefficient	Fractal dimension
0.05	Length	$y = -0.7257x^3 - 3.5478x^2 - 3.9662x + 0.6583$	0.9893	1.80
	Width	$y = 3.6172x^3 + 11.7119x^2 + 13.8192x + 7.1113$	0.9756	1.99
	Thickness	$y = 0.1599x^3 - 0.5560x^2 + 0.5495x + 1.9613$	0.9906	2.34
1.0	Length	$y = 0.5100x^3 + 0.4389x^2 - 0.7488x + 1.0072$	0.9903	1.85
	Width	$y = 3.5912x^3 + 11.6978x^2 + 12.2293x + 6.66415$	0.9669	2.07
	Thickness	$y = 0.7786x^3 + 0.5644x^2 + 0.6630x + 1.6261$	0.9797	2.39
3.0	Length	$y = 1.0023x^3 + 2.6621x^2 + 2.4418x + 2.5842$	0.9936	1.98
	Width	$y = 3.6755x^3 + 11.1111x^2 + 11.8912x + 5.8517$	0.9679	2.09
	Thickness	$y = 0.2468x^3 - 0.4473x^2 + 0.3496x + 1.8566$	0.9781	2.41
5.0	Length	$y = 0.2492x^3 - 0.2844x^2 - 1.0620x + 1.2667$	0.9862	2.01
	Width	$y = 3.1763x^3 + 11.1483x^2 + 10.5508x + 7.8454$	0.9712	2.12
	Thickness	$y = 0.2085x^3 - 0.8226x^2 - 0.0749x + 1.8021$	0.9802	2.45

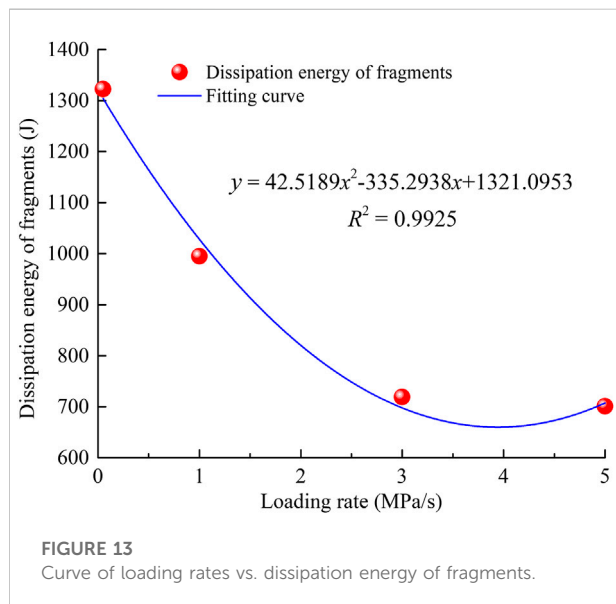


FIGURE 13

Curve of loading rates vs. dissipation energy of fragments.

direction). Second, based on the measurement results, the fractal dimension calculations of length-cumulative quantity, width-cumulative quantity, and thickness-cumulative quantity were carried out according to the fractal dimension calculation method of equivalent edge length-cumulative quantity in granularity-quantity (He et al., 2009). Finally, the $\lg N - \lg (1/s)$ fitting curve (where s is length/width/thickness) is plotted as shown in Figure 12. In this figure, the slope of the straight-line segment of the fitted curve is the fractal dimension, and the specific values are shown in Table 5.

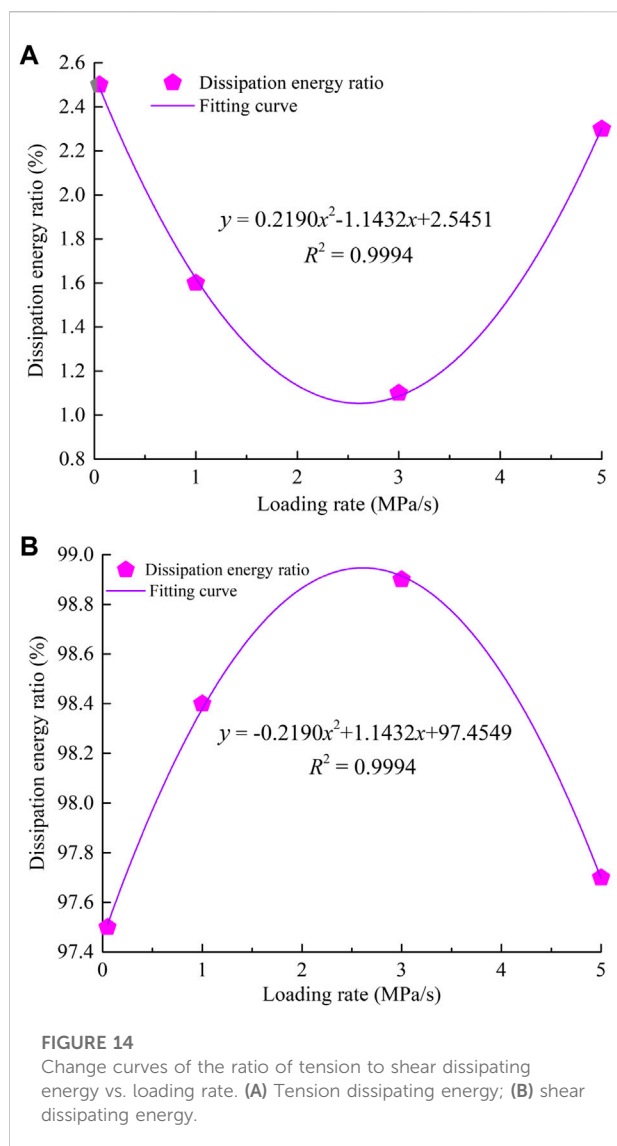
4.3.4 Fractal characteristic analysis of fragments

From Table 3 to Table 5, 1) the fractal dimension of fragments can reflect the failure degree of rock samples, that

is, the larger the fractal dimension D , the more serious the fragments are broken. It shows that the failure degree of rock is positively correlated with fractal dimension. The correlation coefficients of fractal dimensions are all greater than 0.950, indicating that the accumulated number of fragments smaller than the equivalent edge length correlates strongly with the equivalent edge length. 2) Although there are evident discrepancies in the fractal dimensions derived by the three calculation methods, the fractal dimensions exhibit the same trend with different loading rates, that is, they rise as the loading rates increase. This indicates that the greater the loading rate, the less energy is consumed by the crack development and expansion of the rock sample, resulting in a greater amount of elastic strain energy that can be converted into kinetic energy of fragment ejection, which results in varying degrees of rockburst hazard for the rock sample. 3) As the loading rate increases, the crack expansion rate accelerates, intensifying the failure of the rock specimen, reducing its compressive strength, and causing greater fragmentation when the specimen fails. The previous results indicate that the fragmentation categorization method can also be utilized to evaluate the degree of rockburst failure on rock-containing structural surfaces.

5 Discussion

This article discusses the effect of loading rate on the energy dissipation of rockburst fragments in the context of research findings on the fractal characteristics of fragments. According to the energy dissipation estimation method (Su et al., 2016a), Figure 13 depicts the total energy dissipation curve of fragments under different loading rates, and Figure 14 depicts the energy dissipation ratio change curve of tension and shear failure under different loading rates.



From Figure 13, and 14, the greater the loading rate, the lower the energy dissipation of rockburst fragments. It demonstrates that when the loading rate increases, the fragmentation degree of fragments increases, energy dissipation decreases, and the rockburst becomes more serious. 2) When the loading rate is 0.05 MPa/s, 1.0 MPa/s, 3.0 MPa/s, and 5.0 MPa/s, the proportion of shear failure energy consumption of rock fragments to total energy consumption is 97.5, 98.4, 98.9, and 97.7%, respectively. It proves that the energy dissipation of fragments under different loading rates is dominated by shear energy dissipation. In addition, the proportion of tension energy consumption decreases and subsequently increases as the loading rate increases, while the proportion of shear energy consumption exhibits the opposite trend of tension energy consumption.

According to further analysis of the abovementioned results, the occurrence of rockbursts is essentially caused by unstable changes in

the internal energy of rocks. In rock specimens in the loading stage (Figure 4), the loading system applied to the specimen energy is mainly converted into strain energy stored in the specimen and dissipation energy required for fracture closure or expansion. Once the specimen is unloaded, the majority of its stored energy is rapidly transformed into the kinetic energy required for the rapid ejection or throwing of fragments. The greater the loading rate, the specimen in the process of loading and unloading the internal crack development is less adequate. The higher the fragmentation degree, the smaller the corresponding energy dissipation, resulting in the degree of failure to the specimen rockburst will exhibit a stronger dynamic. This also shows that the macroscopic block characteristics of rockburst fragments can reflect the fragmentation degree of rock and that rockburst occurs in the energy input, storage, dissipation, and release are closely associated when a rockburst happens. In judging the level of rockburst failure, the fractal dimension of rockburst fragments can be used as a rockburst reference basis. A large number of engineering practices indicate that the faster the tunnel excavation speed, the greater the degree of failure when the rockburst occurs. Therefore, in the excavation process of underground engineering, the excavation speed can be appropriately reduced to reduce the vertical stress loading rate of the tunnel surrounding rock, so as to effectively avoid the occurrence of severe rockburst.

6 Conclusion

In this article, a complete and accurate reproduction of the entire process of rockburst inoculation-occurrence-development in the test room and a comparative analysis of fragmentation degree, fractal characteristics, and Weibull distribution characteristics of rockburst fragments under different loading rates are presented. The key findings are as follows:

- 1) The rockburst ejection failure process under different loading rates reveals that at a loading rate of 0.05 MPa/s, rock samples experienced static brittle failure of slabbing. At loading rates of 1.0, 3.0, and 5.0 MPa/s, rock samples experienced different degrees of rockburst disaster. The rockburst ejection failure process can be summarized as four stages: grain ejection, rock spalling into plates, rock shearing into fragments, and rock fragment ejection.
- 2) The particle size grouping and mass distribution characteristics of different fragments show that the quality of rockburst fragments is mainly coarse-grained, medium-grained, and fine-grained. With the increase in loading rate, under the action of vertical stress σ_1 , the splitting rock plate caused by tensile stress in the direction of the vertical unloading face increases obviously, and the rock plate is ejected under the action of shear and tensile-shear load, forming large particle-size fragments.
- 3) The statistical analysis results of the Weibull distribution of rockburst fragments under different loading rates show that

the size parameter k represents the average value of fragment size; the smaller the value of k , the more serious the fragmentation degree. The size parameter k gradually decreases with an increasing loading rate. The fragmentation degree of rockburst fragments grows as the loading rate increases.

- 4) The fractal characteristics of rockburst fragments show that the fractal dimension with different loading rates shows a consistent trend, that is, the fractal dimension increases as the loading rate increases. As the loading rate increases, the rate of crack expansion increases, which exacerbates the damage to the rock specimen, reduces its compressive strength, and causes greater fragmentation when the specimen fails.

Data availability statement

The original contributions presented in the study are included in the article/Supplementary Material; further inquiries can be directed to the corresponding author.

Author contributions

Conceptualization, JG and XL; methodology, FS; data curation, FS; writing—original draft preparation, FS and JG; funding acquisition, JF, JG, and XL; formal analysis, FS;

writing—review and editing, FS and JG. All authors have read and agreed to the published version of the manuscript.

Funding

This research was funded by the National Natural Science Foundation of China (52178388, U1810203) and the Natural Science Foundation of Henan Province (212300410146).

Conflict of interest

The authors declare that the research was conducted in the absence of any commercial or financial relationships that could be construed as a potential conflict of interest.

Publisher's note

All claims expressed in this article are solely those of the authors and do not necessarily represent those of their affiliated organizations, or those of the publisher, the editors, and the reviewers. Any product that may be evaluated in this article, or claim that may be made by its manufacturer, is not guaranteed or endorsed by the publisher.

References

- Chen, B. R., Feng, X. T., Ming, H. J., Zhou, H., Zeng, R. H., Feng, G. L., et al. (2012). Evolution law and mechanism of rockburst in deep tunnel: Time delayed rockburst. *Chin. J. Rock Mech. Eng.* 31 (3), 561.
- Chen, Z. Y., Su, G. S., Ju, J. W., and Jiang, J. Q. (2019). Experimental study on energy dissipation of fragments during rockburst. *Bull. Eng. Geol. Environ.* 78, 5369–5386. doi:10.1007/s10064-019-01463-9
- Deng, T., Yang, L. D., and Han, W. F. (2007). Influence of loading form on distribution of marble fragments. *J. Tongji Univ. Sci.* 35 (1), 10.
- Dlouhy, I., and Strnadel, B. (2008). The effect of crack propagation mechanism on the fractal dimension of fracture surfaces in steels. *Eng. Fract. Mech.* 75 (3), 726–738. doi:10.1016/j.engfracmech.2007.03.038
- Fairhurst, C. E., and Hudson, J. A. (1999). Draft ISRM suggested method for the complete stress-strain curve for intact rock in uniaxial compression. *Int. J. Rock Mech. Min. Sci.* 36 (3), 279–289.
- Ge, X. R., and Hou, M. X. (2011). A new 3D *in-situ* rock stresses measuring method: Borehole wall stress relief method (BWSRM) and development of geostress measuring instrument based on BWSRM and its primary applications to engineering. *Chin. J. Rock Mech. Eng.* 30 (11), 2161.
- He, M. C., Wang, Y., Su, J. S., and Liu, D. Q. (2018). Analysis of fractal characteristics of fragment of sandstone impact rock burst under static and dynamic coupled loads. *J. China Univ. Min. Technol.* 47 (4), 699. doi:10.13247/j.cnki.jcmt.000876
- He, M. C., Yang, G. X., Miao, J. L., Jia, X. N., and Jiang, T. T. (2009). Classification and research methods of rockburst experimental fragment. *Chin. J. Rock Mech. Eng.* 28 (8), 1521.
- Hedley, D. G. F. (1992). *Rockburst handbook for Ontario hardrock mines*. Toronto: Toronto Public Library.
- Hu, L. Q., Li, X. B., and Zhao, F. J. (2002). Study on energy consumption in fracture and damage of rock induced by impact loadings. *Chin. J. Rock Mech. Eng.* 21 (S2), 2304.
- Hu, X. C., Su, G. S., Chen, G. Y., Mei, S. M., Feng, X. T., Mei, G. X., et al. (2019a). Experiment on rockburst process of borehole and its acoustic emission characteristics. *Rock Mech. Rock Eng.* 52, 783–802. doi:10.1007/s00603-018-1613-z
- Hu, X. C., Su, G. S., Chen, K., Li, T. B., and Jiang, Q. (2019b). Strainburst characteristics under bolt support conditions: An experimental study. *Nat. Hazards (Dordr)* 97, 913–933. doi:10.1007/s11069-019-03682-5
- Jiang, J. Q., Su, G. S., Liu, Y. X., Zhao, G. F., and Yan, X. Y. (2020b). Effect of the propagation direction of the weak dynamic disturbance on rock failure: An experimental study. *Bull. Eng. Geol. Environ.* 80, 1507–1521. doi:10.1007/s10064-020-01960-2
- Jiang, J. Q., Su, G. S., Zhang, X. H., and Feng, X. T. (2020a). Effect of initial damage on remotely triggered rockburst in granite: An experimental study. *Bull. Eng. Geol. Environ.* 79 (6), 3175–3194. doi:10.1007/s10064-020-01760-8
- Khan, N. M., Ahmad, M., Cao, K. W., Ali, L., Liu, W., Rehman, H., et al. (2022). Developing a new bursting liability index based on energy evolution for coal under different loading rates. *Sustainability* 14 (3), 1572. doi:10.3390/su14031572
- Li, D. J., Jia, X. N., Miao, J. L., He, M. C., and Li, D. D. (2010). Analysis of fractal characteristics of fragment from rockburst test of granite. *Chin. J. Rock Mech. Eng.* 29 (S1), 3280.
- Li, D. J., Zhao, F., and Zheng, M. J. (2014). Fractal characteristics of cracks and fragments generated in unloading rockburst tests. *Int. J. Min. Sci. Technol.* 24 (6), 819–823. doi:10.1016/j.ijmst.2014.10.014
- Li, X., Yao, W., and Wang, C. L. (2021). The influence of multiple dynamic loading on fragmentation characteristics in dynamic compression tests. *Rock Mech. Rock Eng.* 54 (3), 1583–1596. doi:10.1007/s00603-020-02324-8
- Liu, D. Q., Han, Z. J., Wang, C. G., and Hu, T. X. (2021). Experimental study on fragment characteristics of rockburst induced by uni-directional, bi-directional and tri-directional disturbances. *J. Central South Univ. Sci. Technol.* 52 (8), 2793. doi:10.11817/j.issn.1672-7207.2021.08.025

- Liu, D. Q., Hu, T. X., Wang, Y., Ling, K., Han, Z. J., and He, M. C. (2022). Experimental study on the effect of dynamic load frequency for impact rockburst of sandstone. *Chin. J. Rock Mech. Eng.* 41 (7), 1310–1324. doi:10.13722/j.cnki.jrme.2021.0951
- Liu, D. Q., Li, D. J., Zhao, F., and Wang, C. C. (2014). Fragmentation characteristics analysis of sandstone fragments based on impact rockburst test. *J. Rock Mech. Geotechnical Eng.* 6 (3), 251–256. doi:10.1016/j.jrmge.2014.04.001
- Lu, J., Zhang, D. M., Huang, G., Li, X., Gao, H., and Yin, G. Z. (2020). Effects of loading rate on the compound dynamic disaster in deep underground coal mine under true triaxial stress. *Int. J. Rock Mech. Min. Sci.* 134, 104453. doi:10.1016/j.ijrmms.2020.104453
- Ping, Q., Luo, X., Ma, Q. Y., and Yuan, P. (2015). Broken energy dissipation characteristics of sandstone specimens under impact loads. *Chin. J. Rock Mech. Eng.* 34 (S2), 4197. doi:10.13722/j.cnki.jrme.2015.0585
- Si, X. F., Huang, L. Q., Gong, F. Q., Liu, X. L., and Li, X. B. (2020). Experimental investigation on influence of loading rate on rockburst in deep circular tunnel under true-triaxial stress condition. *J. Cent. South Univ.* 27, 2914–2929. doi:10.1007/s11771-020-4518-4
- Su, G. S., Chen, Z. Y., Jiang, J. Q., Mo, J. H., and Shi, Y. J. (2016a). Experimental study on energy dissipating characteristics of rockburst fragments under different loading rates. *Chin. J. Geotechnical Eng.* 38 (8), 1481. doi:10.11779/CJGE201608016
- Su, G. S., Chen, Z. Y., Yin, H. X., Zhang, X. H., and Mo, J. H. (2016b). True triaxial tests on rockburst of granite after high temperatures. *Chin. J. Geotechnical Eng.* 38 (9), 1586. doi:10.11779/CJGE201609005
- Su, G. S., Jiang, J. Q., Feng, X. T., Jiang, Q., Chen, Z. Y., and Mo, J. H. (2018). Influence of loading rate on strainburst: An experimental study. *Bull. Eng. Geol. Environ.* 78, 3559–3573. doi:10.1007/s10064-018-1351-1
- Wang, L., and Gao, Q. (2007). Fragmentation distribution prediction of rock based on damage energy dissipation. *Chin. J. Rock Mech. Eng.* 26 (6), 1202.
- Xia, Y. Y., Lin, M. Q., Liao, L. L., Xiong, W., and Wang, Z. D. (2014). Fractal characteristic analysis of fragments from rockburst tests of large-diameter specimens. *Chin. J. Rock Mech. Eng.* 33 (7), 1358. doi:10.13722/j.cnki.jrme.2014.07.007
- Xie, H. P., and Pariseau, W. G. (1993). Fractal character and mechanism of rock bursts. *Chin. J. Rock Mech. Eng.* 12 (1), 28.
- Xie, H. P., Peng, R. D., and Ju, Y. (2004). Energy dissipation of rock deformation and fracture. *Chin. J. Rock Mech. Eng.* 23 (21), 3365.



OPEN ACCESS

EDITED BY

Shuren Wang,
Henan Polytechnic University, China

REVIEWED BY

Fangtian Wang,
China University of Mining and
Technology, China
Bing Bai,
Beijing Jiaotong University, China

*CORRESPONDENCE

Hongkai Han,
hkh@hpu.edu.cn

SPECIALTY SECTION

This article was submitted to
Geohazards and Georisks,
a section of the journal
Frontiers in Earth Science

RECEIVED 19 August 2022

ACCEPTED 06 September 2022

PUBLISHED 23 September 2022

CITATION

Liu Y, Jia H, Han H, Zuo W, Shi J,
Chang P, Miao J, He Y and Peng J
(2022), Research on the gas migration
trend and mechanism of the transition
flow regime in coal based on MRT-
LBM simulation.

Front. Earth Sci. 10:1022845.

doi: 10.3389/feart.2022.1022845

COPYRIGHT

© 2022 Liu, Jia, Han, Zuo, Shi, Chang,
Miao, He and Peng. This is an open-
access article distributed under the
terms of the [Creative Commons
Attribution License \(CC BY\)](https://creativecommons.org/licenses/by/4.0/). The use,
distribution or reproduction in other
forums is permitted, provided the
original author(s) and the copyright
owner(s) are credited and that the
original publication in this journal is
cited, in accordance with accepted
academic practice. No use, distribution
or reproduction is permitted which does
not comply with these terms.

Research on the gas migration trend and mechanism of the transition flow regime in coal based on MRT-LBM simulation

Yanwei Liu¹, Haojie Jia¹, Hongkai Han^{1*}, Weiqin Zuo¹, Jin Shi²,
Ping Chang³, Jian Miao^{1,4}, Yanyan He¹ and Jie Peng¹

¹School of Safety Science and Engineering, Henan Polytechnic University, Jiaozuo, China, ²College of Literature, Science and the Arts, University of Michigan, Ann Arbor, Michigan, United States, ³WA School of Mines: Minerals, Energy and Chemical Engineering, Curtin University, Kalgoorlie, WA, Australia,

⁴School of Intelligent Engineering, Shandong Management University, Jinan, Shandong, China

In order to reveal the process and mechanism of gas flow in a low-permeability coal seam, a new multiple-relaxation-time lattice Boltzmann method (MRT-LBM) model of gas migration in coal micro/nanopores based on Langmuir monolayer adsorption theory, the slip boundary scheme and Bosanquet effective viscosity was established. The software MATLAB was used to carry out the simulation study of uniform pore gas flow based on the MRT-LBM model, and the results were compared and verified with the porous anodic alumina membrane gas flow experimental results. On this basis, the gas flow in coal pores with different micro/nanopore sizes considering adsorption was simulated. The results show that the dimensionless permeability coefficient increases with decreasing pore size under the same pressure, which reflects the subsequent enhancement of the microboundary constraint effect and reveals that the pore system becomes the main controlling factor of coal seam permeability within the coal matrix in the middle and late stages of coal seam gas extraction, while the role of the microboundary constraint effect needs to be considered. The gas adsorption layer weakens the pore gas flow capacity, but for pores with a radius greater than 16 nm, the apparent change in permeability caused by the adsorption layer is less than 5%, and the adsorption effect can be ignored. N₂, CH₄, and CO₂ enter the transition flow regime under different pressure conditions; with gas extraction, the gas pressure decreases, and the difference in the gas flow characteristics of the three gases increases.

KEYWORDS

transition flow regime, micro/nanopore flow experiment, monolayer adsorption, multi-relaxation-time (MRT), expansion simulation

Introduction

According to the theory of rarefied gas dynamics, when the ratio of the mean free path of the molecules in the fluid to the pore size of coal seam (Knudsen number) is greater than 0.1, the fluid enters the transition flow regime, and the Navier–Stokes equation based on continuum approximation and the thermodynamic equilibrium assumption is invalid.

The gas transport within the micro/nanopores of a deep low-permeability coal seam in the middle and late stages of extraction occurs within the transition flow. Determining the trend and mechanism of coal seam gas migration in the transitional regime is a popular and challenging problem in current research. A precise understanding of the gas migration in low-permeability coal seams would have important directive significance for improving the accuracy of gas extraction prediction and implementing effective measures to increase production.

To accurately describe the gas migration in coal seam micro/nanopores, scholars have established various coal pore diffusion models from the perspective of pore diffusion (Wang et al., 2020a; Liu et al., 2020; Wang et al., 2021a; Zhang et al., 2022). Barrer (1951) first established the classical single-hole diffusion model based on Fick diffusion. Ruckenstein et al. (1971) proposed a dual-porosity diffusion model based on the classical model. Liu (Liu, 2011) extended the double porosity diffusion model to the three-stage diffusion model; although the accuracy was improved, the model was complex and difficult to apply to engineering applications. Li et al. (2021a) established a new model based on the diffusion coefficient-time relationship; this basis simplified the model but did not represent a sufficient physical basis. Liu et al. (2021a) unified the characterization of seepage and diffusion with the concept of the density gradient and established a density gradient-driven desorption diffusion model. Scholars have applied a variety of effective strategies to study coal pore gas diffusion, but they have not reached a unified understanding.

When gas is transported through porous media rich in micro/nanopores, the collision of the gas molecules with the wall increases the gas flow rate, and the gas permeability measured is the apparent permeability. Javadpour (2009) directly added slip flow to Knudsen diffusion flow to represent the total flow in micro/nanopores, leading to the concept of apparent permeability. Wu et al. (2015) coupled the flow of different flow mechanisms according to a certain contribution weight coefficient. However, repeated calculations to a certain extent cannot be avoided by adding different flow regimes. Beskok and Karniadakis (1999) established a model suitable for all flow regimes by modifying the boundary slip condition and introducing the dilution effect coefficient. Liu et al. (2022) showed that the microboundary constraint effect in the transitional region cannot be ignored. The Beskok model was improved by using the effective viscosity to modify the mean free path. Although the apparent permeability model establishes a relationship with Darcy's law, which makes its application more convenient, the above models are mostly simplified or contain more empirical coefficients.

The pore microstructure of coal is extremely complicated, and micro/nanopore gas experiments are difficult and expensive and have a low success rate. Therefore, many scholars simplify the microstructure to micro/nanotube bundles for theoretical and experimental research. A porous anodic alumina membrane

contains a large number of micro/nanotube bundles per unit area, with a simple pore structure and uniform pore size. Liu et al. (2022), Guo et al. (2015) and Wang et al. (2017a) carried out experimental research and model verification of micro/nanopore gas flow with porous anodic alumina membranes. However, when the pore of the membrane is smaller than 20 nm, the pore formation is not uniform, and it is difficult to precisely obtain the pore parameters. In addition, these experiments are easily disrupted and expensive. It is difficult to use this technique in systematic studies on gas migration within micro/nanopores.

The LBM is a mesoscopic simulation method that realizes fluid motion through particle collision and migration with a clear physical background and is an effective simulation method for the transition flow. Combined with experimental methods, it is expected to solve the controversy over the coal pore gas transmission mechanism.

LBM simulations of coal gas migration are currently mostly performed at the macrofracture level (Roslin et al., 2019; Wang et al., 2020b; Li et al., 2021b). Jin et al. (Jin et al., 2019) and Yu et al. (2020) used the LBM to simulate the permeability of the fluid migration process in coal cleat networks. Wang et al. (2022) simulated the seepage characteristics of three-dimensional fracture networks of coal in different loading stages. Yan et al. (2021) studied the gas seepage in coal pore networks by the LBM. They found that the gas seepage velocity and apparent permeability increased with increasing porosity, but they did not consider the wall slip or the microboundary constraint effect.

The LBM has been widely used in the study of nanopore transition-flow in shale. Succi (2002) first proposed a rebound-mirror combined boundary scheme (bounce-back and specular reflection (BSR) slip boundary scheme) that can describe the boundary slip effect. Nie et al. (2002) established the LBM model of the transition-flow based on the relations between the Knudsen number and relaxation time. Wang et al. (2020c) established the microscale gas flow LBM model of shale. Wang et al. (2017b) and Liu et al. (2021b) used the MRT-LBM model to study microscale gas transmission and improved the simulation accuracy.

Coal seam gas migration is a complex multiphase and multi-scale fluid flow. Bai et al. (Bai et al., 2021a; Bai et al., 2021b) studied the coupling flow of multiphase materials and the effect of temperature on adsorption - desorption and migration in porous media by laboratory experiments. Wang et al. (2021b) combined Pore Network Models (PNM), Laplace Semi-Analytical Solvers (SAS) and LBM to study the permeability of tight porous rocks.

In summary, the combination of the mesoscopic LBM simulation method and porous anodic alumina membrane gas flow experiment is an effective tool and developing trend for determining the expression and mechanism of transition flow regime gas migration in coal. The pore parameters of the membrane were accurately characterized by the maximum stable extremum region algorithm. The MRT-LBM model

established for micro/nanopore gas flow in coal was effectively verified by physical experiments. Finally, based on the MRT-LBM model, an extended simulation experiment of coal micro/nanopore gas migration was carried out to reveal the expression of coal micro/nanopore gas flow.

Simulation method

LBM-LBM mathematical model

The LBM has a comprehensible mesoscopic physical background and obtains macroscopic flow information through the numerical solution of the discrete particle density distribution function. The discrete equation of the LBM can be written as (Succi, 2002):

$$f_{\alpha}(r + e_{\alpha}\delta t, t + \delta t) - f_{\alpha}(r, t) = \Omega_{f_{\alpha}} + \delta t F_{\alpha}(r, t) \quad (1)$$

where $f_{\alpha}(r, t)$ represents the discrete density distribution function; e_{α} denotes the discrete velocity; δt is the lattice time step; $\Omega_{f_{\alpha}}$ is the discrete collision operator; and F_{α} denotes the discrete external forcing term.

The accuracy of the model is determined by the collision operator. The MRT-LBM model contains multiple adjustable parameters; the shear viscosity and bulk viscosity are adjustable, with adequate numerical stability (Li et al., 2011). The collision operator of the MRT-LBM model is given by:

$$\Omega_{f_{\alpha}} = -(M^{-1}SM)_{\alpha\beta}(f_{\beta} - f_{\beta}^{eq}) \quad (2)$$

where S is a diagonal relaxation matrix. For the commonly used D2Q9 (two-dimensional nine-velocity) model, the matrix is $S = \text{diag}(\tau_p, \tau_e, \tau_e, \tau_j, \tau_j, \tau_q, \tau_s, \tau_s)^{-1}$, and τ_s and τ_q are the relaxation times related to the dynamic viscosity and boundary scheme, respectively. The other relaxation times can be set to any value but should be greater than 0.5 (Tao et al., 2018), and the values in this paper are (1, 1.1, 1.2, 1, τ_q , 1, 1, τ_q, τ_s, τ_s); f_{β}^{eq} denotes the equilibrium distribution function; M is the transform matrix; and the particle density distribution function f_{β} can be projected to velocity moment space through the transform matrix.

Relaxation time and boundary treatment of the transition flow

When using the LBM to simulate macroscopic flow, the Reynolds number is mandatory. In the simulation of the microscale transition-flow, a dimensionless Knudsen number is needed, and the relationship between the Knudsen number and relaxation time (the time when the distribution of microscopic particles approaches equilibrium from the nonequilibrium state) is determined.

According to rarefied gas dynamics, the Knudsen number which is used to classify gas flow regimes can be defined as (Florence et al., 2007):

$$Kn = \frac{\lambda}{H} = \frac{\mu}{HP} \sqrt{\frac{\pi RT}{2M}} \quad (3)$$

where λ represents the mean free path, nm; p denotes the gas pressure, MPa; R is the gas constant, J/(molK); T is the absolute temperature, K; μ denotes the dynamic viscosity at p and T , mPas; M denotes the molecular weight, kg/mol; and H represents the characteristic length of the flow geometry, nm.

In the microscale LBM simulation, the relations between Kn and relaxation time τ is given by (Nie et al., 2002):

$$Kn = \sqrt{\frac{\pi}{6}} \frac{(\tau - 0.5)}{N_H} \quad (4)$$

where N_H represents the lattice number for the characteristic length of the flow geometry. When $Kn > 0.01$, the gas enters the slip flow regime, and the BSR slip boundary scheme can accurately describe the boundary slip velocity.

When $Kn > 0.1$, the gas enters the transitional regime, and the constraint of the microboundary on the mean free path cannot be ignored. At this time, the mean free path needs to be corrected by the effective viscosity (Liu et al., 2022).

The effective viscosity μ_{eff} can be expressed as (Beskok and Karniadakis, 1999):

$$\mu_{\text{eff}} = \frac{\mu}{1 + \omega Kn} \quad (5)$$

Michalis et al. (Michalis et al., 2010) found experimentally that the parameter ω in the transitional regime generally tends to 2. Li et al. (Li et al., 2011) took ω as a constant value two and obtained satisfactory simulation results by using the MRT-LBM model. From Eqs 5–7, the relaxation time related to dynamic viscosity is given by:

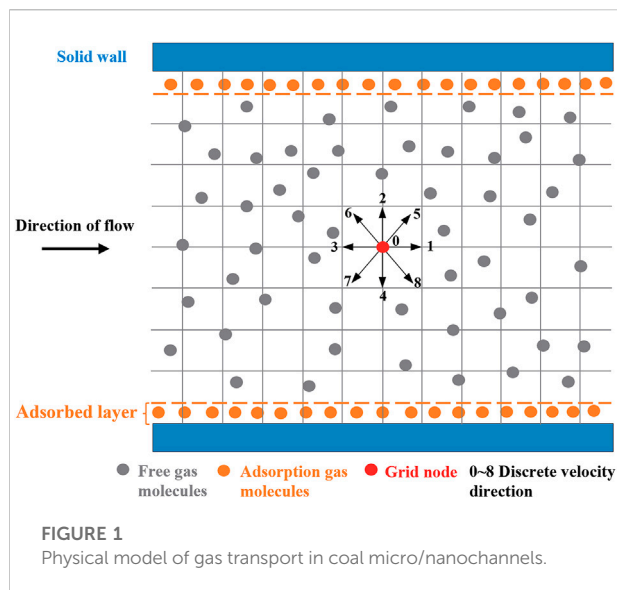
$$\tau_s = \frac{1}{2} + \sqrt{\frac{6}{\pi}} \frac{N_H Kn}{1 + \omega Kn} \quad (6)$$

When the effective viscosity is adopted, the rebound ratio coefficient r_b of the BSR scheme and the relaxation time τ_q related to the second-order slip coefficient also need to be corrected, and the calculation method is given in Reference (Li et al., 2011).

Analysis of adsorption

The adsorption layer is formed under the interaction between gas and solid surface in coal micro-scale pores. The gas adsorption volume of coal can be calculated by the Langmuir equation:

$$V = \frac{abP}{1 + bP} \quad (7)$$



where a represents the maximum monolayer adsorption capacity, m^3/t ; b denotes the Langmuir equilibrium constant, $1/\text{MPa}$; and V is the adsorption amount of adsorbed gas at p , m^3/t .

The adsorption intensity can be represented by the surface coverage, and the adsorption gas surface coverage θ can be expressed as:

$$\theta = \frac{bP}{1 + bP} \quad (8)$$

When the maximum adsorption capacity is reached, according to Langmuir monolayer adsorption theory, the size of the gas flow channel is reduced two times the molecular diameter. Therefore, the effective flow radius r_e of the coal nanopores considering adsorption can be defined as:

$$r_e = r - d\theta \quad (9)$$

where d is the diameter of the gas molecules.

Physical model of gas flow in the transitional regime

Considering that the gas flow in the micro/nanopores is affected by viscous resistance, wall slip, adsorption and the microboundary constraint effect, a physical model of gas flow in the micro/nanopores of coal is established (Figure 1).

Experiment and model validation

The pore structure of coal is complex and unevenly distributed from nanometers to microns, and this structure is

difficult to accurately obtain. Thus, it is difficult to directly study the flow of gas in coal micro/nanopores. Therefore, a porous anodic alumina membrane with uniform pore sizes of micro- and nanopores was selected to study the gas flow in the transitional regime and to verify the model. First, images of the pores of the membrane were obtained by field emission scanning electron microscopy (FESEM), and the pore structure was characterized with maximally stable extremal regions (MSER) in MATLAB. The pore structure parameters of the membrane were obtained, and the intrinsic permeability was calculated. Then, the gas pressure and flow rate were measured through a permeability test experiment on the membrane, and the gas flow of the micro/nanopores was analyzed.

Measurement of micro/nanopore parameters of porous anodic alumina membranes

Porous anodic alumina membranes with a diameter of 35 mm and a thickness of 60 μm were used in the experiment. Limited by the material properties, three kinds of membranes with representative pore sizes (the theoretical mean pore sizes of the membranes were 20–30 nm, 110–150 nm and 200–300 nm) were selected and numbered M-1, M-2 and M-3, respectively. The membranes were scanned by FESEM at Henan Polytechnic University. The scanning results are shown in Figure 2. The magnifications are 67560 times, 30,000 times, and 5,000 times.

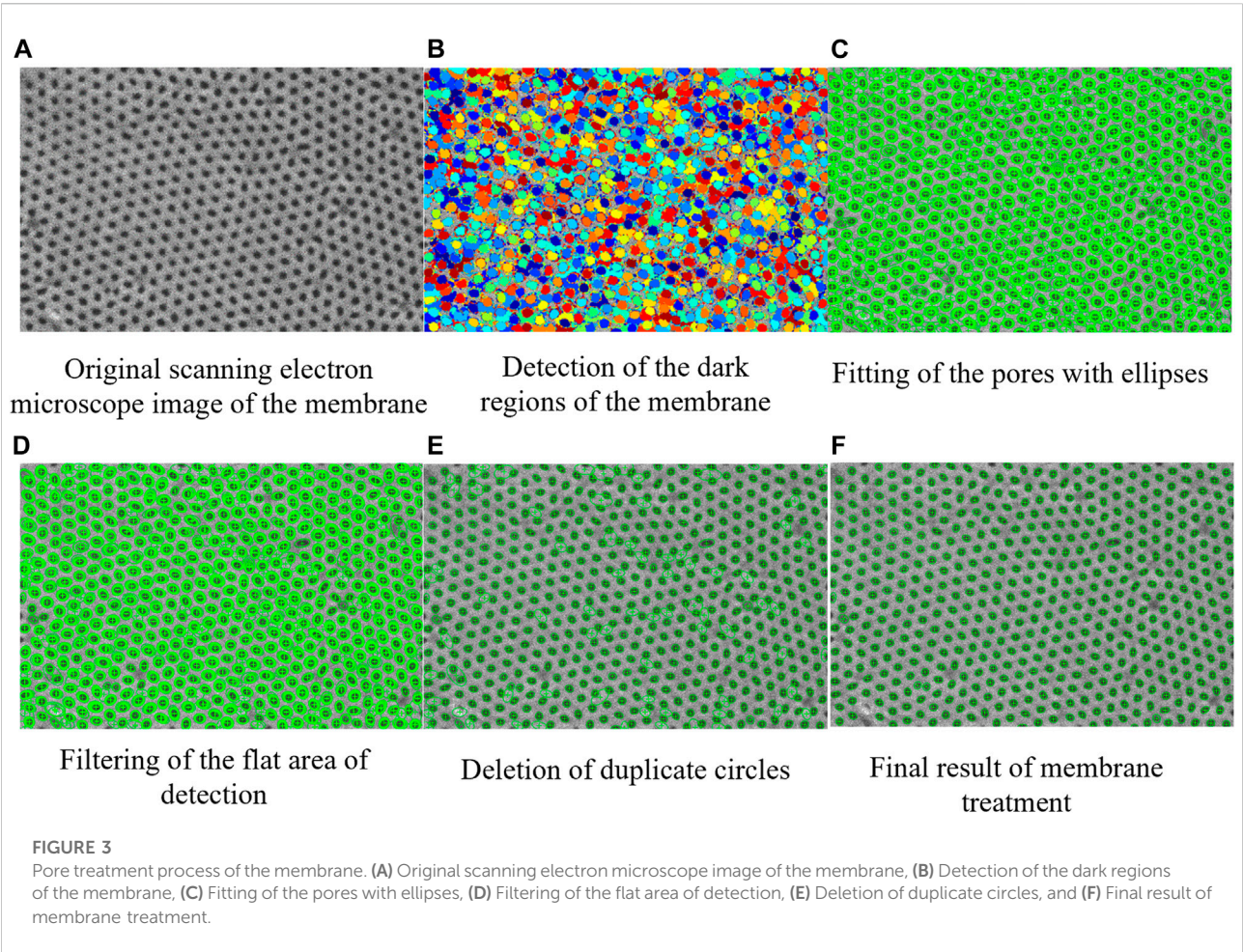
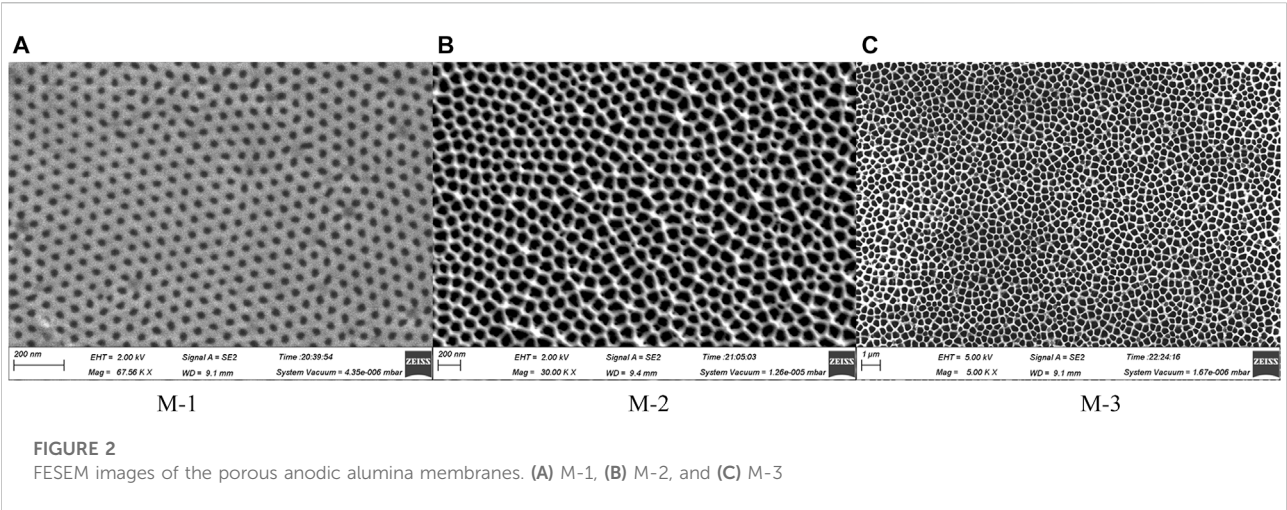
Figure 2 shows that the pore-forming effect of the selected three specifications of the membrane is good, the pore size is relatively uniform, and the pore section tends to be elliptical; these pores closely resemble the pores of a coal body, meeting the requirements of the uniform micro/nanopore gas flow experiment.

The MSER algorithm conducts affine invariant transformation to the image gray level and can be used for multiscale detection. Based on the MSER algorithm, the software MATLAB is used to write the program, and ellipses are used to fit the micro/nanopore edges of the membrane. The treatment process of the M-1 membrane is shown in Figure 3 as an example, and more detailed treatment steps are given in Reference (Liu et al., 2022).

The number and the total area of pores in the detection area were counted, and the porosity and equivalent mean pore size of the membranes were calculated. The Darcy permeability of porous media is related only to the pore structure, which can be calculated by Eq. 10.

$$K_D = \frac{\phi r^2}{8} \quad (10)$$

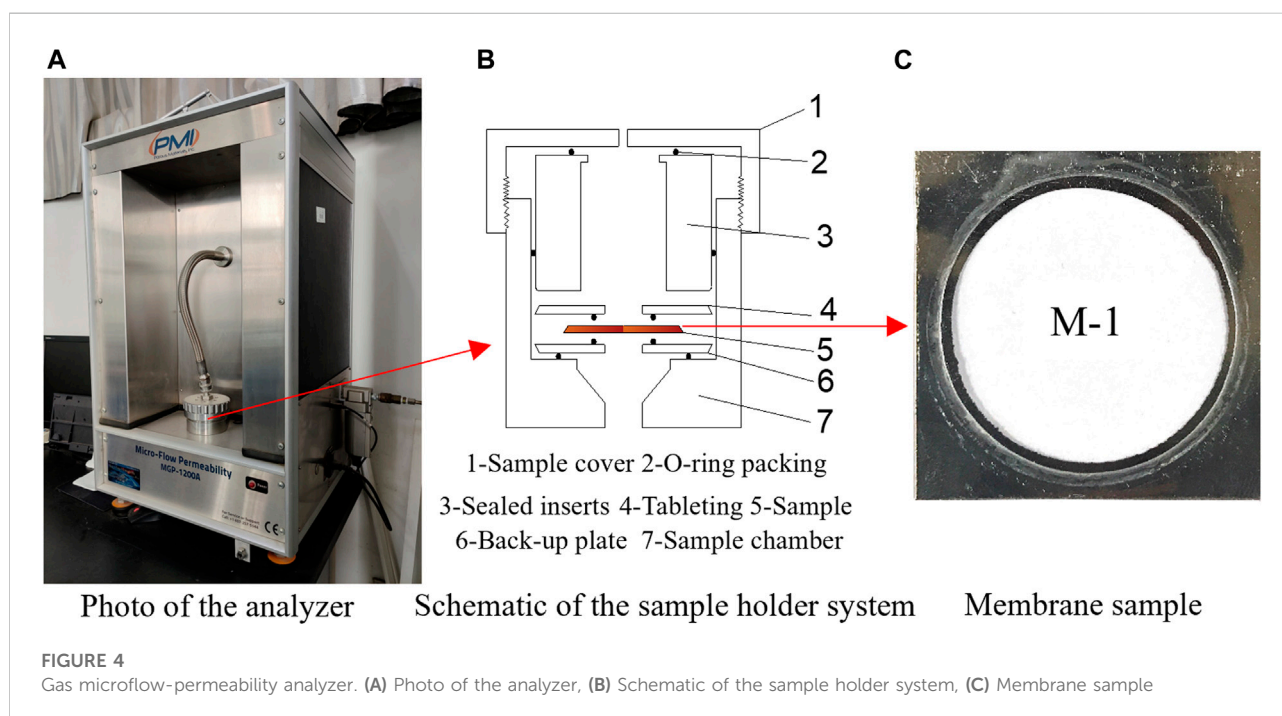
where K_D denotes the Darcy permeability (also known as the intrinsic permeability), 10^{-3} mD ; ϕ represents porosity; and r is the pore radius, nm.



The pore parameters of the membranes obtained by MSER algorithm processing and statistical calculation are shown in Table 1. The table shows that the equivalent mean pore size of the membranes is 34.3–270.3 nm and that the ratio of pore length to pore size is 222–1749; thus, the membranes exhibit the characteristics of tube bundles.

TABLE 1 Pore parameters of the membranes.

Sample	Equivalent mean pore size (nm)	Theoretical mean pore size (nm)	Porosity Φ	Intrinsic permeability K_D (mD)
M-1	34.3	20–30	0.257	0.009
M-2	96.5	110–150	0.299	0.087
M-3	270.3	200–300	0.364	0.831



Gas flow experiment of the transition flow

The gas microflow-permeability analyzer of Henan Polytechnic University was used in the experiment. This equipment can monitor pressure and flow in real time, and the error of the data is 0.15%. A photo of the analyzer, a schematic of the sample holder system and the membrane sample are shown in Figure 4. To ensure that the gas completely passes through the membrane sample, O-ring packing is used to compact the sample. The outlet pressure of the experiment is the local atmospheric pressure (0.10 MPa), and the diameter of the O-ring is 15 mm. More detailed experimental steps are given in Reference (Liu et al., 2022).

To ensure the safety of the experimental process, nitrogen was used instead of methane. Both nitrogen and methane are nonpolar molecules, their molecular diameters and mean free paths are similar, and both have adsorption properties. Moreover, nitrogen is often contained in the gas components of coal seams, and the two are equivalent in terms of gas flow.

Helium is an inert gas that does not adsorb, and its molecular properties are quite different from those of methane and nitrogen, making it suitable for experimental comparison. The physical properties of the three gas parameters are shown in Table 2, and the experimental temperature was 298 K.

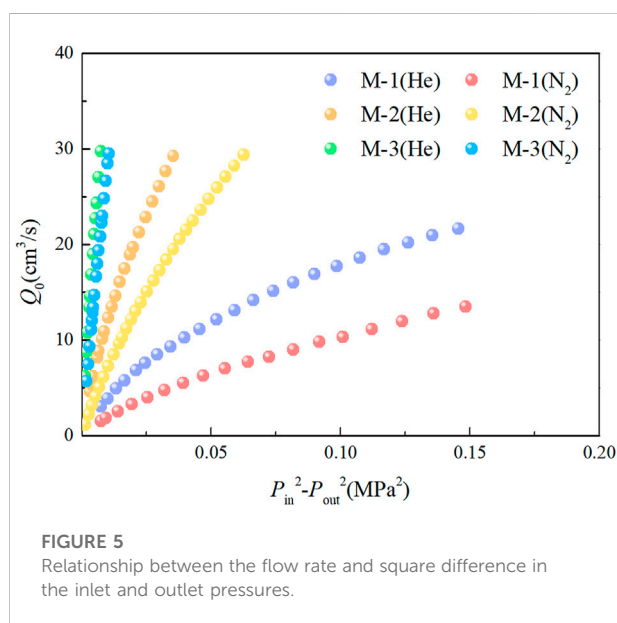
When gas passes through micro/nanopores in porous media, the collisions between the gas and solid wall cannot be ignored. The microboundary constraint effect enhances the gas flowability in the pores, and the gas permeability measured is the apparent permeability. The gas permeability of the membrane samples can be calculated by Eq. 11.

$$K_{app} = \frac{2P_0Q_0\mu L}{A(P_{in}^2 - P_{out}^2)} \times 100 \quad (11)$$

where K_{app} represents the gas permeability (also known as the apparent permeability), mD; P_0 , P_{in} and P_{out} are the standard atmospheric pressure, inlet pressure, and outlet pressure, respectively, MPa; Q_0 denotes the gas flow rate at P_0 , cm^3/s ; μ

TABLE 2 Physical properties of the experimental gases.

Gas	Dynamic viscosity (Pa·s)	Molecular weight (g·mol ⁻¹)	Mean free path (nm)	Molecular diameter (nm)
CH ₄	1.12×10 ⁻⁵	16	54.5	0.41
N ₂	1.78×10 ⁻⁵	28	65.5	0.38
He	1.98×10 ⁻⁵	4	192.7	0.26

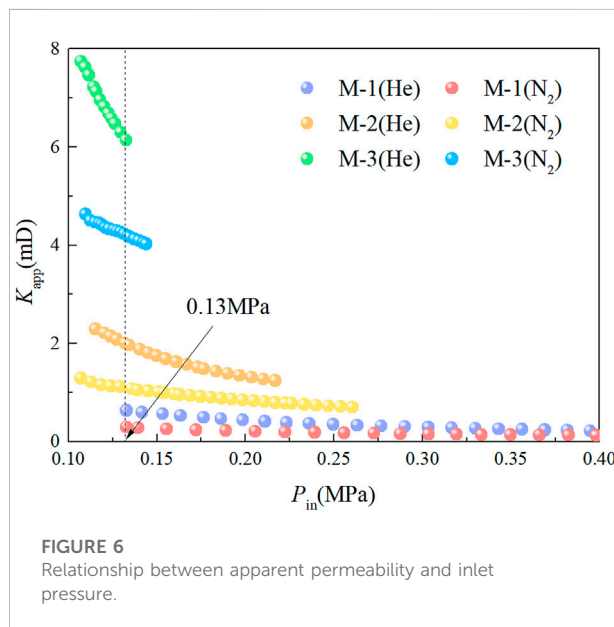


is the dynamic viscosity, mPas; L denotes the flow channel length, cm; and A is the cross-sectional area of the flow channel, cm².

Results and discussion regarding the experiment

To avoid the influence of nitrogen adsorption on the experimental results, the M-1, M-2 and M-3 films were used repeatedly in the experiment, and helium and nitrogen were used successively for the gas penetration experiments. The inlet pressure of the experiment increased gradually with time. The pressure stability in the pipeline system was controlled by the default maximum pressure drop and holding time value of the instrument, and the gas flow and pressure were automatically recorded at each stable timestep. To prevent the membrane from rupturing, the instrument automatically stopped when the maximum pressure (0.40 MPa) was reached. The experimental results are shown in Figure 5.

During the experiment, when the small pore size membrane M-1 (34.3 nm) reaches the set maximum pressure (0.40 MPa), the instrument automatically stops. The medium-pore size



membrane M-2 (96.5 nm) and large-pore size membrane M-3 (270.3 nm) cannot maintain pressure stability when the flow rate reaches approximately 30 cm³/s, and the instrument automatically stops.

As depicted in Figure 5, with an increasing square of the difference in the inlet and outlet pressures, the flow rate shows nonlinear growth. Under the same pressure, the flow rate of helium is greater than that of nitrogen, and the slope of the curve is larger. Combining Eq. 11 shows that the curve slope reflects the apparent permeability. To further analyze the variation in apparent permeability, the relationship between apparent permeability and inlet pressure is shown in Figure 6.

According to Figure 6 and Table 1, the experimental apparent permeability is much higher than the intrinsic permeability of the membranes, and the apparent permeability increases with the decrease of gas pressure in the channel. The results show that the mean free path increases with decreasing pressure and that the proportion of collisions between molecule and the wall out of the total number of collisions increases, which enhances the flow capacity of gas in the pores. For the same membrane, the apparent permeability of helium is higher than that of nitrogen under the same pressure, and the flow rate is larger.

TABLE 3 Numerical simulation schemes.

Gas	Sample number	Lattice length δ_x' (nm)	Relaxation time τ_s'	Simulation lattice $N_x \times N_y$
He	M-1	3.43	7.12	17493*11
	M-2	9.65	6.64	6,218*11
	M-3	27.03	5.62	2,220*11
N ₂	M-1	3.43	6.61	17493*11
	M-2	9.65	5.55	6,218*11
	M-3	27.03	3.90	2,220*11

This shows that under the same conditions, the microboundary constraint effect of helium is stronger, and the flowability is stronger.

When the pressure is approximately 0.13 MPa, the helium flow rates of the M-1, M-2 and M-3 membranes are 1.97, 1.76 and 1.41 times the nitrogen flow rate, respectively. This shows that under the same pressure, the smaller the pore size of the membrane is, the more obvious the difference between the helium and nitrogen flow capacities. When the pressures on the M-1 membrane are approximately 0.20, 0.30 and 0.40 MPa, the helium flows are 1.89, 1.78 and 1.61 times the nitrogen flow. This shows that under the same pore conditions, the lower the pressure is, the more obvious the difference between the helium and nitrogen flow capacities. The experiments show that the apparent permeability of micro/nanoporous media is not only determined by the pore structure but related to the fluid pressure and fluid type.

Verification and discussion of the model

The MRT-LBM model in this paper was used to simulate the flow experiments of helium and nitrogen. The BSR slip boundary scheme was used for the upper and lower walls, and a consistent linear extrapolation scheme was used for the inlet and outlet (Verhaeghe et al., 2009). In the LBM simulation process, the pressure boundary scheme was transformed into the particle density distribution function by $p = \rho c_s^2$, and the local Kn changed with position in time and space. The simulation parameters are given in Table 3.

In the LBM simulation of physics experiments, the real physical units need to be converted into dimensionless lattice units. By non-dimensionalizing all the physical units in Eq. 11, the apparent permeability of the LBM can be written as (Cho et al., 2013):

$$K'_{app} = \frac{2\rho'_{out}v'L'}{c_s'^2(\rho_{in}'^2 - \rho_{out}'^2)} \frac{1}{N_x N_y} \sum_{i=1}^{N_x} \sum_{j=1}^{N_y} u_x(i, j) \quad (12)$$

where K'_{app} represents the apparent permeability in lattice units; ρ'_{in} denotes the inlet density in lattice units; ρ'_{out} denotes the outlet density

in lattice units; v' is the viscosity in lattice units; L' is the channel length in lattice units; N_x is the lattice number in the flow direction; N_y is the lattice number perpendicular to the flow direction; and $u_x(i, j)$ is the velocity of fluid particles in lattice units at the positions i and j .

The microboundary constraint effect causes the apparent permeability of the membranes measured with the experimental gas to be much larger than its intrinsic permeability. The stronger the microboundary constraint effect is, the greater the ratio (dimensionless permeability coefficient) of the two, and the greater the deviation from Darcy's law. The dimensionless permeability coefficient of the LBM simulation can be calculated as follows:

$$K_r = K'_{app}/K'_D \quad (13)$$

where K_r is the dimensionless permeability coefficient and K'_D is the intrinsic permeability in lattice units. A comparison between the experimental and simulation results of helium and nitrogen is shown in Figure 7.

Figure 7 shows that the experimental gas flows all enter the transitional regime, that the Knudsen number of the helium experiment is 1.2–9.7, and that the Knudsen number of the nitrogen experiment is 0.4–3.3. The simulation results of the MRT-LBM model in this paper are in good agreement with the experimental results as a whole, but the deviation of the simulation results increases gradually after $Kn > 8$. This occurs because the parameter ω should be a gradually increasing value (Liu et al., 2022) but is taken as a constant value in the simulation. The dimensionless permeability coefficient K_r increases with increasing Kn , indicating that the microboundary constraint effect enhances the flow capacity of the gas, and the deviation of the flow rate predicted by Darcy's law increases. The minimum equivalent mean pore size of the experimental membrane samples is 34.3 nm, and the maximum inlet pressure is 0.40 MPa. The effect of nitrogen adsorption on the permeability is not found.

Gas flow is essentially a macroscopic velocity transfer caused by molecular collisions. The characteristic size of the flow channel and gas pressure, temperature and molecular properties all affect the molecular collisions, and these factors

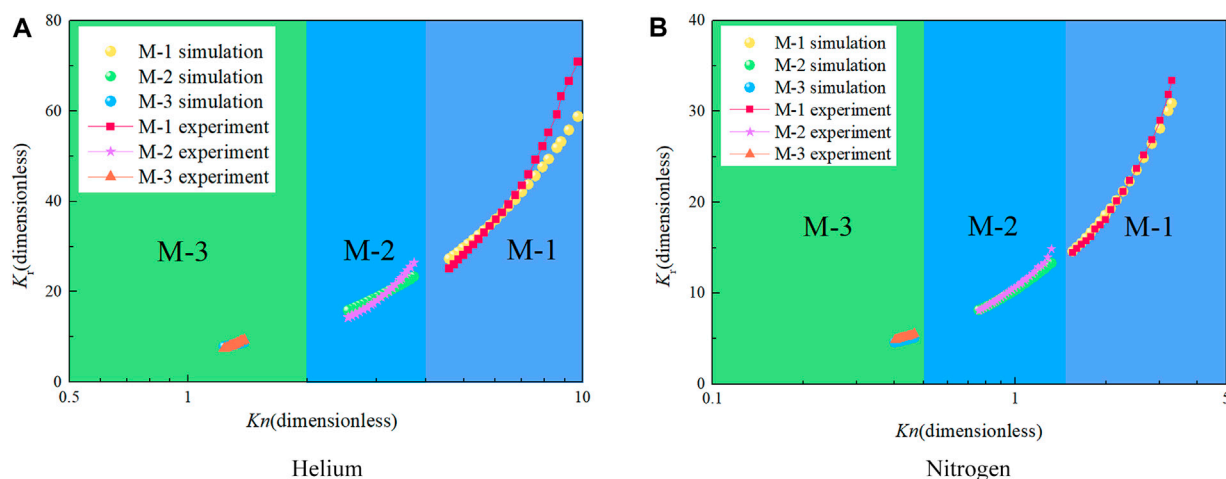


FIGURE 7
Variation in the dimensionless permeability coefficient with Kn . (A) Helium, (B) Nitrogen

can be reflected by Kn . Therefore, under the experimental pressure conditions, the dimensionless permeability coefficients K_r of nitrogen and helium with different micro/nanopore size membranes have the same variation as Kn .

Extended simulation and discussion of transition flow gas flow in coal

Fu et al. (Fu et al., 2005) classified coal pores into two types, where those <65 nm are diffusion pores and those >65 nm are seeping pores by the fractal method. This classification method is convenient for engineering application, but both pore size and gas pressure affect the gas migration regime within pores. According to Eq. 3, the corresponding relationship between the methane flow regime and pressure in pores with different pore sizes under coal reservoir conditions can be calculated (Figure 8).

Figure 8 illustrates that it is necessary to determine the gas flow regime by combining the pore size and pressure to determine the applicable flow mechanism and model. For diffusion pores with radii larger than 8 nm, the slip flow regime is entered when the gas pressure is greater than 6.89 MPa. For seeping pores with radii smaller than 325 nm, when the gas pressure is less than 0.17 MPa, the transitional regime is entered. At this time, the approximation and the thermodynamic equilibrium assumption are invalid, and a higher-order model with higher accuracy is needed; otherwise, large errors occur. The LBM is a mesoscopic simulation method that is suitable for macroscopic and microscopic simulations. Therefore, the MRT-LBM model in this paper is used to carry out extended simulation research on gas migration in micro/nanopores of coal.

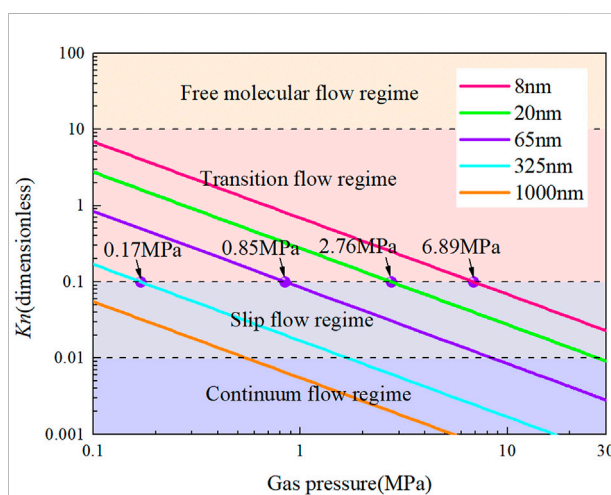
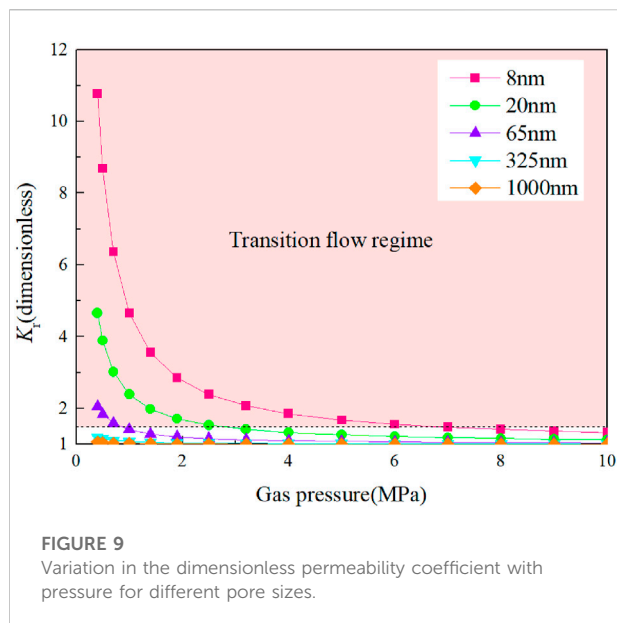


FIGURE 8
Relationship between methane flow regimes and pressure in pores with different sizes.

Effect of pore size and pressure on methane flow

In order to investigate the influence of pore size on methane flow, the flow of methane in micro/nanopores with different pore sizes was simulated, and the relationship between the dimensionless permeability coefficient and pressure can be obtained (Figure 9).

Figure 9 demonstrates that the microboundary constraint effect enhances the gas flowability and that the smaller the pore size and the lower the pressure are, the more significant the enhancement effect on the flowability. For pores with a radius of

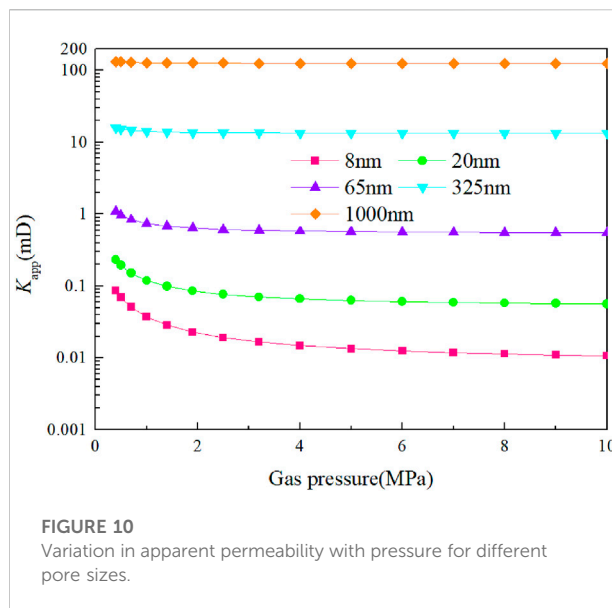


8 nm, at a pressure of 0.40 MPa and 10 MPa, the actual gas flow is 10.8 and 1.3 times that calculated by Darcy's law, respectively. For pores with a radius of 325 nm, the actual gas flow is only 1.2 times that calculated by Darcy's law at a pressure of 0.40 MPa; the pores with radii of 1,000 nm can be neglected.

With the progress of gas extraction, the gas pressure decreases, and the effect of the microboundary constraint on the enhancement of gas flowability is more obvious. However, in the early stage of gas extraction in a low-permeability coal seam, the extraction flow rate is high, and the attenuation is fast. In the later stage, the flow rate is low, and the gas is difficult to extract. Therefore, it is necessary to further analyze the relationship between pore apparent permeability and gas pressure.

Figure 10 shows that with decreasing pore size, the intrinsic permeability decreases, and the apparent permeability decreases. Therefore, the pore size dominates the permeability, and the microboundary constraint effect alleviates the influence of pore size reduction on permeability.

The methane in coal is mainly stored in micropores, and adsorbed methane accounts for 80%–90% of the methane in coal reservoirs (Cheng and Hu, 2021). The desorption process of adsorbed gas is very fast, approximately 10^{-10} – 10^{-5} s, and the desorption of free gas from micropores (<2 nm) into the middle and large pores in the path is very short. In the study of coal seams, the impact of methane desorption and migration in micropores on permeability can be ignored. In the early stage of gas extraction, free gas is released rapidly under drive from the pressure gradient. At this time, the large pores and fractures are the main flow channels and are the main controlling factors of coal permeability. In the middle and late period of extraction, the free gas is released rapidly, the gas pressure drops, and the microporous desorbed gas replenishes the fracture system

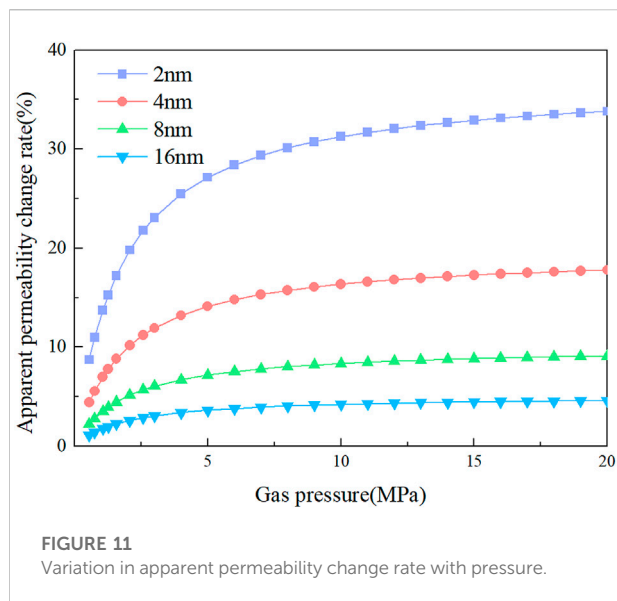


through the pore system. The replenishment velocity of gas through the pore system is less than that of the fracture flow velocity, and with the decrease in pressure, the microboundary constraint effect increases. In the coal matrix and in the mid-late stage of coal seam gas extraction, the pore system becomes the main controlling factor of coal seam permeability. Therefore, it is necessary to accurately understand gas migration through micro/nanopores in low-permeability coal seams.

Effect of adsorption on methane flow

Collectively, a large number of pore structures in coal provides a large specific surface area and has a strong adsorption effect on methane. To investigate the effect of adsorption on methane flow in coal nanopores, the Langmuir equilibrium constant is set to $b = 0.5 \text{ MPa}^{-1}$ to simulate methane flow with and without adsorption at pore sizes of 2 nm, 4 nm, 8 nm and 16 nm, respectively. The variation in the apparent permeability change rate with or without adsorption with pressure is shown in Figure 11.

Figure 11 shows that the adsorption layer weakens the methane flow capacity in the pores and that the magnitude of the weakening increases with increasing pressure and finally tends to be stable. Combined with Eq. 7, it can be seen that when the pressure reaches a certain value, the adsorption amount tends to the maximum adsorption volume and gradually stabilizes. At this time, the coverage $\theta \approx 1$, and the thickness of the adsorption layer tends to the maximum. The apparent permeability change rate considering adsorption increases with decreasing pore size. When the adsorption layer is considered, the apparent permeability of



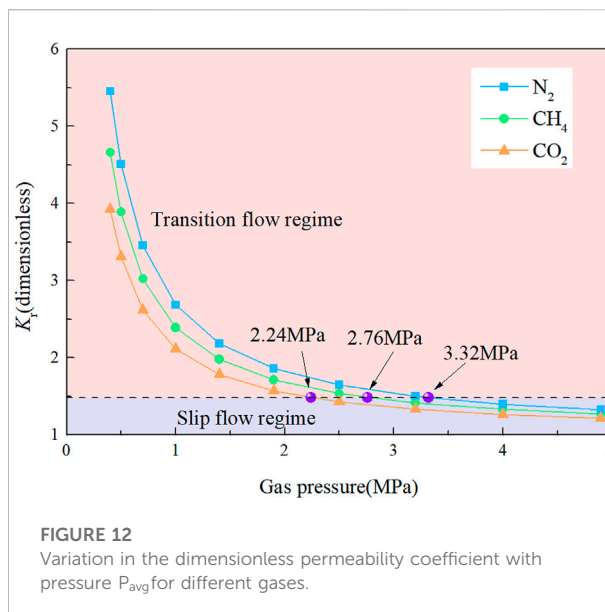
the pores with a radius of 2 nm is reduced by 33.8% at most. For pores with radii greater than 16 nm, the apparent permeability change rate is less than 5%, and the influence of the adsorption layer thickness on the apparent permeability can be ignored.

The surface diffusion of adsorbed gas on the solid wall is driven by the chemical potential gradient. Yang et al. (2020) studied the effect of surface diffusion of nanoporous gas on apparent permeability by combining molecular simulation and LBM simulation. The results showed that the contribution of gas surface diffusion to permeability decreased with increasing pressure and pore size. When the pore size was greater than 20 nm, surface diffusion could be ignored. Surface diffusion makes a greater contribution to permeability in micropores (<2 nm), and gas has a short path through micropores, so it has little effect on the overall permeability of the coal seam.

The temperature conduction have an important influence on adsorption mechanism, Bai et al. (2022) used the smoothed particle hydrodynamics (SPH) method to simulate the heat transfer process in porous media at the pore scale. Yang et al. (2020) research shows that the gas apparent permeability in organic nanopore is enhanced with the increment of temperature.

Difference analysis on the influence of different gas types

Coal seam gas is composed of a variety of gas components, and the common components are N_2 , CH_4 and CO_2 . In order to study the influence of different gas types on the gas flow law of nanopores, the gas flow of three kinds of gas components with a



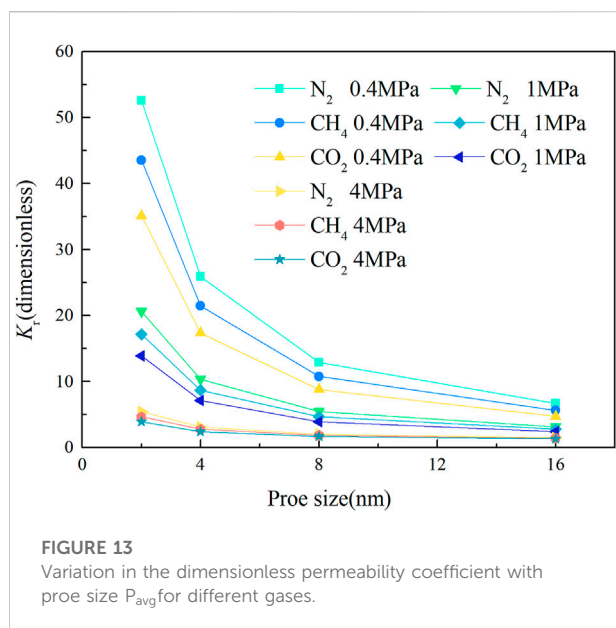
radius of 20 nm was simulated, and the relationship between the dimensionless permeability coefficient K_r and gas pressure is shown in Figure 12.

Figure 12 shows that the effects of the microboundary constraint on different gas flow capacities are different. N_2 , CH_4 and CO_2 enter the transitional regime at 3.32 MPa, 2.76 MPa, and 2.24 MPa, respectively. Under the same pressure of CO_2 , CH_4 and N_2 , the mean free path increases in turn, the microboundary constraint effect on the gas flow capacity increases in turn, and the dimensionless permeability coefficient increases in turn. The dimensionless permeability coefficients of the three gases increase with decreasing pressure, and the difference among the three increases with decreasing pressure. This shows that with gas extraction, the gas pressure decreases, and the difference in the three gas flow characteristics increases.

Figure 13 shows that the dimensionless permeability coefficients of N_2 , CH_4 and CO_2 increase with the decrease of pore size, and the difference between the three increases with the decrease of pore size. It shows that the smaller the pressure and the pore size, the more obvious the microboundary constraint effect, and the greater the difference in the flow characteristics of different gases.

Conclusion

In this paper, a porous anodic alumina membrane gas permeability test and MRT-LBM simulation were used to study the gas migration trend and the mechanism of transition-flow in different micro/nanopores in coal. The following conclusions were obtained:



- 1) A new simulation method for micro/nanopore gas migration in coal based on the MRT-LBM model is proposed. The experimental verification shows that on the basis of Langmuir monolayer adsorption theory, the model of the BSR scheme and effective viscosity can precisely describe gas migration in the transitional regime in coal.
- 2) The microboundary constraint effect in the transitional regime reduces the mean free path, and the gas viscosity decreases. The smaller the pore size and the lower the gas pressure are, the greater the contribution of the collisions between molecules and the wall to the flow, the more obvious the microboundary constraint effect, and the greater the difference of different gas flow. The adsorption layer reduces the effective flow radius of a pore and decreases the flow capacity of methane in the pore.
- 3) The corresponding relationship between methane flow regime and pressure in coal pores with different pore sizes under coal reservoir conditions is investigated. The smaller the pore size is, the higher the pressure of gas flow into the transitional regime, and the microboundary constraint effect increases the permeability of the transition flow. The pore size plays a dominant role in permeability. In the early stage of gas extraction, large pores and fractures are the main circulation channels and are the main factors controlling coal permeability. In the coal matrix and the middle and later periods of gas extraction, the pore system becomes the main factor controlling coal permeability, and with the decrease in pore pressure, the microboundary constraint effect is more obvious.

Data availability statement

The original contributions presented in the study are included in the article/supplementary material, further inquiries can be directed to the corresponding author.

Author contributions

YL and HH designed and modified the theoretical framework and the structures of manuscript; HJ implemented the numerical simulations and prepared the draft of manuscript; JS and PC corrected some Figures and technical terminology; JM, YH, and JP improved some Figures and presentations.

Funding

This work was supported by the program for National Natural Science Foundation of China (Nos. 52174173, 52274188, and 52104190), the Focus R&D and Promotion for Scientific and Technological Project of Henan Province (No. 222102320012), the Key Scientific Research Project Fund of Colleges and Universities of Henan Province (No. 21A440009), the Project Funded by China Postdoctoral Science Foundation (Nos. 2020M682291 and 2022T150194), the Fundamental Research Funds for the Universities of Henan Province (No. NSFRF210307) and the State Key Laboratory Cultivation Base for Gas Geology and Gas Control (Henan Polytechnic University) (Nos. WS2021A05 and WS2021B01).

Conflict of interest

The authors declare that the research was conducted in the absence of any commercial or financial relationships that could be construed as a potential conflict of interest.

The handling editor SW declared a shared affiliation with the authors at the time of review.

Publisher's note

All claims expressed in this article are solely those of the authors and do not necessarily represent those of their affiliated organizations, or those of the publisher, the editors and the reviewers. Any product that may be evaluated in this article, or claim that may be made by its manufacturer, is not guaranteed or endorsed by the publisher.

References

- Bai, B., Jiang, S. C., Li, L. L., Li, X., and Wu, H. Y. (2021). The transport of silica powders and lead ions under unsteady flow and variable injection concentrations. *Powder Technol.* 387, 22–30. doi:10.1016/j.powtec.2021.04.014
- Bai, B., Nie, Q. K., Zhang, Y. K., Wang, X. L., and Hu, W. (2021). Cotransport of heavy metals and SiO₂ particles at different temperatures by seepage. *J. Hydrology* 597, 125771. doi:10.1016/j.jhydrol.2020.125771
- Bai, B., Wang, Y., Rao, D. Y., and Bai, F. (2022). The effective thermal conductivity of unsaturated porous media deduced by pore-scale SPH simulation. *Front. Earth Sci. (Lausanne)*. 10. doi:10.3389/feart.2022.943853
- Barrer, R. M. (1951). *Diffusion in and through solids*. London: Cambridge University Press, 28–29.
- Beskok, A., and Karniadakis, G. E. (1999). A model for flows in channels, pipes, and ducts at micro and nano scales. *Microscale Thermophys. Eng.* 3 (1), 43–77. doi:10.1080/108939599199864
- Cheng, Y. P., and Hu, B. (2021). Main occurrence form of methane in coal: Micropore filling. *J. China Coal Soc.* 46 (09), 2933–2948. doi:10.13225/j.cnki.jccs.2020.1214
- Cho, H., Jeong, N., and Sung, H. J. (2013). Permeability of microscale fibrous porous media using the lattice Boltzmann method. *Int. J. Heat. Fluid Flow.* 44, 435–443. doi:10.1016/j.ijheatfluidflow.2013.07.013
- Florence, F. A., Rushing, J. A., Newsham, K. E., and Blasingame, T. A. (2007). Improved permeability prediction relations for low-permeability sands. *Rocky Mt. Oil Gas Technol. Symposium Society of Petroleum Engineers (SPE) SPE107954 2007 SPE Rocky Mountain Oil and Gas Technology Symposium Denver, CO, United States April 16–18, 2007*. doi:10.2118/107954-MS
- Fu, X. H., Qin, Y., Zhang, W. H., Wei, C. T., and Zhou, R. F. (2005). Fractal classification and natural classification of coal pore structure based on migration of coal bed methane. *Chin. Sci. Bull.* 50 (1), 66–71. doi:10.1007/bf03184085
- Guo, C. H., Xu, J. C., Wu, K. L., Wei, M. Z., and Liu, S. Y. (2015). Study on gas flow through nano pores of shale gas reservoirs. *Fuel* 143, 107–117. doi:10.1016/j.fuel.2014.11.032
- Javadpour, F. (2009). Nanopores and apparent permeability of gas flow in mudrocks (shales and siltstone). *J. Can. Petroleum Technol.* 48 (8), 16–21. doi:10.2118/09-08-16-da
- Jin, Y., Zheng, J. L., Liu, X. H., Pan, J. N., and Liu, S. X. (2019). Control mechanisms of self-affine, rough cleat networks on flow dynamics in coal reservoir. *Energy* 189, 116146. doi:10.1016/j.energy.2019.116146
- Li, Q., He, Y. L., Tang, G. H., and Tao, W. Q. (2011). Lattice Boltzmann modeling of microchannel flows in the transition flow regime. *Microfluid. Nanofluidics* 10 (3), 607–618. doi:10.1007/s10404-010-0693-1
- Li, Q., Liu, D., Cai, Y., Zhao, B., Lu, Y., and Zhou, Y. (2021). Effects of natural micro-fracture morphology, temperature and pressure on fluid flow in coals through fractal theory combined with lattice Boltzmann method. *Fuel* 286, 119468. doi:10.1016/j.fuel.2020.119468
- Li, Z. Q., Peng, J. S., Li, L., Qi, L. L., and Li, W. (2021). Novel dynamic multiscale model of apparent diffusion permeability of methane through low-permeability coal seams. *Energy Fuels*. 35 (9), 7844–7857. doi:10.1021/acs.energyfuels.1c00324
- Liu, L. F., Wang, Y. H., and Aryana, S. A. (2021). Insights into scale translation of methane transport in nanopores. *J. Nat. Gas Sci. Eng.* 96, 104220. doi:10.1016/j.jngse.2021.104220
- Liu, W., Xu, H., Wu, D. Y., Qin, Y. P., Liu, J., and Zhao, W. (2021). Gases migration behavior of adsorption processes in coal particles: Density gradient model and its experimental validation. *Process Saf. Environ. Prot.* 152, 264–277. doi:10.1016/j.psep.2021.06.014
- Liu, Y. W., Du, Y., Li, Z. Q., Zhao, F. J., Zuo, W. Q., Wei, J. P., et al. (2020). A rapid and accurate direct measurement method of underground coal seam gas content based on dynamic diffusion theory. *Int. J. Min. Sci. Technol.* 30 (6), 799–810. doi:10.1016/j.ijmst.2020.07.004
- Liu, Y. W., Jia, H. J., Zuo, W. Q., Han, H. K., Chang, P., Miao, J., et al. (2022). A model for gas transport through nanopores based on effective molecular free path. *J. China Univ. Min. Technol.* 51 (01), 90–99. doi:10.13247/j.cnki.jcmt.001341
- Liu, Y. W. (2011). *Study on gas emission rules, mechanism and dynamic model from coal particle*. Doctoral dissertation. Jiaozuo: Henan Polytechnic University, 123–127.
- Michalis, V. K., Kalarakis, A. N., Skouras, E. D., and Burganos, V. N. (2010). Rarefaction effects on gas viscosity in the Knudsen transition regime. *Microfluid. Nanofluidics* 9 (4–5), 847–853. doi:10.1007/s10404-010-0606-3
- Nie, X. B., Doolen, G. D., and Chen, S. Y. (2002). Lattice-Boltzmann simulations of fluid flows in MEMS. *J. Stat. Phys.* 107 (1), 279–289. doi:10.1023/a:1014523007427
- Roslin, A., Pokrajac, D., and Zhou, Y. (2019). Cleat structure analysis and permeability simulation of coal samples based on micro-computed tomography (micro-CT) and scan electron microscopy (SEM) technology. *Fuel* 254, 115579. doi:10.1016/j.fuel.2019.05.162
- Ruckenstein, E., Vaidanathan, A. S., and Youngquist, G. R. (1971). Sorption by solids with bidisperse pore structures. *Chem. Eng. Sci.* 26 (9), 1305–1318. doi:10.1016/0009-2509(71)80051-9
- Succi, S. (2002). Mesoscopic modeling of slip motion at fluid-solid interfaces with heterogeneous catalysis. *Phys. Rev. Lett.* 89 (6), 064502–064509. doi:10.1103/physrevlett.89.064502
- Tao, S., Zhang, H. L., Guo, Z. L., and Wang, L. P. (2018). Numerical investigation of dilute aerosol particle transport and deposition in oscillating multi-cylinder obstructions. *Adv. Powder Technol.* 29 (9), 2003–2018. doi:10.1016/j.apt.2018.05.007
- Verhaeghe, F., Luo, L., and Blanpain, B. (2009). Lattice Boltzmann modeling of microchannel flow in slip flow regime. *J. Comput. Phys.* 228 (1), 147–157. doi:10.1016/j.jcp.2008.09.004
- Wang, D. K., Liu, S. M., Wei, J. P., Wang, H. L., and Yao, B. H. (2017). A research study of the intra-nanopore methane flow law. *Int. J. Hydrogen Energy* 42 (29), 18607–18613. doi:10.1016/j.ijhydene.2017.04.195
- Wang, D. K., Tian, X. R., Wei, J. P., Zhang, H. T., Yao, B. H., Zhang, H., et al. (2022). Fracture evolution and nonlinear seepage characteristic of gas-bearing coal using X-ray computed tomography and the lattice Boltzmann method. *J. Petroleum Sci. Eng.* 211, 110144. doi:10.1016/j.petrol.2022.110144
- Wang, H. B., Li, T., Zou, Q. L., Cheng, Z. H., and Yang, Z. K. (2020). Influences of path control effects on characteristics of gas migration in a coal reservoir. *Fuel* 267, 117212. doi:10.1016/j.fuel.2020.117212
- Wang, H. Y., Yang, X., Du, F., Wang, G. D., Wang, Y. Y., Zhao, W., et al. (2021). Calculation of the diffusion coefficient of gas diffusion in coal: The comparison of numerical model and traditional analytical model. *J. Petroleum Sci. Eng.* 205, 108931. doi:10.1016/j.petrol.2021.108931
- Wang, J. J., Kang, Q. J., Chen, L., and Rahman, S. S. (2017). Pore-scale lattice Boltzmann simulation of micro-gaseous flow considering surface diffusion effect. *Int. J. Coal Geol.* 169, 62–73. doi:10.1016/j.coal.2016.11.013
- Wang, Q., Li, C., Zhao, Y., and Ai, D. (2020). Study of gas emission law at the heading face in a coal-mine tunnel based on the Lattice Boltzmann method. *Energy Sci. Eng.* 8 (5), 1705–1715. doi:10.1002/esc3.626
- Wang, Y. D., Chung, T., Rabbani, A., Armstrong, R. T., and Mostaghimi, P. (2021). Fast direct flow simulation in porous media by coupling with pore network and Laplace models. *Adv. Water Resour.* 150, 103883. doi:10.1016/j.advwatres.2021.103883
- Wang, Y. D., Xue, J. K., Wang, D. S., and Xue, Q. Z. (2020). Lattice Boltzmann method for simulation of shale gas flow in kerogen nano-pores considering temperature dependent adsorption. *Int. J. Oil Gas Coal Technol.* 23 (4), 409–426. doi:10.1504/ijogct.2020.106145
- Wu, K. L., Li, X. F., and Chen, Z. X. (2015). A model for gas transport through nanopores of shale gas reservoirs[J]. *Acta Petro-lei Sin.* 36 (7), 837889–838848.
- Yan, M., Zhou, M., Li, S. G., Lin, H. F., Zhang, K. Y., Zhang, B. B., et al. (2021). Numerical investigation on the influence of micropore structure characteristics on gas seepage in coal with lattice Boltzmann method. *Energy* 230, 120773. doi:10.1016/j.energy.2021.120773
- Yang, X., Zhou, W. N., Liu, X. L., and Yan, Y. Y. (2020). A multiscale approach for simulation of shale gas transport in organic nanopores. *Energy* 210, 118547. doi:10.1016/j.energy.2020.118547
- Yu, X., Xu, L. C., Regenauer-Lieb, K., Jing, Y., and Tian, F. B. (2020). Modeling the effects of gas slippage, cleat network topology and scale dependence of gas transport in coal seam gas reservoirs. *Fuel* 264, 116715. doi:10.1016/j.fuel.2019.116715
- Zhang, J. X., Li, B., Liu, Y. W., Li, P., Fu, J. W., Chen, L., et al. (2022). Dynamic multifield coupling model of gas drainage and a new remedy method for borehole leakage. *Acta Geotech.*, 1–17. doi:10.1007/s11440-021-01444-x



OPEN ACCESS

EDITED BY

Shuren Wang,
Henan Polytechnic University, China

REVIEWED BY

Jianwei Cheng,
China University of Mining and
Technology, China
Fenhua Ren,
University of Science and Technology
Beijing, China

*CORRESPONDENCE

Zhijia Zhang,
Intukyxyzj@163.com

SPECIALTY SECTION

This article was submitted to
Geohazards and Georisks,
a section of the journal
Frontiers in Earth Science

RECEIVED 01 June 2022

ACCEPTED 05 September 2022

PUBLISHED 27 September 2022

CITATION

Lan T, Zhang Z, Sun J, Zhao W, Zhang M,
Jia W, Liu M and Guo X (2022), Regional
prediction and prevention analysis of
rockburst hazard based on the Gaussian
process for binary classification.
Front. Earth Sci. 10:959232.
doi: 10.3389/feart.2022.959232

COPYRIGHT

© 2022 Lan, Zhang, Sun, Zhao, Zhang,
Jia, Liu and Guo. This is an open-access
article distributed under the terms of the
[Creative Commons Attribution License
\(CC BY\)](https://creativecommons.org/licenses/by/4.0/). The use, distribution or
reproduction in other forums is
permitted, provided the original
author(s) and the copyright owner(s) are
credited and that the original
publication in this journal is cited, in
accordance with accepted academic
practice. No use, distribution or
reproduction is permitted which does
not comply with these terms.

Regional prediction and prevention analysis of rockburst hazard based on the Gaussian process for binary classification

Tianwei Lan, Zhijia Zhang*, Jiawei Sun, Wenqi Zhao,
Mancang Zhang, Weidong Jia, Mingwei Liu and Xutao Guo

College of Mining, Liaoning Technical University, Fuxin, Liaoning, China

Rockburst is a complex dynamic disaster in coal mining and affected by many factors. To accurately predict the rockburst hazard among complex influencing factors, a prediction model of rockburst hazard based on the Gaussian process for binary classification (GPC) was proposed after the identification of the intrinsic relationship between multiple factors of coal mines and rockburst. Through computerized machine learning and integrated intelligent analysis, the non-linear mapping of rockburst hazard and its influencing factors was established. The multi-factor pattern recognition model was constructed using artificial intelligence. The prediction criteria of the rockburst hazard probability and the hazard probability value of the prediction area unit were determined by applying neural network and fuzzy inference methods. In addition, the rockburst hazardous zone was classified, and the corresponding technical scheme for the prevention was put forward. The validity and feasibility of the regional prediction of rockburst hazard based on GPC were verified in the engineering practice. This method is highly targeted and can improve the accuracy and precision of rockburst prediction, thus contributing to the safe and efficient production of coal mines.

KEYWORDS

rockburst, machine learning, regional prediction, multi-factor pattern recognition, prevention technology

Introduction

As a complex dynamic disaster in coal mining, rockburst is very hard to be accurately predicted (Qiao et al., 2021; Zhu et al., 2022). The occurrence of rockbursts is influenced by various factors and is characterized by a regional distribution (Wang et al., 2021a; Cao et al., 2021; Chen et al., 2021). As the depth of mining deepens, the number and frequency of rockbursts in mines increase (Yu et al., 2021; Xue et al., 2022). There are distinctive rockburst modes under different conditions of mining areas, mines, coal seams, structures, and stresses. Traditional linear data analysis is not accurate enough under complex mining conditions (He et al., 2020; Zhang and Jiang, 2020; Lin et al., 2022). Based on the non-linear relationship between rockburst hazard and its influencing factors, the

probability prediction value of unit hazard is determined (Wu et al., 2021a; Chen et al., 2021; Yang et al., 2021; Yang and Zhang, 2021). According to the magnitude of the risk probability value of each cell, the engineering area is divided into four classes, and the regional and quantitative rockburst prediction can be significantly improved by using the multi-factor pattern recognition method.

In the prediction of mine rockburst hazards, machine learning methods have been proposed to predict rockburst hazards with good results (Ullah et al., 2022; Wojtecki et al., 2022; Xiao et al., 2022). Machine learning is a complex and cross-cutting discipline. In the prediction of rockburst hazards in mines, data from multiple sources are analyzed, and then machine learning algorithms are used to continuously learn from previous rockburst events and train computer models. The study of “neural network + machine learning” artificial intelligence prediction techniques allows monitoring and predicting the likelihood of rockburst hazards in coal mines (Wang et al., 2021b; Ke et al., 2021; Zhang et al., 2021). In order to accurately predict rockburst hazards under complex conditions, a rockburst hazard prediction model based on the Gaussian process for binary classification (GPC) was proposed (Hui and Zhang, 2020; Davis et al., 2021).

For the rockburst situation in Jixian Coal Mine, a GPC-based rockburst hazard prediction, prevention, and control technology system was established based on theoretical analysis (Iwata and Tanaka, 2022), and the intrinsic relationship between multiple influencing factors and rockburst was determined using a multi-factor pattern identification method. By dividing the engineering area into prediction units and determining the pattern identification criteria and unit hazard probability values (Gładyr et al., 2021), the rockburst hazard area of the on-site engineering area was classified, and corresponding management measures were proposed (Wu et al., 2021b).

Principles of the Gaussian process for binary classification

Statistically, the Gaussian process is a stochastic process: the distribution of any finite variable set is a Gaussian distribution. In other words, for any integer $n \geq 1$ and any family of random variables \mathbf{X} , the joint probability distribution of the corresponding process state $f(\mathbf{X})$ at time t obeys the n -dimensional Gaussian distribution. All statistical characteristics of the Gaussian process are determined by its mean and covariance function. In the field of machine learning, the Gaussian process refers to a machine learning method based on the Gaussian stochastic process and Bayesian learning theory.

The Gaussian process for binary classification (GPC) model is a kind of classification model based on the machine learning principle of the Gaussian process. In the

GPC model, let an input x correspond to the output value of the binary classification mark y , $y \in \{-1, 1\}$, and the observation data set is $\mathbf{D} = \{(x_i, y_i) | i = 1, \dots, m\}$. The GPC model aims to predict the classification y^* corresponding to the new test input x^* (Ahmad et al., 2022).

For a given x , the $p(y|x)$ distribution is the Bernoulli distribution, and the probability of $y = 1$ is $p(y = 1|x) = \Phi(f(x))$, where $f(x)$ is the potential function, and $\Phi(\bullet)$ is the cumulative probability density function of the standard Gaussian distribution. Generally, the sigmoid function is taken as $\Phi(z) = 1/(1 + e^{-z})$. The function of the sigmoid function is to convert the $f(x)$ constrained by intervals into the value of $[0, 1]$, so as to ensure that the probability value ranges in $[0, 1]$. For simplicity, let $f_i = f(x_i)$, $\mathbf{f} = [f_1, \dots, f_m]^T$, $\mathbf{y} = [y_1, \dots, y_m]^T$, $\mathbf{X} = [x_1, \dots, x_m]^T$.

For a given potential function, the observed value is an independent Bernoulli distribution variable, whose likelihood function is

$$p(\mathbf{y}|\mathbf{f}) = \prod_{i=1}^m p(y_i|f_i) = \prod_{i=1}^m \Phi(y_i f_i). \quad (1)$$

The prior distribution of potential functions is

$$\text{beip}(\mathbf{f}|\mathbf{X}, \boldsymbol{\theta}) = N(\mathbf{0}, \mathbf{K}), \quad (2)$$

where \mathbf{K} is a covariance matrix of order $m \times m$, $\mathbf{K}_{ij} = k(\mathbf{x}_i, \mathbf{x}_j, \boldsymbol{\theta})$, $k(\cdot)$ is a positive definite covariance function related to $\boldsymbol{\theta}$, and $\boldsymbol{\theta}$ is a hyper-function.

The covariance function of the Gaussian process model needs to be satisfied: a non-negative positive definite covariance matrix can be generated for any point set. The commonly used covariance function is the squared exponential function, namely,

$$k_y(\mathbf{x}_p, \mathbf{x}_q) = \sigma_f^2 \exp\left(-\frac{1}{2l^2}(\mathbf{x}_p - \mathbf{x}_q)^2\right), \quad (3)$$

where the hyper-function $\boldsymbol{\theta} = \{\sigma_f, l\}$; the optimal hyper-parameters can be estimated by the maximum likelihood method, as described in the literature.

According to Bayes' rule, after obtaining the actual observation value, a posterior distribution of the potential function \mathbf{f} is obtained as follows:

$$p(\mathbf{f}|\mathbf{D}, \boldsymbol{\theta}) = \frac{p(\mathbf{y}|\mathbf{f})p(\mathbf{f}|\mathbf{X}, \boldsymbol{\theta})}{p(\mathbf{D}|\boldsymbol{\theta})} = \frac{N(\mathbf{0}, \mathbf{K})}{p(\mathbf{D}|\boldsymbol{\theta})} \prod_{i=1}^m \Phi(y_i f_i). \quad (4)$$

The aforementioned equation is the learning process of GPC, and the following is the prediction process of GPC. The conditional probability of the potential function value \mathbf{f}^* corresponding to \mathbf{x}^* is

$$p(\mathbf{f}^*|\mathbf{D}, \boldsymbol{\theta}, \mathbf{x}^*) = \int p(\mathbf{f}_*|\mathbf{f}, \mathbf{X}, \boldsymbol{\theta}, \mathbf{x}_*)p(\mathbf{f}|\mathbf{D}, \boldsymbol{\theta})d\mathbf{f}. \quad (5)$$

The prediction probability of y^* is

$$p(y_*|D, \theta, x_*) = \int p(y_*|f_*)p(f_*|D, \theta, x_*)df_*. \quad (6)$$

When the predicted probability value of Y_* is greater than 0.5, then $y_* = 1$; otherwise, $y_* = -1$. Eqs 5 and 6 have no analytical solutions. Approximate solutions can be obtained by using Laplace's method and expectation propagation method (Villacampa-Calvo and Hernández-Lobato, 2020; Chakir et al., 2022). Let m and A be the mean and variance of the approximate solutions, respectively, and the approximate Gaussian distribution of the posterior distribution of the potential function f is

$$p(f|D, \theta) \approx q(f|D, \theta) = N(m, A). \quad (7)$$

Similarly, the posterior distribution of f_* can be set as an approximate Gaussian distribution:

$$q(f_*|D, \theta, x_*) = N(\mu_*, \sigma_*^2). \quad (8)$$

The mean and variance are

$$\mu_* = K_*^T K^{-1} m, \quad (9a)$$

$$\sigma_*^2 = k(x_*, x_*) - k_*^T (K^{-1} - K^{-1} A K^{-1}) k_*, \quad (9b)$$

where $k_* = [k(x_1, x_*), \dots, k(x_m, x_*)]^T$ represents the prior covariance vector between x_* and training input X . x_* belongs to classification 1 of the prediction probability:

$$q(y_* = 1|D, \theta, x_*) = \Phi\left(\frac{\mu_*}{\sqrt{1 + \sigma_*^2}}\right). \quad (10)$$

Gaussian process for binary classification-based prediction model for rockburst hazard

Main influencing factors of rockburst

The mechanism of rockburst in coal mines is complex. The occurrence of rockburst is controlled by n influencing factors, such as mining depth, stress, geological structure, coal body structure, mining layout, and advancing strength. When n factors are studied, each factor is regarded as an element of a vector, and then n factors constitute an n -dimensional vector. Each combination of n factors is a pattern, which corresponds to a single position in the n -dimensional feature space. Through the study of training samples, the non-linear mapping relationship between rockburst hazard and its influencing factors was established, and a multi-factor pattern recognition model was constructed. The similar patterns were very close together in the feature space, while the different patterns were far apart in the feature space. The task of pattern recognition is to divide the feature space by

certain methods, so that similar patterns can be located in the same region.

Establishment of the Gaussian process for binary classification model

The establishment of the GPC model for the rockburst hazard prediction and the visualization of prediction results are shown in Figure 1.

- (1) Rockburst cases were collected as training samples. It was assumed that there were several rockburst cases (x_i, y_i) ($i=1, 2, \dots, k$), where x_i is the n -dimensional vector of influencing factors of rockburst and y_i represents the grade of the rockburst hazard.
- (2) Through learning the training samples, the optimal hyper-parameters of the covariance function were obtained by the maximum likelihood method.
- (3) According to the theory of the Gaussian process and the Bayesian rule, the training samples were studied by inductive inferencing. The posterior approximate Gaussian distribution of the potential function f^* of the predicted samples was obtained by Eq. 8.
- (4) According to Eq. 10, the hazard probability prediction criteria of rockburst and the hazard probability value of the predicted regional unit were obtained. When the predicted probability value was in a certain critical interval, the rockburst hazard and the range of the hazardous zone were determined.
- (5) Based on the aforementioned modeling steps, the MATLAB program was compiled, and the regional prediction management system was established to visualize the prediction results.

Rockburst hazard classification

According to Article 228 of *Coal Mine Safety Regulation (2022 Edition)*, the following provisions shall be observed in the prevention and control of rockburst in mines: when coal seams with potential rockburst are mined, comprehensive prevention and control measures must be taken, such as prediction of rockburst hazard, monitoring and early warning, prevention governance, validity inspection, and safety protection. The hazard prediction of rockburst is the primary task in implementing comprehensive prevention and control measures.

According to the *Detailed Rules and Regulations for Prevention of Rockburst in Coal Mines (2018 Edition)*, the probability prediction values of rockburst hazard were used to classify the regional hazard in the proposed classification method. Four grades of the regional rockburst hazard were obtained: non-rockburst hazard, weak rockburst hazard, medium rockburst hazard, and strong

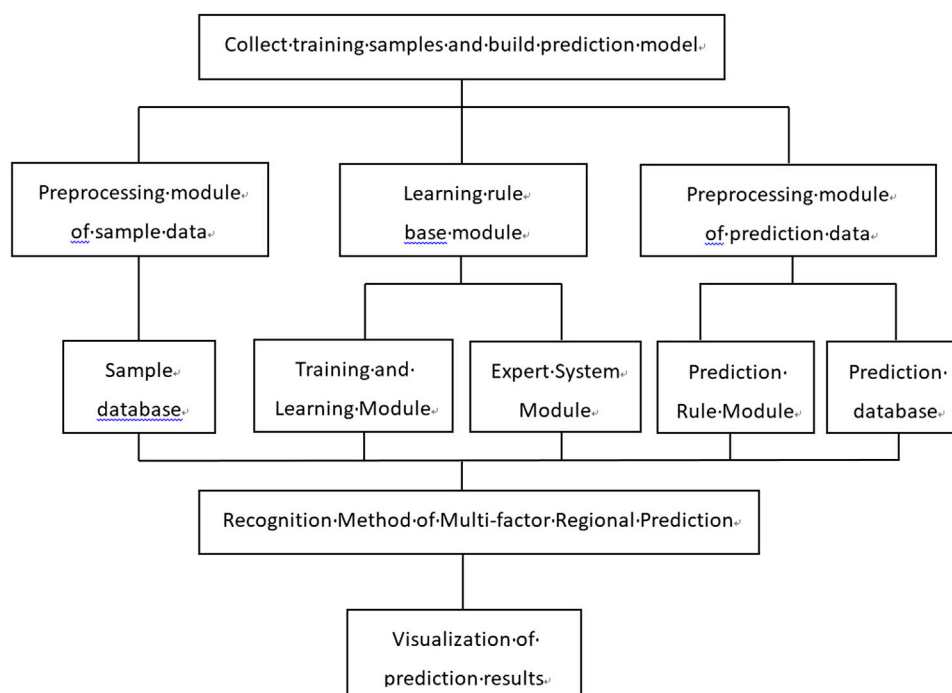


FIGURE 1
Prediction of rockburst hazard based on GPBC.

rockburst hazard. In the actual mining, when excavation roadways or working faces enter different prediction units, the risk of the areas can be determined in advance, and the corresponding preventive measures can be taken in advance.

Cases in the mining project

Introduction of rockburst in Jixian Coal Mine

Jixian Coal Mine was put into operation in 1968. It is currently mined at a depth of 578–733 m and is a deep mining pit. The main coal seams are coal seams 3, 9, and 16. In the backstopping process of Coal Seam 9, rockburst has occurred many times. At present, more than 50 rockbursts have occurred, and the maximum energy released by rockburst was 2.7×10^7 J (Figure 2). With the extension of mining excavation, the threat of rockburst is further strengthened. Rockburst can destroy roadways and mechanical equipment and seriously restrict the safe and efficient production of coal mines. It has become an important scientific problem to be solved urgently.

Establishment of the rockburst hazard prediction model in Jixian Coal Mine

The mining geological and technical conditions of rockburst in Jixian Coal Mine were analyzed. The main influencing factors of rockburst included fracture structure, tectonic stress, roof lithology, mining depth, and mining intensity. According to the different effects of different factors on the rockburst, the Gaussian process for binary classification was applied to analyze the training samples and determine different weights. Then, quantitative analysis was carried out, and the probability prediction model of multi-factor pattern recognition for rockburst hazard was established. The multi-factor pattern recognition technology was applied for the comprehensive intelligent analysis, and then the neural network and fuzzy reasoning method were used to determine the hazard probability of each unit in the prediction zone. The studied zones were divided into finite units, and the impact of each single factor index on the unit was analyzed, and the probability value of rockburst hazard for each unit was predicted.

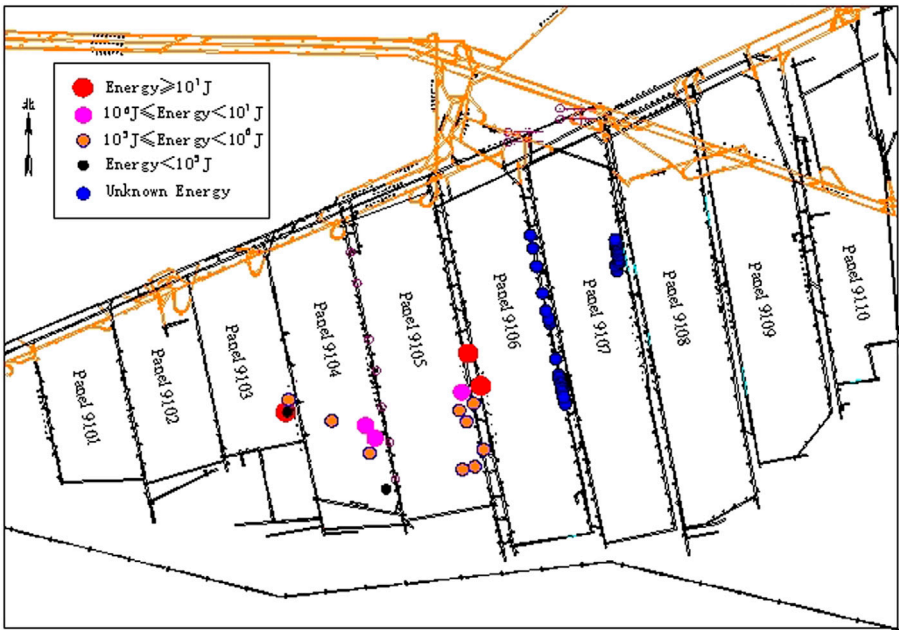


FIGURE 2
Rockburst distribution in working faces of Jixian coal mine.

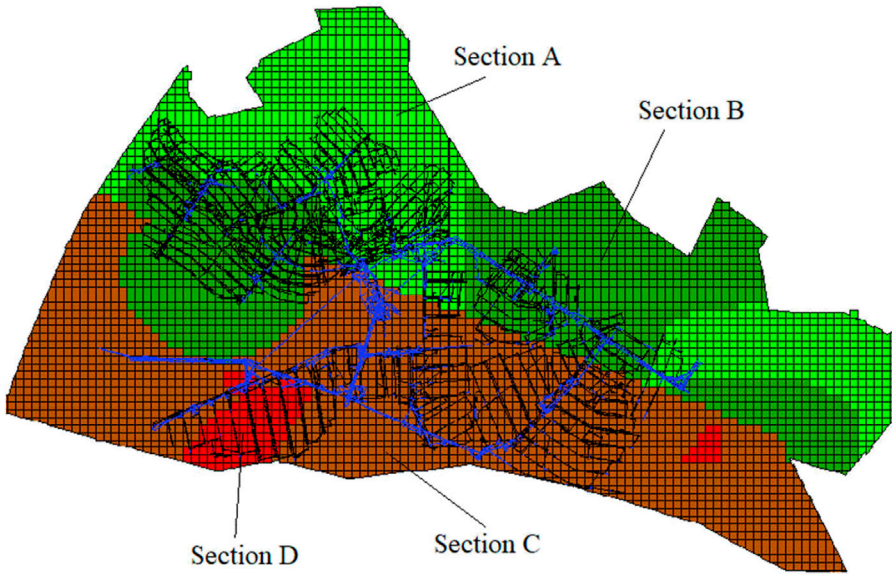


FIGURE 3
Classification results of hazardous zone of rockburst Section A is non-rockburst zone; Section B is weak rockburst zone, Section C is medium rockburst.

TABLE 1 Prediction accuracy of mine rockburst in different grade zones.

Local grade	Critical value	Accuracy rate
None	≤ 0.25	87.49%
Weak	0.25–0.5	63.31%
Medium	0.5–0.75	96.78%
Strong	> 0.75	99.79%
Hazard	Maximum	0.92
Probability	Minimum	0.08
Random variables	μ	0.44
Eigenvalues	σ^2	0.03

Prediction of rockburst hazard in Jixian Coal Mine

According to the risk prediction results of rockburst, Jixian Coal Mine was divided into a total of 4,553 units with a cell grid of 100 m \times 100 m. The influencing factors, such as fracture structure, tectonic stress, roof lithology, mining depth, and mining intensity, were mapped to the unit grid. The comprehensive influence of each factor on the prediction unit was expressed by the probability value, and the hazard probability of rockburst of each unit was obtained by the method of pattern recognition.

The probability values of rockburst hazard in Jixian Coal Mine of 0.25, 0.50, and 0.75 were taken as critical values. If the probability value is less than 0.25, it is the non-rockburst zone,

accounting for 17.6%; between 0.25 and 0.50, it is the weak rockburst hazardous zone, accounting for 52.8%; if it is between 0.50 and 0.75, it is the medium rockburst hazardous zone, accounting for 26.4%; and if it is more than 0.75, it is the strong rockburst hazardous zone, accounting for 3.2%. Figure 3 shows the classification results of the hazardous zone of rockburst.

The multi-factor pattern recognition method based on machine learning completed the sub-unit probability prediction of rockburst hazard. By comparing the rockburst training samples with the predicted samples, the results showed that the prediction results were in good agreement with the actual situation, and the prediction results were highly scientific and reliable. Table 1 shows the prediction accuracy of rockburst in different grade zones.

Prediction results of rockburst hazard in Working Face 4 of Western Mining Area 2 in Jixian Coal Mine

Based on the regional prediction of rockburst hazard in Jixian Coal Mine, the predicted hazard probability values of any working face, any mining area, or any location in the mine field can be obtained. Figure 4 shows the unit probability prediction value of rockburst hazard in the Working Face 4 of Western Mining Area 2.

As shown in Figure 4, Working Face 4 in the Western Mining Area 2 is divided into 12 unit grids in line with 100 m \times 100 m unit grids. There are 10 unit grids with a hazard probability value

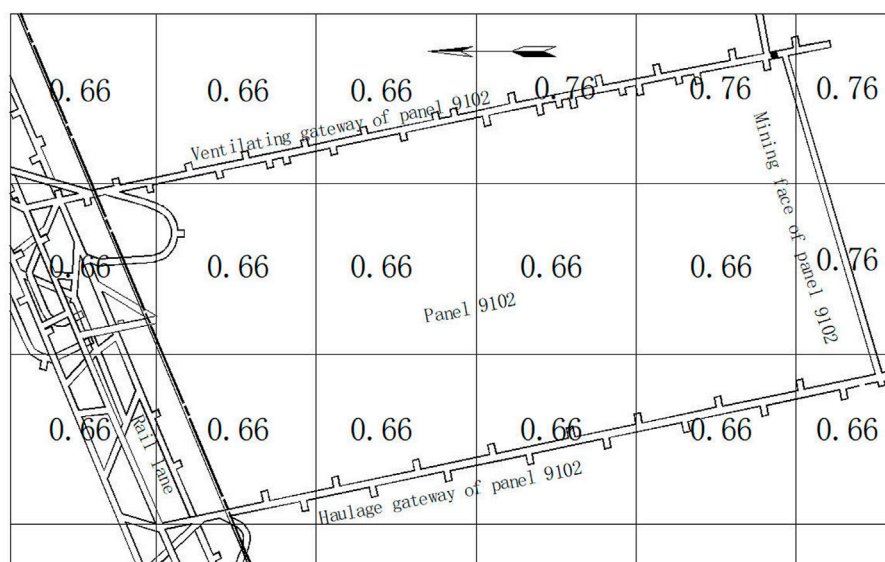


FIGURE 4 Prediction results of multi-factor pattern recognition for rockburst hazard in panel 9102.

TABLE 2 Hazard classification of rockburst and prevention measures in Jixian Coal Mine.

Hazard grade	Probability value of the predicted unit	Suggestions on prevention and control measures
Non-rockburst hazard	≤ 0.25	<ol style="list-style-type: none"> ① Advance all working faces of mining in line with the operation rules ② Conduct the random hazard test in the mining operation
Weak rockburst hazard	0.25–0.5	<ol style="list-style-type: none"> ① Take the single local measures for the hazard relief ② Strengthen the hazard detection in the mining operation. Conduct the mining operation if detection indicators are identified to be safe
Medium rockburst hazard	0.5–0.75	<ol style="list-style-type: none"> ① Take two or more combinations of local hazard-relief measures ② Strengthen the hazard detection in the mining operation. Conduct the mining operation if detection indicators are identified to be safe
Strong rockburst hazard	> 0.75	<ol style="list-style-type: none"> ① Take the comprehensive local measures for the hazard relief ② Strengthen the hazard detection in the mining operation. Conduct the mining operation if detection indicators are identified to be safe ③ Terminate the mining operation and evacuate personnel from hazardous locations, if detection indicator exceeds the limit ④ Take prevention, control measures, and relevant parameters under the guidance of experts; adopt comprehensive measures and methods under special conditions ⑤ Take the next step of the mining operation only through expert argumentation ⑥ Strengthen strong support and structural support of the roadway. Implement relevant measures, such as increasing strong pressure relief, reducing drilling density, and low pressure blasting in deep hole interval

of 0.66, accounting for 83.33% of the predicted unit grids in the working face. Most areas of the working face are medium rockburst hazardous zones. There are two unit grids with a hazard probability value of 0.76, accounting for 16.67%. The area from the middle of the transportation roadway to the open-off cuts of Working Face 4 is the strong hazard rockburst zone, which is also an area prone to stress concentration and rockburst.

Through the aforementioned analysis, it is concluded that the sub-unit prediction with multi-factor pattern recognition can divide the predicted working face into several prediction units, and the probability value of each unit can be obtained. Before the roadway tunneling or mining face advances to different prediction units, the potential rockburst hazard of the location can be determined in advance, so that corresponding control measures can be taken in advance. Compared with the comprehensive index method, the hazard value of Working Face 4 was 0.62, indicating that the multi-factor pattern recognition method improves the accuracy and precision of the prediction.

Regional prevention and control technology of rockburst hazard

By using the probability prediction method with multi-factor pattern recognition, the sub-unit probability prediction of coal seam hazard was realized, and the results were classified in line with the regional prediction grade. In the actual mining, when excavation roadways or working faces enter different prediction

units, the potential rockburst hazard of the location can be obtained in advance, and corresponding preventive measures can be taken in advance. According to the hazard probability value of the prediction unit, when the conditions were suitable, regional measures were first chosen to relieve the hazard, or the corresponding local measures were taken to reduce the hazard. Regional prediction of rockburst provides a scientific basis for taking prevention and control measures against the rockburst, so as to ensure safe production in coal mines. For different hazard grades, the corresponding prevention and control measures were adopted, as shown in Table 2.

Conclusion

For the problem of rockburst hazard area prediction under complex mining conditions, traditional linear data analysis is not an ideal solution. In order to improve the precision and accuracy of prediction results, this article studies the non-linear mapping relationship between rockburst hazard and its influencing factors through machine learning of rockburst hazard training samples and draws the following conclusion based on the principle of the binary Gaussian process and the main influencing factors of rockburst:

- (1) Aiming at the prediction of rockburst hazard under complex conditions, a multi-factor pattern recognition method of rockburst hazard prediction was proposed based on GPC. By learning the training samples, the non-linear mapping

relationship between rockburst hazard and its influencing factors was established, and the probability prediction value of the unit hazard was determined.

- (2) The probability values of rockburst hazard of 0.25, 0.5, and 0.75 were taken as critical values, and the rockburst hazard of Jixian Coal Mine was divided into four grades. The sub-unit probability prediction results of rockburst hazard in Working Face 4 are 0.66 and 0.76 in Western Mining Area 2. Through the sub-unit probability prediction of rockburst hazard, the rockburst prediction is upgraded from point prediction to regional prediction, from single-factor prediction to multi-factor prediction, and from qualitative prediction to quantitative prediction. Moreover, the accuracy of rockburst prediction is greatly improved.
- (3) The prevention and control technology system of hazard prediction of rockburst was established based on GPC. According to the hazard probability value of grid units, the potential rockburst hazard of the mining location can be determined before roadway driving or working face mining advances different prediction units. It provided a scientific basis for taking effective rockburst prevention measures, so as to ensure safe production in coal mines.

Data availability statement

The raw data supporting the conclusion of this article will be made available by the authors, without undue reservation.

Author contributions

TL carried out the main construction of ideas for the study and a detailed split of the overall research problem of the study; ZZ was responsible for constructing the mathematical model, programming, and summarizing the data; JS and WZ classified and processed the field data to provide strong data support for

the team research; WJ and MZ edited the graphs in the manuscript to make the conclusion of the manuscript clearer and concise; and ML and XG collected the raw data for the field real measurements.

Funding

This research was financially supported by the LiaoNing Revitalization Talents Program (XLYC2007042), Liaoning Provincial Education Department Basic Scientific Research Project (Key Project) (LJKZ0325), and National Natural Science Foundation of China (51604139).

Acknowledgments

The authors thank all editors and reviewers for their comments and suggestions.

Conflict of interest

The authors declare that the research was conducted in the absence of any commercial or financial relationships that could be construed as a potential conflict of interest.

Publisher's note

All claims expressed in this article are solely those of the authors and do not necessarily represent those of their affiliated organizations, or those of the publisher, the editors, and the reviewers. Any product that may be evaluated in this article, or claim that may be made by its manufacturer, is not guaranteed or endorsed by the publisher.

References

- Ahmad, M., Amjad, M., Al-Mansob, R., Kaminski, P., Olczak, P., Khan, B., et al. (2022). Prediction of liquefaction-induced lateral displacements using Gaussian process regression. *Appl. Sci.* 12 (4), 1977. doi:10.3390/app12041977
- Cao, A., Liu, Y., Jiang, S., Hao, Q., Peng, Y., Bai, X., et al. (2021). Numerical investigation on influence of two combined faults and its structure features on rock burst mechanism. *Minerals* 11, 1438. doi:10.3390/min11121438
- Chakir, Y., Abouir, J., Aounil, I., and Benouahmane, B. (2022). Two-dimensional Laplace transform inversion using bivariate homogeneous two-point Padé approximants. *Numer. Algorithms* 90, 1153–1174. doi:10.1007/s11075-021-01225-3
- Chen, D., Wang, E.-Y., and Li, N. (2021). Rupture process assessment of rock bursts in a coal mine: Inversion of source parameters and the slip distribution on the rupture surface. *Eng. Fail. Anal.* 130, 105741. doi:10.1016/j.engfailanal.2021.105741
- Davis, C. B., Hans, C. M., and Santner, T. J. (2021). Prediction of non-stationary response functions using a Bayesian composite Gaussian process. *Comput. Statistics Data Analysis* 154, 107083. doi:10.1016/j.csda.2020.107083
- Gladyr, A. V., Tereshkin, A. A., Rasskazov, M. I., and Konstantinov, A. V. (2021). Application of probabilistic clustering analysis to rockburst hazard assessment of rock mass. *IOP Conf. Ser. Earth Environ. Sci.* 773 (1), 012061. doi:10.1088/1755-1315/773/1/012061
- He, M., Li, J., and Ren, F. (2020). Rock burst criterion based on clay mineral content. *Arab. J. Geosci.* 13, 185–188. doi:10.1007/s12517-020-5199-x
- Hui, L., and Zhang, X. (2020). Predictive analysis of impact hazard level of coal rock mass based on fuzzy inference network. *J. Intelligent Fuzzy Syst.* 38 (2), 1509–1518. doi:10.3233/jifs-179514
- Iwata, T., and Tanaka, Y. (2022). Few-shot learning for spatial regression via neural embedding-based Gaussian processes. *Mach. Learn.* 1114, 1239–1257. doi:10.1007/s10994-021-06118-z
- Ke, B., Khandelwal, M., Asteris, P. G., Skentou, A. D., Mamou, A., and Armaghani, D. J. (2021). Rock-burst occurrence prediction based on optimized Naïve Bayes models. *IEEE Access* 9, 91347–91360. doi:10.1109/access.2021.3089205

- Lin, M., Gao, C., Xia, Y., Zhang, D., Liu, X., and Liang, X. (2022). Rock burst initiation and precursors in a model specimen based on acoustic emission and infrared monitoring. *Arab. J. Geosci.* 15 (4), 1–19. doi:10.1007/s12517-021-09423-y
- Qiao, C., Guo, Y.-H., and Li, C.-H. (2021). Study on rock burst prediction of deep buried tunnel based on cusp catastrophe theory. *Geotech. Geol. Eng. (Dordr.)* 39, 1101–1115. doi:10.1007/s10706-020-01547-4
- Ullah, B., Kamran, M., and Rui, Y. (2022). Predictive modeling of short-term rockburst for the stability of subsurface structures using machine learning approaches: T-SNE, K-means clustering and XGBoost. *Math. (Basel)* 3, 449. doi:10.3390/math10030449
- Villacampa-Calvo, C., and Hernández-Lobato, D. (2020). Alpha divergence minimization in multi-class Gaussian process classification. *Neurocomputing* 378, 210–227. doi:10.1016/j.neucom.2019.09.090
- Wang, J., Apel, D. B., Dyczko, A., Walentek, A., Prusek, S., Xu, H., et al. (2021). Investigation of the rockburst mechanism of driving roadways in close-distance coal seam mining using numerical modeling method. *Min. Metallurgy Explor.* 38 (5), 1899–1921. doi:10.1007/s42461-021-00471-2
- Wang, J., Huang, M., and Guo, J. (2021). Rock burst evaluation using the CRITIC algorithm-based cloud model. *Front. Phys.* 8, 593701. doi:10.3389/fphy.2020.593701
- Wojtecki, Ł., Iwaszenko, S., Apel, D. B., Bukowska, M., and Makowka, J. (2022). Use of machine learning algorithms to assess the state of rockburst hazard in underground coal mine openings. *J. Rock Mech. Geotechnical Eng.* 14, 703–713. doi:10.1016/j.jrmge.2021.10.011
- Wu, Z., Pan, P. Z., Konicek, P., Zhao, S., Chen, J., and Liu, X. (2021). Spatial and temporal microseismic evolution before rock burst in steeply dipping thick coal seams under alternating mining of adjacent coal seams. *Arab. J. Geosci.* 14 (20), 1–28. doi:10.1007/s12517-021-08439-8
- Wu, T., Gao, Y., Zhou, Y., and Sun, H. (2021). A novel comprehensive quantitative method for various geological disaster evaluations in underground engineering: Multidimensional finite interval cloud model (MFICM). *Environ. Earth Sci.* 80 (20), 1–18. doi:10.1007/s12665-021-10012-1
- Xiao, Y., Deng, H., Xie, Z., and Lu, H. (2022). Mine ground pressure monitoring and early warning based on deep learning data analysis. *Mob. Inf. Syst.* 2022, 1–12. doi:10.1155/2022/6255119
- Xue, C., Cao, A., Liu, Y., Guo, W., Wen, Y., Hu, Y., et al. (2022). Mechanism and prevention practice of coal burst in deep gradual residual coal pillar area: A case study. *Arab. J. Geosci.* 15 (2), 1–12. doi:10.1007/s12517-022-09527-z
- Yang, Y., Wei, S., and Li, K. (2021). Inverse analysis of dynamic failure characteristics of roadway surrounding rock under rock burst. *Energy Sci. Eng.* 9, 2298–2310. doi:10.1002/ese3.977
- Yang, Y., and Zhang, Z. (2021). Surrounding rock effect on coal burst under unloading condition: A numerical study. *Arab. J. Geosci.* 14 (17), 1–11. doi:10.1007/s12517-021-08120-0
- Yu, Y., Zhu, B., Guo, H., Chen, B., and Geng, D. (2021). Warning index associated with rock burst in deeply buried tunnels. *Int. J. Geomech.* 21, 04021211. doi:10.1061/(asce)gm.1943-5622.0002135
- Zhang, J., Wang, M., and Xi, C. (2021). Prediction and evaluation of rockburst based on depth neural network. *Adv. Civ. Eng.* 2021, 1–11. doi:10.1155/2021/8248443
- Zhang, M., and Jiang, F. (2020). Rock burst criteria and control based on an abutment-stress-transfer model in deep coal roadways. *Energy Sci. Eng.* 8, 2966–2975. doi:10.1002/ese3.715
- Zhu, Z., Wu, Y., and Han, J. (2022). A prediction method of coal burst based on analytic hierarchy process and fuzzy comprehensive evaluation. *Front. Earth Sci. (Lausanne)* 9, 834958. doi:10.3389/feart.2021.834958



OPEN ACCESS

EDITED BY
Shuren Wang,
Henan Polytechnic University, China

REVIEWED BY
Pengfei Shan,
Xi'an University of Science and
Technology, China
Jianwei Cheng,
China University of Mining and
Technology, China

*CORRESPONDENCE
Huaibin Li,
LHB_aust@126.com

SPECIALTY SECTION
This article was submitted to
Geohazards and Georisks,
a section of the journal
Frontiers in Earth Science

RECEIVED 21 August 2022
ACCEPTED 12 September 2022
PUBLISHED 28 September 2022

CITATION
Li H, Zhao X, Dai B, Huang Z and Zhu Q
(2022), Study on the evolution and
prediction of fracture depth of
surrounding rock in deep mining
roadway based on numerical analysis
and borehole detection.
Front. Earth Sci. 10:1024240.
doi: 10.3389/feart.2022.1024240

COPYRIGHT
© 2022 Li, Zhao, Dai, Huang and Zhu.
This is an open-access article
distributed under the terms of the
[Creative Commons Attribution License
\(CC BY\)](https://creativecommons.org/licenses/by/4.0/). The use, distribution or
reproduction in other forums is
permitted, provided the original
author(s) and the copyright owner(s) are
credited and that the original
publication in this journal is cited, in
accordance with accepted academic
practice. No use, distribution or
reproduction is permitted which does
not comply with these terms.

Study on the evolution and prediction of fracture depth of surrounding rock in deep mining roadway based on numerical analysis and borehole detection

Huaibin Li^{1,2*}, Xingdong Zhao³, Bibo Dai², Zujun Huang⁴ and Qiankun Zhu³

¹School of Safety Science and Engineering, Anhui University of Science and Technology, Huainan, China, ²State Key Laboratory of Safety and Health for Metal Mines, Maanshan, China, ³Laboratory for Safe Mining in Deep Metal Mine, Northeastern University, Shenyang, China, ⁴Zhuxianzhuang Coal Mine of Huaibei Mining (Group) Co., Ltd., Suzhou, China

The failure of surrounding rock in deep hard rock roadway is closely related to mining disturbance. In this study, the 13# stope ramp of –767 m level (at a buried depth of 1,197 m) at Hongtoushan copper mine was taken as the engineering background, a comprehensive analysis method of numerical analysis and borehole detection was put forward, and the evolution law of fracture depth of the ramp surrounding rock under the mining influence was obtained. The results show that the maximum tangential stress and fracture depth of the ramp surrounding rock on both sidewalls increase slowly at the initial mining stage. When the ore body above the ramp is mined, the maximum tangential stress and fracture depth of the ramp surrounding rock on both sidewalls increase rapidly, and the two parameters are positively correlated. Based on this, the ratio of the maximum tangential stress of the surrounding rock to the uniaxial compressive strength of intact rock ($\sigma_{\theta\max}/\sigma_c$) and the equivalent radius (a) of the roadway were used as parameters, and an equation for the fracture depth of the roadway surrounding rock was proposed. Through the case analysis, the results show that the proposed equation of fracture depth of the roadway surrounding rock has good prediction accuracy. This study enriches the research on the stability and failure mechanism of the roadway surrounding rock under the mining disturbance, and provides new basis for the support design of mining roadways.

KEYWORDS

ramp, mining influence, numerical analysis, borehole detection, fracture depth equation

Introduction

The overhand cut-and-fill mining method has been widely used in deep metal deposits, and the transportation roadway has generally been arranged at the footwall of the ore body. The deep stope and the roadway surrounding rock are often in a complex stress environment (i.e., high ground stress, high ground temperature, high osmotic pressure, and strong mining disturbance). When the mining stress is greater than the strength of the surrounding rock of the stope (roadway), the spalling, rockburst and other failures of the surrounding rock can be induced easily. As a result, the ore loss and dilution, equipment damage and personnel casualties can be caused, which seriously hinders the normal production of the mine (Read, 2004; Zhao et al., 2013; Abdellah et al., 2014; Zheng et al., 2015; Wei et al., 2022).

At present, research on the failure of the surrounding rock of stope (roadway) induced by deep mining has been widely conducted, and some progress in the mechanics and mining engineering has been obtained. Through borehole television monitoring and acoustic testing, Wang et al. (2015) studied the damage range of roadway surrounding rock, and concluded that the damage range of the roadway surrounding rock under the mining influence is larger than that without mining influence. Based on the numerical simulation method, Zhang and Mitri (2008) explored the key factors affecting the plastic zone of the surrounding rock in the footwall transport roadway. It was found that under the mining influence, the plastic zone of the surrounding rock of the footwall transport roadway increases with the increase of the buried depth of the roadway, and it also increases with the decrease of the distance between roadway and stope. Through the numerical simulation method, Jia et al. (2017) studied the mechanical mechanism and distribution characteristics of the plastic zone of roadway surrounding rock under the non-uniform stress field. The results showed that when the stress around the roadway is greater than the strength of the surrounding rock and the ratio of principal stress around the roadway is large, the shear failure occurs in the surrounding rock, and a butterfly-shaped plastic zone can be formed. Abdellah et al. (2011) evaluated the issue of haulage drift safety in mining activities using probabilistic methods. Aiming at the Linglong gold mine in China, Cai and Lai (2003) investigated the main influencing factors of the stability of the transport roadway by the coupled data mining techniques, and analyzed the acoustic emission signals and monitoring results. Liu et al. (2019) simulated coal seams with different dip angles through the FALC^{3D} software, and discussed the characteristics of floor failure under the mining influence. Waclawik et al. (2017) monitored the stress of the surrounding rock of the roadway under long-wall mining. It was concluded that the stress of surrounding rock changes with the advance of the working face.

The stress change of the surrounding rock in underground engineering is closely related to rock failure. Researchers have conducted many studies on the relationship between stress and

failure of surrounding rock in engineering. Based on the damage situation of the gold mine in South Africa, Ortlepp and Stacey (1994), Ortlepp (2000) divided the damage degree of the roadway by using the ratio of the maximum principal stress to the uniaxial compressive strength. Specifically, when the maximum principal stress is equal to $0.2\sigma_b$, the spalling failure occurs in the surrounding rock, when it exceeds $0.4\sigma_b$, rockburst occurs in the surrounding rock. By using maximum principal stress, minimum principal stress and peak strength σ_b , Wagner and Wiseman (1980) proposed a concept of stress concentration factor. It is concluded that when the stress concentration factor SF is equal to or greater than 0.8, the spalling failure occurs in the roadway surrounding rock. Hoek and Brown (1980) made a more detailed classification of the damage degree of the roadway by using the ratio of the maximum tangential stress of surrounding rock to the uniaxial compressive strength of rock ($\sigma_{\theta\max}/\sigma_c$). When $\sigma_{\theta\max}/\sigma_c$ is equal to 0.34, slight spalling failure occurs in the surrounding rock, when $\sigma_{\theta\max}/\sigma_c$ is equal to 0.42, severe spalling failure occurs in the surrounding rock. Dowding and Andersson (1986) analyzed five typical cases of spalling failure of surrounding rock in tunnels. It is believed that when the ratio of the maximum tangential stress of surrounding rock caused by tunnel excavation to the uniaxial compressive strength of rock ($\sigma_{\theta\max}/\sigma_c$) exceeds 0.35, the spalling failure of surrounding rock occurs, when $\sigma_{\theta\max}/\sigma_c$ exceeds 0.5, the weak or medium rockburst occurs in surrounding rock, when $\sigma_{\theta\max}/\sigma_c$ exceeds 1.0, the strong rock burst occurs in surrounding rock. Based on field-measured data, Martin (1993), Martini et al. (1997), and MartinChristiansson (2009) and Diederichs (2007) fitted empirical formulas with stress intensity ratio and roadway size as parameters, and calculated the fracture depth of the roadway surrounding rock. Perras and Diederichs (2016) predicted the excavation damage zones of the brittle surrounding rock of the underground tunnel by the empirical method and numerical simulation method. Cai and Kaiser (2014) employed numerical simulation and field comparison methods to study the spalling failure strength at the excavation boundary in the field. The results showed that the spalling strength of rock mass at the project site is not 0.4 ± 0.1 times of the uniaxial compressive strength of rock, but generally 0.8 ± 0.05 times of the uniaxial compressive strength of rock. The above research results provide a valuable reference for analyzing the stress, displacement and distribution characteristics of the failure zone of the roadway surrounding rocks under the mining influence. However, there are few studies on the evolution and prediction of the fracture depth of roadway surrounding rock under the influence of deep mining.

The 13# stope ramp of -767 m level (at a buried depth of 1,197 m) at Hongtoushan copper mine, a wide range of spalling failures under the mining influence occurred. Based on this engineering background, the failure mechanism of the ramp surrounding rock was analyzed, and the evolution process of the maximum tangential stress of the ramp surrounding rock during the overhand cut-and-fill mining was obtained by the FLAC^{3D} software. Besides, the fracture depth of the surrounding rock was measured by the borehole detection, the stress-fracture depth evolution process of

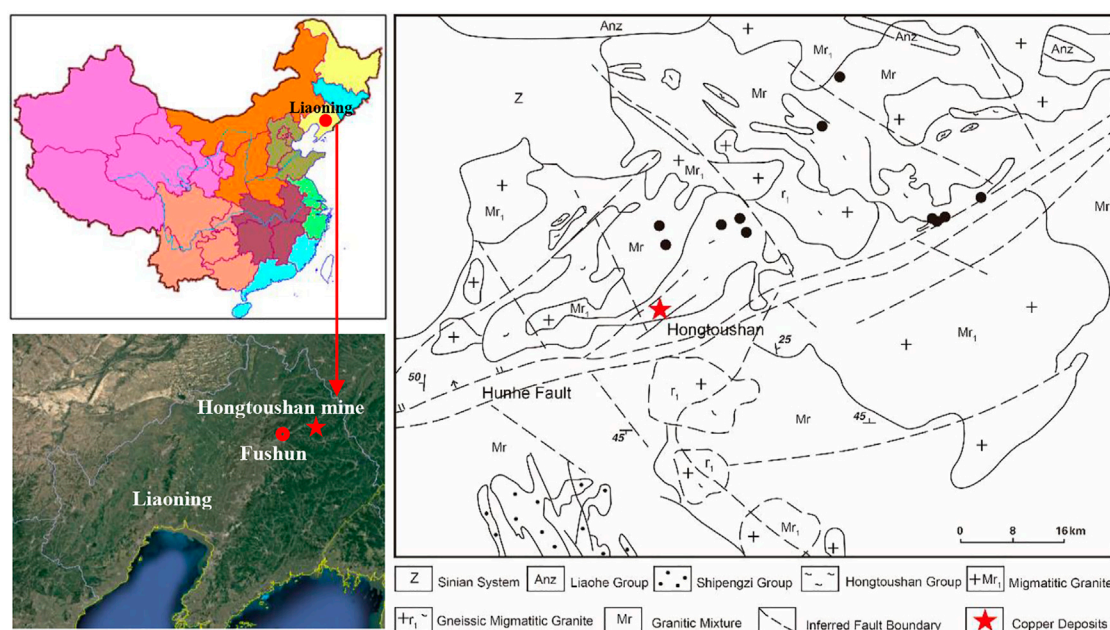


FIGURE 1
Location and regional geology of the Hongtoushan mine.

surrounding rock under the mining influence was comprehensively analyzed, and the equation of rock fracture depth of mining roadway was proposed by using the ratio of the maximum tangential stress of surrounding rock of the roadway to the uniaxial compressive strength of the intact rock ($\sigma_{\theta\max}/\sigma_c$) and the equivalent radius (a) of the roadway. This study provides a basis for supporting design and judgment of the fracture depth of roadway surrounding rock under the mining influence.

Site description

Engineering geology

Hongtoushan copper mine is located in the northeast of Liaoning Province, China (Figure 1). At present, it is one of the deepest non-ferrous metal mine in China, with an exploration depth of 1,657 m and a mining depth of 1,257 m. In this mine, the overhand cut-and-fill mining method was adopted. The 13# stope ramp of -767 m level (at a buried depth of 1,197 m) had a stage height of 60 m, a strike length of 50 m, and a stope span of 30 m, and the dip of the stope is 70°. Parallel blast hole rings were fired at a 3 m extracting height in the horizontal panel and using multiple ring sequences. The stope is backfilled with tailings and cement after every slice mined. Access to cut-and-fill stopes is through ramp located in footwall of each stope and inclined at the same dip as the ore body. The horizontal distance between the ramp and 13# stope is about 20 m. The

horse-shoe-shaped ramp is a cross-section of 3.0 m width and 2.8 m height. To obtain the distribution of the structural planes in the stope and surrounding rock, the on-site engineering geological survey of the hanging wall, footwall and ore body of the stope was carried out by using the scan line method. The rock samples were taken on-site and the rock mechanical experiments were carried out. The quality of the surrounding rock of the stope was classified by rock mass rating (RMR) and rock mass quality (Q) methods. The results showed that the quality of rock mass was generally good. The mechanical parameters of the ramp surrounding rock were estimated based on the Hoke-Brown strength criterion, as shown in Table 1.

The regression equations of the maximum horizontal principal stress, minimum horizontal principal stress and vertical stress are obtained by hollow inclusion stress relief method in the field as follows (Zhao et al., 2019).

$$\begin{cases} \sigma_{h,\max} = 0.0273H - 0.5071 \\ \sigma_{h,\min} = 0.0235H - 3.7780 \\ \sigma_v = 0.0316H - 5.6280 \end{cases} \quad (1)$$

where $\sigma_{h,\max}$, $\sigma_{h,\min}$, and σ_v (MPa) are the maximum horizontal principal stress, minimum horizontal principal stress, and vertical principal stress, and H is the depth (m). According to Eq. 1, the maximum horizontal principal stress $\sigma_{h,\max}$ at -767 m (at a buried depth of 1,197 m) reaches 32.2 MPa with a direction of NW, the minor horizontal principal stress $\sigma_{h,\min}$ is 24.4 MPa in the 167°/60° plane, and the vertical principal stress σ_v is 32.2 MPa.

TABLE 1 Mechanical parameters of rock samples and rock mass.

Site	Rock samples				Rock mass		
	Density/kg m ⁻³	Uniaxial compression strength/MPa	Tensile strength/MPa	Young's modulus/GPa	Uniaxial compression strength/MPa	Tensile strength/MPa	Young's modulus/GPa
Hanging wall	2,714	112.30	6.77	50.60	17.56	0.104	12.00
Ore body	4,224	105.50	7.23	55.20	24.80	0.142	15.69
Foot wall	2,724	132.80	7.49	51.00	36.13	0.402	28.40
Backfill	2,251	2.51	0.53	1.50	2.51	0.051	1.50



FIGURE 2
Spalling failure of the ramp surrounding rock in the 13# stope.

Failure mechanism of the ramp surrounding rock

The ramp of 13# stope was arranged in the hard rock mass of the footwall. Due to its large buried depth and close distance to the stope, this ramp was seriously affected by mining. Figure 2 shows the typical spalling failure of the 13# stope ramp under the mining influence. The ramp excavation breaks the balance of the initial stress field, the stress begins to redistribute, the tangential stress of the ramp surrounding rock increases, the radial stress decreases. As a result, the ramp is in a bidirectional stress state. Under the mining influence, the ramp surrounding rock undergoes several stress adjustments. When the maximum tangential stress in surrounding rock exceeds the strength of the rock mass, the stress-induced brittle failure of surrounding rock can be caused. As it is difficult to obtain the strength of rock mass on-site, Hoek and Brown (1980), Dowding and Andersson (1986), Martin et al. (1999), Cai and Kaiser (2014), and Wang et al. (2012) took the ratio of the maximum tangential stress $\sigma_{\theta\max}$ to the uniaxial compressive strength σ_c of intact rock as

the basis of brittle failure of hard rock. It can be seen that the brittle failure of hard rock can be described by $\sigma_{\theta\max}/\sigma_c$. Based on the empirical relationship between $\sigma_{\theta\max}/\sigma_c$ and fracture depth, the maximum tangential stress of the surrounding rock under the mining influence can be obtained by numerical calculation, and the fracture depth of the surrounding rock of the mining roadway can be quickly calculated with the empirical formula. This equation can provide a reference for the support design.

Analysis method for fracture evolution process of the ramp surrounding rock under the mining influence

Numerical analysis

According to the engineering geological conditions of the 13# stope ramp of -767 m level (at a buried depth of 1,197 m),

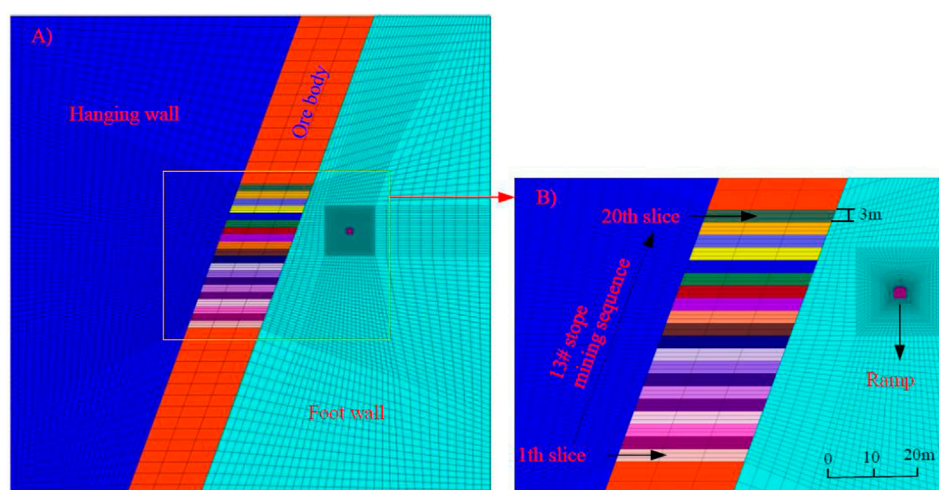


FIGURE 3
Numerical model of the 13# stope and ramp.

a numerical simulation model was established. It was assumed that the calculation model was a plane strain model, and the rock mass was homogeneous and isotropic. The size of the model was 200 m × 200 m (width × high), and the model was divided into 87,520 units, as shown in Figure 3. To ensure the calculation accuracy, the grid at the ramp position was encrypted. The dip angle of the ore body was 70° and the thickness was 30 m. The mixed boundary conditions were adopted in the model. The vertical and horizontal displacements were restricted on both sidewalls and the bottom of the model. Stress constraints were applied on both sidewalls and the top of the model, and the linear-elastic model was used for simulation.

The FLAC^{3D} software was used to analyze the evolution process of the tangential stress of the ramp surrounding rock of the stope under the mining influence. During the model calculation, the ramp was excavated first, and then the 13# stope was mined from the bottom to the top layers by layers. There were 20 layers in total, and each layer was 3 m high. After the stress balance was reached after the mining of the previous layer, the backfilling of the next layer was conducted.

Borehole detection

Borehole detection technology is an intuitive detection method, which can quickly and accurately identify the development of cracks in surrounding rock. At present, the borehole detection method has been rarely used to observe the failure evolution process of the roadway surrounding rock under the deep mining influence in the existing studies. It is

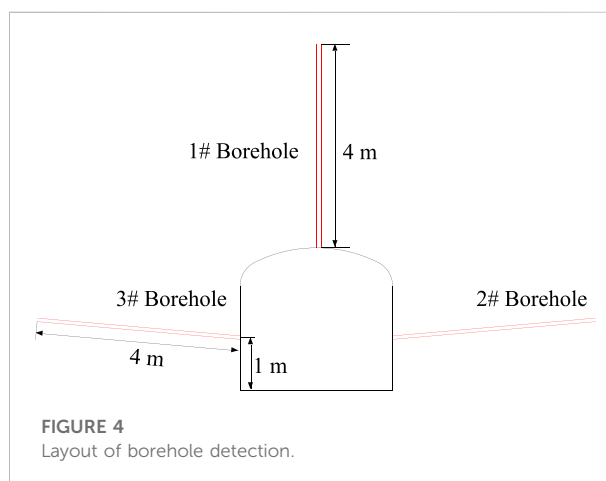


FIGURE 4
Layout of borehole detection.

necessary to use the borehole detection method to further reveal the mining-induced failure evolution of roadway surrounding rock.

The ZKXG100-type borehole camera detection device was used on site to detect the fracture depth of the ramp surrounding rock in the 13# stope. Three detection boreholes with a depth of 4 m and a diameter of 40 mm were drilled on the both sidewalls and roof of the ramp. The both sidewalls of the detection boreholes were 1 m high from the floor, with an upward horizontal inclination of 5°. The roof detection boreholes were set perpendicular to the roof. Figure 4 shows the specific layout of the borehole detection. The field observation is from the first layer mining until the end of the 13# stope mining. When mining the ore body below the 14th layer in the 13# stope, the cracks in

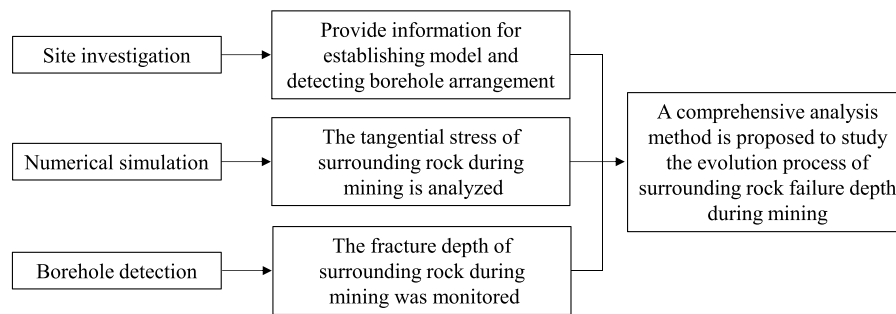


FIGURE 5

Comprehensive analysis method for the fracture depth evolution of the ramp surrounding rock under the mining influence.

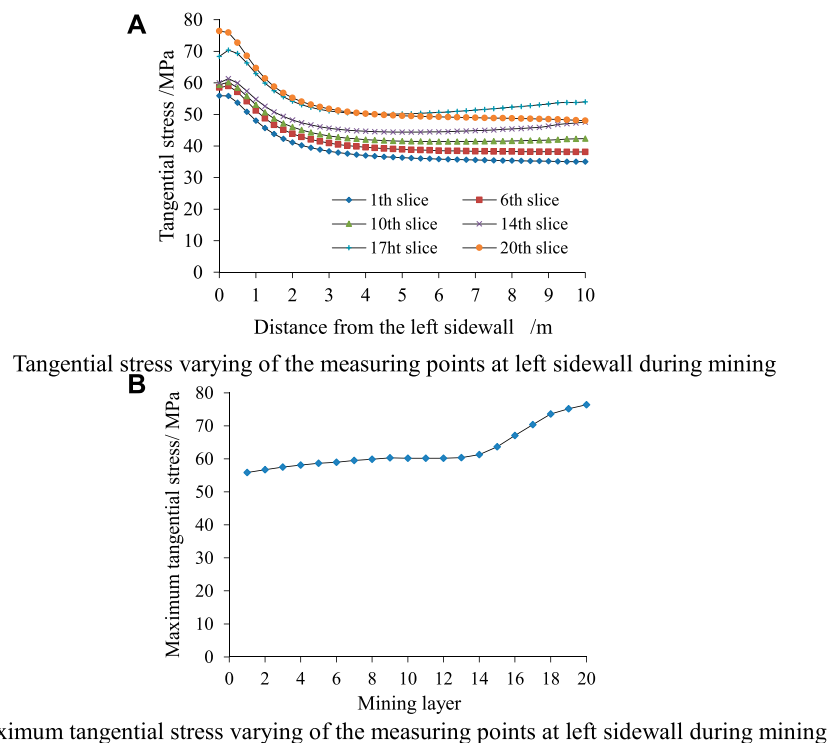


FIGURE 6

Tangential stress varying at left sidewall during mining.

the ramp surrounding rock were not significantly developed and damaged. Therefore, Figure 9 only shows the detection results when mining the ore body above the 14th layer in the 13# stope.

Comprehensive analysis method

To analyze the failure evolution process of surrounding rock of the 13# stope ramp under the mining influence, a comprehensive analysis method combining field investigation,

numerical analysis and borehole detection was proposed (see Figure 5). In the field investigation, the failure characteristics and occurrence mechanism of the ramp surrounding rock were mainly analyzed to provide detailed data for the establishment of the numerical calculation model and the location of the borehole detection. The numerical analysis was used to study the evolution law of the tangential stress of the ramp surrounding rock under the mining influence. Borehole detection recorded the fracture depth of the ramp surrounding rock when different layers were mined.

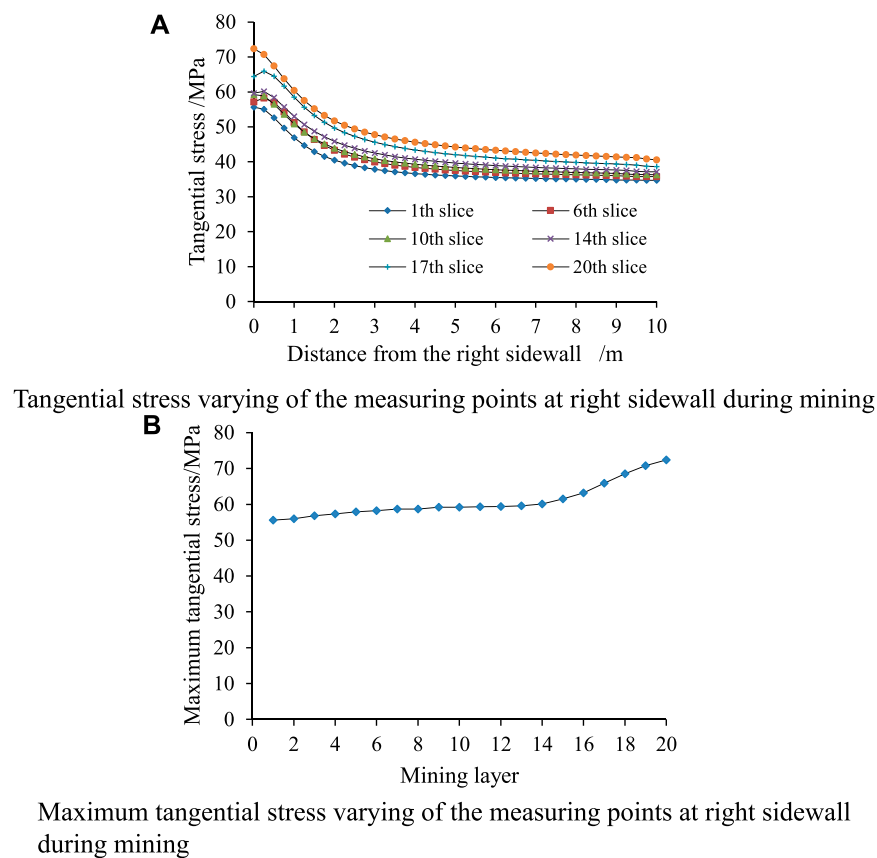
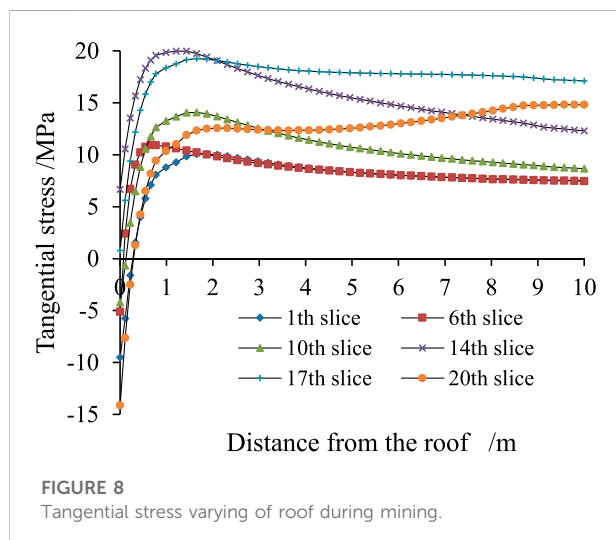


FIGURE 7

Tangential stress varying at right sidewall during mining.



Analysis of stress-fracture evolution of the ramp surrounding rock under the mining influence

Analysis of tangential stress evolution of surrounding rock

To analyze the evolution process of tangential stress of the surrounding rock under mining, measuring points were arranged every 0.2 m along the radial direction 10 m at the left, right and roof of the ramp, and the change of tangential stress at this point was monitored, as shown in Figures 6–8. For simplicity, the compressive stress was set as a positive value and the tensile stress as a negative value.

As shown in Figure 6A, with the increase of radial depth, the tangential stress value of the left sidewall first increases slightly, and then begins to decrease. When the depth is about twice the

TABLE 2 Comparative analysis of the maximum tangential stress and fracture depth of the ramp surrounding rock.

Position\Layered		2	4	6	8	10	12	14	16	18	20
Left sidewall	Maximum tangential stress/MPa	56.7	58.1	59.0	59.9	60.2	60.2	61.3	67.1	73.6	76.4
	Fracture depth/m	0.18	0.20	0.23	0.36	0.42	0.51	0.73	0.91	1.17	1.17
Right sidewall	Maximum tangential stress/MPa	56.0	57.3	58.2	58.7	59.2	59.4	60.1	63.2	68.5	72.4
	Fracture depth/m	0.12	0.15	0.18	0.21	0.24	0.32	0.40	0.53	0.81	0.81

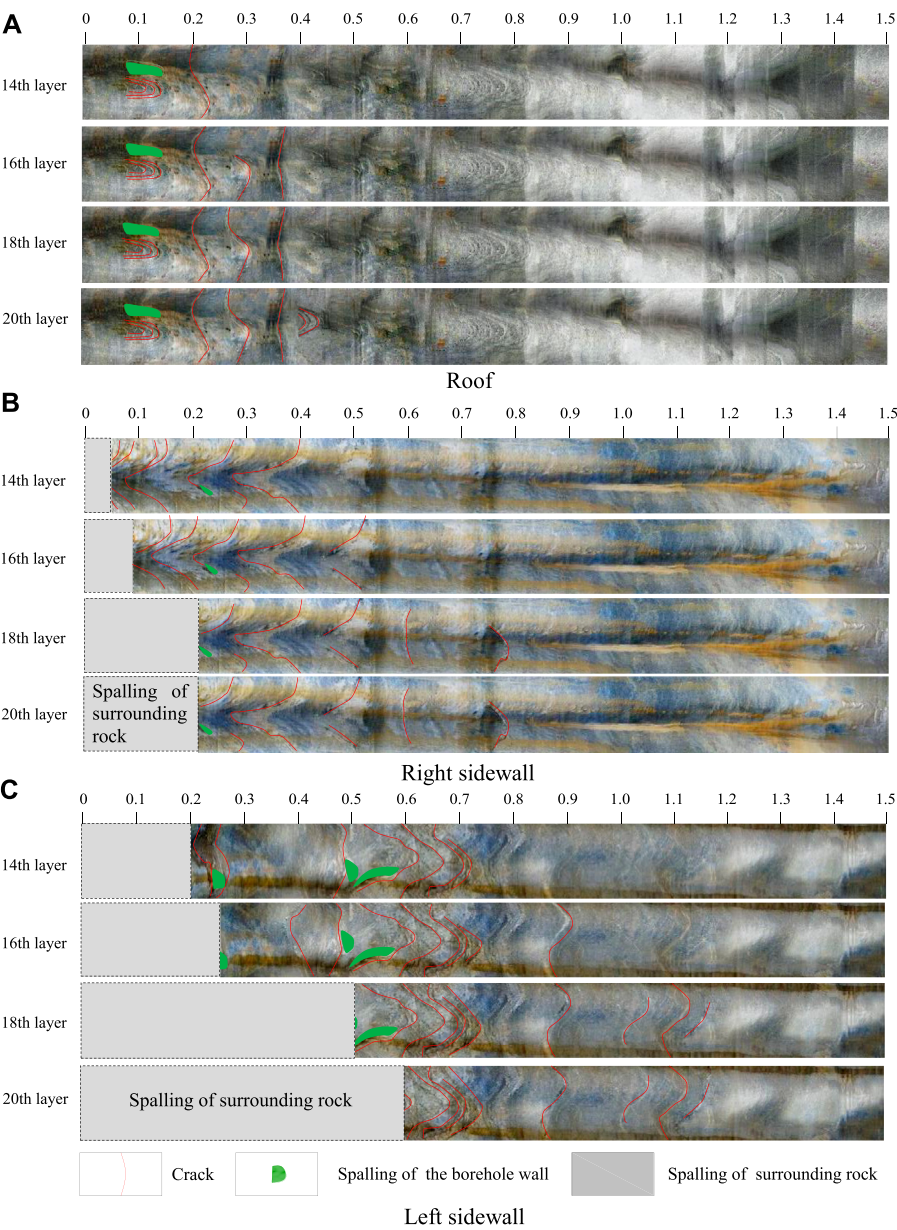
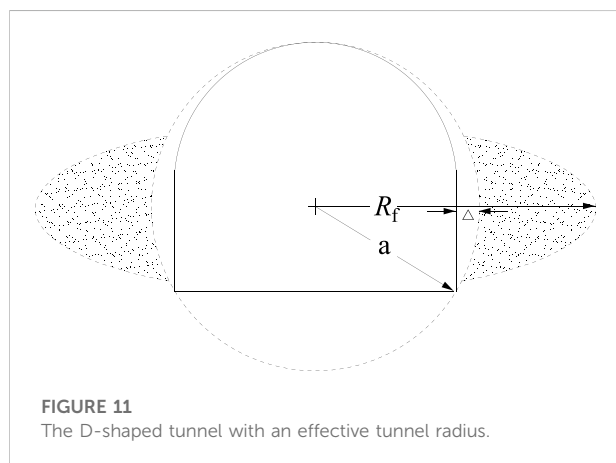
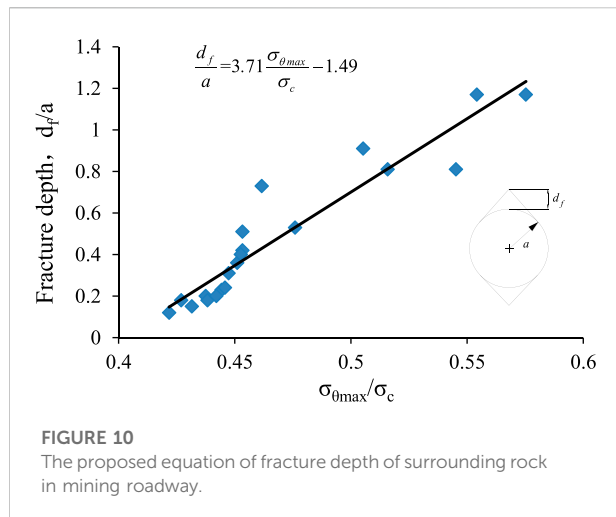


FIGURE 9 Failure of surrounding rock in the 13# stope ramp at different mining layers.



roadway span from the left sidewall, the tangential stress value of this point tends to be stable. As can be seen from Figure 6B, when mining the ore body at the lower part of the ramp, the maximum tangential stress at the left sidewall increases slowly. When mining exceeds the level of the ramp (i.e., the ore body above the 14th layer), the maximum tangential stress increases rapidly,

and then tends to be stable. The maximum tangential stress is 76.4 MPa.

As shown in Figure 7, the tangential stress of the right sidewall has the same evolution law as that of the left sidewall. The difference is that the tangential stress of the right sidewall is slightly smaller than that of the left sidewall during the mining of the same layer. After mining the 20th layer, the maximum tangential stress peak value of the right sidewall is 72.4 MPa.

As shown in Figure 8, the tangential stress value is negative near the roof, and the roof is in the tensile stress zone. With the increase of radial depth, the tangential stress value of the roof changes from negative to positive, and then begins to decrease. When the depth is about twice the roadway span from the roof, the tangential stress value at this point tends to be stable. At the initial stage of mining, there is a tension zone on the ramp roof. When mining to the level near the ramp, the tension zone disappears. With the development of mining, the roof tension zone appears again. The maximum tangential stress value of the ramp surrounding rock during the whole mining process is listed in Table 2.

Analysis of evolution process of fracture depth of the ramp surrounding rock

The damage degree of surrounding rock is mainly judged by observing the development of cracks. The development range of cracks can be regarded as the fracture depth of the surrounding rock. The spalling fracture depth of surrounding rock generally refers to the depth of continuous failure or serious failure of rock mass (Wagner and Wiseman, 1980). Through the borehole detection of the ramp surrounding rock, the failure of surrounding rock in different periods of mining was obtained, as shown in Figure 9. The red line in the figure indicates the crack, the green area indicates the spalling of the borehole wall, and the gray area indicates the spalling of surrounding rock.

When mining the 14th layer, the mining layers are at the same level as the ramp. There are a few cracks on the inner wall of the 1# borehole (in the roof) from the orifice to the position of 0.24 m, and the cracks above the position of 0.24 m are not obvious. A large number of cracks are developed on the inner

TABLE 3 Comparative analysis of different methods for fracture depth of surrounding rock in engineering.

Cases\Methods	Numerical simulation/m	The proposed prediction equation	
		Depth d_f/m	Relative error/%
Underground transportation roadway of a mine in Canada Zhang and Mitri (2008)	3.50	3.22	8.0
Haulage roadway of Mufulira mine Kabwe and Bowa (2016)	0.83	1.01	21.7
Haulage roadway of Garson mine Abdellah et al. (2011)	3.81	3.42	10.2
Ore drawing roadway of Dongguashan copper mine Shu (2021)	2.50	2.21	11.6
Mean relative error/MRE			12.9

wall of the 2# borehole (in the right sidewall) from the orifice to the position of 0.4 m. The spalling with a thickness of 0.05 m in the orifice can be observed, and a small range of spalling appears on the borehole wall at the position of 0.22 m. The cracks above the position of 0.4 m are not developed. A large number of cracks are developed on the inner wall of the 3# borehole (in the left sidewall) from the orifice to the position of 0.73 m. The spalling with a thickness of 0.2 m in the orifice can be observed, and a small range of spalling appears on the borehole wall at 0.25, 0.5, and 0.55 m, respectively. The cracks above the position of 0.73 m are not obvious.

When the 16th layer is mined, the mining layers exceed the level of the ramp. New cracks appear in both sidewalls of the ramp and the roof borehole. Besides, the maximum depth of crack development in the 1# borehole (in the roof) is increased to 0.39 m, and the length of some original cracks is increased slightly. The maximum depth of the failure development in the 2# borehole (in the right sidewall) is increased to 0.53 m, and the depth of spalling failure is increased to 0.09 m. In the 3# borehole (on the left sidewall), the maximum depth of crack development in the 3# borehole is increased to 0.91 m, and the depth of spalling failure is increased to 0.26 m.

When the 18th layer is mined, no new cracks are found in the 1# borehole (in the roof), and only the length of some original cracks is slightly increased. Compared with the previous detection results, new cracks are generated in 2# and 3# boreholes (in the right and left sidewalls), and the crack development depth increases slowly, with the maximum depth of 0.81 and 1.17 m. The new spalling failure occurs in 2# and 3# boreholes (in right and left sidewalls), and the spalling fracture depth is 0.21 and 0.5 m, respectively.

When the 20th layer is mined, new cracks are produced again in the 1# borehole (in the roof), and the maximum depth of crack development increases to 0.44 m. There is no new crack in 2# borehole (in the right sidewall). No new cracks are found in the 3# borehole (in the left sidewall), but the spalling fracture depth is increased to 0.6 m. The fracture depth of the ramp surrounding rock during the whole mining process is summarized in Table 2.

Prediction of fracture depth of the roadway surrounding rock under the mining influence

Through the comprehensive analysis method of numerical analysis and borehole detection, the evolution process of the fracture depth of the surrounding rock under the mining influence is analyzed. As shown in Table 2, the fracture depth of the surrounding rock in the stope increases gradually with the increase of the maximum tangential stress of the surrounding rock, and the mining has a greater influence on the fracture depth of the left sidewall than the right sidewall. Combined with the failure mechanism of the ramp surrounding rock, it can be found

that the brittle failure of hard rock can be described by $\sigma_{\theta\max}/\sigma_c$. The linear fitting of the data (the maximum tangential stress and fracture depth in Table 2) is performed, then the equation of the fracture depth of the surrounding rock of the mining roadway can be obtained (see Figure 10) based on the equivalent radius (a) of the roadway and the ratio of the maximum tangential stress of surrounding rock to the uniaxial compressive strength of intact rock ($\sigma_{\theta\max}/\sigma_c$). When the analyzed roadway section is D-shaped, the effective radius of the roadway should be estimated (Figure 11). The estimated fracture depth of the roadway surrounding rock does not include the distance between the two sidewalls and the boundary of the equivalent circle (Δ). To verify the accuracy of the proposed equation, four engineering cases affected by mining are analyzed (Table 3), and their relative errors are calculated. Then the total error of all cases is predicted and averaged, and the average relative error is 12.9%. The calculation results of the proposed equation for the fracture depth of surrounding rock in mining roadways are in good agreement with the numerical analysis. It indicates that the proposed equation has great practicability and accuracy in predicting the fracture depth of surrounding rock in mining roadway, which can provide a basis for the support design of the engineering site.

Conclusion

Through the comprehensive analysis method of numerical analysis and borehole detection, the evolution process of surrounding rock fracture depth of deep mining ramp in Hongtoushan copper mine was studied. The following conclusions are obtained:

- (1) Numerical simulation is used to analyze the evolution characteristics of the maximum tangential stress of the surrounding rock under the mining influence, and the borehole detection analysis is carried out for the fracture depth of the surrounding rock under the mining influence. The results show that when mining the ore body at the lower part of the ramp, the maximum tangential stress and fracture depth of the two sidewalls of the ramp increase slowly. When mining exceeds the level of the ramp, the maximum tangential stress and fracture depth of the two sidewalls increases rapidly and reach the maximum value at the end of mining, and there is a positive correlation between the two values. In addition, the rock fracture depth of the left sidewall of the ramp is significantly greater than that of the right sidewall under the mining influence. Compared with the mining of the ore body below the ramp, the same level of mining has a greater impact on the fracture of surrounding rock.
- (2) The ratio of the maximum tangential stress of surrounding rock to the uniaxial compressive strength of intact rock

($\sigma_{0\max}/\sigma_c$) and the equivalent radius (a) of the roadway are taken as parameters, and the equation of fracture depth of surrounding rock of the mining roadway is proposed. Through the engineering cases analysis, the proposed equation has good practicability and accuracy.

- (3) This study provides a basis for the stability analysis and support design of surrounding rock under the mining influence.

Data availability statement

The original contributions presented in the study are included in the article/supplementary material, further inquiries can be directed to the corresponding author.

Author contributions

HL conceived and designed the research. QZ performed the field investigations and experiments, presented the numerical simulation. HL and XZ wrote the original manuscript. BD and ZH participated in the data analysis and manuscript modification.

Funding

Key project of Natural Science research in Universities of Anhui Province (KJ 2021A0455), the State Key Laboratory of Safety and Health for Metal Mines (2021-JSKSSYS-02), Research

Start-up Fund for introduction of talents of Anhui University of Science and Technology, NSFC-Shandong Joint fund (Grant No. U1806208) and Research Funds for the Central Universities (N2001033).

Acknowledgments

Great appreciation goes to the editorial board and the reviewers of this paper.

Conflict of interest

Author ZH was employed by the company Zhuxianzhuang Coal Mine of Huaibei Mining (Group) Co., Ltd.

The remaining authors declare that the research was conducted in the absence of any commercial or financial relationships that could be construed as a potential conflict of interest.

Publisher's note

All claims expressed in this article are solely those of the authors and do not necessarily represent those of their affiliated organizations, or those of the publisher, the editors and the reviewers. Any product that may be evaluated in this article, or claim that may be made by its manufacturer, is not guaranteed or endorsed by the publisher.

References

- Abdellah, W., Mitri, H. S., and Thibodeau, D. (2011). Assessment of mine haulage drift safety using probabilistic methods of analysis[J]. *Procedia Eng.* 26, 2099–2111. doi:10.1016/j.proeng.2011.11.2412
- Abdellah, W., Raju, G. D., Mitri, H. S., and Thibodeau, D. (2014). Stability of underground mine development intersections during the life of a mine plan[J]. *Int. J. Rock Mech. Min. Sci.* 72, 173–181. doi:10.1016/j.ijrmms.2014.09.002
- Cai, M., and Kaiser, P. K. (2014). In-situ rock spalling strength near excavation boundaries[J]. *Rock Mech. rock Eng.* 47 (2), 659–675. doi:10.1007/s00603-013-0437-0
- Cai, M., and Lai, X. (2003). Monitoring and analysis of nonlinear dynamic damage of transport roadway supported by composite hard rock materials in linglong gold mine[J]. *Int. J. Minerals, Metallurgy Mater.* 10 (2), 10–15. doi:10.1109/5.771073
- Diederichs, M. S. (2007). The 2003 Canadian geotechnical colloquium: Mechanistic interpretation and practical application of damage and spalling prediction criteria for deep tunnelling[J]. *Can. Geotechnical J.* 44 (9), 1082–1116. doi:10.1139/t07-033
- Dowding, C. H., and Andersson, C. A. (1986). Potential for rock bursting and slabbing in deep caverns[J]. *Eng. Geol.* 22 (3), 265–279. doi:10.1016/0013-7952(86)90028-1
- Hoek, E., and Brown, E. T. (1980). *Underground excavation in rock*[M]. London: Instn Min. Metall, 1–76.
- Jia, H. S., Li, G. S., and Wand, L. Y. (2017). Characteristics of stress-field environment and roof falling mechanism of mining influenced roadway[J]. *J. Min. Saf. Eng.* 34 (04), 707–714. doi:10.13545/j.cnki.jmse.2017.04.015
- Kabwe, E., and Bowa, V. M. (2016). Determination of the appropriate geometry of footwall drifts using numerical analysis technique[J]. *Geotechnical Geol. Eng.* 34 (6), 1955–1969. doi:10.1007/s10706-016-0076-9
- Liu, W., Du, Y., and Liu, Y. (2019). Failure characteristics of floor mining-induced damage under deep different dip angles of coal seam[J]. *Geotechnical Geol. Eng.* 37 (2), 985–994. doi:10.1007/s10706-018-0666-9
- Martin, C. D., Kaiser, P. K., and McCreath, D. R. (1999). Hoek-Brown parameters for predicting the depth of brittle failure around tunnels[J]. *Can. Geotechnical J.* 36 (1), 136–151. doi:10.1139/t98-072
- Martin, C. D. (1993). The strength of massive Lac du Bonnet granite around underground openings. AvailableAt: <http://hdl.handle.net/1993/9785>.
- MartinChristiansson, C. D. R. (2009). Estimating the potential for spalling around a deep nuclear waste repository in crystalline rock[J]. *Int. J. Rock Mech. Min. Sci.* 46 (2), 219–228. doi:10.1016/j.ijrmms.2008.03.001
- Martini, C. D., Read, R. S., and Martino, J. B. (1997). Observations of brittle failure around a circular test tunnel[J]. *Int. J. Rock Mech. Min. Sci.* 34 (7), 1065–1073. doi:10.1016/s1365-1609(97)90200-8
- Ortlepp, W. D., and Stacey, T. R. (1994). Rockburst mechanisms in tunnels and shafts[J]. *Tunn. Undergr. Space Technol.* 9 (1), 59–65. doi:10.1016/0886-7798(94)90010-8
- Ortlepp, W. D. (2000). Observation of mining-induced faults in an intact rock mass at depth[J]. *Int. J. Rock Mech. Min. Sci.* 37 (1), 423–436. doi:10.1016/s1365-1609(99)00117-3
- Perras, M. A., and Diederichs, M. S. (2016). Predicting excavation damage zone depths in brittle rocks[J]. *J. Rock Mech. Geotechnical Eng.* 8 (1), 60–74. doi:10.1016/j.jrmge.2015.11.004
- Read, R. S. (2004). 20 years of excavation response studies at AECL's Underground Research Laboratory[J]. *Int. J. Rock Mech. Min. Sci.* 41 (8), 1251–1275. doi:10.1016/j.ijrmms.2004.09.012

- Shu, J. B. (2021). Stability analysis and control techniques research on the surrounding rock of the ore-drawing roadway in dongguanshan copper mine. *Minerals* 11, 881. doi:10.3390/min11080881
- Waclawik, P., Kukutsch, R., and Konicek, P. (2017). Stress state monitoring in the surroundings of the roadway ahead of longwall mining [J]. *Procedia Eng.* 191, 560–567. doi:10.1016/j.proeng.2017.05.218
- Wagner, H., and Wiseman, N. (1980). The significance of rock fracturing in the design and support of mine excavations[J]. *Eng. Appl. Fract. Analysis* 1980, 399–407. doi:10.1016/b978-0-08-025437-1.50033-4
- Wang, C. H., Song, C. K., and Liu, L. P. (2012). Study of stress characteristics of brittle failures of rock around underground openings[J]. *Rock Soil Mech.* 33 (S1), 1–7. doi:10.16285/j.rsm.2012.s1.001
- Wang, H. W., Jiang, Y. D., and Xue, S. (2015). Assessment of excavation damaged zone around roadways under dynamic pressure induced by an active mining process. *Int. J. Rock Mech. Min. Sci.* 77, 265–277. doi:10.1016/j.ijrmms.2015.03.032
- Wei, W., Mitri, H., and Thibodeau, D. (2022). Stability of haulage drift in the dynamic mine environment. *Int. J. Rock Mech. Min. Sci.* 45, 973–986. doi:10.1016/j.ijrmms.2007.07.020
- Zhang, Y., and Mitri, H. S. (2008). Elastoplastic stability analysis of mine haulage drift in the vicinity of mined stopes [J]. *Int. J. Rock Mech. Min. Sci.* 45 (4), 574–593. doi:10.1016/j.ijrmms.2007.07.020
- Zhao, H., Ma, F., and Zhang, Y. (2013). Monitoring and mechanisms of ground deformation and ground fissures induced by cut-and-fill mining in the Jinchuan Mine 2, China[J]. *Environ. Earth Sci.* 68 (7), 1903–1911. doi:10.1007/s12665-012-1877-7
- Zhao, X., Li, H., and Zhang, S. (2019). Stability analyses and cable bolt support design for A deep large-span stope at the hongtoushan mine, China[J]. *Sustainability* 11 (21), 6134. doi:10.3390/su11216134
- Zheng, J. B., Wang, Q. Z., and Yang, S. (2015). Surround rock deformation and stability control technology of roadway influenced by repeating mining[J]. *Coal Min. Technol.* 3, 76–80. doi:10.13532/j.cnki.cn11-3677/td.2015.03.023

Frontiers in Earth Science

Investigates the processes operating within the major spheres of our planet

Advances our understanding across the earth sciences, providing a theoretical background for better use of our planet's resources and equipping us to face major environmental challenges.

Discover the latest Research Topics

[See more →](#)

Frontiers

Avenue du Tribunal-Fédéral 34
1005 Lausanne, Switzerland
frontiersin.org

Contact us

+41 (0)21 510 17 00
frontiersin.org/about/contact

